Transient Liquid Assisted Growth of YBCO Superconducting Films: Growth Kinetics, Physical Properties and Vortex Pinning

Juri Banchewski

Transient Liquid Assisted Growth of YBCO Superconducting Films: Growth Kinetics, Physical Properties and Vortex Pinning

A dissertation submitted for the degree of

DOCTOR OF PHILOSOPHY IN PHYSICS

by

Juri Banchewski

Supervisor:
Prof. Teresa Puig Molina

Superconducting Materials and Large Scale Nanostructures
Institut de Ciència de Materials de Barcelona (ICMAB-CSIC)

Tutor: Prof. Carles Navau Ros
Doctorat en Física
Departament de Física - Facultat de Ciències
Universitat Autònoma de Barcelona

Noviembre 2020

Memòria que porta per títol **"Transient Liquid Assisted Growth of YBCO Superconducting Films: Growth Kinetics, Physical Properties and Vortex Pinning"** i presentada per aspirar al Grau de Doctor en Física per **Juri Banchewski**

Autor:
Juri Banchewski, M. Sc.

amb el vist i plau de: **Prof. Teresa Puig Molina**, Professora d'investigació del Institut de Ciències de Materials de Barcelona (ICMAB-CSIC) i **Prof. Carles Navau Ros**, Agregat del Departament de Física de la Universitat Autònoma de Barcelona (UAB).
I per a que així consti, signen el present certificat.

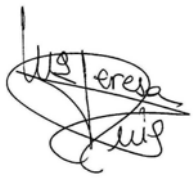

Directora:
Prof. Teresa Puig Molina

Tutor:
Prof. Carles Navau Ros

Bellaterra, 10 de noviembre de 2020

Acknowledgements

These past few years of PhD - rollercoaster wouldn't have been so exciting without a challenging research project, numerous connections to great minds, and sincere friendships. Not even a pandemic could change that after all!

I want to thank, first and foremost, Prof. Teresa Puig, my supervisor and head of the SUMAN group, not only for making this essential part of my personal development possible but especially for the consistent supervision and support. You always had an open mind for new ideas and the willingness to do brainstorming, regardless the long hours. This is rare and highly appreciated!

My deep gratitude goes to Prof. Teresa Puig, Prof. Xavier Obradors, Dr. Susagna Ricart, Prof. Xavier Granados, Prof. Jordi Farjas and Dr. Pere Roura for all the fruitful discussions regarding the doctorate and valuable feedback you gave me to enrich its content. Pere, arguing with you about transient liquids felt like the longest chess game I have ever played. Contrary to chess, we both won! Thank you for that! Also many thanks to Prof. Teresa Puig for giving us private classes on the concepts of superconductivity. Having been a newcomer to the field, it shaped my understanding!

Special thanks go to Dr. Silvia Rasi, Dr. Laia Soler and Dr. Júlia Jareño with whom I did the PhD thesis in parallel and who supplied most of the samples analyzed in this work. Much of the understanding developed throughout these years is a result of the great teamwork, persistence and endurance each of you brought along. It clearly shows that the whole can be greater than the sum of its parts!

I want to acknowledge my colleagues and friends who worked closely with me on the ERC project and with whom I developed my comprehension for the subject: Dr. Silvia Rasi, Dr. Laia Soler, Dr. Júlia Jareño, Lavinia Saltarelli, Diana García, Dr. Albert Queraltó and Adrià Pachecho for various contributions, from the experimental realization of synchrotron experiments to advice in all chemistry related issues; Dr. Roger Guzman, Dr. Bernat Mundet and Dr. Kapil Gupta for the electron microscopy measurements and data treatment. Separate thanks to Kapil for taking that one TEM image to rule my thesis cover!

I am grateful for the help and support by the technical services of ICMAB and particularly to the XRD team with Dr. Anna Crespi, Xavier Campos, and Joan Esquius for all the consultation on how to improve measurements, implement new geometries and the many laughters we had; Dr. Bernat Bozzo from the low temperature service for sharing his know-how on electrical transport measurements, electro-magnetic characterization and corresponding equipment; The Nanoquim team with Luigi Morrone, Neus Romà and Marta Riba for the introduction to the numerous sample preparation techniques available in the clean-room platform; Joshua Bailo and Mariona De Palau for assistance in chemical processes and the countless briefings regarding thermal treatments and experimental preparations for synchrotron experiments.

A special thanks goes to Dr. Cristian Mocuta for three successful years of collaboration, and ongoing, with the DiffAbs beamline, Soleil Synchrotron. Your enthusiasm for science and readiness to get things done, no matter how unconventional or complex, allowed us to explore uncharted grounds. Not to mention all the wake-up calls you took to keep experiments running during night shifts!

I want to acknowledge many more people at ICMAB for sharing their know-how on experimental procedures, theory, data treatment and literature research: Dr. Alexander Stangl, Dr. Juan Carlos Gonzáles, Dr. Bohores Villarejo, Dr. Cornelia Pop, Dr. Ziliang Li, Dr. Joffre Gutierrez, Dr. Jaume Gazquez, Dr. Mariona Coll, Dr. Max Sieger, Dr. Anna Palau, Dr. Narcís Mestres, Dr. Natalia Chamorro, Alejandro Fernández, Jordi Alcalà, Hailin Wang, Pengmei Yu, Yunwei Sheng, Mathieu Mirjolet, Artur Romanov, Pedro Barusco and Pamela Machado. Thanks also to that one student who introduced me to low temperature electrical transport measurements and various experimental techniques from photolithography to sputter deposition of contacts and oxygenation. Also for explaining me the theoretical concept of and difference between $J_{\mathrm{c,iso}}^{\mathrm{weak}}$ and $J_{\mathrm{c,iso}}^{\mathrm{strong}}$!

My deep gratitude goes to all members from the organising committee of the JPhD2019 conference: Artur Romanov, Jan Grzelak, Noemí Contreras, María Tenorio, Miguel Ángel Moreno, Iván Fernández, Martí Gibert, Cristiano Matricardi, Alberto del Moral, Borja Ortín, Soledad Roig, Leticia De Melo, Guillem Vargas and chair Cristina Navarro. It was an honor and pleasure to work with all of you!

Separate thanks to Anna May Masnou for all the input and help in outreach activities!

Not to forget all the people involved in the administration: Sonia Roldán, Pietat Sierra and Marta Vendrell for helping me in bureaucratic matters of any kind. Dr. Mar Tristany, your help and support went far beyond paperwork. You are a cornerstone of the SUMAN group preventing things from collapsing on a daily basis!

The presented work was conducted at the Institut de Ciència de Materials de Barcelona (ICMAB-CSIC). I want to acknowledge the financial support we received throughout the years: The ERC Advanced Grant ULTRASUPERTAPE (EU ERC-AdG-2014-669504); EU COST ACTION Nanohybri (CA16218), MINECO (MAT2014-51778-C2 and FEDER), Generalitat de Catalunya (2017 SGR1519), Programa excelencia Severo Ochoa SEV2015-0496 and Ministerio español de Educación; SOLEIL Synchrotron for granting us beamtime four years in a row to perform in-situ growth studies.

Now, some words to my friends and family who gave me all the support and love needed to withstand this journey.

Artur and Mathieu, my buddies, flatmates, shrinks. I like to think that the unforgettable times we had together are not the last ones, no matter where the next wave brings us!

To Laia, Julia, Alex, Ana, Vish, Ferran and Juanca. Thank you so much for all the trips, vermuts and laughs we had. I couldn't have asked for a warmer welcome to Barcelona. Juanca, you gave me the keys to your flat and to the beautiful, noisy neighbourhood of Gràcia. It keeps me awake at night; I mean... literally!!

To all my friends and colleagues in Barcelona: Bohores, Pengmei, Yunwei, Huan, Mathieu, Alejandro, Jordi, Lavinia, Artur. Thank you for all the funny moments, discussions and memories we shared in the office. Lavinia, thanks for all the (way too sweet) morning coffees and strategic planning on how to advance TLAG to infinity and beyond! Alejandro, for receiving me like family in Galicia (please also thank your cousin for his guidance to Oleiros). Silvia, it was a pleasure to work with you and have a drink once in a while at Plaça del Sol! Pamela, Nico, Tato thank you for all the good time we had together.

My dear friends in Germany: Moheb, Max, Kevin, Jan. Although I was not around much recently, you had nothing else but understanding for it. I can't wait to reunite and revive the good old times!

To my beloved family: My grannies, who kept my belly full and heart warm whenever I came around. Daniel for being the most patient and sincere brother I could wish for. My aunt and parents for their unconditional love, support and trust. I wouldn't have made it this far without you guys.

Abstract

High temperature superconductors (HTS) have been driving research and development programs for about three decades now and are on the verge of entering large scale utilization in the form of Coated Conductors (CCs), a robust and flexible tape architecture that enables textured growth of the rather brittle material class. A remaining bottleneck for widespread CC implementation is the high cost/performance ratio, essentially controlled by the complex and decelerating step of HTS layer growth. In this thesis, we challenge the throughput and cost constraints of conventional growth methods through development of a novel growth technique that combines Chemical Solution Deposition (CSD), an inherently low-cost precursor deposition approach, with a high growth rate, non-equilibrium growth scheme that allows the formation of a transient (Ba-Cu-O) liquid phase prior to crystallization of the final product phase: **T**ransient **L**iquid-**A**ssisted **G**rowth via **CSD** (**TLAG-CSD**).

We employed the new process to grow $YBa_2Cu_3O_{7-\delta}$ (YBCO) thin films, a cuprate-based HTS material with unmatched current carrying performance in applied magnetic field conditions and at high temperatures. The unprecedented properties can only be reached if the electrically anisotropic compound exhibits biaxial texture and provides sufficient nanometric defects to pin vortices, the magnetic flux quanta whose immobilization is a prerequisite to obtaining lossless conduction of electrical current. Hence, not only is the fundamental understanding of the TLAG-CSD process required but also ways to promote epitaxial growth at high rates, avoidance of any current-degrading sources and strategies to enrich the pinning landscape.
To tackle these challenges, we combined several advanced characterization methods: *In-situ* growth experiments with the high luminosity and fast acquisition times (100-500 ms) of a synchrotron facility were carried out to follow growth kinetics under variation of total and oxygen partial pressures, growth temperatures, heating ramps, film thickness/composition and nanoparticle (NP) addition. In particular, we focused first on precursor films that contain only $BaCO_3$ and CuO to facilitate the observation of the liquid characteristics and intermediate reactions, followed by an expansion to the full Y_2O_3-$BaCO_3$-CuO system to study YBCO growth from the transient liquid. The combined set of experiments was successfully summarized in the form of so-called kinetic phase diagrams, a visual representation of the

out-of-equilibrium processes and a road map for its utilization.

Epitaxial, c-axis oriented YBCO films were thoroughly studied via X-ray diffraction, transmission electron microscopy (TEM), low temperature electrical transport and inductive measurements to identify process related limitations and opportunities. This includes probing of the YBCO microstructuture and intrinsic electrical properties to avoid liquid induced substrate reactivity, segregation of secondary phases, while enabling proper CO_2 elimination and oxygen doping of the crystal structure. The continuous tracking of YBCO physical properties throughout the project proved essential for obtaining high current density superconducting films, some of which were further used for in-depth analysis of vortex pinning characteristics and classification of nanometric defects.

Finally, we disclose that epitaxial layer growth rates above $100\,\mathrm{nm\,s^{-1}}$ can be accomplished through the TLAG-CSD approach, surpassing conventional techniques used in CC manufacturing schemes (TFA-CSD, PLD, MOCVD) by up to two orders of magnitude. Superconducting films are demonstrated to reach high epitaxial grain alignment ($\Delta\omega < 0.6^{\circ}$ and $\Delta\phi < 1^{\circ}$), optimal critical temperatures ($T_c = 88$-$92\,\mathrm{K}$) and competitive critical current densities ($J_c = 2$-$5\,\mathrm{MA\,cm^{-2}}$ at self-field and 77 K). We further classify the TLAG-CSD process as highly versatile in enriching the vortex pinning landscape, not only through its capability to promote a high density of stacking faults and small ab-oriented YBCO grains (5-10 nm) in pristine YBCO films but also through its compatibility with preformed nanoparticle addition in nanocomposites, a cost-effective and scalable CSD strategy to improve performance in applied magnetic field conditions. Thus, the concepts and viability experiments revealed in the present work underline the virtue of non-equilibrium growth processes and are envisaged to fuel the field of HTS wire production with new innovation.

Contents

Chapter 1

Introduction and motivation

The mind-boggling phenomena of superconductivity (SC) fascinates the scientific and popular community for more than a century now. After all, there are not many examples of quantum systems that collectively give rise to an accessible, macroscopic appearance such as stable magnetic levitation or lossless conduction of electrical current. Superconductivity is certainly also a field that suffered repeatedly from the euphoria of novel discoveries, followed by the shattering reality of how to make use of those and deal with their limitations. Ever since Kamerlingh Onnes observed the disappearance of electrical resistance in mercury below 4.2 K in 1911, there was a chase for materials that would show this phase transition at higher 'critical temperatures', sustain larger 'critical magnetic fields' and the successful comprehension of the phenomenon within the BCS and Ginzburg-Landau theory [1, 2]. These efforts were fueled by the long-term goal of deriving unprecedented applications for medical, scientific and economic purposes.

Initially, the 1980s did not bear many perspectives for new innovation. A record high transition temperature of 23.2 K was held with Nb_3Ge since 1973 and higher critical temperatures were not predicted, given that material properties which govern the transition according to the BCS theory were not expected to vary much from those that had already been found. Such compounds, nowadays known as low temperature superconductors (LTS) (e.g. Nb_3Sn and NbTi), were integrated into wire architectures and wounded to produce magnetic coils, to date the prime market for SC applications. Due to their superior properties the coils found entrance in medicine, through magnetic resonance imaging (MRI) devices, and fundamental research facilities, such as particle accelerators or high magnetic field labs. Also niche markets exist that make use of the high sensitivity and responsiveness achievable through SC materials, as for instance quantum-interference devices (SQUIDs) based on Josephson junctions. However, larger, commercial markets did not emerge due the restriction that such compounds require operation at liquid

helium temperatures, a costly coolant and intricate in handling.
In that sense, a new era was commenced by Georg Bednorz and Alex Müller in 1986 with the discovery of high temperature superconductivity (HTS) in the $Ba_xLa_{5-x}Cu_5O_{5(3-y)}$ perovskite compound for which they received a Nobel prize in 1987 [3]. Shortly after, a number of layered perovskite structures, including the REBCO material class (RE=rare earth element), were synthesized with critical temperatures well above the boiling temperature of liquid nitrogen, an abundant, cost-effective coolant. This was a milestone insofar as, from the fundamental point of view, HTS does not fit into the framework of the BCS theory, while from the practical perspective SC became abruptly more inviting to be exploited for new applications. The period of time is often termed as the *Woodstock of Physics*, mostly due to the tremendous interest it received globally and frequency of awarded research grants and newly revealed results. The momentum was also big enough to draw the attention to thin perovskite films, in general, whose strongly correlated electron systems are known to exhibit a variety of functional properties, from colossal magnetoresistance to high temperature superconductivity, ferroelectricity and multiferroicity [4, 5].

Nowadays, HTS materials are integrated into, so-called, *2nd generation* (2G) tapes or Coated Conductors (CCs). As the name implies, the wire architecture is not the first to exists. And indeed, the prior approach was to incorporate the brittle ceramic materials into a metallic tube, often silver, through a powder-in-tube (PIT) process. Unfortunately, the benefiting properties of most HTS materials were strongly degraded as PIT does not promote a high degree of textured growth, a prerequisite to achieving high current percolation in these electrically anisotropic materials. Although PIT can be used for some specific materials, such as $Bi_2Sr_2Ca_{n-1}Cu_nO_{2n+4+x}$ (BiSCCO), it was clearly not a suitable approach to exploit the unparalleled properties of REBCO the material class, being the sole candidate for the operation at liquid nitrogen temperatures. A breakthrough achievement was, therefore, the introduction of biaxial texture into flexible metallic tapes, a template that would enable epitaxial growth of materials with low lattice mismatch. In the ensuing years, the SC community successfully faced the highly complex challenge of how to grow the HTS layer over hundreds of meters, while ensuring a homogenous spread of defects at the scale of nanometers.
Such commercially available 2G tapes reach remarkable current carrying capacity of 500 - 700 A at 77 K in 1 cm width and $\leq$ 100 µm in thickness, a performance that could give rise to the next generation of low energy consumption devices and accelerate the transition towards sustainable energy, a shift needed now more than ever [5]. One might hence wonder, why more

than thirty years after the initial discovery of HTS, CCs are not in widespread use.
As summarized by Stephen Blundell, there is an existent inertia in industry regarding new, potentially disruptive technologies [1]:

"*Very often, many of these competing technologies lie dormant, partially developed but never quite making it in the market. This is because it is always easier for an industry to tweak an existing technology than to introduce a radically new one. But then something happens, a minor breakthrough or something dropping in price, and a new technology springs up, seemingly from nowhere, but in fact it has been there all along*."

At present, the demand for HTS wire is compromised for similar reasons. Since the successful deployment of the 2G wire architecture, HTS research and development evolved into a competitive environment to make CCs 'cheaper' and 'better'. The wire affordability is typically evaluated in units of $€\,kA^{-1}m^{-1}$, allowing to tweak the cost/performance ratio either through improvement of the current carrying capacity or decrease in manufacturing costs.[1] Currently, the established techniques to grow the HTS layer (PLD, MOCVD) rely on slow vapor/solid diffusion kinetics, costly vacuum installations and an overall limited delivery of atoms towards the growing front.[2] Hence, intrinsic growth rate limitations prevent the conventional approaches to reach a cost-effective, high throughput manufacturing scheme.
There are two approaches that, if successfully combined, could yield the required drop in cost and increase in fabrication throughput: On the one hand, chemical solution deposition (CSD) is a well establish low-cost, non-vacuum technique that allows to synthesize high quality functional oxide thin films. Especially $YBa_2Cu_3O_{7-\delta}$ (YBCO), an HTS compound of unmatched SC properties, is successfully grown using CSD and the trifluoroacetate metal-organic decomposition approach (TFA-CSD) [6, 7]. On the other hand, intrinsic growth rate limitations can be overcome through liquid assisted processes where atomic diffusivity is drastically enhanced as compared to vapor- and solid-based growth methods. To date, the low-cost benefits of CSD together with the fast crystallization kinetics of melt processes have not been successfully exploited to allow for a higher market penetration of HTS.

[1] To allow for comparison with other materials, the cost reads as "currency per kA and meter in a 1 cm wide tape", hence, gives a price per meter that is capable of carrying one kiloampere.
[2] Typical HTS layer thicknesses lie in a range of 1 - 2 µm.

The present work addresses the remaining bottleneck of cost and throughput constraints through development of a novel growth approach which we entitle **T**ransient **L**iquid **A**ssisted **G**rowth based on **C**hemical **S**olution **D**eposition (**TLAG-CSD**). CSD is employed to deposit uniform metal-organic precursor films to grow epitaxial $YBa_2Cu_3O_{7-\delta}$ layers. The initial precursor solution is modified in a way that allows formation of a transient liquid phase to assist and accelerate the growth of YBCO. While a part of the thesis is devoted to studying crystallization of YBCO *in-situ* under non-equilibrium processing conditions, such as rapid increase in temperature and pressure variations, we also explore the physical properties and vortex pinning characteristics of grown films, essential to define limitations and capabilities of the new process. In particular, the thesis is structured as follows:

- **Chapter 2** comprises some of the main concepts of superconductivity, the interest behind YBCO use for applications and the current state of HTS wire production.
- **Chapter 3** summarizes the experimental procedure and related calculus. This includes sample fabrication, micropatterning techniques, characterization methods and the customized measurements setup used at the synchrotron facility to perform *in-situ* growth experiments.
- **Chapter 4** introduces the basic principles of TLAG-CSD and covers our efforts to study the process *in-situ*. We will define the main reactions, P_{O2} - T paths to reach stable conditions for YBCO growth and give a visual representation of the process in the form of kinetic phase diagrams.
- **Chapter 5** defines strategies of how to increase growth rates, reduce processing temperatures and avoid secondary phase precipitation. It also deals with more exotic crystallization kinetics of the TLAG process, such as YBCO grain reorientation, and how to exploit these to promote epitaxial growth.
- **Chapter 6** overviews our results on the physical characterization of grown films through XRD, TEM, electrical transport and inductive measurements. We will evaluate the texture quality, degree of oxygen doping and percolation state of standard and nanocomposite YBCO samples in order to obtain high current density films.[3]

[3]Preformed nanoparticles are added to the initial precursor solution to obtain YBCO films with artificially induced defects for performance improvements. Such films are termed nanocomposites (NCs).

- **Chapter 7** focuses primarily on vortex pinning characteristics of TLAG films and the identification of nanometric defects that are beneficial for flux immobilization. Four-terminal devices are fabricated via photolithography, deposition of electrical contacts and physical/chemical etching to study the temperature, applied magnetic field and angular dependence of the critical current density.

Chapter 2

Fundamental concepts

Although superconductivity (SC) spans more than a century of wide-ranging research, both experimental and theoretical, it is as recent as 34 years that the field experienced a major upswing in interest with the discovery of high temperature superconductors (HTS). In this introductory part we aim to review some of the fundamental framework governing SC, the peculiarities of the material class under investigation and recent strategies to push HTS towards market applicability. Ultimately, the concepts and approaches discussed here will motivate the individual studies carried out in chapter 4 - 7.

2.1 Introduction to superconductivity

In 1908, the director of the low-temperature laboratory at the University of Leiden, Heike Kamerlingh Onnes, reported the successful liquefaction of helium gas. With a boiling point of 4.2 K in atmospheric pressure, the experimental temperature range could be farther extended towards absolute 0 at that time. K.Onnes initial intentions where to study the temperature dependence of the electrical resistance of highly pure metals, such as platinum and gold. The studies later involved mercury, whose purity was believed to be further improved through repeated distillation.
Three years after He liquefaction, an unexpected observation was made: The electrical resistance of mercury abruptly disappeared below a critical temperature point, T_c. Although a decrease in resistance was expected, the drop appeared on a scale of a few hundredths of a degree and was ascribed to a discontinuous transition. Attempts to induce impurities and intentionally increase electron scattering did not affect the resistance drop. It was, thereafter, suggested that mercury has reached a new state and, given its extraordinary electrical properties may be referred to as *superconducting state* [1, 8]. Similar electrical behaviour was, soon after, found in tin, lead and other metals and by now it is known that about half of the metals in the periodic table can become

superconducting with individual T_c points. The absence of electrical resistance entails that there is no electric field within the material. According to Faraday's law, $\oint \boldsymbol{E} \cdot d\boldsymbol{l} = -\delta\Phi/\delta t$, circular currents must induce a constant magnetic flux. Correspondingly, upon application of an external magnetic field, screening currents must flow to prevent flux changes in the bulk ($\delta\Phi/\delta t = 0$) [2]. As already observed by K.Onnes in 1913, the effect was maintained up to a critical field above which surface currents could no longer sustain flux from entering. At this field the supercurrents collapse and the material transitions into its normal state.
Known as the *Meissner effect*, the next milestone in the field of superconductivity was set by Meissner and Ochsenfeld through the discovery of perfect diamagnetic behaviour ($\chi = -1$). However, although an outer magnetic field can be shielded through the effect of *perfect conductivity* alone, flux lines would tend to be trapped in a normal conductor, while superconductors were found to fully expel the flux lines from the normal state upon cooling through T_c. Such a reversible behaviour implies that there is a thermodynamic critical field, $\mu_0 H_c$, related to the free energy difference between normal (n) and superconducting state (sc)

$$E_c = E_n - E_{sc} = \frac{B_c^2(T)}{2\mu_0} \tag{2.1}$$

with the Helmholtz free energies E_n and E_{sc} of each state in zero field and μ_0 the permeability in vacuum. E_c is commonly referred to as *condensation energy*. Thus, superconductivity could be treated as a thermodynamic phase transition, and its successful microscopic description was achieved by Bardeen, Cooper and Schriefer in the late 50s within the framework of the BCS theory.[1] Although earlier studies by Gorter and Casimir, in 1934, already introduced the concept of a *two-fluid model* with a normal and superfluid condensate of electrons, the full microscopic picture was given through the BCS theory [2]. Here, electrons near the Fermi level of opposite spin and wave vector experience a weak attractive force due to electron-phonon interaction. The result is an electron-electron pairing mechanism into boson-like particles, known as Cooper pairs, that condensate into a macroscopic, quantum coherent state. The superfluid travels through the solid without resistance, while normal electron transport is governed by scattering.

[1] Valid for conventional, low-temperature superconductivity.

2.1.1 Types of superconductors

Already before the appearance of the BCS theory, a different approach by Ginzburg and Landau, known as Ginzburg-Landau (GL) theory, allowed a phenomenological description of the superconducting state through considerations of thermodynamic phase transitions [2]. Particularly, the theory gained again much attention from the 90s onwards due to its capability of correctly predicting aspects of high temperature superconductors,[2] whose macroscopic description remains under debate to this day.
As mentioned earlier, surface currents are generated as means of shielding the bulk of the superconductor from the external magnetic field below T_c. Considering an interface between normal and superconducting phase, the applied magnetic field does not abruptly drop to zero. Instead, the decay follows

$$\mu_0 H(x) = \mu_0 H_a \cdot e^{-x/\lambda} \tag{2.2}$$

with $\mu_0 H_a$ being the applied magnetic field amplitude and λ the *penetration depth* [8]. Ginzburg and Landau introduced a pseudowavefunction ψ, an *order parameter* in the general theory of second-order phase transitions, which is related to the local change of the superconducting electron density

$$n_{sc} \propto |\psi|^2. \tag{2.3}$$

The distance upon which the density of Cooper pairs increases from zero to its maximum value in the bulk is given by the *coherence length*, ξ. Both characteristic length scales, λ and ξ, are used to define the GL parameter

$$\kappa = \frac{\lambda}{\xi} \tag{2.4}$$

In particular, it was Abrikosov who found that depending on the absolute value of κ, the sign of the boundary energy ΔE between normal and SC state changes. He showed that the two regimes are distinguishable at the breaking point of $\kappa = 1/\sqrt{2}$ where the magnetic field penetration characteristics change essentially. This led to the differentiation

$$\kappa = \frac{\lambda}{\xi} \begin{cases} \kappa < 1/\sqrt{2}\text{: type-I SC} \\ \kappa > 1/\sqrt{2}\text{: type-II SC} \end{cases} \tag{2.5}$$

[2] Such as the quantization of magnetic flux lines.

of type-I and type-II superconductors depending on their behaviour in applied magnetic field. An illustration of the normal-to-SC interface and evolution of λ and ξ for the two different cases, $\Delta E > 0$ and $\Delta E < 0$, is shown Fig. 2.1.

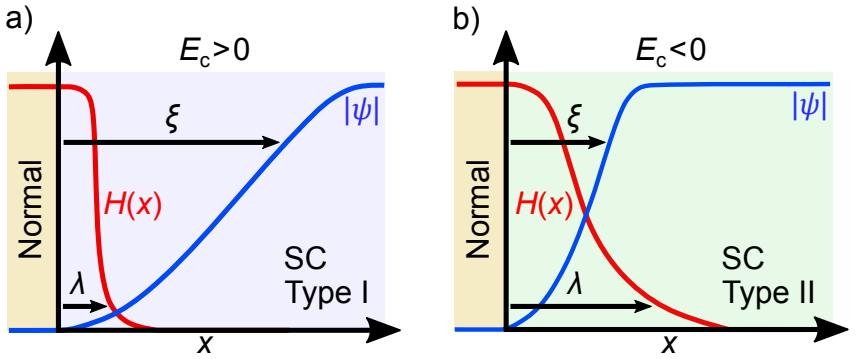

FIGURE 2.1: Schematic view of the spatial evolution of external magnetic field, $H(x)$, and SC electron density, n_{sc}, along an interface of normal to a) type - I and b) type - II SC region. Penetration depths and coherence lengths are included for both cases. Modified from [9].

The positive boundary energy ($\Delta E > 0$) in type-I superconductors yields a minimization of normal-to-SC interfaces. Here, screening currents run through the bulk surface and, with that, full expulsion of the magnetic field is given. The SC remains in the Meissner state up to a critical field value H_c, the exceedance of which results in breaking of the SC state. A schematic representation of the H - T phase diagram is shown in Fig. 2.2a). Most of the previously mentioned superconducting materials and those initially studied by K. Onnes where of type-I.

On the contrary, in type-II superconductors the subdivision of the SC into domains is energetically favoured, allowing quantized flux lines,[3] also referred to as *vortices*, to enter the bulk. The Meissner state is maintained below a lower critical field H_{c1} followed by a mixed state where vortices are present in the superconducting material up to the *upper critical field* H_{c2}. The corresponding illustration of the phase diagram is shown in Fig. 2.2b). Owing to the highly increased upper critical fields of type-II superconductors ($H_{c2} \gg H_{c1}$), these materials are capable of carrying large currents without losses and operate in high magnetic fields. They are, therefore, the only class of superconductors available for high current applications. As we will see in the following, the nature of vortices and the mixed state is responsible for the emerging material science research carried out to tailor the SC properties of type-II superconductors.

[3] With flux quantum $\phi_0 = 2.07 \cdot 10^{-15}$ Tm^2.

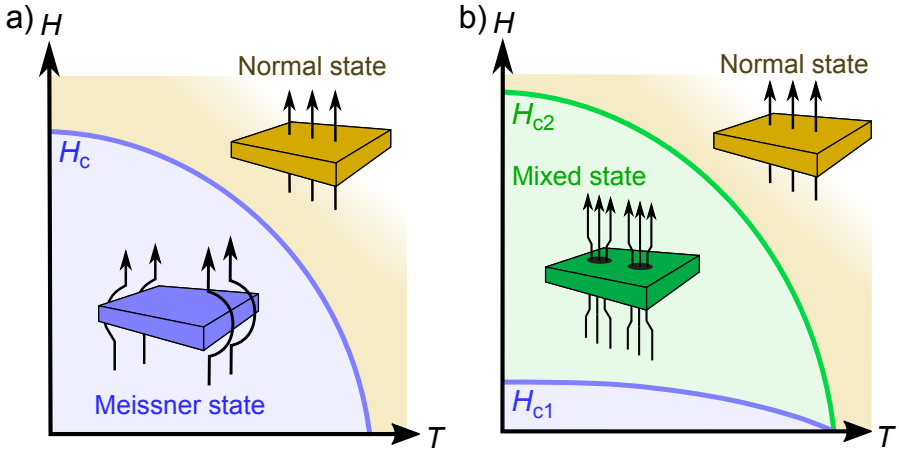

FIGURE 2.2: Illustration of the H - T dependent phase diagram for a a) type - I and b) type - II superconductor.

2.1.2 Mixed state of type-II superconductors

With the discovery of lossless current conduction, K.Onnes promptly envisaged its technological use by winding superconducting wires into coils that produce large magnetic fields. Soon after, such ideas had to be discarded given the low critical fields, H_c, above which the superconducting state is quenched. Most type-I superconductors do not surpass an upper limit of 0.1 T at zero Kelvin having T_c values below 10 K [10]. In this respect, neither the application of high currents could be realized, as the induced self-field of the wire yields a self limitation.

New hope for the actual utilization of superconductivity emerged with the discovery of type-II superconductors having superior magnetic properties. Already in the 40s-50s, a number of niobium-based alloys (e.g. NbN and Nb_3Sb) were found with T_c values in the range of 10 - 20 K and upper critical fields, H_{c2}, reaching 10s of Teslas. First magnets were build soon after, such as the 0.7 T iron-core niobium- and 8.8 T NbTi-wired electromagnet, both operating in liquid helium at 4.2 K [11, 12]. To date, NbTi is used to produce magnetic fields of high uniformity for medical and scientific purposes.

Although the above mentioned examples are cases of low-temperature superconductors, also referred to as *conventional superconductors* as their behaviour is well described through the BCS theory, the superior magnetic properties are in direct connection to the mixed state (Fig. 2.2b)), known as Shubnikov-phase. The transition region is governed by partial entrance of the outer magnetic field in form of quantized flux lines (vortices) that are generated by a circular superconducting current, J_s, flowing around the core. The vortex

core, of radius ξ, consist of normal electrons surrounded by the supercurrent of diameter 2λ. Note that the notation of these vortex characteristic lengths coincides with the magnetic field and order parameter decay in type-II superconductors (Fig.2.1b)). Hence, each vortex can be considered as a cylindrical interface between superconducting and normal region. A schematic drawing of the characteristic vortex parameters is shown in Fig. 2.3a). While ξ is, once again, related to the increase in superconducting electron density, $n_{sc} \propto |\psi|^2$, the magnetic field decay lies within a cylinder of 2λ in diameter.

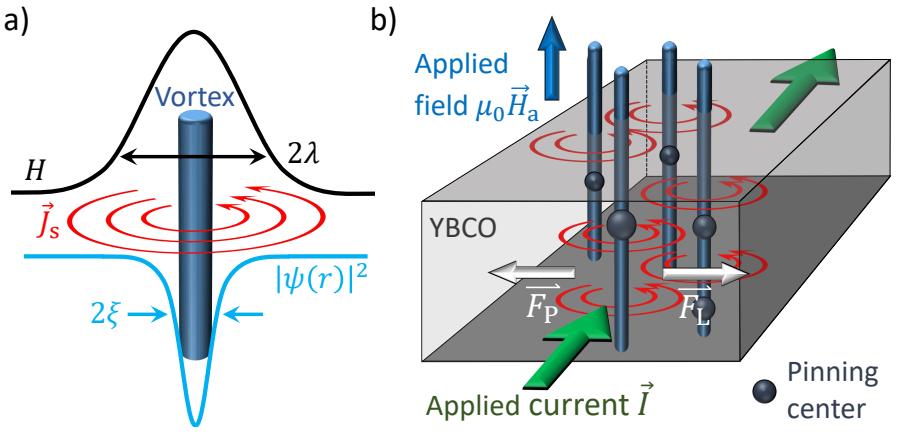

FIGURE 2.3: Mixed state characteristics of a type-II superconductor: a) Vortex with a normal core diameter, 2ξ, induced through supercurrents, J_s, reaching a penetration depth λ. b) Interplay between lorentz-like force, F_L, and pinning force, F_P, upon application of a driving current in applied field conditions.

Given that the vortex core consists of normal electrons, it is of no surprise that the flux tubes interact with structural defects where the superconducting order parameter ψ is reduced by default. As a result the system avoids condensation energy losses by placing the flux lines in locally non-superconducting regions. The strength of interaction is given by the individual pinning force f_p which is, in turn, related to defect dimensionality, distribution and depth of individual pinning potentials, U, that constitute a pinning site [13, 14]. In fact, F_p is in most cases not a simple summation over individual pinning contributions, giving rise to a whole theoretical field dedicated to the, so-called, *summation problem* [14].

Dissipation free current transport in type-II superconductors requires vortices to remain pinned. Vortex motion would, otherwise, result in propagation of the normal electron core and build up of an electric field. Upon application of

a current density J, there is a *lorentz-like force*, F_L, that tends to move the vortices, similarly to a magnetic field acting on a moving charge [2]. F_L is given by

$$\overrightarrow{F_L} = \overrightarrow{J} \times \overrightarrow{B}. \tag{2.6}$$

The force acts in opposite direction to the pinning force (see Fig. 2.3b)) and is responsible for the irreversible detachment of vortices from their pinning potential upon exceedance of a critical current density value, J_c, at the break point

$$|\overrightarrow{J_c} \times \overrightarrow{B}| = |\overrightarrow{F_L}| = |\overrightarrow{F_P}| \tag{2.7}$$

Below J_c ($F_L < F_p$), no electric field is generated along the wire, while above, ($F_L > F_p$), a voltage drop develops non-linearly with applied current, giving rise to the IV-curve characteristics that will be shown in 3.4.4. Hence, the depinning of vortices and, with that, the upper threshold for lossless current conduction are directly linked to the effective defect landscape that immobilizes vortices. A separate discussion on suitable defects for vortex pinning will therefore be given in 2.1.6.

2.1.3 Bean critical state model

The presence of vortices in type-II superconductors results in a large magnetic hysteresis, that can be used to deduce the critical current density through non-distructive inductive measurements (3.2). Upon cooling below T_c in zero field (ZFC) and application of an external magnetic field above H_{c1}, vortices start to nucleate at the outer bulk boundaries and move towards the sample center upon further field increase.
The density of flux lines is highest at the bulk edges and gradually decreases to the insights. A schematic drawing of the vortex distribution is shown in Fig. 2.4 with x pointing to the inner part of the SC bulk, y the current direction and z the applied field and flux line orientation. The density gradient is a consequence of the pinning force opposing the lorentz-like driving force [2]. In the *Bean critical state model*, developed by C.P. Bean, the competing forces and resultant field gradient are used to describe the macroscopic magnetic hysteresis of the mixed state [15].

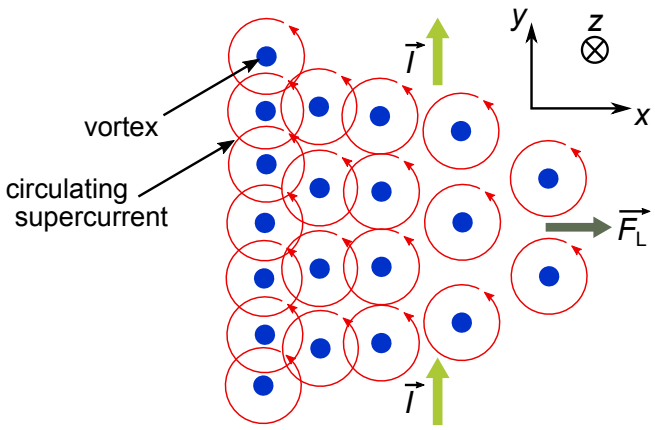

FIGURE 2.4: Penetration of flux lines, pointing in z direction, upon application of a current density in y. A flux line gradient evolves along x due to non-equilibrium pinning forces that reach equlibrium with the lorentz-like driving force. Adapted from [2].

In particular, the simplified model relies on several approximations:

1. **Absence of demagnetizing effects:** The sample volume is treated as infinite slab with the field lines being aligned parallel to the rod direction. Hence, demagnetizing fields can be neglected.

2. **Constant magnetic field slope:** Inside the slab, the magnetic field gradient, arising from the vortex density change, is assumed constant ($\delta B/\delta x = \text{const}$). According to Maxwell equation $\nabla \times \vec{B} = \mu_0 \vec{J}$, the linear change in field translates into precise values of the current density: $+J_c$, $-J_c$ (and 0 if the gradient does not reach the sample center). The circulating current is assumed to be equal to the critical current density J_c, arising as intrinsic property from the overlapping supercurrents of the vortex array (Fig. 2.4).

3. **Absence of creep:** The array of induced flux lines is assumed stable and vortex motion due to thermal fluctuations (flux creep) is neglected. Furthermore, the mixed state initiates at $B_a = 0$, hence, the low critical field is set to zero.

In the simplified approach of the critical state model, J_c does not depend on the applied magnetic field. Although this is not fulfilled in the real case of type-II superconductors, the approach has proven to allow fairly precise estimations of J_c [16]. Fig. 2.5 shows a schematic representation of a magnetic hysteresis loop of a type-II superconducting thin disk. Strictly speaking, J_c is magnetic field independent in the Bean critical state model, whereas here

we show the $J_c(H)$ behaviour of a thin films to resemble a more realistic example as studied in the following. The generated critical current profiles are illustrated in the three inset sketches for different parts of the hysteresis loop, assuming here the Bean critical state model (J_c independent of H) for drawing simplicity.
To reach the saturated, remanent magnetization of the full sample volume, a magnetic field needs to be applied to a value $2H^*$ after ZFC. At this point, the field profile does not change anymore and the applied field reaches a magnitude, high enough to reach the maximum magnetic moment when the field is removed again. The bottom part of the sketch shows the current density values along the slab in-plane axis; at $2H^*$, $-J_c$ is reached until the sample center, followed by $+J_c$ to the outer part. The full current loop, in turn, induces the saturated magnetization, $-m_{sat}$.

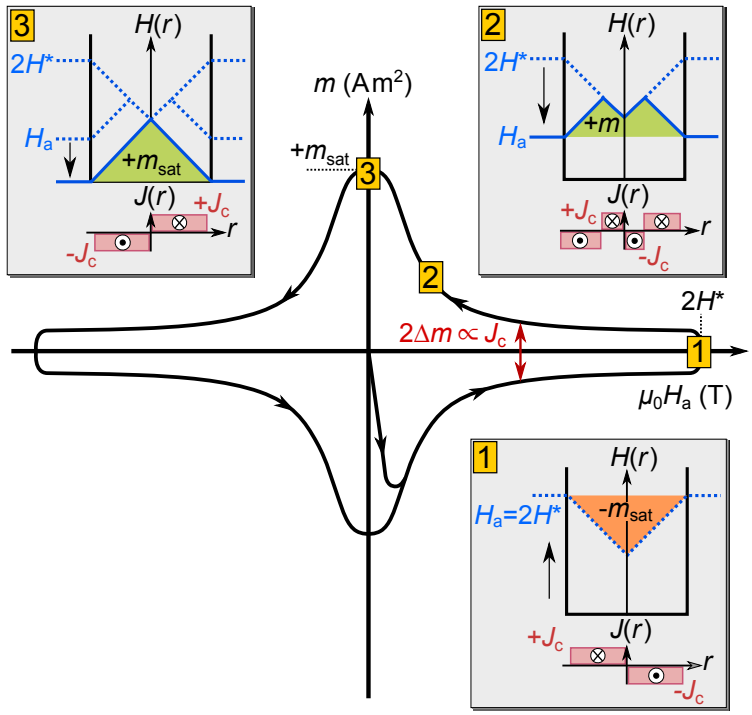

FIGURE 2.5: Magnetization loop of a type-II superconducting thin disk with $H_{c1} = 0$. Insets show the magnetic field penetration characteristics according to the Bean critical state model. Upon ramping of the magnetic field to $2H^*$ the sample reaches a saturation in the remanent magnetization, m_{sat}, when the field is removed. m_{sat} is induced by critical currents reaching the sample center (lower part of inset 3).

When H_a is decreased from $2H^*$, the current stream lines are progressively inverted due to slope change of the magnetic field gradient (Fig. 2.5, sketch 2). This continues until the applied field reaches zero and a remanent magnetization remains. As the field was initially ramped up to $2H^*$, the induced magnetization corresponds to the saturated value. The Bean critical state model can then be used to deduce J_c according to

$$J_c = \frac{3\Delta m}{2r_{eff}} \tag{2.8}$$

where Δm corresponds to the width of the saturated magnetization loop[4]

$$\Delta m = \frac{m_{sat}(\mu_0 H \uparrow) - m_{sat}(\mu_0 H \downarrow)}{2} \tag{2.9}$$

and r_{eff} is the effective radius of a circular area that would cover the full surface of the measured disk [17]. Although demagnetizing effects are known to result in an asymmetry of the magnetic hysteresis, it has been shown that such effects scale with the sample thickness [18], allowing to apply eq. 2.8 to thin superconducting disks as used in this work.

2.1.4 High temperature superconductivity

K. Onnes initial hope of utilizing superconductivity for electric power and magnetic applications found its first realization through a number of conventional superconductors, such as NbTi and Nb_3Sn. Although, to date, these materials are integrated in magnetic coils that produce fields of unsurpassed quality for scientific and medical purposes (e.g. magnetic resonance imaging, particle accelerators, high-field magnets) [19], the entrance of SC in larger markets held off. This is mainly due to the reluctance of most industrial sectors to use cryogenic systems, especially since the cost and handling of liquid helium does not favour such investments.
In this context, a breakthrough discovery was made in 1986 by Bednorz and Müller of high temperature superconductivity (HTS) in the copper oxide ceramic $Ba_xLa_{5-x}Cu_5O_{5(3-y)}$ belonging to the class of type-II superconductivity [3]. One year after, $YBa_2Cu_3O_{7-\delta}$ (YBCO), with a T_c of 93 K, was announced [20] followed by numerous compounds, with a T_c record of 130 - 140 K at ambient pressure. The high critical temperatures opened up the field of superconductivity to cooling through liquid nitrogen, a cost-effective and abundant coolant with a boiling point of 77 K.
The early enthusiasm of HTS discovery was, soon after, dampened by the

[4] Taking upper and lower branch into account.

need to integrate these rather brittle materials into a wire or tape architecture. And although many of the associated technical issues were successfully tackled through tremendous R&D efforts, some challenges, that we will addresses separately in 2.2, persist to date.

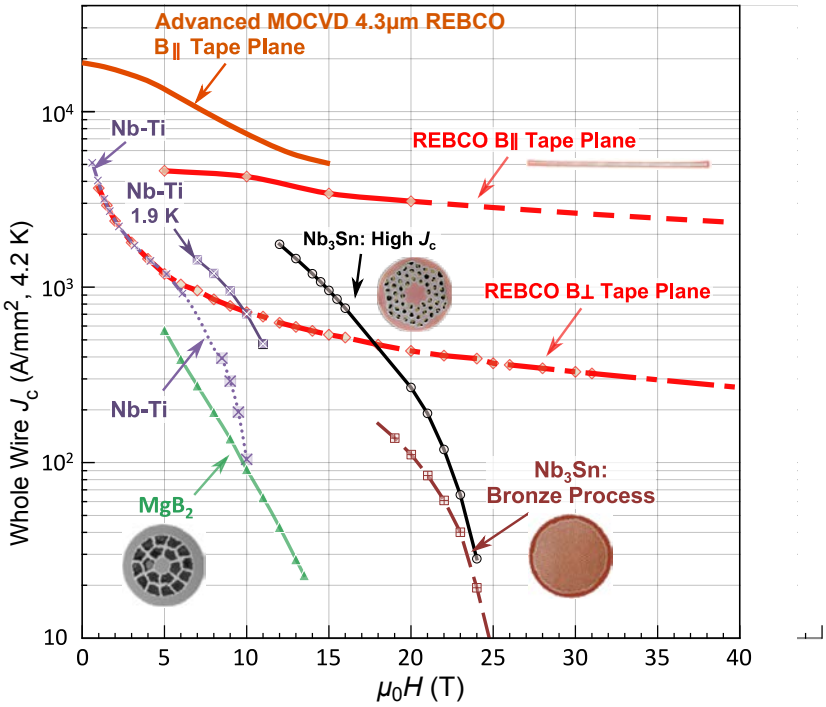

FIGURE 2.6: Comparison of the engineering critical current density versus applied magnetic field for several conventional low-temperature (LTS) superconductors with a REBCO high-temperature superconducting (HTS) tape (shown in red). Graph and additional data obtained from [21, 22].

With regard to new application fields, HTS has game-changing potential: Fig. 2.6 compares in-field critical current densities at 4.2 K of commercially available LTS wires[5] with an HTS tape from the REBCO material class (RE=rare earth elements). Some of the wire and tape cross-sections are included in the figure, insinuating that the underlying architecture of HTS and LTS conductors must be fundamentally different (see 2.2).
Even at the operating temperature of liquid helium (4.2 K), the REBCO tape can outperform LTS materials in the whole magnetic field range as a result

[5] NbTi, Nb_3Sn and MgB_2

of the superior upper critical field.[6] For YBCO, H_{c2} is determined in the order of 170 T at 4.2 K [23]. At low temperatures, HTS materials can particularly be used for high magnetic field applications. For instance, a record high DC magnetic field of 45.5 T could be just recently set at the MagLab research facility through use of an HTS inner coil [24]. Ultimately, such high magnetic fields will increase the resolution of imaging techniques, enlarge the field range for fundamental research and scale down facilities whose size depends on the field.[7] On the contrary, completely new applications are envisaged through use of HTS at high temperatures, where the previously discovered type-II superconductors cannot be utilized at all. This includes, amongst others, power cables and fault current limiters, operating approx. at $\mu_0 H < 1$ T and $T = 77$ K and motors, generators and superconducting magnetic energy storage devices (SMES) requiring $\mu_0 H < 3$ - 5 T and $T = 30$ - 60 K in operational margin [7, 25]. A high interest also lies in the use of HTS for next generation, compact fusion reactors and electric aircraft, allowing to reduce weight and increase efficiency [26, 27].
The HTS material used in the present work is YBCO, one of the most intensively investigated cuprate superconductors. Even though YBCO does not have the highest T_c nor H_{c2}, the compound holds an intrinsic advantage over all other HTS materials that makes it particularly appealing for SC applications. As described previously in 2.1.1, the upper boundary for dissipation free current transport, hence $J_c \neq 0$, is given by $H_{c2}(T)$. While this, indeed, is a sufficient approximation in the LTS case [28], HTS materials are confined by a lower threshold, $H_{irr} \ll H_{c2}$, where a finite electrical resistance evolves from spontaneous vortex motion, resulting in $J_c = 0$ as vortices cannot be pinned.[8] The regime originates from thermal fluctuations becoming stronger than the pinning energy, which yields to melting of the vortex lattice [19]. The characteristic field, $H_{irr}(T)$, is referred to as *irreversibility field* and marks the tolerable limit of loss-free current transport of the HTS $H - T$ phase diagram.

[6] As all HTS materials, REBCO has an intrinsic anisotropy (see 2.1.5), which results in performance changes depending on the magnetic field orientation. This is seen in the different current densities obtained for B$\parallel$ and B$\perp$ to the tape plane (Fig. 2.6).

[7] For instance, the fusion power density is $\propto B^4$, particle accelerator beam energy $\propto B$ and the magnetic resonance imaging resolution sensitivity $\propto B^2$.

[8] In the LTS case H_{irr} lies close to H_{c2}.

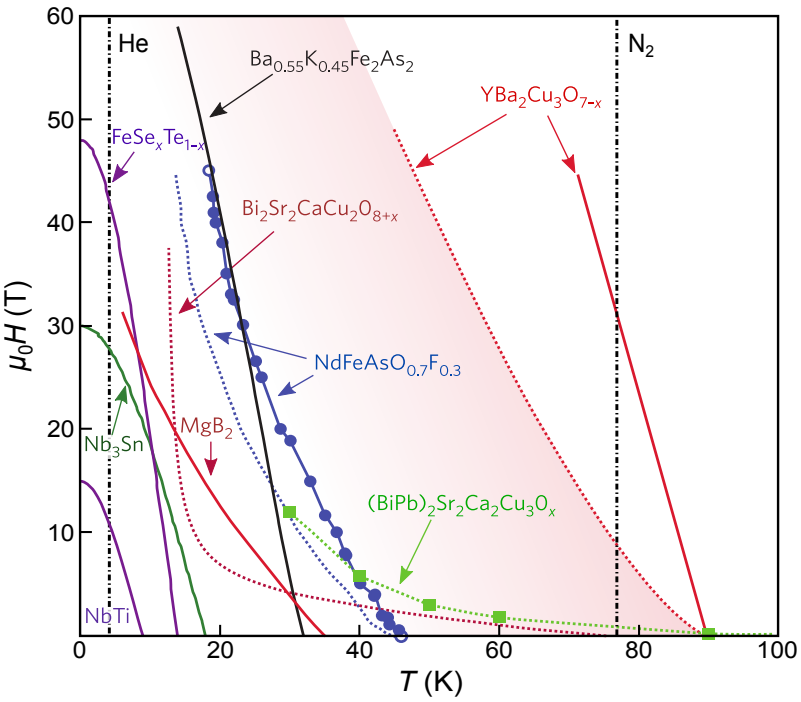

FIGURE 2.7: H - T comparison of upper critical fields, H_{c2} (solid lines), and irreversibility fields, H_{irr} (dashed lines), of type - II superconductors, both LTS and HTS. The operating temperatures of liquid helium and nitrogen are included as black-dashed lines. Data obtained from [29]

Considering upper critical fields and irreversibility lines of different type-II superconductors, both LTS and HTS,[9] the motivation behind integrating YBCO into the next-generation superconducting cables becomes clear [28]. Fig. 2.7 comprises some of the $H_{irr}(T)$ and $H_{c2}(T)$ lines in dashed and solid, respectively. While for most cuprate-based HTS materials, such as $Bi_2Sr_2CaCu_2O_8$ (BSCCO) and $(Bi,Pb)_2Sr_2Ca_2Cu_3O_x$, the upper critical field lines lie well above the one of YBCO (not shown here), $H_{irr}(T)$ does not. In fact, YBCO is the sole candidate with $H_{irr}(T)$ reaching the boiling point of liquid nitrogen (dashaed-black line) and strongly extending the $H - T$ window for potential applications at high fields (> 10 T).

[9] Including NbTi, Nb_3Sn and MgB_2, iron-based pnictides and cuprate compounds.

2.1.5 REBCO crystal structure and laminar anisotropy

The peculiarity of HTS compounds lies in the spatial localization of mobile charge carriers, giving rise to an electrical anisotropy induced by the structural anisotropy. $REBa_2Cu_3O_{7-\delta}$ in particular, where RE can be any rare earth element except Ce, Tb, Pr and Pm [19, 30], is a triple-perovskite[10] with two hole-doped CuO_2-planes being separated by the RE-plane; Y in case of YBCO. As seen in the unit cell in Fig. 2.8 the BaO-planes separate CuO_2-planes from the CuO-chain layers, the latter being responsible for the oxygen deficiency in $YBa_2Cu_3O_{7-\delta}$. For $\delta = 0$ and $\delta = 1$ the structure is considered fully depleted or loaded, respectively. In its depleted state, YBCO exhibits tetragonal structure with $a = b$. A transition to the orthorhombic crystal structure, $a \neq b$ as shown in Fig. 2.8, evolves progressively upon oxygen incorporation at $\delta > 0.65$ [31]. While superconducting currents flow in the CuO_2-planes (highest $|\psi|^2$) [9], CuO-chain layers are considered as *charge-reservoirs* since they provide hole doping into the CuO_2-planes through a charge transfer mechanism [32].

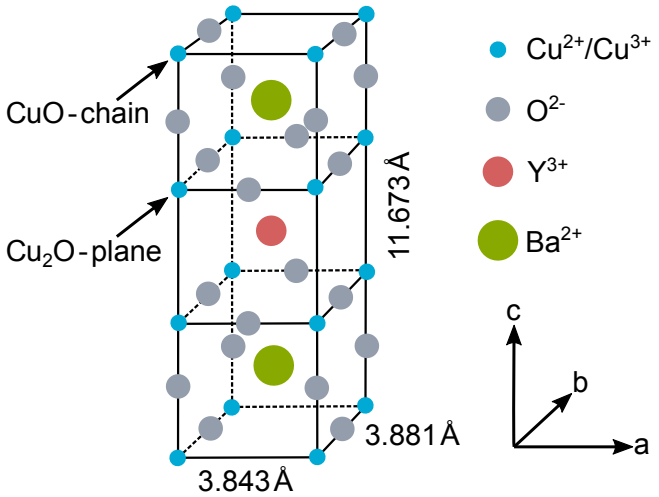

FIGURE 2.8: $YBa_2Cu_3O_{7-\delta}$ orthorhombic unit cell with CuO-chains and CuO_2-planes indicated. Lattice parameters are obtained from the International Centre for Diffraction (ICDD) database [33].

In cuprate-based superconductors, the oxygen content essentially determines whether the structure turns out superconducting and will greatly impact critical temperatures and critical current densities, T_c and J_c, due to its link to the carrier concentration [34]. The complex phase diagram of HTS spans from an antiferromagnetic insulating state when the compound is oxygen depleted,

[10] Unit cell of three ABX_3 blocks, with positive cations A and B in the centre and corners.

towards opening of a pseudogap and *strange metallic* behaviour at increased oxygen concentrations [35]. Although the origin of superconductivity in copper-oxide HTS materials is not fully disclosed, the non-superconducting, pseudogap state is believed to provide insights into the collective electron coupling behaviour of these materials [36].
At low temperatures and within a narrow oxygen doping range ($\delta \approx 0.05$ - 0.06) the SC transition of YBCO is observed with a maximum T_c of 92 - 93 K [37]. At this oxygen concentration, the unit cell exhibits orthorhombic structure due to the uneven occupation of oxygen sites along a- and b-crystallographic directions.

The localization of transport charge carriers within the CuO_2 - planes results in an intrinsic anisotropy of the laminar YBCO structure. This translates into a modulation of the effective electron mass, vortex characteristic lengths and any correlated physical entity, such as H_{c2}, H_{irr} and J_c. The anisotropy magnitude is termed *anisotropy parameter*, γ, and can be expressed as [38]:

$$\gamma = \sqrt{\frac{m_c}{m_{ab}}} = \frac{\lambda_c}{\lambda_{ab}} = \frac{\xi_{ab}}{\xi_c} \propto \frac{H_{c2}^{ab}}{H_{c2}^{c}}. \tag{2.10}$$

We will show in the course of chapter 7 and appendix E, how γ values can be obtained and used for interpretation of transport data.
The anisotropy of HTS materials and quasi-2D nature of superconductivity yields much higher supercurrents along the ab-planes as in c-axis direction [19]. As a consequence, the brittle oxide ceramics require to be grown epitaxially, given a critical threshold in neighbouring grain misalignment to reach the high critical current densities shown earlier in Fig. 2.6. While this is addressed separately in the discussion of tape fabrication strategies (2.2), HTS brings another peculiarity that initiated a competitive environment in material science engineering in the decades after the initial discovery: HTS materials are considered as extreme type-II superconductors due to their large GL values, $\kappa = \lambda/\xi$, with $\lambda > 100$ and $\xi \sim 1$ nm [19]. For YBCO, in specific, $\lambda_{ab} = 135$ nm and $\xi_{ab} = 1.6$ nm for $H//ab$ and $\lambda_c = 890$ nm and $\xi_c = 0.24$ nm for $H//c$ at 0 K [2]. Due to the small coherence length, pinning of vortices requires the introduction of material imperfections on nanometer scale, which is one of the most challenging tasks given that SC wires are requested to reach hundreds of meters in length for most applications.

2.1.6 Vortex pinning in YBCO

In the case of epitaxial films, any interruption of the crystal lattice periodicity is considered as a defect. In particular for YBCO and other laminar type - II

superconductors, defects that enhance the superconducting performance due to vortex pinning need to be distinguished from those that will generate grain discontinuity by decreasing percolation currents. Since the vortex coherence length in YBCO (and HTS in general) is small many structural and atomic defects that generated during growth apply as pinning candidates. However, full current percolation and grain connectivity needs to be ensured to benefit from such contributions. The difficulty is to find ways to control and select the type of defect that one desires to promote.
Over the past decades a variety of defects have been identified in YBCO films, ranging from 0D to 3D in dimension. A schematic overview of the defect landscape is given in Fig. 2.9. Point defects (0D) comprise disruptions at the atomic scale, such as interstitials, impurity atoms or interchange of Y and Ba atomic sites [39]. On the other hand, nanoparticles, locally strained regions, porosity and larger precipitates are 3D disruptions of the superconducting order parameter [40–43].

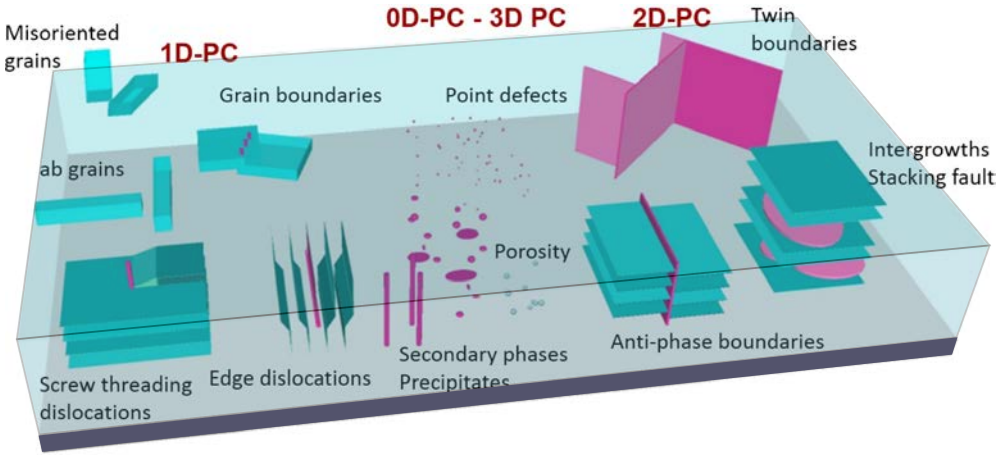

FIGURE 2.9: Schematic overview of possible defects in YBCO films. Defect dimensions range from 0D to 3D, shown in the upper part. Defect regions that can act as pinning sites for vortex immobilization are indicated in pink.

Both, 0D and 3D defects are *isotropic pinning centers* as they contribute equally in all directions of the magnetic field. On the contrary, 1D and 2D defects pin vortices with angular dependent pinning force and are therefore considered as *anisotropic pinning centers*. Dislocations and nanorods are examples of 1D pins, while planar defects, such as stacking faults (SFs), twin boundaries (TBs) and antiphase boundaries perturb the SC structure in 2D [44, 45].
Particularly 3D defects, such as misoriented YBCO grains, coarsened secondary phases or porosity (Fig. 2.9), that reach large sizes with respect to

the superconducting layer, can substantially reduce the superconducting cross-section and decrease the current percolation. Also grain boundaries need to be of high purity and low misalignment to allow for high current percolation along neighbouring grains. Hence, it is essential to promote only such defects that can act as pinning centers or induce secondary defects for pinning, while allowing for a high transmittance of superconducting currents.

The comprised structural defects in Fig. 2.9 can be further categorized as *natural* or *artificial pinning centres* (APCs) depending on whether the defect is formed naturally during growth or introduced artifically through secondary techniques. For instance, SFs and TBs are natural defects that are commonly formed due to stain relaxation and transitioning from tetragonal to orthorhombic crystal structure during oxygenation, respectively [46, 47]. Also the YBCO layered structure itself provides effective pinning along the ab-planes, by localizing vortices within the ab-planes where the superconducting order parameter is reduced. The effect is termed *intrinsic pinning* and attributed to the modulation of the superconducting order parameter ψ along the c-axis direction, with sub-nanometer coherence lengths [48].

Ideally, laminar materials, such as YBCO, should be utilized with magnetic field orientations parallel to the CuO_2-planes. Due to the materials anisotropy, practical values such as $J_c(H)$, H_{c2} and H_{irr} can be considerably elevated for that particular magnetic field orientation. However, the operation margin is strongly confined (few degrees) and actual devices cannot operate with the magnetic field parallel to the ab-planes, making such realizations cumbersome. To optimize the SC performance in certain ranges of the $H - T$ diagram and isotropize the material, sophisticated material science research has been carried out to generate APCs. Such films are then referred to as *nanostructured* YBCO or *nanocomposites* (NCs). The numerous attempts span from ion-irradiation techniques to surface decoration and introduction of secondary phases,[11] ultimately aiming to tune defect size, distribution and density [40, 49–53].

Not all approaches generate defects that act as effective pinning centers by themselves. As demonstrated, for instance, in the case of NC films with added nanoparticles (NPs), the secondary phase tends to agglomerate to sizes of >20 nm during the growth process, unapt to localize vortices with a core diameter of 2-5 nm. However, NP inclusions induce interfacial strain that triggers increased numbers of SFs, a planar, circular defect that is accomodated in the YBCO structure through local strain fields (nanostrain) at its periphery [40, 54, 55]. This, in turn, leads to more isotropic pinning

[11] That result in the integration of nanoparticles and nanorods within the YBCO crystal lattice.

behaviour since local strain fields are shown to act as 3D defect.

In summary, the anisotropic nature of cuprate superconductors and demand to optimize the performance in certain (H, T, θ) regions is currently tackled through precise defect engineering and elaborate strategies to introduce pinning centers. However, not all defects are desirable since large defects can result in obstruction of current percolation, outshining their positive contribution to flux immobilization.

2.2 Superconducting wire fabrication

To motivate the necessity of alternative growth approaches in the field of HTS, as developed in the present thesis, some of the fundamental obstacles to produce superconducting wire, the development of the coated conductor technology and liquid based growth techniques need to be addressed.
HTS superconducting wire is nowadays commercially available from several global providers that continue to improve transport characteristics through close feedback with the consumer [56–58]. However, a major part of the HTS market is still rooted in the production of compact magnetic coils that reach superior performance as compared to those built from conventional type-II materials [24]. What still refrains the technology to enter a broader market of applications is the high production cost of the wire, measured in units of €/kA m, which reads as "euros per kA for a 1 meter of wire of 1 cm in width". Recent estimations show that the cost ratio of wire to final product lies around 5 - 15 % for magnets, 20 - 25 % for cables, fault current limiters and transformers and above 30 % for rotating machines [7]. Nevertheless, past and ongoing proof-of-concept projects demonstrate that HTS will, eventually, allow for lighter, more efficient generators [59], attractive power-grid concepts [60] and, potentially, become the enabling technology for large projects such as the hadron-hadron future circular collider and next-generation fusion reactors [61–64].

The vast leap from the initial discovery of HTS in 1986 to its integration in wire architectures (see 2.2.1) and successful utilization in numerous application fields owes to the persistent R&D efforts undertaken in this field. The

hurdles were challenging. Large devices need kilometers of flexible, superconducting wire with homogeneous properties along its full length.[12] In addition, the brittle ceramic material needs to be grown with a high degree of texture given the anisotropy of the SC state.

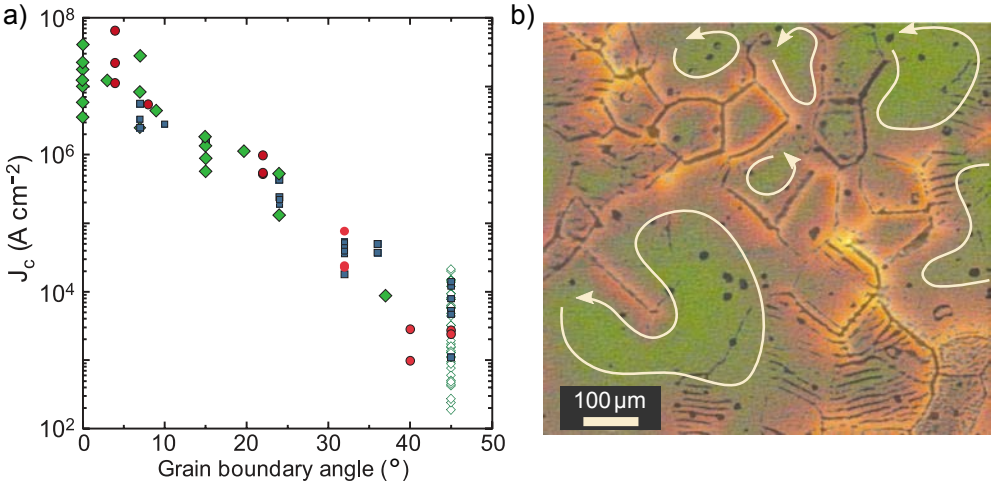

FIGURE 2.10: Grain boundaries influence on percolating state of YBCO films: a) Evolution of J_c values with grain boundary misorientation angle θ. Symbols refer to different studies of YBCO grown on bicrystal $SrTiO_3$ and YSZ substrates (squares and filled rhombs) and bi-epitaxial junctions (open rhombs). b) Magneto-optical image of flux line penetration into a textured YBCO layer with high angle boundaries (black lines). Green and yellow areas correspond to regions of high and poor electromagnetic connectivity, respectively. Data obtained from [28].

Unambiguous evidence that current percolation in HTS materials suffers from grain misalignment was given through studies where the YBCO (00l) tilt could be deliberately altered via growth on $SrTiO_3$ or Y_2O_3-stabilized ZrO_2 (YSZ) bicrystalline substrates [28, 65]. The dependence of the critical current density on the grain boundary angle is shown in Fig. 2.10a). J_c decreases exponentially with the misalignment angle, initiating at a critical threshold of about $\theta_c = 4\text{-}5\,°$. The effect is attributed to insulating edge dislocations that accommodate the tilt and result in Josephson weak-link behaviour. The order parameter is then locally reduced as soon as the width of the insulating region surpasses the coherence length ξ, inducing charge localization at the boundary [7]. Consequently, those regions of the conductor that contain high angle

[12] The weakest link would otherwise degrade the current transport performance of the whole conductor and provide spots where the superconducting-to-normal transition can occur spontaneously during operation, also referred to as *quench*.

grain boundaries are effectively acting as current blockades.
This was further highlighted through imaging of flux penetration along grain boundaries of a textured YBCO film (Fig. 2.10b)). Green areas represent regions that are electromagnetically well connected. Yellow regions, corresponding to poor connectivity, on the other hand, encompass high angle grain boundaries ($\theta_c > 4^o$), seen as dark lines in the optical image.
Hence, the strategy towards high critical current density films, aside from preventing cracks, voids and secondary phase agglomeration, all of which can heavily reduce the percolating cross-section, relies on biaxial texture of the HTS material in use. However, in the early development stage there were no kilometer-long crystalline templates that would transfer the texture into the HTS layer. This required the development of the, so-called, coated conductor (CC) which is to date the cornerstone for implementation of HTS materials into an actual wire architecture.

2.2.1 Development of Coated Conductors

The electrical anisotropy in HTS materials is related to the complex, laminar crystal structure (Fig. 2.8). Considering, for instance, conventional, low T_c type - II superconductors, the crystal lattice exhibits rather simple crystal symmetry, such as Nb - Ti and Nb_3Sn with a body-centered cubic and cubic A15 unit cell structure,[13] respectively [28]. This translates into anisotropy factors $\gamma \sim 1$, hence, negligible angular dependence of SC properties. On the contrary, YBCO and the even more intricate $(Bi,Pb)_2Sr_2Ca_2Cu_3O_x$ (Bi - 2223) compound reach anisotropy values in order of 5 - 7 for YBCO and 50 - 200 for Bi - 2223.
The initial, so-called, *1st generation* approach to incorporate SC materials into a wire architecture was through a "powder-in-tube" (PIT) process that included packing of the SC powder into a copper or silver tube, followed by several rolling and heating steps [28, 39]. The method proved successful for those compounds of low anisotropy, unaffected by grain boundary misalignment. Some of the wires are depicted in Fig. 2.6 showing a round cross-sections with SC filaments embedded in a copper or silver matrix. And even though uniaxial texture could be realized through the PIT process using the anisotropic, high - T_c $Bi_2Sr_2Ca_{n-1}Cu_nO_{2n+4+x}$ (BiSCCO) compound, the low H_{irr} did not enable high temperature applications and restricted its use down to 20 K. A new approach was needed, capable of exploiting HTS to its full potential and open up new application fields in the high temperature range.

[13] Sn atoms occupy the cube-corners and cube-centre sites, while Nb atoms lie in three orthogonal chains.

One of the major achievements came through introduction of texture into flexible metallic substrates, typically ≈100 µm in thickness, either via ion beam-assisted deposition (IBAD) or deformation texturing using the rolling-assisted biaxially textured substrate (RABiTS) [66, 67]. These tape architectures are regarded as approximations to kilometer length single-crystalline substrates, enabling to grow REBCO layers with adjacent grain misalignment below the critical threshold value, θ_c.

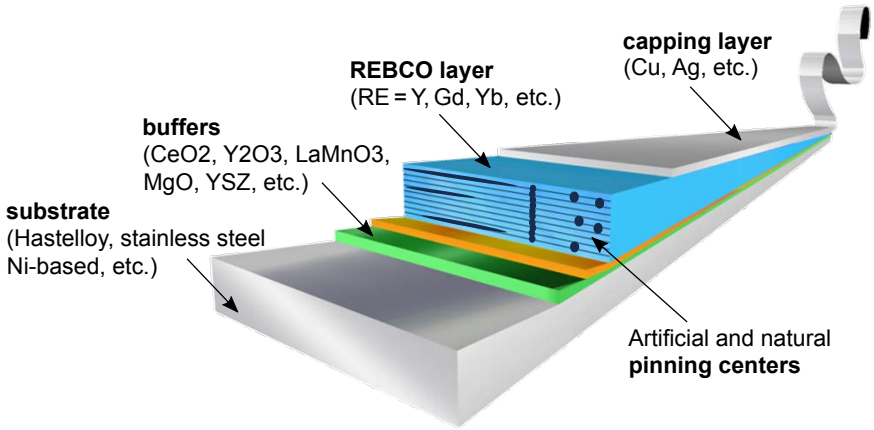

FIGURE 2.11: Illustration of the Coated Conductor geometry to allow for epitaxial growth of REBCO layers, either through ex- or in-situ approaches. Several options are mentioned for substrate and buffer layers to account for the IBAD and RABiT approach [66, 67].

An illustration of the metallic tape with buffer layers and the REBCO HTS material is shown in Fig. 2.11. For IBAD tapes, hastelloy is used as poly-crystalline metallic template and texture is first promoted through the IBAD approach in the overlaying buffers, typically MgO and YSZ. The stack is terminated with an $LaMnO_3$ or CeO_2 layer improve the matching towards the REBCO layer.[14] In case of RABiT tapes, on the contrary, texture is already introduced in the NiW metallic substrate and improved through buffers, such as Y_2O_3, YSZ and CeO_2.[15] Most importantly, much effort has been undertaken to allow for both tape designs to be flexible, non-magnetic and enable the epitaxial growth of oxides with matching lattice parameters to the terminating buffer layer.

[14] To be precise, the hastelloy is first covered with an Al_2O_3 and Y_2O_3 layer before deposition of the IBAD buffer. The multilayer stack adds up to Hastelloy/Al_2O_3/Y_2O_3/MgO/LMO/YBCO, for instance.

[15] Typically, the final stack comprises NiW/Y_2O_3/YSZ/CeO_2/REBCO.

Deposition and growth of the REBCO is either carried out through *in-* or *ex-situ* approaches, depending on whether REBCO crystallization takes place right during film deposition or separately after, respectively. The most established in-situ methods for commercial tape fabrication are Pulsed Laser Deposition (PLD) and Metal Organic Chemical Vapour Deposition (MOCVD). Ex-situ methods are the chemical solution deposition (CSD) approach given by the metalorganic decomposition of triflouracetates (TFA-CSD) and the recently developed Reactive Co-Evaporation and Direct Reaction (RCE-DR) process [25, 68].
The final tape structure incorporates a 1-2 µm thick REBCO layer which is typically capped with a $\sim$ 2 µm silver overlayer and $\sim$ 20 µm copper encapsulation for quench protection, giving a final product of $<$200 µm in thickness and varying widths of 4 mm and 12 mm. Recently, the substrate thickness was decreased to 50-60 µm and some providers even succeeded to lower it down to 30 µm, enabling a higher flexibility of the tape. Due to the fundamental difference of this architecture to the PIT approach, the HTS wire is referred to as 2^{nd} *generation* (2G) tape or Coated Conductor (CC).

In summary, 2G HTS superconducting wires are nowadays available in the form of flexible, resistant tapes, termed Coated Conductors. Several global providers incorporate the REBCO material, typically using Y or Gd as rare earth cation, with a high degree of epitaxial alignment into the stacked structure (Fig. 2.11). A number of strategies, left out here for simplicity reasons, are further utilized to integrate APCs into the REBCO layer and improve its performance in-field and at high temperatures.[16] However, most of the REBCO fabrication approaches rely on growth rate limiting reactions that restrict the process to growth rates below 10 nm s^{-1}. As we will address in the following, liquid mediated growth techniques might overcome such constraints and allow for a higher market penetration of CCs.

2.2.2 Liquid mediated growth approaches

Considering that, performance-wise, commercial HTS tapes reach remarkable current carrying capacity of 500-700 A at 77 K, self-field or 1000-1500 A at 4.2 K, 20 T in 1 cm width, one might ask what is still keeping HTS from entering a broader market of applications. The answer is cost and throughput limitations. At present, the cost/performance ratio of SC wire, measured in units of €/kA m, is still too high. The final cost strongly depends on the operating temperature and magnetic field range, complicating a precise

[16] Such as 1D nanocolumns and 3D platelets in the case of PLD and MOCVD and 3D nanoparticles in TFA-CSD grown YBCO.

cost evaluation. However, typical values settle around $\sim$ 200 €/kA m [69]. Although the price is indeed acceptable for such applications where HTS is a true enabling technology, it can certainly not compete in areas where copper wires are used. For this, the cost ratio should drop considerably towards $\sim$50 €/kA m, approximately by a factor 4 of the current price.

The price reduction can be achieved by different means, including an overall increase in J_c, customization of the CC for a certain application, thickness increase of the REBCO layer (hence, increasing the I_c), substrate layer thinning,[17] increase in manufacturing rates (e.g. through use of multi-lanes, multi-plume lasers) or reduction of raw material costs. However, the largest room for improvement lies in the fabrication throughput itself. The industrially utilized REBCO growth techniques are restricted in intrinsic REBCO growth rates to $< 10\,\mathrm{nm\,s^{-1}}$ due to the reduced atomic diffusivity in vapor-solid and solid-solid reactions [57, 70, 71]. This is where liquid mediated techniques can have a great impact.

The advantage of liquid based techniques lies in the superior diffusivity of cations in the melt. For instance, Y diffusivity in a high temperature (BaO - CuO) melt was shown to reach $4 \cdot 10^{-10}\mathrm{m^2 s^{-1}}$ [72], two orders of magnitude higher than in a YBCO solid [73].[18] This is why growth rates can potentially reach millimeter per hour magnitudes ($100\,\mathrm{nm\,s^{-1}}$), as shown in the case of melt textured grown (MTG) YBCO [6, 74]. The process is commonly used to produce pellets of single-crystalline quality that have no magnetic granularity effects and, hence, are well suited for studies of the YBCO bulk properties.
In MTG, crystallization of YBCO takes place through undercooling of an incongruent melt (Y_2BaCuO_5 + liquid) below the peritectic temperature of YBCO. At these conditions, the system becomes metastable and the melt supersaturates,[19] allowing YBCO to nucleate heterogeneously in presence of a seed crystal of higher melting temperature [75].

[17] For applications, the engineering critical current density, J_e, taking the whole tape thickness into account, is the decisive measure.

[18] Precisely speaking, a melt composition of (3BaO - 5CuO) at 970 °C was used.

[19] The concept of supersaturation, being the driving force for crystallization, will be further addressed in 4.1.

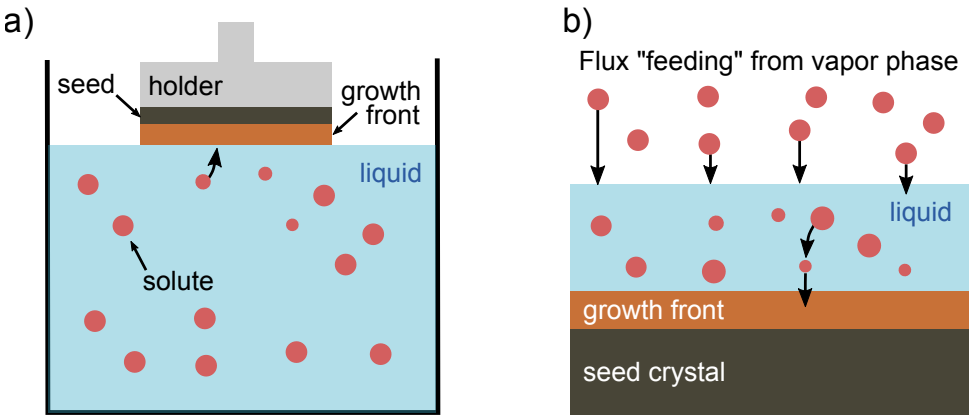

FIGURE 2.12: Growth of HTS thin films through a) Liquid Phase Epitaxy and b) Hybrid Liquid Phase Epitaxy. In both cases, a high temperature melt is saturated with a Y containing solute. Heterogenous YBCO growth is then promoted through a seed crystal. Modified from [76].

To grow YBCO in thin film form, the method Liquid Phase Epitaxy (LPE) was adapted, earlier employed to grow single crystals and non-superconducting phases. A schematic illustration of the process is shown in Fig. 2.12a). A seed crystal is placed on a holder and brought into contact with a high temperature (BaO - CuO) melt, with Y_2O_3 or YBCO as solute. YBCO growth is then achieved at rates up to 50 nm s^{-1} through adjustment of a temperature gradient, with the melt close to the seed crystal being undercooled, hence, supersaturated. In addition, the substrate is rotated to produce forced convection of new supersaturated solute to the growth front [77–79]. Some of the main obstacles in LPE growth lie in the liquid induced reactivity issues with crucible and substrate materials, use of high processing temperatures (∼1000 °C) and the general difficulty of introducing pinning centers, since the equilibrium approach produces single crystalline YBCO with low current carrying capacities. Also the degree in supersaturation cannot be straightforwardly controlled due to the static nature of the process.[20]
Some of these limitations were overcome in more advanced methods such as Hybrid Liquid Phase Epitaxy (HLPE), Pulsed-Laser Tri-Phase Epitaxy (TPE) and Vapor–Liquid–Solid growth (VLS) [80–83]. A scheme of the HLPE process is shown in Fig. 2.12b). A thin liquid layer (50 - 500 nm) is first stabilized and the Y rich solute then fed via PLD. This allows independent regulation of the melt supersaturation through tuning of the laser pulse

[20] The solute concentration in the melt is fixed, while the supersaturation close to the seed decreases due to YBCO growth. Hence, growth rates can fluctuate depending on how efficiently the stagnant liquid layer can be renewed during the process.

frequency. Growth rates up to 35 nm s^{-1} were demonstrated, though in the optimized conditions, YBCO was grown at 12 nm s^{-1} to reach 1.2 MA cm^{-2} at 77 K [84].

The mentioned liquid assisted growth techniques have the potential to reach up to orders of magnitude higher growth rates as compared to the established standard processes. This could, in turn, allow for the necessary cost reduction of CCs, since growth of the REBCO layer is currently the bottleneck step. However, even the most advanced and recent approaches rely on usage of complex installations and high vacuum conditions [68]. Aside from HLPE, TPE and VLS, where the solute is supplied via PLD/MOCVD, also the very recently developed Reactive Co-Evaporation and Direct Reaction liquid based technique (RCE-DR) utilizes ultrahigh vacuum in the order of 10^{-8} bar for the metal evaporation [68].
In addition, liquid based techniques work in near-equilibrium conditions, stabilizing the liquid phase or incongruent melts based on thermodynamic equilibrium data. Crystallization is then either initiated through slight temperature variations or over-saturation of the melt with the solute substance. The downside is that temperature windows for heterogeneous nucleation are rather narrow (few °C), processing temperatures high (800-1050 °C) and the corrosive liquid in contact with substrate and seed for extended time spans. It is also uncertain if liquid based techniques can allow enough flexibility in tailoring defect landscapes for further performance improvement, for instance, through inclusion of secondary phases to produce nanocomposite films.

In the following course we will address these issues in the framework of the TLAG - CSD process, the fundamental principles of which are based on out-of-equilibrium growth kinetics (see 4.1). In particular, we will demonstrate that while growth rates of the REBCO layer surpass any conventional growth method (reaching > 100 nm s^{-1}), TLAG is also compatible with nanoparticle addition to grow nanocomposites, offers a wide epitaxial growth window and intrinsically promotes the formation of nanometric defects that are suitable for vortex pinning.

Chapter 3

Experimental methodologies

In this chapter, an introduction to sample fabrication methods and utilized measurement techniques will be given. Section 3.1 deals with the preparation of films through use of fluorine free metal-organic salts. A brief introduction into the electromagnetic, electrical and structural characterization techniques can be found in 3.2-3.5. *In-situ* X-ray synchrotron measurements and transmission electron microscopy are discussed separately in 3.6 and 3.7, respectively.

3.1 CSD approach to TLAG of YBCO films

As previously introduced in 2.2, tremendous effort has been made to move from the discovery of layered superconducting cuprate perovskites to an actual scheme for wire fabrication. Although the majority of currently established Coated Conductor (CC) fabrication approaches utilize pulsed laser deposition (PLD) as deposition technique, throughput and cost constraints shift the interest towards low-cost methods capable of scaling up and being implemented into reel-to-reel processes.
Chemical **s**olution **d**eposition (**CSD**) is a promising candidate in this sense. It is a highly versatile, low-cost technique that has the potential to supply functional thin films at competitive performance [85–87]. A chemical precursor solution is typically deposited by means of spin-, dip-coating, ink-jet printing, doctor blade etc. under controlled ambient conditions. One of the main advantages lies in the possibility to separate the step of crystallization from the material deposition itself. This frequently overseen difference of CSD compared to physical methods allows to benefit from additive manufacturing, separate control of chemical constituents and integration of nanocrystals from colloidal solutions [7].
In the past few decades, the SUMAN group was strongly involved in the growth and optimization of YBCO films and nanocomposites through the

most widely used solution-based approach that combines **m**etal-**o**rganic deposition with **t**ri**f**luoro**a**cetate solutions (MOD - TFA) [6, 40, 41], early developed by Gupta et al. [88].[1] The use of trifluoroacetate precursors had to be studied throughout each thermal step. The decomposition behaviour of the organic constituents (pyrolysis treatment), the evolution of intermediate phases and the right nucleation conditions were fully explored until epitaxial YBCO films could be grown reproducibly, reaching low grain boundary misalignment and purity.

Fluorinated precursors are used to avoid the formation of the $BaCO_3$ phase which was known to remain stable up to very high temperatures [89]. Carbon residuals were considered to degrade the quality of grain boundaries and be interstitially incorporated in adjacent cites to the CuO_2 planes yielding depression of critical temperatures and current densities at self-field [90]. Instead, pyrolyzed films were optimized to contain a nanocrystalline distribution of CuO, Y_2O_3 and $Ba_{0.72}Y_{0.28}F_{2.28}$ (BYF), the latter transforming to a Ba oxyfluoride (OF) before formation of the YBCO [6]:

$$3CuO + 2Ba(O_xF_y)_2 + \frac{1}{2}Y_2O_3 + 2yH_2O \longrightarrow YBa_2Cu_3O_{7-\delta} + 4yHF \qquad (3.1)$$

Vaporized H_2O is introduced in the process to decompose the $Ba(O_xF_y)_2$, resulting in the release of the toxic hydrogen fluoride (HF) gas. In the later course of the MOD process, and still on-going research, the amount of fluorine was reduced by partial substitution of trifluoroacetate by carboxylates salts, also referred to as low-fluorine approach [91, 92]. The reduction beared many positive aspects, such as decreasing the HF release, higher homogeneity of pyrolyzed films and an overall reduction of the processing time, hence higher CC production yield [93]. Although the development of the low-fluorine approach could highly benefit from the already generated knowledge on TFA, both processes have an intrinsic limitation during the crystallization step to form YBCO. According to eq. 3.1, the reaction takes place through a gas-solid diffusion process which is found to restrict epitaxial layer growth rates to 0.5-1 nm s^{-1}.

Here, we explore the growth of YBCO films and nanocomposites through non-fluorinated precursor salts using a novel, transient liquid mediated process. As will be shown throughout the present thesis, the reaction mechanisms towards formation of the epitaxial YBCO layer, limitations to the process and final film microstructure differ fundamentally from the approaches introduced above. Work on solution design, control of rheological parameters, growth of YBCO films and transmission electron microscopy (TEM)

[1] Nanocomposites refer to superconducting films with added nanoinclusions.

analysis was carried in a collaborative project with six PhD students and four postdoctoral researchers in the framework of an Advanced ERC grant: Pyrolysis studies and growth of pristine YBCO films were mostly carried out by L.Soler, S.Rasi and L.Saltarelli [76, 94]; nanocomposite film growth was investigated by J.Jareño and D.Garcia [95]; ink-jet printed films were focus of Dr. A.Queralto and A.Pachecho; TEM characterisation was undertaken by Dr. R.Guzman, Dr. B.Mundet and Dr. K.Gupta. Their individual contributions will be mentioned throughout this thesis. The main processing steps and thermal profiles to obtain films via TLAG-CSD will be summarized in the following.

3.1.1 Solution preparation and deposition techniques

Commercially available, high-purity acetate salts of Y, Ba and Cu are dehydrated at 50°C overnight in a thermostatic vacuum dryer and later dissolved in two steps in propionic acid and anhydrous alcohol (methanol or butanol).[2] The solvents were found to give full dissolution of the salts at a ratio of 1:1. Additionally, $5\%_{v=v}$ of triethanolamine (TEA) can be added to modify the solution viscosity, and with that influence the decomposition behaviour of the organic matter. The integration of the additive is commonly used to prevent crack formation during the step of pyrolysis and achieve an overall more homogenous coating of the substrate. Special care is taken in keeping the water content below 2% through solution control with a Karl-Fischer device. A higher water content was demonstrated to yield crack formation of pyrolized films [76] and be responsable for degradation of the SC performance of grown films [96]. The prepared solutions are therefore kept in veals filled with argon gas.
Most of the work done in this thesis focuses on two cation stoichiometries, differing in the Ba - Cu ratio: A YBCO-stoichiometric mixture with a Y-Ba-Cu proportion of 1:2:3 (denoted as (2-3) composition) and a Cu-rich mixture of 1:2:4.66 (referred to as (3-7) composition). Exclusively in chapter 5, another yttrium-copper-rich composition corresponding to a proportion of 1.35:2:5.5 is studied for complementary reasons.
The final molar concentrations of the three metals (Y+Ba+Cu) vary in the range of 1 - 1.75 M giving a final film thicknesses of 100 - 250 nm per deposited layer. Thicker layers are obtained through an iteration of solution deposition (3.1.1) and pyrolysis treatment (3.1.2).

Three cubic, single-crystalline substrates were chosen to provide a small lattice mismatch with respect to the basal plane of YBCO: $SrTiO_3$ (STO),

[2] YAc_3 and $CuAc_2$ are obtained from Alfa Aesar; $BaAc_2$ from Sigma Aldrich

$LaAlO_3$ (LAO) and $(LaAlO_3)_{0.3}$ $(SrAlTaO_6)_{0.7}$ (LSAT), all (100) oriented. An overview of the substrate characteristics is given in tab. 3.1. The low lattice mismatch is a requirement to promote c-axis growth and reduce strain induced defect formation [97, 98]. The substrates are 5 x 5 x 0.5mm in size (l x w x h), one-side polished and commercially available from CrysTec [99]. Before solution deposition, all substrates undergo a thermal treatment at 900 °C for 5 h in an oxygen flow of 0.5 L/min. An atomically flat surface termination, free of contaminants, is achieved by these means [76, 85].

Substrate	a [Å]	δ_a [%]	δ_b [%]	δ_{ab} [%]	Strain
LAO	3.791	-1.35	-2.32	-1.84	Compressive
STO	3.905	1.61	0.62	1.12	Tensile
LSAT	3.868	0.65	-0.33	0.16	Tensile

TABLE 3.1: Overview of substrate lattice constants and individual lattice mismatch values (δ_i) with respect to bulk YBCO, using a=3.843Åand b=3.881Å.

Solution deposition is either carried out through spin coating or ink-jet printing. In the former case, a Pyrex microsyringe is used to deposit 15 µl of the precursor solution on top of the polished substrate surface, which is then accelerated in 1 s to 6000 rpm and rotated for 2 min. After homogeneous spread of the solution the sample is placed on a heating plate for 5 min, preset to 70 °C, in order to evaporate solvent remainings. The deposition takes place inside a glove box in a regulated nitrogen environment to create an atmosphere of low humidity and avoid film contamination. Right after solvent evaporation, the sample is transferred to a tubular furnace to undergo the pyrolysis heat treatment.

3.1.2 1st heat treatment: Pyrolysis

The pyrolysis process, also referred to as calcination of metalorganic precursor films, was deeply investigated by thermogravimetric analysis [94] and evolved gas analysis with *in-situ* FTIR [76] before an optimized thermal treatment could be defined: The thermal profile, as depicted in Fig. 3.1, is programmed and carried out with a tubular furnace in a laboratory with controlled humidity atmosphere.

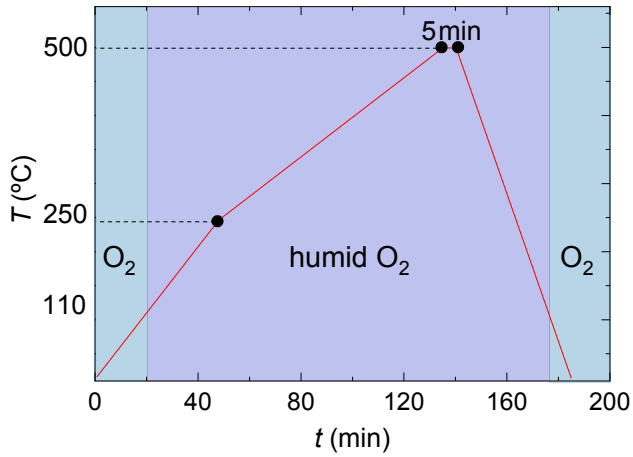

FIGURE 3.1: Optimized pyrolysis heat treatment for a single layer deposition of acetate based precursor solution.

The deposited and dried solution is first heated at a rate of 5 °C/min to a set value of 250 °C; the heating ramp is then decreased to 3 °C/min until a final temperature of 500 °C, followed by a 5 min dwell. The calcination of the ternary compound is finished at this point and the sample is cooled down to room temperature. The whole profile is carried out in an oxygen flow of 0.12 L/min. At temperatures above 110 °C the dry oxygen gas is passed through flasks containing deionized water to reach a humid atmosphere of $P_{H_2O} = 23$ mbar. The use of humid gas is reported and confirmed to prevent the sublimation of copper(II) acetate [100]. After the pyrolysis procedure, a nanocrystalline film with Y_2O_3, $BaCO_3$ and CuO is obtained (4.2) which is subjected to another heat treatment to obtain YBCO.

3.1.3 2nd heat treatment: YBCO Growth

The step of crystallization to form YBCO from pyrolyzed precursor films is subject of on-going research and progressive refinement. Process parameters and approaches to reach the YBCO stability explored in this thesis will be discussed in the following.
Two main routes were investigated to drive the precursor film into a window defined by total pressure (P_{tot}), oxygen partial pressure (P_{O2}) and temperature (T) where stable YBCO nucleation could be reached:

1. ***T*-route:** The temperature route is a 1-step crystallization process. The sample is heated at a constant heating rate and P_{O2} to a high temperature window, followed by a dwell of typically few minutes. The gas

atmosphere is preadjusted using a mixture of N_2 and O_2. The treatment is carried out at atmospheric pressure.

2. **P_{O2}-route:** The second route is a two-step approach where heating is first carried out at a low oxygen partial pressure where YBCO formation is not occurring ($\leq 10^{-5}$ bar below the YBCO instability line [101]). Stable phase formation is then triggered upon P_{O2} increase at constant temperature. P_{tot} is reduced throughout this process to reach the desired oxygen partial pressures either through use of a rotary or a turbomolecular pump.

An illustration of the $P_{O2} - T$ paths of both routes can be found in Fig 4.16 where we derive a phase diagram for the TLAG process. In the particular case of the P_{O2}-route we will identify different characteristic solid phases in the low pressure step of the process. For that reason, the route will further be distinguished in $P_{O2}(BaCu_2O_2)$ - and $P_{O2}(Cu)$ - route to stress the different phases before YBCO growth (see 4.4.2). Here, we only overview the range of explored processing conditions for each route.

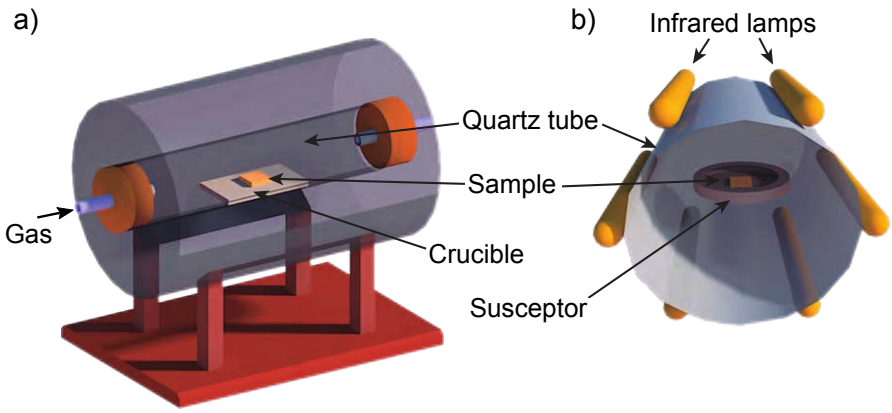

FIGURE 3.2: Schematic representation of the rapid thermal annealing (RTA) furnance used in this work, amongst others, to grow YBCO films through the T - and P_{O2} - route. Modified from [102].

Crystallization is carried out with several in-house furnaces and one setup that was specifically developed to perform *in-situ* growth analysis with synchrotron radiation. A detailed description of the X-ray transparent furnace and experimental setup used at the synchrotron facility is given in 3.6. Relevant experimental conditions of each route are summarized in tab.3.2. The highest heating ramps, reaching $60\,°C \cdot s^{-1}$, were realized with a **R**apid **T**hermal **A**nnealing (**RTA**) furnance, model AS-Micro fabricated by *Annealsys*

and located in the cleanroom facility of ICMAB (Fig. 3.2). The device uses infrared radiation to reach final temperatures up to 1250 °C at maximum rates of 250 °C · s^{-1}. Samples are placed on a SiC-coated graphite susceptor inside a quartz tube and illuminated laterally. Temperatures are read and controlled with a thermocouple located inside the SiC - susceptor and a fast digital PID-controller unit.

	dT/dt [°C · s^{-1}]	T_G [°C]	P_{O2}(I) [bar]	P_{O2}(II) [bar]	gas flow [L/min]
***T*-route**	0.4 - 60	770 - 880	10^{-4} - 10^{-2}	-	0.6/2
$P_{O2}(BaCu_2O_2)$	0.4 - 20	770 - 840	$\sim 10^{-5}$	10^{-4} - 10^{-2}	2
$P_{O2}(Cu)$	0.4 - 5	750 - 840	10^{-8} - 10^{-7}	10^{-4} - 10^{-2}	0.1/0.5

TABLE 3.2: Main growth parameters explored with T-/$P_{O2}(BaCu_2O_2)$-/$P_{O2}(Cu)$-route: Samples are heated with a ramp dT/dt to a growth temperature T_G. Initial and final P_{O2} pressures (I) and (II) are shown, as well as the gas flow rates. Explored ranges are denoted as $x_1 - x_2$, distinct values as x_1/x_2. A total pressure of 1 bar is used in the T - route; $P_{tot} = 5 \cdot P_{O2}$ in both P_{O2} - routes.

All other in-house furnaces, apart from the *in-situ* XRD setup, use a conventional tubular design with resistive heating. Here, samples are placed on a ceramic crucible inside a quartz-tube in the center of the furnace. A temperature calibration is carried out periodically to ensure reproducible thermal profiles.

3.1.4 3rd heat treatment: Oxygenation

Oxygen incorporation into the YBCO crystal structure is key to reaching the superconducting state with high critical temperatures (T_c) and critical current densities (J_c) [31, 103, 104]. After growth, YBCO exhibits a weak orthorhombic structure with a T_c close to 60 K due to the poor occupation of CuO chains by oxygen atoms. Through a separate thermal treatment, which is referred to as oxygenation heat treatment, the sample is exposed to a high oxygen flow at increased temperatures to induce oxygen in-diffusion into the crystal structure.

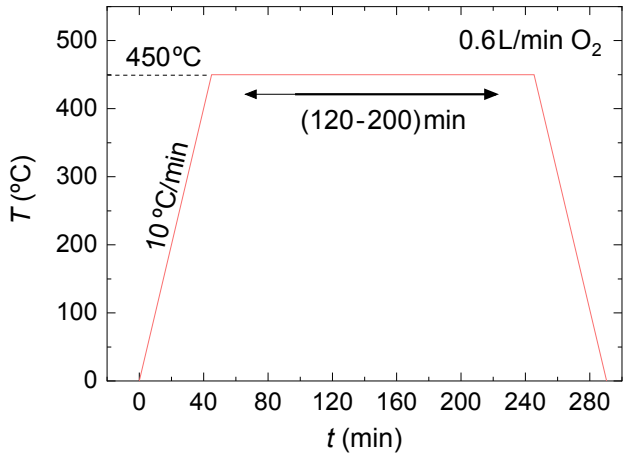

FIGURE 3.3: Standard oxygenation profile for TLAG films. A tubular furnace is used for thermal treatment under 0.6 l/min of oxygen flow.

The doctoral thesis of A.Stangl was devoted to studying oxygen exchange kinetics in YBCO [105]. Fluorine free based YBCO films were found to have reduced porosity as compared to the conventional TFA-MOD process. The densified microstructure was initially assumed to be an obstacle in reaching the optimally doped state of YBCO after growth. *In-situ* **e**lectrical **c**onductivity **r**elaxation (**ECR**) measurements during thermal treatment at 450 °C and an oxygen flow of 0.6 L/min were carried out by A.Stangl to define the dwell time needed to reach highest conductance for a TLAG film. It was found that the same thermal profile as applied to TFA films, as shown in Fig. 3.3, was also suitable for YBCO grown through the TLAG process. Therefore, we could conclude that oxygen is incorporated through defects such as twin boundaries and that film porosity is not a requirement.
The ECR measurements were carried out with one exemplary TLAG film, 90 nm in thickness, grown through the P_{O2}-route. In this thesis we further evaluate the doping state of YBCO and oxygen incorporation into the films via temperature dependent electrical measurements, Hall-effect measurements and XRD for structural analysis (6.1.3).

3.2 Electromagnetic characterization

Inductive measurements were carried out in collaboration with Dr. B.Bozzo, the technician in charge of the low temperature laboratory at ICMAB. A *Quantum Design MPMS XL-7 SQUID* DC magnetometer was used to probe the electromagnetic response of samples at low temperatures. The device is equipped

with a vacuum cryostat and a superconducting coil allowing to sweep fields and temperatures in the range of 0 - 7 T and 1.9 - 400 K, respectively. A magnetic field uniformity with less than 0.01% error is reached in the probed area. The SQUID magnetometer allows to assess sample characteristics, such as critical temperatures T_c and critical current density $J_c(\mu_0 H, T)$ and probe the state of electromagnetic granularity in a quick, non-destructive manner. Grown and oxygenated YBCO films (see 3.1.3 and 3.1.4) are placed perpendicularly to the applied magnetic field of a superconducting magnet. A group of pick-up coils is aligned in the axial direction of the applied field to probe magnetic flux variations according to Faraday's law of induction.
Probe centering and measurement of the magnetic response is carried out through the so called *Reciprocating Sample Option* (RSO), which correlates a periodical sample movement with the current variation induced in the pick-up coils. That way, the Joshepson-Junction based detection system reaches sensitivity in measuring magnetic moments down to 10^{-9} Am^2 (10^{-6} emu) [106]. Each measurement performed in this thesis starts with the cooling of the YBCO film in zero field (ZFC). A brief introduction into the measurement options that are employed when the sample reaches temperatures below T_c is given in the following.

3.2.1 Determination of T_c

Critical temperature measurements are carried out by cooling the sample to typically 20-50 K and applying a small DC magnetic field of ∼200 mT. Such small fields are sufficient to drive the sample into its Meissner state and induce a magnetic moment high enough to be detected by the pick-up coils. The SC layer acts as perfect diamagnet that fully repels the outer magnetic field. While the diamagnetic response is recorded, the sample is warmed up above its transition temperature at a rate of 0.5 °C/min (see Fig. 3.4a)). Tc is defined at the onset where the diamagnetic response if fully suppressed and the material enters its normal state. Additionally, the transition width ΔT_c can be defined as a window where the magnetic moment (m) drops from 90% to 10% of its extrapolated value at 0K (m_0).

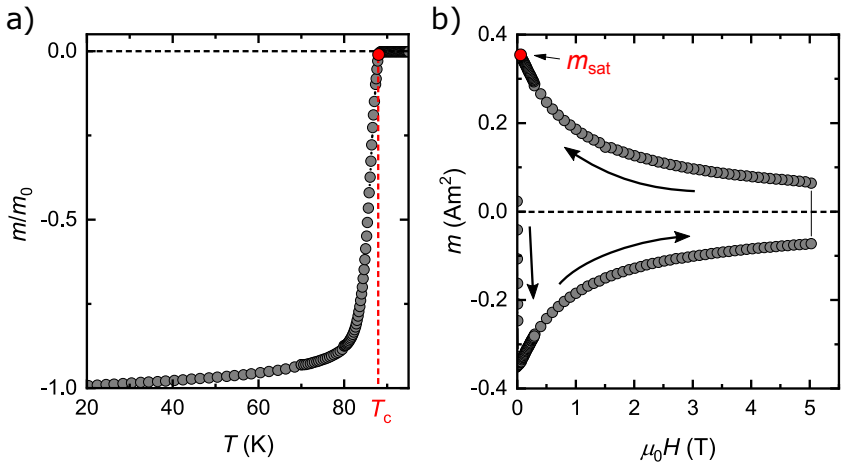

FIGURE 3.4: Exemplary DC magnetization measurements with a SQUID device. After a ZFC, the sample is a) cooled down to 20 K to measure the critical temperature T_c. A DC field of 200 mT is applied to track the diamagnetic response in Meissner state during heating at 0.5 °C/min. The onset T_c is marked with a dashed red line. b) Magnetization measurement at 5 K to obtain J_c after cycling the applied magnetic field to 5 T to reach remanent, saturated magnetization (marked at zero applied field).

3.2.2 Determination of $J_c(\mu_0 H, T)$

As introduced in 2.1.3, the bean critical state model allows to relate the induced saturated magnetization m_{sat} of a film to its critical current density J_c [15]. This allows, taking into account the magnetic field and temperature ranges mentioned above, to investigate the superconducting critical surface $J_c(\mu_0 H, T)$ with the magnetic field parallel to the substrate surface, $H//c$.
An exemplary magnetization measurement is shown in Fig. 3.4b): After a ZFC to 5 K, the temperature is stabilized and the magnetic field ramped to magnetize the sample. When the field is decreased to zero, trapped flux lines create a field gradient resulting in a remanent magnetization. If the upper field value is high enough for flux lines to enter and saturate the entire sample volume ($H \gg 2H^*$, as explained in 2.1.3), the remaining sample magnetization will reach its saturation value. In the ideal case when the YBCO is grown on non-magnetic substrates, upper and lower magnetization branch are symmetrical and can be used to calculate the width of the hysteresis loop according to

$$\Delta M = \frac{m(\mu_0 H \uparrow) - m(\mu_0 H \downarrow)}{2} \propto J_c \tag{3.2}$$

The corresponding critical current density can then be derived using expression 2.8. As the sample magnetic moment is permanently tracked with the RSO measurement configuration, temperature and magnetic field sweeps can be carried out to study characteristics of the critical surface, $J_c(\mu_0 H, T)$.
The SQUID setup is furthermore used to perform studies on films that suffer a diminishment in the percolating critical current density. For TLAG grown films, such J_c reduction could be successfully attributed to granularity effects arising from secondary phase segregation, uncovered film areas or unfavourable conditions for heteroepitaxial nucleation (chapter 6). The technique employed to study granularity contributions is based on previous work done in the SUMAN group by A.Palau et al. and will be introduced in 6.1.5 [107–109].
The measurement options mentioned above serve as a powerful, non-invasive tool to obtain first insights into film quality and SC performance. Throughout this thesis, inductive measurements are used to complement other non-invasive characterization techniques (such X-ray diffraction and Van der Pauw measurements) and categorize samples for deeper electrical transport studies as introduced below.

3.3 Micropatterning

Low-temperature electrical transport measurements are carried out to study the vortex pinning performance of grown films (Chapter 7). To extract information about pinning behaviour, an electric field is applied to the grown layer, high enough to induce a voltage drop that is associated with vortex movement. CSD grown YBCO films can typically sustain applied current densities in the range of 1 - 5 MA·cm^{-2} at 77 K without generating a voltage drop. A film of 250 nm in thickness with a total cross section of 5 mm x 250 nm could hence carry 10 - 60 A at 77 K. To avoid Joule heating effects, such high currents can be applied through pulsed current sources [110]. Experimental setups are then usually restricted in angular accessible range, applied magnetic fields and automation/throughput.
More commonly used, as in this thesis, are commercially available **P**hysical **P**roperty **M**easurement **S**ystems (**PPMS**) that allow a broad temperature, magnetic field and angular characterization but are restricted to a maximum current range of 0.5 - 2 A (depending on the wiring of the accessory equipment).[3] The approach that is then being followed is to narrow down the cross

[3] See 3.4.1 for more information.

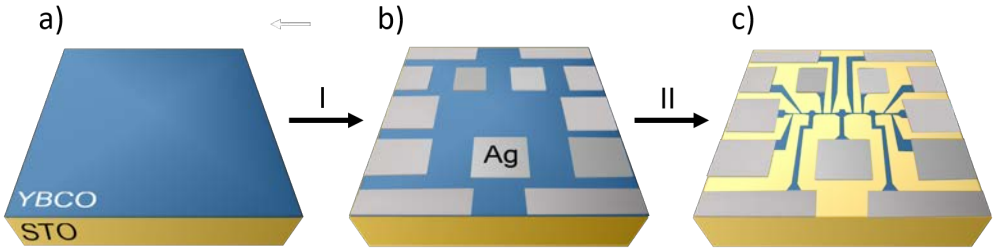

FIGURE 3.5: Succession of micropatterning steps: a) An as-grown YBCO film is prepared for silver contact deposition. Areas to be covered with Ag are exposed through use of photolithography. b) Contact material is deposited via DC-magnetron sputtering with a TSST system. (c) A photolithography step followed by chemical etching enables to transfer a geometry suitable for critical current measurements.

section to a bridge of typically several tenths of µm in width by means of patterning and etching techniques that will be discussed here (shown schematically in Fig. 3.5).
Most of the preparation of an as-grown film for electrical transport measurements was carried out in the in-house cleanroom facility at ICMAB. The first essential step of the process is to obtain electrical contacts with low interface resistivity

$$\rho_c = R_c \cdot A_c \tag{3.3}$$

to minimize Joule heating effects. Here, R_c and A_c denote contact resistance and contact surface area, respectively. J.W. Ekin et al. showed that ρ_c can be reduced to $10^{-10}\,\Omega{\cdot}cm^2$ through use of the noble metals Ag and Au and a post-annealing procedure after contact deposition by magnetron sputtering [111]. The same approach was adapted here to reach a contact resistance of $10^{-6} - 10^{-7}\,\Omega{\cdot}cm^2$, sufficient to suppress Joule heating in the applied range of currents. The processing steps involved to reach the final geometry, as depicted in Fig. 3.5, can be summarized to:

1. Photolithography procedure: Photolithography steps mentioned below are carried out with a *Durham Magneto Optics Ltd.* micro-writer setup. The sample surface is first cleaned with acetone and covered with a positive photoresist (*Microposit(TM) S1813(TM)*) through spin-coating at 5000 rpm for 25 s, followed by curing at 70 °C for 1 min. The micro-writer uses a 385 nm laser light-source that operates at a spatial resolution of 1-5 µm. The area to be laser-drawn is defined using a digital software of the micro-writer system. After exposition, the sample is stirred in a developer solution (*Microposit MF 319*) for 1 min resulting in the removal of photoresist in the illuminated

regions.

2. Contact preparation: A 300-500 nm Ag layer is deposited by means of a TSST sputter system in the clean room facility. The deposition takes place in 0.1 mbar argon atmosphere using target-to-sample voltages of 350-400 V. Photolithography is used to define exact contact location and area dimensions. Ag is hence deposited on a surface partially protected by the photoactive compound. The deposition is followed by a 5-10 s lift-off through ultrasonic cleaning in acetone. Parts that were initially covered by Ag on top of photoresist are removed, leaving behind the geometry shown in Fig. 3.5b). To reach the low contact resistances according to [111], the sample undergoes a thermal treatment at 450 °C for 1 h in oxygen flow, as depicted in Fig. 3.6. The pocedure of contact preparation was refined for TFA-MOD grown films by several PhD students of the SUMAN group and adapted here. Also for TLAG grown films, SQUID measurements were performed after contact preparation showing no degradation of superconducting properties, such as self-field J_c and T_c values.

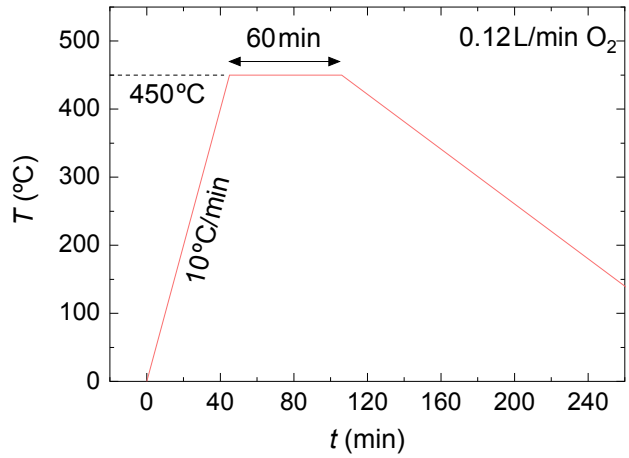

FIGURE 3.6: Thermal treatment of deposited Ag contacts to minimize interface resistivity according to [111].

3. Bridge patterning: To achieve the desired cross section reduction of the probed YBCO, current leads and bridges have to be defined in between the deposited Ag contacts (as depicted in Fig. 3.5c)). Photolithography is once again employed, this time to expose YBCO regions for chemical etching. A digital pattern is aligned and drawn using the known position of the existent Ag pads. After exposition and partial removal of the photoresist, chemical

etching is carried out either in a 1:10 or 1:100 diluted H_3PO_4:H_2O acid solution. The sample is then stirred for 20-30 s until the underlying, transparent substrate is exposed. The remaining photoresist is removed through an ultrasonic bath in acetone. An exemplary YBCO bridge after chemical etching is displayed in Fig. 3.7. Typical bridge dimensions lie in the range of 10-60 µm in width and 200 µm in length. The bridge length is defined by the voltage lead distance. Current leads are patterned wider to make sure the voltage drop is induced in the probed bridge, hence, Joule heating is avoided at the current injection points. After patterning, the sample thickness can be estimated through profilometry along one of the bridge edges.
Patterned samples in their final geometry, as illustrated in Fig. 3.5c), are placed and connected to a commercially available electrical probe (PUCK) that can then be addressed through a PPMS unit.

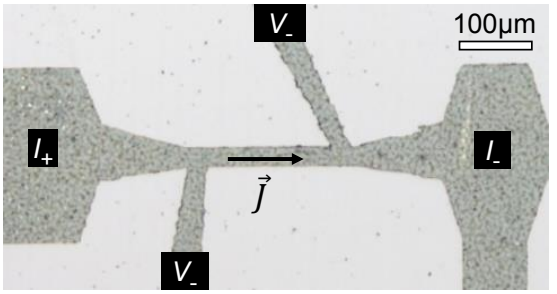

FIGURE 3.7: Optical microscope image of a YBCO bridge after chemical etching. Current/voltage leads as well as the applied current direction are labeled.

3.4 Electrical characterization

Electrical transport measurements were carried out in two main configurations, both using a 4-point probe method to diminish lead and contact resistance contributions. Measurements in Van der Pauw geometry are carried out to probe non-invasively the resistivity and Hall carrier concentration of as-grown films (see 3.4.2) while four terminal sensing on patterned bridges (Fig.3.7) serves to study pinning performance of selected films (discussed in 3.4.4). Both techniques are realised in a PPMS, as introduced below.

3.4.1 Physical property measurement system (PPMS)

A PPMS device supplied by *Quantum Design* is used for the measurements described in 3.4.2 and 3.4.4. The setup includes a vacuum-based helium

cryostat and a longitudinal solenoid magnet that is remotely controlled in a temperature-field range of 1.9 - 400 K and ±9 T, respectively.
Two types of PUCK holders are used to connect a sample geometry to the DC/AC current sources of the PPMS unit: A cylindrical PUCK that is plugged directly into a pin-holder at the bottom of the PPMS and a flat PUCK that serves to explore angular dependencies with a horizontal rotator rod. The former can sustain current values up to 2 A, reaching the upper limit of the current sources, while the latter cannot surpass 500 mA due to the finer external wiring of the rotator. The stationary configuration of the cylindrical PUCK is suitable for studies carried out without magnetic field or those that require only application of $H//c$.[4] This option is primarily chosen for measurements outlined in 3.4.3. The horizontal rotator, however, is mostly used to explore angular pinning characteristics of patterned samples.

3.4.2 Van der Pauw method

Grown and oxygenated films are characterised non-destructively by means of the Van der Pauw technique, which was originally developed to probe resistivity (ρ) and Hall coefficients (R_H) of arbitrarily shaped samples [112]. The derivation is based on the prerequisites that

1. The probed geometry is flat and uniform in thickness
2. No isolated holes are present
3. Contacts are small and set at the boundary

For disc-shaped geometries an error propagation on ρ and R_H can be made if the contacts have finite dimension or are not placed at the circumference of the probed area [112]. Sufficiently small errors, falling below 1% and 7% for ρ and R_H, respectively, can be obtained if the contact-to-border distance and contact size L is one order of magnitude smaller than the disc diameter D.
Van der Pauw derives expressions for the physical measures through a theorem that relates the potential differences measured along the probed geometry according to

$$\exp\left(-\frac{\pi d}{\rho}R_{AB,CD}\right)+\exp\left(-\frac{\pi d}{\rho}R_{BC,DA}\right)=1 \tag{3.4}$$

Here, d stands for the films thickness, ρ is the material resistivity and $R_{AB,CD}$ and $R_{BC,DA}$ denote the resistances measured through permutation of current

[4] Perpendicular to the substrate surface, parallel to the c-axis lattice parameter of YBCO.

direction and voltage read

$$R_{\mathrm{AB,CD}} = \frac{V_{\mathrm{D}} - V_{\mathrm{C}}}{I_{\mathrm{AB}}} \tag{3.5a}$$

$$R_{\mathrm{BC,DA}} = \frac{V_{\mathrm{A}} - V_{\mathrm{D}}}{I_{\mathrm{BC}}} \tag{3.5b}$$

in a configuration as shown in the upper part of Fig. 3.8a). For instance, the resistance $R_{\mathrm{AB,CD}}$ is measured by driving a current from site A to B while measuring the voltage drop between contacts C and D. A solution to eq. 3.4 is given by

$$\rho = \frac{\pi d}{\ln 2} \frac{(R_{\mathrm{AB,CD}} + R_{\mathrm{BC,DA}})}{2} f\left[\frac{R_{\mathrm{AB,CD}}}{R_{\mathrm{BC,DA}}}\right] \tag{3.6}$$

with f being a dimensionless unit that solely depends on the resistance ratio $s = R_{\mathrm{AB,CD}}/R_{\mathrm{BC,DA}}$. A tailor expansion of f for the ideal case that the resistances are similar, $s \approx 1$, is given by

$$f \approx 1 - \left(\frac{s-1}{s+1}\right)^2 \frac{\ln 2}{2} - \left(\frac{s-1}{s+1}\right)^4 \left(\frac{(\ln 2)^2}{4} - \frac{(\ln 2)^3}{12}\right) \tag{3.7}$$

In this work, Van der Pauw measurements are performed on samples of squared shape as depicted schematically in Fig. 3.8b) and c). To obtain resisitivity values, the voltage drops in eq. 3.5a and 3.5b are measured opposite to the current direction (Fig. 3.8b)). This geometry changes in Hall configuration, where the voltage is measured transversal to the applied current direction (Fig. 3.8c)). The current is hence applied and voltage read along the sample diagonals. A magnetic field is applied perpendicular to the current flow resulting in a Lorentz force $\vec{F}_{\mathrm{L}} = q \cdot \vec{v} \times \vec{B}$ on the charge carriers, $\vec{v}$ being their propagation velocity. This results in charge separation until an electric field builds up, high enough to oppose $\vec{F}_{\mathrm{L}}$. The balance of forces yields

$$E_{\mathrm{H}} = \frac{j}{n_{\mathrm{H}}\, q} B \tag{3.8}$$

with q, j, E_{H} and n_{H} standing for the elementary charge, applied current density, Hall electric field and Hall charge carrier density, respectively. The expression can be rewritten to

$$U_{\mathrm{H}} = R_{\mathrm{H}} \frac{I_{\mathrm{applied}}}{d} B \tag{3.9}$$

considering $E_{\mathrm{H}} = U_{\mathrm{H}}/w$ and $I_{\mathrm{applied}} = j \cdot wd$, w being the width of the current cross section. Equation 3.9 describes the Hall effect, formerly derived by

E.Hall [113]. The strength of the applied magnetic field translates into a voltage drop U_H through the constant Hall coefficient $R_H = 1/n_H q$. Given the fact that all quantities in eq. 3.9 are either known or can be measured through the Hall configuration in Fig. 3.8c), the Hall coefficient and with that the charge carrier density, n_H, can be determined through a magnetic field sweep at constant temperature and applied current.
The exact technical realisation of resistivity and Hall measurements as well as the procedure to deduce characteristic physical parameters is discussed in the following.

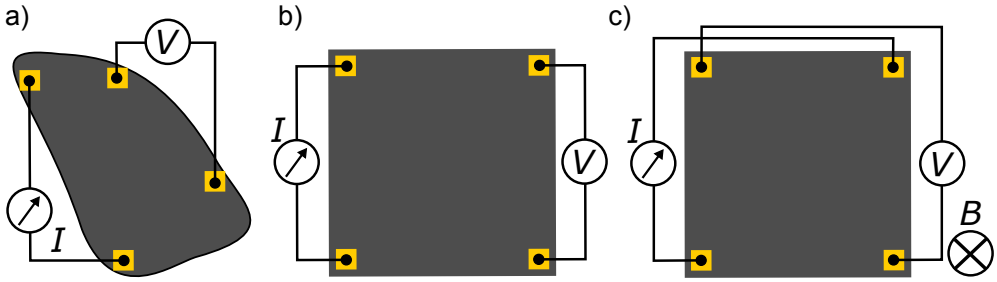

FIGURE 3.8: Schematic respresentation of the Van der Pauw geometry: Resistivity configuration on a a) sample of arbitrary shape and b) square shape as used in this project. (c) Hall effect configuration with the applied magnetic field pointing perpendicular to the sample plane. All geometries are contacted at the sample border.

3.4.3 Hall and resistivity measurements

Measurements in Van der Pauw configuration are carried out using a PPMS of the low-temperature laboratory at ICMAB (3.4.1). Samples are first glued with a varnish of high thermal conductivity on top of a PPMS PUCK holder (see 3.4.1). The geometry edges (Fig. 3.8a)) are then connected through Ag wires to the conducting pads of the PUCK. Samples are bond manually by placing a droplet of conducting silver paint at each sample-to-wire interface. Although Ag paint yields higher contact resistances than sputter deposited contacts, a robust signal in Van der Pauw geometry could be obtained with this approach.
To switch current and voltage directions, according to eq. 3.5a and 3.5b, the pins of the PUCK need to be reconfigured at each measurement point. This is done automatically with a custom made switch-unit that is interconnected between PPMS source and PUCK.
Exemplary data obtained with the two configurations of Fig.3.8b) and c) is

shown in Fig. 3.9: Resistivity is probed as a function of temperature to primarily obtain T_c and ΔT_c values (Fig. 3.9a)).[5] Transition temperatures are determined following the maximum derivative criterion (shown as $T_{c,deriv}$ in the bottom part of the graph). It provides a simplified way to attribute sample inhomogeneities to multiple-peak appearances in the $d\rho/dT$ curve [114].
The approach to estimate the transition width, ΔT_c, is adopted from [115]. Here, a linear behaviour of the form

$$\rho(T) = \rho_0 + c \cdot T \tag{3.10}$$

is fitted to $\rho(T)$ in a range of 150-300 K. The intercept window of the data with 90% and 10% of the linear fit is then defined as ΔT_c (shown in the inset of Fig. 3.9a). In addition, room temperature and 0 K resistivities are extracted from eq. 3.10.

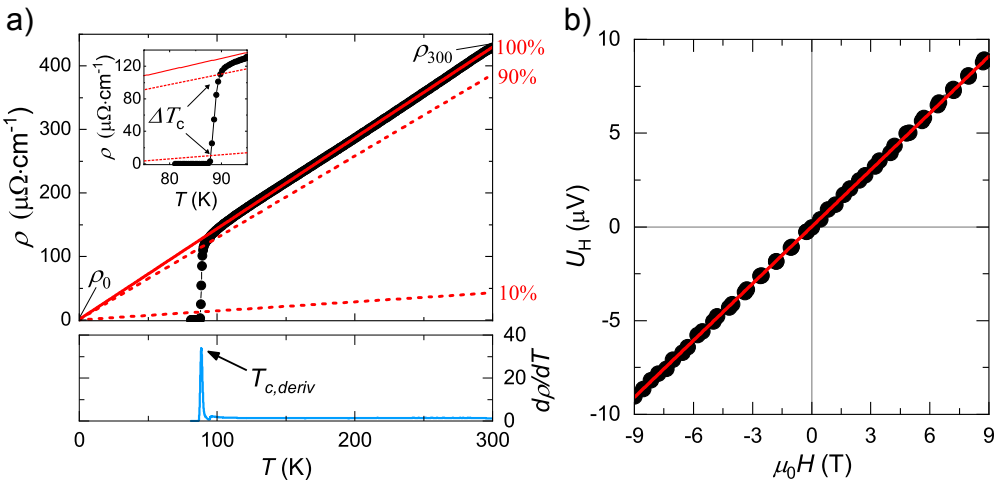

FIGURE 3.9: Measurements performed in Van der Pauw geometry to obtain the a) temperature dependent resistivity behaviour: T_c values are determined through the maximum derivative criteria (blue curve); the transition width, ΔT_c , is defined through normal state resistivity decrease from 90% to 10%. Room temperature and 0 K resistivity are extracted through linear fitting of $\rho(T)$ from 150-300K b) Hall coefficient R_H through linear fitting of the Hall voltage $U_H(B)$ at room temperature

The normal-state temperature range between 95-300 K is typically scanned at a high ramp of 5 °C/min. To ensure temperature stabilization around T_c, however, the ramp is reduced to 0.5 °C/min. The reduced heating/cooling rate around the transition is significant to reduce systematic errors on the T_c

[5] Resistivity values are obtained using eq. 3.6.

values obtained.[6]
Hall measurements are carried out at room temperature to extract the carrier density $n_{H,300K}$ from a linear fit of the Hall voltage (Fig. 3.9b)). The voltage response in eq. 3.9 is obtained by averaging two different contact configurations along the full field range of ± 9 T and through use of an alternating applied current. That way, offset contributions resulting, for instance, from contact misalignment and sample inhomogeneities can be averaged out.

3.4.4 Critical current measurements

Samples to be investigated in their pinning performance are micropatterned to a 4-point bar geometry, as described in 3.3. Two contacts are used to drive a current along the YBCO ab-planes of any patterned bridge while two others are separated by a known distance of 200 µm to sense the voltage drop. The geometry is shown in Fig. 3.10a).
The current-voltage characteristics can be fully controlled and monitored through the PPMS software. Samples are either mounted in stationary configuration or on a rotator arm with a step resolution of 0.01°. In both cases, magnetic fields are applied in maximum Lorentz force configuration, pointing perpendicular to the current direction at all angles θ, defined as the angle enclosed by the magnetic field and YBCO c-axis direction. Two types of measurements are carried out with the device in Fig. 3.10a), resistance measurements similar to those obtained in Van der Pauw geometry and critical current measurements. In the former case, a small AC-current of 0.01 mA at 33 Hz is applied to deduce the resistivity according to

$$\rho = \frac{A_{\text{cross}}}{l} R \tag{3.11}$$

where l and A_{cross} denote length and cross-sectional area of the bridge and R stands for the measured resistance. This measurement option is either used to probe transition temperatures of patterned tracks before a deeper investigation below the critical point or in combination with applied magnetic fields to obtain irreversibility lines.
In case of critical current measurements, the current is ramped up to a setpoint value I_{max} through a predefined number of pulses. A voltage criterion is preset to avoid track burning, so that the current increase is shut down as soon as the threshhold voltage is overcome. An exemplary IV-curve, with the voltage translated into an electric field along the track, E, is shown in Fig. 3.10b). The curve exhibits an exponential increase of the electric field with current,

[6] See Fig. A.1 for more information.

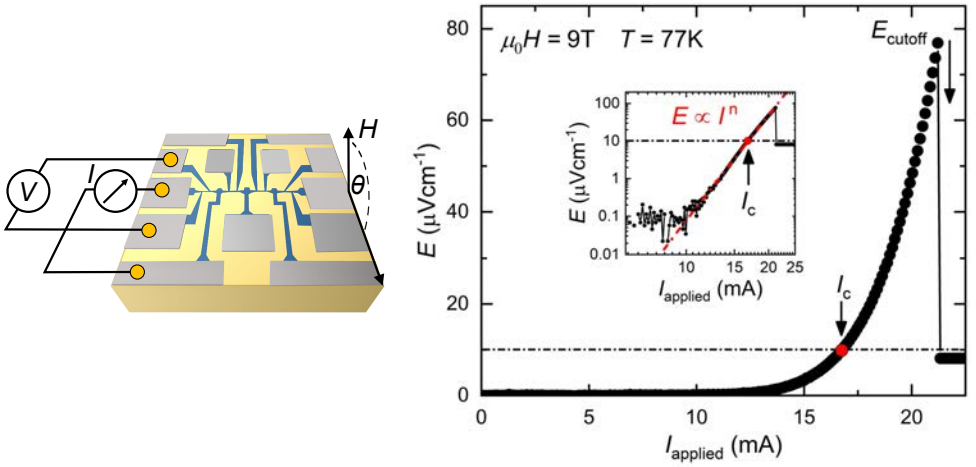

FIGURE 3.10: a) Experimental scheme of a patterned sample to carry out IV measurements. b) An exemplary curve is obtained at 9 T and 77 K. Critical current I_c and cutoff electrical field E_{cutoff} are denoted. The inset shows a more accurate determination of I_c and the n-value through linear fitting (red line) in double-logarithmic scale.

following $E \propto I^n$.[7] The critical current, I_c, is defined as the current needed to produce an electric field of 10 μmV/cm (marked as red point in the graph). A more robust approach, being less affected by noise and Joule heating, is to obtain I_c and n-values through linear fitting of the IV-curve in double-logarithmic scale (shown in the inset of Fig. 3.10b)). Here, the curve is fitted from a field value of 50 μV/cm until the cutoff is reached. The n-value and I_c are then deduced from the linear slope and the 10 μV/cm electric field criterion, respectively. IV-curves are measured to obtain information about the critical surface $J_c(\mu_0 H, T, \theta)$. Each measurement point requires a stabilized magnetic field and temperature, especially given the fact that the measured bridge is driven into a resistive regime with every IV-curve.

3.5 Structural characterization

A Bruker D8 Advance and D8 Discover diffractometer were used to perform structure measurements on TLAG films. The former of the two machines is equipped with a **G**eneral **A**rea **D**etector **D**iffraction **S**ystem and will hereafter be simply referred to as **GADDS**. Both diffractometers opperate with a copper source that has three characteristic emission lines, CuKα_1, CuKα_2 and CuKβ

[7] N-values are typically related to vortex creep characteristics [116].

corresponding to $\lambda = 1.5406$ Å, 1.5418 Å and 1.3922 Å, respectively.
Due to the wide angular range detectable in GAADS (up to 30° in 2θ and 60° in χ), it is a widely used technique to quickly probe the texture quality of films, orientation of secondary phases and especially for phase identification [76, 117]. Here, GAADS measurements were performed exclusively to probe the orientation of crystallographically aligned phases such as nanoparticles from colloidal solutions or YBCO ab-oriented grains. A brief introduction and applicability of the technique will be given in the discussion of results in Chapter 6. Most of the characterization in this thesis, however, was done with the newly acquired D8 Discover diffractometer. A discussion on the utilized measurement options and extracted structural information will be given in the following.

3.5.1 Bruker D8 Discover X-ray diffractometer

The Bruker D8 Discover is a high resolution X-ray setup that enables a fast exchange of auxiliary equipment and measurement options. Each combination of incoming/diffracted beam optics, detector operational mode and scanning geometries were initially tested to adjust for a sufficiently high resolution at reduced integration times.

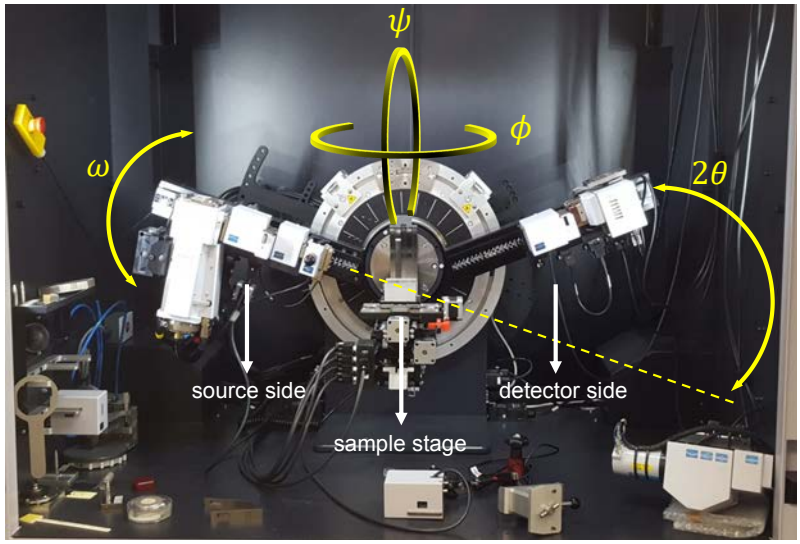

FIGURE 3.11: Bruker D8 Discover diffractometer: Main degrees of freedom are depicted in yellow. White arrows indicate source/detector side and sample stage.

The setup, shown in Fig. 3.11, consists of a vertical goniometer that enables the rotation of incoming and diffracted beam arms around the sample stage, mounted in the center.
The main accessible angles are depicted with respect to the sample stage. Incoming and diffracted beam angles, ω and θ, are accessed via motorized arm movements while the sample rotational angles, χ and ϕ, are addressed through tilt and rotation of the stage. The full setup can be divided into three parts:

1. Source side: The incoming beam arm is equipped with an X-ray twist-tube that is operated at a voltage of 40 kV and 40 mA of current. The tube can be easily rotated allowing to allocate beam intensity in point- or line-focus. While most measurements are done in line-focus to increase the illuminated sample area it is worth switching to point-focus when operating at high angles of χ (as the sample moves from a fully horizontal position at $\chi = 0°$ to a vertical one at $\chi = 90°$). According to the chosen beam focus option, additional slits and collimators can be used to confine the beam and reduce divergence. The incoming beam arm contains additional variable slot holders for modules that further affect the beam properties: A Göbel mirror is used to increase beam intensity while further decreasing the divergence. This is done through a curved multilayer X-ray mirror that parallelizes the incident beam [118]. The Göbel mirror is typically mounted in combination with a double-bounce Ge(220) monochromator to reduce the contribution of the CuKα_2 and CuKβ radiation.

2. Sample stage: Samples are mounted on a glass substrate giving an amorphous scattering background. Up to eight samples can be placed at once and addressed through XYZ movement of the stage. Additionally, a tilted stage is available that allows sample inclination in two degrees of freedom. This option is particularly beneficial when working at $\chi = 90°$, enabling to obtain direct in-plane structural information [119, 120].

3. Detector side: For all measurement geometries, discussed in the following, a motorized detector slit module together with a 1-dimensional *LynxEye* detector are used. The detector achieves high angular resolution while decreasing data acquisition times due to its 192 silicon-based detector strips that simultaneously attribute scattered intensity to a whole range of 2θ values. Each strip has a spatial resolution of 75 µm, which translates into a total angular field view of 1.93 °. The detector opening can be narrowed down to any number of operating strips to increase resolution.

3.5.2 Scanning geometries

The components listed in 3.5.1 serve as a powerful technique to investigate lattice parameters, strain induced lattice deformations, secondary phases and the texture-quality of epitaxial films.
X-ray diffraction is based on the constructive interference of a monochromatic wave being scattered at different crystallographic planes of a crystal. The incoming wave encloses an angle θ with a set of parallel lying planes and picks up a phase depending on the length of the optical path it runs through. Known as Bragg's law [121], the condition for constructive interference is

$$2d_{hkl} \sin\theta = n\lambda \tag{3.12}$$

where d_{hkl} denotes the interplanar spacing of crystallographic planes with miller indices (hkl) and $n\lambda$ is the optical path difference, n being an integer number and λ the wavelength. A crystal can be regarded as a three-dimensional grating that produces such interference conditions for various sets of planes. Typically, diffraction conditions are expressed through a Fourier transformation of the *real* space lattice, referred to as *reciprocal* space representation. While an introduction into the main concepts exceeds the scope of this thesis, a discussion of main scanning geometries and practices to extract structural information will be given here.[8]
Three geometries are used to probe the reciprocal space in different directions and relate the position and broadening of diffraction spots to the real lattice. Exemplary measurements are shown in Fig. 3.12. The sample exhibits primarily out-of-plane texture, however, some misoriented grains are also present. In $\theta - 2\theta$ geometry, short **T2T**, incoming and diffracted beam arm enclose the same angle θ with respect to the (00l) planes of YBCO.[9] The movement of both arms is then performed at constant velocity to measure exclusively along the out-of-plane direction (lower left sketch in Fig. 3.12).

[8] Please refer to the work of B.E.Warren [122], V.K. Pecharsky [123] and M.A.Moram et al. [120] for a general introduction to the subject.

[9] Although centering is carried out with respect to the (h00) planes of the substrate, the plane orientations coincide.

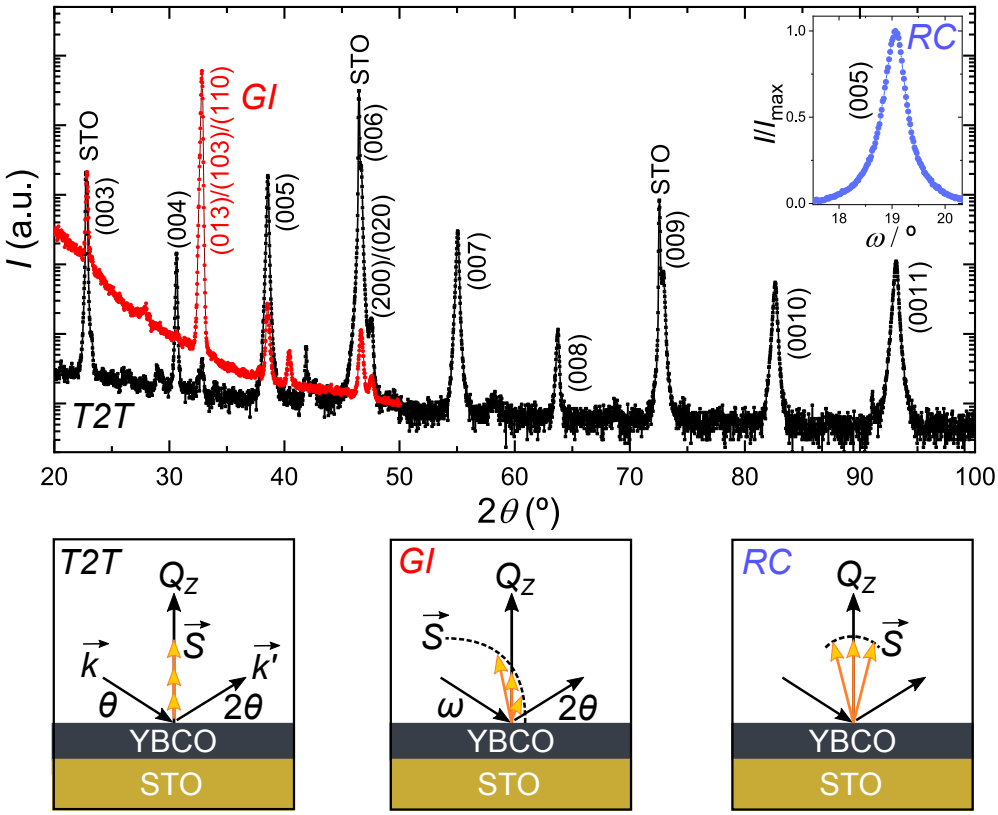

FIGURE 3.12: Most common XRD geometries performed with the Bruker D8 Discover diffractometer. Scans in $\theta - 2\theta$ (black line), grazing-incidence (red line) and rocking curve (blue line) geometry are shown in the upper graph. Illustrations of different probing directions are shown below.

The probing direction is defined by the vector

$$\vec{S} = \vec{k}' - \vec{k} \tag{3.13}$$

which corresponds to the momentum transfer of incidence and diffracted beam vectors $\vec{k}$ and $\vec{k}'$ [120]. Fig. 3.12 shows a T2T measurement over a 2θ range of 20 - 100 °. Note that the most intense peaks can be attributed to the (00l) and (h00) planes of YBCO and STO, respectively, with the whole intensity confined in a narrow region of the reciprocal space. The signal of randomly oriented phases, however, is strongly suppressed due to the spherical distribution of intensity in all directions (seen in the low intensity given by the (013), (103) and (110) plane).

To amplify the signal of misoriented phases, the **g**razing-**i**ncidence (**GI**) geometry is used. Here, a small incidence angle ω is fixed at 0.7 - 1° and the

detector arm driven through a range of 2θ values. That way, the illuminated sample area remains constant, other than in the T2T-geometry, where the probed volume is gradually reduced. In GI-geometry, the probing vector $\vec{S}$ moves along a curved path as depicted in the central sketch of Fig. 3.12, sensing mostly phases that have no distinct texture.[10] Plotted above the T2T pattern in Fig. 3.12, the GI scan shows a change in intensity distribution: (013)/(103)/(110) planes are amplified as compared to the (00l) peak family, resembling the peak proportions of a YBCO powder pattern [124]. **R**ocking-**c**urves (RC) are recorded to probe the out-of-plane orientation of epitaxially aligned grains (c-axis tilt). This is done by keeping the angle between source and detector arm fixed while scanning ω (shown for the (005) reflection in the inset of Fig. 3.12). The constant angle between both arms ensures that the Bragg condition in eq. 3.12 remains unchanged providing exclusively information on the misalignment angle of c-axis grains.

3.5.3 Lattice parameter determination

T2T measurements, introduced in 3.5.2, are used to determine the out-of-plane lattice parameter of YBCO. Oxygenated YBCO exhibits an orthorhombic structure with lattice spacing

$$\frac{1}{d_{hkl}^2} = \frac{h^2}{a^2} + \frac{k^2}{b^2} + \frac{l^2}{c^2} \tag{3.14}$$

where a, b and c denote the unit cell parameters. In principle, the knowledge of one single (00l) peak position would serve to determine the c-axis lattice constant by introducing $d_{00l} = c/l$ in eq. 3.12. However, the measure would be strongly affected by systematic errors such as sample misalignment, curvature and machine uncertainty.
A method was early developed by J.B. Nelson and D.P. Riley who showed that systematic errors are diminished at $\theta = 90°$ [125]. As such high diffraction angles are not accessible, an extrapolation function of the form

$$\frac{1}{2}\left(\frac{\cos^2(\theta)}{\sin(\theta)} + \frac{\cos^2(\theta)}{\theta}\right) \tag{3.15}$$

was proposed and shown to scale linearly with the lattice parameters determined through each peak position. An example of the Nelson-Riley method is shown in Fig. 3.13. High angle (00l) peaks with $l > 5$ are fitted by Lorentzian

[10] Depending on detector opening, beam divergence and the probed path trajectory, oriented phases can also contribute by coincidence. This can be avoided or tested through variation of the incidence angle ω or sample rotation along ϕ.

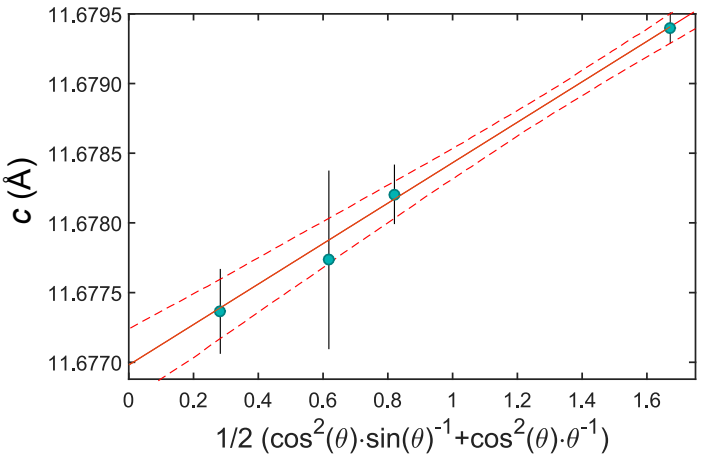

FIGURE 3.13: Nelson-Riley extrapolation of the c-axis lattice constant to $\theta = 90°$. Error bars are obtained from least-square fitting of (00l) peaks. Linear fit and uncertainty interval are represented by solid and dashed red lines, respectively.

peak profiles with linear background

$$f(x) = y_0 + b \cdot x + \frac{2A}{\pi} \frac{w}{4(x - x_c)^2 + w^2}. \tag{3.16}$$

T2T patterns are obtained after centering each sample on the substrate (200) Bragg reflection and calculation of an offset to a known reference value. The wrong knowledge of this reference will directly affect the measured peak positions of YBCO and propagate non-linearly with θ. Hence, reference peak positions were obtained through fine grinding of an $SrTiO_3$ and $LaAlO_3$ single crystalline substrate and Rietveld analysis of the powder pattern. The results are listed in table 3.3. The deviation of measured substrate peak positions to those in tab.3.3 are fitted with a third degree polynomial to obtain a correction function $\Delta_{\text{ref-meas}}(\theta)$.

Substrate	(100)	(200)	(300)	(400)	a (Å)
LAO	23.466	47.980	75.185	108.857	3.788
STO	22.758	46.482	72.584	104.222	3.904

TABLE 3.3: Substrate reference peak positions obtained through powder diffraction and Rietveld refinement. The peak positions are used to calculate a polynomial correction function.

The correction is applied to each fitted YBCO peak position (x_c value of eq. 3.16) to be included in the Nelson-Riley extrapolation. The final out-of-plane lattice constant of YBCO is then obtained from the axis intercept of the linear fit function in Fig. 3.13.

3.5.4 Nanostrain analysis

The broadening of Bragg reflections, as being probed in the symmetrical T2T configuration (see 3.5.2), is caused by finite crystallite sizes and local strain deviations, also known as nanostrain [117].[11] This information is convoluted in the integral breadth β_{total} of each peak, which, for the Lorentzian peak shape, adds up linearly according to

$$\beta_{\text{total}} = \beta_{\text{inst}} + \beta_{\text{g}} + \beta_{\epsilon} \tag{3.17}$$

with β_{inst}, β_{g} and β_{ϵ} standing for instrumental, crystallite size and strain contributions, respectively. The integral breadth is defined as the width of a rectangle having the peak height while comprising the total peak area (sketch in Fig. 3.14). Expressions for β_{g} and β_{ϵ} are given by the Scherrer equation [126] and the Stoke-Wilson relation [127]

$$\beta_{\text{g}} = \frac{K\lambda}{D \cdot \cos\theta} \tag{3.18a}$$

$$\beta_{\epsilon} = \epsilon \cdot \frac{\sin\theta}{\cos\theta} \tag{3.18b}$$

where D and ϵ stand for particle size and nanostrain. The constant K is a shape factor, typically in the range of 0.9-1 [128]. Equation 3.18a and 3.18a can be used to derive the Williamson-Hall relation

$$\beta_{\text{total}} \cdot \cos\theta = 4\epsilon \, \sin\theta + \frac{\lambda}{D} \tag{3.19}$$

which is routinely used in literature to obtain D and ϵ from a linear fit, as shown in Fig. 3.14 [129]. The approach involves fitting of YBCO (00l) reflections at high angles, where peak shapes are well described by Lorenzian profiles. Measured β values are corrected to account for instrumental broadening using a LaB6 specimen of single crystalline quality.

[11] Precisely speaking, the size refers to the length of a coherently scattering, crystallographic domain.

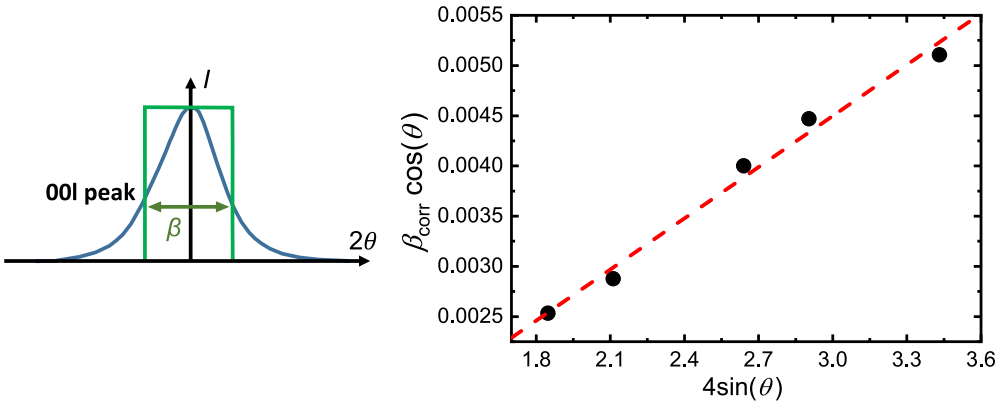

FIGURE 3.14: Exemplary peak profile showing the integral breadth, defined as peak area/I_{max} (left) and a Williamson Hall analysis carried out to extract crystallite sizes and nanostrain values (right).

3.6 *In-situ* growth experiments with synchrotron light

In order to validate TLAG as an ultra-fast, non-equilibrium growth approach, a profound study of intermediate reactions, crystallization kinetics and limitations had to be carried out. Initial quench studies of the crystallization step, performed by L.Soler, suggested that reactions take place on sub-second time scales [76]. It appeared beneficial to explore the phase diagram at increased heating ramps (several °C/s), in controlled gas atmospheres and through various P_{O2}-T paths (3.1.3). The high demands set through growth kinetics and experimental scheme could only be met with the high luminosity and advanced data acquisition tools given at a synchrotron facility. As a major part of this thesis is devoted to styding TLAG growth kinetics via synchrotron radiation, the technical implementations will be discussed here.

3.6.1 DiffAbs beamline: Experimental setup

In-situ growth experiments were carried out in three consecutive years in collaboration with Soleil Synchrotron, **DiffAbs** (**Diff**raction and **Abs**orption) beamline. DiffAbs is devoted to studying fast phase transitions by means of hard X-ray photons in the energy range of 3-23 keV. The beamline is equipped with a 6 axis diffractometer, several sample environments for thermal profiles in controlled atmospheres and multiple detectors (0D point and 2D CCD) compatible with ultra-fast data acquisition in the range of hundred milliseconds.

A number of preliminary tests was carried out with the local beamline contact Dr. C.Mocuta to find a setup configuration that covers a sufficient angular opening and increased signal-to-noise ratio at high acquisition rates. A summary of the experimental specifications and equipment provided by the beamline is given in Tab 3.4.

Energy E	18 keV
Energy resolution $\Delta E/E$	10^{-4}
Flux f	10^{12} ph/s
Beam size HxW	250 x 300 μm^2 (FWHM)
Beam divergence	0.24 x 3.5 $mrad^2$ (vert. x horiz.)
Data acquisition	0D point detector
	XPAD 2D area detector
Sample environment	Anton Paar
	DHS900/DHS1100

TABLE 3.4: *In-situ* measurement configurations and equipment used at the DiffAbs beamline, Soleil synchrotron.

An energy of 18 keV was adjusted through use of a reference STO single crystal with known lattice parameter. The energy is chosen in the upper limit of the available window to cover a broader range of recorded angles (see also 3.6.2) while ensuring sufficient separation of overlapping peaks. A zero-dimensional detector was used for substrate alignment and texture measurements and a two-dimensional **h**ybrid **p**ixel **a**rea **d**etector (**XPAD**) for *in-situ* tracking of the evolving phases during growth.
A commercially available domed heating stage (AntonPaar, DHS900) was mounted in first run experiments and later substituted by the newer model, DHS1100. Both heating stages allow rapid temperature increase at rates of several °C/s and operation in vacuum and controlled gas atmospheres, though the newer model accesses a wider temperature range up to 1100 °C instead of 900 °C. Fig. 3.15a) depicts the mounted setup including 2D detector, sample stage and incoming beam. The point detector, not shown here, is simultaneously mounted underneath the XPAD. The sample is fixed with elastic clamps on a heating plate made of aluminum nitride (Fig. 3.15a), inset) and covered with an X-ray transparent dome made of graphite, PEEK or aluminum with kapton windows. The diffractometer is operated through use of several independent motors that allow precise adjustments down to 0.001°.

All Eulerian coordinates that are accessible through motorized movements are depicted in yellow: (x, y, z) refers to translational motions of the sample stage, (φ, χ and ω) to the sample azimuth, elevation and incidence angle; 2θ represents the detector angle.

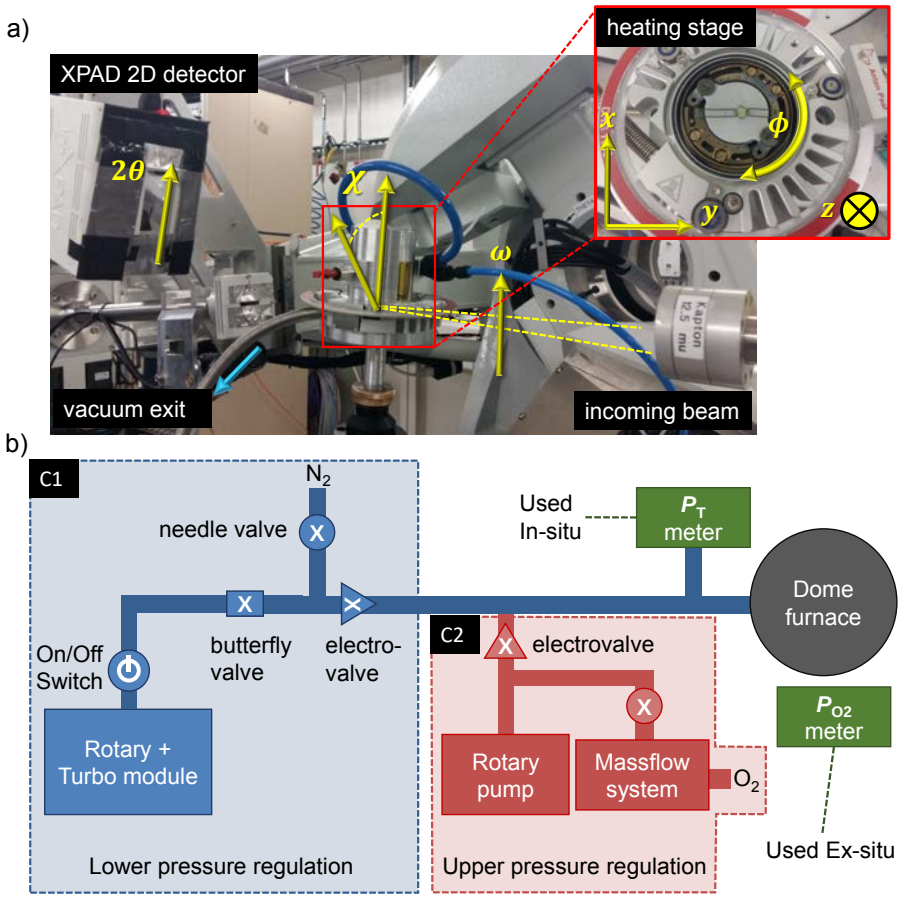

FIGURE 3.15: Soleil experimental setup: a) Measurement configuration showing 2D detector, domed heating stage (inset) and incoming beam; main motorised movements are highlighted in yellow. The tube connection marked by the blue arrow leads to the b) gas control unit and vacuum circuits, depicted schematically.

As already discussed in 3.1.3, samples are grown through three main configurations: A fast temperature increase at 1 bar of total pressure (isobaric conditions at different oxygen partial pressures) and jumps from lowered P_{tot}/P_{O2} pressures towards increased final values (keeping the temperature constant). In order to emulate these growth approaches while allowing to

switch between both, the sealed dome furnace is connected to an in-house designed vacuum unit that was mounted on-site at DiffAbs. Fig. 3.15b) shows a schematic representation of the setup: Remotely controllable electrovalves separate two vacuum circuits (C1 and C2). Needle and butterfly valves are used to independently regulate each circuit before the experiment. The growth routes can hence be emulated with minor changes to the setup:

T-route: The two available gas bottles (nitrogen with < 10 ppm purity and air) are both connected to the massflow system of one circuit while the other remains closed. In this configuration the pyrolyzed sample is heated at 0.4-4.5 °C s^{-1} in $P_{tot} = 1$ bar and $P_{O2} = 10^{-2} - 10^{-4}$ bar and the rotary pump is not active.

P_{O2}-route: To induce rapid changes in pressure with precise P_{O2} adjustment, all vacuum pumps are in use and the two circuits preset and separated through electrovalves. The sample is then heated at a base pressure of $P_{tot} = 10^{-5} - 10^{-6}$ bar (C1 opened, C2 closed) to a desired temperature and the switch performed remotely (C1 closed, C2 opened). Target values of P_{tot} and P_{O2} varied in the range of $10^{-4} - 1$ bar and $10^{-2} - 10^{-4}$ bar, respectively.

As can be seen in Appendix Fig. A.2, the entrance of cold gas during pressure switches causes temperature drops whose height scales with the difference of initial and final pressure. This can be attributed to the small thermal mass of the heater and a slow response of the PID controller. Such drops are undesired and were not found to appear in in-house furnaces. They will hence be considered with greater care in the discussion of results in Chapter 4.

3.6.2 Data acquisition and treatment

Detector position and beam energy were initially adjusted to cover an angular range of $2\theta = 10° - 20°$ and $\chi = -9 - 9°$. Pyrolyzed films contain primarily orthorhombic $BaCO_3$, monoclinic CuO and cubic Y_2O_3. Fig. 3.16 depicts an exemplary grazing incidence measurements performed in-house with the Bruker D8 Discover diffractometer (CuKα energy of 8.04 keV). All precursor phases are randomly oriented and appear in a 2θ range of 22° - 42°. The visibility at DiffAbs can hence be covered by the angular window mentioned above, giving the fact that the beam energy is more than double of CuKα.
Three stationary configurations were used to record the phase evolution,[12] 2θ fixed at 16 ° to retain the same angular range:

[12] No *in-situ* motorized movements were performed during the acquisition.

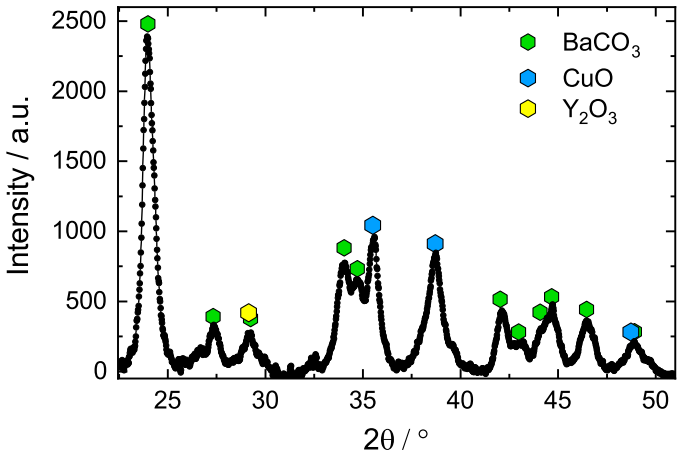

FIGURE 3.16: Grazing incidence measurement of pyrolyzed sample of the (3-7) eutectic composition (see 3.1.1). Symbols indicate literature peak positions obtained from the International Centre for Diffraction (ICDD) database [33].

($\omega = 4°, \chi = 0°$): The incidence angle ω is lowered to increase the illuminated sample area. This geometry is chosen to enhance the signal of polycrystalline phases.

($\omega = 7.9 - 8.1°, \chi = 0°$): ω and 2θ are adjusted in proximity of the (005) Bragg reflection of the epitaxial YBCO layer (literature values range from 16.7 - 17 ° in $2\theta°$ for oxygen deficient YBCO [105]). The exact Bragg condition is avoided to prevent oversaturation of the detector. Precursor phases appear diminished in this configuration due to the smaller illuminated sample area.

($\omega = 6.7°, \chi = 45°$): Nanoparticles from colloidal solutions were found to be epitaxially embedded in the grown YBCO matrix [95]. To study the kinetics of reorientation, the cubic (110) plane was tracked at a chi elevation angle of 45 ° meeting the Bragg condition at $\omega = 6.7°$.

Image recording at a rate of 100-500 ms/frame and a predefined temperature profile were simultaneously initiated in any of the three configurations listed above. Temperatures and frames could later be synchronized through an independent machine time that is saved in each log file. Fig. 3.17a) shows exemplary frames, acquired in Bragg condition with the YBCO (005) reflection, during constant heating at a rate of 4.5 °C s^{-1} at P_{tot} and P_{O2} of 1 bar and 1 mbar, respectively.

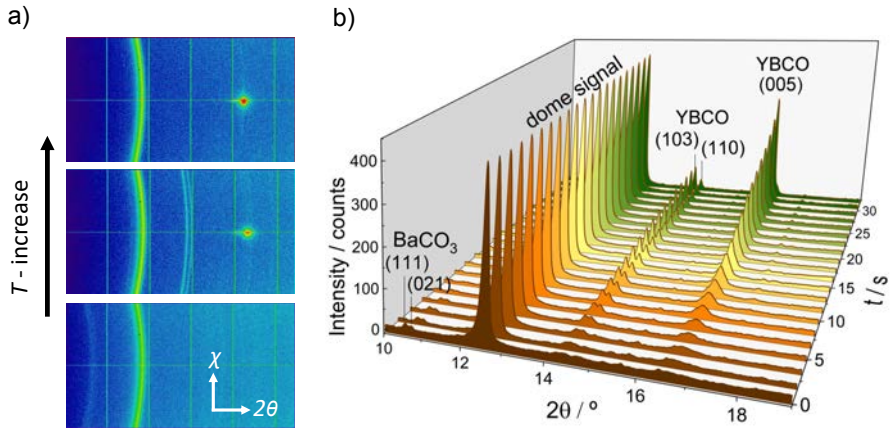

FIGURE 3.17: a) Exemplary raw data obtained at a rate of 100 ms per frame with the 2D detector during temperature increase at 4.5 °C s^{-1}. b) Integrated intensity in χ as evolution of time.

Single frames show the distribution of intensity in the preadjusted window of χ and 2θ. Polycrystalline phases, such as $BaCO_3$, homogeneously nucleated YBCO grains or heater dome phases give an even intensity spread along χ in a confined range of 2θ, in contrast to the epitaxial layer which gives a broadened diffraction spot. DiffAbs provides the acquired images in a raw format that has to be further processed to obtain ($2\theta, \chi$, Intensity) matrices. The intensity can then be summed in χ to follow the evolution in the out-of-plane direction, 2θ. Fig. 3.17b) shows the total image intensity, represented as $I(2\theta)$, as function of time. The elimination of one angle facilitates further data treatment on expense of texture information.
Depending on the chosen P-T profile and acquisition times, 1.000-40.000 frames were recorded per experiment. In order to reduce computational times, tools had to be developed to allow fast extraction and display of information. Consequently, a graphical user interface to visualize data and several processing routines for data treatment were developed and shared amongst other users.[13] The following options are available to process and analyze *in-situ* data and will be referred to in the discussion of Chapter 4 and 5:

1. **I($2\theta, \chi$) patterns:** Two-column files are generated for each image through integration of intensity in one angular direction. That way, intensity profiles as shown in Fig. 3.17b) can be extracted for any custom area and be illustrated as function of time or temperature.

[13] All scripts were developed with Matlab version 2015a and can be provided upon request

2. **Tracking of maximum intensity:** The two column files from (1) are used to follow the maximum intensity in specified angular ranges. The intensity is then exported as function of time and temperature. This approach allows fast access to the evolution of crystalline phases, however, peak-shape changes due to coarsening and mosaicity can falsify the actual evolution. The routine should hence only be used to describe reactions qualitatively or to identify temperature windows for further treatment.

3. **Tracking of total intensity in custom area:** Intensity is integrated for a given $(2\theta - \chi)$ area and exported as function of time and temperature. The approach considers the total fraction of the phase being followed and is hence not affected by coarsening effects.

4. **Peak fitting:** Least-square fitting with multiple and single Lorentzian profiles and linear background (as described in eq. 3.16) is carried out using a set of patterns from (1). Coefficient bounds are first defined for one single scan through manual, graphical input. For that purpose, anchor points are set to restrict the total fitting range, peak positions and widths. The anchor points are then transferred to all other patterns through search of the anchor x-position. Refined fitting values for all patterns are exported as function of scan number, time and temperature. The procedure is more time consuming than the approaches (2) and (3), however, it allows to follow peak shape changes and track the total, integrated intensity given by a phase.

3.7 Scanning transmission electron microscopy

Scanning **t**ransmission **e**lectron **m**icroscopy (**STEM**) was carried out by Dr. B.Mundet, Dr. R.Guzmann and Dr. K.Gupta to study the crystalline state, film composition and defect microstructure of grown YBCO epitaxial layers throughout this project. As TEM images are recurrently used to gain complementary information about growth, secondary phases and nanoscale defects along the present thesis, a brief introduction to the main imaging modes and specimen preparation is given here. A more detailed description of the technique, however, can be found elsewhere [130].
STEM is a technique that stands out for its real-space atomic resolution through use of a highly collimated electron beam of typically several hundreds keV. After ejection and acceleration of electrons from a filament, a set of consecutive electromagnetic coils corrects the beam for aberration and rasters a specimen thin enough to allow transmission of the charged particles. The impinging electrons interact with the sample matter and scatter elastically

onto trajectories described by Rutherford scattering. Multiple annular and circular detectors are placed at increasing angles with respect to the direct beam to extract different contrast in electron-matter interaction. Simultaneously, an **E**lectron **E**nergy **L**oss **S**pectrometer (**EELS**) can be placed in the central position of the out-coming beam path to collect inelastically scattered electrons that have lost a part of their initial kinetic energy. An electromagnetic prism is then used to spatially separate electrons according to their energy loss. The advantage of STEM lies in the simultaneous use of the detectors mentioned above. The main imaging modes and the type of information extracted can be summarized as follows:

- **H**igh-**A**ngle **A**nnular **D**ark-**F**ield (**HAADF**): Also referred to as Z-contrast imaging, the technique reconstructs images through electrons that undergo Rutherford scattering in the range of 100-200 mrad. These high angles are reached by electrons that scatter at the atomic nucleus, making the imaging mode sensitive to Z^2, Z being the atomic number. The heavier elements appear in higher contrast as compared to lighter ones. The main advantage of this technique lies in the straightforward interpretation of the contrast since signal contributions by coherent scattering are reduced. It can hence be seen as a direct visualization of the atomic structure.

- **L**ow-**A**ngle **A**nnular **D**ark-**F**ield (**LAADF**): Electrons are collected at lower angles as compared to HAADF, mostly in the range of 10-50 mrad. The imaging mode is susceptible to lattice deformations that cause a dechanneling effect of electrons from their initial path. Especially when working with YBCO, the imaging mode is commonly used to detect strain fields associated with secondary phase inclusions and accommodation of planar defects.

- Energy loss analysis (STEM-EELS): Amongst others, the chemical composition can be examined through inner shell excitations of the probed material. Incoming electrons transmit a part of their energy at distinct core loss edges giving rise to characteristic energy loss spectra. The simultaneous use of EELS with Z-contrast imaging allows to perform elemental mapping with sub-angstrom resolution.

The sample preparation was carried out either through mechanical thinning or **f**ocused **i**on **b**eam etching (**FIB**). Though both techniques provide electron-transparent lamellas with a thickness below 100 nm, FIB etching allows to make precise area selections and reduce thickness gradients of the probed volume. The majority of images included in this work did not require a precise

choice of the probed region; specimen were hence obtained via mechanically thinning in most cases.

Chapter 4

Transient Liquid Assisted Growth via Chemical Solution Deposition

In this chapter, the foundation to **t**ransient **l**iquid **a**ssisted **g**rowth based on **c**hemical **s**olution **d**eposition (**TLAG-CSD**) will be given, summarizing some of the fundamental achievements within the advanced ERC project [131, 132]. At first, a TLAG scheme and basics on nucleation from liquids will lay the groundwork for the understanding developed in chapter 4 and 5. The phase evolution and kinetics of the simplified (Ba - Cu - O) binary mixtures will then be studied with regard to melting and later extended to the full ternary (Y-Ba-Cu-O) system. This will allow the construction of kinetic phase diagrams for the non-equilibrium growth approach developed here. Main routes into the YBCO stability window will be introduced and an overview of the governing reactions given. Most of the findings, presented here, are derived from *in-situ* growth experiments carried out at the DiffAbs beamline, Soleil Synchrotron.

4.1 Introduction to TLAG-CSD

As motivated in chapter 1 and further discussed in 2.2, a commercial market for HTS is kept from emerging due to high manufacturing costs of the superconducting tape. The REBCO layer has to be grown on buffered metallic substrate over hundreds of meters with high epitaxial quality and thicknesses in the range of micrometers [7]. This challenging task is currently dealt with through use of costly vapor deposition techniques, complex fabrication schemes and, most importantly, low intrinsic growth rates of the superconducting layer. There has been hence a strong momentum for liquid assisted equilibrium growth approaches that could potentially yield the desired cost

reduction [25, 68, 80, 81]. However, also these approaches rely on physical deposition methods (PLD, MOCVD) which hinders a cost-effective production scheme.
Here instead, we explore a technologically simple, low-cost approach that utilizes chemical solution deposition methods together with a non-equilibrium, kinetically driven liquid assisted process: **T**ransient **l**iquid **a**ssisted **g**rowth based on **c**hemical **s**olution **d**eposition (**TLAG-CSD**). The whole process is governed by four major steps to obtain YBCO superconducting films:

1. **Preparation of stable solutions:** The chemical, metal-organic solution to be deposited through CSD methods needs to be stable, e.g. all salts are well dissolved in appropriate solvents. This is not only essential to allow for the solution usability over a period of weeks/months but to ensure the right stoichiometry of the mixture, homogeneous deposition and avoidance of impurities in the film.

2. **Pyrolysis heat treatment:** The pyrolysis heat treatment aims to decompose the organic matter and produce precursor films based on oxides and carbonates of Y_2O_3, $BaCO_3$ and CuO of uniform film thickness. A homogeneous spread and nanocrystallinity of precursor phases is required to avoid inhomogeneities in the conversion to YBCO grown film and allow for enhanced reactivity of all involved phases towards YBCO.

3. **$BaCO_3$ elimination and growth of YBCO:** As will be introduced below, the growth of YBCO through TLAG-CSD requires decomposition of $BaCO_3$ and the right nucleation conditions to promote epitaxial, c-axis YBCO growth. Both points are a prerequisite to obtaining films with high superconducting properties.

4. **Film oxygenation:** The grown YBCO crystal structure needs to be oxygenated, involving a separate heat treatment, to reach the superconducting state with high T_c and J_c values.

In the present chapter the focus is set on the growth of YBCO and the involved reactions. A thorough analysis of chemical solutions and the pyrolisis step can be found in the PhD theses of Dr. Silvia Rasi, Dr. Laia Soler, Dr. Júlia Jareño [76, 94, 95]. Pyrolysed films used in this work are prepared through non-fluorinated metal-organic precursors (see 3.1.2) to obtain nanocrystalline layers of the binary $BaCO_3$-CuO (Ba - Cu - O) and ternary $BaCO_3$-CuO-Y_2O_3 (Y-Ba-Cu-O) systems.[1]
First of all, the decarbonisation of $BaCO_3$ is of major importance to avoid carbon retention in the final YBCO structure. Carbon and carbon based species

[1] The chemical instability of BaO results in $BaCO_3$ as the product phase.

can result in T_c depression and reduction of the critical current density if incorporated into the YBCO structure or retained at the grain boundaries [90, 133, 134]. $BaCO_3$ powders decompose according to

$$BaCO_{3(s)} \longrightarrow BaO_{(s)} + CO_{2(g)}. \tag{4.1}$$

When powders are thermally treated alone, the decarbonisation takes place at temperatures exceeding 900 °C [89, 135, 136], both in air and inert argon atmosphere. The peritectic decomposition temperature of YBCO lies in the same range, which led to the common believe that $BaCO_3$ as initial phase was unsuitable for YBCO manufacturing [89, 137]. It is the catalytic behaviour of CuO that was later found to lower the decarbonisation temperature down to 700°C [89, 94] changing the reaction in 4.1 to

$$BaCO_{3(s)} + Cu_xO_{(s)} \longrightarrow BaCu_xO_{2(s)} + CO_{2(g)} \tag{4.2}$$

x being the oxidation state of copper. Further decrease in reaction temperature was achieved by Sobolik et al. [138], down to 620 °C, who investigated the influence of particle size and sample environment on reaction temperatures. A higher reactivity of nanometric over micrometric sized particles was attributed to the improved diffusion of cations during reaction.

Now, the presence of CuO enables the formation of a (Ba - Cu - O) solid intermediate [139], which in turn reacts with CuO to form a liquid phase. The binary (Ba - Cu - O) system is a well known eutectic with P_{O2}-T dependent melting characteristics [140, 141]. It is the formation of the very same liquid phase that is advantageously used to promote TLAG. The main idea behind TLAG is based upon the kinetic preference of the ternary $BaCuO_2$, CuO and Y_2O_3 system to form a eutectic (Ba - Cu - O) liquid phase (with the presence of dispersed Y_2O_3 solid nanoparticles) in a region of the phase diagram where YBCO is the equilibrium phase. As any crystallization process requires to overcome an energy barrier of nucleation (which delays its formation through an incubation time, see 4.1.3), transient liquids that are not predicted in the equilibrium phase diagram can precede the reaction pathway since they can emerge instantaneously. An equivalent kinetic preference of liquid formation over crystallization was already observed in the synthesis of germanium nanowires [142].
A scheme of the TLAG process is shown in Fig. 4.1: As the liquid (Ba - Cu - O) phase is formed upon heat treatment, Y_2O_3 nanoparticles dissolve and supersaturate the fluid giving rise to YBCO nuclei. Epitaxial layer growth can then be promoted at the substrate interface via a non-equilibrium kinetically driven process if the processing window is properly chosen.

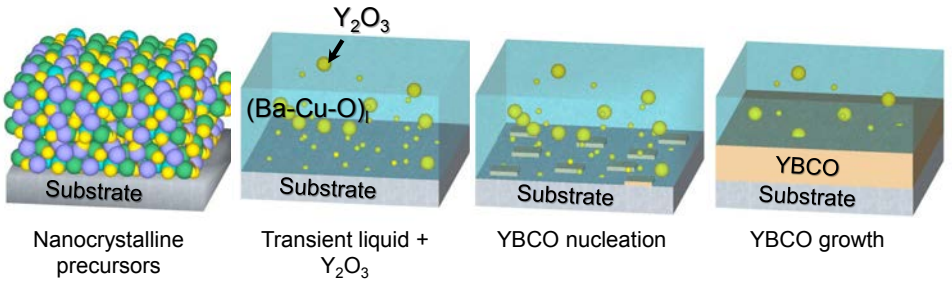

FIGURE 4.1: Schematic representation of the TLAG process after synthesis of a stable metal-organic solution and deposition through CSD methods: A pyrolyzed nanocrystalline film containing $BaCO_3$, CuO and Y_2O_3 is heat treated to undergo a eutectic liquid reaction. The dispersed Y_2O_3 nanoparticles supersaturate the liquid medium yielding crystallization of the YBCO phase.

Similar to other liquid based growth techniques, atomic mobility is expected to be highly enhanced allowing for fast precipitation of any stable solid phase in the conditions of growth. For instance, it was demonstrated in earlier work that Y diffusivity in a (Ba - Cu - O) liquid can reach $4 \cdot 10^{-8} \mathrm{m^2\,s^{-1}}$ as compared to $8 \cdot 10^{-12} \mathrm{m^2\,s^{-1}}$ in a solid medium. In that manner, much higher growth rates are anticipated. In the following sections, a brief introduction into the general concepts of melt formation, melt supersaturation, nucleation and growth, all being key aspects of the TLAG-CSD scheme, will be given. A broad discussion on crystallization from melts can further be found in [143–145].

4.1.1 Melt formation

Based on classical thermodynamics, melting is regarded as a first order phase transitions where a rigid, solid phase of long-range order transits into a disordered fluid. The critical temperature point were solid and liquid state exhibit equal Gibbs free energies, $\Delta G = 0$, is commonly referred to as melting point, T_m. Here, the solid system undergoes an abrupt change in latent heat and volume while the transformation takes place [145]. One of the widely established models to describe the process of melting was developed by Frederick Lindemann in 1910, who based his work on the vibrational instability of the crystal lattice.[2] Here, the event of melting is related to the exceedance of atomic thermal vibrations beyond a critical length upon which the lattice collapses due to

[2]Another frequently used criterion was developed by Max Born. Here, melting is related to the disappearance of the shear modulus in the liquid state. In this macroscopic picture, the

neighbouring collisions. The derivation of the so called *Lindemann criterion* is made through relating the absolute temperature, T, and the thermal vibration energy via the equipartition theorem [147]:

$$m(2\pi\nu)^2 \mathrm{d}x^2 = k_\mathrm{B} T \tag{4.3}$$

Here, $\mathrm{d}x$, ν, m and k refer to the RMS thermal average amplitude of vibration, the frequency, atomic mass and Boltzmann constant, respectively. The criterion can be written in a general form assuming that at T_m, the vibrational distance $\mathrm{d}x$ reaches a critical fraction c_L of the near-neighbour atomic distances a,[3] with $\mathrm{d}x{=}c_\mathrm{L} \cdot a$. T_m can then be expressed as

$$T_\mathrm{m} = \frac{m(2\pi\nu)^2 c_\mathrm{L}^2 a^2}{k_\mathrm{B}} \tag{4.4}$$

In its modern formalism, the frequency ν is further related to the Debye frequency allowing for a relation of melting temperatures with the characteristic bulk properties of the material. Also, a structure dependency was later added to the empirically derived theory and c_L was found to vary for bcc, fcc or hcp metal [145]. It should be noted that the Lindemann criterion is based on a simple harmonic picture of oscillating atoms where melting is described solely through consideration of the solid state, excluding the liquid characteristics. Nevertheless, due to its simplicity and success in predicting melting temperatures, it is widely used nowadays [145, 147].
Although the discussion above considers melting as a discontinuous, abrupt collapse of the crystal stability at T_m, experimentally it is often found that the phase transition takes place over a finite temperature interval. Any source of disorder can introduce gradients in melting points and create regions of shifted transition characteristics. This causes melting to be progressional, often referred to as **continuous melting**. For instance, the disruption of a large crystal into polycrystalline grains can yield transition broadening due to size effects and grain boundary energy contributions. It is, however, evidenced, that continuous melting is not solely influenced by intrinsic properties of the crystal but also surface related effects.

The influence and importance of surface melting was pointed out by Tammann at the same time when Lindemann derived his criterion [147]. Due to reduced coordination of surface atoms, as compared to their interior counterpart, the surface layers are thermally less stable. Similar to the developed

solid looses its rigidity at T_m due to lattice instability. For further reading, please refer to [145] or the original work of M.Born [146].

[3] First estimations by Lindemann gave critical fraction values of c_L~10% [148].

picture of stable, solid nuclei formation in 4.1.3, the surface of a crystal can function as a site for heterogeneous melt nucleation. In fact, it is nowadays accepted that surfaces can exhibit structural changes such as reconstruction, deconstruction, pre-roughening and wetting well below the bulk melting temperature [145]. Surface melting can hence be regarded as wetting of a solid crystal by its own melt.

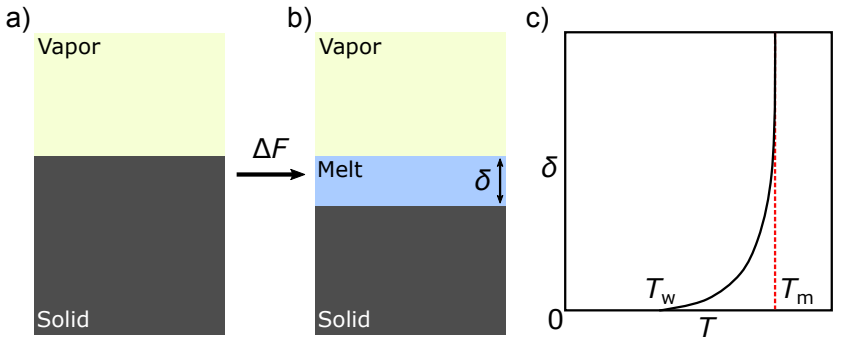

FIGURE 4.2: Schematic illustration of a continuous melting transition: (a) A crystal system in equilibrium with the vapor phase. (b) Formation of a quasi-liquid layer of width δ. (c) Evolution of δ with temperature. The wetting and melting temperature, T_w and T_m, are denoted. Modified from [145].

Fig. 4.2 summarizes the progression of a liquid layer having the width δ. Already at temperatures below the bulk transition point (T_m), the free energy of the system can be reduced by an energy difference, ΔF, if a quasi-liquid layer (QLL) is created (Fig. 4.2). The layer is referred to as "quasi-liquid" layer since structural and electronic properties are found intermediate between equilibrium solid and liquid phase [149]. Hence, the solid-liquid-vapor interface, shown in Fig. 4.2b), exhibits a lowered surface energy as compared to the non-wetted solid in Fig. 4.2a). The formation of the liquid layer initiates at temperatures referred to as wetting temperature, T_w, and an increase in thickness is observed upon reaching the melting point Fig. 4.2c). The thickness of the layer diverges at T_m, that is where the whole crystal transforms into a melt.

The occurrence of surface melting prior to the bulk can also be understood in the simple framework of the Lindemann criterion: At the same temperature, surface atoms vibrate with higher amplitudes than those within the solid, reaching the critical neighbour distance for $T < T_m$ [145, 150]. The first direct observation of surface melting was realized by Frenken et al. on a pure Pb(110) system through temperature-dependent ion scattering measurements [148] and later confirmed by various other authors [145]. Also areas of

enriched defect density, such as grain boundaries and dislocations were observed to show pre-melting behaviour due to the low coordination of atoms.

The discussion made above underlines that the presence of surfaces plays a crucial role in the melting characteristics of a system. However, until now we have considered only sharp and flat interfaces, regardless of curvature and size effects. Nanometric systems, such as nanoparticles, exhibit, aside from their large surface, additional size- and curvature-related contributions.
Kofman et al. investigated small Pb nanoparticles ranging from several nm to 100 nm in size, embedded in a SiO_2 and Al_2O_3 matrix [151]. Here, it is shown that melting is initiated through an outer liquid shell (Fig. 4.3) whose thickness, δ, increases for particles with higher curvature. This is in agreement with early work done by Pawlow, who predicted melting point depression as a function of nanoparticle size and surface energy back in 1909 [152].

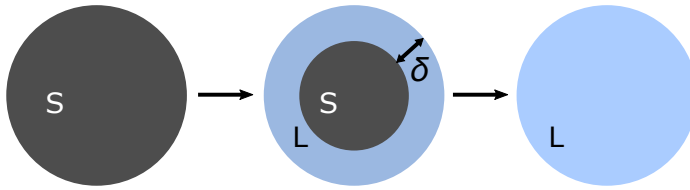

FIGURE 4.3: Three configurations representing the melting of a particle: A solid particle is wetted by a liquid skin which increases in thickness δ until the whole volume is absorbed (left to right). Modified from [151].

Similar to the wetting of solid, flat surfaces, several models were developed to describe the temperature evolution of the liquid skin thickness δ [145]. Here, the Gibbs free energy of the different configurations in Fig. 4.3 is derived and the difference, ΔG, minimized with respect to δ.[4] Experimentally, melting is typically observed to follow an inverse trend with particle size, according to $T_m \propto 1/D$, where D denotes the particle diameter [153, 154]. Although most models imply the initiation of melting at the surface, it has also been observed that particles can reach a critical size, $D < D_c$, below which they melt abruptly [145].
On the contrary to melting point depression, it has also been demonstrated that nanoparticles can be substantially superheated above the bulk melting temperature. This can either be realized by embedding the particles in a material of higher T_m [155] or through realization of an epitaxial relationship between particle and surrounding matrix [154].

[4] See the example of the *liquid skin model* in [145, 151].

Melting point depression and size related effects are commonly studied in pure, single-phase systems. It has, however, also been observed that multi-phase alloys exhibit similar trends to those discussed above. As summarized in the review work of Q.S. Mei et al. [145], experimental observations on multi-phase systems reveal:

1. Free-standing nanoparticles show a size-dependent melting point depression governed by the impact of surface melting.
2. Epitaxially embedded particles do not show considerable melting point depression. In some cases the epitaxial relation can even lead to melting point elevation.
3. Phase-boundaries of multi-phase alloy particles can provide additional venues for heterogenous melt nucleation enhancing the melt formation.

As will be presented in the microstructure analysis in 4.2, precursor CSD films exhibit a high density of surfaces, interfaces and record nano-metric sizes of cations, down to 5 nm. Size related effects on melting and reactivity of phases will hence also be considered here.

4.1.2 Melt supersaturation

The TLAG process involves two phase transitions, one being the formation of a (Ba - Cu - O) melt, the other crystallization from the melt. The driving force for crystallization is typically derived by considering the free energies of initial (liquid) and final state (solid) [143]. A convenient representation of that driving force is often reduced to the chemical potential difference of both phases, $\Delta\mu = \mu_l - \mu_s$. Also referred to as **supersaturation**, the quantity is a measure for the metastability of a solution with higher solute concentration as it can actually dissolve in given thermal conditions. It can hence be expressed according to

$$\Delta\mu = k_b T \log\left(\frac{C}{C_{eq}}\right) \tag{4.5}$$

where C and C_{eq} denotes the actual and equilibrium concentration of the solute in the liquid, respectively. An alternative formulation is often given through the **relative supersaturation**, σ, which reads

$$\sigma = \frac{C - C_{eq}}{C_{eq}} = \frac{C}{C_{eq}} - 1 \tag{4.6}$$

There are different ways a crystallization process can emerge from a saturated liquid. Fig. 4.4 shows a schematic $C(T)$ diagram for a dissolved solute. In the

unsaturated state, the solute concentration is below the solubility limit and crystallization will not occur. The region is separated by the saturation line from a metastable zone, called *Oswald-Miers* regime, where the solute concentration exceeds the equilibrium concentration. Here, nuclei can be formed upon reaching a critical size to remain stable. The duration for this to happen is often introduced as **induction period of nucleation**, τ.

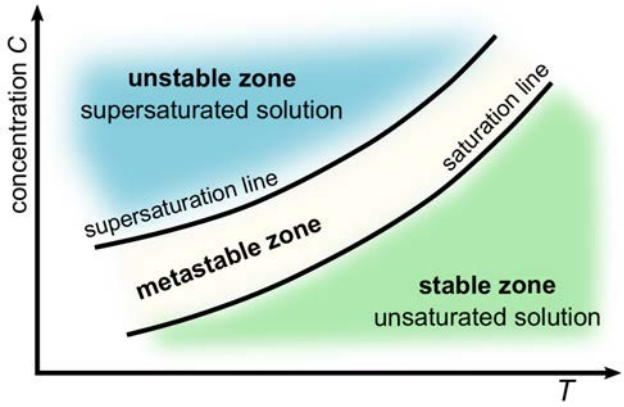

FIGURE 4.4: Schematic representation of a concentration-temperature diagram, inspired by [143]. The stable, metastable and unstable zone of a liquid defines where crystallization does not occur, is highly improbable and emerges instantaneously, respectively. The relative supersaturation σ relates to the width of the metastable zone.

Further increase in saturation and crossing of the supersaturation line results in an unstable liquid and sudden nuclei precipitation. The difference of metastable and unstable zone lies in the abrupt drop of induction times. Although nucleation in the metastable zone is restricted, seed crystals can promote the formation of nuclei with decreased surface area (further discussed in 4.1.3). From Fig. 4.4 it is evident that crystallization can either be triggered through concentration increase or temperature decrease. Both strategies are being followed in melt-based processes, also with regard to YBCO synthesis. For instance, in **m**elt-**t**extured **g**rowth (MTG) of YBCO, crystallization is realized through slow undercooling of an incongruent melt below the peritectic temperature of YBCO [74, 75].[5] Although, here, the dissolution of the (211) phase can shift the overall concentration of the melt and complicate the process, the main driving mechanism is attributed to the decrease in temperature. In **h**ybrid **l**iquid **p**hase **e**pitaxy (HLPE), on the contrary, crystallization

[5] YBCO melts incongruently into a (Ba - Cu - O) liquid phase with dispersed Y_2BaCuO_5 (211) particles above the peritectic temperature.

is induced through flux feeding from a vapor phase and supersaturation tuning [81]. Here, a thin (Ba - Cu - O) liquid layer is first stabilized and a YBCO flux fed through a physical vapor technique, such as **p**ulsed **l**aser **d**eposition (PLD).
Typically, supersaturation tuning in any of the melt-based processes is a challenging task which requires precise control and readjustment of the solute amount.
In TLAG, however, we develop a kinetically driven growth model with the Y_2O_3 amount being fixed by the initial solution stoichiometry. The supersaturation of the melt can then be tuned through processing conditions such as growth routes ($P_{O2} - T$ paths), heating ramps and liquid properties, all of which are key parameters with regard to realizing epitaxial YBCO growth.

4.1.3 Nucleation and growth process

The framework of the **c**lassical **n**ucleation **t**heory (CNT) was formulated more than 90 years ago by Volmer and Weber, Farkas, Becker and Doerin and lays to date the groundwork for the description of growth phenomena and even advanced computational approaches, such as molecular dynamics [144].
Within the thermodynamic description of the CNT, particle clusters of any size are treated as macroscopic objects, being separated from the surrounding liquid by a vanishingly thin interface. This, so called *capillarity approximation*, is used to derive a thermodynamic description for nuclei formation. Stable nuclei are formed upon reaching a critical nucleus size, r^*, needed to overcome the free energy of formation, given by

$$\Delta G = \underbrace{4\pi r^2 \gamma_s}_{\text{surface term}} - \underbrace{\frac{4\pi}{3\nu} r^3 \Delta\mu}_{\text{volume term}} \tag{4.7}$$

The system gains energy due to the volume increase of the solid phase. Here, $4\pi r^3/3$ stands for the total volume of a homogeneously nucleated cluster of size r. It is divided by the unit volume ν of one single molecule (or unit cell in the case of YBCO). At the same time, it is unfavourable to create a new surface, given by $4\pi r^2 \gamma_s$, with γ_s being the interfacial free energy. Thus, the energy barrier for stable nucleation arises from the interplay of these two energy terms of opposite sign [144].
An expression for the critical nuclei radius r^*, above which the volume term dominates, can be derived by determining the maximum of eq. 4.7, according

to $d(\Delta G)/dr = 0$. r^* is then given by

$$r^* = \frac{2\gamma_s \nu}{\Delta\mu}. \tag{4.8}$$

Accordingly, the energy barrier for spherical/homogenous nuclei can be calculated by substituting r through r^* in eq. 4.7, yielding

$$\Delta G^*_{\text{hom}} = \frac{16\pi}{3}\frac{\gamma_s^3 \nu^2}{\Delta\mu^2}. \tag{4.9}$$

Note that critical radius and energy barrier are inversely proportional to the supersaturation. A higher solute concentration will hence reduce the energy needed to induce stable nucleation. **Homogeneous** nucleation requires no participation of other particles (seeds) or interfaces and the correspondent surface term is increased due to the spherical shape of the nucleus. The surface is however reduced in case of **heterogenous** nucleation which takes place at secondary sites such as defects, interfaces and substrate crystals [143].

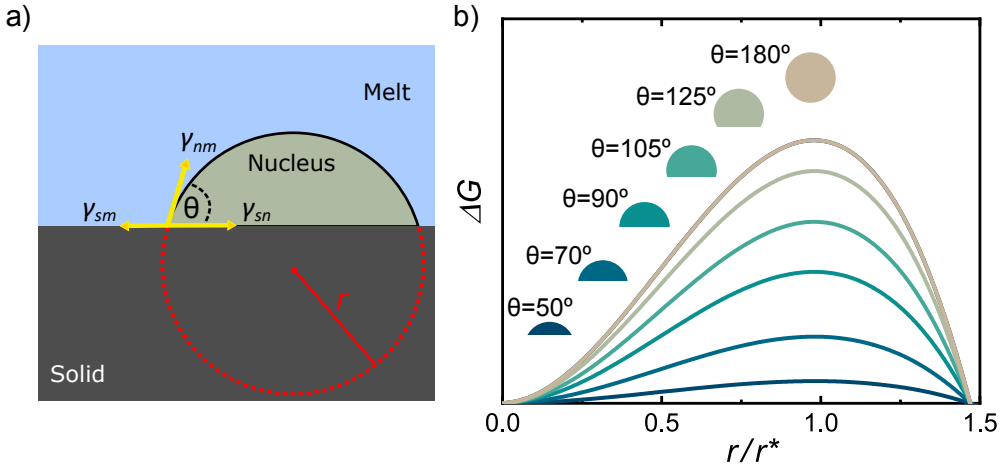

FIGURE 4.5: Overview of heterogeneous nuclei formation: (a) Schematic representation of a heterogeneous nucleus enclosing the angle θ with the underlying solid surface. The contact angle is described by Young's equation (4.12). Dashed red line and radius r account for a homogeneous nucleus of the same curvature. (b) Free energy of formation for different contact angles.

In a first and simple approximation, heterogenous nuclei, being in contact with the surface of another solid, take the shape of a sphere-segment or "cap", as shown in Fig. 4.5a). The cap has a curvature of radius r and encloses an

angle θ with the solid surface, called wetting angle. Due to the geometrical reduction of volume and surface of the nuclei, the free energy of change for heterogenous nuclei is derived to include a correction factor $f(\theta)$, with $0 < f(\theta) < 1$, as compared to the case of a homogenous nucleus [143, 144]. The function, having the form

$$f(\theta) = \frac{(1-\cos(\theta))^2(2+\cos(\theta))}{4} \tag{4.10}$$

is used as a shape factor to correlate heterogeneous and homogeneous nucleation barriers according to

$$\Delta G^*_{\text{het}} = \Delta G^*_{\text{hom}} \cdot f(\theta) \tag{4.11}$$

Fig. 4.5b) shows how the free energy of formation varies for nuclei of different wetting angles. Each function is plotted against the cap radius, normalized to the critical radius r^*. The wetting characteristics are described by Young's relation

$$\gamma_{\text{sm}} = \gamma_{\text{sn}} + \gamma_{\text{nm}}\cos(\theta) \tag{4.12}$$

which is a balance of the surface tensions γ_{sm}, γ_{sn} and γ_{nm} given by the substrate-melt, substrate-nucleus and nucleus-melt interface, respectively.
Fig. 4.6 summarizes the free energies of formation for homogeneous and heterogeneous nucleation. Real examples of crystals nucleated in the bulk and at the substrate interface, identified through TEM measurements of TLAG films, are shown in the insets.

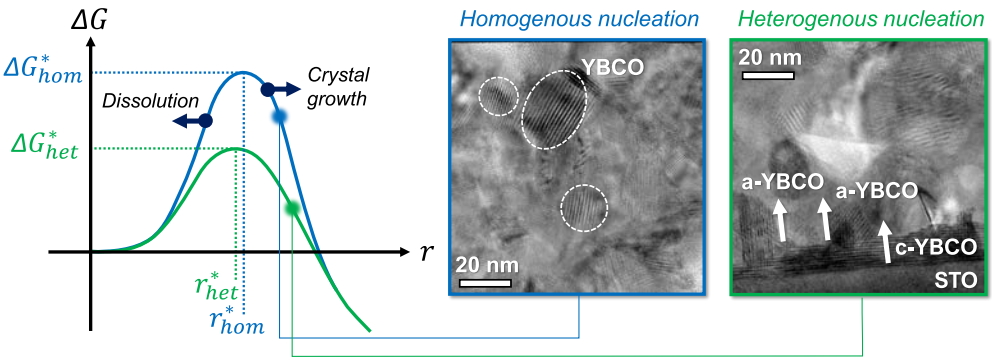

FIGURE 4.6: Competing nuclei formation in TLAG growth of YBCO: Stable homogeneous and heterogeneous nuclei are formed upon surpassing the critical radii. Both type of nuclei can be encountered (insets) if a high supersaturation is reached during growth. Inspired by [144].

As the relation $\Delta G^*_{het} < \Delta G^*_{hom}$ is always fulfilled according to eq. 4.11, one might expect preferential growth of the epitaxial layer over spontaneously nucleated grains in the bulk of the liquid layer. Homogenous nuclei and heterogenous a/b-oriented grains can, however, become competitive with c-oriented grain growth at increased supersaturation.[6] This is shown through exemplary curves of free energies of formation versus supersaturation in Fig. 4.7. The values are adapted from [76, 156]. ΔG_{hom} is additionally added assuming $f = 0.5$ in eq. 4.11. While for low supersaturation values ΔG^*_{het} has an increased difference to the barrier for homogeneous nucleation, promoting c-axis nucleation (green region), the margin shrinks upon $\Delta\mu$ increase. At high supersaturation a/b-oriented particles can also become competitive, reaching a cross-over with ΔG^*_{het}. Here mixed nucleation (heterogeneous and homogeneous) are possible, as highlighted by the colored region.

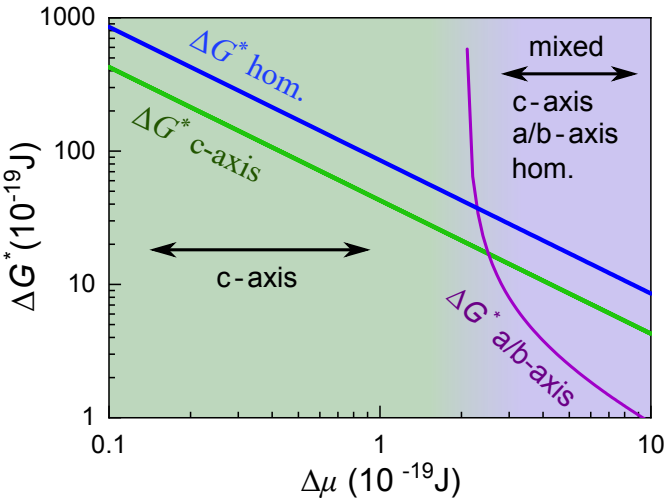

FIGURE 4.7: Free energies of formation, ΔG_i, as function of supersaturation for homogeneous and heterogeneous nuclei (c- and a/b-axis oriented). ΔG_{hom} is exemplified using eq. 4.11 with $f(\theta) = 0.5$. The figure is modified from [156].

The relative supersaturation in TLAG is estimated to exceed classical melt-based growth techniques, such as LPE, HLPE and MOCVD [76]. A supersaturated liquid has always a finite probability to allow spontaneous formation of homogeneous nuclei, even though they are energetically less favoured than heterogeneous ones. This can be understood through consideration of different, in parallel acting nucleation rates for each nuclei type. According to CNT,

[6] a/b-oriented grains are 90° rotated with respect to the epitaxial layer as seen in the TEM inset in Fig. 4.6.

the nucleation rate

$$I = I_0 \exp(-\frac{\Delta G_i^*}{k_B T}) \tag{4.13}$$

follows the form of the Boltzmann-weighted probability function. Here ΔG_i^* stands for the individual energy barriers and I_0 includes the kinetic contributions governing the growth of a nucleus [157].
Expression 4.13 is derived presuming that the exchange of particles between nucleus and liquid is governed through a stochastical process and that the induction time to surpass the critical radius is larger than the time needed for the nucleus to grow to macroscopic dimensions. When these conditions are met, the process becomes time independent [144]. The prefactor I_0 is typically expressed in the form

$$I_0 = \rho_s Z A_{\text{kin}} \tag{4.14}$$

with ρ_s being the nucleation site density, Z the Zeldovich factor[7] and A_{kin} a kinetic factor to account for the attaching rate of particles that arrive with a certain frequency at the nucleus and rearrange to form the crystalline phase. In diffusion limited processes, A_{kin} relates with the diffusion coefficient $D(T)$ which itself follows an Arrhenius type behaviour of the form

$$D(T) = D_0 \exp(-\frac{E_d}{k_B T}) \tag{4.15}$$

with prefactor D_0 and diffusion activation energy E_d [158]. Considering eq. 4.13, the nucleation rate hence adopts the proportionality

$$I \propto \exp\left(-\frac{E_d}{k_B T}\right) \exp\left(-\frac{\Delta G_i^*}{k_B T}\right) \tag{4.16}$$

where the first and second term account for the atomic mobility and nucleation inertia of the system, respectively. Considering a liquid being cooled below its melting point T_m (supercooling), an approximation can be made for all influencing quantities in eq. 4.16 which will depend on the degree of supercooling ΔT. The nucleation rate then follows a peak-shape distribution as shown in Fig. 4.8.

[7] Taking into account that nuclei above their critical size might still destabilize without forming the crystalline phase.

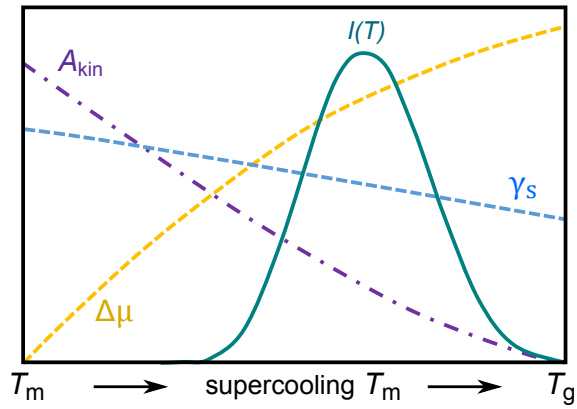

FIGURE 4.8: Illustration of the nucleation rate for a supercooled liquid. In a diffusion limited process, the steady state nucleation rate $I(T)$ exhibits a dome-shape due to the cummulative contributions of $\Delta\mu$, γ_s and A_{kin}. T_g stands for the liquid glass transition temperature. Adapted from [144].

The temperature dependence of $\Delta\mu$, γ_s and A_{kin} is adapted from [144]. The resulting, dome-shaped nucleation rate, $I(T)$, can then be understood as follows: Although the diffusivity of a congruent melt close to its melting point (T_m) is high, nucleation rates are suppressed due to the increased energy barrier to form stable nuclei.[8] At temperatures close to the glass-liquid transition (T_g), however, the low viscosity of the liquid dominates and does not allow for high diffusivity.
It should be noted that although crystallization in the TLAG process is also driven by a supersaturated liquid, the physical origin of the latter and its temperature dependence is more complex. We aim to induce supersaturation by dissolution of Yttria initially embedded in nanoparticle form through ultrafast kinetic conditions. The approaches followed in TLAG to reach final growth conditions will rely either upon very fast increase in temperature or fast isothermal pressure jumps. Liquid diffusivity is then not restricted by temperature as in the case of supercooled systems. The degree of supersaturation and, with that, the nucleation rate will therefore depend on Y_2O_3 dissolution kinetics, Y diffusion through the liquid, Y kinetics at the solid film interface, liquid amount and liquid properties. The complexity associated to the theoretical framework of the involved mechanisms has yet to be developed. In this thesis, we aim to give insights on these aspects.

The limitations and hindrances that arise upon crystal growth from solutions are decoupled from those in the initial stage of nuclei formation. During

[8] The supersaturation $\Delta\mu$ is low here.

growth, stable nuclei coarsen and coalesce towards larger grains until these merge and the process is terminated by grain boundary zipping and strain relaxation. In this course, several separate stages can govern the growth velocity of a crystal [81]:

1. Convective transport of solute towards the growth front.
2. Volume diffusion of solute particles through a 'stagnant' liquid layer of thickness δ.
3. Exchange kinetics of solute particles between the adjecent volume at the growing front and the close-packed terrace where the particles are adsorbed.
4. Surface kinetics, such as diffusion limited transport of adsorbed particles on the terraces between steps.
5. Kinetics of incorporation of adsorbed particles at steps, diffusion along steps, and integration into the crystal at a kink.

Any of the above mentioned points can be rate-limiting with regard to crystal growth if they constitute a part of the reaction scheme. For instance, as in the case of hybrid liquid phase epitaxy (HLPE), the solute particles (Y-rich phase) are fed from a vapor flux, while a (Ba - Cu - O) liquid layer of thickness δ is stabilized independently and the whole liquid layer then needs to be crossed by the solute molecules towards the growth front. Hence, points 1 and 2 need to be considered unless the liquid layer is negligibly thin. In this simplified case, the steady state growth rate can be estimated, as will be done for the TLAG process in 5.1.
In general, the different mechanisms discussed above are hardly separable. This is why they are commonly categorized either into surface or diffusion limited kinetics, allowing to make growth rate estimations [78, 81]. However, the thermodynamic driving force that governs growth rates and remains a key parameter in solution growth is the supersaturation. Depending on its degree, the epitaxial layer formation can take place through spiral growth, 2D growth or 3D roughening going from a low to a high supersaturation degree, respectively [76, 159]. Also the associated defect landscape varies with the growth type. While at low saturation the YBCO crystal structure incorporates few defects and is of single-crystalline quality [74, 84], growth techniques of increased supersaturation typically allow for generation of nanometric defects that suit the purpose of vortex pinning [25, 84]. Throughout the following chapters we will motivate that the TLAG can be classified as a high supersaturation growth approach judging by epitaxial layer growth rates and

defect characteristics.

In summary, a brief introduction into melting, nucleation and growth were given in this section. In 4.1.1 it is motivated that nanometric sized systems can exhibit different melting characteristics from their bulk counterparts. The state of precursor films with regard to crystalline structure, size and distribution of cations is key to obtaining the kinetic preferences of TLAG. Before a discussion on the involved reactions and growth kinetics is made, we will hence consider the crystalline state of CSD derived precursor films in the following.

4.2 Crystalline state of pyrolyzed films

As introduced in 3.1, films were prepared through the fluorine-free metal-organic decomposition route. The pyrolysis heat treatment, being the precedent step before growth, aims to decompose the organic matter and generate a nanocrystalline precursor film that contains only Y_2O_3, $BaCO_3$ and CuO. A high thickness homogeneity, small particle sizes (tens of nanometers) and a uniform distribution of precursor phases is essential to allow for rapid transformations during growth and prevent inclusion of secondary phases within the film. In this section the state of precursor films is evaluated through TEM and XRD measurements, prior to our discussion on the *in-situ* growth analysis.[9]

Considering a one-layer pyrolyzed film (Fig. 4.9a)), a dense microstructure was identified with precursor phases in proximity to each other. These are found to reach the desired nanometric sizes as depicted in the inset figures. Average grain diameters of $BaCO_3$, CuO and Y_2O_3 and their crystal structures are listed in tab. 4.1. A minor proportion of $BaCO_3$, not shown here, is further found to exhibit monoclinic structure with a reduced crystallite size down to 2 -6 nm. It is shown in previous work by S.Rasi and L.Soler [76, 94] that if the monoclinic phase is present in high amount, the decarbonation process can be retarded. Here, however, monoclinic $BaCO_3$ is only given in scarce amounts and was not observed to affect the decarbonization kinetics.

[9] Cross-sectional TEM was carried out using the imaging modes discussed in 3.7.

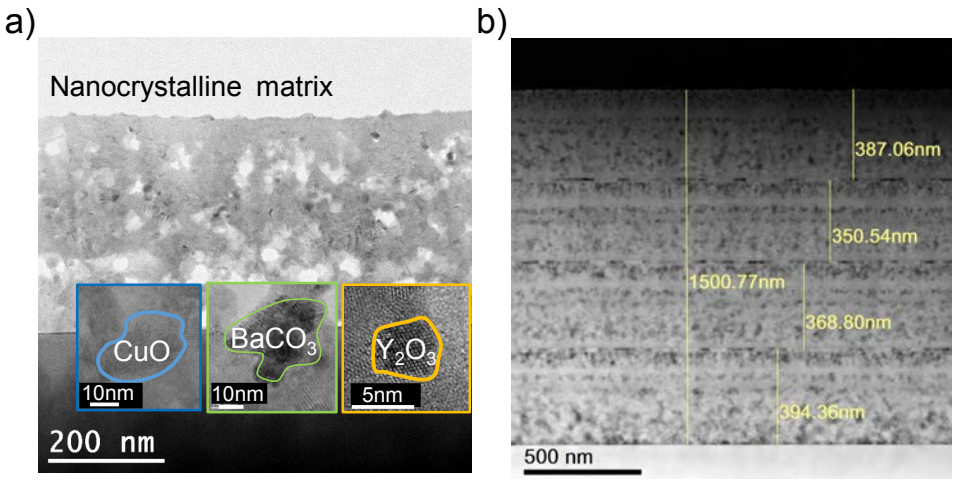

FIGURE 4.9: TEM cross sectional analysis of pyrolysed films through the FF metal-organic decomposition approach: a) Bright-field transmission electron microscopy image of a single-layer film. Inset shows an enlargement of the crystalline precursor phases. b) STEM-HAADF image of a four-layer pyrolysis reaching a total thickness of 1500 nm. Yellow lines represent characteristic lengths of deposited layers.

A four-layer pyrolysed film is further shown in Fig. 4.9a): The STEM-HAADF imaging technique allows a direct correlation of contrast and atomic density. The dark contrast areas can hence be directly related to pores in the structure. Their origin is thought to originate from CO_2 release during the pyrolysis process [6]. A thickness of 1500 nm was estimated by Dr. K.Gupta, taking into account the periodicities encountered throughout the film.[10]

	Grain size (nm)	Structure
$BaCO_3$	10-30	orthorhombic
$BaCO_3$	2-6	monoclinic
CuO	15-40	monoclinic
Y_2O_3	4-6	cubic

TABLE 4.1: Size and structure quantification of crystalline phases in pyrolysed films

Overall, films present a high degree of uniformity in thickness and compactness ($1 \pm 0.2\%$ of porosity). Such homogeneous, multideposited films were achieved just recently via CSD through addition of an amine to the initial

[10] Porosity and densified regions were compared with a single-deposited layer.

solvent mixture, known to increase viscosity and improve the deposition homogeneity.
The values denoted in tab. 4.1 roughly comprise the average size distribution of crystalline phases identified from a set of TEM images. Also deviations towards even smaller values were encountered for the CuO and $BaCO_3$ phase. In addition, a part of the pyrolized layer is found in the amorphous state (yellow encircled regions in Fig. 4.10b)). To confirm the presence of amorphous grains, one pyrolyzed film of (3-7) composition (see nomenclature in 3.1.1) was measured by **g**razing **i**ncidence (GI) X-ray diffraction after pyrolysis and then post-annealed at 500 °C for 5 h and remeasured again. The temperature is chosen below the decarbonization temperatures that will be identified in 4.3 and 4.4. The high temperature treatment aimed to promote crystallization of the amorphous regions.
The GI-measurements are shown in Fig. 4.10a). The identified precursor phases ($BaCO_3$ monoclinic/orthorombic, CuO and Y_2O_3) in the as-pyrolized and heat treated film are labeled with markers. The background profiles are further included for both measurements through dashed lines. The initial, as-pyrolized precursor film contains some $BaCO_3$ monoclinic which transforms into the orthorhombic structure after annealing. The focus of the analysis is however set on the CuO phase evolution due to the compromised detectability of Y_2O_3 and the partial conversion of monoclinic $BaCO_3$ to the orthorhombic structure.

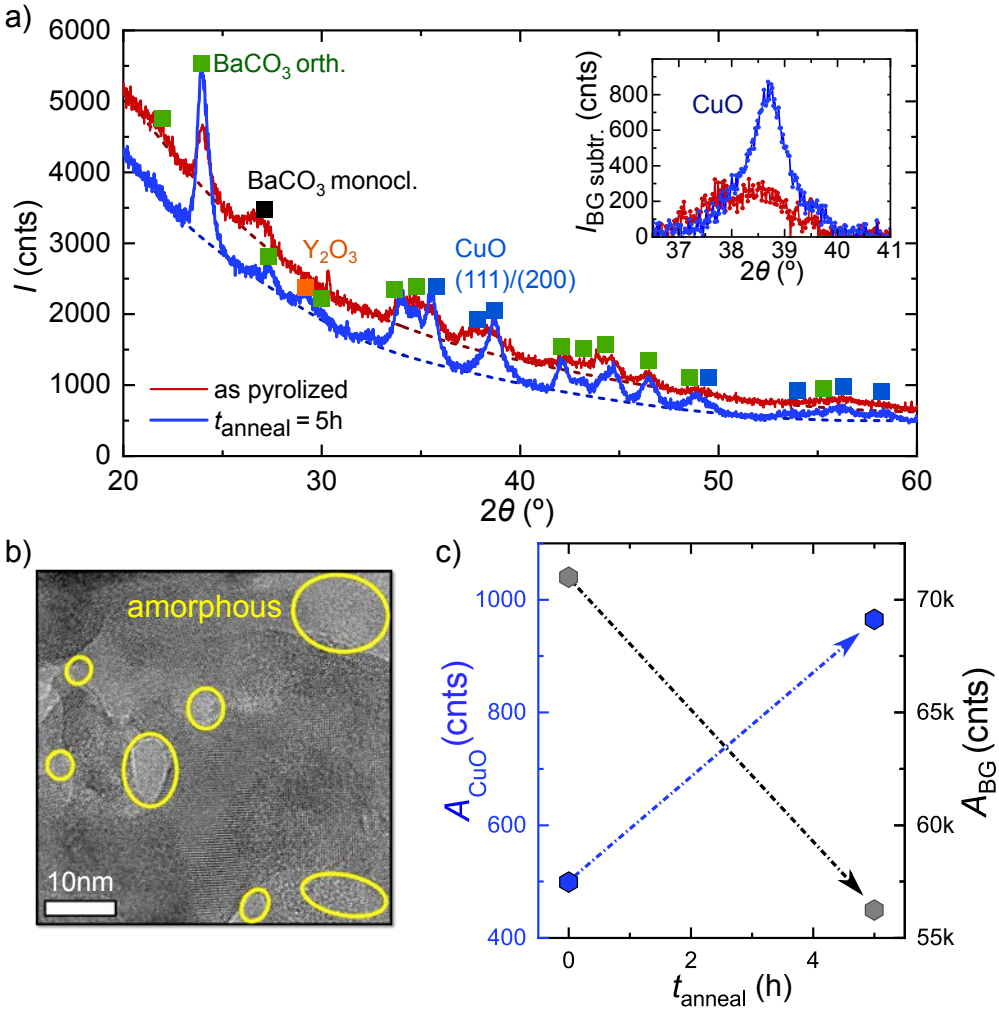

FIGURE 4.10: Identification of amorphous matter: (a) GI-XRD measurements of an as-pyrolyzed film and after annealing at 500 °C for 5 h. Inset shows the CuO (111)/(200) peaks after background subtraction. (b) Exemplary TEM image with amorphous regions (encircled in yellow) in an as-pyrolized film. (c) Integrated area intensities, A_{CuO} and A_{BG}, of the CuO (111)+(200) reflections and the background intensity, respectively.

The combined area intensity of the CuO (111) and (200) planes, A_{CuO}, and of the background intensity, A_{BG}, are plotted against the annealing time in Fig 4.10c). Amorphous phases are known to result in one/two broad maxima in the X-ray diffraction pattern [160].[11] After post-annealing, the background

[11] The background intensity is thought to be a sum of two amorphous signals, one originating from the glass substrate holder, the other from the precursor film.

intensity decreases from > 70k to < 57.5k counts (Fig. 4.10c)). Concurrently, the integrated CuO intensity reaches almost double of its initial value, suggesting that a part of the CuO is indeed in the amorphous state in the as-pyrolized film. The change in CuO evolution is further shown through the background subtracted intensities of the CuO (111) and (200) reflections (Fig. 4.10a), inset). In summary, we have analyzed the state of precursor films which are used in the following for *in-situ* growth experiments. These are found to exhibit a dense microstructure with nanometrically sized precursor phases which should allow for rapid transformations in the TLAG process. We further confirm, using the example of the CuO phase, that a fraction of the precursors are amorphous in the as-pyrolyzed films. This fraction will, hence, remain hidden to detection through X-rays unless crystallization takes place during the temperature profiles. Nevertheless, it can be concluded that the CSD approach followed here allows to produce precursor films with a nanocrystalline microstructure suitable to undergo rapid transformations.

4.3 Study of the (Ba-Cu-O) binary system

With the aim to study transient liquid assisted growth of YBCO through *in-situ* XRD experiments, we first focus on the simplified system that contains only $BaCO_3$ and CuO in pyrolyzed film form. This will allow us to study the underlying reactions and kinetics before extending those efforts to the full complexity of YBCO growth.

The melting behaviour of pseudo-binary BaO-CuO mixtures in film and powder form has been subject of intensive research already shortly after the discovery of superconductivity in the La(Y)-Sr(Ba)-Cu-O perovskites [161–164]. Especially flux methods were considered promising in synthesizing the layered cuprate structure due to the feasibility of the approach to fabricate single-crystalline quality specimen for anisotropy studies of the novel material class [163, 164]. However, studies of the binary melting characteristics showed differences due to the crystalline state of the investigated mixtures. For instance, the phase diagram constructed by T.B. Lindemer [161] includes similar melting temperatures as obtained by M. Nevrira [140] and W. Zhang [162], all three of which worked with grinded powders. Downshifts in melting temperature up to 150°C were later stated by P.Y. Chu for CSD films from metal trimethylacetate and hydroxide based precursors [141] and reinforced for metal-acetate based CSD films by P. Vermeier [165].

The aforementioned authors came to construct a pseudo-binary phase diagram, as shown in Fig.4.11, by carrying out quench studies in different gas atmospheres. At low temperatures, $BaCuO_2$ and CuO phases are found in solid form if $BaCO_3$ decomposition took place or was initiated at the quenched temperature. The eutectic line defines the onset temperature, T_E, for compositions of all (Ba-Cu) ratios where melting starts to take place. At the eutectic point, that is where the (Ba-Cu) ratio is equal to 3(BaO)-7(CuO) or (3-7), the full mixture melts congruently. In all other cases, the mixture melts partially and either $BaCuO_2$ or CuO remain solid up to the liquidus temperature, T_L, where a homogeneous melt is formed.
However, studies that were involved in the construction of a phase diagram, as shown in Fig.4.11, utilize low heating ramps, typically $\leq 0.15\,°C\,s^{-1}$, and differ significantly in precursor characteristics. Besides, phases and reactions were determined through quenching and post-characterization by XRD and SEM. The identification of a liquid phase or partial melting is then cumbersome, particularly since crystallization can occur while the quenched sample is cooled down. The approach being followed in the TLAG process is fundamentally different from previous growth methods. High heating ramps in the range of ≤ 0.4 - $60\,°C\,s^{-1}$ are used to preserve small precursor sizes and promote fast reactivity of phases at the right growth conditions. Hence, by studying the (Ba - Cu - O) system we aim to develop a framework for the specific, nanocrystalline precursor films achieved in this work via CSD and derive an according phase diagram using the non-equilibrium process conditions to emulate YBCO TLAG.
In total, the three (Ba-Cu) ratios denoted in Fig. 4.11, (2-3), (3-7) and (4-11) were explored to grow YBCO films, though the majority of experiments shown in this chapter and chapter 5 will comprise (2-3) and (3-7) films. Only the (2-3) composition equals the (Ba-Cu) ratio of YBCO, while the other mixtures are copper-rich. We have varied the copper concentration as means of tuning the supersaturation conditions. Copper-rich melts are expected to allow for a higher equilibrium Y concentration in the melt, which decreases the relative supersaturation according to eq. 4.6. As will be introduced in 5.1.4, this strategy was explored to reduce the optimal window for c-axis YBCO growth with regard to lower the processing temperatures.

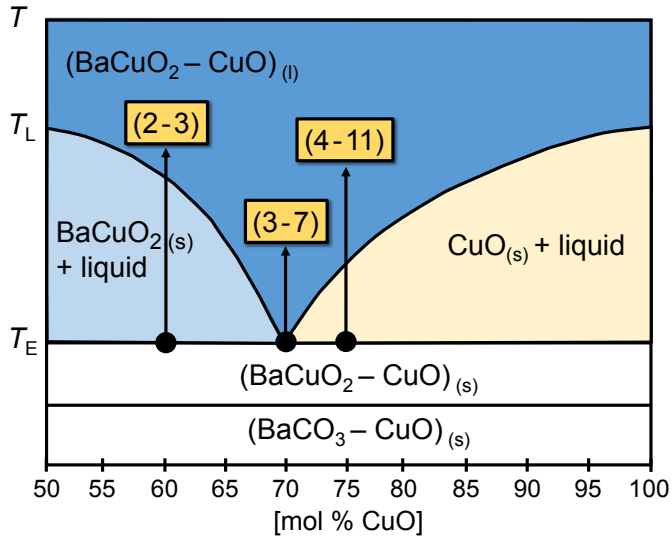

FIGURE 4.11: Schematic $BaCuO_2$-CuO phase diagram adapted from [140, 141]. Characteristic temperatures are dependent on atmosphere, distribution and grain sizes of precursor phases and specimen type (powders or films). Cation compositions studied here, are included in form of $(x - y)$, x and y referring to the amount of Ba and Cu. Although, strictly speaking, carbon and CO_2 should not be included in equilibrium phase diagrams, the $BaCO_3$ and CuO solid phases are kept here being the initial precursor phases in our CSD films.

The binary films studied in the following are of (3-7) composition prepared on MgO single crystal substrates to diminish its reactivity with the highly corrosive (Ba - Cu - O) melt. The *in-situ* growth experiments were carried out at Soleil Synchrotron with the setup described in 3.6.

4.3.1 Phase evolution of binary (3-7) films

To probe the involved kinetics, binary films with a cation concentration of 1M were heat-treated at 0.2 bar, 1 mbar and 0.25 mbar of oxygen partial pressure (P_{O2}), 1 bar of total pressure (P_{total}). An X-ray transparent, domed heating stage, as introduced in 3.6, was used to heat the films at the maximum rate of 4.5 °C s^{-1} to temperatures well above the eutectic temperatures denoted in literature [161]. The thermal profiles are included in Fig.B.1, Appendix B. Each 100 ms a 2D-XRD scan was acquired which can be converted into an intensity versus 2θ profile through count integration in the χ angle. The highest heating rate is chosen here to replicate non-equilibrium thermal conditions as targeted for the final TLAG process. A custom Matlab graphical user interface,

developed in this thesis, was then used to identify phases and temperature windows of interest for further data analysis (see 3.6). Tab.4.2 summarizes all phases that could be observed during the annealing processes with the according 2θ ranges and Bragg reflections.

	Miller indices (hkl)	2θ range (18 keV) [°]	Structure
$BaCO_3$	(111)/(021)	10.00-11.25	orthorhombic
CuO	(111)	16.63-17.27	monoclinic
Cu_2O	(111)	15.53-16.49	cubic
$BaCuO_2$	(611)	13.09-13.47	cubic
$BaCu_2O_2$	(103)/(200)	13.39-13.94	tetragonal

TABLE 4.2: Overview of phases observed in the thermal evolution of binary mixtures on MgO upon heating at 4.5 °C/s, P_{O2}=0.2 bar, 1 mbar, 0.25 mbar, P_{tot}=1 bar. Miller indices refer to the peaks being followed in the analysis. Fitting was carried out in the denoted 2θ ranges. All phases were identified using the ICDD database [33].

The crystallographic planes, denoted in tab.4.2, have no overlap with other phases allowing to track their evolution through fitting with Lorentzian peak profiles. Exemplary fits of the (111) and (021) reflection of $BaCO_3$ are shown in Fig.4.12a) for a temperature window of 600-750 °C at P_{O2}=0.2 bar where the decomposition process takes place. For visibility reasons, only 10% of the acquired data are fitted. A smaller step size and bigger temperature range are, however, chosen to show the evolution of fitted peak intensity and area in Fig.4.12b). A double Lorentzian profile with linear background function were found to reach robust fit conversion with R^2 values close to 1 at reasonable processing time.[12]
Note that peak area and intensity show a discrepancy at the onset of $BaCO_3$ decomposition (Fig.4.12b)). This can be attributed to broadening mechanisms that influence the maximum peak intensity, however, leave the area intensity unaffected. For that reason, the peak area, being a more robust measure for the actual phase amount [123], is further used to define characteristic temperatures (Fig.4.12c)): Reactions that involve the initial or final product, typically show an asymptotic behaviour on one side of the integrated intensity. To determine onset and final temperatures of the reactions, T_{on} and T_f, we look at 90% and 10% of the saturated value of each curve, exemplified in Fig.4.12c)) through dashed red lines.

[12] An overview on the methods to track *in-situ* phase evolution is given in 3.6.2.

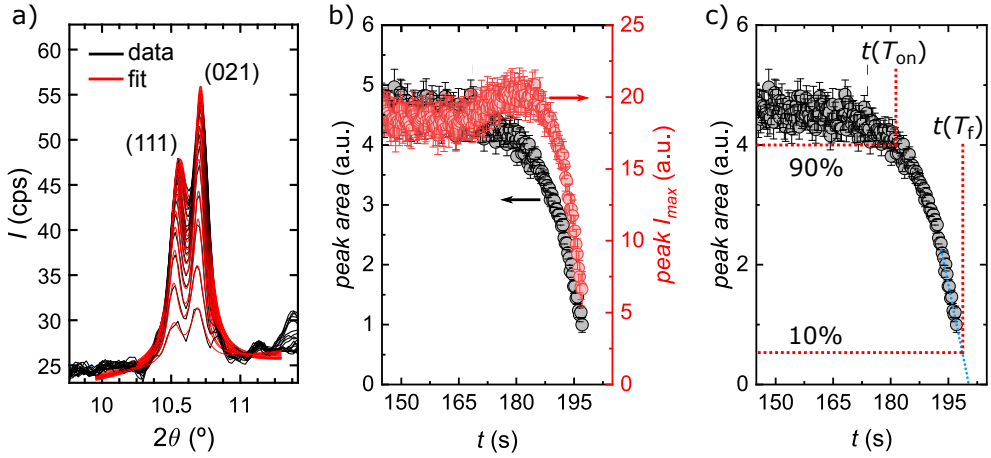

FIGURE 4.12: Exemplary fitting procedure to obtain characteristic temperatures, phase evolution and crystallite sizes: (a) $BaCO_3$ double peak fitting in temperature range of 600 - 750 °C. (b) Evolution of peak intensity and area as a function of time. Alternatively, the fitted values can be represented as function of temperature. (c) Determination of onset and final temperatures, T_{on} and T_f, at 90% and 10% of the maximum measured value of each phase.

The fitted values in Fig.4.12c) are cut at the point when the recorded intensity becomes insufficient for the fit to converge. An extrapolation of the missing data is then obtained through linear fitting of the integrated intensity tails (dashed blue line in Fig.4.12c)). The same approach is carried out on both sides of intermediate phases whose intensity follows a dome-shaped evolution.[13] Errors on characteristic temperatures are obtained at $\pm 5\%$ of the 90% and 10% criterion. The same procedure, as discussed above, is applied to all identified phases in tab.4.2.

The temperature and time evolution of phases of the three binary (3-7) films, heated at a P_{O2} of 0.2 bar, 1 mbar and 0.25 mbar at 4.5 °C s^{-1}, is shown in Fig. 4.13. For enhanced visibility, the curves are normalized to their maximum peak area values. Each of the binary films initiates from the precursor phases $BaCO_3$ and CuO. Upon heating and at temperatures above 650 °C the precursor phases take part in different reactions that vary with P_{O2}.

[13] Phases that appear as intermediate product, not shown here.

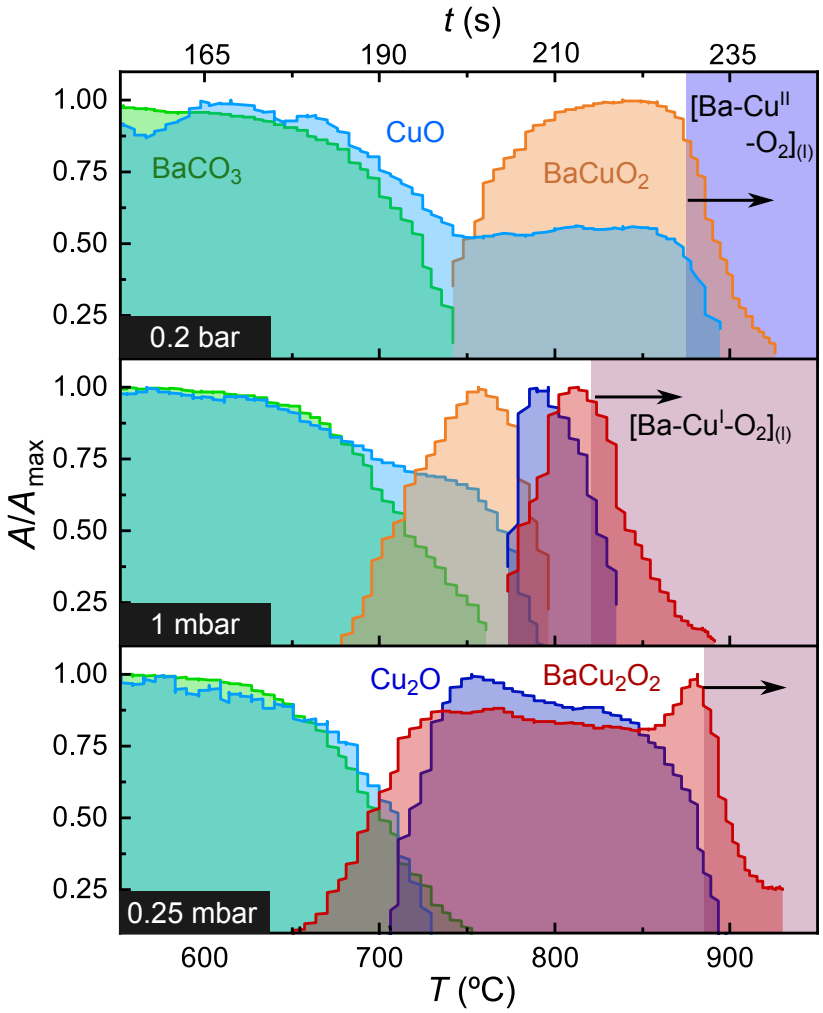

FIGURE 4.13: Time and temperature dependent phase evolution of (3-7) binary films heated with a ramp of 4.5 °C s^{-1} at 0.2 bar, 1 mbar and 0.25 mbar of P_{O2} (from top to bottom), shown as normalized area intensity A/A_{max}. The identified phases from tab. 4.12 are labeled. Complete disappearance of all crystalline phases and melt formation is indicated through coloured regions and arrows.

A discussion of the involved reactions and temperatures can be made for the different P_{O2} ranges (see below). The equations in this section are not adjusted and kept general to account for the use of films with varying $BaCO_3$ to CuO ratio (e.g. (2-3), (3-7)).

High P_{O2} (200 mbar) increasing temperature:
At the highest explored oxygen partial pressure the $BaCO_3$ and CuO signals start to decrease at 665 ± 15 °C. This temperature range is largely unchanged for the lower partial pressures. When treated alone, $BaCO_3$ would decomposes into BaO through CO_2 release at much higher temperatures (eq. 4.1). Here, however, a reaction with CuO takes place to form $BaCuO_{2\,(s)}$. The phase further reacts with CuO above 870 ± 5 °C, yielding complete disappearance of any crystalline signal in the XRD spectra. The absence of crystalline phases suggests that a liquid, based on $BaCuO_2$ and CuO, is formed. The full binary reaction (BR) reads as follows:

$$\textbf{BR1: } BaCO_{3(s)} + CuO_{(s)} \rightarrow BaCuO_{2(s)} + CuO_{(s)} \rightarrow [Ba - Cu^{II} - O]_{(l)}. \quad (4.17)$$

The liquid phase is denoted with the copper (+2) valence state as Cu^{II}. Alternatively, we suggest that $BaCO_3$ and CuO can directly react to the liquid phase according to

$$\textbf{BR2: } BaCO_{3(s)} + CuO_{(s)} \rightarrow [Ba - Cu^{II} - O]_{(l)}. \quad (4.18)$$

This is supported by the fact that all $BaCuO_{2\,(s)}$ forms after a delay in temperature in these experiments. While the precursor phases initiate the reaction at 665 ± 15 °C, the $BaCuO_{2\,(s)}$ intermediate does not form until $> 700 \pm 15$ °C. The formation of $BaCuO_{2\,(s)}$ requires an incubation time to overcome the critical radius and crystallize into the solid phase. Given the high heating ramps in TLAG, it may well happen that the (Ba - Cu^{II} - O) liquid temperature is reached before the crystallization of $BaCuO_{2\,(s)}$ occurs, as we will see in further examples of this thesis. Reaction BR2 is also proposed here to account for the high YBCO growth rates that we will identify already at these low temperatures (5.1.1). Note that also here all phase transformations take place on a scale of only 10-20 s suggesting that a liquid is involved as soon as $BaCO_3$ reacts with CuO at temperatures above 650 °C (as shown in the proposed kinetic phase diagram in Fig. 4.15). For visibility reasons, we have included only the abrupt disappearance of all solid phases (Fig. 4.13) which is from here on referred to as (Ba - Cu^{II} - O)$_{(l)}$ "full liquid region".

Intermediate P_{O2} (1 mbar) increasing temperature:
At 1 mbar the overall reaction path becomes more complex. Similar to the experiment in air ($P_{O2} = 200$ mbar), $BaCO_3$ and CuO form $BaCuO_{2(s)}$. Further advancing in temperature, however, results in Cu reduction from (II) to (I) in oxidation state and the formation of the reduced phases Cu_2O and $BaCu_2O_2$ at 760 ± 5 °C. At temperatures above 818 ± 6 °C also the reduced phases decrease

in intensity leaving no crystalline signal behind. This suggests that full melting of the solid phases is also rendered possible coming from the $BaCu_2O_{2\,(s)}$ phase. The full reaction towards the full liquid region is then

$$\begin{aligned}\textbf{BR3: } & BaCO_{3(s)} + CuO_{(s)} \rightarrow BaCuO_{2(s)} + CuO_{(s)} \\ & \rightarrow BaCu_2O_{2(s)} + Cu_2O_{(s)} \rightarrow [Ba - Cu^{I} - O]_{(l)}.\end{aligned} \tag{4.19}$$

In agreement with the previous discussion, coexistence of solid phases and liquid formation can be postulated according to

$$\begin{aligned}\textbf{BR4: } & BaCO_{3(s)} + CuO_{(s)} \rightarrow BaCuO_{2(s)} + CuO_{(s)} \\ & \rightarrow [Ba - Cu^{II} - O]_{(l)} \rightarrow [Ba - Cu^{I} - O]_{(l)}.\end{aligned} \tag{4.20}$$

Here, we include that the observed copper valance change ($Cu^{II} \rightarrow Cu^{I}$) can also take place in the liquid phase, hence, allowing $(Ba\text{-}Cu^{II}\text{-}O)_{(l)}$ to transform to $(Ba\text{-}Cu^{I}\text{-}O)_{(l)}$.

At low P_{O2} (0.25 mbar) increasing temperature:

At the lowest oxygen partial pressure, no $BaCuO_2$ intermediate phase is formed at all and the precursor phases react directly towards the reduced phases. Similar to the above two cases, two reaction paths are proposed:

$$\textbf{BR5: } BaCO_{3(s)} + CuO_{(s)} \rightarrow BaCu_2O_{2(s)} + Cu_2O_{(s)} \rightarrow [Ba - Cu^{I} - O]_{(l)} \tag{4.21}$$

$$\textbf{BR6: } BaCO_{3(s)} + CuO_{(s)} \rightarrow [Ba - Cu^{I} - O]_{(l)} \tag{4.22}$$

Up to now, we have considered the time and temperature dependent evolution of phases to define the main reaction paths in the binary (3-7) system at different oxygen partial pressures. All three experiments are carried out under rapid heating at 4.5 °C/s, hence, the involved transformations occur at time scales of seconds. This might suggest that partial melting occurs all along the heating profile, initiated at the onset of $BaCO_3$ reaction with CuO. As motivated in 4.1.1, the melting transition can be considerably downshifted in temperature due to size effects of the reacting phases. Given $BaCO_3$ and CuO grain diameters in the range of nanometers in the CSD films used here (4.2), we therefore propose partial melting to take place at reduced temperatures. In turn, the use of increased heating ramps to preserve small particle sizes might be a viable strategy to promote melting at these low temperatures. In addition, we note that the final product of all binary reactions (BR1-BR6) is a full liquid phase, either $(Ba\text{-}Cu^{II}\text{-}O)_{(l)}$ or $(Ba\text{-}Cu^{I}\text{-}O)_{(l)}$ with copper (+2)

or (+1) valance state depending on the P_{O2} of the experiment. The emergence of the full melt is identified through disappearance of the (Ba - Cu - O) solid phases, leaving no trace of any crystalline signal. Further indications of melting can be suggested considering the evolution of particle sizes in the following section.

4.3.2 Crystallite size evolution of phases in binary (3-7) films

As peak fitting has been employed for the analysis in 4.3.1, crystallite sizes can be estimated by means of eq. 3.18a given the integral breadth of each peaks. Debye-Scherrer crystallite sizes as a function of time and temperature are shown for all three binary experiments in Fig. 4.14. Fitted values are presented for temperature ranges where a reliable fit could be attained.
For all experiments, initial particle sizes for $BaCO_3$ and CuO (at 550 °C) reach an average of 35 ± 2 nm and 16 ± 2 nm, respectively. Although Debye-Scherrer particle sizes do not need to coincide with real-space microscopy values, the order of magnitude obtained here is in good agreement with TEM results from 4.2.
Upon heating, precursor particle sizes monotonically increase, even above the point where $BaCO_3$ reaction with CuO occurs. Taking the example of $BaCO_3$ at P_{O2} =0.2 bar, the evolution ends in a broader stray of values due to low signal of the remaining phase. The constant increase in particle sizes might be explained by coarsening of the phases at elevated temperatures [76] and the reaction of small sized particles prior to big ones.[14]
A decrease in particle sizes is, however, observed in those high temperature regions where all crystalline phases disappear, hence, the previously identified $(Ba\text{-}Cu^{II}\text{-}O)_{(l)}$ or $(Ba\text{-}Cu^{I}\text{-}O)_{(l)}$ full liquid region. The temperature margin where full liquid emergence was observed previously is included in Fig. 4.14 through coloured regions. For instance at 0.2 bar and $T = 850 - 920$ °C, CuO and $BaCuO_2$ grain sizes appear to decrease in the $(Ba\text{-}Cu^{II}\text{-}O)_{(l)}$ melting window. A similar trajectory is observed for the lower two pressures in the $(Ba\text{-}Cu^{I}\text{-}O)_{(l)}$ melting window. Hence, the crystallite size can be used as additional measure to sense the emergence of the full liquid, complementary to the evolution of the absolute phase signal.

[14] The Debye Scherrer size, which is an average of the crystallite size distribution, would hence shift to bigger values.

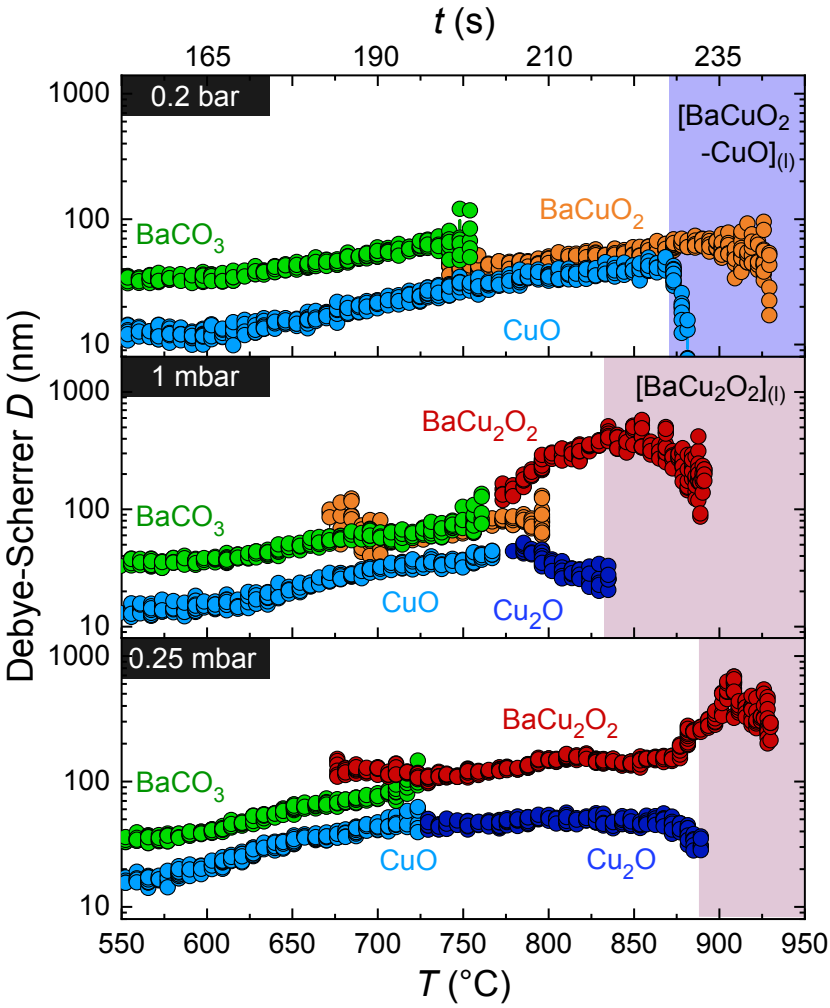

FIGURE 4.14: Time and temperature dependent crystallite size evolution of (3-7) binary films for 0.2 bar, 1 mbar and 0.25 mbar of P_{O2}, heated at 4.5 °C s^{-1} (from top to bottom). Grain sizes D were calculated using the Debye-Scherrer equation 3.18a with the integral breadths obtained from fitting with Lorentzian profiles.

We further observe that at P_{O2} =1 mbar and $T = 775 - 820$ °C the $BaCu_2O_2$ phase grows rapidly to crystallite sizes in the range of 400 nm. Such an increase in size on a scale of $\Delta t \approx 10$ s might suggest an enhanced diffusion of cations through a liquid medium, hence indicate melting below the full liquid regions. The presence of liquid at these low temperatures will further be suggested through studies of YBCO growth growth rates in 5.1.2.

The analysis of crystallite sizes can give complementary information on the involved reactions. For instance, considering the matching size of CuO and Cu_2O at 1 mbar and 0.25 mbar it can be suggested that at least a part of CuO grains undergo the valence change and do not participate in the aforegoing reactions (e.g. $BaCuO_{2(s)}+CuO_{(s)} \rightarrow (Ba\text{-}Cu^{II}\text{-}O)_{(l)}$). A similar observation was made in [138], where upon fast heating at 100 °C s^{-1} in reduced oxygen atmosphere copper reduction took place and CuO could not be preserved. Hence, we can conclude that particle size analysis might be a viable approach to study such non-equilibrium process kinetics, and is shown here to provide additional insights into melting and the copper reduction process. The method will further be employed throughout chapter 5 in the context of YBCO growth.

4.3.3 Kinetic phase diagram of the binary system

The aforegoing findings, including phase transformations and onset/final temperatures of reactions, can be used to construct the $P_{O2} - T$ dependent, kinetic phase diagram shown in Fig. 4.15. We term this visual representation of the process *kinetic phase diagram* since, contrary to equilibrium processes, the temperature was constantly increased at a high ramp of 4.5 °C s^{-1}. Such non-equilibrium processing conditions favour the preservation of small particle sizes to enhance reactivity which is the base of the TLAG scheme. Hence, the kinetic phase diagram should be regarded as a compact illustration of the main process characteristics being representative for the type of precursor films used in this work (size and distribution of phases), the employed heating ramp and film composition.
The coexisting phases observed via *in-situ* XRD experiments are visualized in Fig. 4.15 through $P_{O2} - T$ regions that are labeled accordingly.[15] Measured onset and final temperature values, according to the 90% and 10% criterion, are represented through markers and interpolated by dashed lines (see legend). For comparison, the correspondent literature values are included as solid lines. The melting line $BaCuO_{2(s)}+CuO_{(s)} \rightarrow [BaCuO_2\text{-}CuO]_{(l)}$ and solid-solid transformation $BaCuO_{2(s)}+CuO_{(s)} \rightarrow BaCu_2O_{2(s)}$ were obtained from TGA analysis on micron-sized powders [161, 166],[16] while the copper reduction line ($CuO \rightarrow Cu_2O$) is deduced from standard Gibbs free energy of formation calculus [167]. Reference values for the elimination of $BaCO_3$ through reaction with CuO are not included due to the high discrepancy of the reported values (700 °C in [89] and 900 °C in [136]). Nevertheless, both authors attribute the reduced decomposition temperatures to the catalytic activity of

[15] Taking into account the discussion on the proposed binary reactions.
[16] Onset temperatures are determined at the point of rapid mass-loss.

CuO. The reference melting line of the reduced $BaCu_2O_2$ phase was obtained in [101] via post-characterization methods.

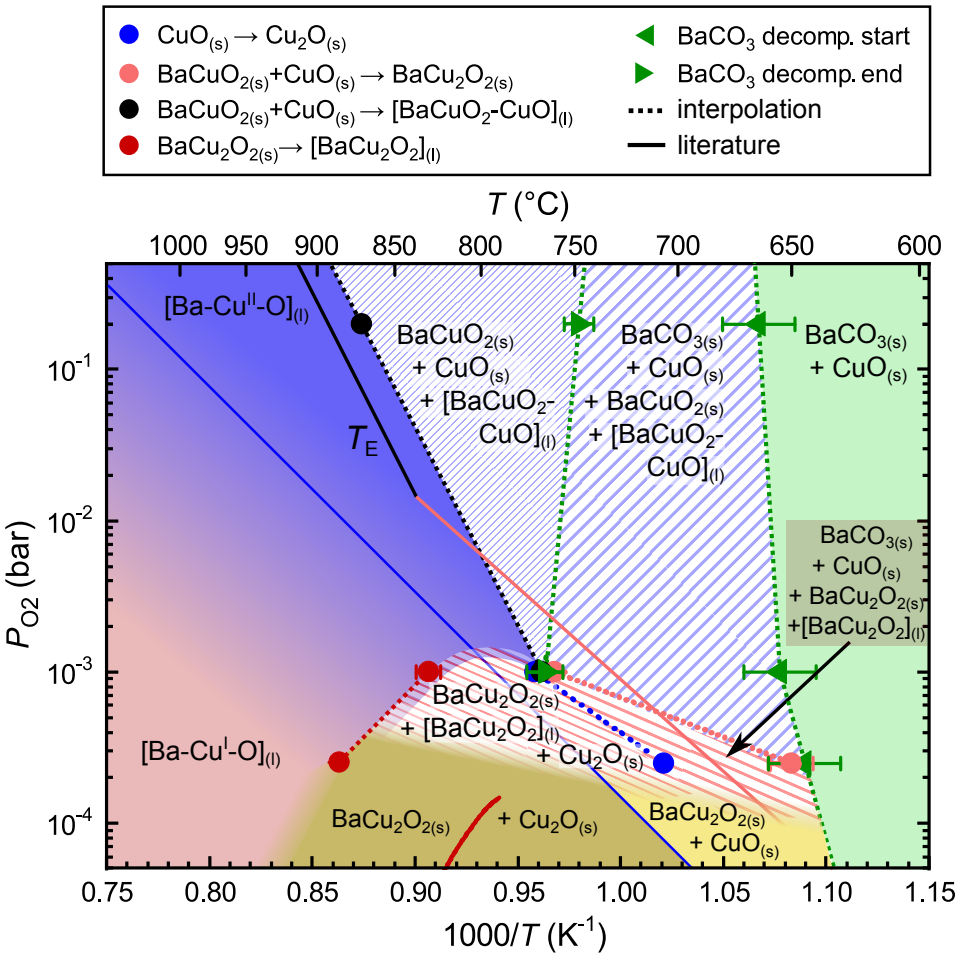

FIGURE 4.15: Binary kinetic phase diagram constructed from *in-situ* XRD results of (3-7) films heated at 4.5 °C s^{-1} (Fig.4.13): Dashed lines connect experimental values (markers), solid lines represent literature values [101, 161, 166, 167]. Measured values are obtained through the 10% and 90% criteria of the normalized phase evolution. Error bars stretch ±5% around these values. The main reactions defined in 4.3.1 (eq. 4.17-eq. 4.22) are included through labeled regions. Areas of uniform color indicate full solid and full liquid regions; dashed regions suggest coexistence of liquid and solid phases. The color gradient in the full liquid region implies that melting is achieved from solid phases with a continuous variation of the Cu oxidation state from (I) to (II). Full solid regions in the lower part of the diagram are obtained from experiments that include pressure variations (4.4.2).

The binary kinetic phase diagram in Fig. 4.15 allows to draw several conclusions about the TLAG-CSD process characteristics and how it compares with equilibrium processes:

1. **$BaCO_3$ elimination:** Decarbonization takes place through reaction with CuO in an approximate temperature range of 650 °C to 750 °C. Even the upper temperature limit of 750 °C is strongly reduced as compared to sole $BaCO_3$ powders which typically decompose at temperatures well above 900 °C [89, 135, 136]. More than that, the values compare with experiments performed on binary (Ba - Cu - O) films that were heated with low ramps of 0.16 °C s^{-1} [136, 141]. We employed, however, 4.5 °C^{-1} and full decomposition could be reached within $\Delta t \approx 20$ s. While most authors argue that diminished decomposition temperatures can either be attributed to the catalytic influence of CuO [89] or enhanced reactivity of nanosized particles [138], none of the studies explores the system at the high heating ramps used here. Hence, we could demonstrate that complete $BaCO_3$ elimination can be achieved under these non-equilibrium, kinetic conditions. This might be attributed to the nanocrystallinity of precursor phases and presence of amorphous matter in the CSD films in addition to an acceleration of the reaction in the presence of the liquid.

2. **Full liquid region:** We have identified that liquid formation is rendered possible coming from (Ba - Cu - O) solid phases with a continuous variation of the Cu valence state from (+2) to (+1). At increased oxygen partial pressures $BaCuO_{2(s)}$+$CuO_{(s)}$ is found to melt resulting in no crystalline byproducts observable via XRD. At reduced oxygen partial pressures, however, also $BaCu_2O_{2(s)}$+$Cu_2O_{(s)}$ is found to melt. As in these particular experiments the copper valance state is shown to change, also liquid properties such as viscosity, reactivity and ability to solubilise $CuO/Cu_2O/Y_2O_3$ might vary. We have included a color gradient between both liquid regions to also account for possible changes in liquid characteristics due to the varying oxidation state of copper.

3. **Low temperature melting:** We have also suggested partial melting at low temperatures, previous to the apparent disappearance of the solid phases. This is included in Fig. 4.15 through dashed regions. The presence of low-temperature melts below equilibrium melting points was suggested in previous work for binary $BaCO_3 + CuO$ films at 620 °C [141], in Vapor-Liquid-Solid growth of YBCO at 750 °C [168] and for hybrid liquid phase epitaxy grown YBCO films at 770 °C [81], amongst others. The origin is believed to be related to the formation of a quasi-liquid layer through surface melting and crystallite size effects. Low

temperature melting or partial melting can also be suggested here given the nanometric size of phases in CSD pyrolysed films (4.2) and the fast conversion rates observed in all experiments. In that sense, the use of high heating ramps might be a key parameter to preserve small particle sizes, avoid coarsening of intermediate phases.

The derived kinetic phase diagram overviews all involved reactions in binary (3-7) mixtures and lays the groundwork for YBCO growth through the TLAG-CSD methodology. While the following sections aim to extend our knowledge to the full ternary (Y-Ba-Cu-O) mixtures, the results throughout chapter 4 and 5 will be related to the growth kinetics observed here.

4.4 Nucleation and growth of YBCO

Analogously to the binary experiments, the *in-situ* growth studies are expanded here to the full ternary Y_2O_3 - $BaCO_3$ - CuO (Y - Ba - Cu - O) system. We will first define the main $P_{O2} - T$ routes explored to bring the precursor films into a region of the phase diagram where growth of YBCO is achieved. Main reactions, limitations and potentialities of each route, as well as the correspondent kinetic phase diagrams will then be developed.

4.4.1 TLAG routes for YBCO growth

The binary kinetic phase diagram is used here to define the explored $P_{O2} - T$ routes into regions of the phase diagram where transient liquid assisted growth of YBCO is expected (Fig. 4.16). In particular, we have investigated two different approaches to grow YBCO: A steady increase in temperature keeping P_{O2} constant, denoted as T -route, and a two-step approach heating first at a low oxygen partial pressure where YBCO is not stable ($\leq 10^{-5}$ bar), followed by a P_{O2} increase into the stable region for nucleation and growth, entitled P_{O2} -route. The range of processing conditions is summarized in 3.1.3. The two different routes are represented through arrows in Fig. 4.16. Specifically for the P_{O2} -route we have encountered that different characteristic solid phases are formed depending on the chosen P_{O2} for the low pressure step. For that reason, the route will further be subdivided into $P_{O2}(BaCu_2O_2)$ - and $P_{O2}(Cu)$ -route to stress the different phases before YBCO growth (see 4.4.2).
Liquid assisted growth of YBCO is expected in those regions of the phase diagram where a melt can emerge and where YBCO is the stable solid phase, hence, the nucleation barrier can be overcome to form stable nuclei (4.1.3). Taking the binary phase diagram as a reference, the potential region for YBCO growth extends to the full $P_{O2} - T$ window where the liquid phase can form

(brown dashed line), confined by the $BaCO_3$+CuO decomposition onset at low temperatures and the YBCO peritectic and instability lines, T_P and T_{ins}, at high temperatures, respectively [101, 169]. At T_P, YBCO is reported to melt incongruently to Y_2BaCuO_5 + liquid, while above T_{ins} stable YBCO nucleation cannot be achieved [101].[17]

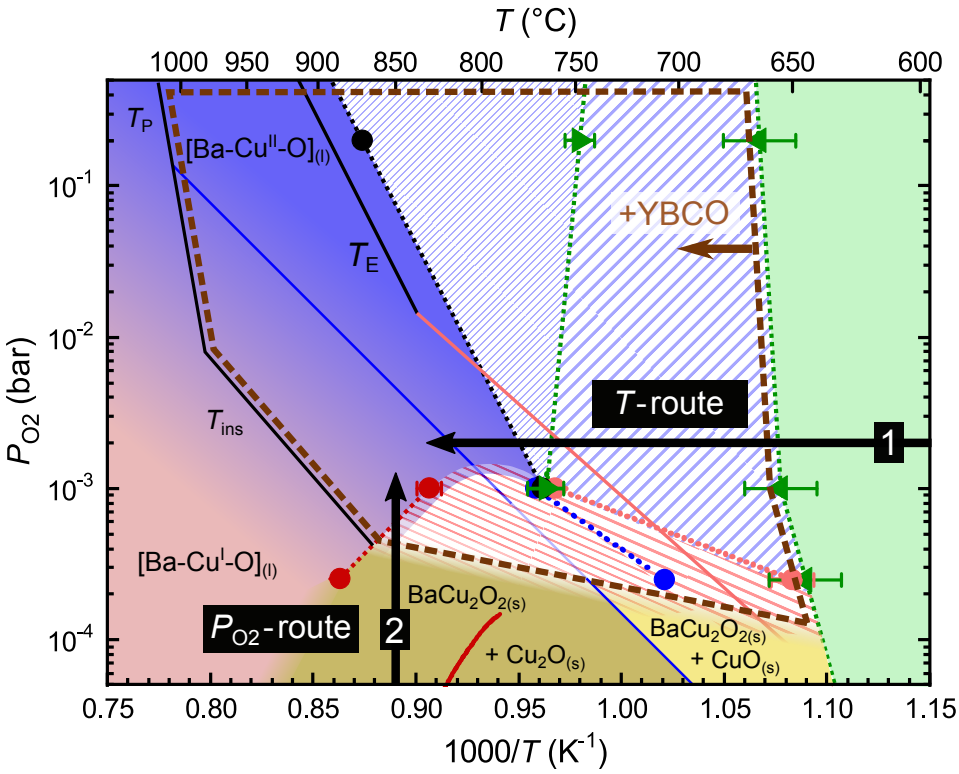

FIGURE 4.16: Main TLAG $P_{O2} - T$ growth routes: In the T-route heating is carried out at constant P_{O2}, $P_{total} = 1$bar into the (Ba - Cu$^{I/II}$ - O) full liquid region of the phase diagram. The P_{O2}-route is a two-step approach where the growth temperature is first reached at $P_{O2} = \leq 10^{-5}$ bar, $P_{total} = P_{O2}/5$; YBCO is not stable here. A pressure jump is then performed in isotherm conditions into the stable region. YBCO peritectic and instability lines (T_P and T_{ins}) are obtained from [101, 169]. The binary kinetic phase diagram is used for illustration (Fig. 4.15).

In the T-route the evolution of phases takes place progressively upon heating, similar to the binary experiments discussed earlier. The one-step approach might hence hold an intrinsic, kinetic complexity since a wide region of the

[17] Precisely speaking, YBCO nucleation is not achieved at reduced oxygen partial pressures below the instability line.

phase diagram is crossed where other solid phases coexist with YBCO, so may become competitive.[18] The approach also relies on rapid elimination of $BaCO_3$ to benefit from a wide range of processing conditions. In order to decouple YBCO growth from such competing kinetics and to simplify the reaction path, the P_{O2}-route was explored. In the following, we will hence define the governing reactions of each route and give a visual representation of the ternary system in form of kinetic phase diagrams.

4.4.2 YBCO growth through $P_{O2}(BaCu_2O_2)$- and $P_{O2}(Cu)$-route

As mentioned previously, growth of YBCO through the P_{O2}-route aims to decouple the reaction path since $BaCO_3$ decomposition and YBCO growth take place in two separate steps. In this section we define the governing reactions to obtain YBCO through pressure jumps into the stable region of growth.
At the synchrotron facility, P_{O2}-route experiments were carried out through use of two separated circuits with controlled gas and pressure regulation. A more detailed description of the setup is given in 3.6. Heating is first carried out at an oxygen partial pressures of P_{O2} =10^{-5}- 10^{-7}bar until the growth temperature, T_{final}, is reached. The desired oxygen partial pressure is adjusted through decrease of the total pressure, P_{total}=$P_{O2}/5$, using a rotary and turbo molecular pump in series.
Let us first consider the evolution of phases for a film of (3-7) composition upon heating at 0.4 C° s^{-1} to T = 850 °C, $P_{O2} = 10^{-5}$ bar, shown in Fig. 4.17a). In this initial base-pressure step CuO undergoes a valence change and a reaction to the reduced phases, Cu_2O and $BaCu_2O_2$, takes place according to

$$\begin{aligned} BaCO_{3(s)} + CuO_{(s)} + Y_2O_{3(s)} &\longrightarrow BaCO_{3(s)} + Cu_2O_{(s)} + Y_2O_{3(s)} \\ &\longrightarrow BaCu_2O_{2(s)} + Y_2O_{3(s)}. \end{aligned} \tag{4.23}$$

The formation of solid phases with copper (+1) valence state is in agreement with the binary phase evolution where at $P_{O2} = 0.25$ mbar the reduced phases are found stable (Fig. 4.13). Also the elimination of $BaCO_3$ is achieved independently of YBCO growth being one of the main advantages to this approach. As the final phase before YBCO growth is $BaCu_2O_2$, we will refer to this route from now on as $P_{O2}(BaCu_2O_2)$ - route.

[18] As well as a/b-oriented YBCO grains and homogeneous nucleation since the supersaturation strongly changes during heating.

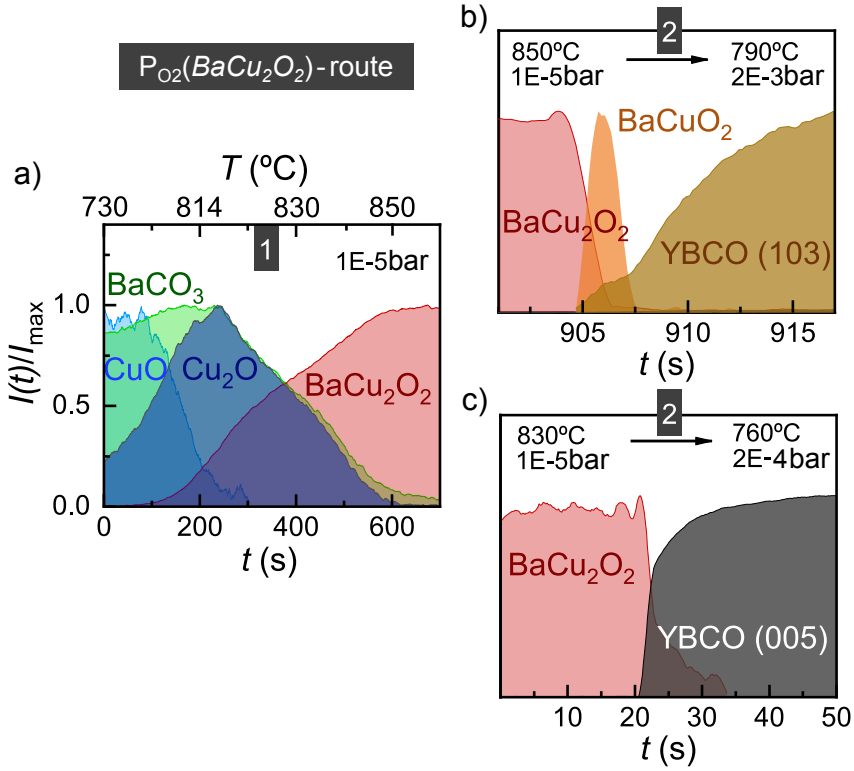

FIGURE 4.17: Phase evolution of ternary films, (3-7) composition, in the $P_{O2}(BaCu_2O_2)$-route approach. (a) Heating is carried out in the low pressure step at 0.4 °C s^{-1} to $T = 850$ °C, $P_{O2} = 10^{-5}$ bar. (b) and (c) show two different P_{O2} jumps from 850 °C and 830 °C to $2 \cdot 10^{-3}$ bar and $3 \cdot 10^{-4}$ bar of P_{O2}, respectively. The $P_{O2} - T$ paths towards the growth conditions are illustrated in Fig. 4.18.

Transient liquid assisted growth of YBCO in the $P_{O2}(BaCu_2O_2)$-route is achieved through P_{O2} increase at constant temperature. This ideal, isothermal case could not be realized with the experimental setup at the synchrotron facility due to the small heater mass and entrance of cold gas. Especially when the jump involved a big change in total pressure, a considerable temperature decrease occurred (see Appendix Fig. A.2). Nevertheless, the reactions could be studied throughout non-linear $P_{O2} - T$ paths as shown in Fig. 4.18, curved arrows. In particular, two experiments are discussed here where melting is expected from the $BaCuO_2$ and $BaCu_2O_2$ solid phases, Fig. 4.17b) and (c), respectively.

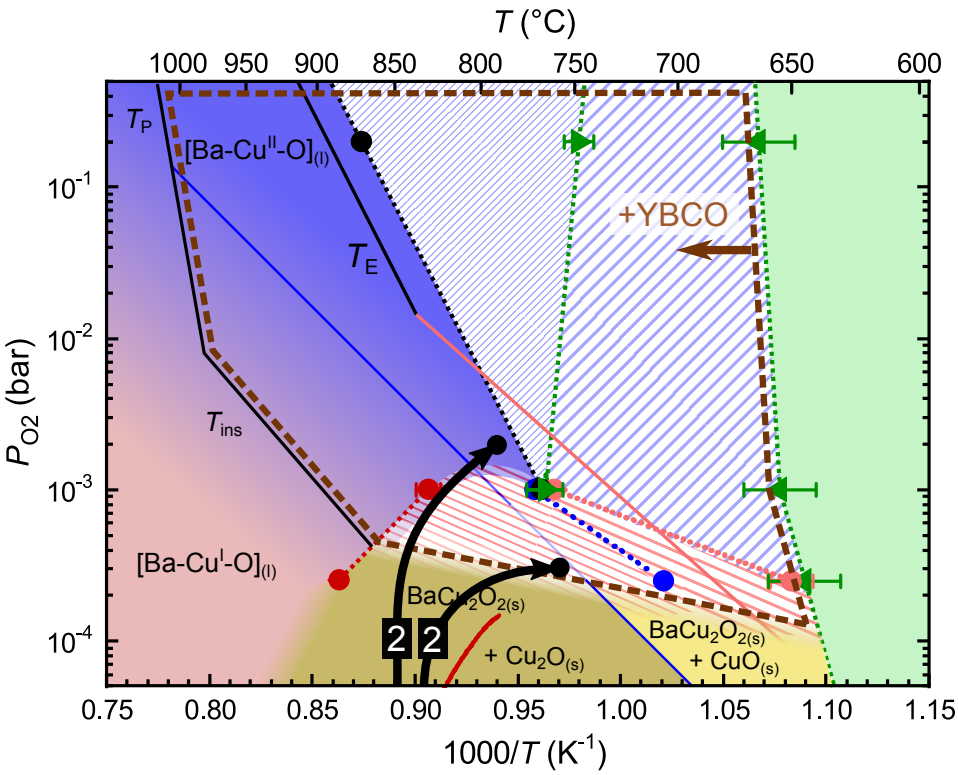

FIGURE 4.18: Illustration of the non-linear $P_{O2} - T$ paths of the two $P_{O2}(BaCu_2O_2)$ - route experiments in Fig. 4.17b) and (c), respectively.

In both cases the initial $BaCu_2O_2$ solid phase that was formed in the low pressure step disappears abruptly (in few seconds). When the P_{O2} jump is placed into the region with the $BaCuO_2$ solid phase and (Ba - Cu^{II} - O) liquid (Fig. 4.18), a short-lived $BaCuO_2$ is found as intermediate phase that rapidly decomposes (Fig. 4.17b)). Hence, both, $BaCuO_2$ and $BaCu_2O_2$ solid phases are not stable in these regions of the phase diagram, in agreement with the binary experiments carried out through the T - route. However, when the P_{O2} jump is placed in the $[BaCu_2O_2]_{(s+l)}$ region (Fig. 4.17c)), $BaCu_2O_2$ melts directly giving rise to YBCO.

The same phase analysis is carried out lowering further the base pressure. A high vacuum is created to reach base pressure values below $< 10^{-6}$ bar.[19] The route represents a phase evolution path which is governed by all stages of copper reduction (Fig. 4.19, left side). Similar to the $P_{O2}(BaCu_2O_2)$ - route,

[19] At the synchrotron facility, such low pressure values could be reached through evacuation of the dome with the turbo molecular pump operating at maximum capacity.

copper changes the oxidation state from (II) to (I), however, at even higher temperatures metallic copper is formed. The route will therefore be referred to as $P_{O2}(Cu)$ - route in the following. The absence of any crystalline (Ba - Cu - O) phase suggests the presence of an amorphous/nanocrystalline BaO and Y_2O_3 phase. The reaction reads

$$BaCO_{3(s)} + CuO_{(s)} + Y_2O_{3(s)} \longrightarrow BaO_{(s)} + Cu_{(s)} + Y_2O_{3(s)}. \tag{4.24}$$

The formation of metallic copper is not expected under these conditions. Its appearance at temperatures as low as 750 °C might be due to the formation of some carbon monoxide (CO) from the elimination of $BaCO_3$, significantly reducing the local oxygen atmosphere [94]. Upon pressure change to P_{O2}=10^{-3} bar, $Cu_{(s)}$ oxidizes and reacts with BaO to give rise to $BaCu_2O_2$ which is further consumed towards the YBCO phase (Fig. 4.19, left side). This is once again in agreement with the binary kinetic phase diagram, were the $BaCu_2O_2$ solid phase was observed in this $P_{O2} - T$ window.
In summary, the full reaction path of the pressure routes can be formulated as follows.

$P_{O2}(BaCu_2O_2)$-route (step 1 at $P_{O2} = 10^{-5}$bar):

$$\begin{aligned} BaCO_{3(s)} + CuO_{(s)} + Y_2O_{3(s)} &\rightarrow BaCu_2O_{2(s)} + Cu_2O_{(s)} \\ &\rightarrow [Ba\text{-}Cu^{I/II}\text{-}O]_{(l)} + Y_2O_{3(s)} \rightarrow YBa_2Cu_3O_{7-\delta} \end{aligned} \tag{4.25}$$

$P_{O2}(Cu)$-route (step 1 at $P_{O2} < 10^{-6}$bar):

$$\begin{aligned} BaCO_{3(s)} + CuO_{(s)} + Y_2O_{3(s)} &\rightarrow BaO_{(s)} + Cu_{(s)} + Y_2O_{3(s)} \\ &\rightarrow [Ba\text{-}Cu^{I/II}\text{-}O]_{(l)} + Y_2O_{3(s)} \rightarrow YBa_2Cu_3O_{7-\delta} \end{aligned} \tag{4.26}$$

The first line of eq. 4.25 and eq. 4.26 is attributed to the low pressure step. Here, the base oxygen partial pressure determines which phases stabilize. Growth of YBCO can then be carried out in the (Ba - $Cu^{I/II}$ - O) liquid region. Note that also here, in accordance with the binary case, the reactions are stoichiometrically not adjusted and kept general to account for the use of different film compositions. For instance, when growth is carried out with the (3-7) mixture, excess copper will be remain after YBCO growth is completed and segregated to the surface under the right processing conditions.

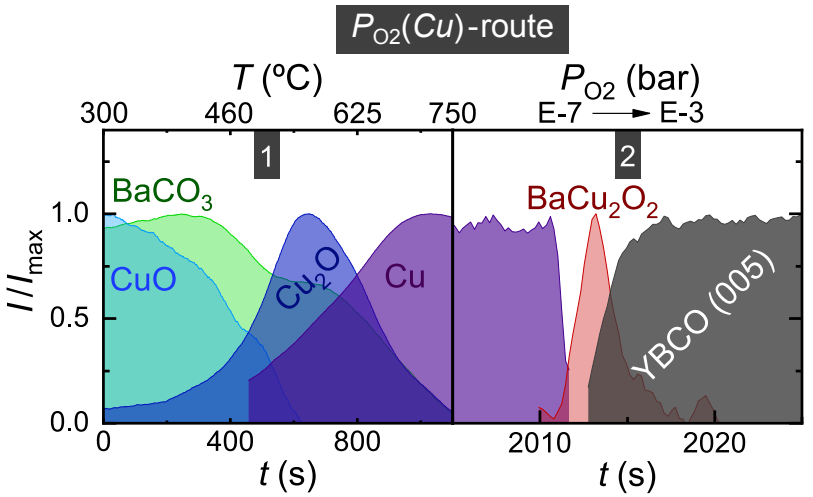

FIGURE 4.19: Evolution of phases for a ternary film of (2-3) composition in the *Cu* - route approach. The thermal conditions of the base pressure step and YBCO growth step: 0.4 C° s^{-1} to 800 ºC, $P_{O2,base} = P_{total}/5 = 10^{-7}$ bar) (left hand side) and $P_{O2,growth} = 10^{-3}$ bar at $T = 750$ ºC (right hand side)

We also note that although a fundamentally different path into the liquid region was explored here with the full ternary mixture, the observed phases are in good agreement with those from binary experiments carried out through the *T* - route approach. This reinforces that TLAG is a highly non-equilibrium process since the (Ba - Cu - O) kinetics are in agreement with the binary mixtures, hence, allowing for a transient melt to precede and assist the growth of YBCO. Nevertheless, the exact position of lines and regions have to be adjusted for the route explored here. An according ternary kinetic phase diagram for the pressure routes is currently constructed by Dr. S.Rasi.

4.4.3 YBCO growth through *T*-route and construction of kinetic phase diagrams

At the synchrotron facility, the growth of YBCO through the *T* - route was explored varying film composition (stoichiometric and copper-rich), heating ramp (0.4 - 4.5 ºC s^{-1}) and oxygen partial pressure ($P_{O2} = 10^{-4}$ -10^{-2} bar, $P_{total} = 1$ bar). Similar to binary experiments the evolution of crystalline phases could be probed in a wide temperature range allowing to construct kinetic phase diagrams also for the ternary mixtures studied here (Y_2O_3, $BaCO_3$, CuO). In this section we aim to define the YBCO growth characteristics using films of (2-3) and (3-7) composition, heated at 0.4 ºC and 4.5 ºC s^{-1}.

The influence of P_{O2} and heating ramps on the progression of phases is shown in Fig. 4.20a) and b), respectively, all of which are films of (2-3) composition.

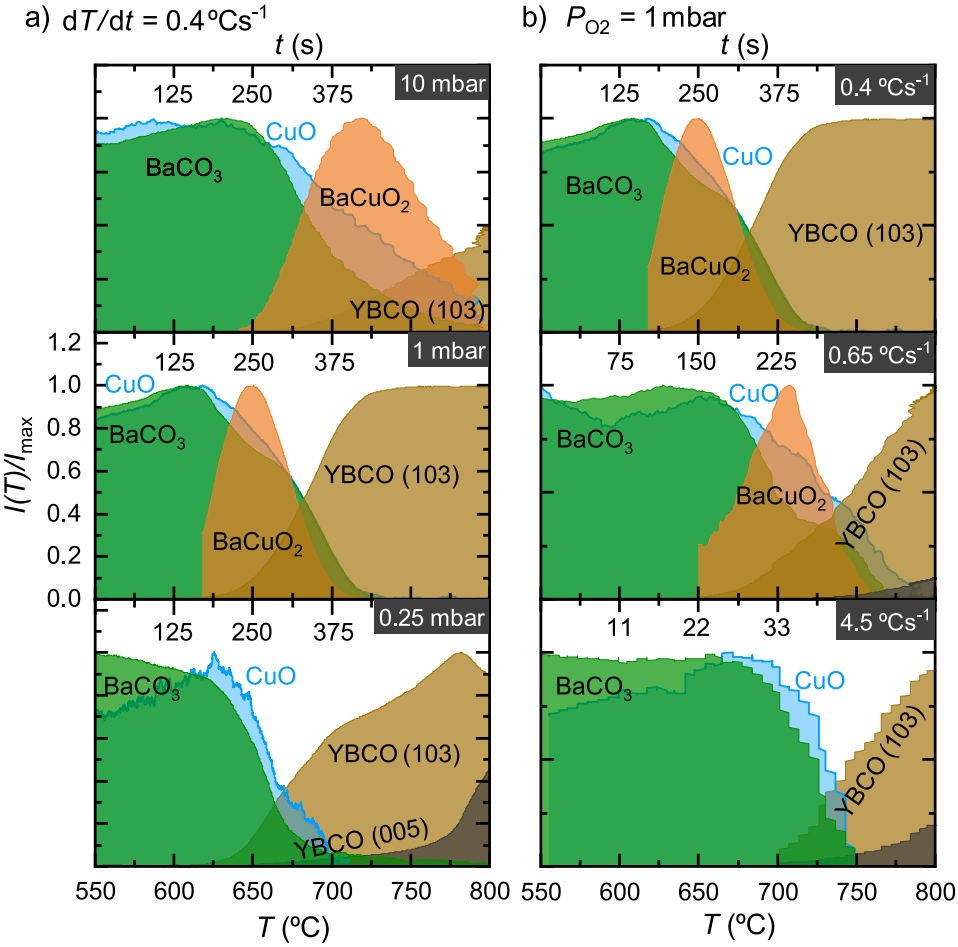

FIGURE 4.20: Time and temperature evolution of phases in (2-3) ternary films: a) P_{O2} dependence using a heating ramp of 0.4 °C s^{-1} and b) Heating ramp dependence at 1 mbar of P_{O2}. Heating ramp and P_{O2} values are labeled in each figure. The curves were obtained following the maximum diffracted signal of each phase and normalization to the maximum value (3.6). YBCO (103) and (005) signals originate from a diffraction ring and spot in the 2D-XRD images, respectively.

The initially tracked precursor phases are $BaCO_3$ and CuO; Y_2O_3 could not be followed due to the nanocrystallinity of the phase. As shown through TEM analysis of pyrolized films very small nanoparticles are obtained in that case (tab. 4.1). For improved visibility, each identified phase is normalized to its

maximum value. The saturation of the epitaxial layer signal, YBCO (005), is reached at higher temperatures and is not shown here. A separate discussion on the evolution of YBCO at these increased temperatures is made in the following.

Considering first the P_{O2} dependence (Fig. 4.20a)), it is apparent that $BaCO_3$ decomposition is achieved at reduced temperatures also in the ternary case, hence, not being a hindrance to YBCO growth. In the range of pressures explored, the decomposition is completed upon reaching $770 \pm 10\,°C$ through reaction with CuO. At 10 mbar and 1 mbar, a solid $BaCuO_2$ intermediate is detected together with homogenous YBCO nuclei.[20] However, other than the solid $BaCuO_2$ which follows a dome-shaped evolution, YBCO increases monotonously. This illustrates that even though $BaCuO_2$ is formed as solid intermediate at the reduced heating ramp of $0.4\,°C\,s^{-1}$ the actual stable phase and final product is YBCO. At $P_{O2} = 0.25$ mbar, no (Ba - Cu - O) solid intermediate is detected at all. Note that at 650 °C, the intensity of $BaCO_3$ is reduced by half while the YBCO is just at the onset of its formation, suggesting that a liquid phase is assisting the transformation.

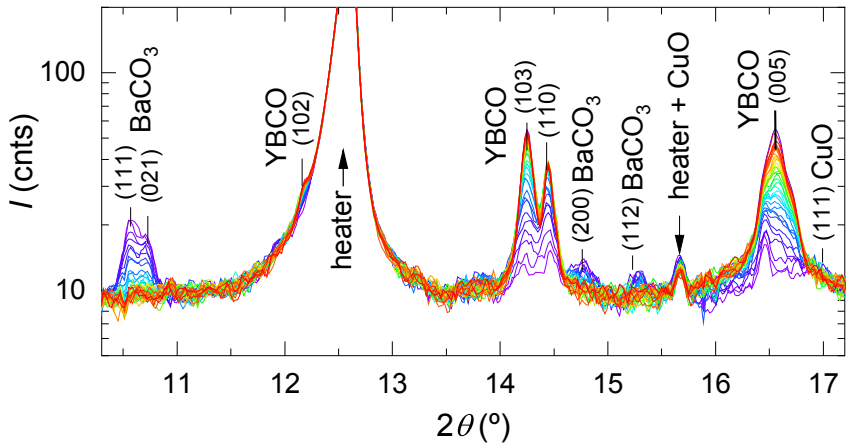

FIGURE 4.21: $I(2\theta)$ scans of a ternary (2-3) mixture heated at $0.4\,°C\,s^{-1}$, $P_{O2} = 0.25$ mbar shown for a temperature range from 640 °C (purple) to 750 °C (red). Curves were obtained through χ-integration of 2D-XRD images acquired each 100 ms.

The raw $I(2\theta)$ data for the experiment at $P_{O2} = 0.25$ mbar (Fig. 4.20a)) is shown in a temperature range of $T = 640 - 750\,°C$ in Fig. 4.21. For better

[20] The (103) crystallographic plane is attributed to randomly oriented YBCO grains. The according 2D scans show an intensity ring at the $2\theta_{(103)}$ peak position.

visibility, one scan each 4 °C is plotted. Also here it is seen that $BaCO_3$ decomposition is completed before the full film is crystallized to YBCO (see light blue curve). Thus, YBCO evolves from non-crystalline matter, possibly the (Ba - Cu^{I} - O) liquid phase in agreement with the binary kinetic phase diagram (Fig. 4.15).
Fig. 4.20b) further shows the evolution of phases at P_{O2} = 1mbar varying the heating ramp. An increase from 0.4 °C s^{-1} to 0.65 °C s^{-1} yields a delayed formation of the $BaCuO_2$ intermediate solid phase. At 4.5 °C s^{-1} the $BaCuO_2$ solid phase is completely absent and a direct conversion to YBCO takes place. This suggests that the formation of the crystalline $BaCuO_2$ phase is not mandatory for the reaction towards YBCO and only a byproduct of the kinetically driven process.

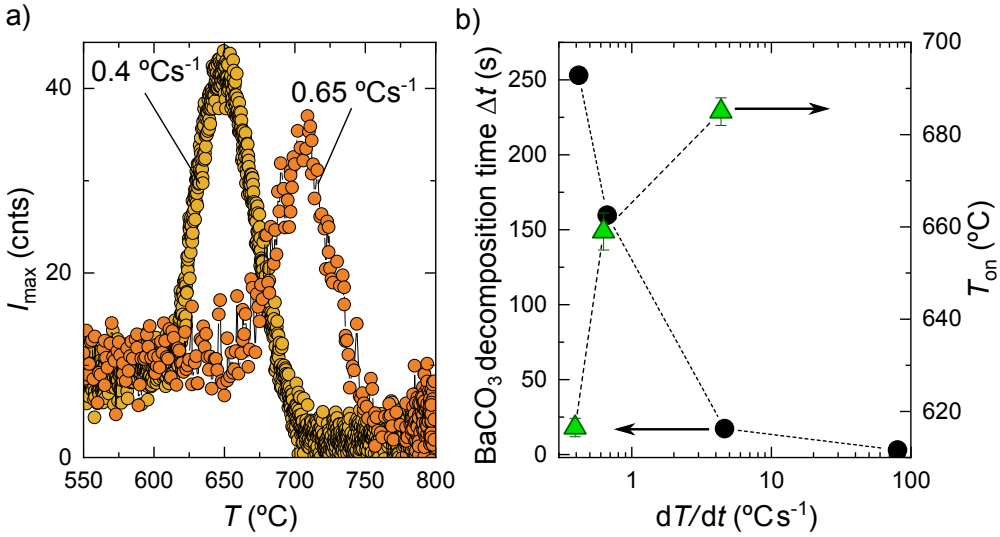

FIGURE 4.22: Analysis of $BaCuO_2$ and $BaCO_3$ solid phases under heating ramp variation: (a) Absolute intensity (I_{max}) of the $BaCuO_2$ (600) reflection as a function of temperature. Different heating ramps are labeled. (b) $BaCO_3$ decomposition times (Δt) and onset temperatures (T_{on}) obtained from the experiments in Fig. 4.20b). One additional point is included in for a sample heated at 80 °C s^{-1} to 800 °C and quenched after 3 s. Full $BaCO_3$ elimination was then confirmed via in-house XRD [76].

The heating ramp influence on the $BaCuO_2$ evolution and decomposition behaviour of $BaCO_3$ is further studied in Fig. 4.22. As shown through the absolute intensity of the $BaCuO_2$ (600) reflection (Fig. 4.22a)), the increase in heating ramp results in a temperature shift of the maximum signal together with a decrease of the overall maximum intensity reached. Both trends can be understood considering the decomposition behaviour of $BaCO_3$ (Fig. 4.20b)).

Elevation of the heating ramp results in the decomposition window being pushed to higher temperatures. Simultaneously, the decomposition time (Δt) drops by an order of magnitude for $0.4 \rightarrow 4.5\,^{\circ}\mathrm{C\,s^{-1}}$ and two orders of magnitude for $0.4 \rightarrow 80\,^{\circ}\mathrm{C\,s^{-1}}$.[21] The use of increased heating ramps hence pushes all reactions, including the crystallization of $BaCuO_{2(s)}$, towards higher temperatures.[22] In turn, the growth of YBCO can benefit from reduced formation of competing phases and take place in the full liquid region of the phase diagram where nucleation and growth are expected to be accelerated. The influence of the thermal profile on YBCO growth rates and on phase coarsening are thoroughly studied in 5.1.1, 5.1.3 and 5.3.1.

In order to overview all observed phases/reactions in ternary mixtures, we have exploited the time and temperature evolution of phases, as shown in Fig. 4.20, to construct kinetic phase diagrams for each composition and heating ramp. Note that until now we have discussed the characteristic growth mechanisms using the example of (2-3) films. The analysis was, however, also carried out for copper-rich (3-7) mixtures employing heating ramps of $0.4\,^{\circ}\mathrm{C\,s^{-1}}$ and $4.5\,^{\circ}\mathrm{C\,s^{-1}}$.
Given the two stoichiometries and heating ramps explored, four ternary kinetic phase diagrams were developed in total, comprising the reaction time-scales and involved solid phases (Fig. 4.24 and Fig. 4.25). The according heating ramps and compositions are labeled in each diagram. Markers identify the different phases that appear during growth and $BaCO_3$ decomposition onsets. Owing to space constraints the corresponding legend is shown separately in Fig. 4.23.
The four diagrams are constructed by adapting $BaCO_3$ decomposition and $BaCuO_2$ solid regions, adding of the YBCO peritectic/instability line and indicating where transient liquid growth of YBCO can take place (dashed brown region). A time axis is included to emphasize the change in reaction duration for different heating ramps, evidencing the relevance of process kinetics in TLAG. The binary kinetic phase diagram is, however, used here as a reference for all four cases. This can be justified taking the results and trends of the present and following chapter into account.
As seen in the set of diagrams (Fig. 4.24 and Fig. 4.25), phases which can be observed simultaneously during YBCO growth are in good agreement with the defined $P_{O2} - T$ regions of binary mixtures. Considering, for instance, the case of (2-3) and (3-7) films heated at $0.4\,^{\circ}\mathrm{C\,s^{-1}}$ (top diagram

[21] This effect was attributed to an accelerated CO_2 out-diffusion process in presence of a liquid phase [76, 94].

[22] Given the required incubation time for stable nuclei formation, a decrease in the amount is expected.

in Fig. 4.24 and Fig. 4.25), the $BaCuO_2$ solid intermediate phase could only be detected at increased oxygen partial pressures ($P_{O2} \geq 1$ mbar). Also the reduced $BaCu_2O_2$ phase could be observed for the (2-3) film treated at 4.5 °C s^{-1} ($P_{O2} = 0.25$ mbar), where the phase is expected according to the binary kinetic phase diagram. Such competing solid phases primarily appear at low temperatures initiated at the onset of $BaCO_3$ reaction with CuO. The phases are found stable at reduced temperatures where we suggested the coexistence of solid and liquid phases (dashed regions).

While the detected phases are in agreement with the binary system, the diagrams further emphasize the kinetic nature of the TLAG approach. This becomes evident when comparing the reaction time scales and characteristic temperatures upon heating ramp increase from 0.4 °C s^{-1} to 4.5 °C s^{-1}, both for (2-3) and (3-7) ternary mixtures. The $BaCO_3 + CuO$ reaction and YBCO formation windows are both pushed to higher temperatures upon heating ramp increase, while the reaction duration drops by approximately one order of magnitude, seen in the time axes of Fig. 4.24 and Fig. 4.25. Note that in all considered experiments the YBCO layer growth is completed upon arrival at high temperatures. Hence, growth rates must be considerably increased when elevated heating ramps are used. In some particular cases we even observed the decomposition of YBCO above a certain temperature threshold (Fig. 4.25).

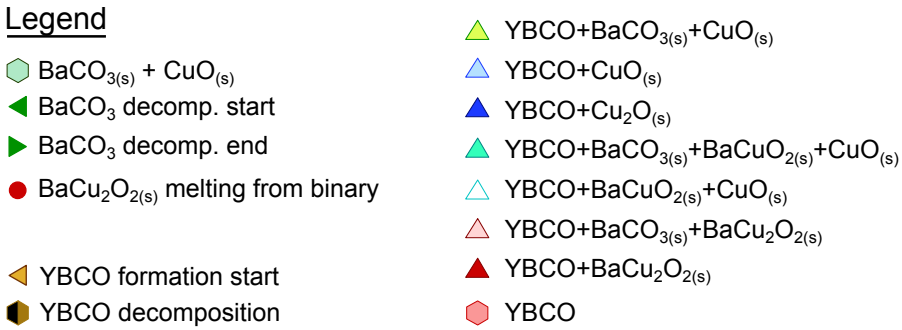

FIGURE 4.23: Attribution of solid phases and reactions to the different markers in Fig. 4.24 and Fig. 4.25. Phases were identified from $I(2\theta)$ curves acquired *in-situ* during growth.

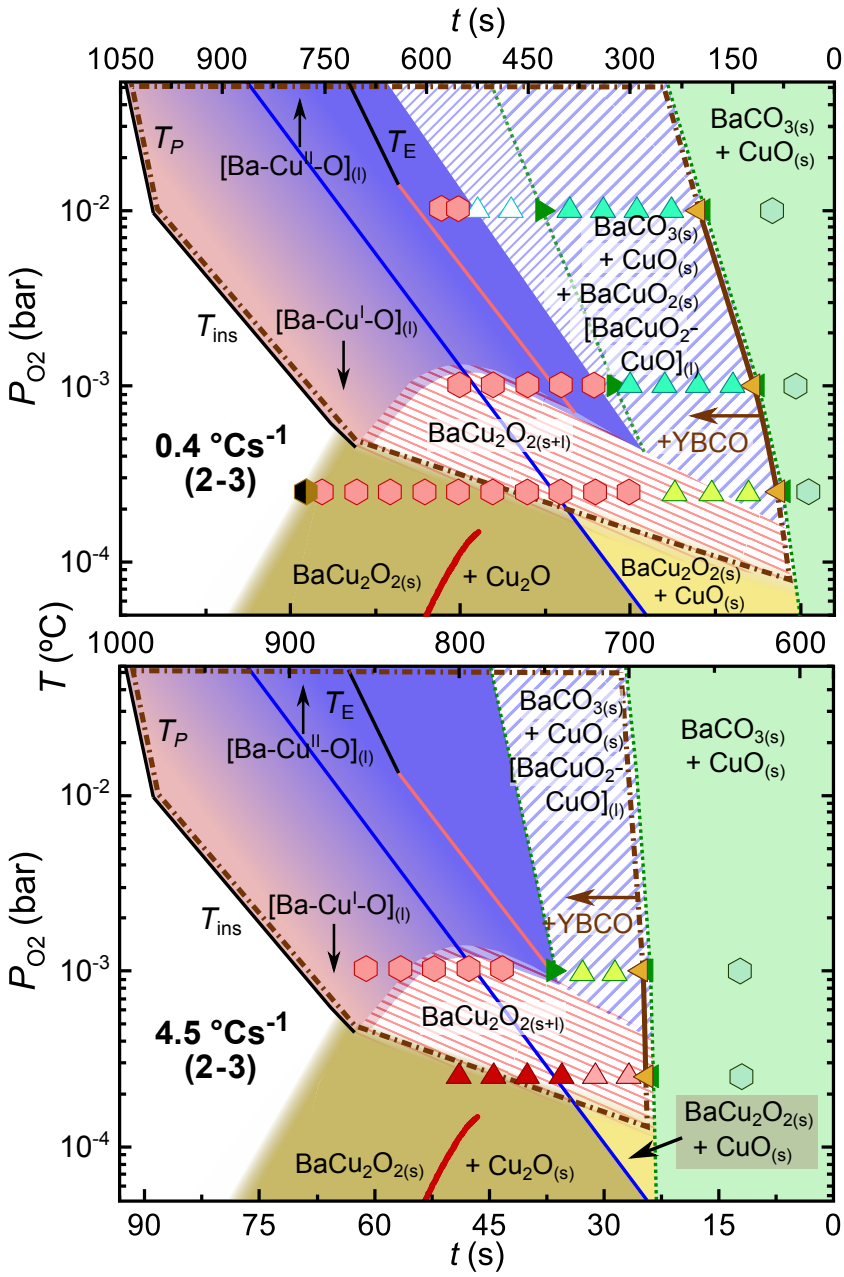

FIGURE 4.24: Ternary kinetic phase diagrams of (2-3) films heated at 0.4 ºC s^{-1} (top) and 4.5 ºC s^{-1} (bottom), $P_{\text{total}} = 1$ bar. Markers indicate the different solid phases and reactions observed in each T - route experiment (legend in Fig. 4.23). All solid lines are adapted from Fig. 4.15 and Fig. 4.16.

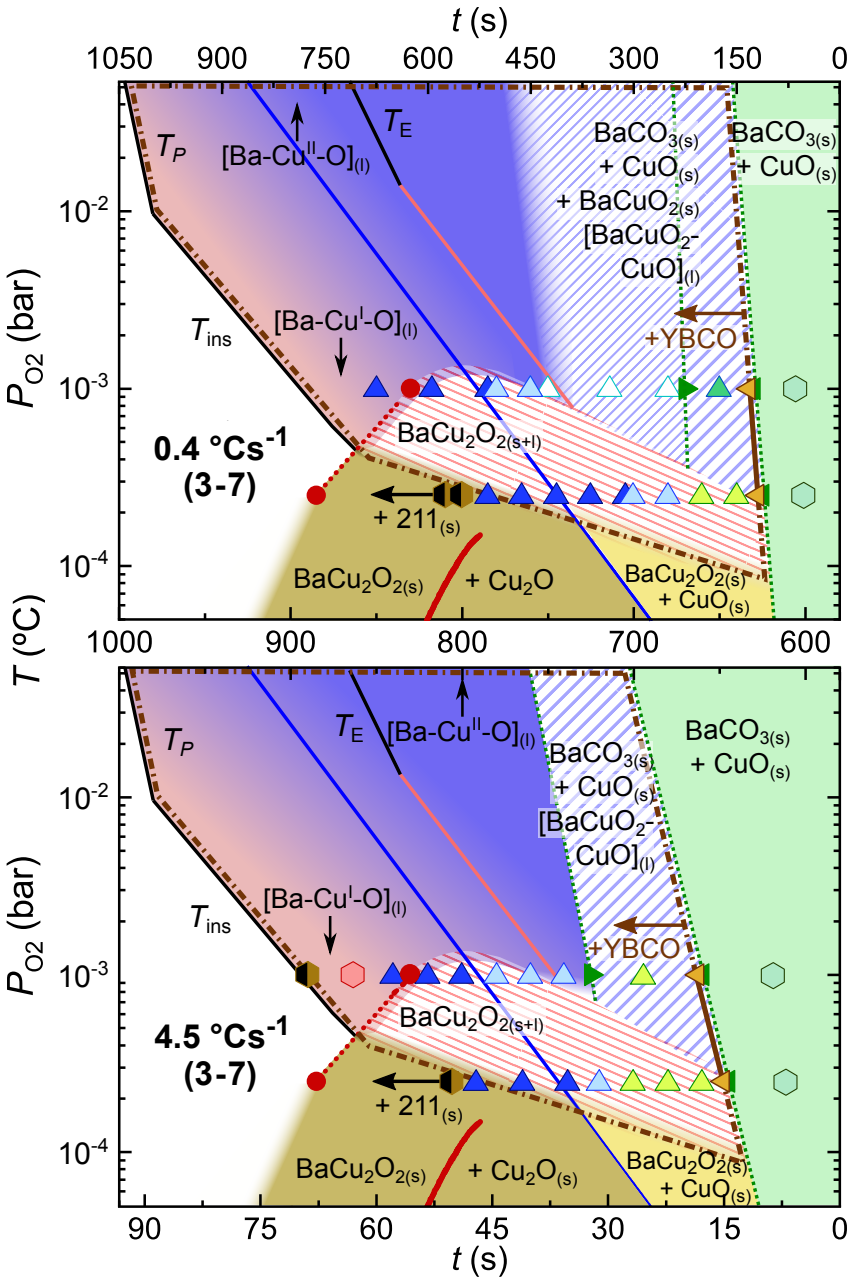

FIGURE 4.25: Ternary kinetic phase diagrams of (3-7) films heated at $0.4\,^{\circ}\mathrm{C\,s^{-1}}$ (top) and $4.5\,^{\circ}\mathrm{C\,s^{-1}}$ (bottom), $P_{\mathrm{total}} = 1$ bar. Markers indicate the different solid phases and reactions observed in each T-route experiment (legend in Fig. 4.23). All solid lines are adapted from Fig. 4.15 and Fig. 4.16.

All four diagrams are quantitatively different, demonstrating the relevance of visualizing the underlying processes for each set of conditions. Also the characteristic competing phases during YBCO growth are found to change. For instance, when working with ternary (3-7) mixtures (Fig. 4.25) it is more likely to encounter partial CuO coarsening and its independent evolution during YBCO growth. As in the binary case, these crystallites are found to undergo the valence change in proximity to the equilibrium CuO→Cu_2O line. Hence, summarising the reactions through the visual form of kinetic phase diagrams allows for a facilitated assessment of growth conditions that promote only the formation of YBCO.

Potentially, all appearing secondary phases during YBCO growth could limit the film performance if the superconducting cross-section is reduced or grain boundaries contaminated [170, 171]. For that reason, the focus in chapter 5 is separately set on how to promote growth of epitaxial YBCO at high growth rates. However, although secondary phases ($BaCuO_2$, CuO, Cu_2O) can be formed along the ramp it is also seen in the kinetic phase diagrams that heating into the full liquid region can result in their dissolution. As seen for both film compositions at 4.5 °C s^{-1} and P_{O2} = 1 mbar, only the YBCO phase is detected in the (Ba - Cu^I - O) full liquid region even allowing to dissolve the Cu_2O phase in the melt.

In addition to the disappearance of competing solid phases in the (Ba - Cu^I - O) full liquid region we observe that the diffracted intensity of homogeneously nucleated YBCO grains (random grains) also diminishes upon heating into the (Ba - Cu^I - O) melt. Taking the example of the (2-3) film heated at 4.5 °C s^{-1} at P_{O2} = 1 mbar (Fig. 4.20b)), the phase evolution at elevated temperatures is shown in Fig. 4.26, both in absolute and normalized intensity (top and bottom graph, respectively). Random YBCO crystals that initiate from homogeneously nucleated sites, are represented through the (103) crystallographic plane.[23] The epitaxial layer is shown through the (005) reflection.

Both, epitaxial and randomly oriented YBCO grains are starting to grow during $BaCO_3$ decomposition. We notice that the nucleation density of YBCO random nuclei is higher at low temperatures, while that of epitaxial nuclei reaches its maximum upon further temperature increase. This might be attributed to the temperature dependence of the equilibrium concentration C_e of Y in melt, yielding an overall higher supersaturation at low temperatures [76]. At high supersaturation, the system will hence have an increased probability to surpass the Gibbs free energy barrier to form stable homogeneous nuclei (4.1.3).

[23] In 2D-XRD images, the intensity is spherically spread due to the random alignment of these grains.

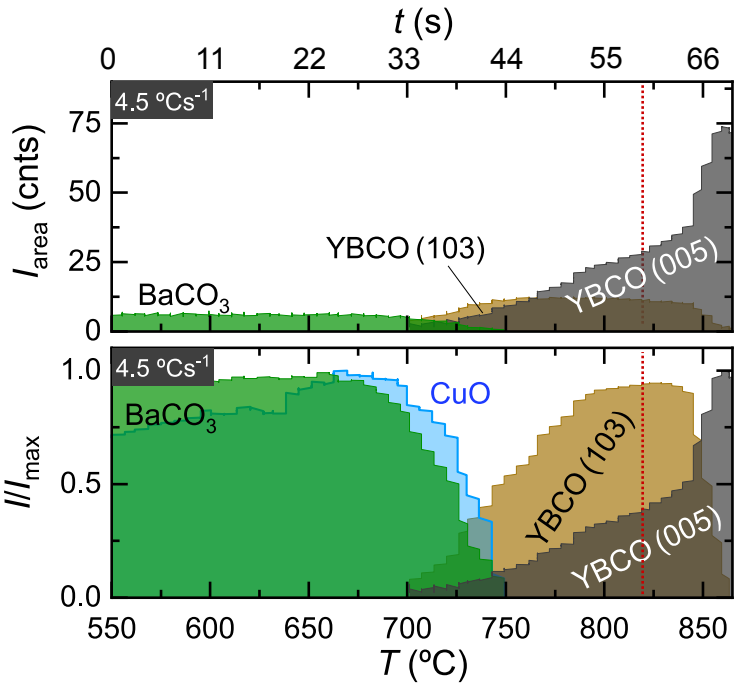

FIGURE 4.26: Time and temperature evolution of phases of a (2-3) ternary film heated at 4.5 °C s^{-1}, P_{O2} = 1 mbar. Top and bottom graphs show the peak area intensity and normalized intensity, respectively. The dashed red line marks the temperature where the (Ba - Cu^{I} - O) full liquid region is identified according to binary experiments.

Upon heating into the (Ba - Cu^{I} - O) full liquid region (red dashed line at T = 818 °C), the (103) vanishes followed by an increase and saturation of the epitaxial layer signal. We will attribute this rather unexpected phenomenon to YBCO grain reorientation during growth (5.2) and study its efficiency with respect to the chosen film composition and process parameters. Here however, it can be anticipated that growth mechanisms fundamentally change in the identified full liquid region of the kinetic phase diagrams.

In summary, we studied YBCO growth through the T - route approach for different film compositions, heating ramps and P_{O2} values through *in-situ* XRD synchrotron experiments. This enabled us to construct different kinetic phase diagrams which are adapted to the binary (Ba - Cu - O) diagram (4.3.1). Several points can be concluded from the aforegoing discussion:

1. Crystallization of YBCO can be realized through steady increase of temperature at constant heating ramps and oxygen partial pressures (explored for $P_{O2} = 2.5 \cdot 10^{-4} - 10^{-2}$ bar, P_{total} = 1 bar and 0.4/4.5 °C s^{-1}).

Depending on the final $P_{O2} - T$ region of growth, two main reaction paths can be formulated

$$\begin{aligned} BaCO_{3(s)} + CuO_{(s)} + Y_2O_{3(s)} &\rightarrow [Ba\text{-}Cu^{II}\text{-}O]_{(l)} + Y_2O_{3(s)} \\ &\rightarrow YBa_2Cu_3O_{7-\delta} \end{aligned} \tag{4.27}$$

$$\begin{aligned} BaCO_{3(s)} + CuO_{(s)} + Y_2O_{3(s)} &\rightarrow [Ba\text{-}Cu^{II}\text{-}O]_{(l)} + Y_2O_{3(s)} \\ &\rightarrow [Ba\text{-}Cu^{I}\text{-}O]_{(l)} + Y_2O_{3(s)} \rightarrow YBa_2Cu_3O_{7-\delta} \end{aligned} \tag{4.28}$$

Growth of YBCO can either be achieved through the Cu^{II} or Cu^{I} based melt. However, particular results are obtained for each individual set of growth conditions. We have therefore not included here in the general reactions that, eventually, secondary solid phases can form along the thermal profile as their appearance is not mandatory to obtain the final YBCO product and can be fully avoided through tuning of processing conditions.

2. The elimination of $BaCO_3$ is influenced by the utilized liquid composition and heating ramp, showing that decomposition onset temperatures can be as low as 610 °C (Fig. 4.24). However, for all explored P_{O2} values and heating ramps, full decarbonization is reached at 770 ± 10°C. This is an essential demonstration that the TLAG process is not limited by the high decomposition temperatures reported for bulk $BaCO_3$ powders in agreement with the binary system studied earlier.

3. Several indications were given suggesting that the ternary kinetic phase diagrams resemble the binary one, though precise modifications are observed for each particular case (liquid composition, heating ramp). In the present chapter, we argue through the characteristic phases that appear in different $P_{O2} - T$ regions and through the change in growth kinetics upon entrance in the full liquid region (e.g. random YBCO grain disappearance in favour of the epitaxial layer). Further justification is given in chapter 5 where we explore YBCO epitaxial growth rate dependencies on processing parameters, the phenomena of random YBCO grain disappearance and the influence of solid phase coarsening during growth.

Finally, we note that the binary (3-7) kinetic phase diagram is used here as foundation also for ternary films of (2-3) composition. Although we have justified that the underlying (Ba - Cu - O) kinetics might not be strongly affected by this change in composition, a binary kinetic phase diagram should further

be developed for the (2-3) case to adjust the experimentally determined lines and regions. The results obtained further support the need to construct such kinetic phase diagrams for each variation in process conditions and discourage the use of thermodynamic phase diagrams to analyze TLAG mechanisms and results.

4.4.4 Ultrahigh growth rates in the TLAG process

The validation of TLAG as an ultrahigh growth rate approach was one of the key objectives of this project. Up to now we have considered only the reaction paths of different routes and conditions, omitting the evolution of the epitaxial layer. Although strategies towards high YBCO conversion rates are laid out in 5.1, the maximum achieved growth rates of each processing route (4.4.1) is anticipated here for complementary reasons.

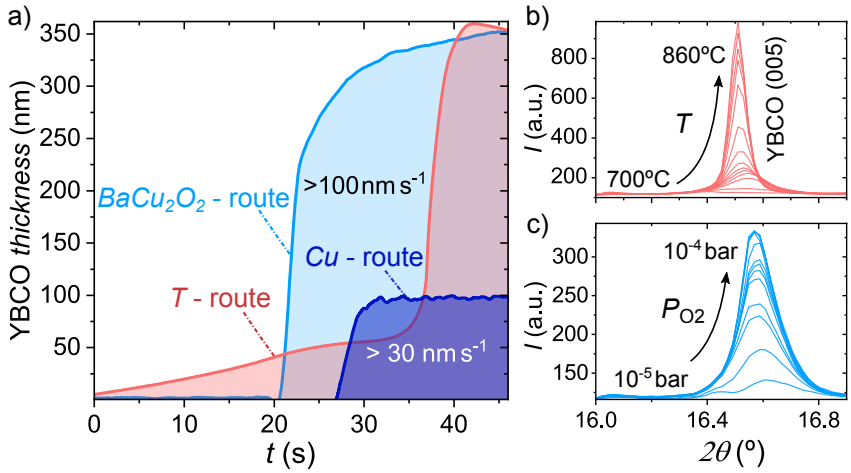

FIGURE 4.27: Growth rate estimation for the three main TLAG routes: (a) YBCO layer thickness evolution as a function of time for T-route (P_{O2} = 10^{-3} bar, (3-7) composition), $P_{O2}(BaCu_2O_2)$-route (T = 850 °C, $P_{O2,base}$ = 10^{-5} bar, $P_{O2,final}$ = 10^{-4} bar, (3-7) composition) and $P_{O2}(Cu)$-route (T = 800 °C, $P_{O2,base}$ = 10^{-7} bar, $P_{O2,final}$ = 10^{-3} bar, (2-3) composition). (b) and (c) show the (005) epitaxial reflection for the T- and $P_{O2}(BaCu_2O_2)$-route experiment.

Growth rates can be estimated through changes in the (005) diffraction spot intensity given by the YBCO epitaxial layer growth. For this purpose, the raw $I(2\theta)$ signals, shown exemplary for the T- and $P_{O2}(BaCu_2O_2)$-route in

Fig 4.27b) and c), are tracked and renormalized to the YBCO layer thickness.[24] The epitaxial layer evolution for T -, $P_{O2}(BaCu_2O_2)$ - and $P_{O2}(Cu)$ -route is shown in Fig 4.27a). For visibility reasons, the time column of each signal was adjusted by a constant value. T - and $P_{O2}(BaCu_2O_2)$ - route grown samples gave a final thickness of 350 nm, while a thinner was used in the $P_{O2}(Cu)$ - route.
All three approaches demonstrate growth rates of the epitaxial layer well beyond values reported for solid-solid and vapor-solid limited processes, such as PLD ($<10\,nm\,s^{-1}$) and TFA-CSD ($<2\,nm\,s^{-1}$). In particular, derivative values from the curves in Fig 4.27a) yield a maximum of $132\,nm\,s^{-1}$ in the T -route, $120\,nm\,s^{-1}$ in the $P_{O2}(BaCu_2O_2)$ - route and $36\,nm\,s^{-1}$ in the $P_{O2}(Cu)$ - route case. Among all experiments carried out at the synchrotron, these values belong to the highest observed. The lower growth rate obtained in the $P_{O2}(Cu)$ -route might be explained by the reduced temperature chosen for the pressure step ($T = 800\,°C$). Hence, the TLAG process can be classified as a highly non-equilibrium growth approach capable of reaching the ultrahigh growth rates prospected earlier in this chapter. In fact, even higher growth rates ($100\text{-}1000\,nm\,s^{-1}$) could be recently confirmed in-house by Dr. A.Queraltó through *in-situ* electrical resistance measurements during growth. These first results were obtained through the $P_{O2}(BaCu_2O_2)$ - route and placement of the growth conditions in the full liquid region of the phase diagram.

4.4.5 State-of-the-art TLAG films

In-situ growth experiments carried out at the DiffAbs beamline have given us insights into the main reaction paths and classified TLAG as a non-equilibrium growth approach capable of reaching growth rates in the range of $100\,nm\,s^{-1}$. In this last section, we overview state-of-the-art TLAG films of each processing route to complement the aforegoing findings of this chapter. A broader discussion on physical properties and how growth conditions correlate with the final film performance is, however, carried out in chapter 6.

Exemplary images of the surface and cross section of TLAG films are presented in Fig. 4.28. Under optimized growth conditions, the YBCO layer exhibit a porous-free, closed microstructure, as commonly observed through liquid mediated techniques (Fig. 4.28c)). Such films typically reach critical current densities in the range of 1 - 5 $MA\,cm^{-2}$ at 77 K (discussed below) showing a distribution of secondary phase segregations on the surface (Fig. 4.28a) and

[24] Saturation of the signal is reached upon completion of the layer. Final thicknesses were confirmed through transmission electron microscopy measurements.

b)). The morphology is likely to arise from a high heterogeneous nucleation rate allowing to push excess material to the top. The composition of the segretations is usually Ba-Cu-O and CuO (the last specially for copper-rich liquid compositions).[25]

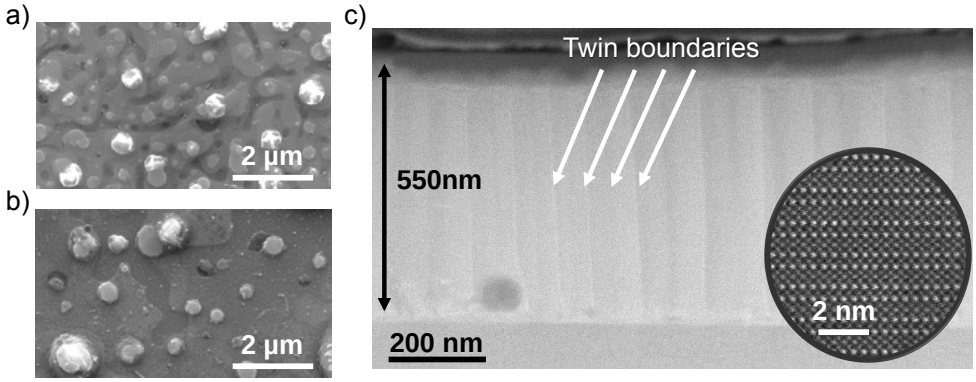

FIGURE 4.28: Scanning electron microscopy image of pristine TLAG film grown through the (a) $P_{O2}(BaCu_2O_2)$ - route and (b) T - route. (c) STEM cross section image of a 550 nm thick YBCO layer (T - route) with the twin boundaries indicated. The inset is a high resolution STEM image showing the YBCO atomic structure.

The epitaxial quality is further studied via high resolution X-ray diffraction measurements, shown in Fig. 4.29, for samples grown through different routes. A nanocomposite film with 12 mol % of $BaZrO_3$ (BZO) nanoparticles from colloidal solutions is also included. In $\theta - 2\theta$ geometry, the scans show predominantly the $(00l)$ peak family, apart from substrate reflections and some minor secondary phases. As introduced above, minor phases can be located on the film surface and do not necessarily reduce the superconducting cross-section of the film.
Rocking curves and ϕ - scans (seen in the insets of Fig. 4.29) provide additional texture information. Full width at half maximum values below 0.8 ° and 0.6 ° for $\Delta\phi$ and $\Delta\omega$ settle in the lower range of reported values suggesting that grain boundary misalignment is not a hindrance to current percolation in TLAG grown films.

[25] Confirmed by EDX measurements.

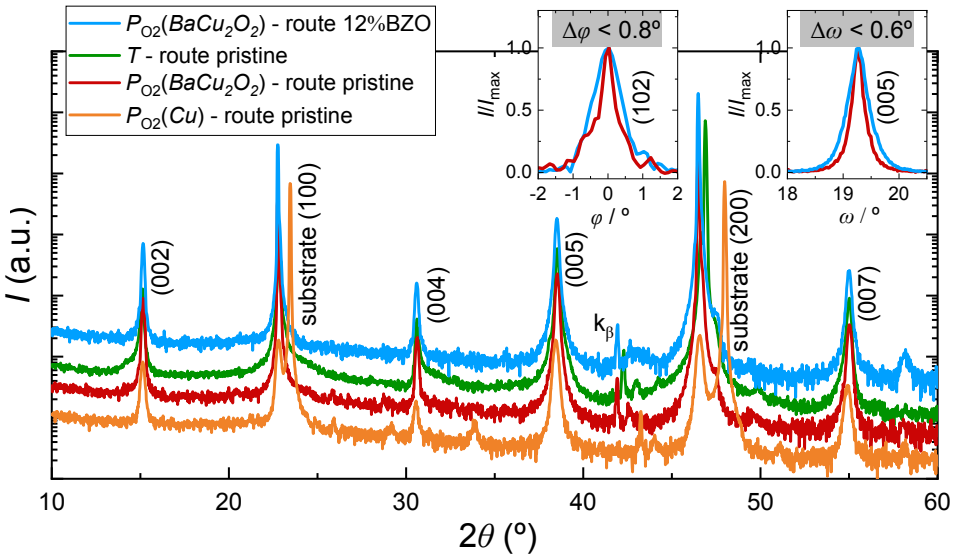

FIGURE 4.29: HR-XRD measurements in $\theta - 2\theta$ geometry of different TLAG samples. Samples are grown in $P_{O2}(BaCu_2O_2)$-, $P_{O2}(Cu)$- and T-route on STO, LSAT and LAO substrate, respectively. Insets show ϕ- and ω-scans of the (102) and (005) reflection. The full width at half maximum values $\Delta\phi$ and $\Delta\omega$ are included.

Throughout this project, grown films were probed with a SQUID device (3.2) and through resistivity measurements in Van der Pauw geometry (3.4.2) to assess the temperature and magnetic field dependence of the critical current density $J_c(T, H)$ together with critical temperatures T_c.
$J_c(T)$ and $\rho(T)$ measurements of the best films grown through each route are shown in Fig. 4.30. High critical temperatures ranging from 88 - 92 K can be achieved with all investigated routes and for nanocomposite films (Fig. 4.30b)). As will be further argued in chapter 6, there is no indication of grain contamination through carbon residuals.[26] Also very low room temperature resistivity values in a range of $\rho_{300K} = 250\text{-}360\ \mu\Omega\,cm$ can be achieved through most of the explored approaches. Comparable values are reported for PLD and TFA-CSD grown YBCO [172, 173]. The increased ρ_{300K} for the $P_{O2}(Cu)$-route is related to secondary phases that disrupt the current percolation in that particular approach (6.1.4).

[26] Carbon contamination is known to degrade percolating currents and T_c values [90, 133, 134].

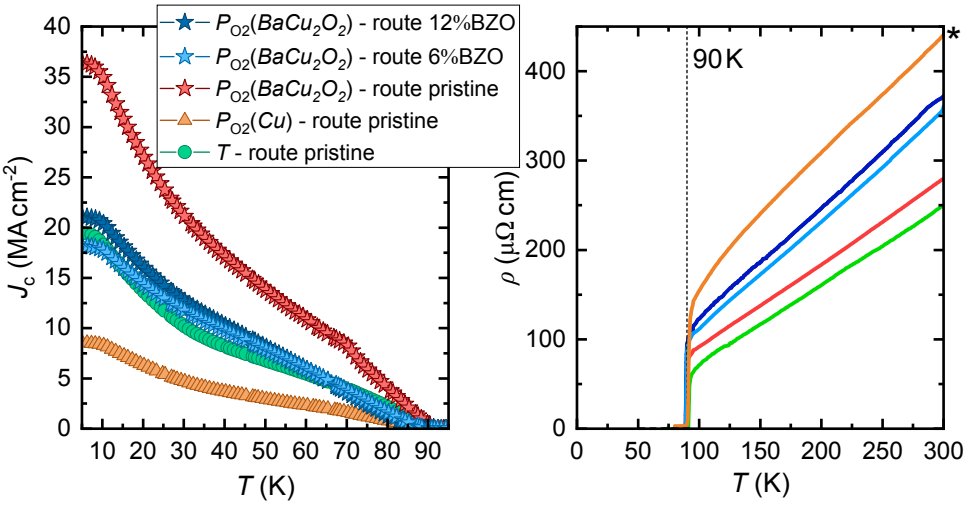

FIGURE 4.30: (a) DC magnetization measurements of the critical current density J_c as a function of temperature and (b) Transport resistivity measurements in Van der Pauw geometry of the best TLAG films pristine and nanocomposite films. Resistivity values of the curve with an asterisk symbol were divided 2 for improved visibility.

Maximum J_c values at self-field and 77 K are spread in a range of 1-5 MA cm^{-2} for film thicknesses of 100 -250 nm (Fig. 4.30a)). As will be discussed throughout chapter 6 the reproducibility and upper limit of achievable critical current densities was found to rely on film composition, process parameters and the growth route itself. For a comprehensive discussion on the growth optimization, the reader is further advised to consider the PhD theses of L.Soler (optimization of the T - and $P_{O2}(BaCu_2O_2)$ - route) [76], S.Rasi ($P_{O2}(Cu)$ - route) [94] and J.Jareño (nanocomposite film growth) [95]. At this point it can, however, be concluded that all growth routes discussed earlier allow for the fabrication of YBCO films with high critical temperatures (88 - 92 K), high texture quality ($\Delta\phi < 0.8^{\circ}$, $\Delta\omega < 0.6^{\circ}$) and competitive current carrying capacity (1-5 MA cm^{-2} at self-filed and 77 K).

4.5 Conclusions

A foundation to transient liquid assisted growth based on chemical solution deposition (TLAG-CSD) is developed in this chapter. Besides discussing basic concepts on melting and crystallization from liquids, we have established a processing scheme that combines non-equilibrium growth conditions with nanometric reactant sizes achieved via CSD.
TLAG is a kinetically driven growth model which beneficially triggers the

formation of a transient liquid phase that, in turn, accelerates the crystallization process towards the final product phase. This is achieved through melting of the solid (Ba - Cu - O) system in a region of the phase diagram where YBCO is the thermodynamically predicted phase. Y is dissolved in the liquid phase having a high diffusion constant which gives rise to growth rates beyond those achieved in conventional solid-solid and vapor-solid limited processes. Epitaxial layer convertion rates above $100\,\mathrm{nm\,s^{-1}}$ could be successfully demonstrated through the approach developed here.

Insights into the determining reactions and kinetics were obtained through *in-situ* growth experiments under synchrotron radiation. Only the high luminosity and acquisition times given at the synchrotron facility (100 ms per 2D-XRD frame) allowed us to resolve the rapid transformations involved. In particular, we studied two types of nanocrystalline precursor systems employing high heating ramps ($0.4/4.5\,^{\circ}\mathrm{C\,s^{-1}}$) at different oxygen partial pressures: Binary (Ba - Cu - O) and ternary (Y-Ba-Cu-O) mixtures. The former system is used to facilitate the observation of melting of the (Ba - Cu - O) solid phases while the latter extends the reaction paths to its full complexity to grow YBCO. In summary, several key results were acquired on the principles of the TLAG-CSD process:

1. **Construction of binary kinetic phase diagram:** The rapid phase transformations of binary mixtures in non-equilibrium processing conditions are visualized in the form of a $P_{O2} - T$ dependent *kinetic phase diagram*. The diagram is derived for a heating ramp of $4.5\,^{\circ}\mathrm{C\,s^{-1}}$, (3-7) composition through a set of experiments where the $BaCO_3$-CuO precursor films are brought to $T > 800\,^{\circ}\mathrm{C}$ at different P_{O2} values. In particular, we find that liquid formation is rendered possible both from the ($BaCuO_2$-CuO) and ($BaCu_2O_2$-Cu_2O) solid phases having copper (2+) and (1+) valence states, respectively. We therefore suggest that liquid properties (e.g. viscosity, reactivity and supersaturation) might continuously vary from a (Ba - Cu^{I} - O) melt with copper (+1) oxidation state (low P_{O2}) towards a (Ba - Cu^{II} - O) melt with copper (+2) oxidation state (high P_{O2}).

2. **$BaCO_3$ reaction with CuO:** The decomposition of $BaCO_3$ was successfully realized in all gas atmospheres and under various $P_{O2} - T$ paths at temperatures low enough for YBCO processing. The low decomposition temperatures and fast decomposition times are a result of $BaCO_3$ reaction with CuO, both given in nanocrystalline form in the precursor films.

3. **Different $P_{O2} - T$ processing routes:** Considering the derived kinetic phase diagrams, a large $P_{O2} - T$ window is defined suitable for YBCO

processing. We explored several paths to reach final growth conditions, entitled T -, $P_{O2}(BaCu_2O_2)$ - and $P_{O2}(Cu)$ route, all of which differ in intermediate phases and reaction complexity. Epitaxial YBCO films with critical current densities at self-field and 77K in the range of $1-5\,\mathrm{MA\,cm^{-2}}$ can be obtained by these means.

4. **Transient liquid assisted growth of YBCO:** For the particular case of the T - route we constructed four kinetic phase diagrams, one for each composition ((2-3) and (3-7)) and heating ramp ($0.4\,^{\circ}\mathrm{C\,s^{-1}}$ and $4.5\,^{\circ}\mathrm{C\,s^{-1}}$). The binary kinetic phase diagram is used as reference due to the agreement of detected solid phases. The necessity of constructing individual diagrams is demonstrated through the strong variation in reaction time scales, temperatures and characteristic solid phases for each set of processing conditions. For instance, it could be shown that the increase in heating ramps results in a temperature shift of the full YBCO reaction path while the reaction duration decreases by an order of magnitude. The derivation of such diagrams is strongly recommended for the ongoing exploration of the TLAG process, specifically with regard to identifying the most suitable YBCO growth conditions.

Finally we note that these studies should be extended to more film compositions and to wider $P_{O2}-T$ regions. For instance, we have used the (3-7) binary kinetic phase diagram as reference to construct the (2-3) ternary one. Although we find agreement in the evolution of phases for both systems, a (2-3) binary diagram should be constructed to confirm these results. Also the large $P_{O2}-T$ margin where the full-liquid region is identified invites for YBCO growth at high rates and increased oxygen partial pressure where growth would take place in the (Ba - Cu^{II} - O) melting region. These objectives are intended to be addressed in follow up experiments at the synchrotron facility.

Chapter 5

Toward the kinetic control of the TLAG process

While the main reactions, routes and limitations of TLAG were focus of the aforegoing part, the present chapter explores the versatility of the approach with regard to c-axis YBCO growth, decrease of growth temperatures and the effect of random grain reorientation. In particular, we will define process parameters and competing crystallization kinetics that have the most influence on the quality of the grown layer. *In situ* synchrotron measurements will, once more, be employed to follow structural changes during the heating process. The observed findings will be correlated with TEM images of grown and quenched films. In addition, a new approach to obtain kinetic information from 2D X-ray diffraction measurements will be developed in 5.2.1.

As introduced earlier, TLAG growth can be realized through a temperature increase process at a fixed oxygen partial pressure (T - route) or through a two step approach that involves initial heating at low pressure followed by a pressure increase at a fixed temperature ($P_{O2}(Cu)$ - and $P_{O2}(BaCu_2O_2)$ -route). In this chapter, however, the choice of experiments is limited to the T - route for the following reasons:

1. **Temperature stability:** In the particular pressure experiments at Soleil synchrotron, the fast entrance of cold gas to reach the final P_{O2} conditions resulted in a sudden decrease of temperature in the sample space. Even though we attempted to compensate it, the drops could not be avoided, possibly due to the small volume of the sample environment and slow kinetic response of the furnace. Some of the drops are shown

in Appendix Fig. A.2 reaching up to 73 °C, especially when the pressure jump was carried out from $P_{total} < 10^{-5}$ bar to $P_{total} = 1$ bar. A precise $P_{O2} - T$ attribution of involved structural changes is hence compromised for detailed analysis. In the T - route process, however, the temperature stability was much higher allowing us to perform a thorough analysis.

2. **$BaCO_3$ decomposition and coarsening:** Although $BaCO_3$ decomposition can be realized in each of the developed routes, the decomposition in the T - route is much simpler. For instance, CO_2 elimination in the $P_{O2}(BaCu_2O_2)$ -route takes 8 min as compared to < 20 s in the T - route (see Appendix C, Fig. C.1). Phase coarsening due to the increased times for $BaCO_3$ decarbonation, might then play an additional, inestimable role when studying growth kinetics, which is beyond the present study.

3. **Constant heating ramp in the T - route process:** Kinetic processes vary for the different routes. Here we have studied the most straightforward approach, i.e. using predefined heating ramps in the T - route process. Any changes in liquid characteristics and impact of growth conditions can hence be tracked more easily given the crossing of a large temperature window.

Ternary Y_2O_3 - $BaCO_3$ - CuO films are prepared according to 3.1. Heat treatment is carried out at $P_{total} = 1$ bar varying the heating ramp, P_{O2} pressure and precursor composition (Fig. 4.11). Two layer pyrolysed films are considered here, giving an estimated YBCO epitaxial layer thickness of 350 - 450 nm after growth.

5.1 Promoting c-axis growth at high growth rates

Since the successful development of ion beam-assisted deposited buffered templates (IBAD) [67] and rolling-assisted biaxially textured substrates (RABiTS) [66] the HTS community seeks to grow thick REBCO tapes with high current carrying capacity. That being a major challenge, a high yield of the employed fabrication process is an additional obstacle for the produced tape to become cost-competitive. As previously introduced, the utilization of melt based techniques can resolve throughput constraints due to the potentially high intrinsic growth rates of the process (2.2.2).
Supersaturation is an essential control parameter to reach fast conversion rates. As it is shown by A. Kursumovic et al., the steady state growth rate,

G, scales linearly with the relative supersaturation σ according to

$$G = \left[\frac{1}{k} + \frac{\delta}{D}\right]^{-1} \sigma \frac{C_{\text{eq}}}{C_{\text{xt}}} \tag{5.1}$$

where k, δ, D, C_{xt} and C_{eq} denote the kinetic coefficient, liquid layer thickness, volume diffusion coefficient, Y concentration in the grown crystal and equilibrium Y concentration in the melt, respectively [81]. With the factors k and D the expression accounts for growth that is either limited by surface kinetics or diffusion of solute through the liquid medium to the growth front. For instance, as assumed in the case of hybrid liquid phase epitaxy (HLPE), eq. 5.1 can be reduced to

$$G \approx k\sigma \frac{C_{\text{eq}}}{C_{\text{xt}}} \tag{5.2}$$

if a liquid BaO - CuO layer is stabilized thin enough ($\delta \approx 100\,\text{nm}$) to suppress the diffusion term. Note that in HLPE a thin liquid layer is stabilized prior to solid flux feeding from the vapor phase. Hence, the whole distance δ needs to be crossed towards the growth front.

Although the TLAG process is considerably different from the HLPE case, a similar approximation as above (eq. 5.2) can be made for TLAG due to the homogeneous spread of Y_2O_3 in a liquid layer of BaO - CuO, hence, short diffusion lengths towards the gorwth front ($\delta \rightarrow 0$). The kinetic coefficient k, given in units of $\text{m}\,\text{s}^{-1}$ varies with T and P_{O2}, while supersaturation changes with the actual and equilibrium concentration of Y in the medium.

Not all liquid assisted processes imply high growth rates for the reasons mentioned above. For instance, in Vapor-Liquid-Solid epitaxy (VLS) and its modified form, pulsed-laser tri-phase epitaxy (TPE), the feed of solute and with that the supersaturation is kept low enough to produce single-crystal quality films at rates not higher than $0.25\,\text{nm}\,\text{s}^{-1}$ [82, 174]. Rates in the range of $10\,\text{nm}\,\text{s}^{-1}$ are employed in hybrid liquid phase epitaxy (HLPE), with an estimated relative supersaturation of $\sigma \approx 10$, and liquid assisted molecular beam epitaxy (MBE) [80, 81].

In TLAG, the order of magnitude of the relative supersaturation (eq. 4.6) can be estimated taking into account real and equilibrium concentrations of Y in the melt:

1. **Equilibrium concentration C_{eq}**: The equilibrium concentration depends on the solubility of Y which is primarily controlled by temperature and copper amount of the liquid composition. Copper and temperature increase yield a decrease in supersaturation if the total concentration of Y in the melt, C, remains unchanged. For the growth conditions employed here, C_{eq} is estimated in the range of 0.01-0.6 mol% [76].

2. **Supersaturated concentration** C: Precursor films contain the whole amount of Y in Y_2O_3 particle form. Therefore, the actual Y amount in the melt might reach very high values as compared to approaches that rely on vapor-phase melt feeding techniques. As estimated in [76] through consideration of the thermodynamic phase diagram of $BaCuO_2$ - Y_2O_3, C might reach 10 mol%.

For these estimated concentration values, σ can vary orders of magnitudes. For instance, an upper estimation of $C = 10$ mol% yields $\sigma = 10 - 1000$ depending on the exact C_{eq}. This would translate, according to eq. 5.2, into growth rates up to 1000 nm s^{-1} for $k \approx 10^{-5}$ - 10^{-6} m s^{-1} [84] and $C_{xt} = 17$ %, the Y concentration in the YBCO solid. Accordingly, for a lowered supersaturated concentrations of $C = 1$ % the growth rate would reach a maximum of 100 m s^{-1}, similar to the maximum values demonstrated in 4.4.4. With the obtainable growth velocities TLAG categorizes as high - σ growth approach. This is further evidenced by the occurrence of homogeneous nucleation (4.4.1) and a high amount of defects such as dislocations, stacking faults and nano-inclusions in the grown layer (chapter 7). Low - σ growth techniques, on the contrary, favour defect-free, large grain sizes (tenth of µm).
Estimating supersaturation and growth rate values is a challenging undertaking already in equilibrium processes where the liquid composition and solute supply can be confined to a certain degree. In TLAG, the kinetic, non-equilibrium nature of the process further complicates such calculus. For instance, we have seen through construction of kinetic phase diagrams in 4.3.3 and 4.4.3 that a large $P_O - T$ window is crossed in the T - route approach where solid and liquid phases can coexist. It can be expected that at these reduced temperatures atomic mobility is compromised and that other solid phases can compete with YBCO growth. High growth rates in the mixed solid-liquid region might hence rely on proper tuning of process conditions to avoid phase coarsening and preservation of small particle sizes in order to promote liquid formation at these low temperatures. In the high temperature region, however, we expect to reach full liquid formation. Here, other factors might play an essential role, such as diffusivity of Y in the melt, liquid supersaturation and surface kinetics (4.1.3).
In the following sections we will therefore develop an understanding of control parameters that can be used to get into favourable supersaturation conditions for c-axis growth. This involves the $P_{O2} - T$ dependence (5.1.1), influence of heating ramps (5.1.2) and composition changes (5.1.4). The combined understanding of all will further be used to motivate TLAG growth opportunities at low temperatures (5.1.4) and promote homogeneous to heterogeneous growth conversion (5.2).

5.1.1 P_{O2} - T influence on epitaxial layer growth rates

Within the ERC project, the T - route was explored for a P_{O2} window of 10^{-4} - 10^{-2} bar, $P_{total} = 1$ bar. It seemed beneficial to work at these reduced oxygen partial pressures allowing to reduce processing temperatures and while promoting YBCO c-axis growth. At the synchrotron facility, experiments were primarily carried out at a P_{O2} of 1 mbar and 0.25 mbar to cover this region of interest. Two exemplary growth experiments of (2 - 3) and (3 - 7) composition, heated at 1 mbar and $dT/dt = 4.5\,°C\,s^{-1}$, are shown in Fig. 5.1.
The YBCO (103) evolution is obtained through integration of the whole ring intensity given in each 2D frame at $2\theta = 14° - 14.33°$ and $\chi = -9 - 9°$ (Fig. 5.1a)). To track the epitaxial layer signal a more confined window is chosen ($2\theta = 16.1° - 16.8°$, $\chi = -2° - 2°$) and recalculated into an effective layer thickness. Both signals can then be resolved in temperature and time (Fig. 5.1b)).

Both experiments show a similar evolution of the two types of grain orientations, independent of the chosen stoichiometry. Homogeneous and heterogeneous nuclei initiate to grow in parallel in region 1, labeled in Fig. 5.1b). That is where the 2D X-ray frame in Fig. 5.1a) shows a sharp diffraction spot on the position of the (005) and two equally distributed intensity rings at the (110) and (103) peak positions.
In region 2, a sharp intensity drop of grains with random orientation is registered while the epitaxial layer signal further increases and saturates in region 3. Following the 2D frames, the ring intensities diminish until complete disappearance while some intensity concentrates around (005) spot. Although a full characterization of the involved kinetics is the focus of section 5.2, it appears that c-axis growth is most notably promoted at high temperatures, initiating in region 2. Instantaneous growth rates during temperature increase, G_{inst}, can be estimated through derivation of the curves in Fig. 5.1b). This is done for a temperature range of 700 - 870 °C and shown in Fig. 5.2.[1] The previously denoted regions 1-3 are included.

[1] The stray of points results from the signal variation at each given temperature. Temperatures are recorded every 0.6 s by the Anton Paar heater unit, while 2D-XRD images are acquired every 100 ms.

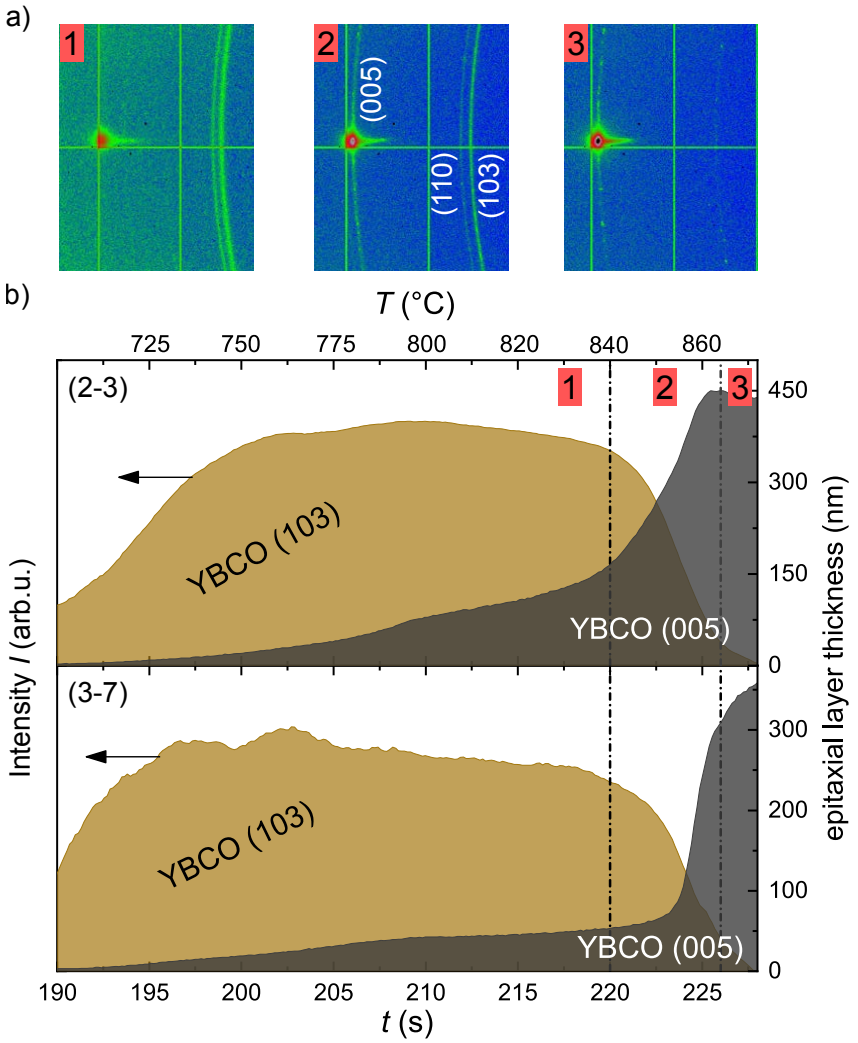

FIGURE 5.1: a) 2D-XRD images acquired during heating in regions 1-3, seen in b). b) Phase evolution of randomly oriented grains, YBCO (103), and epitaxial layer, YBCO (005), for two films of (2-3) and (3-7) composition (see labels). Dashed lines mark window of (103) intensity decrease. The thermal conditions are: 4.5 °C s^{-1}, T_{final} = 870 °C, P_{O2} = 1 mbar. Epitaxial layer thicknesses are estimated taking into account TEM images of comparable films. The (103) signal is amplified for better visibility.

Already at low temperatures (700 - 750 °C) both compositions reach epitaxial growth rates up to 8 nm s^{-1} which is almost 10 times higher than reached in the solid-solid based TFA-CSD processes [6]. This speaks for the presence of a low temperature melt as suggested in 4.4.3 and incorporated into the kinetic phase diagrams. Approaching region 2, both films run through a minor

drop in their growth speed. The dip appears more pronounced in the film of (3-7) composition. In region 2, the rates visibly increase passing through a maximum of 74 nm s^{-1} and 132 nm s^{-1} for the (2-3) and (3-7) composition, respectively. The maximum is followed by a decrease as the layer formation is complete in region 3.

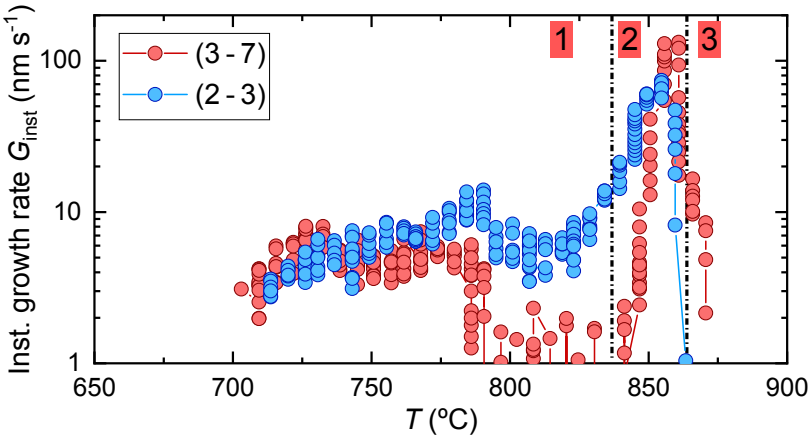

FIGURE 5.2: Instantaneous epitaxial layer growth rates obtained by deriving the curves in Fig. 5.1b) as a function of temperature. Dashed lines and numeration of the three different regions are included.

To relate the evolution of epitaxial layer growth rates to possible underlying reactions, all phases of the (3-7) film were tracked along the heating procedure. The correspondent normalized intensities are shown in Fig. 5.3a) as a function of time and temperature. From the initial precursor phases only $BaCO_3$ could be tracked due to the nanocrystallinity and high amorphous fraction of CuO and Y_2O_3. Some of the CuO crystallizes during heating (signified by the arrow around 660 °C), saturates towards 770 °C (labeled as point 1) and undergoes a valance change, CuO→Cu_2O, upon further temperature increase (point 1→2). In the final stage of growth (point 3→4) we observe the disappearance of the crystalline Cu_2O together with the YBCO (103) ring intensity and a rapid increase of the epitaxial layer signal.
The evolution of CuO and Cu_2O for the points 1 - 4 is further shown through $I(2\theta)$ scans in Fig. 5.3b). An additional scan without index depicts the relevant 2θ region at room temperature (lowest in the graph). CuO and Cu_2O (111) planes develop in agreement with the integrated intensity evolution in Fig. 5.3a). At room temperature there is no signal of any of the two phases. However, CuO partially crystallizes along the ramp and undergoes a valence change as already observed for binary (Ba - Cu - O) films in 4.3.

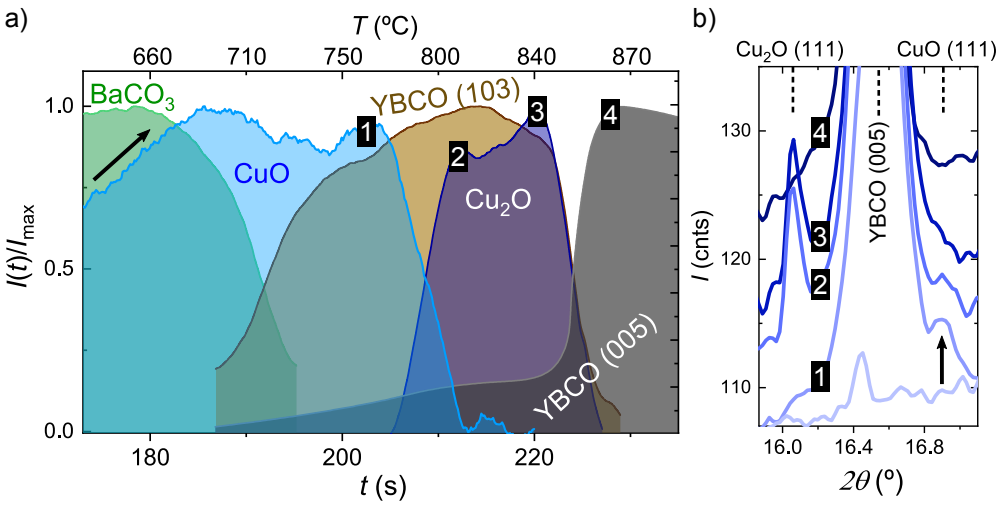

FIGURE 5.3: Time and temperature dependent phase evolution of the (3 - 7), copper-rich, film from Fig. 5.2b). Labeled points 1-4 indicate minimum and maximum values of the CuO and Cu_2O signals. b) $I(2\theta)$ evolution of the Cu_2O (111) and CuO (111) planes for the points 1 - 4 in a). The lowest scan without indexing is obtained at room temperature.

Considering the phase evolution in Fig. 5.3 the progression of instantaneous layer growth rates in Fig. 5.2 can be interpreted. In particular, three characteristic features seen in Fig. 5.2 can be addressed considering all results:

1. **High growth rates in region 1:** The growth rates encountered in this region are already well above those of conventional processes. According to the kinetic phase diagrams derived for ternary (3-7) mixtures (Fig. 4.25) this is the temperature range at $P_{O2} = 1$ mbar where a low temperature (Ba - Cu^{II} - O) melt together with solid phases are proposed to coexist. Considering the phase evolution in Fig. 5.3 the presence of solid phases can further be confirmed here given the CuO crystallization and valance change to Cu_2O. We therefore propose that growth rates remain compromised when mixed solid-liquid regions of the phase diagram are crossed, shown here through crossing of the (Ba - Cu^{II} - O) mixed region.

2. **Ultra-high growth rates in region 2:** The maximum epitaxial layer growth rates are achieved when the full (Ba - Cu^{I} - O) liquid region is entered (840 - 860 °C). Again in agreement with the derived kinetic phase diagram (Fig. 4.25), we observe that three independent signals coincide in their evolution in this temperature margin: The disappearance of the Cu_2O signal, drop in YBCO (103)/(110) intensity and the simultaneous, rapid increase of the (005) epitaxial layer signal. This is also where we

observe a maximum in G_{inst} of 132 nm s^{-1} in the (3-7) film. Hence, it can be suggested that YBCO growth rates experience an additional increase when the (Ba - Cu^{I} - O) full liquid region is reached.

3. **Growth rate dip in region 1:** As mentioned earlier, the $G_{inst}(T)$ curves show a minor dip which initiates at 770 °C before the (Ba - Cu^{I} - O) full liquid region is entered. The origin of the decrease can only be speculated at the present moment and requires additional experiments. For instance, few is known about what determines the amount of the low temperature melt. If the melt is formed only by those precursor phases that lie below a critical size, as motivated in chapter 4, its amount might be limited yielding to the observed decrease in G_{inst}. The appearance of the dip also coincides with the temperature window where the copper valence change takes place (point 1 $\rightarrow$ 2 in Fig. 5.3). This might, in turn, result in liquid property changes (e.g. viscosity, diffusivity) which could influence the growth behaviour.

So far, melting of the reduced $BaCu_2O_2$ phase could only be evidenced in the $P_{O2}(BaCu_2O_2)$ and $P_{O2}(Cu)$ - route where it appeared as stable, crystalline phase in the low pressure step. The coinciding, disrupted evolution of three independent signals (Cu_2O, YBCO (103)/(110) and YBCO (005)) further confirms that an additional melt emerges at high temperatures in the T - route, ascribed to the (Ba - Cu^{I} - O) liquid at $P_{O2} = 1$ mbar.
We also note that in the case of the copper-rich (3-7) composition, studied here, not all CuO/Cu_2O is incorporated in the liquid phase. Hence, the nominal (3-7) liquid composition is not reached for these particular processing conditions in the T - route. The amount of segregated copper phases cannot be estimated from the *in-situ* experiments and should be addressed in future experiments through quench studies and post-characterisation of grown films. In this chapter, however, we take advantage of the CuO/Cu_2O phase evolution to study the general degree of coarsening in films and evaluate how this affects YBCO growth.

The interpretation of the growth rate dependence with temperature is further supported considering two (3-7) films heated at a P_{O2} of 1 mbar and 0.25 mbar, 4.5 °C s^{-1}. The G_{inst} values of both samples are transferred into the correspondent kinetic phase diagram and shown in Fig. 5.4. As can be seen in the light-blue color ($G < 5$ nm s^{-1}), both films initiate the growth at reduced rates and accelerate upon further temperature increase. In the whole region where liquid and solid phases are assumed to coexist, ($BaCu_2O_{2(s+l)}$, G_{inst} does not exceed 20 nm s^{-1} for both oxygen partial pressures. The only zone where

ulta-high growth rates above 100 nm s^{-1} are reached, lies in the full (Ba - Cu^{I}-O) liquid region, previously defined through observance of melting of the solid $BaCu_2O_2$ phase in (3-7) binary films (4.3.1). Also a slight drop in growth rates in proximity to the $CuO \rightarrow Cu_2O$ reduction line, as seen before for films heated at 1 mbar, is observed here for both films (encircled by a dashed black line in Fig. 5.4). As mentioned earlier, this effect needs to be further examined in future experiments, for instance through larger variations of oxygen partial pressure or use of films with varying particle sizes of precursor phases to explore the effect of particle size on melting.

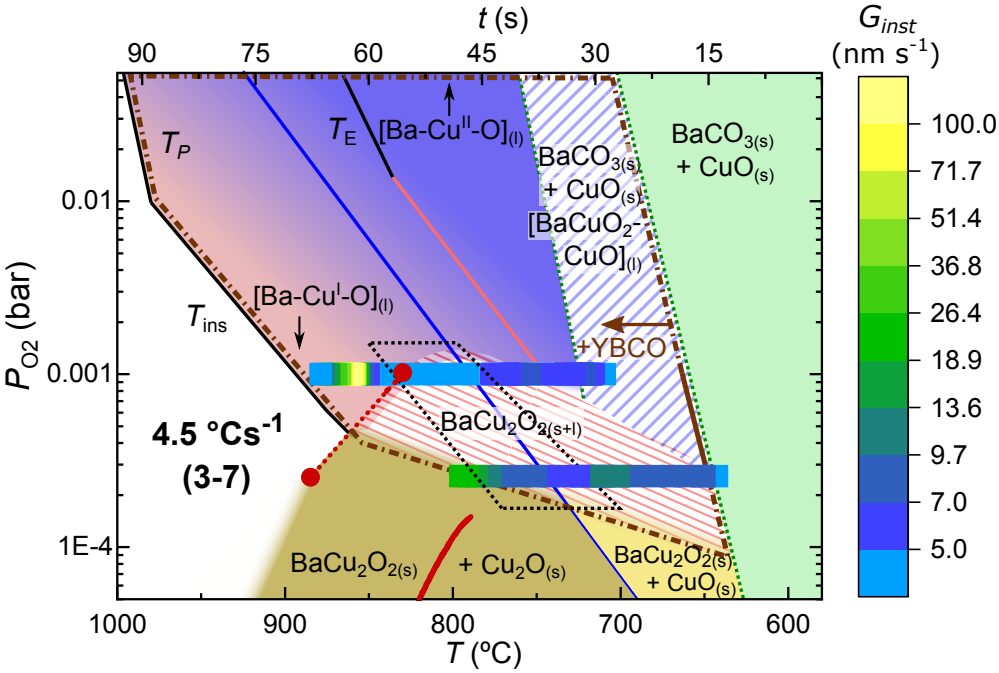

FIGURE 5.4: Attribution of instantaneous growth rates (color scale) to $P_{O2} - T$ conditions for two films of (3-7) composition, heated at $dT/dt = 4.5\,°C\,s^{-1}$, at 1 mbar and 0.25 mbar. YBCO instability lines, $CuO \rightarrow Cu_2O$ and $BaCu_2O_2$ melting lines are adapted from Fig. 4.25. Dashed, black line confines the window where a growth rate decrease is observed.

In summary, the growth of films through the T - route could be successfully exploited to estimate epitaxial layer growth rates during heating (G_{inst}), allowing to access process kinetics as a function of temperature. With the attempt to judge on the $P_{O2} - T$ dependence of YBCO conversion rates, we have evidenced that even for the generally high growth rates of the TLAG process G_{inst} can vary by an order of magnitude depending on where the film is placed in the kinetic phase diagram. The most noticeable change in G_{inst} is

observed when growth takes place in the (Ba - Cu^{I} - O) full liquid region that we identified in 4.4.3. In particular, the coinciding evolution of the Cu_2O, YBCO (103) and YBCO (005) signals together with a leap increase in growth rates is suggested here as an indicator for the emergence of a full liquid with a Cu valance (+1) at this P_{O2}. This hypothesis will further be backed up with an in depth analysis of the YBCO intensity evolution in section 5.2.
In regions of the phase diagram where the presence of liquid and solid phases are suggested, growth rates lie below 20 nm s^{-1}, though still up to 10 - 20 times higher than obtained in the TFA-CSD approach [6]. However, an additional 5 - 10 fold increase is registered when the samples are heated above the $BaCu_2O_2$ melting line into the full liquid region (up to 132 nm s^{-1}). Considering the sensitivity of YBCO growth rates on $P_{O2} - T$ conditions and the good agreement of results with the derived kinetic phase diagrams, the exploration of growth in wider $P_{O2} - T$ regions should further be envisaged, especially for $P_{O2} > 1$ mbar. This is currently addressed through *in-situ* resistance measurements of YBCO film growth at increased oxygen partial pressures in the full liquid region.

5.1.2 Heating ramp influence on epitaxial layer growth rates

Up to now only experiments at the maximum heating ramp of 4.5 °C s^{-1} were considered. In 4.4.3 it is argued that the increase of heating ramp can considerably change the progression of phases. For instance, at 0.4 °C s^{-1} and $P_{O2} = 1$ mbar a crystalline $BaCuO_2$ intermediate phase could be detected, absent at the highest ramps. This is a confirmation of the kinetic driving force of the non-equilibrium TLAG process since crystallization of the $BaCuO_2$ intermediate phase could occur at low heating ramps while it is hindered at increased heating ramps where the nanocrystalline/amorphous $BaCuO_2$ directly reacts with CuO to form the liquid phase.
A growth rate comparison of (3-7) films heated at 0.4 °C s^{-1} and 4.5 °C s^{-1} is shown in Fig. 5.5 for $P_{O2} = 1$ mbar and 0.25 mbar. At reduced heating ramps, the epitaxial layer initiates to grow at lower temperatures. This can be directly related to the shift in $BaCO_3$ decomposition towards lower temperatures (4.4.3). A more significant difference can be noted comparing the absolute values: At the same temperatures, films heated at 4.5 °C s^{-1} are capable of reaching YBCO conversion rates one order of magnitude above those heated slowly. Taking the example at $P_{O2} = 1$ mbar and $T = 730$ °C, growth rates of $5 - 7$ nm s^{-1} and $0.20 - 0.25$ nm s^{-1} are estimated for 4.5 °C s^{-1} and 0.4 °C s^{-1}, respectively. A similar discrepancy is observed for the two films processed at $P_{O2} = 0.25$ mbar and samples of (2-3) composition (not shown here).

The difference in achievable growth rates under heating ramp variation might be interpreted taking into account the derived kinetic phase diagram. At low temperatures, growth takes place in the mixed solid-liquid region in the (Ba - Cu^{II} - O) melt.[2] As mentioned earlier, increased heating ramps are likely to result in less coarsening of intermediate phases whose grain sizes are essential for melt formation. Hence, the samples that are heated at 0.4 °C s^{-1} might be affected stronger by phase coarsening and fewer melt formation. If coarsening is the limiting factor at these reduced temperatures, liquid properties might be changed due to stoichiometry variations. At low temperatures, one can also expect a different liquid viscosity and/or Y diffusivity in the melt.
In addition, the high temperature region where TLAG profits from the full liquid emergence cannot be reached by those films heated slowly as the epitaxial layer growth is completed along the ramp. This can be observed in Fig. 5.5 at P_{O2} = 1 mbar. While the film heated at 4.5 °C s^{-1} experiences a maximum in the epitaxial layer growth at high temperatures of 840 - 860 °C, the film heated slowly reaches an earlier maximum due to completion of the layer along the ramp.

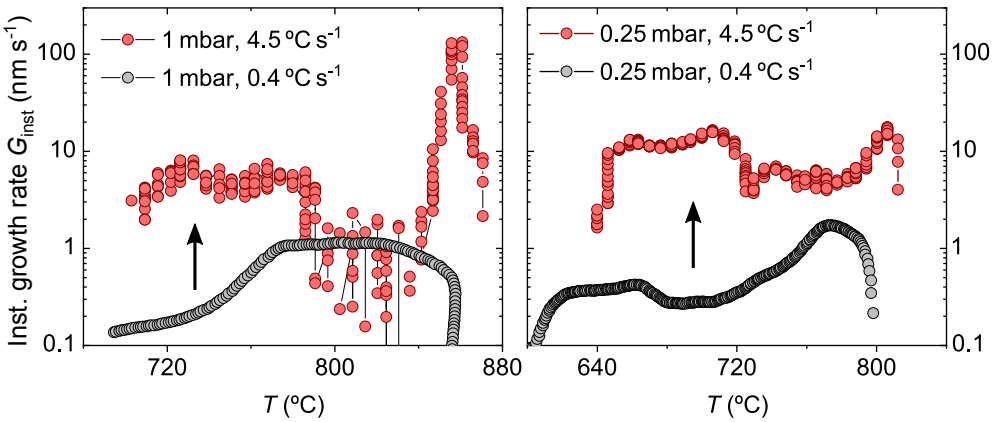

FIGURE 5.5: Heating ramp influence on the instantaneous epitaxial layer growth rates of (3-7) films heated at 0.4 °C s^{-1} and 4.5 °C s^{-1} at a P_{O2} of 1 mbar and 0.25 mbar. Growth rates are calculated using the derivative criteria of the YBCO (005) integrated intensity.

The application of increased heating ramps is proposed to be beneficial with regard to the avoidance of phase coarsening and capability of reaching the full liquid region of the phase diagram. A similar influence of heating ramps on the coarsening of phases was suggested in frame of the $P_{O2}(Cu)$ - route where increased heating ramps proved beneficial in the reduction of copper

[2] See kinetic phase diagrams in 4.4.3.

grain sizes at low pressures [94]. In the T-route, growth takes place along the ramp and at the targeted final growth temperature. The use of increased ramps is, hence, substantial to shorten the time needed to reach the most favourable c-axis growth conditions. In addition, the heating ramp increase brings the growth process to higher temperatures were the liquid viscosity is expected to decrease and Y solubility in the melt to rise. Overall, we see that the combination of such contributions allows to access higher growth rates through elevation of the heating ramp. Finally, we note that depending on the T, P_{O2} and heating ramp conditions, liquid properties may also vary with the copper oxidation state ((Ba-Cu^{I}-O)$\rightarrow$(Ba-Cu^{II}-O)).

The general trend in the increase of growth rates upon rapid heating is represented in Fig. 5.6. An average heating ramp is calculated taking into account the time needed to reach final growth conditions. Maximum YBCO growth rates are determined through the maximum derivative of the YBCO (005) signal and normalization to the nominal layer thickness.
Although all films run through the same range of temperatures, the highest conversion rates are achieved when growth conditions are reached faster, both at P_{O2} =1 mbar and 0.25 mbar. An increase in growth velocities up to two orders of magnitude can be accomplished that way. However, even for the same heating ramps, there is a strong stray of points. As for the case of 4.5 °C s^{-1} and P_{O2} =1 mbar, growth rates can range from 18 nm s^{-1} to 132 nm s^{-1}.

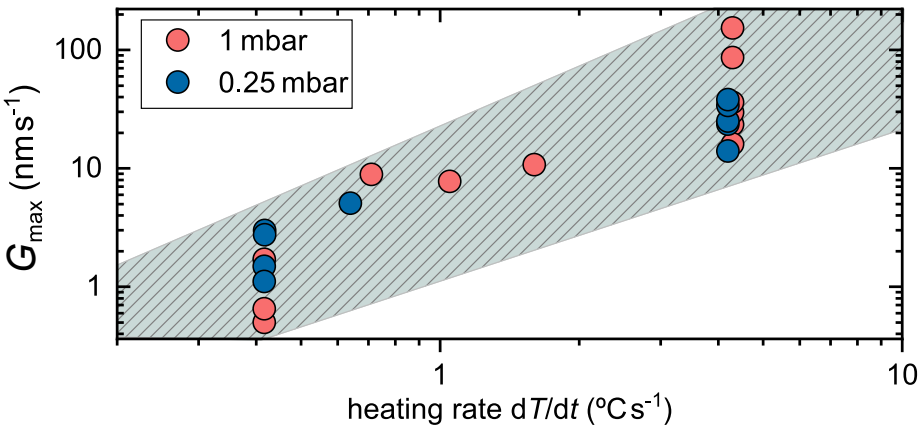

FIGURE 5.6: Maximum growth rates obtained with derivative criteria as a function of the heating ramp. Values are shown for 1 mbar and 0.25 mbar of P_{O2}. The shaded region is a guide to the eye for the upward trend. Only films of (3-7) composition are considered here

To give a possible explanation for the variation of growth rates, seen in Fig. 5.6, the phase evolution and degree of coarsening is evaluated in more detail for three films shown in the following.

5.1.3 Influence of copper valance state and coarsening on epitaxial layer growth rates

Three experiments are considered to relate the growth rate change to the underlying reaction mechanisms, all of which are two-layer pyrolyzed films of (3-7) composition and a molar concentration of 1.75 M. The samples are heat treated with the profiles shown in Fig. 5.7. A final thickness of 400 nm is obtained for all three cases. For simplicity reasons, the samples will be referred to as S1-S3.
Sample S2 and S3 are heated at the maximum rate of 4.5 °C s^{-1} to a temperature of 860 °C. These two films are estimated to reach the upper and lower limit in the stray of points at 4.5 °C s^{-1} in Fig. 5.6, with 18 nm s^{-1} and 132 nm s^{-1}, respectively. S1, on the contrary, is initially preset to reach 750 °C at the maximum rate and switched to a flatter ramp towards 860 °C. Here, the growth rate does not surpass 9 nm s^{-1}.

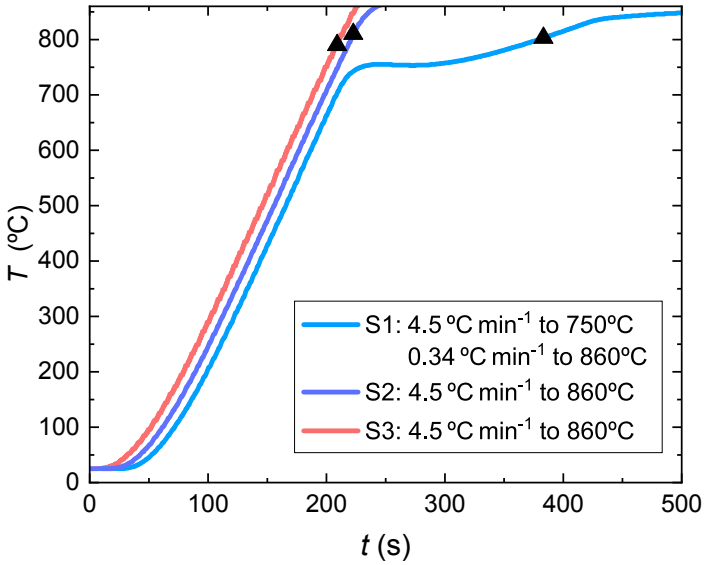

FIGURE 5.7: Temperature profiles of three (3-7) films of 1.75 M molar concentration treated at $P_{O2} = 1$ mbar: Two films are ramped up at 4.5 °C s^{-1} to 860 °C (S2 and S3); S1 is first heated at 4.5 °C s^{-1} to 750 °C followed by a decrease of ramp to 0.34 °C s^{-1} towards 860 °C (S1). Markers indicate the point where copper reduction takes place.

The change in heating profile for S1 aims to amplify coarsening contributions at elevated temperatures. The decrease in heating ramp is chosen in a temperature window before copper reduction occurs ($CuO \rightarrow Cu_2O$). The black markers in Fig. 5.7 signify where the valence change takes place for each experiment.[3] In particular, the copper progression is considered here for several reasons. On the one hand we have seen in the previous section (5.1.1) that changes in growth rates might be linked to a change in copper valance state.[4] Although this change was sensed through solid phases, also the melt is expected to undergo the valence change and potentially change its characteristics (e.g. viscosity, diffusivity, supersaturation). On the other hand, it was motivated through the derivation of kinetic phase diagrams that copper segregation is a frequently observed process that runs in parallel to YBCO growth when copper-rich compositions are used. A change in liquid properties might then also be influenced by the degree of copper segregation/coarsening which we deliberately aim to amplify here.

CuO, Cu_2O and epitaxial layer signals are shown in Fig. 5.8 for the three experiments whose thermal history is depicted in Fig. 5.7. As mentioned in 5.1.1, the detection of the CuO signal at room temperature is compromised due to the nanocrystallinity/amorphous state of the phase. However, at elevated temperatures a part of the CuO is found to crystallize as shown for all three films in Fig. 5.8. Hence, it can be regarded as a trace phase that allows to obtain information about the copper valance state.

The role of CuO as a trace phase becomes evident considering the intensity evolution in Fig. 5.8. While the epitaxial layer is formed, the coarsened crystallites undergo a valence change at temperatures ranging from 786 - 816 °C. At these transition temperatures the epitaxial layer completion of S2 and S3 (Fig. 5.8b) and c)) rages from 40-50 %. The film grown through the mixed ramp profile (S1) is at 65 %, in agreement with the decrease in heating ramp. The maximum YBCO epitaxial layer growth rates of all three experiments are included in the figure labels.

[3] Identified through temperature dependent analysis of phases.

[4] The appearance of a dip in G_{inst} (Fig. 5.2) was found to coincide with the $CuO \rightarrow Cu_2O$ reduction in temperature (Fig. 5.3).

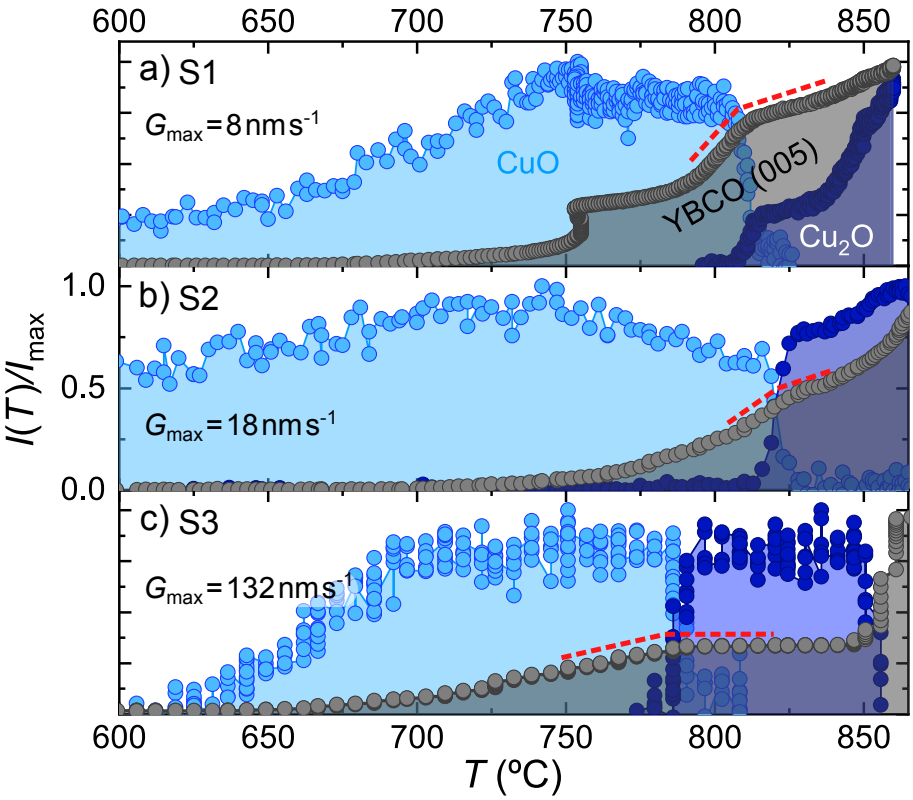

FIGURE 5.8: Normalized CuO, Cu_2O and YBCO (005) signal for the three films that are grown through the temperature profiles in Fig. 5.7. a) S1: 4.5 °C s^{-1} to 750 °C, followed by a switch to 0.34 °C s^{-1} up to 860 °C. b)/(c) S2/S3: 4.5 °C s^{-1} to 860 °C. The phase evolution is obtained through $(2\theta - \chi)$ area integration of the 2D frames. The change in YBCO growth rate upon copper reduction is marked through dashed red lines (- - - - -). The maximum instantaneous growth rate, G_{max}, of each experiment is included as figure label.

In proximity to the copper reduction temperatures, the epitaxial layer is registered to decrease in growth rate even though the temperature is further raised, as seen by the dashed-red lines. This is indicative that the valence change, observed in solid copper crystallites, reflects also a simultaneous property change of the melt. Advancing further in temperature, the growth velocity of S1 and S2 increases only marginally. Here, the reduced Cu_2O phase follows an upward trend. This can be attributed to the fact that Cu_2O is partially aligned with the (111) plane parallel to the substrate surface. Such a preferential orientation could affect the absolute registered intensity values depending on the phase amount allocated in the diffraction spot. It can hence

not be confirmed that the actual amount of Cu_2O keeps increasing in these two experiments.
The YBCO epitaxial layer growth rate for S1 and S2 does not exceed 9 nm s^{-1} and 18 nm s^{-1}, respectively. This might be related to the actual amount of copper in the melt if coarsening of the phase is favoured. As it is extensively discussed in [76], the copper concentration is predicted to affect the equilibrium Y concentration C_{eq} in the (Ba - Cu - O) melt and with that the overall relative supersaturation σ. In addition, melt property changes (e.g. viscosity and reactivity) could further influence growth rates through changes in diffusivity, surface kinetics and the actual Y concentration, C, in the liquid phase (eq. 5.1).

While moderate conversion rates are reached for S1 and S2, a maximum of 132 nm s^{-1} is achieved for S3, Fig. 5.8c). In that particular case the solid Cu_2O is shown to disappear in a temperature window of 840 - 860°C where the full liquid region is reached according to the kinetic phase diagrams. We have discussed previously in 5.1.2 that growth rates depend significantly on the utilized heating ramp and that this dependence might be a result of enhanced coarsening of precursor and intermediate phases. However here, all three experiments undergo a similar temperature treatment (Fig. 5.7). To evaluate whether the films are distinguishable in their coarsening state of precursor and intermediate phases we can, hence, use the CuO and Cu_2O solid phases for further analysis.
A comparison of the absolute CuO intensity for the three films is shown in Fig. 5.9a). The curves are acquired through integration of counts in a confined 2θ window of 16.95°-17.19° around the CuO (111) reflection, $\chi = -9° - 9°$.[5] A constant offset was subtracted to remove any secondary contributions to the signal.
Comparing the intensity evolution in Fig. 5.9a), it appears that the absolute amount of segregated, crystalline CuO can vary even though all films have the same nominal composition. The segregation is strongest for the film S1, which is heated with a mixed ramp profile (switch to 0.34 °C s^{-1} above 750 °C). Here, the sample spends considerably more time in the temperature window 700 - 800 °C where the crystalline CuO is found stable.

[5]The phase is randomly oriented, hence a ring intensity is observable in the 2D images.

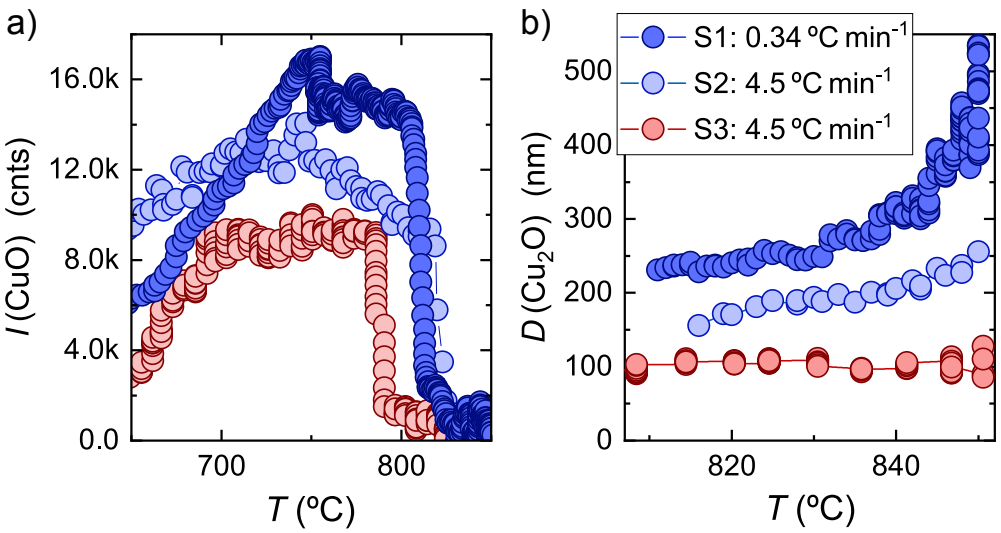

FIGURE 5.9: CuO and Cu_2O (111) signal evolution of (3-7) films shown in Fig. 5.8: a) Absolute CuO intensity obtained through tracking of counts in $(2\theta - \chi)$ window of $2\theta = 16.95^{o}$-17.19^{o} and $\chi = -9^{o}$-9^{o}. CuO crystallizes first along the ramp below T =700-750ºC, followed by a rapid drop when the valence change takes place. b) Debye Scherrer crystallite sizes of Cu_2O phase calculated through peak fitting with Lorentzian profiles.

The Bragg reflection of the Cu_2O (111) plane is well isolated of any other phase. Here, peak fitting can be used to estimate the size of coarsened crystallites right after the CuO→Cu_2O reduction took place. Debye Scherrer grain sizes of the reduced phase are plotted in Fig. 5.9b). The film reaching highest YBCO epitaxial layer growth rates (S3), shows the weakest coarsening effect of Cu_2O grains (red markers). Values saturate at approximately 100 nm. S1 and S2, however, surpass this estimate by a factor of 2-3, reaching values above 200 nm.
Given the reduced amount of CuO segregation and disappearance of Cu_2O crystallites in S3, it can be suggested that reaction kinetics are changed as compared to S1 and S2. It seems that in this particular case the contribution of coarsening is less pronounced even allowing for Cu_2O dissolution in the full (Ba - Cu^{I} - O) liquid region. This is also the film of (3-7) composition whose growth velocity evolution is discussed in 5.1.1.[6]

These findings complement our previous assumptions, namely that the coarsening state of phases might contribute to the overall reaction speed and

[6]The abrupt growth rate increase was suggested to arise from entering in the (Ba - Cu^{I} - O) full liquid region.

growth of YBCO, here exemplified through the evolution of CuO and Cu_2O solid phases. Until now, we attributed the change in growth rates either to where the sample is placed in the phase diagram or which heating ramp is employed. Here, however, the understanding is further extended to a dependence on thermal history of each individual case and changes in coarsening. This is, in fact, also in agreement with our current understanding of the kinetic phase diagrams. In those regions where liquid and solid phases coexist, coarsening of any of the involved precursor or intermediate phases might slow down the reaction towards YBCO. In this context, the use of increased heating ramps and processing conditions to minimize such contributions become central points of the TLAG process. It should also be mentioned that the maximum accessible heating ramps at the synchrotron facility (< 4.5°C s^{-1}) are not the optimal ones that we will define in chapter 6 for T - route grown films. Improved film performance was achieved at 20°C s^{-1}, where coarsening contributions are expected to be further diminished.
It should also be emphasized that although we center the analysis here around the coarsening degree of the CuO/Cu_2O phase, the associated changes in growth rates are not suggested to be directly affected by the presence of these coarsened crystallites. The shown trends should rather be considered as a result of liquid property changes (e.g. viscosity, diffusivity of Y, supersaturation) and all the intermediate steps involved in YBCO growth (4.1.3) since the presence and coarsening of solid CuO/Cu_2O phases implies a change of liquid composition (less Cu in the liquid). Hence, the coarsening of CuO/Cu_2O might be only indicative for such background processes, elsewise not observable via X-ray diffraction.

5.1.4 Strategies towards low temperature processing

The decrease of processing temperatures in YBCO manufacturing is a highly desirable goal, mainly for two reasons: Cost-reduction due to lower furnace operating temperatures and avoidance of substrate and buffer reactivity with the corrosive liquid phase, which is amplified at increased temperatures [77]. Reactivity phases are known to degrade film performance through contamination of the REBCO crystal structure [175].
As summarized in 4.4.5 and 6.1.2 for the TLAG case, the use of high heating ramps and increased temperatures ($dT/dt > 20$°C/s, $T > 800$ °C) can result in interface reaction of substrate and liquid phase. Two main strategies are explored here to reduce processing temperatures: Variation of P_{O2}, placing the sample in different parts of the kinetic phase diagram, and increase of copper concentration in the initial precursor composition to increase the c-axis window at lower temperatures due to reduced supersaturation of the melt [76,

132].
The latter of the two approaches arises from the fact that Y solubility is reported to change upon (Ba - Cu - O) flux composition changes [176]. Fig. 5.10a) shows the equilibrium Y concentration for the case of a (3-5) and (3-7) melt composition. Values are extracted from [84, 177, 178] and extended to lower temperatures. At any given temperature the melt with higher copper concentration allows to solubilize more Y. This can be converted into a temperature dependent supersaturation, $\Delta\mu$, and relative supersaturation, σ, using eq. 4.5 and 4.6, respectively. The curves are plotted in Fig. 5.10b) for both liquid stoichiometries. Here, the actual Y concentration in the liquid (C) is estimated to 10%, extrapolated from the high temperature liquidus line, (Ba - Cu - O) melt + Y_2O_3 [76].

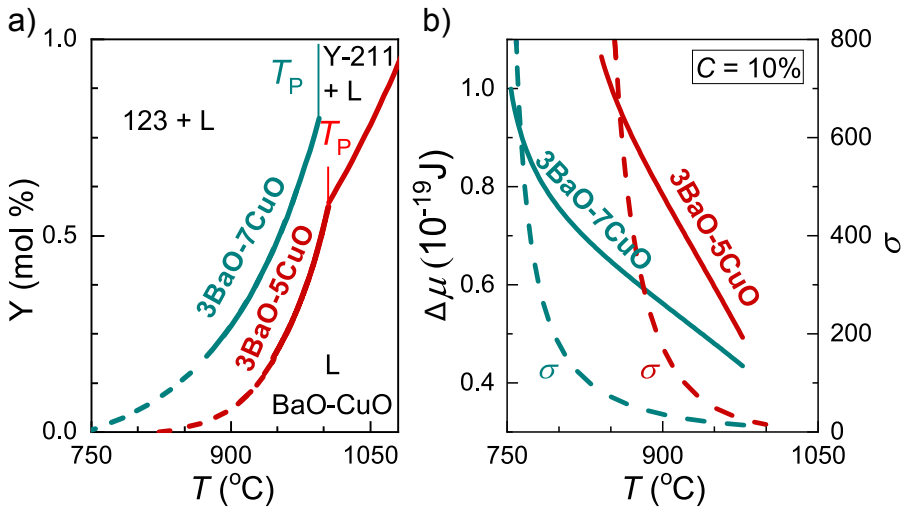

FIGURE 5.10: Exemplary supersaturation calculus for (3-5) and (3-7) melt compositions: Temperature dependence of a) Y equilibrium concentration C_{eq} and b) supersaturation values $\Delta\mu$ (solid lines) and σ (dashed lines) for a fixed, real Y concentration $C = 10\%$. The dashed lines in a) are extrapolations of the equilibrium values from [84, 177, 178]. Courtesy of L.Soler [76].

From Fig. 5.10b) it can be concluded that for similar temperatures and Y concentrations (C) in the melt, supersaturation decreases with copper enrichment. Correspondingly, the same supersaturation can be reached at reduced temperatures if a copper-rich melt is employed. With regard to TLAG processing, the use of copper enriched solutions might hence become an additional parameter to control supersaturation and widen the region to promote YBCO c-axis growth.

The two mentioned strategies are explored here through *in situ* XRD measurements of films with varying copper concentration and through changes in oxygen partial pressure, hence, heating into different regions of the kinetic phase diagram.

The YBCO intensity evolution of three films of different (Ba-Cu) composition are shown in Fig. 5.11. The three mixtures (2-3), (3-7) and (4-11) have a $BaCuO_2$ to CuO ratio of 25%, 30% and 40%, respectively.[7]
In Fig. 5.11a), the combined integrated intensity of the (110) and (103) reflections is shown as a function of temperature. To obtain the evolution, a fixed 2θ range is chosen, covering both diffraction rings. The intensity is then tracked for the full angular range in χ. A constant background is subtracted to eliminate background contributions such as heater signal and diffuse scattering. Absolute intensity values are comparable given the similar nominal thickness of the grown films and overlapping background intensities.
As introduced in the previous chapter, crossing of the low temperature window allows for nucleation of homogeneous grains. This can be understood, considering that the supersaturation decreases when increasing temperature (Fig. 5.10b)) for any of the compositions. Due to the low solubility of Y at low temperatures, supersaturation values can be high enough to allow for formation of homogeneous nuclei whose Gibbs free energy barrier is higher than those of heterogeneous ones (eq. 4.11).
It appears, however, that the proportion of randomly nucleated grains can vary with the composition used. Although the estimations in Fig. 5.10 are made from equilibrium solubility curves and shifts in temperature can be expected for the TLAG process, the downward trend of randomly nucleated grains with increased copper concentration is in agreement with the theoretical prediction: At the same temperatures, the copper-rich melts have decreased supersaturation. A reduction in nucleation and growth rates is, hence, expected according to eq. 4.13 and eq. 5.2, resulting in a reduced amount of random YBCO as heating ramp increases.
Simultaneously, a change in the evolution of the YBCO epitaxial signal is registered for the three compositions (Fig. 5.11b)). The intensity of the YBCO (005) reflection is normalized to unity to compare the overall advancement in the growth of the epitaxial layer. The film with highest copper content, previously observed to yield the lowest YBCO random fraction (Fig. 5.11a)), is now seen to promote growth of the epitaxial layer at lower temperatures ($\sim$ 50ºC in difference). In agreement with former findings [132], the epitaxial

[7] An overview is further given in Fig. 4.11.

layer formation advances in the copper-rich melts where the optimal supersaturation window for c-axis growth is reached at reduced temperatures.

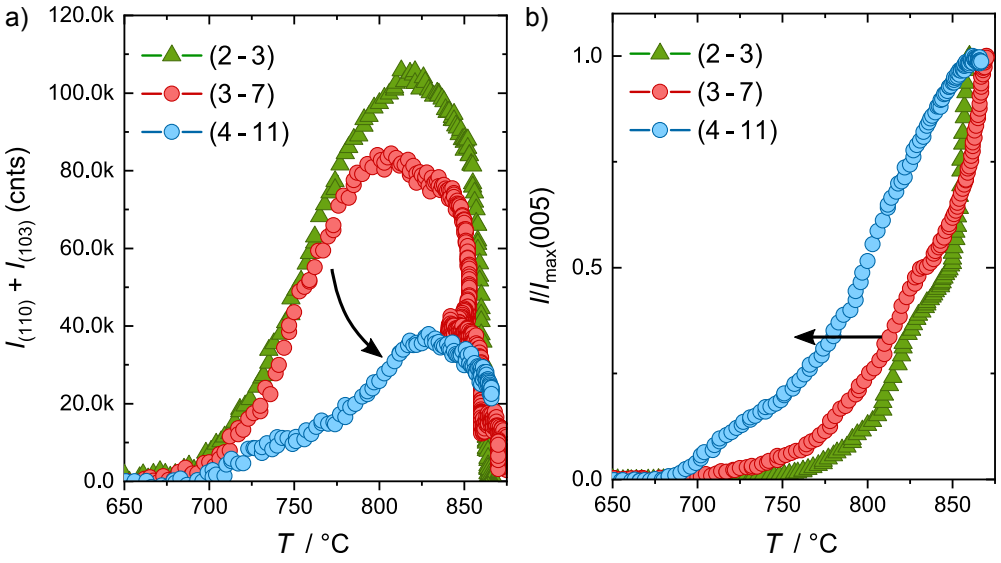

FIGURE 5.11: YBCO temperature dependent signal evolution for the three different precursor compositions (4-11), (3-7) and (2-3) heated at 4.5 °C s^{-1} to 860 °C at P_{O2} = 1 mbar: a) Combined intensity of (110) and (103) diffraction rings in absolute counts. b) Normalized (005) signal of the epitaxial layer.

In the second approach to promote c-axis YBCO growth at reduced temperatures, we looked into the evolution of epitaxial layer growth rates for films of (2-3) and (3-7) composition heated at 4.5 °C s^{-1}, P_{O2} = 0.25 mbar and P_{O2} = 1 mbar. The instantaneous epitaxial layer growth rates are shown in Fig. 5.12, comprising all four experiments. Both (2-3) and (3-7) films, heated at P_{O2} =0.25 mbar, initiate the growth at rates higher than 5 nm s^{-1} and a temperature of 640 -650 °C, well below the temperatures registered for the experiments at 1 mbar ($\sim$ 700 °C). This shift might be a result of the P_{O2} - T dependence of the kinetic phase diagrams. At reduced oxygen partial pressures growth takes place almost entirely in the melt originating from the $BaCu_2O_2$ phase.

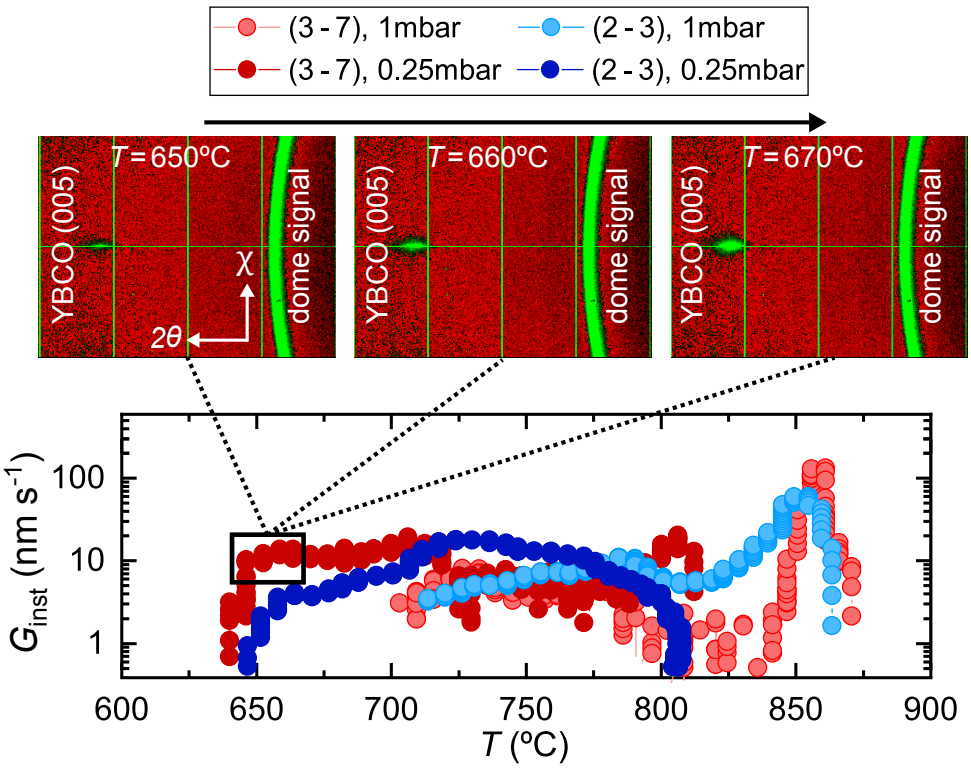

FIGURE 5.12: Epitaxial layer growth rates for (2-3) and (3-7) compositions heated at a maximum ramp of 4.5 °C s^{-1} at P_{O2} = 1 mbar and 0.25 mbar. 2D X-ray scans in the top show the time evolution of the (3-7) film, P_{O2} = 0.25 mbar in a temperature range of 650 - 670 °C.

The combined effect of film composition and P_{O2} dependence is further shown to allow for very high epitaxial layer growth rates, up to 10 nm s^{-1} at 650 ºC, for the copper-rich (3-7) mixture heated at P_{O2} =0.25 mbar. The 2D-XRD images for this (3-7) film are included in Fig. 5.12 in a temperature window of 650 - 670 ºC. One frame each 10 ºC is plotted and the color scale adjusted just above the background noise level. It is clearly seen that apart from the heater dome signal, there is only the YBCO epitaxial reflection, given by the (005) plane, advancing in temperature. If random nuclei are also formed at these conditions their signal must lie within the noise range. In this window, supersaturation seems to be in the right conditions to promote primarily heterogeneous nucleation.

The preferential growth of the epitaxial layer at low temperatures, for the (3-7) film heated at P_{O2} =0.25 mbar, is further shown through $\theta - 2\theta$ scans of the

relevant temperature region (Fig. 5.13). Once again it is visible that heterogeneous nucleation precedes the homogeneous one, at temperatures below 700 °C.

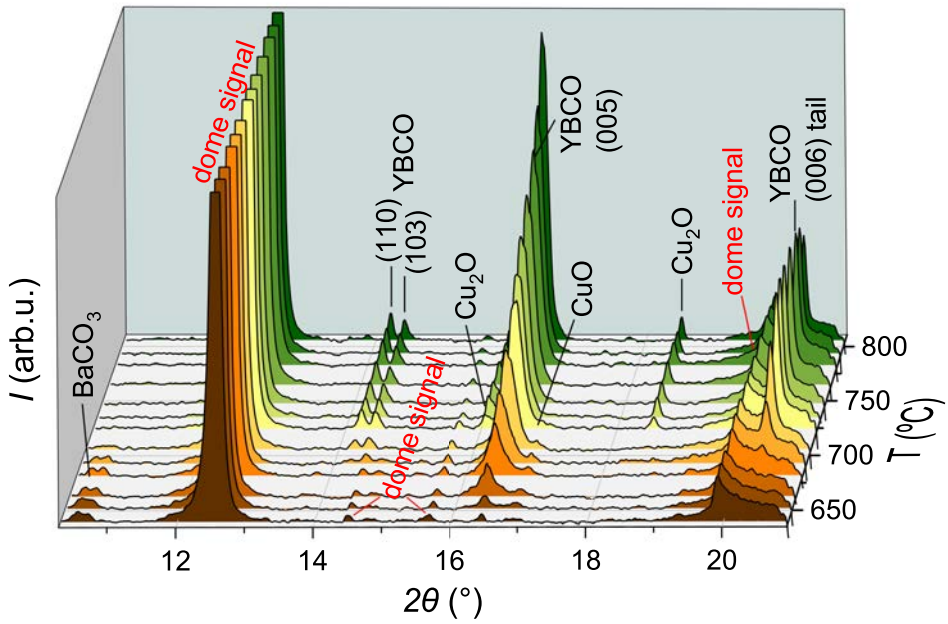

FIGURE 5.13: Temperature evolution of $\theta - 2\theta$ curves for a (3-7) film heated at $P_{O2} = 0.25$ mbar, $dT/dt = 4.5\,°C\,s^{-1}$. The scans are shown from the onset of YBCO epitaxial layer formation until completion of the film growth. The dome signal at 12.5 ° is cut to 250 counts.

Above 710 °C, CuO to Cu_2O reduction and the formation of homogeneous grains are observed. A diminishment of the YBCO (110)/(103) signal, as identified for the films at 1 mbar (5.3a)), does not take place. This effect will particularly be addressed in the following section.

To conclude, through variations of the oxygen partial pressure (P_{O2}) and film composition, keeping the heating ramp constant at $4.5\,°C\,s^{-1}$, we could promote high growth rates at low temperatures with the copper-enriched composition working at P_{O2} =0.25 mbar. Precise dwell experiments at reduced temperatures should further explore such favourable conditions for c-axis growth. Although at these $P_{O2} - T$ conditions the ultra-high growth rate values of $> 100\,nm\,s^{-1}$ could not be achieved, possibly due to the low temperature, presence of solid phases and liquid properties, it is remarkable that epitaxial YBCO growth can already take place at temperatures as low as 650 °C

and growth rates of 10 nm s^{-1}. This is approximately ten times higher than achieved in the TFA-CSD approach [6]. Not only do these results invite for further experiments varying film stoichiometry and P_{O2}, but also underline that the TLAG process is capable of promoting high growth rates at low temperatures if the non-equilibrium benefits of the process are properly exploited. As argued throughout this section, this includes preservation of small particle sizes[8] and placement of the growth conditions into regions of the phase diagram where low temperature melting is expected.

5.2 Homogeneous to heterogeneous growth conversion

In the aforegoing part the focus was set on the essential process parameters that enable TLAG processing at high rates and low temperatures. Through *in-situ* tracking of instantaneous epitaxial growth rates, crystallite sizes and phase intensity we could validate and extend our understanding of the kinetic phase diagrams derived in chapter 4. These tracking procedures also underline the significance of synchrotron radiation to study highly non-equilibrium, kinetically driven processes such as TLAG. Here, we develop another approach to obtain information from the 2D-XRD images and apply the new method to a surprising phenomenon observed already previously, namely the disappearance of randomly oriented YBCO crystallites upon heating.
As already suggested from the phase evolution in Fig. 5.1, the diffracted intensity of randomly nucleated YBCO grains, observable through the (110) and (103) planes, is found to diminish while the epitaxial layer proceeds to grow along the heating ramp. The effect was observed at P_{O2} =1 mbar and T =840-860 °C, both for films of (2-3) and (3-7) composition. Given that the phenomenon occurs at high temperatures where we expect to reach the (Ba - Cu^{I} - O) full liquid region, it should be elucidated whether the TLAG process can promote reorientation of crystallites under certain conditions. A demonstration of random grain reorientation would be insofar significant as the mechanism is rarely observed, especially in YBCO processing, and could become an additional strategy to promote c-axis growth.

5.2.1 Intensity tracking procedure

With the aim to identify whether the disappearance of diffracted intensity, coming from random YBCO grains (Fig. 5.1), is a result of grain reorientation we benefit here from the fact that the intensity is acquired through 2D-XRD

[8] Allowing to avoid coarsening of precursor and intermediate phases.

imaging with a certain angular range ($2\theta/\chi$ opening of approximately 10°-21°/-9°-9°, respectively). This allows to track the intensity in individual areas of each 2D image briefly introduced in 3.6.2 and decide whether reallocation takes place from one angular window to another.

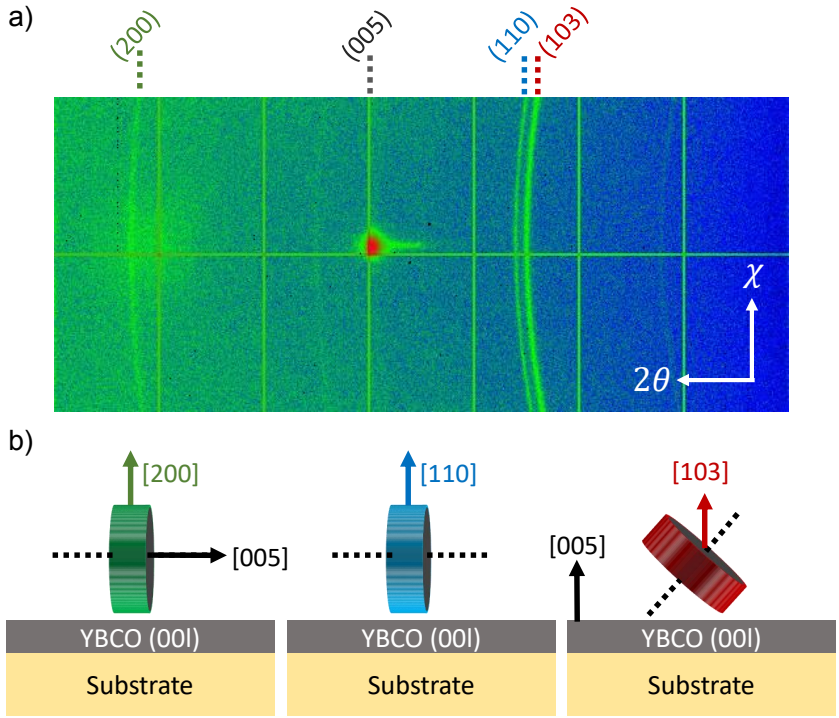

FIGURE 5.14: Intensity distribution with different grain orientations: a) 2D-XRD frame with the main YBCO diffraction planes identified. The scan is chosen for a case where the epitaxial layer is partially grown, together with some randomly oriented YBCO grains. b) Schematic representation of plate-like grains with different orientations. Dashed lines represent the direction perpendicular to (00l) planes. The notation $[h\,k\,l]$ specifies the diffracted direction with respect to the $(h\,k\,l)$ plane [120].

Let us, for instance, consider one single frame where the epitaxial layer is partially formed together with homogeneously nucleated grains (Fig. 5.14a)). All diffracted intensity coming from the YBCO phase is confined in a (005) diffraction spot and evenly distributed intensity rings at 2θ positions that fulfill Bragg's law.[9]

[9]Note that incident and outgoing diffraction angles are chosen in Bragg's condition with the (005) plane, allowing to follow randomly oriented grains as well as the epitaxial layer evolution.

The main diffraction planes of YBCO are denoted in the top of the 2D scan. In the initial stage of growth, YBCO crystallizes in its tetragonal structure with the (103) plane giving the strongest signal, followed by the (110), (200) and (005) planes.[10] Now, the intensity distribution in Fig. 5.14 comes partially from the epitaxial layer and partially from misoriented, random YBCO grains. This explains the bright, confined spot at the 2θ position of the (005) reflection and the rings coming from the (103), (110) and (200) planes. A ring around the (005) spot is hardly observable and requires proper intensity integration.

A schematic drawing of plate-like grains and epitaxial layer that would yield the diffracted pattern in Fig. 5.15a) is shown in Fig. 5.15b).[11] The grains are drawn in disc-shape assuming that YBCO grows anisotropically faster in a- as compared to the c-axis direction [179, 180]. For each of the depicted platelets the c-axis direction is identified through a black-dashed line. Also a YBCO epitaxial layer is included, disproportionate in size for the sake of simplicity.

Now, the subdivision of the diffracted space and attribution to different YBCO grains allows to track intensity reallocation if a reorientation processes are involved. In particular, we will track the intensity in three distinct areas of each 2D image and resolve it in time/temperature (see Fig. 5.15a)). Region 1 confines the total intensity given by the (110) and (103) plane (χ = -9°-9°), termed $I_{(103)+(110)}$. Region 2, on the contrary, comprises angles $|\chi| > 2°$ to follow high angle grains that settle around the c-axis alignment, $I_{(005)\,\mathrm{ring}}$. Finally, the signal of the epitaxial layer itself, I_{epit}, is tracked in region 3 where the angular range is confined to $|\chi| < 1°$.

[10] See PDF:00-039-1496 of the ICDD crystallographic database. For YBCO powders the intensity of the (005) plane is 10 times lower than for the (103).

[11] Precisely speaking, grain orientations as illustratively shown here would result in diffracted intensity only along the 2θ axis and $\chi = 0$. The ring sections in Fig. 5.14a) arise from a spread of angles around the crystallographic planes in Fig. 5.14b)

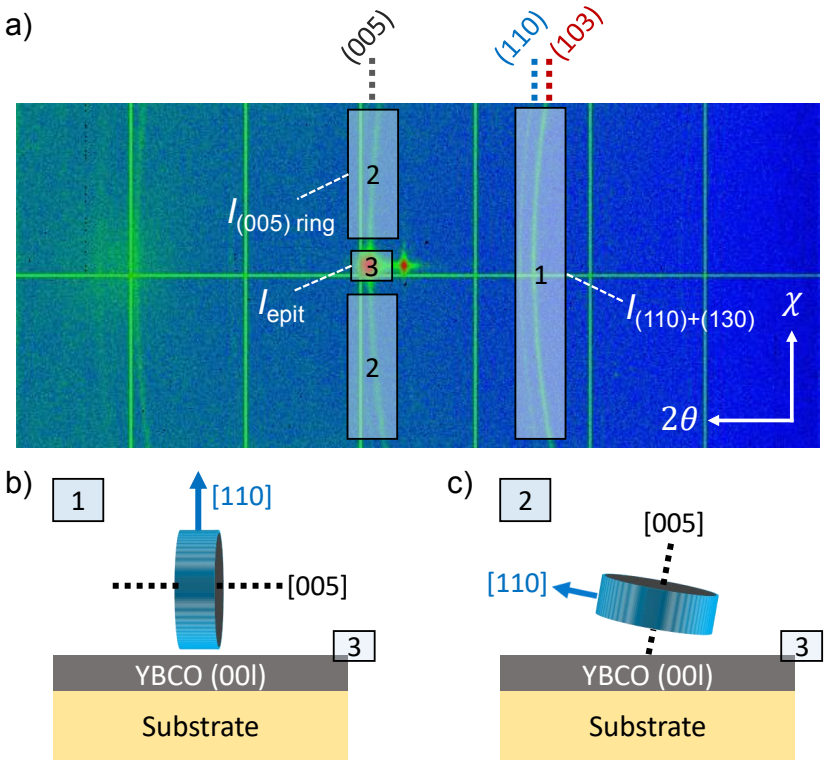

FIGURE 5.15: Random nuclei evolution: a) 2D scan with three custom regions that are integrated to track intensity in different parts of the angular range. b) YBCO grain alignment to give the intensity rings in a), shown exemplary for the (110) plane. Dashed lines represent the direction perpendicular to (00l) planes.

The chosen areas for intensity integration are suited to track reorientation mechanisms. This is illustrated through the example of a grain whose (110) plane is initially parallel to the substrate (00l) planes, giving the (110) intensity ring in region 1 (Fig. 5.15b)). Upon rotation of the same crystallite towards the epitaxial layer (Fig. 5.15c)) the intensity would disappear from region 1 as soon as a tilt angle higher than $\pm 9°$ is reached and be registered in region 2 when its (005) plane encloses angles smaller than $\pm 9°$ with the substrate surface.

The tracking procedure will be employed in the following to identify the underlying conversion mechanism and confine process parameters that benefit the restructuring phenomenon.

5.2.2 Identification of process conditions for YBCO random grain reorientation

In the previous discussion of this chapter, the evolution of phases, particularly the disappearance of the (103) and (110) diffraction rings, is shown for a P_{O2} of 1 mbar (5.1.1). Here, we aim to explore this signal evolution in more detail at different oxygen partial pressures, taking advantage of the tracking method in 5.2.1. The ring intensity around the (005) diffraction spot ($I_{(005)\ \mathrm{ring}}$) and the (103)/(110) polycrystalline rings ($I_{(103)+(110)}$) can give complementary information whether an intensity reallocation takes place. In addition, the (005) diffraction spot, given by the epitaxial layer itself, is tracked as third area to account for grains that have low misalignment with respect to the c-axis growth direction (I_{epit}). These three regions are integrated and resolved in time and temperature for two (3-7) films heated at P_{O2}= 0.25 mbar and 1 mbar. The according progression of all signals is shown in Fig. 5.16.

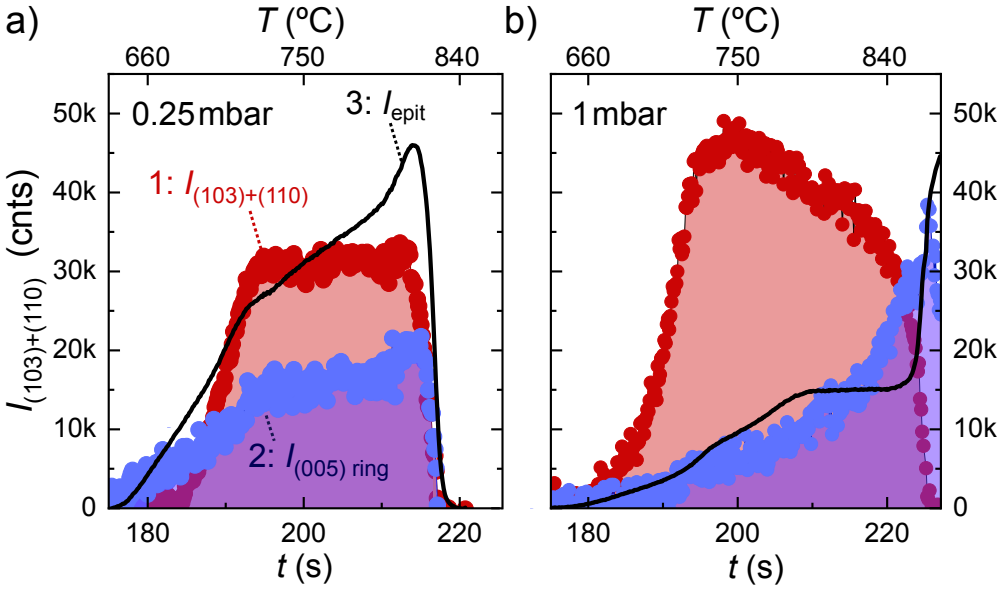

FIGURE 5.16: Custom integration of intensity in areas defined in Fig. 5.15 for two (3-7) films heated at P_{O2} = 0.25 mbar and 1 mbar with a heating ramp of 4.5 °C s^{-1}. Purple and red curves show the evolution of the ring intensities; black solid lines are obtained through integration of the (005) epitaxial layer signal at $|\chi| < 1°$. The intensity scale applies only to the polycrystalline ring intensities $I_{(005)\ \mathrm{ring}}$ and $I_{(103)+(110)}$.

Considering first the film heated at 0.25 mbar, it is observable that the tracked intensity of all three regions develops concurrently.[12] After all signals reach saturation, a drop follows simultaneously at 800-810 °C.[13] The coinciding disappearance of YBCO signals in all integrated areas of the 2D scans suggests that the YBCO phase decomposes at this temperature.
The decomposition of YBCO at P_{O2} =0.25 mbar can further be confirmed considering the emerging phases at these temperatures. A compact representation of the phase evolution at 0.25 mbar is given in Fig. 5.17a), in the form of a 2θ and T dependent colormap. All YBCO signal, including the epitaxial layer (indicated as (005)), vanishes at temperatures above 800-810 °C giving a decomposition into crystalline $BaCu_2O_2$ and Y_2BaCuO_5 (short, 022 and 211). Appearance of crystalline 211 is in agreement with YBCO stability diagrams as derived by T.B. Lindemer and J.L. MacManus-Driscoll [101, 139].

The responsible mechanism for the (103)/(110) intensity disappearance changes upon P_{O2} increase. At 1 mbar the integrated signals in region 1 and 2, $I_{(005)\ \mathrm{ring}}$ and $I_{(103)+(110)}$, evolve decoupled from each other, opposite to the evolution at 0.25 mbar (Fig. 5.16b)). Firstly, most of the intensity accumulates and saturates in the (103) and (110) ring (red curve). At this point the ring intensity around the (005) diffraction spot is below 25 % of its maximum value (purple curve). The intensity drop of $I_{(103)+(110)}$ coincides with an increase in $I_{(005)\ \mathrm{ring}}$. It appears that at 840-860 °C a reallocation of the signal takes place. Also a minor decrease in $I_{(005)\ \mathrm{ring}}$ is obtained after a delay as compared to $I_{(103)+(110)}$ drop. In the meanwhile, the epitaxial layer signal (solid black line) increases monotonously and reaches a maximum at 850-860 °C suggesting that kinetics change considerably at this increased P_{O2}. According to the kinetic phase diagram in 4.4.3, the temperature range where intensity reallocation from region 1 to 2 takes place coincides with the melting of the solid $BaCu_2O_2$ phase, hence, entrance into the (Ba - Cu^{I} - O) full liquid region.

[12] A downward temperature shift of the epitaxial layer signals, $I_{(005)\ \mathrm{ring}}$ and I_{epit}, is in agreement with the growth temperature reduction at these low P_{O2} values (5.1.4).

[13] The onset temperatures for the signal decrease are determined through the 90% criterion, as used for the construction of the kinetic phase diagrams in 4.4.3.

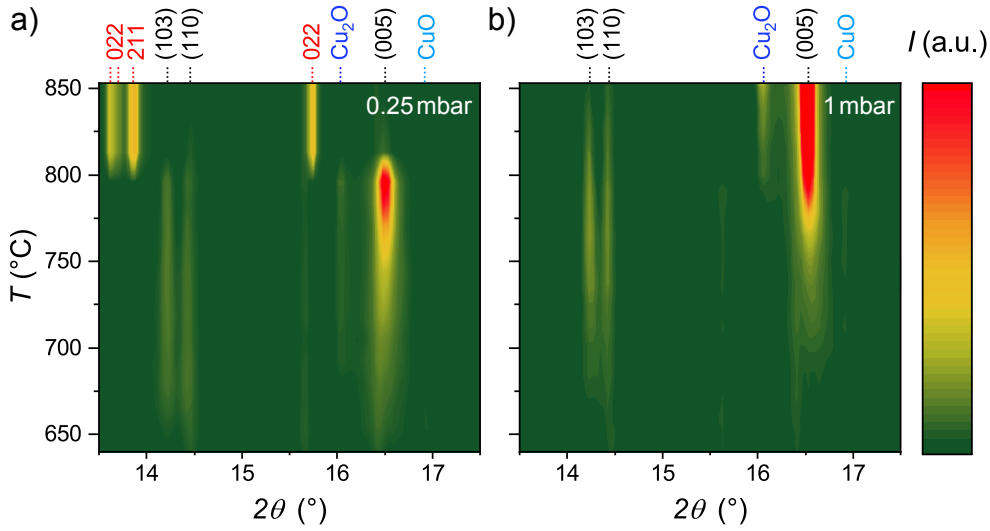

FIGURE 5.17: Evolution of phases at 0.25 mbar and 1 mbar through 2θ - T dependent color mapping, shown in a) and b), respectively. 2θ positions of the identified phases are labeled in the top. $BaCu_2O_2$ and Y_2BaCuO_5 are denoted as 022 and 211, respectively. Numbers in brackets refer to YBCO (*hkl*) planes. Both films are of (3-7) composition heated with a ramp of $dT/dt = 4.5\,°C\,s^{-1}$.

The difference is further observed in the 2θ - T colormap (Fig.5.17b)). Contrary to the reduced pressure, no crystalline 022 and 211 are found upon (103)/(110) ring intensity disappearance. At temperatures above 850 °C only the YBCO (005) and the Cu_2O (111) reflection persist, in accordance to the phase evolution in 5.1.2.

The correspondent 2D-XRD frames of the experiment at 1 mbar are shown in Fig. 5.18. The scans are chosen in the temperature window where the progressive intensity reallocation takes place. In agreement with the integrated curves, random YBCO grains evolve simultaneously with the epitaxial layer in the initial stage of the growth process (800 °C). As mentioned previously, the soft ring around the (005) diffraction spot requires integration for proper visibility. At 850 °C, $I_{(103)+(110)}$ is considerably decreased while a ring around the epitaxial (005) spot forms. At the final temperature of 860 °C, that is where the epitaxial layer signal is found to saturate, most of the (103)/(110) intensity has disappeared. The remaining, visible rings ((005), (103) and (110) at 860 °C) seem to have a grainy intensity spread.[14] This is a sign of single coarsened grains that fulfill Bragg's law only in distinct directions.

[14]Other than at 800 °C, the intensity seems to be distributed non-uniformly in narrow, bright spots along the ring.

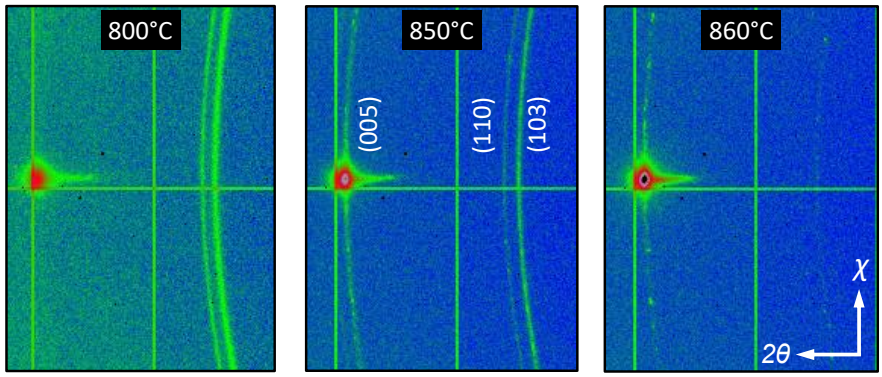

FIGURE 5.18: 2D scans acquired at 800 °C, 850 °C and 860 °C for a (3-7) film heated at $P_{O2} = 1$ mbar. The 2θ range is confined to 13.7 ° - 17 °. Main YBCO crystal planes are labeled. The same contrast range is chosen for all scans.

5.2.3 TEM analysis of quenched and grown films

In the previous part of this section (5.2.1 and 5.2.2) we have introduced a method based on customized tracking of intensity in 2D-XRD images which allows to detect whether YBCO grains reorientate or decompose. In particular, we argued that grain reorientation is possible when growth is carried out at high temperatures in the (Ba - Cu^{I} - O) full liquid region of the phase diagram. These findings are further complemented here via TEM analysis of grown and quenched films.

Samples were prepared following the standard pyrolysis process (3.1.2) and quenched in a rapid thermal annealing furnace capable of heating at 0.4 - 60 °C s^{-1} and cooling at 80 °C s^{-1}, located in the clean room facilities of ICMAB (3.1.3); TEM characterization was carried out by Dr. R. Guzman and Dr. K. Gupta.

Several TEM images of a quenched film of (2-3) composition are shown in Fig. 5.19. The sample is heated at a rate of 20 °C s^{-1} to 680 °C and cooled to room temperature right after. The bright-field high resolution imaging mode allows to identify phases through identification of diffraction planes and fast Fourier transform. Considering the phase diagram in Fig. 4.24, a quench temperature of 680 °C and oxygen partial pressure of $P_{O2} = 10$ mbar places the sample at the onset of $BaCO_3$ decomposition and YBCO formation. This is confirmed by the TEM images in Fig. 5.19: The image in Fig. 5.19a) shows a cross section of the whole layer having a total thickness of 280 nm. The only YBCO phase found at this initial stage of growth is located at the LSAT substrate interface, indicated through arrows. A magnification of that region

is shown in Fig. 5.19b) and c). The thin layer visible in the first frame is attributed to c-axis YBCO, approximately 10 nm in thickness. Also an a-axis grain is found on top of the c-YBCO (Fig. 5.19b)), indicative for the high supersaturation expected for TLAG growth. The image in Fig. 5.19c) shows that the $BaCO_3$ phase coexists with first heterogeneous nuclei and that the decomposition process of $BaCO_3$ is a direct limitation to YBCO formation in this route, as discussed previously in 4.4.3.

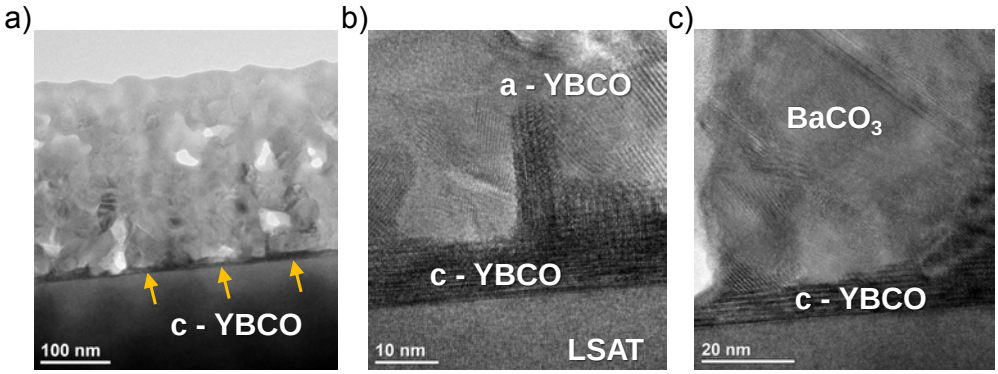

FIGURE 5.19: Bright-field HRTEM images of a (2-3) film heated at 20 °C s^{-1}, P_{O2} = 10 mbar and quenched at 680 °C, no dwell. Cooling is performed at a rate of 80 °C s^{-1}. a) Full cross-section of the film. Arrows mark heterogeneous nuclei at the interface to LSAT substrate. b) Area with a- and c-axis grain. c) Area were YBCO growth and $BaCO_3$ decomposition proceed simultaneously.

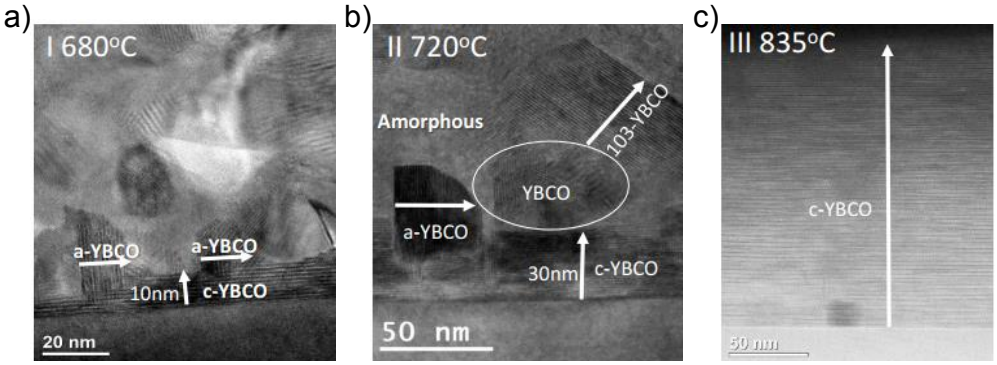

FIGURE 5.20: Two quenched films at a) 680 °C and b) 720 °C and c) a grown layer at 835 °C, t_{dwell} = 2 min after heating at 20 °C s^{-1}, P_{O2} = 10 mbar, (2-3) composition. A cooling rate of 80 °C s^{-1} was applied in all cases. The crystallographic orientations of YBCO are indicated.

In addition to the film quenched at 680 °C, a quench at 720 °C and a grown film at 835 °C are included in Fig. 5.20. The increase in quench temperature results in further advancing of the YBCO phase amount. Epitaxial YBCO grains are found to reach an average size of 30 nm, while randomly oriented YBCO nuclei are also present in the bulk, labeled as (103)-YBCO (Fig. 5.20b)). The surrounding material has no crystalline structure. This is in agreement with *in situ* synchrotron experiments were apart from YBCO growth only decomposition of $BaCO_3$ and reaction with CuO takes place (eq. 4.27 and eq. 4.28). The amorphous phase can therefore be either attributed to remaining precursor phases or the intermediate liquid phase.
Upon heating to 835 °C and a dwell of 2 min (Fig. 5.20c)), a full conversion of the layer is reached. The TEM image shows a section that has preferably c-axis YBCO. In other parts, embedded ab-grains can typically be found in the *T* - route.[15] The high amount of misoriented grains, as seen in the quenched samples, is, however, not observed in the grown film. Assuming that the increased amount of random grains in quenched films is not induced upon cooling, given the high cooling rate of 80 °C s^{-1}, it can hence be suggested that random grain reorientation took place in order to reach the high c-axis fraction of the film grown at 835 °C, P_{O2} =10 mbar. In fact, this is also consistent with our previous suggestion that the reorientation process is induced in the full liquid region of the phase diagram. Note that while the films quenched at 680 °C and 720 °C are treated at $P_{O2} - T$ conditions where liquid and solid phases are expected, this is not the case for the grown film at 835 °C and P_{O2} =10 mbar. We also remark that these preliminary structural results should be considered with caution since the kinetic phase diagrams in 4.4.3 were derived using the maximum available heating ramp of 4.5 °C s^{-1} of the *in-situ* setup. Here, however, the films are heat treated at 20 °C s^{-1} which will be defined as the optimal ramp to grow YBCO films through this route (see discussion in 6.1).
In conclusion, we have motivated that the TLAG process is capable of inducing reorientation of randomly oriented YBCO grains. This phenomenon has been rarely observed in YBCO manufacturing and especially not at such short timescales as found here. Due to its potentiality to improve the quality of grown films, we attempt to define processing conditions and characteristics of the TLAG process that benefit the efficiency of reorientation in the following.

[15] The defect structure encountered in grown films and its influence on the pinning performance will be thoroughly discussed in chapter 7.

5.3 Promoting YBCO random grain reorientation in the TLAG process

In the previous two sections (5.1 and 5.2) we laid out strategies towards increasing epitaxial layer growth rates and identified that the TLAG process allows for random YBCO grain reorientation in favour of the c-axis layer. Both aspects of the process are found to be promoted if the final growth conditions are placed in the full liquid region of the phase diagram. In particular, we found that highest YBCO epitaxial growth rates are achievable when the heating ramp is increased and coarsening of solid phases avoided. To explore whether the efficiency of random YBCO grain reorientation is also influenced by the presence of solid phases, we explore the effect here in films of varying copper concentration and through variation of the heating ramp. All shown films are heat treated at P_{O2} =1 mbar were reorientation is found to take place upon crossing of the $BaCu_2O_2$ melting line (4.4.3).

5.3.1 Influence of copper coarsening on YBCO grain reorientation

The use of copper-rich compositions was shown to result in fewer homogeneously nucleated YBCO grains during heat treatment and to promote c-axis growth at reduced temperatures (5.1.4). While both aspects are beneficial to improve the film quality and reduce processing temperatures, we have also observed for copper-rich films of (3-7) composition that some of the CuO can coarsen along the ramp (5.1.3). The solid phase was then used as trace element to evaluate whether coarsening impacts the epitaxial layer growth rates. A similar link is examined here with regard to the efficiency of the YBCO random grain reorientation process.

Three films of precursor composition (2-3), (3-7) and (4-11) are considered in the following, heat treated with a ramp of 4.5 °C s^{-1}, P_{O2} = 1 mbar.[16] As introduced previously in 5.2.1, misoriented YBCO grains can be tracked in two custom areas of each 2D-XRD frame: The ring surrounding the (005) epitaxial layer diffraction spot, $I_{(005)\,\mathrm{ring}}$ ($|\chi| > 2°$), and the (103)/(110) polycrystalline rings, $I_{(103)+(110)}$ (χ = -9°-9°).

The time and temperature evolution of $I_{(005)\,\mathrm{ring}}$ and $I_{(103)+(110)}$ is depicted in Fig. 5.21 for the three different compositions. All samples run through the same thermal profile with a final dwell temperature of 860-870 °C. The point where each film starts to approach the dwell temperature (> 850 °C) is marked in the upper axis. A dashed-black line is further included at 818 °C to indicate

[16] The compositions correspond to a $BaCuO_2$ to CuO ratio of 25%, 30% and 40%, respectively.

the melting temperature of the $BaCu_2O_2$ solid phase, determined in 4.3 for binary mixtures. That is where we expect to enter the full liquid region at this oxygen partial pressure.
Independent of the film composition, the high angle grain intensity ($I_{(103)+(110)}$) runs through a maximum upon heating. The intensity decrease is registered to initiate at the temperature where melting of the $BaCu_2O_2$ solid phase is expected for all three cases. The drop in $I_{(103)+(110)}$ further coincides with an increase in $I_{(005)\ \mathrm{ring}}$. In 5.2.2 we concluded that such an intensity reallocation is a sign of YBCO grain reorientation, where high angle grains disappearance is followed by an increase of grains with alignment close to the c-axis direction.

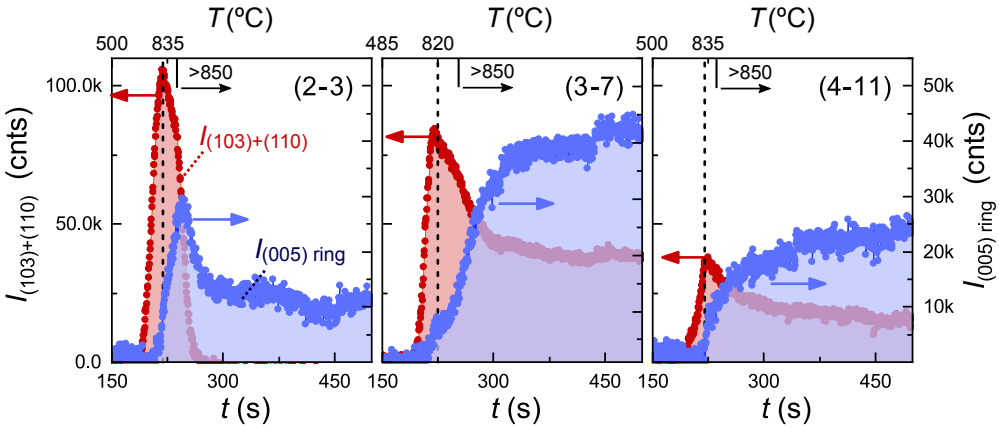

FIGURE 5.21: Custom integration of intensity in areas defined in Fig. 5.15 for films of (2-3), (3-7) and (4-11) composition, heated at 4.5 °C s^{-1}, P_{O2} = 1 mbar. Purple and red curves show the time and temperature evolution of the ring intensities $I_{(005)\ \mathrm{ring}}$ ($|\chi| > 2°$) and $I_{(103)+(110)}$ (χ = -9°-9°). Dashed-black lines mark T = 818 °C where melting of $BaCu_2O_2$ is observed for binary mixtures (Fig. 4.15).

The efficiency of reorientation appears to be highest for the film of (2-3) composition since all intensity attributed to high angle grains vanishes when reaching the dwell temperature. Also the accumulated signal around the (005) spot ($I_{(005)\ \mathrm{ring}}$) declines shortly after. In the copper-rich compositions, on the contrary, $I_{(103)+(110)}$ decreases only by half while the $I_{(005)\ \mathrm{ring}}$ signal saturates at a constant value. This means that high angle grains only partially reorientate while low angle ones accumulate around the epitaxial layer alignment.
The improvement in random YBCO grain reorientation in the film of (2-3) composition can further be confirmed considering the intensity spread in χ, shown in Fig. 5.22. For this purpose, a 2D image was integrated in a 2θ window that covers the whole (005) reflection. The frame is chosen on the dwell

where the epitaxial layer signal is found to saturate and the process is defined as complete.
In agreement with the integrated signal, $I_{(005)\,\mathrm{ring}}$, from Fig. 5.21 the $I(\chi)$ scans show an increased intensity at angles $|\chi| > 1°$, a result of grain accumulation around the YBCO c-axis direction. Such grains, regardless of those having even higher misalignment angles ($I_{(103)+(110)}$), can become a hindrance to the film performance reducing the current percolation. This was shown through studies of how grain misalignment affects the grain-boundary critical current in YBCO bicrystals [65, 181]. It could be shown that if adjacent grains enclose angles higher than 4° - 5° a drop in the percolating currents arises.

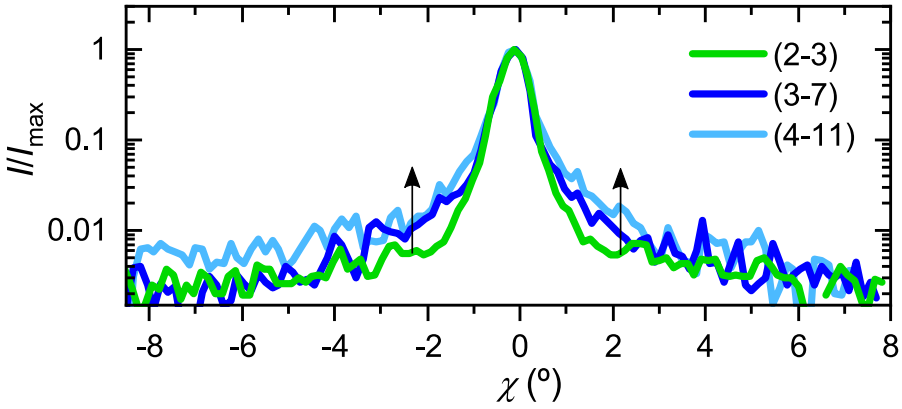

FIGURE 5.22: Normalized intensity as function of χ for the three films of Fig. 5.21. Integration is carried out in a 2θ window of 16.33° - 17° to obtain only the signal of the (005) reflection. Arrows highlight the intensity increase for $|\chi| > 1°$.

In order to understand whether the efficiency of grain reorientation might be linked to competing crystallization processes during growth, the phase evolution of the three films of varying composition is further considered in Fig. 5.23 as function of time and temperature: As seen for the stoichiometric mixture, (2-3), $BaCO_3$ decomposition takes place through reaction with CuO to form a transient liquid phase that assists homogeneous and heterogeneous YBCO growth (eq. 4.27 and eq. 4.28). When the temperature exceeds 818 °C, that is where melting of the $BaCu_2O_2$ solid phase was identified (see phase diagram in Fig. 4.15), a rapid drop in the intensity given by high angle grains, YBCO (103), is registered while the epitaxial layer signal saturates.
The reaction kinetics become more complex using the copper-rich compositions. An increased fraction of the initial CuO phase is in the amorphous/nanocrystalline state seen in the lowered signal at 500 °C. As already introduced in 5.1.3 some of the CuO crystallizes and coarsens along the ramp,

followed by a valance change to Cu_2O. This impeding, kinetically influenced coarsening effect is the main difference observed here between stoichiometic and copper-rich mixtures. It also coincides with a less drastic drop of YBCO (103) intensity in the films of (3-7) and (4-11) composition, suggesting that the coarsened particles might complicate the reorientation process either as direct blockades or due to liquid property changes.

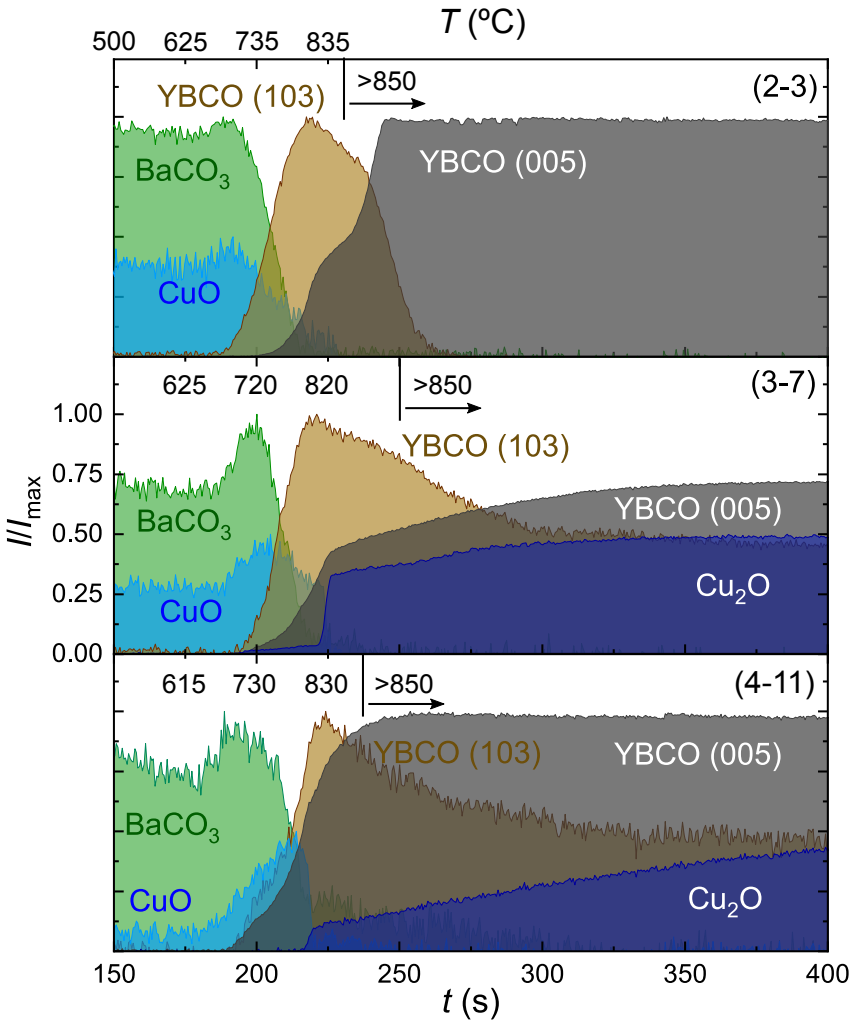

FIGURE 5.23: Time and temperature evolution of phases for films of (2-3), (3-7) and (4-11) composition, heated at 4.5 °C s^{-1}, P_{O2} = 1 mbar. For enhanced visibility, $BaCO_3$ and YBCO intensities are normalized to 1; CuO and Cu_2O to 0.5. The signals are obtained through integration of counts in the full χ range of (-9 - 9°) except for the epitaxial YBCO (005) signal where the window is narrowed to χ = -2° - 2°.

A relation between copper coarsening and the reorientation of randomly oriented YBCO crystallites can further be suggested considering a film of copper-rich composition where the Cu_2O solid crystallites are found unstable upon crossing of the $BaCu_2O_2$ melting line, hence, dissolve in the (Ba - Cu^I - O) full liquid region (Fig. 5.24). Although the film is also of (3-7) composition and shows a similar initial coarsening evolution of the copper phases as in Fig. 5.23, the disappearance of the Cu_2O solid phase in the high temperature melt coincides with a drop in the YBCO (103) intensity, attributed earlier to reorientation. For this particular film the Cu_2O grain sizes were shown previously to be reduced (∼100 nm) as compared to those films where the phase remains stable at high temperature (> 200 nm), see Fig. 5.9b). Hence, the simultaneous decrease of the YBCO (103) intensity together with the dissolution of the Cu_2O solid phase reinforces that phase coarsening can impede the reorientation process in the (Ba - Cu^I - O) full liquid region.

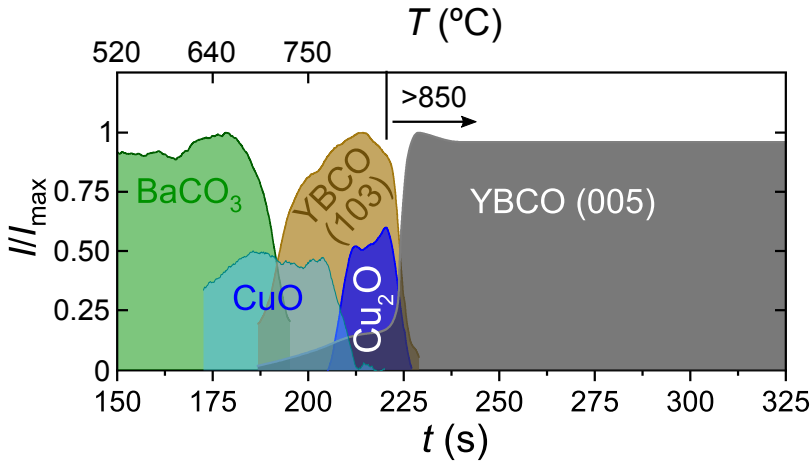

FIGURE 5.24: Phase evolution of a (3-7) films heated at 4.5 °C s^{-1}, P_{O2} = 1 mbar where Cu_2O solid phase is observed to disappear at temperature above the $BaCu_2O_2$ melting point obtained in 4.3 (818 °C). Curves are obtained and normalized as described in Fig. 5.23.

To complement these findings with direct structural observations, we performed TEM measurements of the samples in Fig. 5.23 after growth. In particular, the analysis was focused on those regions of the TEM cross-section where misaligned YBCO grains could be encountered, assuming that in these parts the reorientation process did not succeed.
Fig. 5.25 comprises the results for the (2-3) and (4-11) film, being the two mixtures of lowest and highest copper content. In general, the (2-3) film is found to exhibit a high degree of epitaxy throughout the layer (Fig. 5.25a)). In

some parts of the cross-section misaligned YBCO grains are found embedded in the epitaxial YBCO matrix, seen in the inset of Fig. 5.25a). The enclosed YBCO grains are typically accompanied by strong lattice bending of the surrounding ab-planes and a high density of $YBa_2Cu_4O_8$ (248) stacking faults. Such regions were further evaluated through EELS compositorial mapping (Fig. 5.25c)), showing that the YBCO phase (yellow color) is interrupted by CuO/Cu_2O inclusions (blue color).

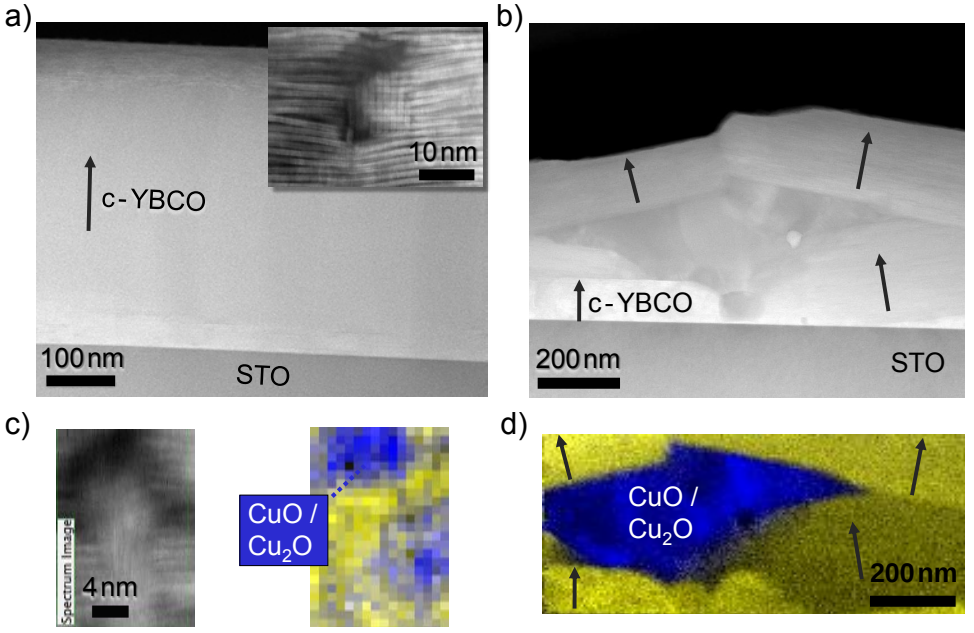

FIGURE 5.25: TEM analysis overview of samples grown through the T-route at 4.5 °C s^{-1}, P_{O2} = 1 mbar, T =860 - 870 °C: a) Cross-section of the (2-3) composition film; A misaligned YBCO grain is shown in the inset image. b) Cross-section of the copper-rich film, (4-11) composition; Arrows point along the c-axis direction of YBCO grains. c) and d) show EELS compositional mapping of the films in a) and b), respectively. The areas comprise regions with misaligned YBCO grains. Yellow and blue colors correspond to YBCO and CuO/Cu_2O phases, respectively. The EELS map in c) was acquired in the region shown on the left.

The severity with which the YBCO epitaxial layer is interrupted and size of CuO/Cu_2O inclusions are both clearly intensified in the film of (4-11) composition (Fig. 5.25b)). Large YBCO grains (> 200 nm) show an increased misalignment with respect to the substrate surface, seemingly blocked by a CuO/Cu_2O segregation in the center (200-400 nm in size) whose composition is confirmed through EELS mapping in Fig. 5.25d). The TEM analysis, hence,

confirms the trends observed through *in-situ* measurements.

In summary, we suggest that phase coarsening, here shown through *in-situ* XRD and TEM analysis of the CuO and Cu_2O solid phases, can impede the beneficial phenomenon of YBCO random grain reorientation in the (Ba - Cu^I - O) melting region. This effect is especially amplified when copper-rich compositions are used, where the coarsening of CuO/Cu_2O appears to be facilitated.
Ideally, copper-rich compositions should give rise to a (Ba-Cu-O) melt of increased copper concentration. The growth of YBCO, having the equivalent stoichiometry of (2-3), would then induce the segregation of excess CuO/Cu_2O during growth. If these particles coarsen and get trapped in the layer, they would reduce the superconducting cross-section and, with that, the current carrying capacity. Hence, such segregations should be preferably pushed to the film surface. The growth of continuous YBCO layers therefore requires control over this pushing/trapping mechanism and avoidance of any coarsening effects upon heating, achievable through tuning of process parameters (e.g. $P_{O2} - T$, heating ramps) and film composition.
Although we have seen that copper-rich compositions tend to promote CuO/Cu_2O coarsening and that these phases are suggested to block the process of random grain reorientation, it should be noted that up to now the process conditions of *in-situ* growth experiments were restricted to P_{O2} =1 mbar and a heating ramp of 4.5 °C s^{-1}. In the following, we will motivate that changes in heating ramps can influence the reorientation process and that such studies should be extended to the full phase diagram.

5.3.2 Heating ramp influence on YBCO grain reorientation

In the aforegoing part of this chapter, we have disclosed that coarsening of phases has to be avoided in the TLAG process to promote high epitaxial layer growth rates (5.1.3) and allow for random YBCO grain reorientation (5.3.1). The impact of coarsening on the reorientation process is further explored here through variation of the heating ramp during growth.
As discussed in 5.1.3, the degree of copper coarsening might be influenced by the chosen thermal profile. The strongest CuO signal and, hence, amplified coarsening contribution, was obtained through heating at 4.5 °C s^{-1} to 750 °C, followed by a flatter ramp of 0.3 °C s^{-1} towards the final growth temperature (T = 860 °C). In this section, the change of heating ramp at 750 °C is explored as a parameter to control the effect of CuO coarsening and its impact on the state

of the grown films.[17] In particular, three films of (3-7) composition, denoted as f1-f3, are considered here: f1 and f2 are initially heated at the maximum ramp of 4.5 °C s^{-1} to 750 °C; a switch to 0.3 °C s^{-1} and 1 °C s^{-1} is then realized towards 860 °C, respectively. f3 is heated continuously at 4.5 °C s^{-1} to 860 °C. The thermal profiles are summarised in Appendix C.2, Fig. C.2.
Post-analysis of the grown films was carried out at ICMAB by means of XRD and SEM measurements. The results are shown column-wise in Fig. 5.26 for the three films, f1-f3, with highest to lowest heating ramp above 750 °C (from left to right).

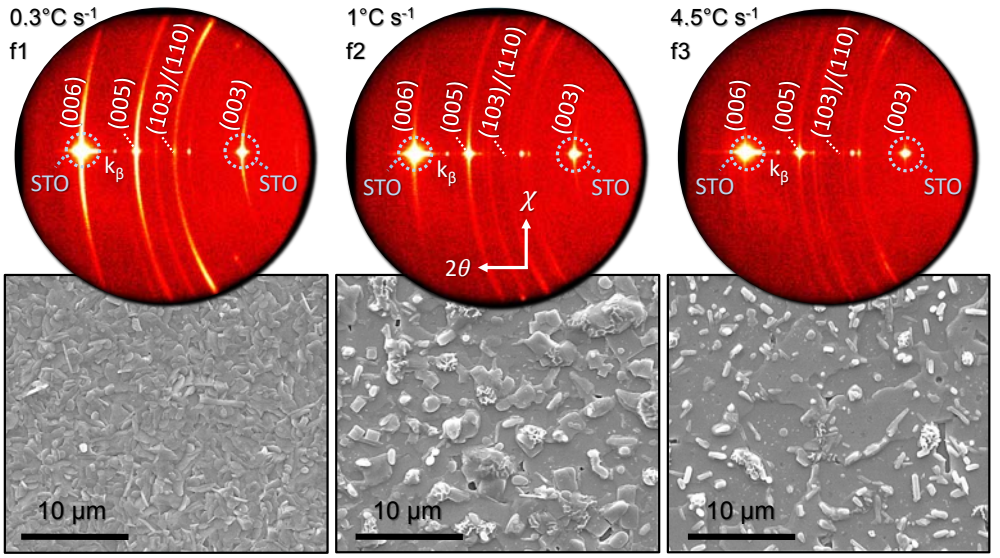

FIGURE 5.26: Post-characterization of (3-7) films, f1-f3, grown through the temperature profiles in Appendix C.2, Fig. C.2. 2D-XRD GAADS measurements (upper part) and SEM surface images bottom part) overview the film quality (texture and surface) after growth. XRD results are obtained for a $2\theta/\chi$ range of (13° - 55°)/(-34°-34°), respectively. The sample notation is labeled in the top.

The 2D-XRD measurements in the upper part of the graph confirm that the texture quality varies with the time period spent at $T > 750$°C. Since the same contrast limits were chosen for all measurements, the intensity distribution can be qualitatively compared. Best visible in the χ broadening of the (005) diffraction spot, the film heated at 0.3 °C s^{-1} (f1) shows the highest proportion of misoriented grains. The diffraction spot gets gradually sharper and ring intensities, $I(103)/I(110)$, weaker upon heating ramp increase (f2-f3).

[17] The high temperature is chosen below the [$BaCu_2O_2$] melting line to promote coarsening in the mixed solid-liquid region.

The change in texture quality is in agreement with the surface characteristics bottom part of Fig. 5.26): f1 presents a spiky miscrostructure all along the sample surface. Such inclined, plate-like grains can be attributed to misoriented YBCO crystallites [182].[18] Upon heating ramp increase, interconnected terraces, distinguishable through a uniform grey color, become pronounced. The highest homogeneity is reached for f3, though still some plate-like grains are present.

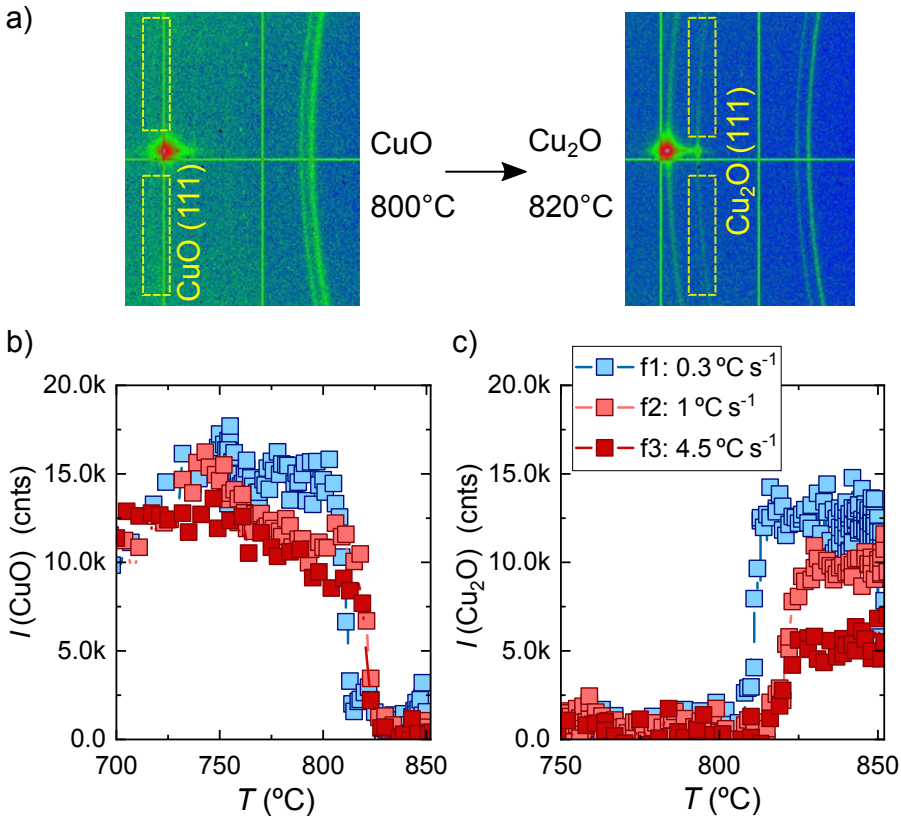

FIGURE 5.27: Copper reduction process and coarsening in (3-7) films grown through mixed-ramp profiles (Appendix C.2, Fig. C.2). Samples f1-f3 are heated at 4.5 °C s^{-1} to 750 °C; the ramp denoted in the legend is then used towards $T = 860$ °C, $P_{O2} = 1$ mbar. a) Integrated areas of the 2D-XRD scans (yellow-dashed regions) to follow the CuO and Cu_2O ring intensities. b) CuO (111) evolution as a function of temperature. (c) Cu_2O (111) evolution as a function of temperature.

[18]The plate-like form arises from the anisotropic growth speed of YBCO in a- and c-axis direction.

To explore whether the structural differences are influenced by the change in thermal profiles, we have, once more, analysed the evolution of the CuO/Cu_2O solid phases. The CuO/Cu_2O (111) signals are obtained through count integration in the areas encircled by the yellow-dashed lines in Fig. 5.27a). The integration is done for $|\chi| > 1°$ to exclude any signal given by epitaxial phases. The CuO and Cu_2O signals are tracked in a range of 700-850 °C to cover the valance change ($CuO \rightarrow Cu_2O$) at ∼800-820 °C and the region where reorientation of YBCO random grains takes place. As can be seen in the Appendix Fig. C.2 this is also the temperature window where the thermal profiles deviate most due to the change in heating ramp.
The integrated CuO/Cu_2O signals are shown in Fig. 5.27b) and Fig. 5.27c) suggesting that the decrease in heating ramps is indeed a measure to amplify the segregation process. While at 700 °C a similar response, I(CuO), is obtained for all three films, the curves start to deviate for the temperature region where different heating ramps are used. Correspondingly, the discrepancy is also seen in the Cu_2O signal after the valence change took place (Fig. 5.27c)). At this P_{O2} and above 750 °C, in agreement with the kinetic phase diagram, a region with the $BaCu_2O_{2(s)}$ and $Cu_2O_{(s)}$ phase is crossed prior to reaching the full liquid. Hence, if the heating ramp is decreased, coarsening of the Cu_2O might be promoted. Given the enhanced copper segregation at reduced heating ramps, these findings are in agreement with the observed structural tendencies in Fig. 5.26. As already suggested in 5.3.1, the coarsened copper phase might impede the reorientation process resulting a higher fraction of YBCO grains which could not realign in the full liquid region of the phase diagram.

To complement these findings with a film where no copper segregations could be detected, we further consider a (2-3) film heated at 4.5 °C s^{-1} to 860 °C, $P_{O2} = 1$ mbar. Fig. 5.28 shows the XRD and SEM data in accordance to the (3-7) samples in Fig. 5.26. As compared to (3-7) case the texture seems profoundly improved. Most of the diffracted intensity is confined in spots of the YBCO (00l) peak family. A minor fraction of off-axis grains might, however, still be expected given the soft intensity streak around the (005) reflection.

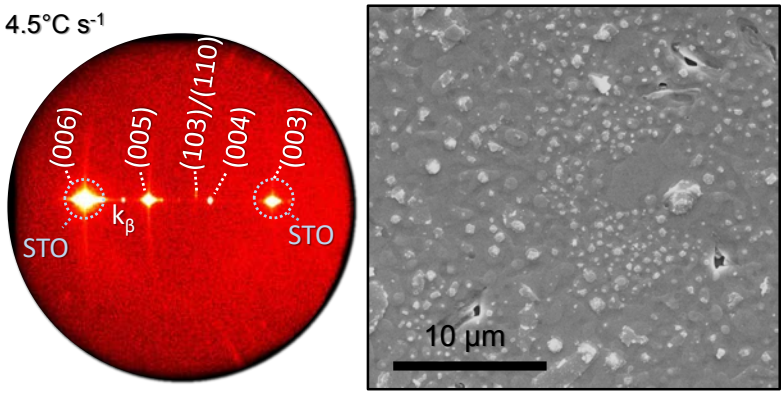

FIGURE 5.28: 2D-XRD measurement and SEM surface of a (2-3) film heated at 4.5 °C s^{-1} to 860 °C, P_{O2} = 1 mbar. The measurement characteristics are summarized in Fig. 5.26.

The SEM image shows aside from droplet-like segregations a closed microstructure with few pores and smooth contrast. Such a surface morphology is typical for films having a high epitaxial quality as evidenced by TEM images on (2-3) compositon films (not shown here).
Several (2-3) films grown at the synchrotron facility are further characterized via SQUID magnometometry and electrical measurements. As can be seen in Fig. 5.29a) two films reach reproducibly 0.8 MA cm^{-2} at 77 K and 6-7 MA cm^{-2} at 5 K for an estimated thickness of 450 nm. Also a high critical temperature of T_c = 90 K and transition width of 2.6 K are reached indicating that films do not suffer from liquid reactivity with the substrate nor carbon retention (see Fig. 5.29b)).
The improved epitaxial quality, surface morphology and current carrying capacity of (2-3) films could be associated with the absence of CuO/Cu_2O phase coarsening.[19] The segregated phase might locally influence liquid stoichiometry, trigger the formation of secondary trace phases or directly impede the reorientation process. Misoriented YBCO grains would then additionally reduce the effective cross section of the film.

[19]The (3-7) films from Fig. 5.28 do not reach 1 MA cm^{-2} at 5 K and self-field.

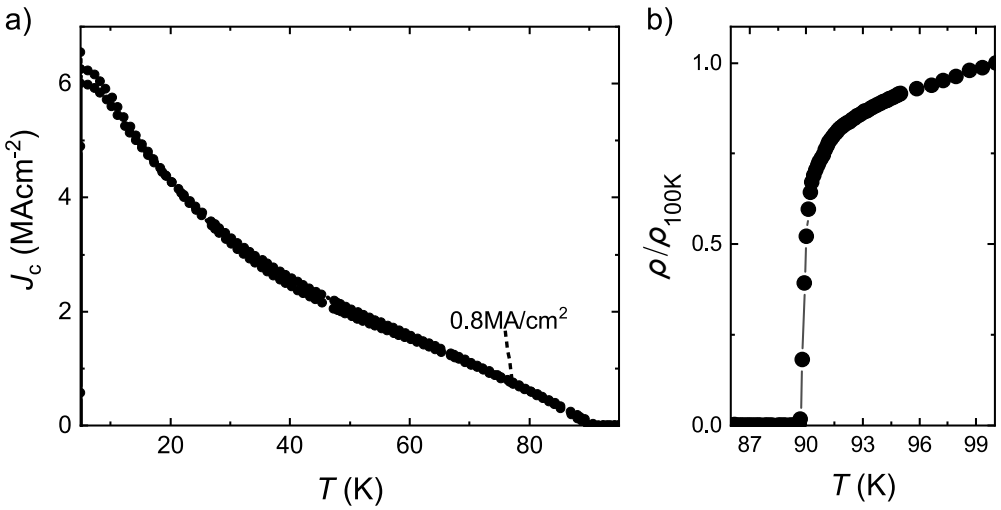

FIGURE 5.29: a) SQUID $J_c(T)$ and b) Van der Pauw, T_c measurement of (2-3) films grown at the synchrotron facility. Samples are heat treated with the thermal conditions denoted in Fig. 5.28.

To conclude, TLAG growth through the T - route requires additional understanding of how phase coarsening can be minimized, allowing to benefit from random YBCO grain reorientation and enhance the current carrying capacity of grown films. This is particularly of importance when working with off-stoichiometry mixtures where liquid composition changes allow to profit from reductions in process temperatures and decrease the amount of homogeneously nucleated grains along the ramp (see section 5.1.4). Until now, we have explored the influence of heating ramps on the CuO/Cu_2O solid phase evolution in films of (3-7) composition. The tendencies suggest that coarsening can be diminished through heating ramp increase allowing to improve film texture and morphology.

We also note that up to now the *in-situ* growth experiments were performed at P_{O2} =1 mbar where the reorientation process takes place upon heating into the (Ba - Cu^{I} - O) melting region (T >818 ºC). Considering the derived kinetic phase diagrams in 4.4.3, these studies should now be expanded to wider regions of $P_{O2} - T$ conditions. For instance, experiments at increased P_{O2} values would allow to explore whether the (Ba - Cu^{II} - O) full liquid region can also promote reorientation.[20] As this melt can already be reached at temperatures as low as 750-800 ºC and with different copper oxidation state, more understanding can be generated on how the reorientation process is influenced by differences in liquid characteristics that arise from the continuous change in Cu valence upon P_{O2} increase.

[20] Or how the reorientation is affected by working in a melt of increased copper valance state.

5.4 Epitaxial alignment of preformed nanoparticles

2D-XRD images, acquired *in-situ* during YBCO growth, could be beneficially exploited to obtain angular information of intensity reallocation (5.2). This was then used to explain the disappearance of the signal coming from randomly oriented YBCO grains. As a result, the integration of counts in specified angular ranges of each XRD frame allowed us to attribute this effect to grain reorientation when the film reached the (Ba - Cu^{I} - O) full liquid region of the phase diagram. A similar customized treatment of XRD scans is applied here to suggest that other crystalline phases can also reorient during growth of YBCO.
As will be laid out in chapter 6 and 7, YBCO nanocomposite (NC) films with $BaZrO_3$ (BZO) and $BaHfO_3$ (BHO) nanoparticles (NPs) from colloidal solutions were grown to further improve the superconducting performance. An exceptionally high fraction of NPs was found to be epitaxially embedded in the YBCO c-axis layer, an effect which has never been observed in CSD grown YBCO films to this extent (see 7.1.3 and Fig. 6.35). These results are further complemented here through *in-situ* studies of the NP evolution during growth, aiming to motivate that reorientation takes place. For the sake of completeness the synchrotron results are already included here, although NC films will be studied in more detail in the following chapters.

Preformed NPs from colloidal solutions were synthesized in cubic structure giving an average diameter of 4-5 nm (Fig. 6.34). At room temperature, hence, in the pyrolized film containing Y_2O_3, $BaCO_3$ and CuO, the NPs remain hidden to X-ray diffraction measurements. The effect was attributed to the nano-crystallinity and partial amorphization of the surface [95]. After YBCO growth, however, the particles are well visible having a preferential alignment within the YBCO matrix. This has been confirmed in-house and at the synchrotron facility.
Knowing how particles would orient during growth, we could prealign the setup to be in Bragg condition with the BHO (110) plane, the strongest reflection of the cubic structure. Heating was then carried out with the maximum ramp of 4.5 °C s^{-1} to 850 °C in a P_{O2} of 1 mbar using a film of (3-7) composition with 24% in molar percentage of BHO. In the case of standard YBCO films, these process conditions were shown to allow for reorientation of randomly oriented YBCO grains at temperatures above 820 °C, hence in the full (Ba - Cu^{I} - O) liquid region (see kinetic phase diagrams in 4.4.3).
A similar evolution is obtained here for the NC film. Fig. 5.30 shows $\theta - 2\theta$ scans for a temperature window of T =820-850 °C, obtained through integration of the 2D-XRD scans in χ. As expected for this temperature range, the

signal coming from randomly oriented YBCO grains is observed to diminish. This is seen in the drop of intensity given by the YBCO (102), (103) and (110) reflections. Simultaneously, a peak appears which we attribute to the BHO (110) reflection.

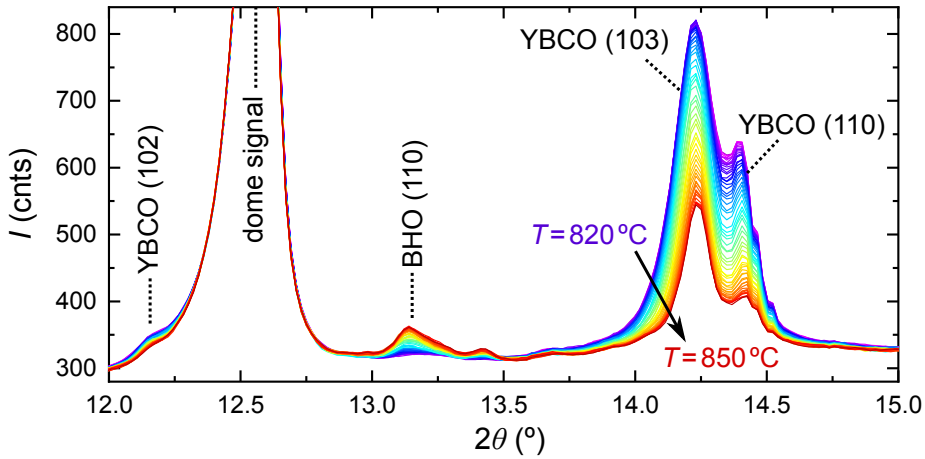

FIGURE 5.30: $I(2\theta)$ scans of a nanocomposite (3-7) film with 24% of $BaHfO_3$ (BHO) heated at 4.5 °C/s, P_{O2} = 1 mbar, shown for a temperature range from 820 °C (purple curve) to 850 °C (red curve). Curves were obtained through χ-integration of 2D scans acquired each 160 ms. The range of temperatures is chosen in the full liquid region of the kinetic phase diagrams derived in 4.4.3.

The full temperature evolution of the YBCO (103) and BHO (110) peak intensities is further shown in Fig. 5.31a), normalized to the maximum value for better visibility. In agreement with the $\theta - 2\theta$ scans, a drop of the YBCO (103) and increase of the BHO (110) signals are observed for $T > 820$ °C. To confirm that the appearing nanoparticles are epitaxially aligned, the 2D-XRD images are converted to $I(\chi)$ scans, covering the whole NP peak in Fig. 5.30 ($2\theta = 13.04$ °- 13.37 °). The corresponding scans are summarized in Fig. 5.31b), showing a peak of the BZO (110) reflection in χ. Hence, considering that the BHO (110) reflection has a width in 2θ and χ (Fig. 5.30 and Fig. 5.31) it can be concluded that the appearing phase exhibits a preferential orientation.

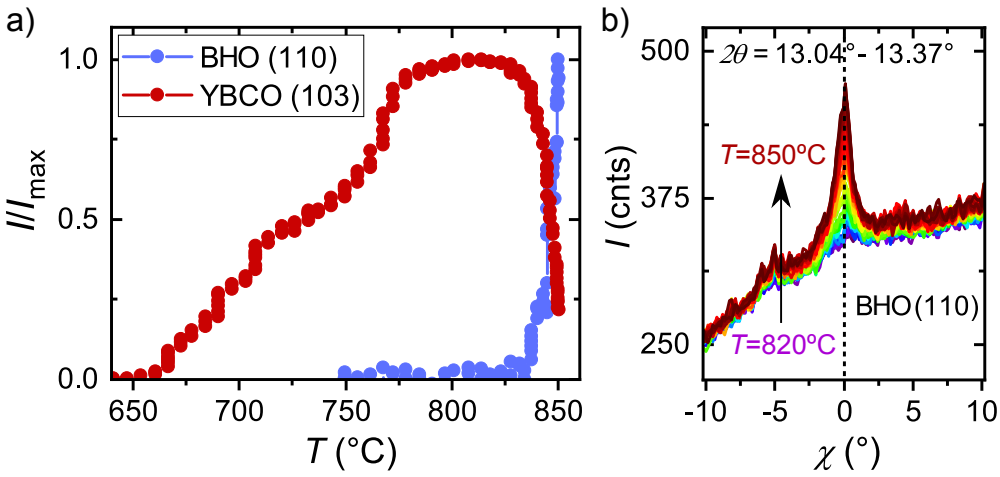

FIGURE 5.31: Phase evolution using a (3-7) nanocomposite film with 24% BHO heated at 4.5 °C s^{-1}we, $P_{O2} = 1$ mbar: a) Normalized temperature dependence of the YBCO (103) and BHO (110) signals. b) $I(\chi)$ scans of the BHO (110) reflection in a temperature range of 820 °C (purple curve) to 850 °C (red curve). The scans were obtained in a 2θ window of 13.04°-13.37° to cover the full BHO (110) reflection.

The above mentioned findings suggest that the appearance of NPs is linked to the kinetics in the full liquid region of the phase diagram. Given the fact that in the same $P_{O2} - T$ range reorientation of random YBCO grains takes place (5.2), a similar scenario might be expected for the BZO/BHO phase.

NP reorientation in the full liquid region can further be suggested taking into account the 2θ- and χ-dependent peak broadening evolution of the BHO (110) signal. The broadening of XRD peaks is typically a convolution of several contributions including instrumental broadening, sample curvature, finite particle sizes, non-uniformal strain, localized defects (e.g. stacking faults and dislocations) and the grain orientation itself (tilt and twist) [120]. Different measurements options (e.g. ϕ-, ω- and θ-2θ -scans) are used to probe specific directions of the crystal lattice and, with that, comprise only a part of the broadening effects. For instance, while ϕ-scans are commonly used to probe the degree of grain rotation/twist, ω-scans or rocking curves suit to evaluate the grain tilt.

Only few information can be obtained from the measurements of the BHO (110) reflection in Fig. 5.30 and Fig. 5.31b). A proper evaluation of different broadening contributions is typically carried out through deconvolution of the different angular dependencies which require probing of multiple reflections. This is done, for instance, in the case of θ-2θ-scans through the Williamson-Hall analysis to separate particle size from non-uniform strain

broadening contributions (3.5.4). Nevertheless, some preliminary conclusion can already be draw from the analysis of one single reflection probed in different angular directions.
The 2θ and χ FWHM values of the BHO (110) reflection, $\Delta 2\theta$ and $\Delta\chi$, are shown in Fig. 5.32a) and b), respectively. Peaks were fitted with Lorentzian profiles in a temperature window where the increasing BHO signal reaches sufficient intensity. While the $\Delta 2\theta$ values remain unchanged, $\Delta\chi$ decreases approximately by half, from $\sim 3\,^{\circ}$ to $< 1.5\,^{\circ}$. The broadening in 2θ is primarily caused by small particle sizes, instrumental contributions and non-uniform strain. It appears however, that none of these contribution vary in the temperature range where the BHO signal increases (Fig. 5.31). Hence, also the NP size might be assumed constant in the considered range. On the contrary, the peak width decreases considerably in χ direction, which is mostly sensitive to the particle orientation and size [120].

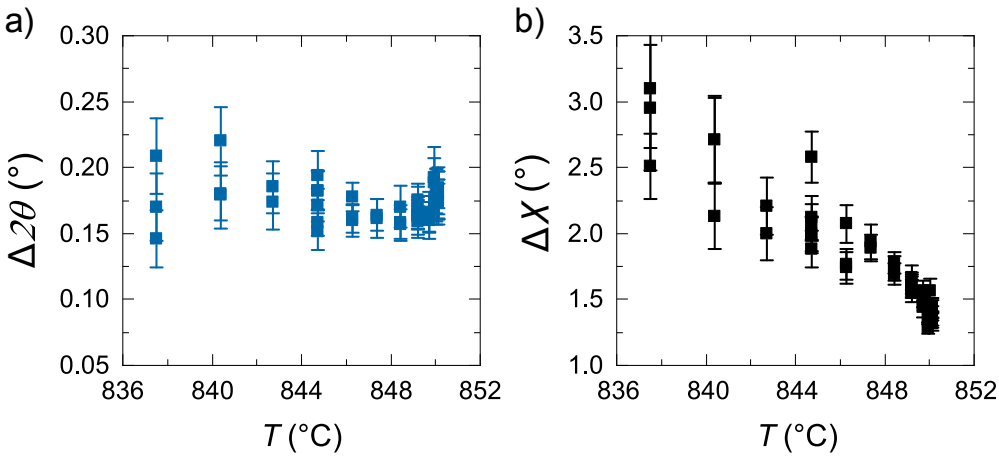

FIGURE 5.32: Temperature evolution of the BHO (110) peak widths (FWHM) using the a) 2θ- and b) χ-scans from Fig. 5.30 and Fig. 5.31b), respectively. Least-square peak fitting was carried out with Lorentzian profiles.

Considering the disproportionate narrowing of the peak in χ, in addition to the temperature independent 2θ width evolution, an improvement of the NP phase alignment/texture might hence be suggested. Emergence of the full liquid at temperatures $> 820\,^{\circ}$ together with the growing YBCO c-axis front might promote NP reorientation as means of minimizing the interface energy between YBCO and BHO. After growth, pole figures were recorded of the BZO (110) reflection and compared to a pristine YBCO film without NPs. As seen in Fig. 6.34c), nanoparticles exhibit a preferential alignment as

anticipated here.

In conclusion, the epitaxial embedment of NPs is proposed here to take place in the same region of the phase diagram where random YBCO grain reorientation was suggested earlier (5.2), namely the (Ba - Cu^{I} - O) full liquid region. Although nanocomposite films will be discussed in greater detail in the following chapters, some of the results were anticipated here in the framework of the *in-situ* growth studies. It appears that the TLAG process allows for rapid reorientation during growth, possibly enabling to reduce interface energies. Future studies of reorientation processes should include probing of several reflections during one experiment or fast acquisition of pole figures to enable a proper deconvolution of different broadening contributions and changes in texture.

5.5 Conclusions

While in the previous chapter the focus is set on the general understanding of TLAG, including development of kinetic phase diagrams, main reactions paths and growth route opportunities, the present chapter looks into different kinetic aspects of the process through growth of YBCO in the T - route.
In particular, changes in heating ramps, $P_{O2} - T$ conditions and sample composition are explored in order to

1. **Avoid phase coarsening during growth**
2. **Promote high growth rates of the epitaxial layer**
3. **Reduce processing temperatures**
4. **Favor random YBCO grain reorientation towards the epitaxial layer alignment**

From the combined observations it can be concluded that the TLAG process classifies as highly non-equilibrium growth approach of high supersaturation. We have evidenced that ultra-high growth rates up to $132\,\mathrm{nm\,s^{-1}}$ are rendered possible in the (Ba - Cu^{I} - O) full liquid region of the kinetic phase diagrams. Employment of increased heating ramps to reach these growth conditions are suggested to allow for an enhanced reactivity of all involved phases towards the final YBCO epitaxial layer.
Growth in the full liquid is also demonstrated to yield an exotic, kinetically driven effect which has not yet been observed at such short time scales in YBCO manufacturing, namely the reorientation of randomly nucleated

YBCO grains in favour of the epitaxial c-axis layer alignment. The efficiency of the reorientation process is suggested to be promoted when coarsening of precursor and intermediate phases can be avoided, possibly through use of increased heating ramps. This is not only a confirmation of our present understanding of the kinetic phase diagrams but also underlines the non-equilibrium nature and associated benefits of this novel process.
Within the range of the probed $P_{O2} - T$ conditions and maximum accessible heating ramps, the use of copper-rich compositions bears additional complexity. In agreement with theoretical predictions of melt supersaturation, copper-rich compositions show the desirable trend of widened temperature windows for c-axis growth and decrease in the amount of homogeneous grain nucleation at lower temperatures. Strikingly, we could demonstrate YBCO epitaxial layer growth rates up to $8\,\mathrm{nm\,s^{-1}}$ at temperatures as low as 650 °C, approximately ten times higher than obtained in CSD methods based on vapor-solid and solid-solid limited reactions. However, the use of copper-rich compositions also seems to allow for CuO/Cu_2O solid phase segregation during growth. These crystallites are shown to block the reorientation process and be encapsulated into the grown layer. Misaligned grains and copper segregations would then prohibit high percolating currents. The use of copper-rich compositions to benefit from the desirable trends mentioned above, therefore, requires additional understanding of how to prevent formation of these solid phases in the *T* -route TLAG process. In this context, the effect of increasing the heating ramp is shown to have a positive influence and should be combined in future studies to explore wider ranges of $P_{O2} - T$ conditions.

Finally, we point out that the presented studies of the involved growth kinetics settle in rather complicated region of the phase diagram, where a large window in $P_{O2} - T$ is governed by the coexistence of melt and solid phases. Also the probed full liquid region at $P_{O2} = 1\,\mathrm{mbar}$ is, for now, based on the (Ba - Cu^{I} - O) melt. It would, however, be essential to extend these efforts to increased oxygen partial pressures were melt properties (e.g. viscosity, reactivity, supersaturation) might change with increasing copper valance state. The liquid region of higher copper oxidation state extends to much lower temperatures (750-800 °C) at high P_{O2} and might therefore be attractive for YBCO manufacturing.
Several PhD and postdoctoral students pursue these efforts in the facilities of ICMAB and at the synchrotron. First results through quench studies of (3-7) films in our in-house institution confirm that reorientation of random YBCO grains takes place in the same temperature window as defined here. Efforts are also undertaken to explore composition changes through more efficient

ways. In that framework, combinatorial chemistry approaches are employed together with ink-jet printing by Dr. A.Queralto and A.Pacheco to produce compositionally graded films. Through collaboration with beamline scientist Dr. C.Mocuta a novel geometry could be developed and successfully implemented to study *in-situ* growth of composition graded films via continuous X-ray beam reallocation during the experiment. The approach will allow for high-throughput investigations of the TLAG process and facilitate the search for optimal growth conditions. A detailed description of the approach is laid out in the work of Dr. A.Queralto et al. [183].

Chapter 6

Physical characterization of TLAG films

The fabrication of high performance REBCO films requires careful choice of growth parameters that are essential to the process. In the TLAG case, such efforts are summarized in the aforegoing chapters. *In-situ* synchrotron measurements are demonstrated as mandatory tool to resolve sub-second reactions and track crystallization kinetics. However, beyond the work done to understand TLAG growth mechanisms and obtain *c* -axis oriented YBCO films, a thorough analysis of the physical properties of grown layers is required to pinpoint process limitations and obtain high critical current density films. The epitaxial YBCO crystal structure requires a certain oxygen content, grain and grain-boundaries need to be free of contaminants and nano-scale defect have to be given in order to increase the pinning performance. Here, the discussion is centered around the efforts made to reach high current density films and track down macroscopic influences that alter the performance.
Superconducting samples are characterized by means of XRD, electrical and inductive magnetic measurements to relate growth routes and process conditions with the final film properties. The first part (6.1) mostly focuses on the analysis of pristine YBCO films. In particular, the discussion is made with regard to the different growth routes (4.4.1), each of which is found to have unique limitations and opportunities to obtain high performance films. The analysis is then extended to TLAG nanocomposite films from colloidal solutions grown through the $P_{O2}(BaCu_2O_2)$ - route approach (6.2).

6.1 Path towards high percolating currents: Current limiting sources in TLAG grown pristine films

When it comes to performance optimization of YBCO films, a clear distinction has to be made on the physical factors that define the measured critical current density $J_c(H,T,\theta)$. In the practical sense, it is the threshold up to which current can be applied without entering into an energy-dissipative regime. In the electrodynamic discription this is where pinning and Lorentz force, F_P and F_L, are equal. As J_c is defined through the balance of these forces and F_P is a summation over all vortex pinning centers, the critical current density is directly affected by the pinning landscape [28, 184]. Highest pinning forces are reached when defects have a size of $\sim 2\xi$,[1] appear in comparable density to the amount of vortices and have maximum pinning potential U. For that reason most studies that aim to increase J_c are either focused on introducing artificial pinning centers or through condensation energy changes [105, 185, 186].
Taking into account that J_c is a physical property reflecting the strength of vortex-defect or vortex-vortex interaction, depending on the magnetic field regime, the interpretation of the measured value itself can be misleading, particularly when it comes to a newly developed growth method. Let us, for instance, consider the two types of measurement techniques introduced in chapter 3 to determine J_c. The value can either be deduced through inductive measurements and application of the Bean critical state model (eq. 2.8) or electrically via patterning of a bridge of known cross-section A_{cross} and measurement of the critical current I_c. In the latter case the calculation is done according to $J_c = I_c / A_{cross}$. Both approaches yield only an approximation of the actual J_c value as the local properties are not evaluated and percolation hindrances not accounted:[2]

- The equation used to evaluate the critical current from the measured total magnetic moment (e.g. via SQUID, VSM) considers the case of a perfect single crystal. The presence of precipitates, high angle grains and weak-link grain boundaries, however, subdivides the volume into minor fractions. This yields a reduction of the sensed magnetic moment due to formation of minor magnetisation loops and an overall reduced sample magnetization. The measured, percolating intergrain J_c is diminished while the intrinsic grain current density, also referred to as intragrain J_c, is unaffected [16].

[1] $\sim 2\xi$ being the vortex core diameter, $2\xi \approx 3$-4 nm for YBCO.
[2] Samples are assumed homogeneous with current flowing uniformly throughout the volume.

- Transport current density is directly influenced by A_{cross} which is of unknown value when percolation hindrances are given in the film. A proper estimation of the local J_c would hence require knowledge of the effective cross section at each position.

Therefore, the measured J_c will be the percolative one in YBCO films that suffer from macroscopic defects. The critical current associated to the superconducting grains will, however, remain hidden unless specific methods are used to probe the intrinsic state of the grain [108]. As anticipated in 4.4.5, high critical current densities in the range of 1 - 5 MA cm^{-2} at 77 K can be reached for TLAG grown films with the investigated $P_{O2} - T$ routes. Limitations arising in the TLAG process were up to now related to phases that segregate along the thermal profile, detectable through their crystallinity and visibility with X-rays and TEM. J_c diminution would then be simply a result of cross section reductions. However, such conclusions can only be drawn after considering all possible performance related limitations in TLAG growth. A distinction can be made according to sources that affect the intragrain state and those that limit the percolation capacity.

J_c reduction due to intragrain state:

1. **Phase purity:** The TLAG process entails two potential sources that can affect the purity of the YBCO phase. Residual carbon from the **$BaCO_3$ decomposition process** can alter the superconducting properties through substitution of copper in CuO planes by CO_3 carbonate groups [133, 134, 187]. Proper $BaCO_3$ decomposition in the TLAG approach is, therefore, not only substantial to all successive reactions but also to avoid contamination of the YBCO structure. Similar effects can arise from **liquid induced interfacial reactivity** issues. The highly corrosive nature of the melt allows its reaction with the substrate interface at high temperatures [77], yielding impurity substitution in the YBCO unit cell [188], typically accompanied with a decrease in T_c [175, 189, 190]. In addition, macroscopic secondary phases can be formed due to liquid reaction with substrate material, reducing the film cross-section [132].

2. **Oxygenation of YBCO:** After growth, YBCO typically exhibits a weak orthorhombicity of the crystal structure [105]. As-grown films do not surpass $T_c > 60$ K given the low amount of oxygen in the CuO-chains. The oxygenation procedure in 3.1.4 aims to incorporate oxygen into the chain sites. Holes are then doped from the chains into the CuO_2-planes via charge transfer [32]. High T_c and J_c values are reached in the optimally to over-doped range with a hole concentration $p \approx 0.16$ -0.19,

referring to the amount of charges per copper atom in the CuO_2-planes [34, 105].

J_c reduction due to compromised percolation:

4. **Texture quality:** Studies of the ab-plane tilt of YBCO on STO bicrystals show an exponential drop of J_c across the grain boundary for tilt angles θ higher than the critical angle $\theta_c = 4\text{-}5\,°$ [28, 65, 181].[3] The sensitivity to misorientation is due to insulating edge dislocations that accommodate the tilt.[4] At angles above θ_c the boundary becomes a Josephson weak-link, locally reducing the order parameter as the width of the insulating region surpasses the coherence length ξ.

5. **Purity of grain boundaries:** Accumulation of secondary phases in grain boundaries can be considered as a separate limitation factor to percolating currents since they function as weak-links between neighbouring grains [191]. This is independent of the grain boundary tilt angle and can be considered as direct barrier. The impact is found to scale with YBCO grain sizes as increased amounts of impurities are accumulated at the grain interfaces for larger grown grains, i.e. for low nucleation densities. [170, 192].

6. **Superconducting cross-section:** Reduction of the YBCO cross-section is the most straightforward limitation to the percolating state. Such contributions, also termed granularity effects, arise whenever non-superconducting matter is embedded in the epitaxial layer yielding to a reduction of the effective cross-section. As shown for porous and artificially multi-granular YBCO films, the overall measured J_c decreases while the local, intragrain J_c shows no reduction [107–109, 193].

Due to the few knowledge existing on ultrafast, non-equilibrium growth of YBCO, the superconducting performance of TLAG films needed to be optimized taking all of the above mentioned points into account. Throughout the course of this thesis, microstructural, electrical and inductive measurements were employed to study potential limitations in each of the investigated TLAG growth routes in order to obtain films of high superconducting performance. In the following, the different subjects serve as a guideline to evaluate their relevance to the process.

[3] See also discussion in 2.2 on HTS tape manufacturing.
[4] Yielding a localized under-doping of the grain boundary.

6.1.1 YBCO texture quality

In a first approach, we evaluate the texture quality as potential limitation to reaching high current density TLAG films. Throughout the project, a first assessment of the degree of texture was obtained via 2D X-ray diffraction measurements (GADDS). The XRD signal is acquired with an angular opening of 2θ and χ of (13° - 55°) and (-34°-34°), respectively.[5] The wide opening allows to categorize those films that reach preferential c - axis growth, seen in a confined spot of the YBCO (005) reflection.
The efforts to define process parameters and influencing factors to obtain c - axis YBCO growth in every TLAG growth route are summarized in the PhD theses of L.Soler [76], J.Jareño [95] and S.Rasi [94], in addition to the present work. To evaluate the degree of texture, we narrow the analysis here, however, only to those films that have already no polycrystalline diffraction rings coming from highly misoriented YBCO grains.
As anticipated in 4.4.5, the TLAG process allows for a high epitaxial alignment of c - axis YBCO grains. This was exemplified with high resolution XRD measurements of three pristine and one nanocomposite (NC) film grown through the main $P_{O2} - T$ paths (Fig. 4.29). Such measurements are performed with the experimental setup described in 3.5 on samples that already show strong c - axis texture in the 2D scans (routinely carried out after growth).

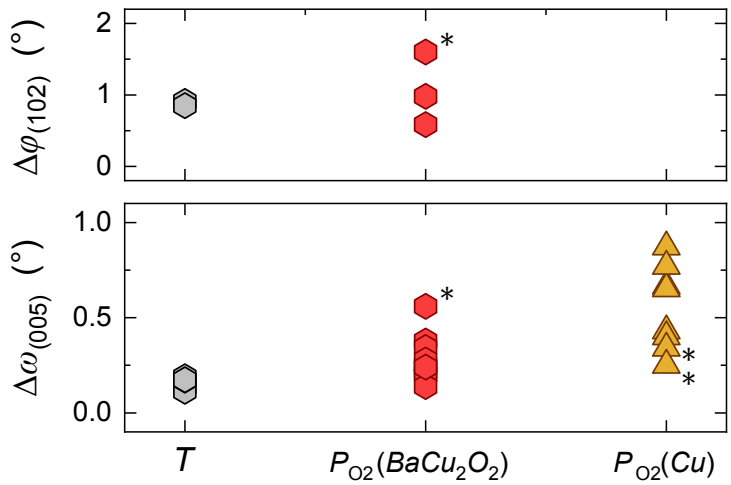

FIGURE 6.1: Overview of $\Delta\omega_{(005)}$ and $\Delta\phi_{(102)}$ values obtained for films from the three main routes (T - , $P_{O2}(BaCu_2O_2)$ - and $P_{O2}(Cu)$ - route). The range of growth conditions is summarized in tab. 3.2. Values obtained for thick films (800 - 1000 nm in thickness) are identified with asterisk symbols.

[5] See, for instance, the measurement in Fig. 5.26.

High resolution XRD measurements include probing of the out-of-plane direction, perpendicular to the substrate (00l) planes ($\theta - 2\theta$ geometry), a rocking curve scan of the YBCO (005) reflection and in some cases a ϕ - scans of the YBCO (102) reflection. While the first geometry provides information about the c - axis lattice parameter and local strain deviations, the latter two scan types quantify the misorientation degree of c - axis grains. The rocking curve translates into out-of-plane tilting of the c - oriented grains and the ϕ - scans into an in-plane rotation of the grain.
Rocking curves and ϕ - scans of films processed in the different $P_{O2} - T$ paths of this work (T -, $P_{O2}(BaCu_2O_2)$ - and $P_{O2}(Cu)$ - route) are fitted with Lorentzian peak profiles to extract the FWHM values $\Delta\omega_{(005)}$ and $\Delta\phi_{(102)}$, respectively. A route-dependent overview of these values is given in Fig. 6.1. The range of $\Delta\omega_{(005)}$ and $\Delta\phi_{(102)}$ values stretches from 0.1° - 0.9° and 0.6° - 1.6°, respectively.
The samples are grown in the wide range of P_{O2}/T conditions, denoted in tab. 3.2. It appears that the epitaxial quality of TLAG grown films is high, independent of the exact processing conditions. The $\Delta\omega_{(005)}$ values shown here settle in the lower range of reported values and are comparable to those obtained in liquid-assisted, equilibrium process, such as liquid phase epitaxy (LPE) and hybrid liquid phase epitaxy (HLPE) [78, 81].

YBCO thick films

Fig. 6.1 also comprises three thick YBCO films that have recently been obtained through multi-deposition by spin-coating, one grown in the $P_{O2}(BaCu_2O_2)$ -, the other two in the $P_{O2}(Cu)$ - route (800 - 1000 nm in thickness). The $\Delta\omega_{(005)}$ and $\Delta\phi_{(102)}$ values lie close to those of 100 - 400 nm thick films. Hence, the epitaxial quality seems not to be affected by an increase in thickness, similar to other liquid based approaches [28, 78].
The high degree of c - axis grain alignment is further confirmed through θ - 2θ measurements on three thick films from each processing route (Fig. 6.2). Apart from a minor fraction of misoriented YBCO ab-grains, denoted as ($h\,k\,0$) reflections, and a scarce amount of parasitic solid phases, the avoidance of which requires further growth optimization, the scans show a pronounced signal by the (00l) peak family up to very high angles.
The surface and cross-section of the $P_{O2}(BaCu_2O_2)$ - route grown thick film is further shown through SEM imaging in Fig. 6.3. The SEM micrograph of the top-view indicates a dense, pore-free surface, typical for liquid based growth techniques (Fig. 6.3a)).

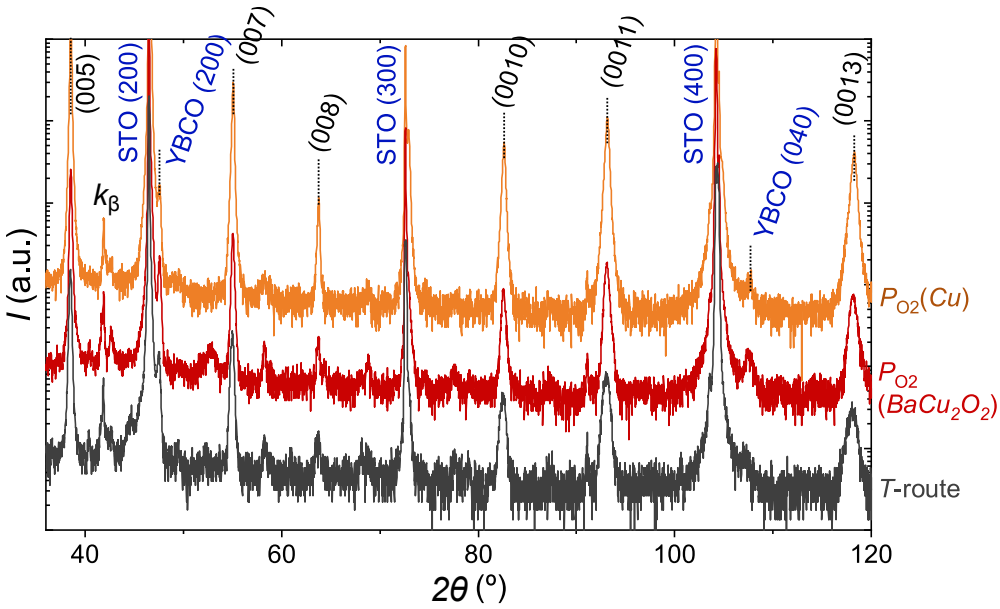

FIGURE 6.2: θ-2θ measurements of three thick YBCO films grown through the T-, $P_{O2}(BaCu_2O_2)$- and $P_{O2}(Cu)$- route (see labels). YBCO $(00l)$, $(h\,k\,0)$ planes as well as STO substrate peaks are denoted.

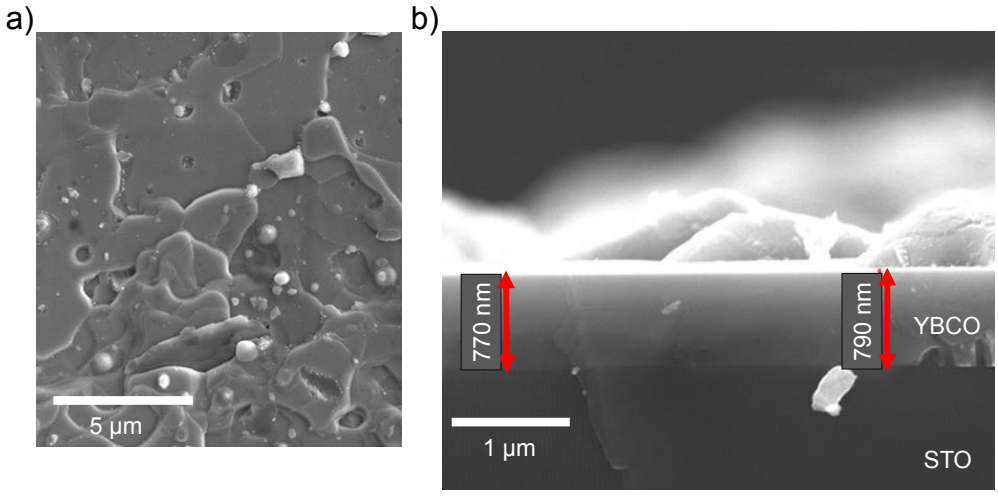

FIGURE 6.3: Scanning electron microscopy images of a thick YBCO film (800 nm) grown through the $P_{O2}(BaCu_2O_2)$- route: a) Surface- and b) Cross-section view.

The J_c of the thick film is determined through inductive measurements to reach 0.4 MA cm^{-2} and 3.2 MA cm^{-2} at 77 K and 5 K, respectively. Such values are reduced as compared to the peak values achieved for TLAG grown thin films.[6] The texture quality being a potential limitation to J_c can, however, be excluded here given the high degree of grain alignment. The particular film shown in Fig. 6.3 has a measured $\Delta\omega_{(005)}$ and $\Delta\phi_{(102)}$ value of 0.56° and 1.6°, respectively, at an estimated thickness of up to 800 nm (Fig. 6.3b)).

YBCO grown on LMO buffered hastelloy metallic tape

The texture analysis from above is further extended to a 180 nm thick YBCO film, grown through the $P_{O2}(BaCu_2O_2)$ - route on industrial Hastelloy C276 tape, provided by SUNAM.[7] The Ni-based hastelloy substrate is polycrystalline and covered with a sequence of buffer layers to promote texture in the final layer. A full sequence, bottom to top, includes 40 nm of Al_2O_3, 7 nm of Y_2O_3, 7 nm of Y_2O_3, 10 nm ion-beam-assisted (IBAD) MgO, 20 nm homoepitaxial MgO and 40 nm $LaMnO_3$ (LMO). The texture is promoted first in the IBAD MgO layer and terminated with the LMO layer having an in-plane lattice mismatch of 2% to the orthorhombic YBCO phase.[8] Measurements in $\theta - 2\theta$ geometry of SUNAM tape alone and with YBCO on top are shown in Fig. 6.4a), red and black curve, respectively. As introduced in 3.5, the XRD signal of polycristalline phases appears strongly diminished in this configuration due to the reduced illuminated area and confined detector opening. This is seen in the low intensity of the Hastelloy reflections. The diffracted signal of the epitaxial MgO and LMO layers, on the contrary, is enhanced despite the low thickness of these buffer layers.
The grown YBCO film exhibits strong c - axis texture, seen in the sole presence of the (00l) peak family. The evaluation of the texture quality is done in relation to the LMO, being the last buffer in the stack. A comparison of the YBCO (006) / LMO (200) rocking curves and YBCO (102) / LMO (111) ϕ - scans is shown in Fig. 6.4b) and c), respectively. The choice of crystallographic planes is made given their close interplanar spacing.

[6] A maximum of 5.5 MA cm^{-2} was achieved for a 100 nm thick film from the $P_{O2}(BaCu_2O_2)$ - route.

[7] The alloy includes 16% Mo, 15% Cr, 6% Fe, 4%W, 2.5%Co, 2.5%Mn, 2.5%V and 51.5% Ni.

[8] Averaged value assuming YBCO in-plane lattice constants of a = 0.382 nm and b = 0.389 nm.

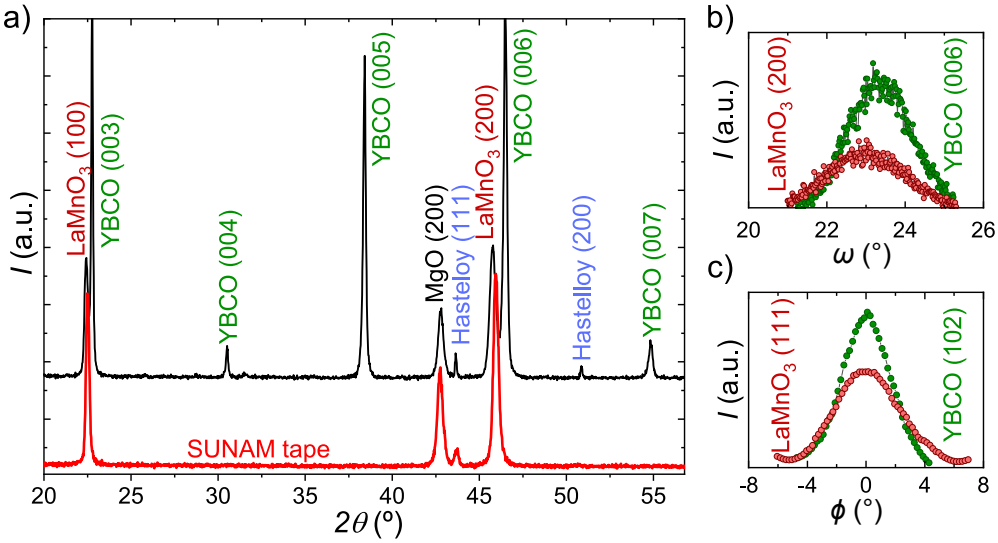

FIGURE 6.4: XRD results of a YBCO TLAG thin film grown on hastelloy SuNAM substrate: a) $\theta - 2\theta$ measurement showing YBCO cube-on-cube texture on the (100) LMO buffer layer (black curve), and SUNAM tape without YBCO (red curve). (b) Rocking curve of the YBCO (006) and LMO (200) reflection. (c) ϕ - scan of the YBCO (102) and LMO (111) reflection.

	$\Delta\omega$ [°]	$\Delta\phi$ [°]
$YBa_2Cu_3O_{7-\delta}$	2.53	4.4
$LaMnO_3$	3.51	5.84

TABLE 6.1: Overview of mistilt and rotation degree of heterogeneous YBCO grains on SUNAM tape: $\Delta\omega$ values of YBCO (006) and LMO (200) and $\Delta\phi$ values of YBCO (102) and LMO (111) reflection obtained from the XRD scans in Fig. 6.4.

The FWHM values are summarized in tab. 6.1. The YBCO texture is found to be improved as compared to the LMO buffer. Such texture-curing has already been observed in other growth techniques, for instance, in PLD-grown YBCO [194] and the liquid assisted RCE-DR process [195, 196].
Considering the aforegoing results on the texture quality of TLAG films, varying thickness, processing routes and substrates, it can be concluded that the current carrying performance of these films does not suffer from high grain-boundary angles. The range of $\Delta\omega_{(005)}$ and $\Delta\phi_{(102)}$ values (Fig. 6.1) compares to the lowest reported in literature and lies well below the critical angle (θ_c), a

threshold above which weak-link behaviour is expected to affect J_c [65]. In addition, the grown films exhibit similar texture characteristics as other liquid-based techniques, such as the generally low degree of grain misalignment and its invariability upon thickness increase [28, 78, 81].

6.1.2 YBCO phase purity: $BaCO_3$ decomposition and liquid induced reactivity

$BaCO_3$ decomposition and carbon contamination

The grain purity is further examined here since contamination of the YBCO crystal structure can result in suppression of the superconducting state. In the TLAG process, two main sources of contamination are considered: Carbon retention from the $BaCO_3$ decomposition process and liquid induced reactivity phases arising from substrate dissolution. Full decomposition of $BaCO_3$ was previously demonstrated through *in-situ* synchrotron analysis for each of the probed $P_{O2} - T$ paths (4.4). The films had ranging thicknesses of 400 - 450 nm. Here, we expand the analysis to thicker films where the CO_2 removal might encounter further complications.

	dT/dt [°C · s^{-1}]	T_{Growth} [°C]	$P_{O2,Base}$ [bar]	$P_{O2,Growth}$ [bar]	$P_{tot,Growth}$ [bar]
S1/T	5	860	-	10^{-3}	1
S2/$P_{O2}(BaCu_2O_2)$	0.4	845	10^{-5}	10^{-3}	$5 \cdot 10^{-3}$
S3/$P_{O2}(Cu)$	0.4	840	10^{-7}	$2 \cdot 10^{-3}$	10^{-2}

TABLE 6.2: Processing conditions three thick YBCO films, S1 - S3, grown through different routes (T -, $P_{O2}(BaCu_2O_2)$ - and $P_{O2}(Cu)$ - route). Only one oxygen partial pressure is used in the T - route. $P_{tot,Base} = 5 \cdot P_{O2,Base}$ for S2 and S3.

Three thick precursor films are obtained through CSD multideposition and processed to give a 800 - 1000 nm thick YBCO layer (confirmed via cross-section SEM images). The samples, labeled as S1 - S3 are grown through the three main routes with the growth conditions denoted in tab. 6.2. S1 and S3 consist of 5 layers, (2-3) composition, 2 M in concentration; S2 is composed of 8 layers, (3-7) composition of 1 M.
As a first attempt to show that no $BaCO_3$ remainings persist after growth,

diffraction measurements in grazing incidence geometry are performed before and after the crystallization process (Fig. 6.5). In this configuration, the randomly oriented precursor phases have enhanced detectability (3.5).

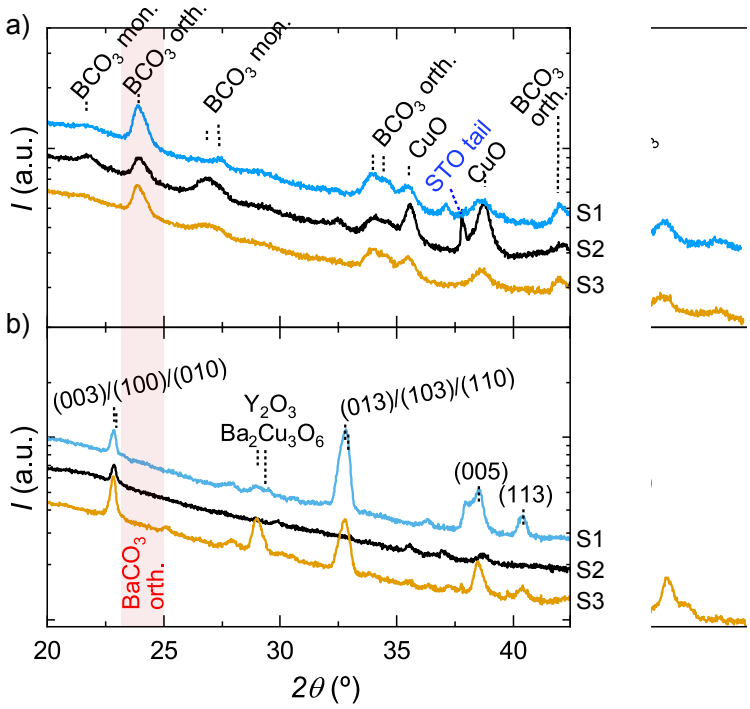

FIGURE 6.5: GI-XRD measurements of samples S1 - S3 (tab. 6.2) (a) before growth and (b) after growth. Reflections without labels correspond to crystallographic planes of YBCO. The sample nomenclature is denoted on right-hand side.

An overview of the measurements is shown in Fig. 6.5a) and b), depicting precursor films and grown YBCO layers, respectively. Note that in this geometry, the probing vector (eq. 3.13) moves along a circular path as shown in Fig. 3.12. If an epitaxial reflection is not crossed by coincidence, only ring intensities arising from randomly oriented phases are detected that way.
The GI-measurement of the precursor films show predominantly the presence of orthorhombic and monoclinic $BaCO_3$ and CuO.[9] Y_2O_3 particles remain hidden due to the nano-crystallinity of the phase. Regarding the grown films, the crystalline phases can be attributed to misoriented YBCO grains and secondary phases whose identification is not primary here. Most importantly,

[9]TEM analysis of precursor films further confirmed that the monoclinic phase is given in reduced amount as compared to the orthorhombic phase (4.2).

there is no sign of $BaCO_3$ remainings, as highlighted by the red-shaded region in Fig. 6.5b). The absence of crystalline $BaCO_3$ is a first requirement for full conversion to YBCO in the TLAG process. A second assessment is to evidence that there is no C retention at the grain boundaries or C incorporation into the YBCO structure.

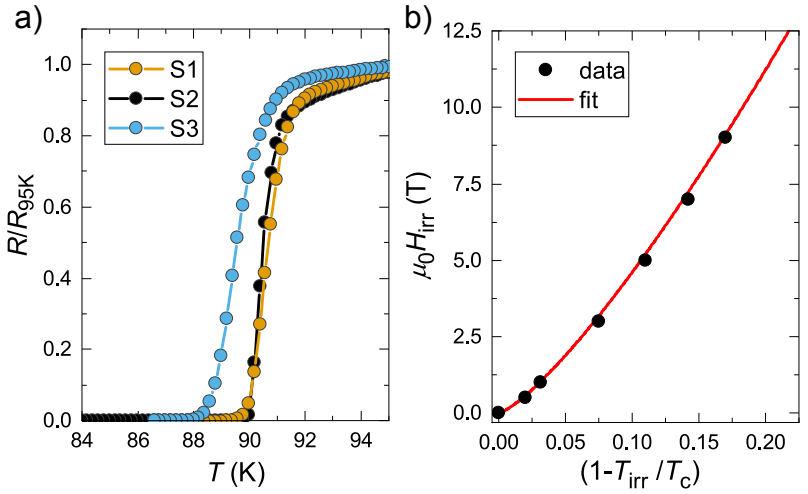

FIGURE 6.6: Transport measurements of thick YBCO TLAG samples (processing conditions in tab. 6.2): a) Transition temperatures obtained via Van der Pauw method. b) Irreversibility line determination from transport measurements on patterned YBCO bridge with a $R(T_{irr})/R(100\,K) = 0.001$ criterion. A fitting is carried out according to eq. 6.1.

The samples discussed here do not surpass a J_c threshold of $0.4\,MA\,cm^{-2}$ at 77 K and $3.2\,MA\,cm^{-2}$ at 5 K and require a refined growth optimization to avoid remaining secondary phases. However, to confirm that films are free of contaminants and of high phase purity, electrical measurements are conducted in two configurations. Superconducting critical temperatures are probed in Van der Pauw, four-point geometry (3.4.2) showing high transition temperatures of 89 - 90 K for all three thick films (Fig. 6.6a)). In addition, the irreversibility line is determined for sample S2. The film is micropatterned to a four-point bar geometry (3.4.4) and the superconducting transition remeasured under applied magnetic fields of 0.5, 1, 3, 5, 7 and 9 T for $H // c$. Irreversibility temperatures T_{irr}, as shown in figure 6.6c), are obtained from ρ(T) curves following the criterion $\rho(T_{irr})/\rho(100\,K) = 10^{-3}$ [197]. An extrapolation to higher magnetic fields is done through fitting of the power-law

$$H_{irr} = H_0 \left(1 - \frac{T_{irr}}{T_c}\right)^{\alpha} \tag{6.1}$$

with the fitting parameters H_0 and α [198, 199]. The fitted curve is included in Fig. 6.6c) as solid red line. The irreversibility line, with $H_{irr}(77K) = 8\,T$ is comparable to other pure YBCO systems [200, 201]. Also the exponent $\alpha = 1.3$ lies in a typical range of 1-2 for YBCO with varying defect landscapes [197]. It is, therefore, safe to conclude that TLAG films do not suffer from carbon retention typically seen in a depression of transition temperatures [134].

Effects of liquid reactivity

A similar discussion can be made on interface related reactivity issues encountered in the TLAG process. When ultrahigh heating ramps, as used in this work, meet the formation of corrosive melts, reactivity phases and YBCO impurity substitution become a major concern. Initially, TLAG growth was explored through the *T* - route varying oxygen partial pressure, heating ramps and substrates ($SrTiO_3$ (STO), $LaAlO_3$ (LAO) and $(LaAlO_3)_{0.3}$ $(SrAlTaO_6)_{0.7}$ (LSAT)).[10] This was to find the most reproducible conditions for heterogeneous nucleation while avoiding substrate dissolution by the liquid phase.
Let us, for instance, consider three films of stoichiometric composition grown through the *T* - route at 750 °C, 770 °C and 810 °C on STO, P_{O2} =1 mbar and a heating rate of $60\,°C\,s^{-1}$.[11] All three samples reach full epitaxy of the YBCO phase itself [76]. However, SEM surface imaging shows needle-like structures that interrupt the epitaxial layer with exposed substrate surface in the near surroundings (Fig. 6.7). Terraces of light and dark grey color and needle structures are identified by EDX analysis as YBCO, substrate and Y_2BaCuO_5 (211) phase, respectively.

[10] Also different buffer layers, such as PLD-grown YBCO, PLD $LaMnO_3$, CSD Nd_2CuO_4 and CSD $LaMnO_3$, have been used showing no changes in the observed trends.

[11] Films heated at $60\,°C\,s^{-1}$ are considered here as extreme case; As will be shown in the following, optimal growth is obtained for $\leq 20\,°C\,s^{-1}$.

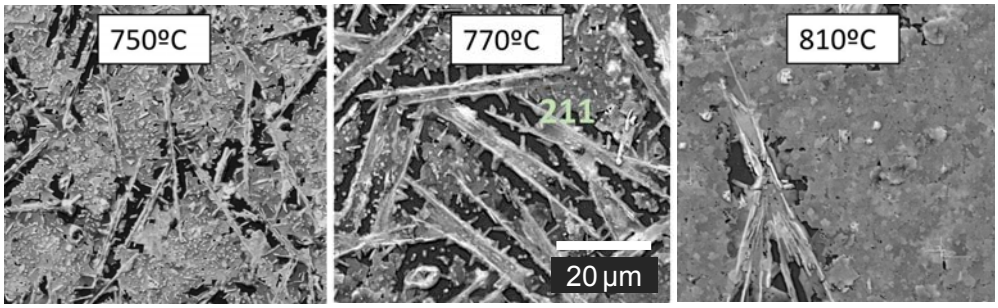

FIGURE 6.7: SEM surface images of (2-3) films heated at 60 °C s^{-1}, $P_{O2} = 10^{-3}$ bar to different T_{Growth}. The needle-like structures are identified through EDX measurements as Y_2BaCuO_5 (211) phase.

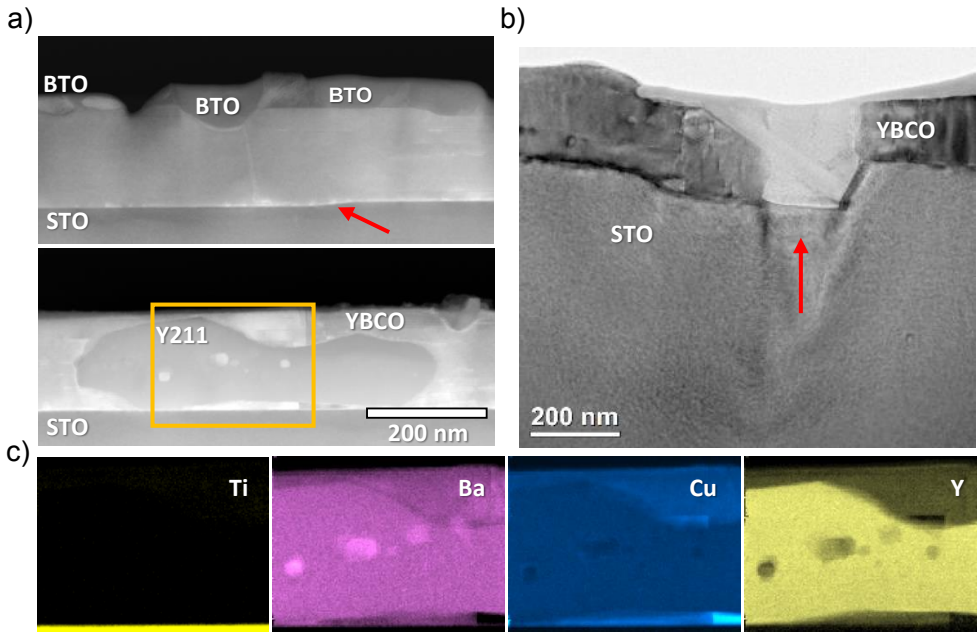

FIGURE 6.8: TEM overview on reactivity issues in *T* - route for grown film on STO. Growth is carried out with (2-3) composition, heated at 60 °C s^{-1}, $P_{O2} = 10^{-2}$ bar to $T_{Growth} = 835$ °C. a) $BaTiO_3$ (BTO) and 211 solid phases blocking the conducting cross-section of the film. Red arrow marks a step in the STO substrate due to liquid dissolution. b) Magnification of strongly dissolved substrate area. c) Identification of BTO phase through EELS mapping.

The presence of needles is accompanied by substrate reactivity phases, as shown in the TEM analysis in Fig. 6.8. On STO, we find the growth of $BaTiO_3$

(BTO) of macroscopic sizes in the range of 200-400 nm (shown in the upper part of Fig. 6.8a)). The reactivity phase incorporates Ti from the STO substrate and is found in proximity to places where interface reactivity is observed. A step in the substrate is marked by a red arrow in Fig. 6.8a).
Strong substrate dissolution with a step exceeding 100 nm in height is further shown in Fig. 6.8b). Other regions present large-areas of the 211 phase (Fig. 6.8a), bottom part), in agreement with the SEM results. The phase consistency (both for BTO and 211) is confirmed through EELS analysis (3.7), and shown exemplary for BTO in Fig. 6.8c).
The observed secondary phases are a severe and direct limitation to the conducting cross-section of the films. This is shown for films heated at the maximum rate of 60 °C s^{-1}, P_{O2} =1 mbar and 10 mbar on STO substrate.
Considering SQUID measurements of the superconducting transition,[12] contamination of the actual, intrinsic YBCO phase might further be suggested: Fig. 6.9 shows inductive measurements of the transition for samples heated at different ramps to a final growth temperature of T = 835 °C. Shown exemplary for three films on STO subtrate, the transition onset shifts towards lower temperatures upon heating ramp increase from 0.4 °C s^{-1} to 40 °C s^{-1}, Fig. 6.9a).

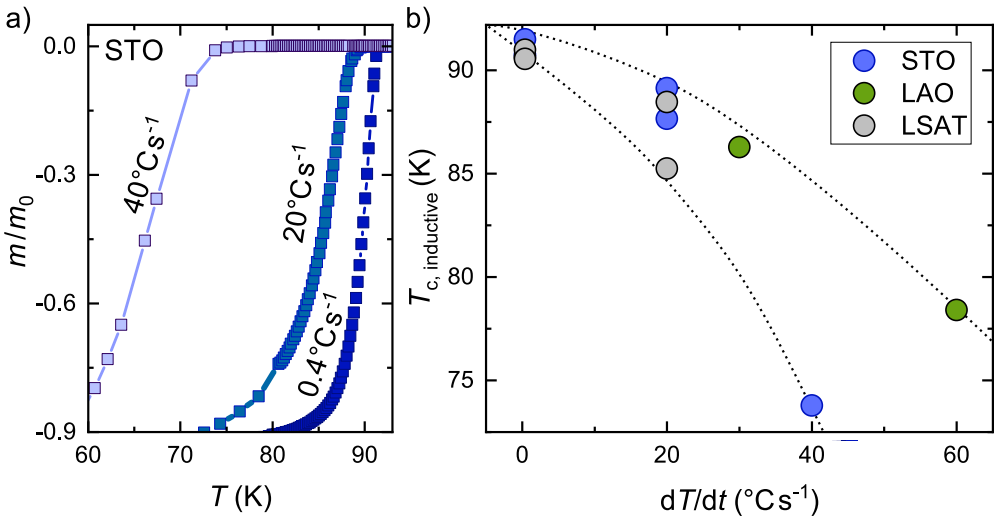

FIGURE 6.9: Inductively measured a) SC transition of (2-3) films grown at 0.4, 20 and 40 °C s^{-1}, $P_{O2} = 10^{-3}$ bar, T_{Growth} = 835 °C on STO. b) Onset T_c values for (2-3) films grown on STO, LAO and LSAT at different heating ramps.

[12] Measured at a DC field of 200 mT in Meissner state (3.2.1).

The observed trend appears to be similar for all chosen substrates. Onset values where the normalized magnetic moment m/m_0 initiates the decrease, that is where we define T_c (3.2.1), were further extracted for the three substrates used in this work (Fig. 6.9b)). Also for films grown on LSAT and LAO a declining trend is observable upon heating ramp increase.
A confirmation that neither LAO nor LSAT withstand the corrosive nature of the liquid phase is given in Fig. 6.10. The TEM images show two grown films heated at $60\,°C\,s^{-1}$ to $T = 835\,°C$. As indicated by the red arrows, both substrates present regions where the interface is attacked by the liquid phase. Also local formation of the 211 phase could be identified via TEM [76], not shown here.

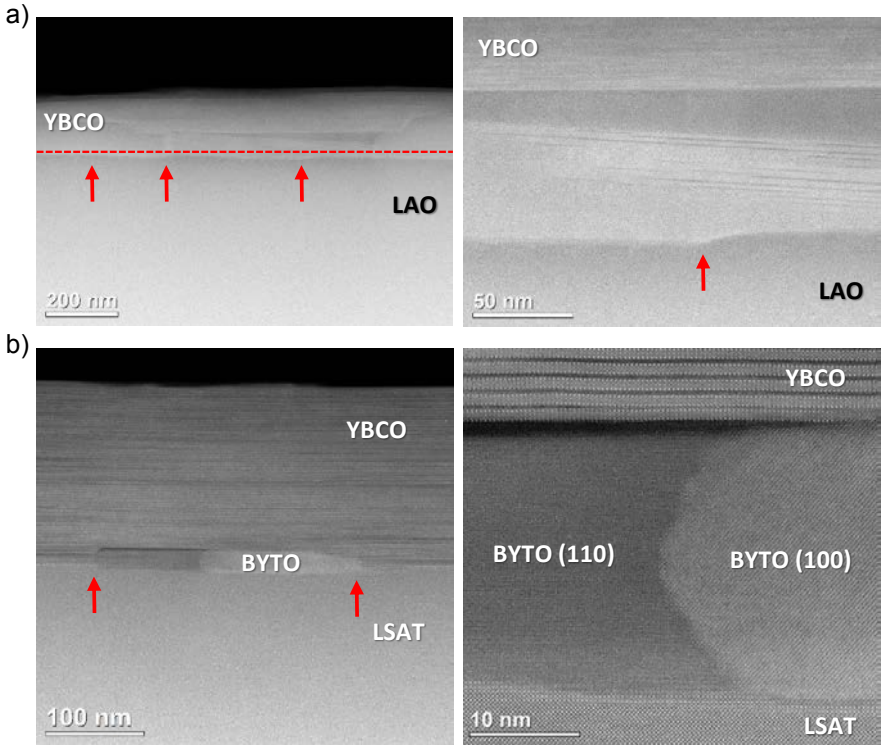

FIGURE 6.10: TEM overview on reactivity issues in T - route for grown films on a) LAO and b) LSAT substrate. Growth is carried out in both cases at $60\,°C\,s^{-1}$, $P_{O2} = 10^{-2}$ bar, $T_{Growth} = 835\,°C$. Dissolved substrate regions are indicated through red arrows.

On LAO, the presence of La in the YBCO bulk and on the surface are confirmed through EELS mapping. Aside from steps in the LAO interface, no other solid reactivity phases are formed (Fig. 6.10a)). This is different in the

case of grown films on LSAT. Here, crystalline Ba_2YTaO (BYTO) is observed, primarily (110) and (100) oriented. Typically, BYTO grains are found right at the dissolved substrate interface.
The superconducting performance of TLAG films that are processed through the *T* - route at increased heating rates ($> 20\,°C\,s^{-1}$) is strongly compromised. For instance, J_c values do not exceed $1\,MA\,cm^{-2}$ at 5 K. This can be attributed to off-stoichometry phase formation, such as the 211 phase, substrate reactivity phases and badly wetted areas in proximity to such macroscopic defects (Fig. 6.7). The previously shown inductive measurements of the transition temperature further suggest that an intrinsic contamination of the YBCO phase might be given. To confirm that the T_c decrease is not simply arising from a weak electromagnetic response of the films, electrical measurement are conducted to probe the SC transition.

A set of Van der Pauw resisitivity measurements of grown films on LSAT and STO are shown in Fig. 6.11. Room temperature resistivity values, ρ_{300K}, of 250-500 $\mu\Omega$ can be obtained for films grown at 0.4 - 20 $°C\,s^{-1}$ (Fig. 6.11a)). The lower limit of 250 $\mu\Omega$ is in good agreement with reported values $\rho_{300K} = 300\,\mu\Omega$ and $200\,\mu\Omega$ for YBCO CSD [173] and single crystal films [172], respectively. Increased resistivity values can be attributed to electron scattering at localized inhomogeneities and nanoscale defects encountered in TLAG films (6.1.4 and 7.1). For films processed at higher heating ramps, such as $40\,°C\,s^{-1}$ (Fig. 6.11a)), resistivity values show a strong increase and a shift of the superconducting transition towards lower temperatures.
A decline in transition temperatures with heating ramp increase is shown for more films in Fig.6.11b). T_c values are determined following the maximum derivative criterion (3.4.3) and plotted as a function of heating rate. The dashed black lines highlight the outer bounds in the stray of points. Films processed at rates of 0.4 - 20 $°C\,s^{-1}$ present high T_c values in the range of 90 - 92.5 K. A decrease is observed for two films heated at $40\,°C\,s^{-1}$. The visible downward trend of critical temperatures with heating rate is in agreement with the inductive measurements introduced earlier (Fig. 6.9). Together with the microscopy results it can be suggested that the application of high heating ramps ($>20\,°C\,s^{-1}$) yields substrate induced reactivity, thus the formation of secondary phases and contamination of the actual YBCO phase with atomic elements of the substrate material. In case of STO, copper substitution through Ti, according to $YBa_2(Cu_{1-x}T_x)O_z$, would results in the seen suppression of superconductivity [175].

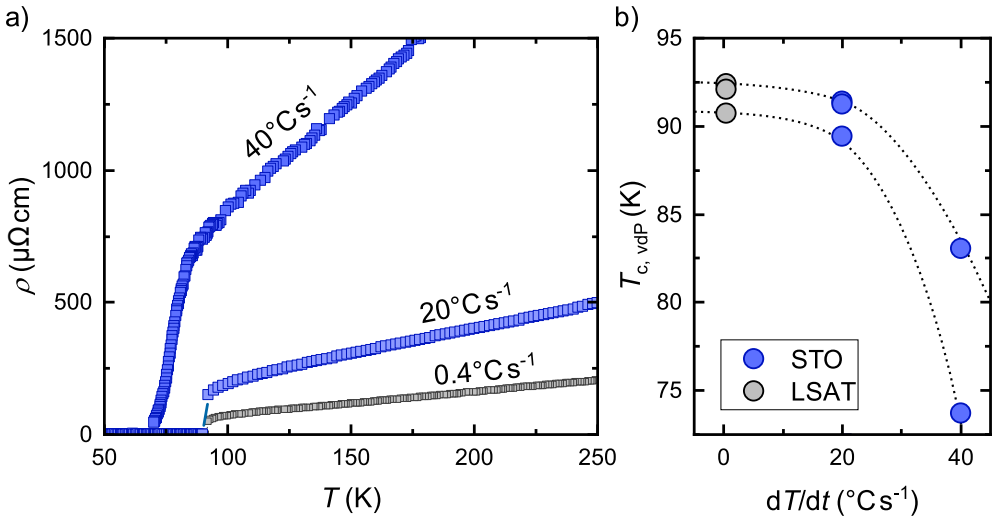

FIGURE 6.11: Van der Pauw resistivity measurements of a) SC transition of (2-3) films heated at 0.4, 20 and 40 °C s^{-1}, $P_{O2} = 10^{-3}$ bar to $T_{Growth} = 835$ °C. b) Derivative T_c values for (2-3) films grown on STO and LSAT at different heating ramps.

To conclude, the T-route can suffer from localized regions of substrate dissolution by the corrosive melt when heating ramps above 20 °C s^{-1} are employed to drive the film towards high temperatures. This can be specifically attributed to the use of increased heating ramps since $P_{O2} - T$ variations and use of different substrates/buffers did not resolve the observed issues [76, 95]. Formation of macroscopic BTO and BYTO grains are found when growth is carried out on STO and LSAT, respectively. In addition, interface reactivity seems to be always accompanied by the Y-rich 211 phase which might be a result of the off-stoichiometry created by the substrate-liquid reaction. The remaining phase mixture might be depleted in Ba atoms, favouring the formation of the 211 phase. Also contamination of the YBCO phase itself with substrate elements (e.g. Ti) can be suggested given the drop in critical temperatures obtained from inductive and electrical measurements. A full understanding of the enhanced substrate reactivity at the highest heating ramps has yet to be developed. A possible explanation might lie in the liquid phase amount, melt supersaturation, temperature and time period the liquid is in contact with the substrate interface. The use of high heating rates might preserve a narrow particle size distribution and allow a more abrupt liquid formation. At the same time, the increased rates would compromise dissolution of Y_2O_3 nanoparticles, hence, reduce the supersaturation of the melt [132], while the main reactions are pushed to higher temperatures where reactivity is promoted.

In the T - route liquid reactivity issues can be avoided when using heating rates $\leq 20\,°C\,s^{-1}$ or through identification of non-reactive buffer layers. However, the intrinsic complexity of this growth approach lies in the crossing of a wide temperature window where liquid and YBCO phase become stable (Fig. 4.25). This is further coupled to the decomposition behaviour of $BaCO_3$. In an attempt to decouple the reaction path and reduce the time of liquid phase being in contact with the substrate, the pressure routes were developed (eq. 4.25 and eq. 4.26).
In the $P_{O2}(BaCu_2O_2)$ - and $P_{O2}(Cu)$ -route, growth was carried out on STO and LAO substrate, respectively. Considering TEM, XRD and electrical transport results, no significant reactivity issues, that would affect the superconducting properties (T_c, J_c), could be identified in the $P_{O2}(Cu)$ -route nor $P_{O2}(BaCu_2O_2)$ -route [76, 94]. The only case of liquid reactivity was observed in the $P_{O2}(BaCu_2O_2)$ -route when working on STO substrate, close to the YBCO instability line. Fig. 6.12 shows an STEM image of an oriented BTO nanoparticle of 20-25 nm in diameter as a reaction product between the (Ba - Cu - O) liquid and the STO substrate. The composition of the enclosed grain is determined in the same region through EELS mapping, shown on the right-hand side of the figure. All films, grown through the $P_{O2}(BaCu_2O_2)$ - route, were explored for 0.5 mbar and 1 mbar of P_{O2}, (3-7) composition, varying the temperature. The BTO phase is primarily observed at the reduced oxygen partial pressure of 0.5 mbar when working closer to the YBCO instability line.

The preferential alignment of the BTO phase could further be confirmed via high resolution XRD measurements.[13] As can be seen in the $\theta - 2\theta$ scans, Fig. 6.13a), both films grown at 1 mbar ($T = 830\,°C$ and $850\,°C$) show primarily the YBCO (004) and (005) reflections. Only the film grown at 0.5 mbar presents an additional reflection at $2\theta = 31.60\,°$ which we identified as $BaTiO_3$ (110) plane. Debye-Scherrer grain sizes vary in the range of 20-40 nm, in agreement with crystallite dimension observed through electron microscopy. BTO crystallizes in tetragonal structure with $a = 4.00$ Å and $c = 4.02$ Å. With the $(h\,k\,0)$ planes parallel to the YBCO ab-planes, the phase could potentially accomodate with a lattice mismatch of $< 1\%$ in-plane and $< 3\%$ out-of-plane with respect to the orthorhombic YBCO lattice.

[13] A confirmation through 2D XRD scans is carried out in [76].

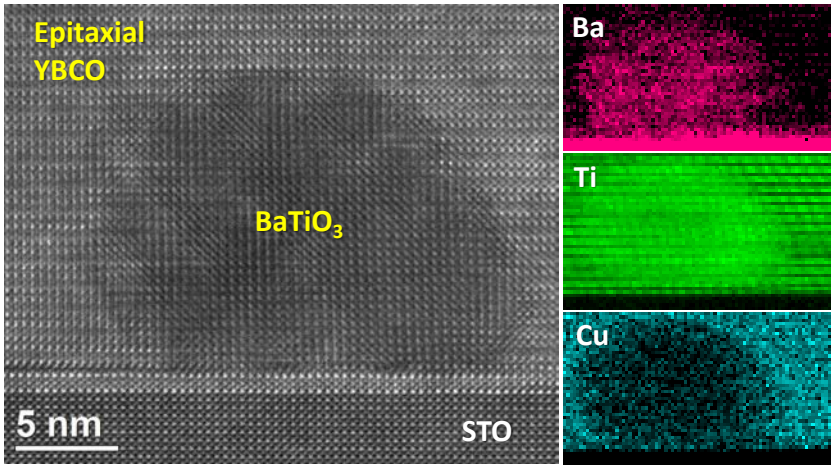

FIGURE 6.12: STEM measurement of epitaxially embedded BTO particle (right-hand side) and EELS mapping of the same region (left-hand side) for a YBCO film grown through the $P_{O2}(BaCu_2O_2)$ - route. BTO particles could only be identified close to the substrate interface.

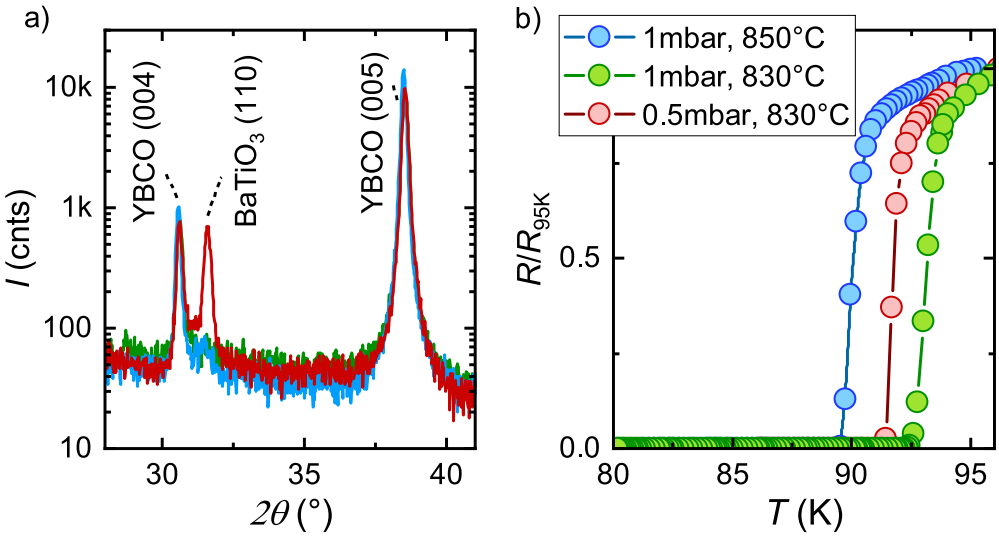

FIGURE 6.13: XRD and resistivity measurements of samples grown in $P_{O2}(BaCu_2O_2)$ - route varying $P_{O2,Growth}$ and T_{Growth} (see legend). a) $\theta - 2\theta$ scan showing a pronounced BTO (110) reflection for the film grown at 0.5 mbar. b) SC transition with $T_{c,deriv} > 90$ K for all films. The color code in the legend applies to both graphs.

Contrary to reactivity issues in the T - route for growth on STO, we find no influence of the BTO phase on the film performance. Van der pauw resistivity

measurements of the superconducting transition are show in Fig. 6.13b) for the films with and without BTO phase. High T_c values (90 - 92.5 K) are reached for all samples suggesting that the YBCO phase is not contaminated.[14] Hence, even though scarce amounts of liquid induced substrate reactivity could be found at the lowest explored oxygen partial pressure, the initial intention of preventing liquid reactivity issues through the pressure route approach could be realized and the incorporation of Ti in the structure avoided.

The most noticeable difference of the pressure approaches to grow YBCO films is the reduced appearance of substrate reactivity with the liquid phase. It could be argued that the occurrence and severity of substrate dissolution relies on the time period of the liquid being in contact with the substrate interface. In the T - route, increased heating ramps were suggested to result in compromised Y_2O_3 dissolution while liquid might be formed in a wide temperature window. The consequent extended time period of liquid in contact with the substrate might then promote liquid induced reactivity. In the pressure approaches, however, the film is transferred immediately to a temperature window where nucleation rates are high, hence the time of liquid-to-substrate contact is reduced.

In summary, we have evaluated several potential hindrances to reaching high critical currents in TLAG YBCO films:

1. **Texture quality:** The degree of c - axis grain alignment is found to be generally high in TLAG grown films. Presented $\Delta\omega$ and $\Delta\phi$ values compete with the lowest values reported in literature, typical for liquid based processes. This is valid for all investigated growth routes of this work and a YBCO layer thickness of up to 1 µm. Therefore, grain misalignment is considered to have less relevance to the current percolation even in the case of thick TLAG films.

2. **$BaCO_3$ decomposition:** In addition to *in-situ* synchrotron measurements (chapter 4) and structural and electrical characterization of thin TLAG grown films (Fig. 4.29 and Fig. 4.30), the elimination of $BaCO_3$ is extended here to thicker films of 800-1000 nm. XRD measurements show no crystalline residuals of the precursor phase as well as no C retention in grain boundaries or C incorporation in the YBCO structure, in agreement with high T_c values (>89 K) obtained through transport measurements [134].

[14] In the T - route, a degradation of T_c is evidenced when reactivity phases are present.

3. **Liquid induced interface reactivity:** Liquid reactivity with the substrate interface can have deteriorating consequences for the film performance. This is shown to be primarily an issue when growth is carried out through the T - route at heating ramps $> 20\,°C\,s^{-1}$, confirmed for growth on LAO, STO and LSAT substrate. The deteriorating effect is suggested to be promoted through growth conditions that do not allow rapid coverage of the substrate interface by the epitaxial YBCO phase, hence, increasing the time period of the liquid being in contact with the substrate. Reactivity issues can either be avoided through a reduction of heating rates or film processing through the pressure routes. A solution might further be given through identification of non-dissolvable buffer materials. First promising results are currently obtained for YBCO films grown on $LaMnO_3$ (LMO) buffer layers, as used in the case of hastelloy SUNAM substrates (Fig. 6.4).

While the first two points are evidenced in numerous cases to be of no concern to the performance of TLAG grown films, the avoidance of interfacial reactivity requires a proper choice of growth conditions. Films presented in the following part are either grown through the pressure routes or at $0.5 - 20\,°C\,s^{-1}$ in the T - route, both being means to avoiding reactivity influences.

6.1.3 Doping state and charge carrier density of grown films after oxygenation thermal treatment

Proper oxygen incorporation into the YBCO crystal structure is pivotal to reaching high critical current density films. As introduced in 2.1.5, $YBa_2Cu_3O_{7-\delta}$ is an oxygen deficient structure composed of three perovskite blocks with Y and Ba atoms in the central positions. The deficiency $(7 - \delta)$ arises from the partial occupation of $CuO_{1-\delta}$ chains with oxygen atoms. The chains function as charge reservoirs, providing carriers to the superconducting CuO_2-planes [9]. Each incorporated oxygen atom supplies the structure with two electron holes, resulting in partial doping of the CuO_2-planes via charge transfer [32]. This, so called, **doping effect**, is crucial for the electronic state of YBCO. Superconductivity in YBCO can be strongly altered, to the point of complete disappearance, through variation of holes per copper atom, p, in the CuO_2-planes. Also the superconducting film performance scales with the hole concentration [31, 34, 103]. The T_c dependence is parabola-like with a maximum at $p = 0.16$ (**optimally doped**), while J_c keeps increasing up to $p = 0.19$ in the **overdoped** state [34, 105]. At lower concentrations the material is considered as **underdoped**.
Oxygen incorporation into the YBCO structure is typically done through a

post-thermal treatment after the film is crystallized. As discussed in 3.1.4, the standard oxygenation procedure established in the SUMAN group to reach good superconducting performance includes a temperature dwell at 450 °C at high oxygen flow (Fig. 3.3). This was initially optimized for TFA-CSD YBCO films. Oxygen incorporation is believed to be limited through bulk-/grain-boundary diffusion and defects that provide paths of migration [105]. Concerns whether the same oxygenation procedure should be adapted for TLAG samples emerged given the dense microstructure (Fig. 4.28) and high epitaxial quality of these films (Fig. 6.1). Hence, the doping state of TLAG grown YBCO needs to be revised in order to affirm the suitability of the thermal treatment also for the films studied here and discard the oxygenation treatment as a cause of low J_c.

For most compounds, information about the doping state and oxygen content is obtained through destructive methods, such as iodometric titration and weight-loss measurements [31]. In YBCO, however, we benefit from the correlation of the doping level with the orthorhombicity of the unit cell and charge carrier density [31, 105, 202]. It is reported that p scales proportionally with the charge carrier density, n, while the unit cell deforms for different oxygen concentrations [31, 202]. Both measures can be assessed through non-destructive XRD and electrical characterization as introduced in 3.4 and 3.5. In particular, the charge carrier density is obtained through room temperature Hall effect measurements in Van der Pauw geometry ($n_{H,300K}$).
First of all, let us consider the processing conditions of the grown films under consideration. We are comparing samples from different processing routes since the $P_{O2} - T$ history is found to have the strongest impact on the microstructure of the YBCO layer (see 6.1.4). $P_{O2} - T$ ranges and heating ramps are summarized in tab. 6.3; film compositions, substrates, YBCO layer thicknesses and range of $J_c(5K, 0T)$ values are listed in tab. 6.4.

Growth route	dT/dt [°C · s^{-1}]	T_G [°C]	$P_{O2,Base}$ [bar]	$P_{O2,G}$ [bar]	$P_{tot,G}$ [bar]
T	$0.4 - 20$	$770 - 860$	-	$10^{-4} - 10^{-3}$	1
$P_{O2}(BaCu_2O_2)$	$0.4 - 20$	$830 - 840$	10^{-5}	$10^{-4} - 10^{-3}$	10^{-6}
$P_{O2}(Cu)$	$0.17 - 20$	830	10^{-7}	$10^{-4} - 10^{-3}$	10^{-8}

TABLE 6.3: Growth condition limits of each investigated route: dT/dt, T_G, $P_{O2,G}$, $P_{O2,G}$ and $P_{tot,G}$ refer to heating ramp, growth temperature, initial and final P_{O2} and total pressure during growth. The base total pressure is $P_{tot,Base} = 5 \cdot P_{O2,Base}$.

Growth route	Composition	Substrate	t [nm]	$J_c(5K, 0T)$ [MA cm^{-2}]
T	(2-3)/(3-7)	STO/LSAT	$100 - 450$	$2.9 - 16.6$
$P_{O2}(BaCu_2O_2)$	(3-7)	STO	$100 - 800$	$3.1 - 34$
$P_{O2}(Cu)$	(2-3)/(3-7)	LAO	$100 - 900$	$1.4 - 8.9$

TABLE 6.4: Film compositions, substrates, thicknesses t and $J_c(5K, 0T)$ values of samples in tab. 6.3. The YBCO thickness is estimated through TEM/SEM cross-sectional images and the nominal molar concentration of films. J_c is obtained via inductive measurements (3.2).

The processing conditions are limited by several constraints. In the T - route, growth below 770 °C leads to enhanced homogeneous nucleation giving rise to randomly oriented YBCO grains (chapter 5 and [76]). The heating ramps are confined to $0.4 - 20°C\,s^{-1}$ to avoid substrate reactivity shown in the previous part (6.1.2). In the pressure routes, the $P_{O2} - T$ growth window is narrowed to the heterogeneous nucleation region encountered for these approaches [76, 94, 95]. $J_c(5K, 0T)$ values, obtained from inductive measurements (tab. 6.4) show a wide stray with a lower limit of 1-3 MA cm^{-2}. In particular, we want to answer here if the lowered critical current density could be attributed to a poor oxygenation of the YBCO structure.

Fig. 6.14a) summarizes the range of Hall carrier densities, $n_{H,300K}$, for films grown through the above mentioned processing conditions (3.4.2). Three of the Hall effect measurements are depicted in Fig. 6.14b), shown in the color code of each route. The slope dU_H/dB relates to the Hall coefficient R_H (eq. 3.9).[15] The latter yields the carrier density according to $R_H = 1/n_H q$.

[15] At known film thickness and applied current $I_{applied}$.

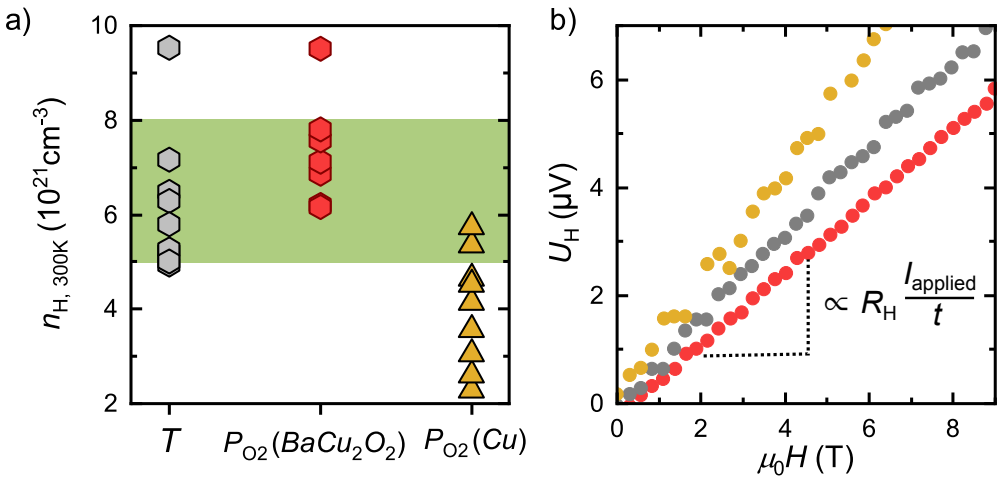

FIGURE 6.14: Overview of Hall measurements in Van der Pauw configuration: a) Room temperature Hall carrier densities, $n_{H,300K}$, for films from different routes. For $n_{H,300K} = (5\text{-}8)10^{21}$ cm^{-3} (marked in green) high $J_c(5K, 0T)$ and T_c values (>20 MA cm^{-2} and >90 K) are be obtained in TFA-CSD YBCO [105]. b) Raw measurements of the Hall voltage for one film of each route showing a difference in slopes.

The measured $n_{H,300K}$ values (Fig. 6.14a)) show a certain fluctuation in the range of $(5-9.5)10^{21}$ cm^{-3}, $(6-9.5)10^{21}$ cm^{-3} and $(2.6-5.7)10^{21}$ cm^{-3} for T-, $P_{O2}(BaCu_2O_2)$- and $P_{O2}(Cu)$-route, respectively. To conclude whether the achieved oxygen concentration is sufficient to allow for high critical current densities and critical temperatures, a green-colored region is included at $(5\text{-}8)10^{21}$ cm^{-3} being close to the optimally doped values reported for YBCO [203]. In particular, the denoted range has been identified as suitable to reach high $J_c(5K, 0T)$ and T_c values of >20 MA cm^{-2} and >90 K in TFA-CSD YBCO films [105]. As illustrated in Fig. 6.14a), TLAG films grown through the T- and $P_{O2}(BaCu_2O_2)$-route lie in the region where high superconducting performance is rendered possible. Considering the upper values of both routes, it is also noticeable that some films show a tendency towards the overdoped region, which is a very promising path for J_c improvement via increase of condensation energy but beyond the work of this thesis [105]. Films from the $P_{O2}(Cu)$-route, on the contrary, show a tendency towards $n_{H,300K} < 5{\cdot}10^{21}$ cm^{-3} which can be considered as underdoped.

The range of $n_{H,300K}$ values is in agreement with high transition temperatures obtained from electrical transport measurements. As shown in Fig 6.15, most films reach high critical temperatures above 90 K. A slight decline below 90 K becomes apparent for $P_{O2}(Cu)$-route grown YBCO films where we also observe the downward tendency in carrier concentration. The minor decline of

T_c values for the films with highest carrier concentrations ($>8{\cdot}10^{21}$ cm^{-3}) is also an expected behaviour in the overdoped regime and should be affirmed through additional analysis.

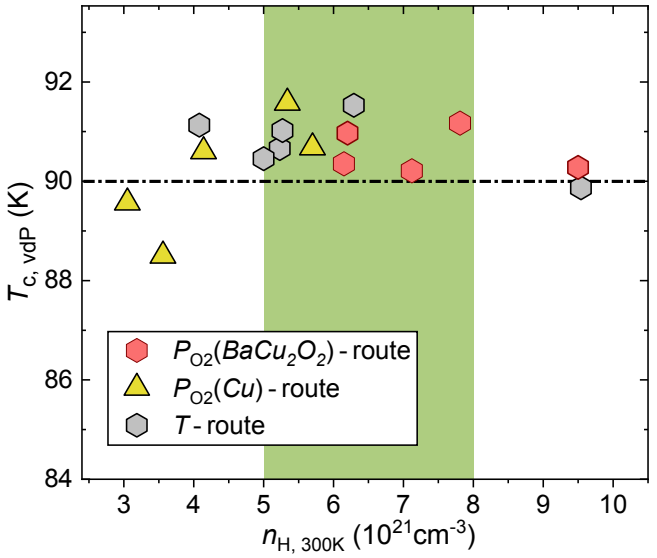

FIGURE 6.15: T_c dependence on charge carrier density $n_{H,300K}$ for films from different routes. For $n_{H,300K} = (5\text{-}8)10^{21}$ cm^{-3} (marked in green) high $J_c(5K, 0T)$ and T_c values (>20 MA cm^{-2} and >90 K) are be obtained in TFA-CSD YBCO [105].

The increased oxygen depletion in films from the $P_{O2}(Cu)$ - route can further be suggested taking into account the linearity of $\rho(T)$ measurements. Fig. 6.16a) shows the resistivity as function of temperature for three thin films (100-250 nm), one of each route. The curves are linearly fitted in the high temperature range of 150 - 300 K (eq. 3.10). An enhanced deviation from the linear dependence is observed for the film grown through the $P_{O2}(Cu)$ - route, from 150 K towards the transition (yellow curve). This is further confirmed through the normalized resistivity curves, $(\rho(T)\text{-}\rho_0)/cT$, in Fig. 6.16b). The downward trend is characteristic for underdoped films whose charges are partially trapped in pseudo-gap states and do not contribute to the normal state resistivity [203, 204]. Similar results are obtained for thick TLAG films (800-1000 nm) as shown in Appendix Fig. D.1. Notice that here again, we can observe for some films (in particular the $P_{O2}(BaCu_2O_2)$ -route sample in Fig. 6.16b)) an upturn of the normalized resistivity which would also be expected in the overdoped regime [105].

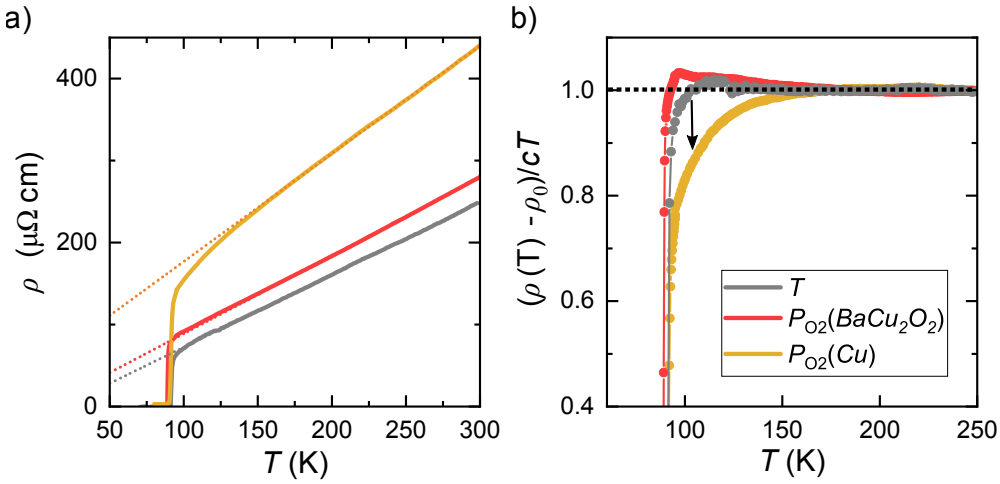

FIGURE 6.16: Resistivity measurements of samples from different routes. a) $\rho(T)$ dependence indicating a deviation from linearity towards T_c. Dashed lines are linear fits carried out at 150 - 300 K. The $\rho(T)$ curve of the $P_{O2}(Cu)$ - route film was devided by a factor of 2 for visibility reasons. b) Normalized resistivity $(\rho(T) - \rho_0)/cT$ as a function of temperature for the same three films.

A low oxygen concentration in $P_{O2}(Cu)$ - route grown films, as compared to the other routes, can also be sensed through structural analysis via high-resolution XRD measurements. As a result of bond-length variations, oxygen incorporation into the YBCO matrix yields a shrinkage of the c - axis lattice parameter [103]. Hence, a decrease of the charge carrier density, being a result of oxygen depletion in the Cu - O chains, typical comes along with an expansion in c .

Out-of-plane lattice parameters are determined through the Nelson-Riley method (3.5.3) and shown as a function of carrier densities in Fig. 6.17. The grey-shaded region marks a possible correlation between both quantities, in agreement to studies on TFA-CSD and PLD films where the oxygen content was modified intentionally [105]. Most of the $P_{O2}(Cu)$ - route grown films are found in the lower range of carrier densities having elongated c -axis lattice parameters (11.67 - 11.74 Å). The three films encircled by a dashed-black line are of 100 nm thickness, grown on LAO. Due to the smaller substrate in-plane lattice parameter of the (3.791 Å), as compared to YBCO (a=3.843 Å, b=3.881 Å), the increase in c values might also be affected by in-plane, compressive strain. However, strained films of 100 nm on LAO typically show an elongation of c towards 11.69 Å, at most [105]. The strong increase in c values should, therefore, not arise from strain contributions alone but be indeed affected by the reduced oxygen content in these films. For the other two routes

we can confirm that c-axis values are in agreement with an optimal oxygen doping of the YBCO crystal structure.

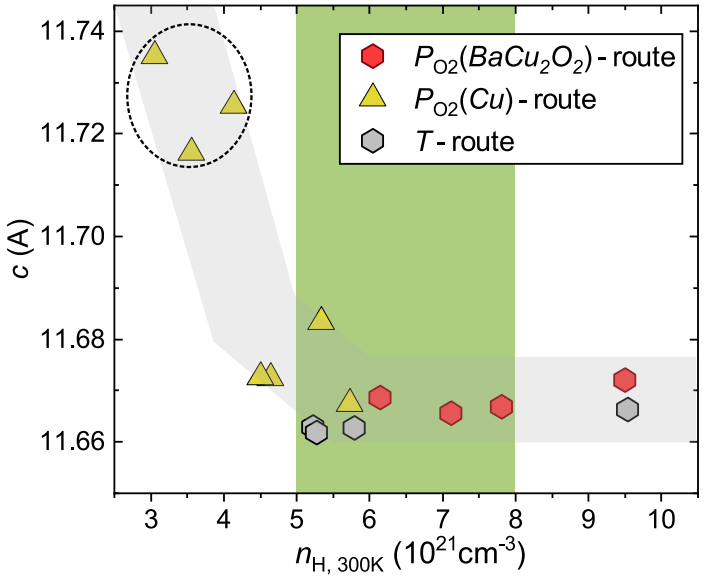

FIGURE 6.17: c-axis evolution with $n_{H,300K}$ for samples from different routes. For $n_{H,300K} = (5\text{-}8)10^{21}$ cm^{-3} (marked in green) high $J_c(5K, 0T)$ and T_c values (>20 MA cm^{-2} and >90 K) are be obtained in TFA-CSD YBCO [105]. Dashed black circle marks samples from the $P_{O2}(Cu)$-route showing a strong elongation of the lattice parameter.

In summary, we have evaluated the oxygenation state of TLAG samples and compared the physical properties with those of optimized films from the TFA-CSD process [105]. The range of carrier densities as shown here for the T- and $P_{O2}(BaCu_2O_2)$-route grown films is in agreement with the identified margin where high $J_c(5K, 0T)$ and T_c values are rendered possible in the TFA-CSD case. We can therefore conclude that decreased J_c values for YBCO films of both routes are not a result a poor oxygen doping. However, we find that oxygen incorporation meets additional hindrances in the case of $P_{O2}(Cu)$-route grown films, seen in a downward tendency of $n_{H,300K}$ values, elongation in the c-axis lattice parameter and increased deviation of $\rho(T)$ from linearity towards the critical temperature. A possible complication of oxygen incorporation in these films will further be suggested in the next section remains, however, subject of additional studies for this particular growth route.

6.1.4 Superconducting cross-section reductions

Up to now, we have analyzed several factors that could limit the performance of TLAG films, including the epitaxial quality of films, YBCO phase purity and oxygenation of the crystal structure. Within the course of this thesis, we concluded that none of these potential issues is relevant enough to yield a considerable decrease of J_c. Reactivity phases and contamination of the YBCO grain can either be avoided through tuning of processing parameters or choice of the growth route (6.1.2). Also the post-annealing process for oxygen incorporation into the YBCO crystal structure is found to be uncritical for most of the investigated films and routes. However, even for the optimized growth conditions, summarized in tab. 6.3 and tab. 6.4, there is a considerable deviation of J_c values in each route. In this section, we will evaluate the main reason we ascribe to possible J_c degradation in the TLAG process: Bad percolation due to reduction of the superconducting cross-section.
In order to examine the percolation nature of grown films and its correlation with critical current densities, we measured room temperature resistivity values, ρ_{300K}, in Van der Pauw 4-point geometry for a variety of films from different processing routes. The physical measure is sensitive to defects that alter the superconducting cross-section yielding to enhanced electron scattering in the normal state [193].
As a result, a universal correlation between inductively measured $J_c(5K, 0T)$ and ρ_{300K} values is found, independent of route and precise growth conditions. This is summarized in Fig. 6.18. An increase of J_c values is observed for $\rho_{300K} < 500\,\mu\Omega\,cm$. There must hence be an additional limitation that cannot be tracked through critical temperatures, neither through lattice parameters and the Hall carrier density, as done in the aforegoing part.
In particular, the clear correlation between both values has several implications for the TLAG process and future evaluations of the film quality:

1. Measurements of the room temperature resistivity can be used as a first assessment of the superconducting performance of films. Being a non-destructive, cost-effective and fast measurement procedure, the throughput of sample screening can be highly increased as compared to transport or inductive characterization.

2. ρ_{300K} values below $500\,\mu\Omega\,cm$ can be targeted to reach considerable improvements in critical current densities.

3. The optimized growth conditions of the T - and $P_{O2}(BaCu_2O_2)$ -route allow to go below this critical limit and reach high current percolation. In fact, the minimum values obtained here, ranging from 250-260 $\mu\Omega\,cm$,

settle amongst the lowest ones obtained for YBCO films of high crystalline quality [173, 205].

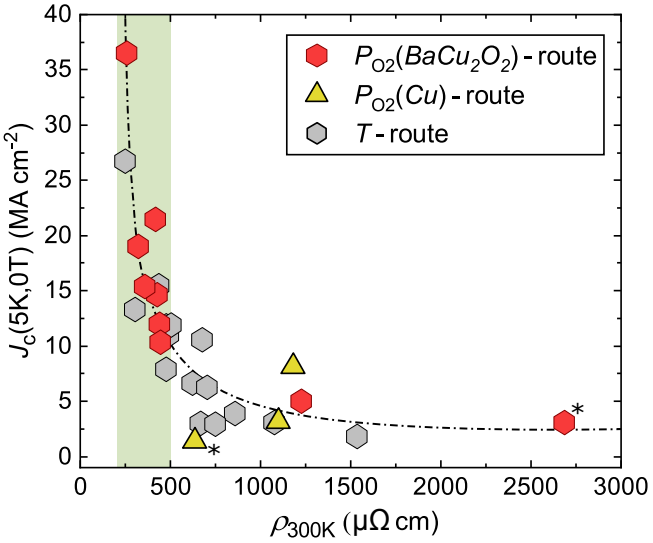

FIGURE 6.18: Scaling of inductively measured $J_c(5K, 0T)$ values with room temperature resistivities ρ_{300K}. Independent of the growth route, values follow a trend, shown by the dashed black line as guide to the eye. The majority of films lies in a thickness range of 100 - 400 nm; two thick films (800 - 1000 nm) are identified with asterisk symbols.

The scaling of critical current densities with resistivity values was already observed in previous work for TFA-CSD grown YBCO films [173, 193, 197]. The increase in normal state resistivity was attributed to the presence of pores, being the prime source of cross-sectional reduction in the TFA-CSD process. This was further confirmed through artificially induced pores via lithography techniques [109]. On the one hand, an increased amount of pores reduces the overall volume fraction of the epitaxial YBCO phase. Hence, the full YBCO volume, used in the critical state model to calculate J_c (eq. 2.8), breaks down into magnetization loops of minor radius and induces percolating currents. As shown by A. Palau et al. for films with significant high angle grain boundary contributions,[16] the measured J_c becomes a "percolating", grain-boundary current density J_c^{GB}, reduced as compared to the intragrain current density J_c^{Grain} [107, 108]. In the subsequent section we will introduce the method used to obtain both current densities.
On the other hand, an increase in pore density also affects the normal state

[16] Having the same impact on the current percolation as pores.

resistivity since additional interfaces are created and scattering of electrons promoted. However, since TLAG grown films exhibit a dense structure (Fig. 6.3) but tend to generate secondary phases due to the rapid process kinetics, we can propose that this is the actual origin of the trend depicted in Fig. 6.18, similar to porous films. In the following part we will hence summarize the main route-specific percolation hindrances through a set of TEM, XRD and inductive measurements.

To begin with the *T* - route, the approach relies on proper control of competing crystallization kinetics. For instance, it is shown in 6.1.2 that the use of the highest heating ramps (20 - 60 °C s^{-1}) yields liquid induced reactivity phases, formation of Y_2BaCuO_5 and badly wetted substrate areas close to those defects. As discussed previously, this is a result of extended time periods of liquid-to-substrate contact at high temperatures, allowing the reaction to take place. On the contrary, lowered heating rates promote homogeneous nucleation along the ramp. Though homogeneous grains are demonstrated to undergo reorientation upon further temperature increase, the mechanism can be hindered through coarsening of phases, for instance CuO segregations (5.2). These competing mechanisms are also evidenced through TEM analysis. An overview of macroscopic defects encountered in the *T* - route ($\leq$ 20 °C s^{-1}) is given in Fig 6.19. With copper-rich compositions we typically encounter an increase of large interruptions of the epitaxial layer. Such holes might result from bad wetting of the substrate by the liquid phase (Fig 6.19a), yellow arrows). Also large CuO segregations (> 100 nm) can be found impeding the connectivity of *c* - axis grains (Fig 6.19b)). Both defect types can be attributed to the copper enrichment of the composition. As shown through *in-situ* synchrotron experiments, CuO solid coarsening is only observed in (3 - 7) films (5.3.1). On the contrary, bad wetting in (3-7) compositions might arise from a low viscosity of melt (Fig. 5.10). This would promote an increased mobility of the (Ba - Cu - O) liquid, generating voids especially for low nucleation density conditions [76]. Note that the presence of voids and CuO segregations should not affect the intrinsic properties of the grain, yet limit the percolation through the grain (Fig. 6.18). In the *T* - route also ab-grains and YBCO grains of varying orientations are commonly encountered within the epitaxial layer (Fig 6.19c)). Such grains are typically accompanied by strong bending and distortions of the surrounding YBCO lattice which can be beneficial for the pinning performance if they are kept in the nanometer size range (see chapter 7). However, it is evident that the formation of grains with growth directions other than c - YBCO is more probable in this route due to crossing of the large YBCO stability window (Fig. 4.25).

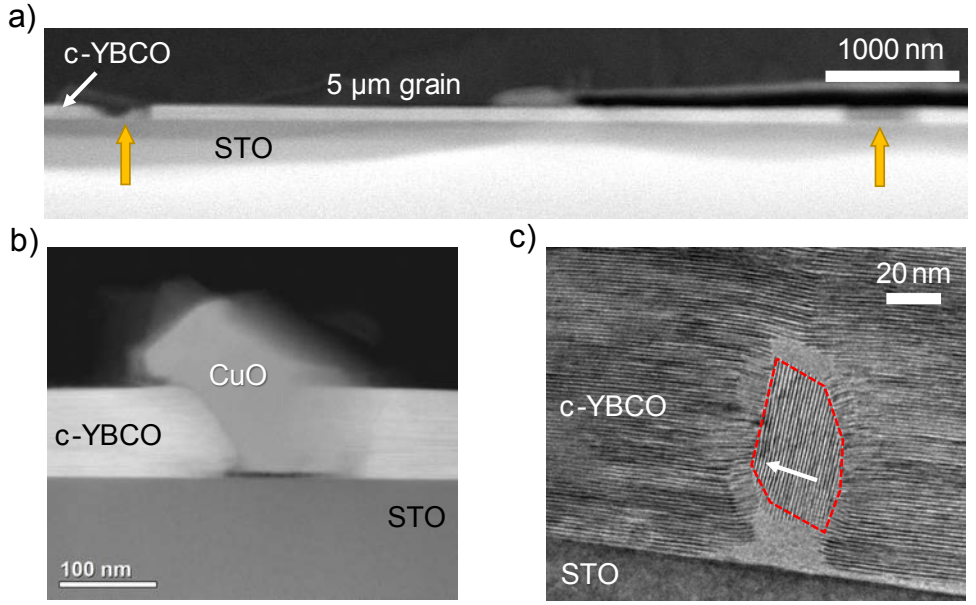

FIGURE 6.19: TEM overview of percolation hindrances in T - route grown films. Images show a) areas of bad substrate wetting and b) CuO solid segregations for films of (3-7) composition. c) Embedded, misoriented YBCO grain in the c - axis layer. Observed in films of (2-3) composition.

The fundamental change of YBCO growth through the pressure routes reflects in the observed microstructural differences. The main percolation hindrance identified in the $P_{O2}(BaCu_2O_2)$ approach is the increased formation of ab-grains.[17] Inductively measured $J_c(77K, 0T)$ values are found to decrease with the volume fraction of ab-oriented grains for films of same thickness, processed at P_{O2} =$10^{-4} - 10^{-3}$ bar and T = 800-830 °C (Fig. 6.20). The volume fraction is calculated through a similar methodology as proposed in [207]. Here, an in-plane reflection, in our case the (102) plane, is fully integrated through 2D-XRD scans (GAADS, ω - scans). As ab- and c-oriented grains have a displacement of the same reflection in χ, the ratio of integrated (102) intensities can be converted to volume fraction, considering the geometrical change in X-ray spot size upon χ variation [207].
TEM images confirm that ab-grains are the predominant source of cross-section reductions and additional interfaces (Fig. 6.20b)). In the T - route, the volume percentage of ab-grains in this range of P_{O2} - T conditions and 20 °C s^{-1} does not surpass 2%, considerably lower than that observed here

[17] Due to the high resistivity of YBCO in c - axis direction, ab-grains are considered to block the percolating current [206]

in the $P_{O2}(BaCu_2O_2)$ - route [76]. The supersaturation in the pressure approach can hence be suggested higher than in the T - route, given the increased amount of ab-nucleation.[18] Therefore, fine tuning of process conditions is required to avoid ab-grain formation and ensure full c-axis epitaxy.

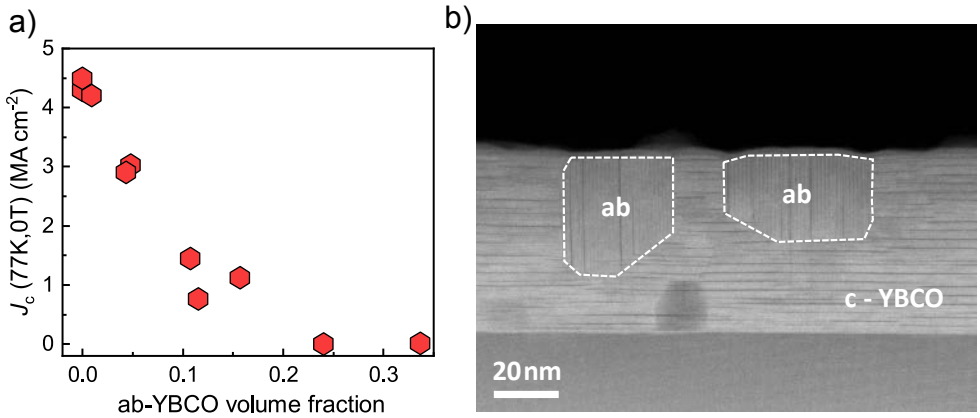

FIGURE 6.20: Main percolation hindrance in the $P_{O2}(BaCu_2O_2)$ - route: a) $J_c(77K, 0T)$ evolution with ab-YBCO volume fraction, determined through GAADS ω - integration and application of the methodology in [207]. b) STEM image showing the inclusion of ab-grains in the epitaxial layer as direct limitation to the conducting cross-section of the film.

In agreement with the $P_{O2}(BaCu_2O_2)$ - route the increased ab-nucleation is also confirmed in the $P_{O2}(Cu)$ approach [94]. However, the more severe inter-grain limitation of this route can be attributed to coarsening of the metallic copper in the low pressure step. Fig. 6.21a) shows an overview of EELS maps acquired for three films that are quenched in the low pressure step. Heating is performed through different ramp profiles (see labels) towards the growth temperature in order to study the influence of the ramp on copper coarsening. Although metallic copper sizes appear to diminish from > 200 nm at 0.4 °C s^{-1} to a finer spread in the mixed ramp profile and at 5 °C s^{-1}, local segregation of larger grains (80 - 200 nm) persist in both cases.
Accordingly, the coarsened copper creates local off-stoichiometry that can severely affect the growth kinetics. Some of the phases and compositions that could be identified in the grown films are shown in Fig. 6.21b). Apart from the metallic copper itself, having oxidized to CuO, the grown films can contain Y_2O_3 and BaO precursor phases and other (Y - Cu - O) and (Ba - Cu - O) products, all of which will severely affect the percolating performance of the films. Therefore, this route seems to be the most complicated one in avoiding

[18] A higher supersaturation would decrease the Gibbs free energy barrier for heterogeneous ab-nucleation yielding an increased ab-volume fraction (Fig. 6.20).

percolation hindrances since the formation of metallic Cu delays all successive reactions and promotes coarsening of the non-reacted phases.

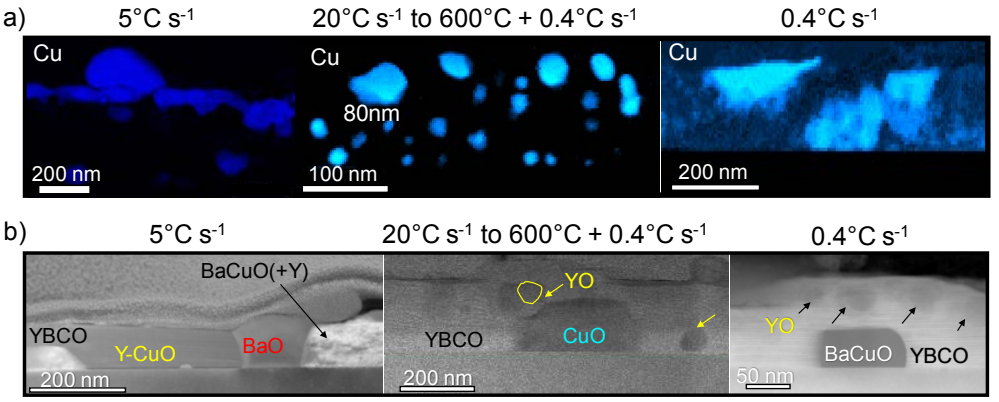

FIGURE 6.21: Limitations to current percolation in $P_{O2}(Cu)$ - route: a) EELS mapping of quenched films from the vacuum step (at $P_{O2,Base} = 10^{-7}$ bar, $T = 830°C$). Different heating ramps (included as labels) are used to study the effect of metallic copper coarsening. b) TEM images of representative grown film processed through same thermal history as in a) (at $P_{O2,Growth} = 10^{-3}$ bar $T_{Growth} = 830°C$).

In summary, it can be suggested that the current carrying capacity of TLAG films primarily relies on the effective cross-section of the epitaxial layer which can be reduced through route-specific secondary phases, misoriented YBCO grains and voids in the structure. As discussed in the introductory part, the network of macroscopic defects would result in a diminished percolating critical current density. However, we could also demonstrate that TLAG films with a normal state resistivity below 500 μΩ cm can be obtained through the T- and $P_{O2}(BaCu_2O_2)$ - route, reaching a minimum of 240 - 260 μΩ cm and high critical current densities up to 20 MA cm^{-2} (T - route) and 36 MA cm^{-2} ($P_{O2}(BaCu_2O_2)$ - route) using the optimised growth conditions of both approaches. Comparable resistivity values are reported for YBCO films of high crystalline quality [173, 205]. In addition, the correlation between J_c and ρ_{300K} values is further proposed as viable tool for a first assessment of the superconducting performance through Van der Pauw measurements. The approach might allow for a higher throughput of screened samples and be used to facilitate the exclusion of growth conditions.

6.1.5 Electromagnetic grain size influence on percolating currents

In order to obtain information about the actual state of the YBCO grain (J_c^{Grain}) and conclude that the sole potential limitation to TLAG grown films is due to

cross-sectional reductions, we employ a methodology that enables to evaluate the electromagnetic granularity of the film. The method was developed in the PhD thesis of Anna Palau and employed in several studies using YBCO films [16, 107–109, 193, 197]. The inductive, non-invasive technique, also referred to as *Palau method*, allows to obtain simultaneous information on the critical current density within the grains, J_c^{Grain}, and across the grain boundaries (percolating current density), J_c^{GB}, through DC magnetization minor loops.

As reported in [16, 109], electromagnetic granularity typically manifests itself in a characteristic feature of the magnetic hysteresis loop. The elsewise symmetric curve reaching the maximum magnetization at $\mu_0 H_{\text{applied}} = 0\,\text{T}$ for films, develops an asymmetric displacement of the magnetization maximum towards positive applied magnetic field values $\mu_0 H_{\text{applied}} > 0\,\text{T}$. The same feature is observed for TLAG films with varying degrees of secondary phases.

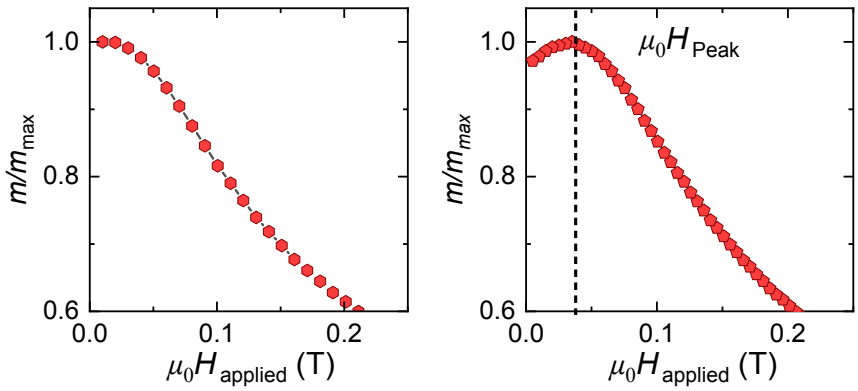

FIGURE 6.22: Normalized magnetic hysteresis at $T = 5\,\text{K}$ for two samples with increasing degree of electromagnetic granularity (left to right). The granular sample shows an asymmetric peak in the hysteresis loop at $\mu_0 H_{\text{Peak}} > 0$. Both samples are grown through the $P_{O2}(BaCu_2O_2)$ - route giving a YBCO thickness of 100 nm.

Normalized hysteresis loops of two TLAG films grown through the $P_{O2}(BaCu_2O_2)$-route are shown in Fig. 6.22, reaching a $J_c(5\text{K}, 0\text{T})$ of $36\,\text{MA}\,\text{cm}^{-2}$ and $5\,\text{MA}\,\text{cm}^{-2}$, respectively. The film with reduced current density shows a pronounced peak at $\mu_0 H_{\text{Peak}} = 0.04\,\text{T}$. The film of lowered $J_c(5\text{K}, 0\text{T})$ has an increased room temperature resistivity of $1230\,\mu\Omega\,\text{cm}$, well above the critical threshold we defined in the previous section, while the high J_c film reaches $260\,\mu\Omega\,\text{cm}$. Hence, the appearance of a peak in the hysteresis

loop coincides with the presence of secondary phases and percolating hindrances in the YBCO film.
The origin of the peak can be understood considering the evolution of magnetic field lines upon ramping of $H_{applied}$. Fig. 6.23a) shows a schematic representation of a granular film when the magnetic field is increased after a zero field cool (ZFC). The magnetic field penetrates the entire superconducting film crossing grains and grain boundaries.

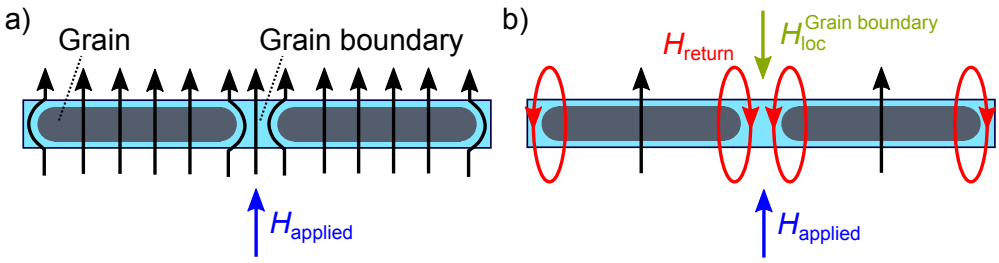

FIGURE 6.23: Schematic representation of magnetic field distribution in a granular film upon a) ramp up and b) decrease of the applied magnetic field. Adapted from [197].

Upon decrease of $H_{applied}$ (Fig. 6.23b)), the field lines will no longer return at the sample edges, as it would be the case for a single crystal, but through the network of non-superconducting phases and grain boundaries. The local magnetic field at the grain boundary H_{loc}^{GB} can be expressed as the vectorial sum over applied and return field $H_{applied}$ and H_{return}, giving

$$H_{loc}^{GB} = H_{applied} - H_{return}. \tag{6.2}$$

Maximum magnetization is reached when applied and return field cancel out, hence $H_{loc}^{GB} = 0$. Upon further decrease of $H_{applied}$ to 0, local and return field will be equal, $H_{applied} = -H_{return}$ yielding a reduction of the overall magnetization and a peak in the return branch (Fig. 6.23b)). Now, the position of H_{Peak} depends on whether the maximum applied field, H_m, is sufficient to saturate all grains. Therefore, when the applied field is cycled towards increasing set point values H_m, the peak position shifts until saturation at $H_m(H_{peak}^{Sat})$. Exemplary DC magnetic field cycles are depicted in Fig. 6.24a). The peak evolution is further shown in the inset.

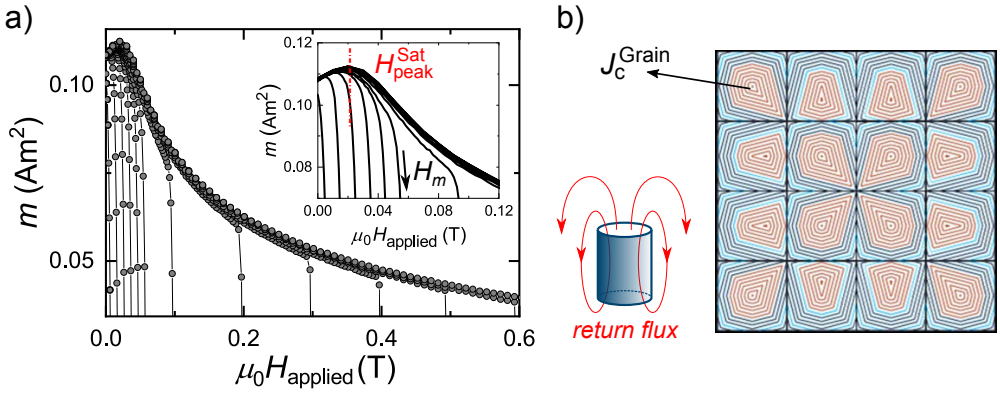

FIGURE 6.24: Illustration of the *Palau method* using the example of a granular TLAG film grown on STO substrate: a) Magnetic hysteresis loops at 5 K with DC-field set values of $\mu_0 H_m$ =0.01-0.8T. Inset shows a magnification of the peak saturation at H^{sat}_{peak} when a sufficiently high field H_m is applied. (b) Schematic picture of current stream lines in a granular sample. Non-superconducting secondary phases, weak-links, voids etc. break down the sample into finite current domains. Each domain (cylindrical representation on the left) allows for a return field at the grain boundary.

Fig. 6.24b) shows the current stream lines for a granular film whose grain magnetization is saturated [16]. The bean critical state model now applies to each single grain with critical current density J_c^{Grain} (shown in red). It is demonstrated that the measured J_c from the remanent magnetization is solely determined by the percolating current of the grain boundaries [197]. The actual J_c^{Grain}, hence, remains hidden through the standard measurement approach (see 3.2). The *Palau method* relates the saturated peak position H^{Sat}_{peak} and the applied saturation field $H_m(H^{Sat}_{peak})$ to the actual intragrain current density J_c^{Grain} and an average electromagnetic grain size D according to

$$J_c^{Grain} = \frac{H_m(H^{Sat}_{peak})}{2 f_1 D} \tag{6.3a}$$

$$\frac{H^{Sat}_{peak}}{H_m(H^{Sat}_{peak})} = f_2. \tag{6.3b}$$

Here, f_1 and f_2 are numerically calculated dimensionless functions that depend on the ratio D/t of grain diameter and thickness, respectively.[19] The determination of J_c^{Grain} and D is done through tracking of the peak position and maximum applied magnetic field H_m. A plot of these two values

[19] The full theoretical framework can be found in [16].

at three different temperatures is exemplary shown in Fig. 6.25a) for a TLAG film grown through the T - route. The obtained J_c^{Grain} values are further shown in Fig. 6.25b) together with J_c^{GB} (determined from eq. 2.8).

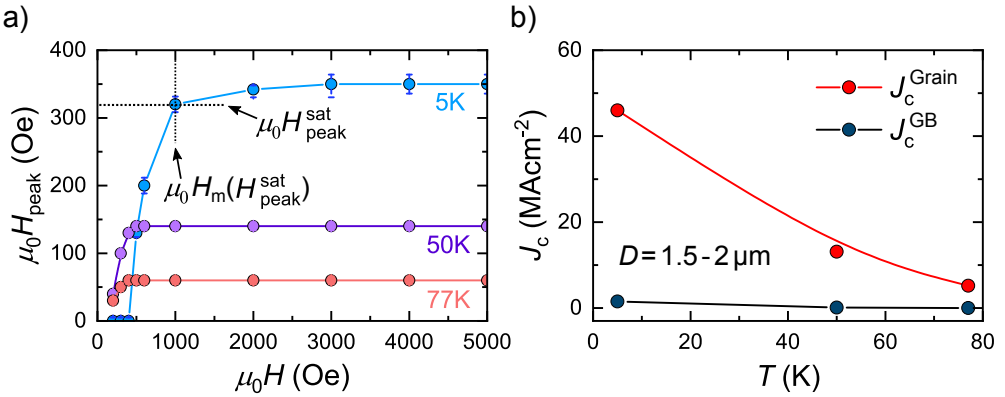

FIGURE 6.25: Exemplary determination of J_c^{Grain} and the electromagnetic grain size D through *Palau method* on a film grown through the T - route, 250 nm in nominal thickness: a) Evolution of the hysteresis peak upon ramping of the magnetic field to increasing H_m values at 5 K, 50 K and 77 K. The peak position saturates at H^{sat}_{peak} and an applied field value of $H_m(H^{Sat}_{peak})$. J_c^{Grain} and D are then determined through eq. 6.3a and 6.3b. b) Temperature dependence of grain and grain-boundary critical current density J_c^{Grain} and J_c^{GB}.

It appears that at any given temperature the grain critical current is increased. For instance, $J_c^{Grain} = 46\,MA\,cm^{-2}$ at 5 K, while $J_c^{GB} = 1.54\,MA\,cm^{-2}$. Similarly at 77 K, J_c^{Grain} reaches $5\,MA\,cm^{-2}$, while J_c^{GB} is reduced down to $0.2\,MA\,cm^{-2}$. This is an indication that the reduction of J_c^{GB} does not arise from grain contamination and that the full avoidance of percolating hindrances would allow an increase of the critical current density towards $46\,MA\,cm^{-2}$ at 5 K and $5\,MA\,cm^{-2}$ at 77 K.

To further confirm that the actual grain critical current is unaffected, the analysis is extended to films processed in the optimized conditions of the different routes (tab. 6.3 and 6.4). An overview of J_c^{Grain} and J_c^{GB} values achieved with each approach is given in Fig. 6.26a). J_c^{Grain} values (full symbols) for the $P_{O2}(BaCu_2O_2)$ - and T - route lie in the range of 46 - 82 $MA\,cm^{-2}$. The fluctuation in J_c^{Grain} might be a result of varying pinning landscapes, as will be motivated in chapter 7. The values compare with the highest reported critical current densities for YBCO CSD and PLD grown films, suggesting that any degradation of the critical current densities (open symbols) is of granular nature. In fact, values in the range $82\,MA\,cm^{-2}$ are not obtained by default for

YBCO films and have so far only been achieved through sophisticated additional oxygenation procedures [105].

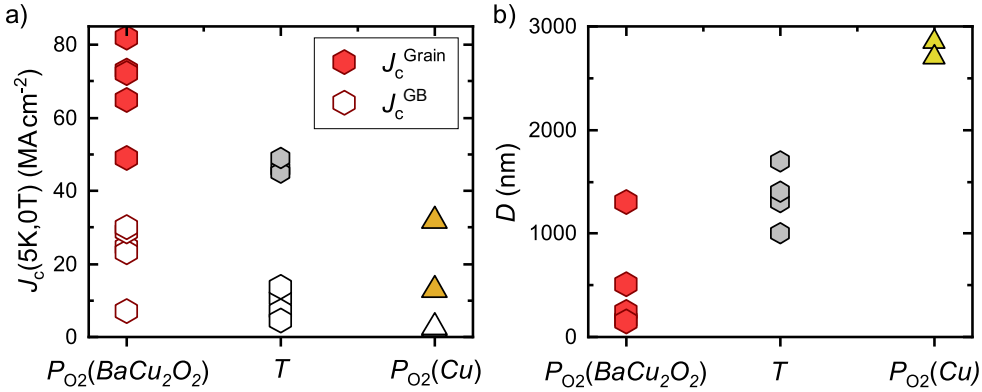

FIGURE 6.26: Summary of results from the *Palau method* for TLAG films from different routes: a) Grain and grain-boundary critical current density J_c^{Grain} and J_c^{GB} at 5 K. b) Electromagnetic (EM) grain size D.

In the $P_{O2}(Cu)$-route, however, J_c^{Grain} is found comparably reduced (13-32 MA cm^{-2}). As suggested in 6.1.3, grown films from this route might have the additional obstacle of oxygen incorporation after growth. The reduced J_c^{Grain} might hence reflect the higher oxygen depletion in these samples. This might further be proposed considering the electromagnetic grain sizes in Fig. 6.26b). While $D \leq 1.7$ µm for all films of the former two routes, $P_{O2}(Cu)$-route grown films give increased values of 2.7 µm. Whether the oxygen incorporation in these films is hindered due to an increase in grain sizes or a larger amount of secondary phases blocking the diffusion (Fig. 6.21) should be considered in additional studies. For instance, electrical conductivity relaxation measurements, as carried out in [105], should give insights into oxygen diffusion kinetics.

The discrepancy of J_c^{Grain} and J_c^{GB} can be primarily attributed to the route specific percolation hindrances, summarized in 6.1.4. The presence of non-superconducting volume can yield to cross-sectional reductions and an overall granular behaviour, as reported for porous films and coated conductors with considerable grain-boundary contributions [16, 109]. For TLAG films, a correlation is further found between grain sizes D and J_c^{GB}. The route-independent tendency is shown in Fig. 6.27. Highest percolating current densities are achieved in the $P_{O2}(BaCu_2O_2)$-route where the average grain size can reach minimum values of 150 nm. The dependence of the percolating critical current density on grain sizes was earlier suggested by V. Solovyov et al.

[170, 208]. Larger grains would yield to an increased accumulation of undesired material at the grain boundaries and lead to the deterioration of the grain boundary quality.

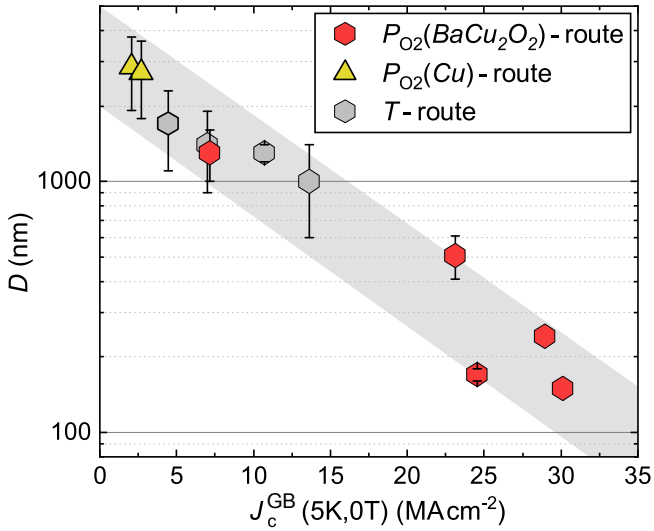

FIGURE 6.27: Correlation of electromagnetic grain sizes D with the grain-boundary critical current density J_c^{GB}. Different routes further show a separation in the achievable grain size.

A grain size contribution might further be suggested considering only $P_{O2}(BaCu_2O_2)$ - route grown films. As shown in Fig. 6.27, one particular sample has a reduced J_c^{GB} and increased D as compared to the rest. Growth conditions and results from the *Palau method* for these five films are summarized in tab. 6.5. The similarity in grain critical current densities, within a range of 50 - 82 MA cm^{-2}, cannot explain a decrease of J_c^{GB} down to 7 MA cm^{-2} (marked in red).

In the previous sections we have identified two potential sources that can reduce the conducting cross-section of $P_{O2}(BaCu_2O_2)$ - route grown films, oriented $BaTiO_3$ particles (Fig. 6.12) and YBCO ab-grains (Fig. 6.20). Fig. 6.28 depicts θ - 2θ XRD-scans in a range where both limiting phases can be observed. The four films with electromagnetic grain sizes of 150 - 500 nm are shown in green, the film with $D = 1300$ nm is depicted in red. The $BaTiO_3$ (110) and YBCO (200) signal of the film with strongly reduced J_c^{GB} is not superior to the rest of the samples. Hence, it can be proposed that apart from the amount of undesired phases an additional role is attributed to their distribution. Decreased grains sizes are an indication of high nucleation density and a diminished pushing effect of undesired elements towards the grain boundaries.

Hence, the grain-boundary quality enhances allowing for higher percolating currents [170, 208].

T_{Growth} [°C]	$P_{\text{O2,Growth}}$ [bar]	EM D [nm]	J_c^{GB} [MA cm^{-2}]	J_c^{Grain} [MA cm^{-2}]
820	$5 \cdot 10^{-4}$	500	23	65
820	$5 \cdot 10^{-4}$	150	28	72
830	$5 \cdot 10^{-4}$	240	30	82
830	10^{-3}	170	25	73
830	10^{-3}	1300	7	50

TABLE 6.5: Comparison of electromagnetic grain sizes D, grain and grain-boundary critical current density J_c^{Grain} and J_c^{GB} for five films processed at T_{Growth} and $P_{\text{O2,Growth}}$ through the $P_{O2}(BaCu_2O_2)$ - route. Values that show a strong deviation from the rest are included in red.

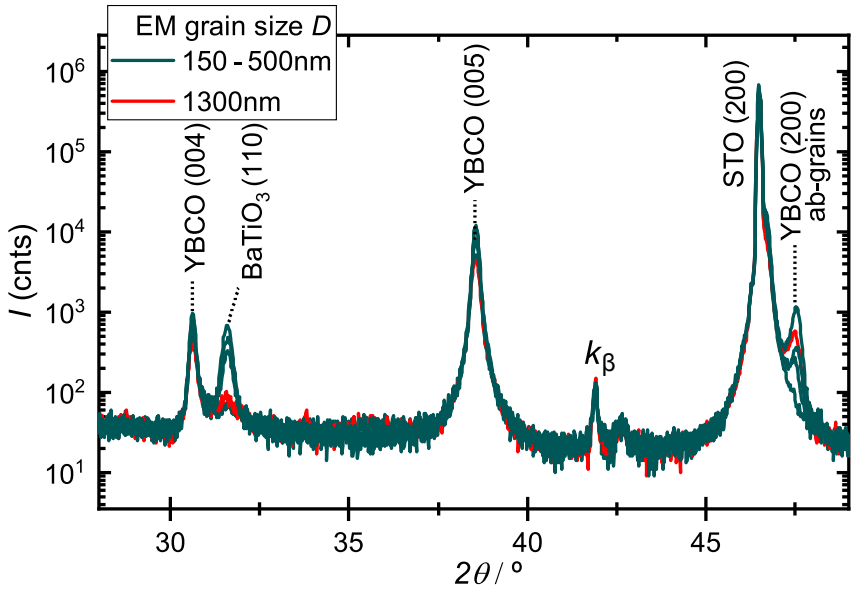

FIGURE 6.28: XRD measurements in $\theta - 2\theta$ configuration of the five films in tab. 6.5. Samples with $D = 150$ - 500 nm are shown in green, the film with increased D of 1300 nm is depicted in red.

In summary, we perform a series of inductive measurements on TLAG samples that exhibit a peak in the positive return branch of the magnetic hysteresis loop. The feature is characteristic for films, which accumulate non-superconducting matter within the layer [16, 109, 193]. Since grain contamination and strong oxygen depletion of the YBCO structure could be excluded in the previous part as detrimental influence on the superconducting performance, we attribute the decrease in measured J_c primarily to route-specific, cross-sectional reductions, as summarized in 6.1.4. This is demonstrated through the high intragrain critical current densities obtained by the *Palau method*. In addition, achieving epitaxial YBCO growth at reduced grain sizes (i.e. high nucleation density) might be a necessity to contain any competing secondary phase formation and avoid deterioration of the grain boundary quality. Overall, the control of the nucleation density should be undertaken through proper tuning of the supersaturation conditions.

6.2 Current limitations in TLAG nanocomposite films from colloidal solutions

In order to enhance the pinning performance of TLAG grown pristine films, we explored the embedment of preformed $BaZrO_3$ (BZO) and $BaHfO_3$ (BHO) nanoparticles (NP) from colloidal solutions into the YBCO crystal structure. In CSD methods, NPs can either be synthesized simultaneously during YBCO growth through spontaneous segregation, or independently stabilized and incorporated into the initial YBCO precursor solution. The later approach is used here and termed *preformed nanoparticle method*, since NP synthesis and YBCO growth are decoupled.
As discussed in 2.1.6, various approaches have been developed over the past few decades to introduce defects that create localized regions with low superconducting order parameter. In these, so-called, nanocomposite (NC) films, the pinning landscape proves effective if the defect density matches the vortex density at sizes of the vortex core diameter $2\xi \approx 4\text{-}5\,\text{nm}$. In addition, defect dimension (0D, 1D, 2D or 3D) and orientation will heavily alter the angular and in-field performance of films.
The approach followed here is one of the most promising strategies with regard to improving the in-field behaviour while reducing angular anisotropy of the laminar YBCO structure. In particular, the use of NPs from colloidal solutions provides a base for:

1. **Controlled tuning of NP characteristics:** The prime benefit of preformed NP synthesis is that it enables a precise pre-determination of NP size and shape allowing to reach smaller sizes than the *in-situ* methods.

If, in addition, process parameters are optimized to avoid NP coarsening during growth of YBCO, the use of preformed NPs allows for higher particle densities and lower sizes as compared to spontaneous segregation methods [209].

2. **Increased isotropic pinning:** NPs trigger the formation of secondary defects, such as stacking faults (SF) and vacancies [116]. This is an effect of stress relaxation when mismatched particles accommodate in the YBCO structure. While most NPs typically exceed the vortex core diameter, and do not pin vortices by themselves, the associated secondary defects do provide a pinning landscape. The performance of YBCO nanocomposite films is found to be decreased in anisotropy as compared to pristine YBCO [40, 41].

3. **Isotropic core pinning:** The additional pinning of vortices by NPs themselves would yield a strong performance increase. Up to very recently, core pinning could only be achieved through self-assembled PLD nanorods whose diameter matches 2ξ. Unfortunately, nanorods are 1D defects that enhance pinning in a certain range of angles of the applied magnetic field. Recent efforts in NP miniaturization and employment of high heating ramps have shown, however, that NPs can also be embedded at nanometric sizes [210].

The compatibility of preformed $BaMO_3$ (M = Zr, Hf) nanoparticles (NP) with CSD methodologies was earlier demonstrated by the SUMAN group for YBCO growth through solid-solid reactions [30, 116, 209, 210]. Here, however, we deal with a corrosive melt that can potentially dissolve any of the utilized single crystal substrates and an ultrafast growth process that might push all the NPs to the film surface. It is, hence, of prime importance to demonstrate that the use of NPs in the TLAG approach is also feasible. Furthermore, we want to address the question which impact the addition of nanoparticles has on the final YBCO physical properties discussed in the previous sections.
The analysis is confined to NC films grown through the $P_{O2}(BaCu_2O_2)$ - route. All the work done on the optimization of NC growth through different TLAG routes and on the stability of NPs in the YBCO solution was carried out in the PhD thesis of J.Jareño [95]. The films analyzed here in physical properties are of 100 nm in thickness, crystallized at $T_{Growth} = 830\,°C / 835\,°C$ and $P_{O2} = 10^{-3}$ bar, which are the optimized conditions defined in [95]. Tested NP concentrations were 6%, 12%, 24% and 32% in molar percentage.

6.2.1 Limitations to high critical current densities

Similar to the discussion made on pristine YBCO films (6.1), we aim to define, at first, the main limitations in order to know how to overcome those and obtain high performance TLAG nanocomposite films. NC films of high epitaxial quality could be fabricated in the optimized conditions of the $P_{O2}(BaCu_2O_2)$-route. Fig. 6.29 shows an overview of high resolution XRD measurements carried out on samples of varying NP concentration (see labels). Primarily YBCO (00l) and STO (h00) reflections are recorded in the θ-2θ configuration (Fig. 6.29a)). The presence of NPs does not show a strong influence on the degree of epitaxial grain alignment. This is confirmed through ω- and ϕ-scans in Fig. 6.29b) and c). $\Delta\omega$ and $\Delta\phi$ values below 0.6 ° and 0.8 ° lie within the range of values we find for pristine TLAG films (Fig. 6.1).
Although all films exhibit a high epitaxial grain alignment, the inductively determined critical current density strongly varies with NP percentage. Fig. 6.30a) shows an overview of self-field J_c values at 5 K and 77 K as a function of the NP amount. The fluctuation of the critical current density for samples of the same nominal NP percentage is given by the error bars. High $J_c(5K, 0T)$ and $J_c(77K, 0T)$ values in the range of 15 - 23 MA cm^{-2} and 1 - 5 MA cm^{-2} are obtained only for films containing 6% and 12% of BZO/BHO. Further increase of the NP amount to 24% and 32% results in a drop of J_c by one order of magnitude.
The primary cause of cross-section reduction in the $P_{O2}(BaCu_2O_2)$-route was up to now attributed to the increased formation of ab-YBCO grains (6.1.4). This is further confirmed for TLAG nanocomposites as seen in Fig. 6.30b) for films containing 6% and 12% of BZO/BHO. Above an ab-volume fraction of 5%, the critical current density is considerably reduced down to 0.2 - 0.5 MA cm^{-2}.

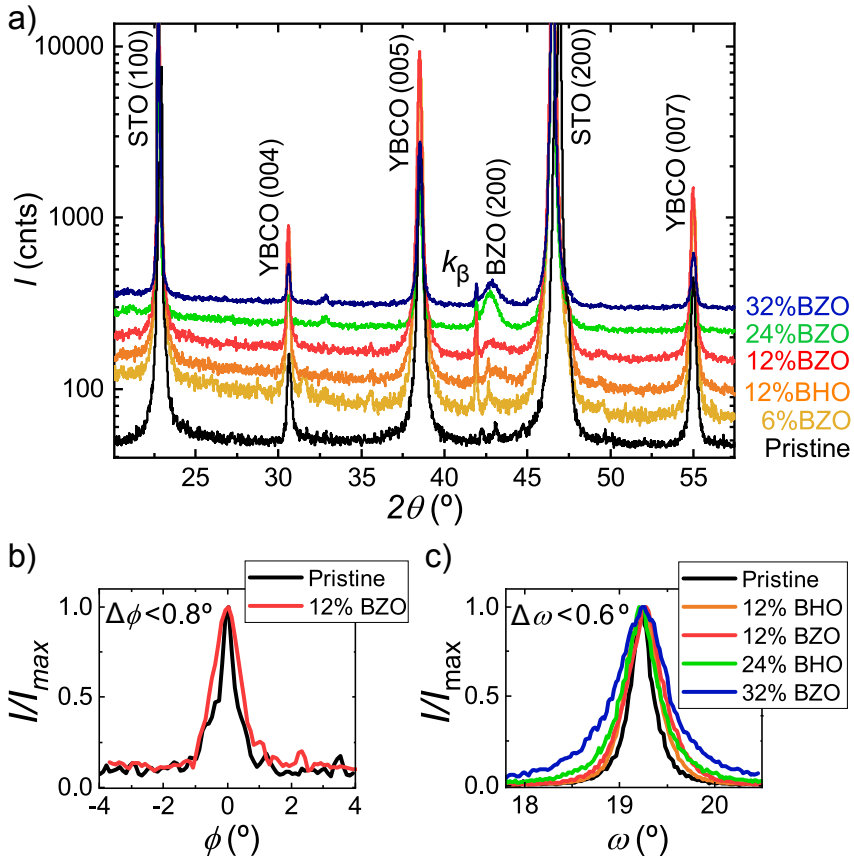

FIGURE 6.29: Overview of XRD analysis on TLAG nanocomposite (NC) films: a) $\theta - 2\theta$ measurements of NC films with varying percentages of nanoparticles (NP) ranging from 6% to 32% of $BaZrO_3/BaHfO_3$ (short: BZO/BHO). A pristine film is included for comparison. b) ϕ-scans of (102) reflection and c) Rocking curves (ω-scans) of (005) reflection for pristine and NC films.

The critical threshold of 5% appears lowered as compared to pristine films (Fig. 6.20). Here, $J_c(77K, 0T)$ values could be maintained in a range of 0.8-1.5 MA cm^{-2} above 10% of ab-YBCO, indicating that the presence of NPs can additionally complicate the current percolation. This is confirmed by STEM measurements of films with varying NP concentration. Fig. 6.31 depicts the cross-section of a 12%BZO and 24%BHO NC film of 2.2 MA cm^{-2} and 0.2 MA cm^{-2} at 77K, respectively. The sample with lower concentration

is found to have a better dispersion of small NPs leaving enough c-YBCO volume for the percolation of current. At increased NP percentages, a higher degree of NP agglomeration is observed (Fig. 6.31, right-hand side). The cross-section image shows an ab-grain of 40 nm in addition to a high degree of NP accumulation.

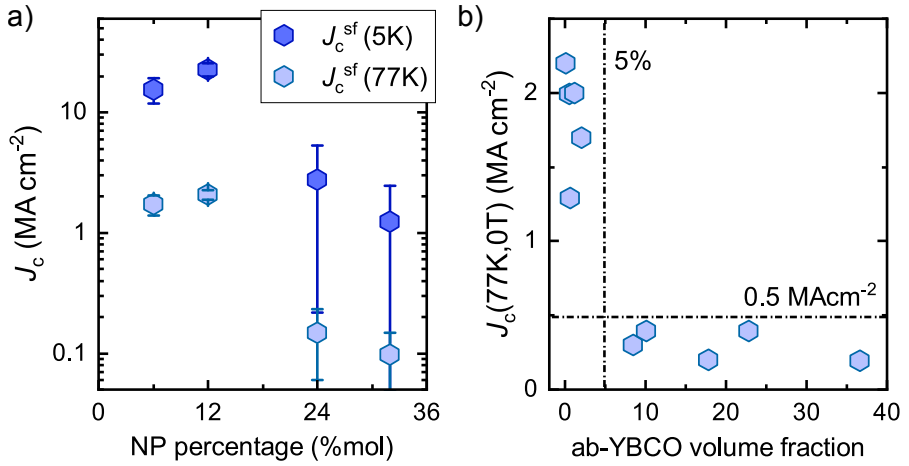

FIGURE 6.30: a) Dependence of inductively measured J_c values at self field, 5 K and 77 K, on NP percentage. Error bars summarize the fluctuation of obtained values at the same NP percentage. b) Ab-grain volume fraction for films containing 6 % and 12 % of BZO/BHO as a function of J_c(5 K,0 T).

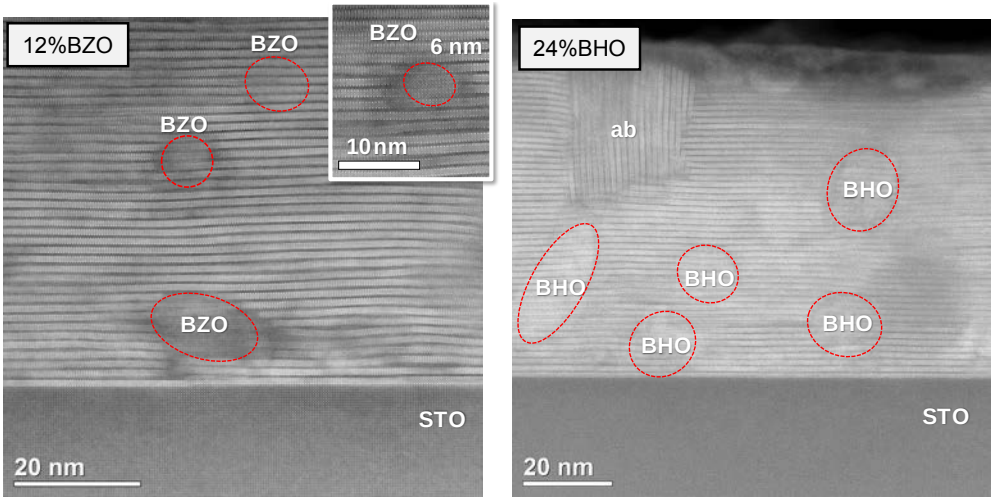

FIGURE 6.31: STEM images of a 12 % BZO and 24 % BHO NC film, left- and right-hand side, respectively. Inset shows that particles of 6 nm in diameter can be found in the YBCO layer.

The increased ab-grain fraction and NP agglomeration are summarized to be the sole limitation to high percolating currents in TLAG NC films [95]. We will further confirm here that critical temperatures and Hall carrier densities show no indication of grain contamination nor a low oxygen content (6.2.2). While the proper embedment of NPs is subject of on-going research and in constant feedback with the growth optimization of pristine YBCO growth, it is important to point out that high critical current densities can be achieved for NC films through the TLAG process. In fact, inductive measurements of the intragrain critical current density J_c^{Grain} suggest promising film performance if percolative hindrances can be fully avoided. An exemplary measurement of the magnetic hysteresis loop following the *Palau method* (6.1.5) is shown in Fig. 6.32a).[20] The resulting J_c^{Grain} values for samples of increasing NP percentage are summarized in Fig. 6.32b).
As compared to pristine films, lying in a range of 48 - 83 MA cm^{-2}, higher critical current densities with a maximum of 138 MA cm^{-2} are obtained for NC films. This indicates an increased pinning performance of films with NP addition and the successful integration of the secondary phases into the YBCO.

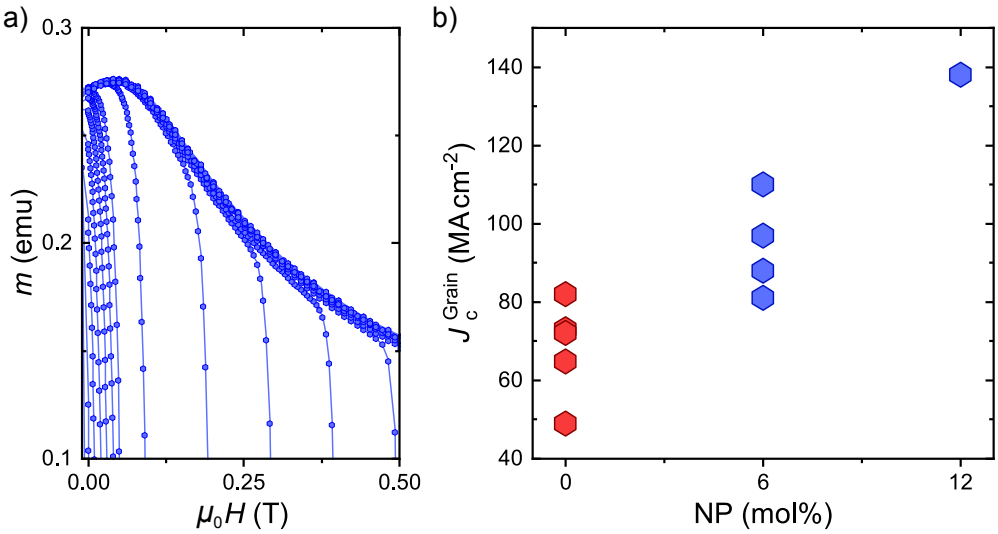

FIGURE 6.32: Application of *Palau method* on NC films: a) Magnetic hysteresis loops at 5 K for a 6% BHO NC film showing saturation of the peak position. b) Comparison of J_c^{Grain} values of pristine and NC films of 6% and 12% BZO/BHO.

[20]The saturated magnetization and applied field of saturation are evaluated as previously demonstrated in Fig. 6.25

A proper incorporation of particles into the YBCO crystal stucture is further evidenced through the in-field performance of films. The inductively measured $J_c(H)$ behaviour of the best $P_{O2}(BaCu_2O_2)$-route grown pristine film is compared with two nanocomposites of 12% BHO/BZO in Fig. 6.33 at 77 K and 5 K.

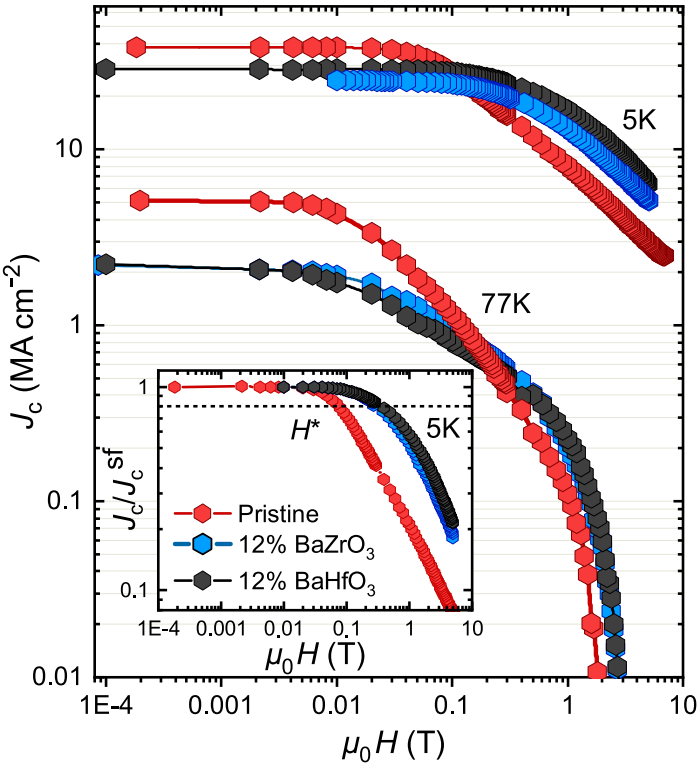

FIGURE 6.33: Inductive critical current density J_c as a function of the magnetic field at 5 K and 77 K for a pristine YBCO film and a 12% BZO and 12% BHO NC film. All three samples are grown at $T_{Growth} = 835\,^{\circ}C$ and $P_{O2,Growth} = 10^{-3}$ bar. The inset shows the normalized $J_c(H)/J_c^{sf}$ curves at 5 K. The H^* parameter is defined with the criterion in eq. 6.4. The nanocomposite films outperform the pristine one at a cross-over fields of $\mu_0 H = 0.1$ - 0.2 T at both temperatures.

Although both NC films have an initially lowered J_c at self-field, by up to 55%, the pristine YBCO is outperformed at a cross-over fields of $\mu_0 H = 0.1$ - 0.2 T at both temperatures. This is further emphasized through the normalized $J_c(H)$ dependence in the inset of Fig. 6.33. The nanocomposites present a smoother in-field behaviour as highlighted by the dashed line at

$$J_c(\mu_0 H^*)/J_c^{sf} = 0.8 \tag{6.4}$$

The crossover field $\mu_0 H^*$ can be defined as transition between single-vortex pinning regime and vortex-vortex interaction regime [30].[21] While the pristine film falls below 80% at 0.075 T, the self-field plateau of NC films is extended towards 0.3 - 0.4 T, implying an increased density of defects capable to pin vortices.
To summarize, first indications that the addition of nanoparticles induces changes in the YBCO structure is given here. While the texture quality is shown not to be affected by the secondary phase, the percolation state of films meets additional complications given the already increased ab-nuclei formation in this growth route. Nevertheless, for NC films where NP agglomeration could be avoided, a promising pinning performance is found in applied field conditions, outperforming pristine YBCO. We also observe a strong increase in intragrain critical current densities obtained through the *Palau method*, indicative for a richer pinning landscape of NC films. As will be seen in the following, this might be attributed to the capability of the TLAG process to epitaxially enclose NPs at nanometric small sizes, promoting a high density of stacking faults and bending of the YBCO lattice.

6.2.2 Epitaxial nanoparticle enclosure in YBCO crystal lattice

As demonstrated earlier in 5.2, TLAG growth drives homogeneously nucleated YBCO grains to realign towards the epitaxial layer during growth. This is further observed for initially misoriented NPs which accommodate in epitaxial relation with the YBCO lattice (shown through *in-situ T* - route experiment in 5.4). Also in the $P_{O2}(BaCu_2O_2)$ - route, the secondary phase is found to exhibit texture. A first indication of the epitaxial embedment of particles can be suggested considering the $\theta - 2\theta$ measurements in Fig. 6.29a). The only diffracted signal identified from the $BaZrO_3/BaHfO_3$ phase is given by the (200) reflection at $2\theta \approx 43\,°$, although other, more intense diffraction peaks are expected for the cubic structure.[22] The outstanding nature of the phenomenon, given the short time scales of reactions and crystallization, is rendered possible through liquid assistance and the non-equilibrium TLAG process kinetics. In this section, we aim to support this finding through a larger study of electrical, inductive and structural measurements.
Fig. 6.34a) shows a TEM image of $BaHfO_3$ NPs in the colloidal solution before addition to the YBCO solution. Particles reach a homogeneous size dispersion in a range of 4 - 5 nm. After growth, the epitaxial enclosure is verified

[21] In the SUMAN group, the criteria is arbitrary chosen to $J_c(\mu_0 H^*)/J_c^{sf} = 0.9$. Here we modify it to 0.8 to diminish granularity contributions.

[22] According to powder diffraction references from the ICDD database a higher intensity is given by the (110) and (211) planes [33].

through STEM measurements (Fig. 6.34b)), with $BaMO_3$(100)//YBCO(100) and $BaMO_3$(100)//YBCO(001). The relatively high lattice mismatch of 8-9 % of the cubic phase with respect to the orthorhombic YBCO lattice might be responsible for a high density of 248 stacking faults and YBCO lattice bending encountered close to the secondary phases.[23]

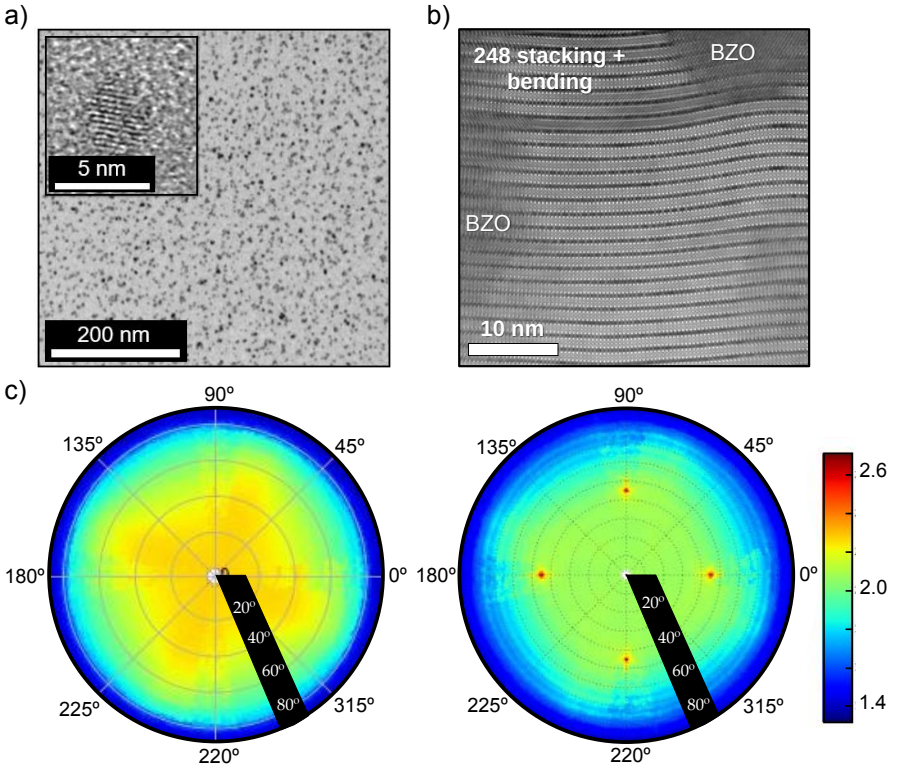

FIGURE 6.34: Microscopy and XRD analysis of NP evolution starting from the colloidal solution to the final integration in the YBCO film: a) TEM image of BHO NPs in the colloidal solution, 4 - 5 nm in average diameter. b) STEM image of a 12%BZO NC where the particles are found in epitaxial relation with the YBCO matrix. The surrounding area shows YBCO lattice bending and a high density of 248 stacking faults. c) Pole figures of pristine (left) and 24% BZO NC film (right) at the BZO (110) peak position of 30.11 °. 4-fold symmetric reflections are seen only in the NC case and attributed to the (110) plane. Poles were recorded at Soleil Synchrotron, DiffAbs beamline.

The epitaxial relationship is further identified through pole figures at the BZO/BHO (110) peak position ($2\theta = 30.12\,°$) for a pristine and a 24% BZO

[23]The density of SFs lies beyond the already increased one in pristine TLAG films, associated to the fast growth kinetics (see discussion in chapter 7).

nanocomposite film (Fig. 6.34c)). Only the NC shows the presence of a four-fold symmetric reflection at $\chi = 45\,°$. Both, symmetry and in-plane position, match the BZO (110) plane if epitaxial alignment of the particles is given.
The known NP orientation can further be used to extract the volume percentage of the randomly oriented fraction. A methodology was early introduced by A.Llordes et al. using 2D-XRD integration of any given NP plane. [117]. Typically, the (110) reflection, being the strongest peak of the cubic phase, is fully integrated through an ω-scan (similarly to a rocking-curve, see 3.5.2). The procedure covers an angular opening ($2\theta - \chi$), large enough to record the epitaxial (110) spot intensity I_{spot} and the randomly distributed ring intensity I_{ring} of the same reflection.[24] An examplary 2D-XRD image is shown in Fig. 6.35a) with the BZO (110) intensity primarily confined in a diffraction spot. The image is acquired through ω-integration of 1h with the GAADS diffractometer.[25] The random fraction $I_{\text{rnd}}/I_{\text{epit}}$ can then be calculated according to

$$\frac{I_{\text{rnd}}}{I_{\text{epit}}} = \frac{I_{\text{ring}} \frac{360}{\Delta\chi} \cdot 4\pi}{8 \cdot I_{\text{spot}}}. \tag{6.5}$$

The ring intensity is obtained in a $\Delta\chi$ and $\Delta 2\theta$ range of 30 ° and 1.5 °, respectively. The value is corrected by a factor $4\pi(360/\Delta\chi)$ assuming a spherical distribution of intensity in 360 °. Accordingly, the spot intensity is multiplied by 8 taking the full symmetry of the reflection into account.
The procedure is repeated for samples with varying NP percentage (6 - 32 %) and compared to TFA grown films from previous work of the group [40, 117]. The latter films include BZO nanoparticles which spontaneously segregate during growth. The comparison is shown in Fig. 6.35b). In the TLAG process, the volume fraction of randomly oriented particles does not surpass 10% at any given, nominal NP concentration. It appears that the system is capable of minimizing incoherent interfaces and reducing surface energy through epitaxial enclosure of the secondary phase. In the TFA process, however, BZO particles are enclosed in majority without any preferential orientation ($I_{\text{rnd}}/I_{\text{epit}} > 60\%$). This is a surprising outcome since growth rates of YBCO in the TLAG process are orders of magnitude higher than in the TFA approach. The occurrence of reorientation is hence not governed by the speed of YBCO crystallization but other influences. For instance, it might be suggested that the presence of a liquid phase in addition to the recently achieved size reduction of NPs (down to 4 - 5 nm) allows the rotation at these short time scales.

[24] Nanoparticles without orientation will contribute to I_{ring} while epitaxially ones diffract into I_{spot}.
[25] The time was initially optimized to have a sufficient signal-to-noise ratio.

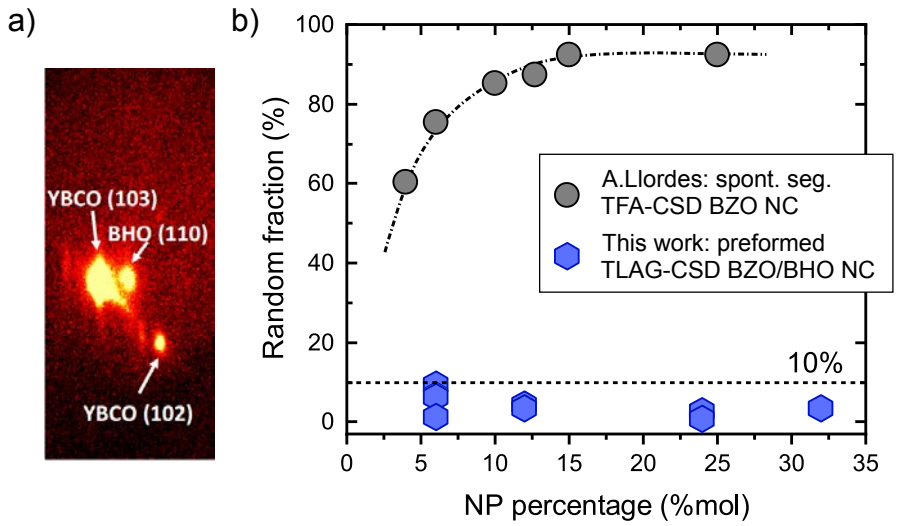

FIGURE 6.35: XRD analysis of the epitaxial embedment of NPs in the YBCO structure: a) 2D-frame of the BZO/BHO (110) reflection, recorded through an ω-scan with the GAADS diffractometer. The frame is used to determine the random fraction of NPs according to eq. 6.5 b). Comparison of the random fraction of TLAG NC films (6%-32%) with spontaneously segregated BZO TFA NC films. Data for the TFA films is acquired from the PhD thesis of A.Llordes [117].

The epitaxial accommodation of particles can further be suggested to influence the YBCO crystal structure. Fig. 6.36 depicts $\theta - 2\theta$ measurements of three films (pristine YBCO, YBCO+12%BHO and YBCO+24%BHO) at high angles were lattice constant changes can be easily observed through peak displacements in 2θ.
All three films contain ab-grains, indicated by the (400) reflection at 107.37°. The (400) peak position shows no visible changes with NP content. In contrast, a strong shift to lower 2θ values is observed for the (0013) reflection with increasing NP concentration. Peak positions and lattice parameters are inversely correlated (eq. 3.13). The downward shift in (00l) peaks is hence indicative for an expansion of the c-axis and in agreement with a matching of NP and YBCO lattice. No change is, however, observable in the ab-grain lattice, signifying that particles are only enclosed in the epitaxial, c-oriented YBCO fraction.

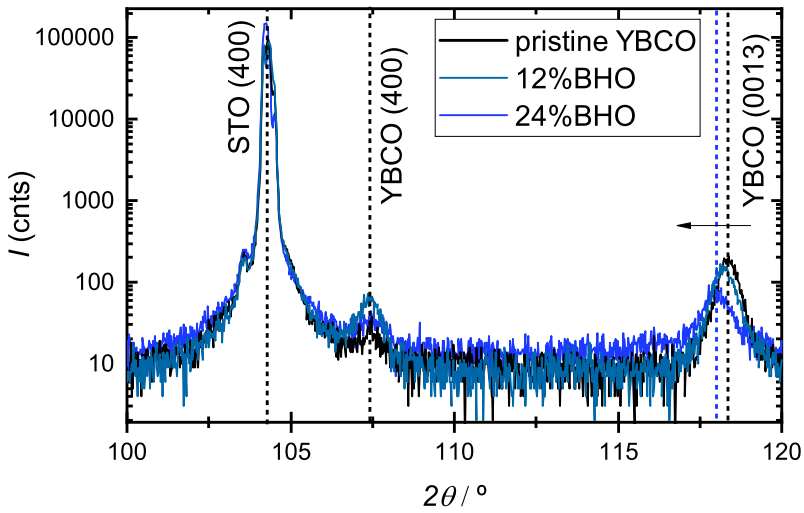

FIGURE 6.36: XRD $\theta - 2\theta$ scans of pristine YBCO and two NC films containing 12% and 24% of BHO. A visible shift is given for the (0013) reflection with NP inclusion, related to an elongation of the c - axis lattice parameter in the epitaxial YBCO layer. The (400) reflection, arising from ab-grains remains, however, unchanged in the peak position.

The aforementioned improved in-field performance and c - axis elongation of NC films is summarized in Fig. 6.37. H^* values, representative for the crossover between vortex-defect and vortex-vortex interaction, are calculated according to criteria 6.4. Lattice parameters are determined through the Nelson-Riley method (3.5.3). All pristine YBCO films lie in a confined region of $\mu_0 H^* < 0.1$ T and $c < 11.67$ Å, while NCs extend the range of values up to $\mu_0 H^* = 0.38$ T and $c < 11.69$ Å.

A correlation between the two physical parameters might be suggested if the associated elongation of the lattice in c triggers strain relaxation in some parts of the lattice. As mentioned earlier, the cubic BMO lattice is mismatched by up to 8% with regard to the YBCO c - axis. An elongation of the cell parameter even up to the maximum determined value of 11.69 Åwould not correspond to a fully strained film, hence, the lattice must release the strain in parts of the structure.[26] YBCO is known to form 248 stacking faults (SFs) upon strain release [211], which are observed in increased amounts for the NC films presented here (Fig. 6.34). Nevertheless, an in-depth TEM study of NP-YBCO interfaces and strain mapping is required to confirm this.

To verify that the denoted increase in c - axis lattice parameters is not a result of oxygen depletion in NC films, resistivity and Hall carrier density measurements are further carried out in Van der Pauw geometry. The measurements

[26] The uniformal strain can be estimated to reach 0.04%.

proved sensitive in the response on oxygen concentration in pristine films (6.1.3) and are once more employed here.

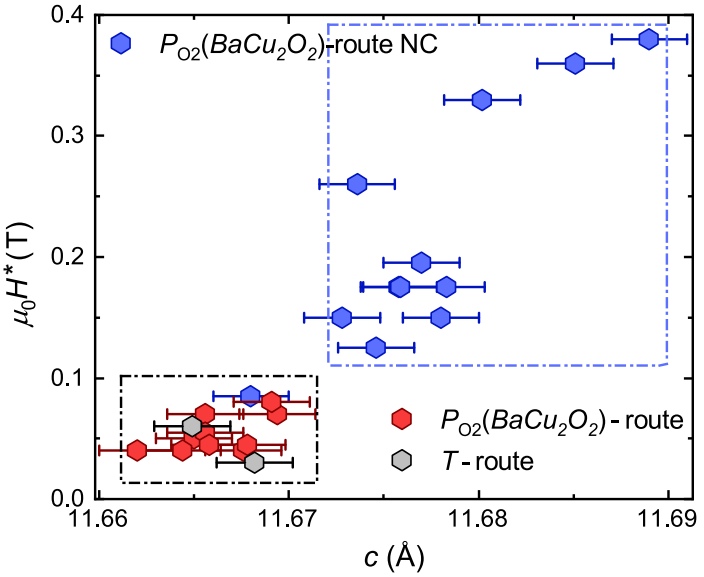

FIGURE 6.37: Correlation of $\mu_0 H^*$ values, obtained through 0.8* criterion of $J_c(H)$ at 5 K (eq. 6.4), with the c - axis lattice parameter of the epitaxial layer. Pristine films from the T - and $P_{O2}(BaCu_2O_2)$ -route are shown together with NCs which expand both physical measures to higher values (distinguished through dashed regions)

Fig. 6.38a) summarizes the obtained T_c and $n_{H,300K}$ values for films of varying percentages of BHO/BZO NPs (6 - 32 %). The margin in carrier concentration obtained for NCs is in good agreement with pristine samples of the same route. The $n_{H,300K}$ values lie in a range of $(6-9.8)10^{21}$ cm^{-3} suggesting that films are optimally doped (green shaded region). However, a minor decrease in critical temperatures with a minimum of 87.58 K is observed for NC films. The T_c diminishment cannot be attributed to an increase in transition width ΔT_c as can be seen in the resistivity measurements in Fig. 6.38b). Independent of the NP concentration the transition width appears unchanged (within ± 0.2 °C). The slight T_c drop might, however, be indicative for a uniformal strain that persists in these films. This is further supported by a correlation between the critical temperature and c -axis lattice parameter. As seen through a comparison of $P_{O2}(BaCu_2O_2)$ -route grown pristine and NC films in Fig. 6.39, the slight drop in T_c for NC films coincides with an expansion of the out-of-plane lattice constant. A similar effect is reported for PLD-grown films with self-assembled BHO nanocolumns [212]. Here, the c - axis is shown

to increase with the nanocolumn mol percentage as a result of lattice constant matching of both phases.

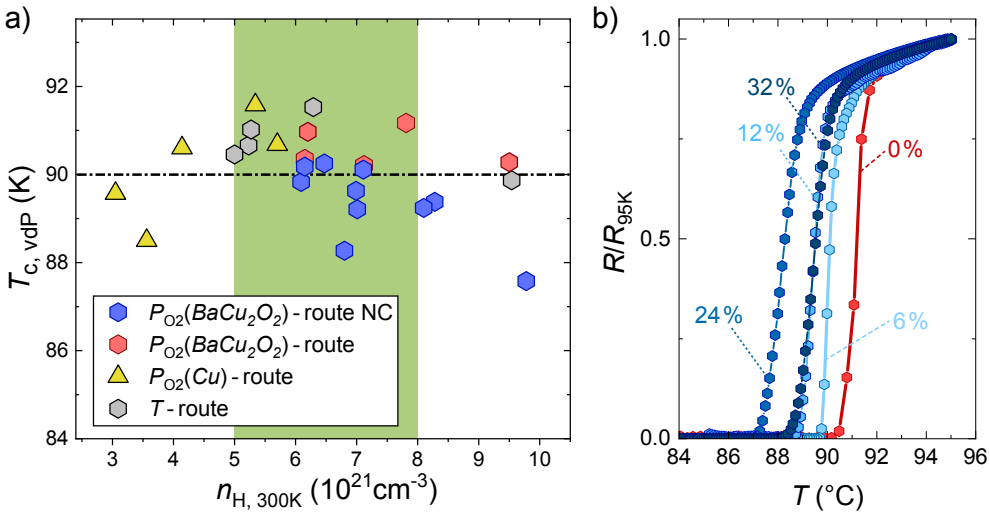

FIGURE 6.38: Transport measurements in Van der Pauw geometry of pristine and NC films: a) T_c versus room-temperature Hall carrier concentration ($n_{H,300K}$). For $n_{H,300K} = (5-8)10^{21}$ cm^{-3} (marked in green) high J_c(5K, 0T) and T_c values (> 20 MA cm^{-2} and > 90 K) are obtained in TFA-CSD YBCO [105]. b) Normalized resistance measurements of the SC transition for samples with varying NP percentages of BZO/BHO.

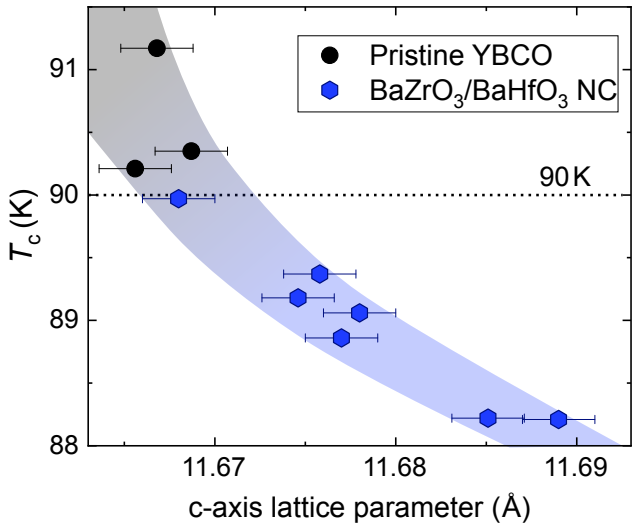

FIGURE 6.39: T_c as a function of c-axis lattice parameter for $P_{O2}(BaCu_2O_2)$-route grown pristine and BZO/BHO NC films.

To conclude, NP addition triggers structural and electrical property changes that suggest the proper incorporation of the secondary phase into the YBCO layer. TEM analysis could further be employed to track NPs of 5-6 nm in diameter in various NC films, though even smaller particles might be present in the layer that remain undetected due to their size and orientation.[27] Epitaxial embedment of NPs to the degree shown here (>90% in volume fraction) has not yet been reported in literature and might bear novel characteristics in the SC state of NC films. Until now, we have evidenced that NC films exhibit an enhanced in-field performance and increased intragrain critical current densities through inductive measurements. Further insights into the SC performance will be given in the discussion of electrical transport measurements in chapter 7.

6.3 Conclusions

With the aim to track down limitations to the current carrying capacity of TLAG films, we have performed a thorough analysis of different physical properties indicative for performance constraints. The TLAG process relies on proper $BaCO_3$ decomposition and the utilization of a very reactive melt. In addition, crystallized YBCO layers are typically found to exhibit a closed and dense microstructure. These circumstances were initially thought as potential complication to reaching high critical current densities. In particular, the removal of carbon, liquid induced substrate dissolution and oxygen incorporation into YBCO crystal structure needed to be addressed as possible influences on the film performance.
As a result, neither the decomposition of $BaCO_3$ nor the oxygenation of grown YBCO films is found to be a critical issue.[28] This is coherently confirmed through XRD, TEM and electrical analysis of films grown through the T-, $P_{O2}(BaCu_2O_2)$- and $P_{O2}(Cu)$-route. Concerning substrate dissolution by the intermediate liquid phase, the effect is evidenced to have a greater impact in the T-route where growth is carried out through consequent, interconnected reactions. Here, a wide temperature window is crossed where the liquid phase becomes stable while YBCO growth rates are determined by $P_{O2} - T$ conditions, melt supersaturation and liquid properties (e.g. viscosity, diffusivity). In this regard, heating ramps are found to have the strongest influence on the final state of the film, being the key processing parameter

[27] The epitaxial alignment of particles and lattice matching complicates the identification of the secondary phase.

[28] A complication of oxygen incorporation in the case of the $P_{O2}(Cu)$-route is suggested, however, not the primary source of reduced critical current densities.

to balance the time of liquid existence against the speed of surface coverage by the YBCO phase. Films that are processed in the T - route at heating ramps above $20\,°C\,s^{-1}$ show dissolved substrate regions, formation of off-stoichiometry phases and diminished T_c values as a result of YBCO grain and grain-boundary contamination. Interface dissolution can be avoided by different means. Either the growth is carried out in the T - route at heating ramps $\leq 20\,°C\,s^{-1}$, on non-reactive buffer layers, or through the pressure routes where no strong reactivity is observed. This might be attributed to an increased supersaturation of the pressure approaches allowing to suppress competing nucleation mechanisms.

The prime source of performance decrease of TLAG grown samples is attributed to route-specific percolation hindrances that compete with YBCO growth. Secondary phases, misoriented YBCO nuclei and voids in the epitaxial layer can essentially reduce the superconducting cross-section of the film. While in the $P_{O2}(Cu)$ - route, the low pressure step is found to promote coarsening of the metallic copper and the consequent imbalance of the film homogeneity during growth, the T - and $P_{O2}(BaCu_2O_2)$ - route allow for the fabrication of high performance films with critical current densities in the range of 2-5 $MA\,cm^{-2}$ at 77 K and self-field.

The $P_{O2}(BaCu_2O_2)$ - route is further demonstrated suitable to enable $BaZrO_3$ (BZO) and $BaHfO_3$ (BHO) nanoparticle addition from colloidal solutions. High critical current densities up to $2.2\,MA\,cm^{-2}$ at 77 K and improved in-field performance as compared to pristine samples are evidenced at a maximum concentration of 12mol% of the secondary phase. Even though a high epitaxial quality of the YBCO layer is maintained up to 32% of BZO/BHO, further growth optimization is required to avoid nanoparticle (NP) agglomeration at these high concentrations.

Surprisingly, NPs are found epitaxially enclosed in the YBCO matrix, in contrast to gas-solid based processing schemes (TFA-CSD) where the secondary phase is primarily randomly orientated. We attribute this finding to the recent miniaturization of particles down to a size of 4 - 5 nm in diameter, allowing to rotate in the transient liquid phase as a means of reducing surface energies. The coherent interfaces are found to results in strong YBCO lattice bending and increased formation of stacking faults. Both defect types might promote improved pinning performances as motivated here and further explored in the following chapter.

Chapter 7

Vortex pinning and correlation with defect landscape of pristine and nanocomposite TLAG films

In the previous chapters, we have thoroughly analysed the TLAG process from the step of YBCO crystallization to macroscopic defects in already grown films that can degrade the current carrying capacity. These efforts yielded fundamental insights into competing crystallization kinetics, allowed us to confine processing conditions and define route-specific obstacles to fabricate high critical current density films. However, when it comes to the actual use of Coated Conductors (CCs), a broad characterization of the $J_c(H, T, \theta)$ dependence becomes pivotal for a proper classification of these newly developed films into potential application fields.

For instance, cables and fault current limiters (FCLs) operate in self-field conditions or at low magnetic field (< 1 T), while transformers, motors, generators and magnets will require several Teslas in operational margin [7]. For that reason, great efforts are undertaken from the material science point of view to tailor precise defect landscapes of CCs with regard to the final application requirements. In that sense, not only is a characterization of TLAG grown films necessary due to their widely unknown pinning properties, but also owing to given concerns whether liquid assisted growth techniques are capable of providing sufficient defects for vortex pinning. Liquid mediated, equilibrium growth processes are typically found to produce highly defect-free films of single crystalline quality [74, 84].

To answer these questions we aim to examine TLAG grown films with regard to nanoscale defects and vortex pinning characteristics through a series of structural and low-temperature, transport measurements on micropatterned bridges. In particular, we want to relate these findings to YBCO films grown through the well established TFA-CSD approach whose microstructure and

its link to transport properties is well understood. The films under consideration in the present chapter are all grown in the optimized conditions of the T- and $P_{O2}(BaCu_2O_2)$-route (derived throughout chapter 6) giving critical current densities at self-field and 77 K in the range of 1.2 - 5.5 MA cm^{-2}. The raw data of samples grown through the conventional TFA-CSD approach was kindly provided by Dr. F.Vallès [30].

7.1 Nanoscale defects in TLAG grown films

A profound understanding of electrical transport characteristics can only be derived considering the nanoscale defects that govern the pinning landscape. In this section we aim to give an overview of defects encountered in TLAG films that apply for pinning of vortices. However, this should first be set into perspective given past and recent efforts to enhance the pinning performance of CCs.

The term "nanoscale" refers solely to those defects that range from several nanometers to tenth of nanometers in size, lying close to the vortex core diameter of YBCO, $2\xi \approx 3$ - 4 nm (H//ab and 0 K). The strength and effectivity of the pinning sites relates to their size r and depth of the created pinning potential U which ultimately translates into pinning force [14]. A "good" defect constellation is given when the density, size and condensation energy allow for an optimum accommodation of a large number of vortices, which ultimately is what governs J_c; that means, defects with a high individual pinning force. In addition, large transport currents require the avoidance of percolation problems (good grain connectivity) so that the full effective cross section is deployed.

As summarized in 2.1.6, a variety of defects apply as potential pinning candidates in YBCO films [39]. Some of these defects can be generated during the growth step of YBCO, referred to as *natural pinning centers*, other can be intentionally introduced altering strongly the pinning landscape, what has been termed *artifical pinning centers* (APCs) [52, 209, 213–218]. A distinction of approaches and resulting types of defects can be categorized as follows:

1. Addition of nanometric secondary phases: The most common approach to alter the defect landscape is through integration of secondary phases, giving rise to so-called nanocomposite (NC) films. It is distinguished whether the secondary phase segregates spontaneously during the YBCO crystallization step or is stable all along the growth procedure, hence prepared independently and later introduced in the growth process. For instance, in PLD growth, secondary compounds such as $BaZrO_3$, $BaHfO_3$

or $Ba_2Y(Nb/Ta)O_6$ are initially added to the PLD target allowing for a self-assembly of nanocolumns into aligned arrays along the c-axis of YBCO [43, 44, 51].[1] The nanocolumn diameter, typically ranging from 5 - 10 nm, can be well predicted through elastic strain models as a result of interface strain relaxation [219–221].
Spontaneous segregation of secondary phases is also utilized in CSD methods. Here, the secondary phase segregates in nanoparticle (NP) form, typically ranging from 5 - 20 nm in diameter [7, 40, 222, 223]. In contrast, preformed nanoparticles, as used in this work, allow independent optimization and miniaturization of NPs and subsequent addition to the YBCO precursor solution. This approach is exclusive to CSD methods since precursor deposition and YBCO growth take place separately [132, 210]. For all NC films pinning is achieved through a synergetic combination of core pinning by the secondary phases and secondary defects that are formed to accommodate strain.[2] As for instance in the CSD case, NP/YBCO interfaces are shown to trigger the formation of $YBa_2Cu_4O_8$ intergrowths, also referred to as 248 stacking faults (SFs), which in turn promote local strain deviations (nanostrain). The nanostrained regions suppress cooper-pair formation yielding higher pinning efficiencies and an increase in isotropic pinning [40, 41].

2. Rare-earth (RE) addition/substitution: RE-addition ($Y_xRE_{1-x}BCuO$) or complete Y substitution (REBCO, RE = Gd, Sm, Eu, Nd etc.) was demonstrated to increase J_c at self-field and in some cases improve the in-field performance. Although the exact interplay of pinning mechanisms is still under debate, the increased critical currents might be attributed to the correlation of T_c with the ionic RE radius, point-like cation disorder and strain fields [39, 225–227].

3. Irradiation techniques: Irradiation with light ions such as electrons, protons, neutrons (typically 1 - 3 MeV) induces randomly distributed defects, while heavy ions (>100 MeV) typically generate columnar defects due to the increased kinetic energies [39, 228, 229]. Both types of defects lie in a size range of angstrom to nanometers and serve as optimal vortex pinning centers, allowing for controlled tuning of the pinning efficiency. However, irradiation of kilometer-long wires is neither practical nor cost-effective.

[1] Also segregation of Y_2O_3 platelets and mixed composites can be achieved this way.

[2] Up to now, core pinning by the secondary phase itself is primarily evidenced in the case of PLD nanocolumns, although latest studies also suggest the effect can be achieved through preformed NPs when combined with non-equilibrium process kinetics that diminish coarsening contributions [209, 224].

Hence, the technique is rather used for research purposes to understand vortex physics of different defect types or endurance studies of REBCO wires that are to be exposed to radiation [230].

4. Substrate surface decoration: Substrate surface decoration/modification, typically with oxide nanostructures, prior YBCO growth can trigger disruptions, distortions and strain fields in the grown layer [50, 213, 231]. Enhancement in the in-field performance are typically attributed to increased isotropic pinning and c-axis correlated defects. It remains, however, to be demonstrated if the approach is compatible with thicker films (> 1 µm) since the effect is localized near the substrate interface making the translation of a fault throughout the whole layer cumbersome.

5. Naturally formed defects: Generation of defects during growth (e.g. oxygen vacancies, dislocations, twin boundaries, SF) can be considered as additional methodology to introduce pinning centers. Due to their formation during the step of growth, without the use of any secondary means, these defects can be referred to as *naturally derived defects*. Especially non-equilibrium growth schemes can produce more complex YBCO microstructures. As shown, for instance, for the recently developed CSD flash heating process (FH), the YBCO structure exhibits distortions and SFs all along the layer. This is possibly related to strain relaxation mechanisms due to increased nucleation densities and reaction kinetics [224]. Also liquid assisted techniques, such as hybrid liquid phase epitaxy (HLPE) and reactive coevaporation by cyclic deposition and direct reaction (RCE-DR), are demonstrated to allow for embedment of Y_2O_3/Gd_2O_3 nanoparticles, hence, giving rise nanocomposite defect landscape as introduced in point 1 [25, 84].

The spectrum of methods summarized here highlights the efforts undertaken to introduce APCs and naturally derived defects into the YBCO structure to further push the film performance. The need to do so is particularly given since most of the conventional growth methods have room for improvement with regard to enhancing the isotropy of the HTS layer and the in-field performance. Taking as a reference the trifluoroacetate metalorganic decomposition approache (TFA-MOD) [6], the pristine YBCO microstructure[3] typically exhibits coherent twin-boundaries (TB) along the c-axis direction and a low density of SFs at the YBCO/substrate and surface interface layers, respectively [45, 54, 224, 232, 233].[4] These, so-called, correlated defects provide a contribution to pinning only in confined angular ranges (H//ab and H//c, see 2.1.6).

[3] Without any introduction of APCs.

[4] Coherent TBs cross the whole YBCO layer with a boundary spacing of $\sim$ 40 - 80 nm.

Although SFs are known to increase the film isotropy for the reasons mentioned earlier, their limited appearance in pristine films, only at the interfaces, reduces this desirable effect. A similar microstructure is obtained for pristine PLD films [105]. On the contrary, other growth approaches (e.g. RCE-DR, FH-CSD) have demonstrated to intrinsically yield enriched pinning landscapes and improved pinning characteristics of films already due a preferential formation of natural defects [25, 224]. As TLAG is a highly non-equilibrium process, a similar scenario might, hence, be envisaged for the films studied here. We will, therefore, classify TLAG in its ability to promote pinning centers and set the findings in context to present growth methods.

7.1.1 TEM analysis of *T*-route pristine YBCO films

TEM analysis of TLAG grown films has been routinely carried out by Dr. R.Guzman, Dr. B.Mundet and Dr. K.Gupta throughout the ERC project. Although many films and cross-sections were characterized with different imaging modes (3.7), we summarize here the overall tendencies observed for different processing routes and growth conditions.
To begin with the defect landscape of *T*-route grown films, we concluded in 6.1 that the heating ramp greatly affects the film microstructure. Heating ramp dependent changes are further found on the nanoscale: Fig. 7.1 comprises STEM images of films grown at 0.4 °C s^{-1} giving a final YBCO thickness of 250 -300 nm.

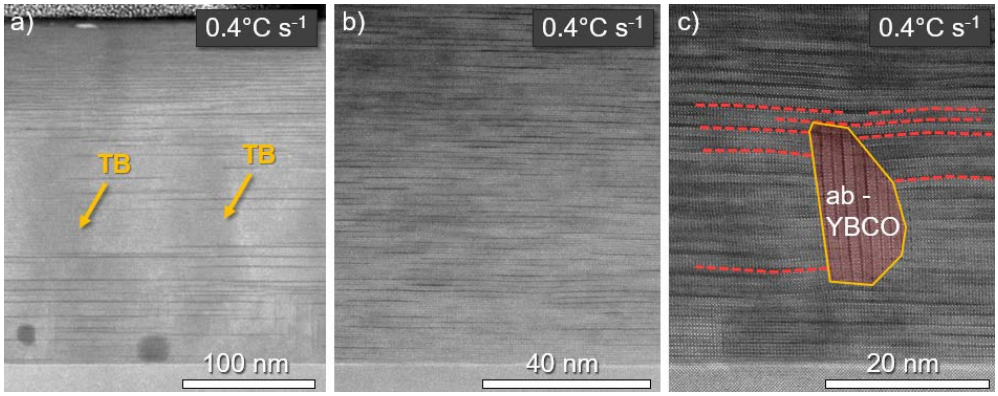

FIGURE 7.1: Z-contrast, STEM images of (2-3) TLAG pristine films processed through *T*-route, heated at 0.4 °C s^{-1} to T_{Growth} = 835°C, $P_{O2} = 10^{-3}$ bar, LSAT substrate. The images show a) 248 stacking faults (SFs) and partially distorted twin boundaries (TBs), b) high density of SFs throughout the full thickness and c) misaligned ab-grain (encircled in yellow) surrounded by SFs and lattice bending (red lines). All films reach an estimated thickness of 250 -300 nm.

For the lowest explored heating ramp a mixed defect landscape is observed. Some regions resemble a rather "TFA-like" microstucture (Fig. 7.1a)) where twin boundaries (TBs) stretch across a large layer fraction [233, 234]. The coherence of such twin-domains is typically perturbed in the surface region and at the substrate interface where a higher number of 248 stacking faults (SFs) accumulate. Both defect types are commonly observed in YBCO films and can be distinguished here through their darker contrast.[5] Other areas, however, show increased amounts of short SFs (∼10 nm in diameter) across the full thickness (Fig. 7.1b)) and nanometric YBCO grains of varying orientations embedded in the c-axis epitaxial YBCO layer (Fig. 7.1c)). In the latter case the YBCO structure exhibits, aside from a high density of SFs, strong lattice bending close to the misoriented grain. Enclosed, nanometric ab-YBCO grains,[6] as observed here for pristine YBCO films, have not been reported in literature. The YBCO lattice bending and increased amounts of SFs are rather pursued and realized through introduction of APCs (see aforegoing section).

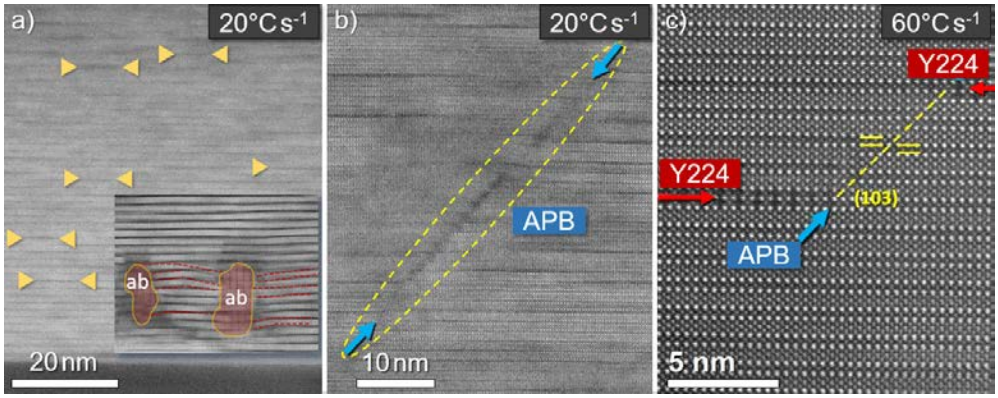

FIGURE 7.2: Z-contrast, STEM images of (2-3) TLAG pristine films processed through *T*-route at increased heating ramps of 20 °C s^{-1} and 60 °C s^{-1}, T_{Growth} = 835°C, P_{O2} = 10^{-3}-10^{-2} bar, LSAT substrate. The heating ramp is labeled in each frame. Different sections show a) short 248 SFs (yellow arrows) and enclosed ab-grains (inset) b) an antiphase boundary (APB) and c) $Y_2Ba_2Cu_4O_9$ intergrowths (red arrows) terminated and connected through an APB (blue arrow). All films reach an estimated thickness of 250 -300 nm.

While films processed at 0.4 °C s^{-1} vary in microstructure from a rather TFA-like constellation to regions with high SF density + nano-inclusions,

[5] In Z-contrast imaging any variation of the atomic sequence or changes in the atomic number Z will modulate the Rutherford scattering characteristics (3.7)

[6] YBCO grains which are oriented with the ab-planes perpendicular to the film surface.

a more homogeneous distribution of SFs and completely new defects are observed at increased heating ramps. In particular, we consider samples grown at 20 °C s^{-1} and 60 °C s^{-1} (Fig. 7.2).
The defect landscape of films heated at 20 °C s^{-1} is mostly constituted of uniformly distributed, short SFs (Fig. 7.2a)). Also embedded ab-YBCO grains and YBCO lattice distortions are encountered in some parts of the layer. However, as in the previous case, the prime defect is given by the intergrowths observed throughout the whole TEM cross-section. This is in contrast to samples grown at 0.4 °C s^{-1} where regions with coherent TBs could also be found (Fig 7.1a)).
Another peculiarity of grown films at these high rates is the formation of antiphase boundaries (APBs), seen in Fig. 7.2b). Although APBs are detected in scarce amounts, their formation is indicative for the out-of-equilibrium nature of the crystallization process. Typically, the defect is observed parallel to the c-axis as a result of mismatching atomic planes upon rapid coalescence of neighbouring grains [39, 235]. Here, however, the enclosed angle between ab-planes and APB ranges from 45 - 48 °.
A similarly substantial change in microstructure is evidenced upon heating ramp increase to 60 °C s^{-1}. Surprisingly, few 248 SFs are formed and the microstructure resembles defect-free, single-crystalline YBCO. Some regions show, however, defects that have rarely been observed in other processes. For instance, aside from 248 SFs, we find $Y_2Ba_2Cu_4O_9$ (224) intergrowths which results from intercalation of an additional Y - Cu - O perovskite block. Such 224 intergrowths are typically found in proximity to each other, connected through an APB along the YBCO [103] direction (Fig. 7.2c)). Up to now only observed in few examples of PLD-grown YBCO, 224 intergrowths are reported to be insulating, hence a potential candidate for vortex pinning [234, 235]. However, a characterization of the pinning characteristics would require stabilized growth conditions where these faults can be promoted in higher amount. This could be, for instance, combined with a future growth optimization on LMO buffers to resolve reactivity issues encountered at these high heating ramps (6.1.2).

To conclude, TLAG films processed through the *T*- route tend to accommodate defects that are usually not obtained in pristine CSD YBCO films. In particular, we observe a high density of short 248 stacking faults, given by the intercalation of an extra Cu-O atomic layer into the YBCO stacking order.[7] The disc-like, 2D defect is terminated through partial dislocations which are known to generate YBCO lattice distortions and local strain deviations [40,

[7] SFs of 10 nm in diameter are commonly found to be uniformly distributed along the whole layer thickness.

54, 55, 236] (see also 2.1.6).
The driving force for the formation of stacking faults is known to arise from stress relaxation mechanisms, hence, dissipation of strain energy. Stress formation is typically rooted in coalescence of neighbouring YBCO grains, mismatch with buffers/substrate interfaces and the enclosure of secondary phases [40, 54, 55]. However, since SFs in TFA-CSD YBCO are formed in moderate amount and rather at the surface/substrate interfaces, the increased density in TLAG films must arise from the out-of-equilibrium growth kinetics. In particular, we find that the density, type and defect distribution in *T*-route grown films might be strongly influenced by the utilized heating ramp. Given the fact that the TLAG is a new process with complex nanometric defect constellations, the observed trends deserve further studies including films grown at different processing conditions.
In summary, the defect landscape at different heating ramps comprises:

1. **0.4 °C s^{-1}:** Increased density of short SFs (down to 10 nm in diameter), enclosed misoriented YBCO grains and YBCO lattice bending. Partially coherent TBs, perturbed at the top and bottom interfaces, are further found in some sections of the layer.

2. **20 °C s^{-1}:** High density of short SFs, enclosed misoriented YBCO grains and YBCO lattice bending (similar to 0.4 °C s^{-1}). However, no coherent TBs could be identified in any of the considered films. Also APBs, enclosing an angle of 45 - 48 ° with the ab-planes were for the first time observed at these elevated heating rates.

3. **60 °C s^{-1}:** A comparably fault-free microstructure as compared to 0.4 °C s^{-1} and 20 °C s^{-1} is obtained. However, more exotic defects and novel defect-defect correlations are formed, such as 224 intergrowths connected through [103] oriented APBs.

The enriched defect landscape in *T*-route grown films portrays a promising scenario for the superconducting performance and cost-effectiveness of the wire. Not only would this allow to enrich defects at low-cost, as compared to the methods introduced earlier (7.1), but potentially allow tailoring of pinning landscapes through processing conditions. Eventually, the generation of certain defect types in a controlled manner should further be explored and remains future work.

7.1.2 TEM analysis of $P_{O2}(BaCu_2O_2)$-route pristine YBCO films

A revision of the nanoscale defect constellation for $P_{O2}(BaCu_2O_2)$-route pristine films is further carried out here. As this growth approach relies on rapid pressure jumps at constant temperature, crystallization of YBCO is carried out in a more confined temperature window. One of the consequences is that the heterogeneous nucleation region is reached in a kinetically different manner than through the T-route approach. Hence, a change in defect landscape can also be expected.

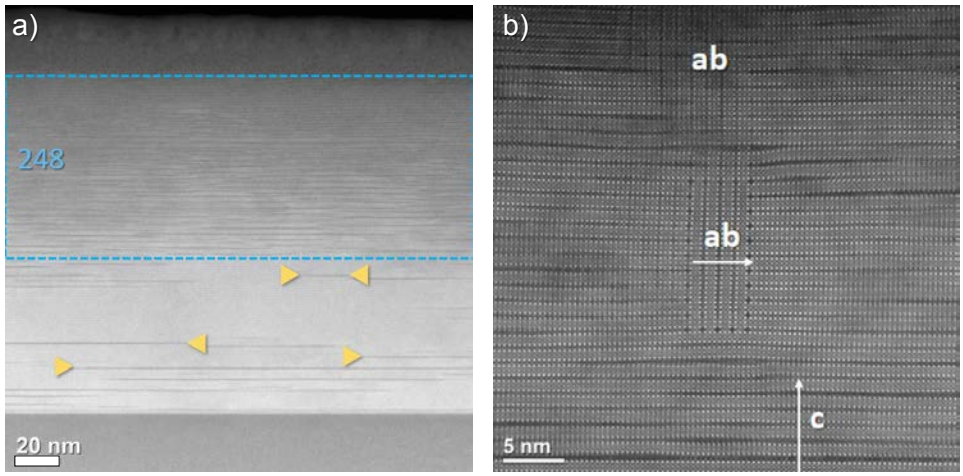

FIGURE 7.3: Z-contrast, STEM images of (3-7) TLAG pristine films grown through $P_{O2}(BaCu_2O_2)$-route at $T_{Growth} = 840°C$, $P_{O2} = 10^{-3}$ bar, STO substrate. Images show a) YBCO area with block of correlated 248 SFs (encircled in blue) and some isolated, long SFs (yellow arrows) b) SFs surrounding ab-grains enclosed in the epitaxial YBCO. Film in a) and b) reach a thickness of 200 nm and 100 nm, respectively.

$P_{O2}(BaCu_2O_2)$-route pristine films typically show a high amount of long SFs surrounded by a non-distorted, uniform YBCO matrix. Fig. 7.3 summarizes the observed trends. Although some short SFs (10 nm) can be found in minor amount, the majority of faults reaches large coherence lengths of >150 nm. Fig. 7.3 depicts some of the 248 SFs exceeding the image size (yellow arrows). Also a substantial part of the YBCO layer thickness ($>50\%$), is perturbed by a high density of long SFs (encircled by dashed blue line in Fig. 7.3a)). Note that, other than in T-route grown films, the high density of SFs is not accompanied by heavy lattice bending nor nanometric inclusions of misoriented YBCO grains (Fig. 7.2a)).
Hence, the general defect scenario we encounter for $P_{O2}(BaCu_2O_2)$-route

pristine films is a high density of long SFs and few lattice bending of the surrounding YBCO matrix. Nevertheless, nanometric ab-grains could be identified in scarce amount in some parts of the TEM cross-section generating few bending of the adjacent planes Fig. 7.3b). Although this defect is rarely observed as compared to *T*-route grown films, both processing routes can generate ab-grain inclusions.
The cause of microstructural differences between both routes (SF length and degree of distortions) can only be speculated at the present moment. Possible answers might lie in the observed reorientation mechanisms of random YBCO grains, differences in supersaturation and YBCO growth rates for the particular growth conditions used. Although this needs to be elucidated in future studies, covering a larger spectrum of processing conditions, the rich defect variety in TLAG films is unambiguous and a consequence of the non-equilibrium nature of the process.

7.1.3 TEM analysis of $P_{O2}(BaCu_2O_2)$-route YBCO + $BaZrO_3$/$BaHfO_3$ nanocomposites

Some of the findings on nanocomposite films were already anticipated in 6.2. The microstructure and defect constellation are further laid out here in the context of pristine films. $P_{O2}(BaCu_2O_2)$-route grown $BaZrO_3$/$BaHfO_3$ nanocomposites (BZO/BHO NCs) were prepared containing varying nanoparticle (NP) mol percentages from 6% - 32%.
XRD measurements of NC films revealed that the majority of NPs (> 90% in volume) are epitaxially enclosed in the YBCO crystal lattice yielding an elongation of the unit cell in c-direction. In comparison to pristine films, highly increased intergrain critical current densities (J_c^{grain}), slightly reduced critical temperatures ($T_c \approx 88$ K) and smoothed $J_c(H)$ behaviour were attributed to the proper NP incorporation into the YBCO layer.
An overview of STEM images of films with varying NP percentages (6% - 24%) is given in Fig. 7.4. A commonality of all NCs is the high amount of SFs covering uniformly the full YBCO cross-section. This is already observed at the lowest NP percentage of 6%BZO (Fig. 7.4a)). The highly faulted microstructure is further accompanied by strong lattice bending as seen in the inset of Fig. 7.4a). A similar nanometric defect constellation is observed for the two films with increased NP concentrations (Fig. 7.4b) and c)), even though for concentrations $\geq$24mol% further growth optimization is required to avoid NP agglomeration (Fig.6.30a)).
Although additional TEM analysis needs to be carried out to understand how

the increased SF density and lattice distortions are generated,[8] the difference in microstructure between $P_{O2}(BaCu_2O_2)$-route grown pristine and NC films is substantial. Note that we have identified rather large SFs and no strong bending of lattice planes in the $P_{O2}(BaCu_2O_2)$-route (Fig. 7.3).

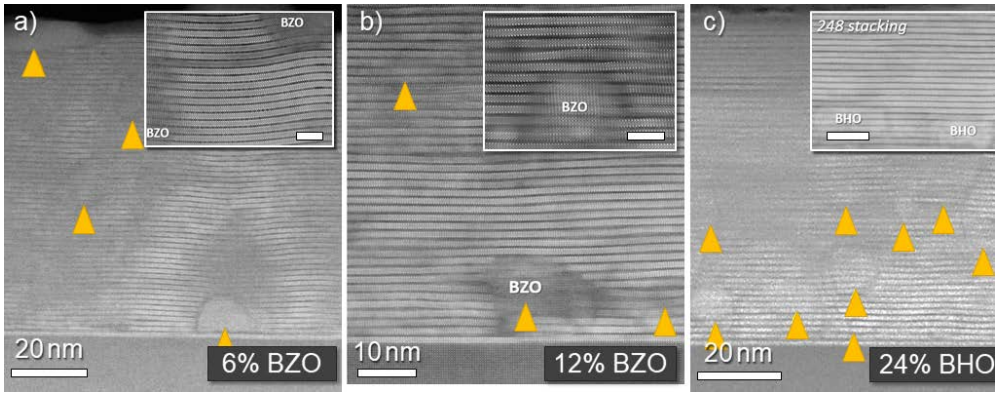

FIGURE 7.4: Z-contrast, STEM images of (3-7) TLAG NC films grown through $P_{O2}(BaCu_2O_2)$-route at $T_{Growth} = 830°C$, $P_{O2} = 10^{-3}$ bar, STO substrate. Images show the NP distribution (yellow arrows), SFs and the extent of lattice bending for a) 6% BZO b) 12% BZO and c) 24% BHO NC film. All films reach an estimated thickness of 90 nm.

In summary, we have shown that a variety of defects are formed in TLAG films, all of which suit the purpose of vortex pinning due to their nanometric dimension. This appears to be intrinsic to the TLAG process itself since a high amount of 248 SFs, small ab-oriented YBCO grains (5-10nm), antiphase boundaries (APBs) and 224 intergrowths are already identified in pristine YBCO. Ultimately, small ab- and misoriented YBCO grains are enclosed due to the competing homogeneous/heterogenous nucleation, while 248/224 SFs and APBs might be formed as a means of stress relaxation [55, 234, 235]. The complex microstructure might be, therefore, a result of the kinetic growth mechanisms of TLAG favored by the high supersaturation conditions employed.

Finally, the introduction of nanoparticles (NPs) from colloidal solutions is shown to create strong YBCO lattice bending and further increase the SF density. The change in microstructure is particularly apparent considering $P_{O2}(BaCu_2O_2)$-route grown pristine films where relatively long SFs (> 150 nm) and few bending is observed. These microstructural changes might be associated with NP reorientation during growth and epitaxial alignment within the

[8] For instance, through strain- and EELS-mapping and studies of the NP/YBCO interfaces [54, 237]

YBCO matrix (5.4 and 6.2.2). In addition, NPs themselves are embedded successfully into the YBCO epitaxial layer at nanometric sizes, potentially acting as core pinning centers if NP size matching with the vortex diameter can be achieved.

7.2 Influence of nanoscale defects on effective anisotropy and single vortex pinning regime

While the aforegoing part lays out the complexity of possible defect constellations in TLAG films and underlines the out-of-equilibrium nature of the process, the influence of defects on physical properties, both structurally and electrically, needs to be addressed.
In a first approach, the influence of defects is examined here through consideration of the anisotropy of YBCO. The anisotropy in YBCO crystal structure and electronic conductivity transfers to a modulation of the vortex parameters ξ and λ with temperature and magnetic field orientation. Thereby, any physical measure that relies on ξ and λ, and hence relates to the vortex properties, will depend on magnetic field, direction of the magnetic field and temperature, such as the critical current density J_c, upper critical field $H_{c2}(T)$ and irreversibility field $H_{irr}(T)$. Summarized through the vortex anisotropy parameter, γ (eq. 2.10), the strength of the vortex core modulation scales with the change of electron mass, m_c and m_{ab}, along the different crystallographic planes.[9]
Blatter et al. derived a scaling factor $\epsilon(\theta)$ (eq. E.1) which allows to separate isotropic from anisotropic pinning contributions to the above listed physical properties through introduction of an effective magnetic field $H_{eff} = \epsilon(\theta)H$, H being the applied magnetic field [239, 240]. The, so called, "Blatter scaling" or "isotropic collapse", allows to evaluate the anisotropy of physical magnitudes, such as $H_{c2}(T)$, $H_{irr}(T)$, J_c, where γ (induced by the structure anisotropy of YBCO) has a direct effect. However, it also allows to identify the defects that contribute to vortex pinning beyond this scaling, i.e. those which appear at specific directions where this scaling is not achieved. Such defects are referred to as anisotropic defects to distinguish them from the isotropic ones. The latter contribute similarly to vortex pinning in any magnetic field direction.
In this section we aim to evaluate the general degree of isotropy in TLAG films

[9] The γ parameter is also referred to as "mass anisotropy" [238]

through determination of the effective mass anisotropy. However, the determination of γ values bears an additional complexity which needs to be addressed previously. According to eq. 2.10, γ is intrinsic to the electronic state of YBCO. If the value is obtained through the Blatter scaling approach it typically gives $4-6$ for YBCO films [241, 242]. These values are demonstrated to be independent of the vortex pinning characteristics, hence, the same for pristine and nanocomposite films as the electronic structure remains unchanged [242]. However, in CSD-nanocomposites, the determination of γ through scaling of magnitudes that rely on vortex pinning ($H_{irr}(T)$, J_c) was shown to give decreased values ($1.5-4$) for nanocomposite films [40, 41, 242]. This led to the introduction of an empirical effective anisotropy, γ_{eff}, and a generalized angular factor

$$\epsilon_{eff}(\theta) = [\cos^2\theta + \gamma_{eff}^{-2}\sin^2\theta]^{1/2}. \tag{7.1}$$

Although γ_{eff} indicates that the isotropy of quantities related to pinning (J_c, H_{irr}) can change, those properties that depend only on the intrinsic mass anisotropy are unperturbed (i.e. H_{c2}), meaning that the electronic properties of YBCO are unchanged. This was demonstrated through measurements of H_{c2} at high field installations [40, 242]. In the following, we make use of γ_{eff} values to determine the overall pinning isotropy of TLAG films.

7.2.1 Irreversibility line scaling $H_{irr}(T)$

The determination of γ_{eff} values from the isotropic scaling of irreversibility lines (ILs) is a common practice to evaluate the vortex pinning properties of a system in pristine and nanocomposite films [242]. These values are further utilised for the scaling of $J_c(\theta)$ curves as will be shown in 7.3.

ILs are obtained through resistance measurements of the SC transition on patterned 4-terminal bridges under varying applied magnetic fields of 0 - 9 T. To conduct the scaling, the change of ILs with the magnetic field orientation is further needed. For that reason, the bridge is mounted on a rotor device allowing to determine the IL in maximum Lorentz force configuration for different angles (3.4.1). An introduction to Blatter scaling and the determination of γ_{eff} values from irreversibility line measurements is further given in Appendix E.

An exemplary IL scaling for a $P_{O2}(BaCu_2O_2)$-route grown pristine film is shown in Fig. 7.5a) using $\gamma_{eff} = 5$, as commonly obtained for pristine TFA-CSD films. A sketch of the measurement geometry, with H perpendicular to the applied current $\vec{J}$ at all angles is included in the same figure. The angle θ is enclosed between the magnetic field direction an the c-axis of YBCO.

From Fig. 7.5a) it is apparent that the acquired lines do not collapse in any of the given angular ranges for a γ_{eff} value of 5. The deviation is visible for

$2\theta = 40° - 70°$ and further enhanced at H//c and H//ab where most of the anisotropic defects are located.[10] Therefore, the TLAG film does not follow the same scaling behaviour as pristine TFA-CSD films where the collapse is achieved for $\gamma_{eff} = 5$ [30, 241, 242].
Instead, the overlap of ILs at $40° - 70°$ is reached for $\gamma_{eff} = 2.7$ (Fig. 7.5b)), considerably lower than for pristine TFA-CSD films. Once again, the H//ab and H//c directions do not scale given the increased amount of anisotropic pinning centers acting in these orientations.

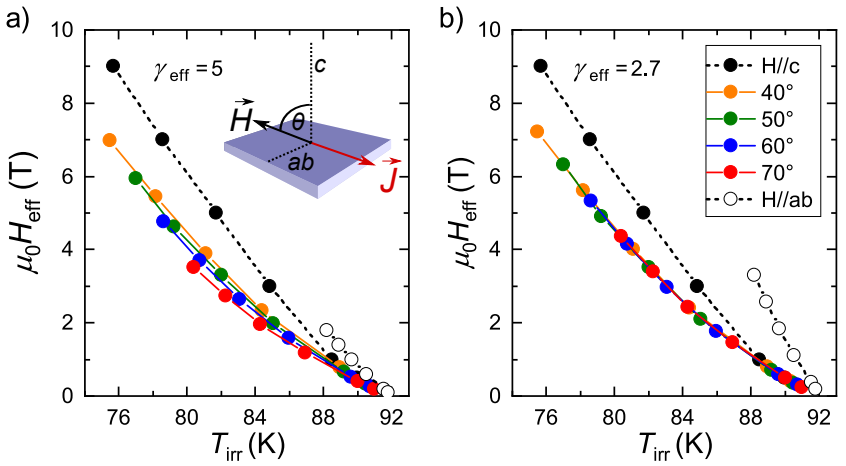

FIGURE 7.5: Determination of the effective anisotropy factor, γ_{eff}, through Blatter scaling of angular-dependent irreversibility line (ILs) measurements: a) Exemplary Blatter scaling for a $P_{O2}(BaCu_2O_2)$-route grown pristine TLAG film with $\gamma_{eff} = 5$, as typically used for pristine TFA-CSD films. The collapse is not achieved for any of the given ILs as seen in the divergence at different θ angles. Each line is measured in maximum Lorentz-force configuration as shown in the inset sketch. b) The collapse of ILs at $\theta = 40° - 70°$ is reached for a lowered γ_{eff} of 2.7.

The lowered γ_{eff} value is not an individual case. An overview of effective anisotropy factors for pristine and nanocomposite TLAG films is given in Fig. 7.6. Also two pristine TFA-CSD films are included for comparison. The latter lie, with $\gamma_{eff} = 4 - 5$, in a typical range as obtained for standard YBCO [241].
All TLAG films show a decrease in γ_{eff} as compared to the TFA-CSD case. Values range from 2.3 to 3.5 with the 6%BZO NC film constituting the lower

[10] These comprise correlated ab-pinning and stacking faults (SFs) for H//ab and twin boundaries (TBs) for H//c.

limit. Accordingly, the overall isotropy of these films is higher since the magnetic field requires a weaker modulation, $\epsilon(\theta, \gamma_{\text{eff}})$, to reach the same scaling as pristine TFA samples. Such behaviour, already for T - and $P_{O2}(BaCu_2O_2)$ - route grown pristine films, resembles the case of TFA NCs rather than of pristine YBCO [40].

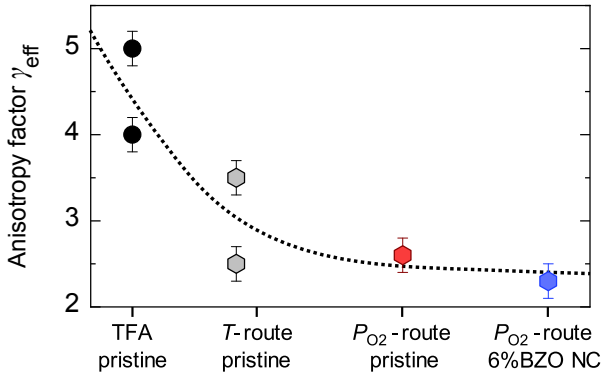

FIGURE 7.6: Overview of γ_{eff} values obtained for TLAG films (pristine and NCs) through Blatter scaling of ILs, as exemplified in Fig. 7.5. Pristine TFA-CSD films are included as reference. Error bars are included to account for the uncertainty of the scaling approach.

The decrease of γ_{eff} for NCs with APCs was attributed to strong isotropic pinning contributions, acting predominantly at medium-high temperatures and a wide range of magnetic fields [40, 41]. Hence, the irreversibility line, separating vortex solid from vortex liquid state, is specifically sensitive to strong isotropic defects. The origin of strong isotropic pinning in TFA-NCs leads back to the increased SF formation. SFs accommodate strain that is generated through the additional NP/YBCO incoherent interfaces and are integrated into the unfaulted YBCO structure through partial dislocations [54, 55]. Such localized regions of dislocations were demonstrated to suppress cooper pair formation and act as strong, isotropic pinning centers with a modified isotropy [40]. Therefore, the tailoring and optimization of NC films intentionally aims to increase the density of SFs and with that the overall isotropic performance of the conductor. Here, however, a similar degree of isotropy is reached for TLAG pristine films without the inclusion of the randomly oriented nanoparticles

7.2.2 Nanostrain and enlargement of single-vortex pinning regime

Partial dislocations, surrounding the disc-like SFs, are known to shape the pinning behaviour in-field as well as in temperature and angular dependence [40, 243]. However, before conducting a complete characterization of transport properties (7.3), the previously observed increase in isotropy should also be motivated from structural and inductive measurements. This allows to ascertain whether the isotropy of TLAG samples increases for the same reasons as formerly reported for TFA NCs [40].
As introduced in the previous section, partial dislocations are formed at the periphery of SFs to accommodate the fault in the YBCO crystal lattice. TEM analyses have revealed that at these dislocation points large strain (1-3%) is localized, and it was theoretically proposed that 1% of tensile strain is able to suppress cooper pair formation. Therefore, these nanometric, localized regions are able to accomodate large amounts of isotropic strain, commonly referred to "nanostrain", which act as isotropic core-pinning sites [40, 54, 243, 244].
In particular, two physical measures are known to scale with the density of SFs and the associated localized strain regions [40, 245]:

1. **Smoothed $J_c(H)$:** SFs provide several channels to vortex pinning. While the SFs themselves act as anisotropic 2D defects in H//ab, the isotropic contribution arises from a high density of Cu and O vacancies within the fault (0D defects) and partial dislocations at the border (1D defect) [244]. As a result, the single vortex pinning regime, characterised by $\mu_0 H^*$ (6.4), increases as compared to films with a low SF density [245].

2. **XRD peak broadening:** Local strain deviations, given by the accommodation of SFs in the YBCO structure, yield θ dependent broadening of XRD reflections due to the inhomogenous distribution of the c-axis parameter. A value for nanostrain can be obtained through the so-called Williamson–Hall plot (3.5.4) where the non-uniform strain generated by SFs is separated from other line broadening contributions [40, 117].

The determination of both values, nanostrain and $\mu_0 H^*$, is exemplified in Fig. 7.7 for a pristine and 12%BZO NC TLAG film from the $P_{O2}(BaCu_2O_2)$-route.[11] Both films present a relatively high nanostrain of ϵ =0.18-0.21, shown in the Williamson-Hall plot in Fig. 7.7a). Typically, TFA-CSD YBCO values lie below $\epsilon = 0.125$ [210], indicating that both films incorporate an increased amount of SFs. Also the $\mu_0 H^*$ values (eq. 6.4) are elevated as compared to

[11] See also method discussed in 3.5.4 on the determination of the nanostrain.

TFA-CSD case, which settle below 0.05 T. As can be seen in the $J_c(H)$ dependence and normalized field dependence (Fig. 7.7b) and inset) pristine and NC TLAG film exceed that threshold considerably with $\mu_0 H^* = 0.09$ T and 0.24 T, respectively. A separate discussion is given in the following to address the 2-3 fold increase in $\mu_0 H^*$ values of NC TLAG films as compared to the pristine ones.

The analysis from above is applied to pristine TLAG films grown through the optimized conditions of the T - and $P_{O2}(BaCu_2O_2)$ -route (Fig. 7.8).[12] The γ_{eff} values from Fig. 7.6 are indicated for the three individual samples of both routes. A grey-shaded region is further added to confine the range of pristine TFA-CSD values [30]. Only samples that reach self-field critical current densities above 1 MA cm^{-2} at 77 K are considered. This constraint is made to diminish potential contributions to the non-uniform strain arising from grain connectivity issues (e.g. grain boundary zipping during island coalescence), termed mesostrain or microstrain [246].

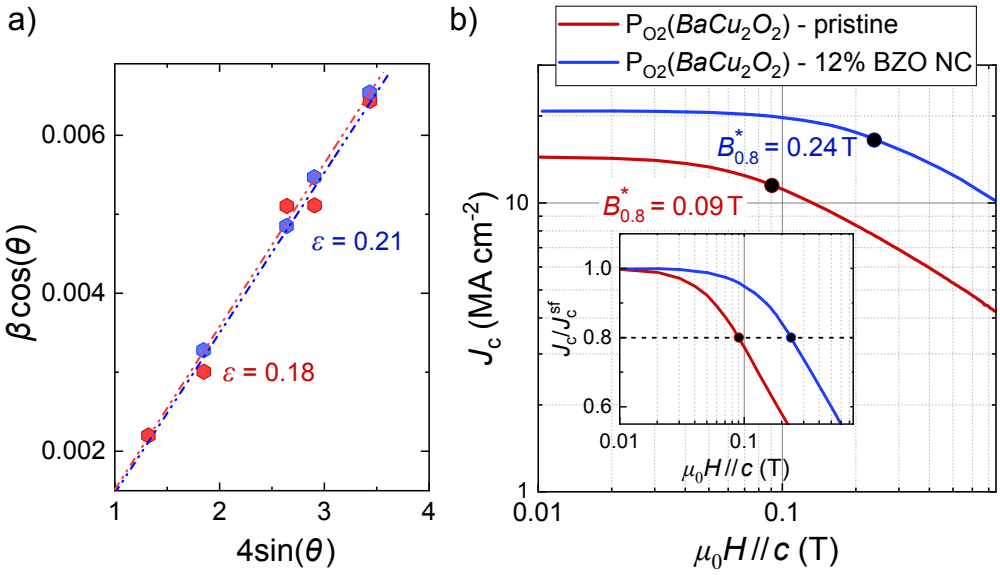

FIGURE 7.7: Exemplary determination of nanostrain and $\mu_0 H^*_{0.8}$ values for a pristine TLAG and 12%BZO NC film from the $P_{O2}(BaCu_2O_2)$-route: a) Williamson-Hall analysis of the XRD peak broadening contributions (3.5.4). b) $J_c(H)$ dependence and normalized field dependence (inset) obtained from magnetic inductive measurements at 5 K. The color code in the legend applies to both graphs.

[12] See tab. 6.3 for the exact growth conditions.

As anticipated earlier, nanostrain values (ϵ) are found increased and the plateau for single-vortex pinning ($\mu_0 H^*$) elongated. While standard TFA films do not surpass an upper limit of 0.125% and 0.06 T in ϵ and $\mu_0 H^*$, respectively, a 2-3 fold enhancement is obtained for TLAG samples. In particular, films from the *T* - route, that is where we observe the highest densities of short SFs and embedded ab-grains, define the upper nanostrain limit with 0.25%.
Overall, the upward tendency of $\mu_0 H^*$ with ϵ values can be well understood given the increased SF density, lattice distortions and novel defects such as enclosed nanometric ab-grains and 224 intergrowths, identified microscopically in TLAG grown films (7.1). As mentioned previously, especially SFs are a source of local strain deviations that can act as additional pinning sites. However, such tendencies were up to now primarily observed in TFA-NC films where the effect is pursued on purpose [40, 41]. Hence, the TLAG process enables pinning enhancements already in pristine YBCO films underlining the advantage of the non-equilibrium growth approach to supply increased defect densities and more complex pinning scenarios.

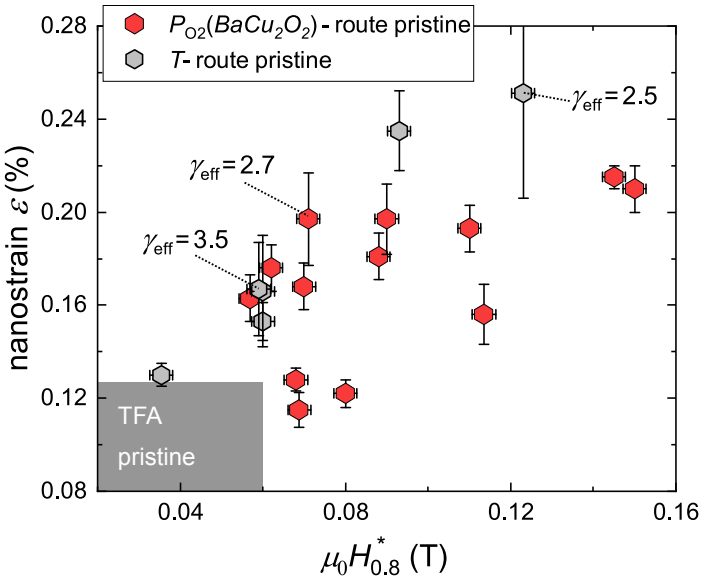

FIGURE 7.8: Evolution of nanostrain, ϵ, with single vortex pinning plateau, characterized by $\mu_0 H^*_{0.8}$ at H//c, 5 K (eq. 6.4). Gray shaded region marks the range of values of pristine TFA-CSD films. Samples which were characterized through Blatter scaling of angular-dependent IL measurements (Fig. 7.6) are labeled with the according γ_{eff} value.

The data from Fig. 7.8 is further complemented with results on $P_{O2}(BaCu_2O_2)$-route grown BHO/BZO NCs and shown in Fig 7.9a). As highlighted by the

dashed-blue rectangle, TLAG NC films lie in a similar nanostrain range as pristine films (approx. 0.13%-0.28%), while the $\mu_0 H^*$ region extends by a factor 2-3.

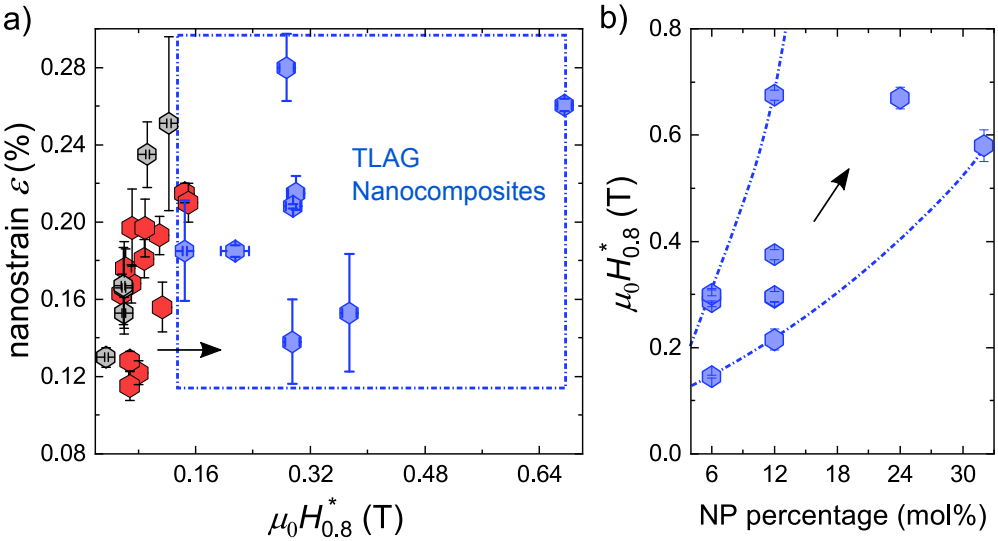

FIGURE 7.9: Analysis of nanostrain, ϵ, and $\mu_0 H^*_{0.8}$ values including TLAG NC films grown through the $P_{O2}(BaCu_2O_2)$-route: a) Evolution of ϵ with $\mu_0 H^*_{0.8}$ in comparison to pristine samples. Arrow and dashed-blue rectangle highlight the increase in $\mu_0 H^*_{0.8}$ of NC films without further increase in ϵ. b) Correlation between $\mu_0 H^*_{0.8}$ and nominal NP percentage.

Such an outcome is unexpected since in TFA-NC films the increase in $\mu_0 H^*$ is primarily attributed to larger amounts of SFs which in turn increase the non-uniform strain. Here, however, $\mu_0 H^*$ appears to increase independently from the associated nanostrain. Therefore, we suggest that the presence of NPs has an additional influence on the single-vortex pinning plateau other than through formation of faults and distortions.

This is, in fact, in agreement with previous results (6.2) showing that a fraction of NPs could be successfully incorporated into the YBCO matrix at very small sizes (4-6 nm), lying in a similar range as the vortex core diameter. Hence, contributions to pinning by NPs as core pinning centers might be proposed given the independent increase in $\mu_0 H^*$. This can further be suggested considering the $\mu_0 H^*$ increase with NP percentage (Fig 7.9b)). The single-vortex pinning plateau elongates through increase of the nominal concentration. If the increase in $\mu_0 H^*$ was caused by a secondary defect that scales with the NP percentage we would expect to find differences in the microstructure of films (Fig. 7.4). Besides a high density of SFs in all NC films

we observe, however, no additional defects that increase with NP percentage and would simultaneously remain undetected to the XRD strain broadening analysis from above.

In summary, TLAG growth is evidenced to naturally drive the YBCO to form a high amount of 248-intergrowths (SFs). Also more exotic defects, such as small ab-oriented YBCO nanograins (5-10nm), 224-intergrowths and antiphase boundaries, could be found under certain processing conditions, though 248 SFs are suggested to be the prime defect in these films. The complex microstructure, in turn, is shown to smooth the decay of J_c as a function of magnetic field and reduce the effective anisotropy ($\gamma_{eff} \leq 3.5$) already in pristine TLAG films as compared to the conventional TFA-CSD route. This is demonstrated, up to now, through a series of structural (TEM and XRD) and inductive measurements. The observed trends require further characterization through electrical transport measurements on patterned bridges to confirm the influence of SFs.
Finally, the successful incorporation of NPs into the YBCO matrix (Fig. 7.4) is shown to induce pinning enhancement without considerable changes in the degree of local strain deviations. This is used to argue that a part of NPs, which maintain their nanometric size of 4-6 nm, might function as core pinning sites in these novel NC films. The reason why core pinning by NP inclusion was not achieved until now might lie in the very recent miniaturization of NPs down to 3-4 nm in diameter [209], their successful stabilization in the YBCO solution [95] and rapid TLAG crystallization kinetics that suppress NP coarsening during thermal treatments [132]. A similar advantageous microstructure and suggestion of NPs as core pinning sites is made in the novel Flash Heating process of TFA-CSD films where rapid thermal treatment is used to avoid NP coarsening [210]. The combination of rapid, non-equilibrium growth schemes and independent NP control in colloidal solutions might, therefore, enable efficent, isotropic core pinning with the CSD methodology. Ultimately, such films could out-perform PLD films where core pinning is achieved only one-directional, not isotropically, through nanocolumns that segregate during growth [43, 44, 51, 52].

7.3 Influence of nanoscale defects on current transport

While the previous part of the chapter is centered around identification of nanometric structural defects in TLAG films and how these alter various

macroscopic measures (γ_{eff}, ϵ and $\mu_0 H^*$), the analysis here is exclusively focused on electrical transport measurements at low temperatures. In particular, we have identified 248-intergrowths (SFs) as the most commonly occurring defect in TLAG pristine and NC films. However, although such faults are also observed in YBCO from other processes, such as TFA-CSD and PLD growth [55], the density, length and distribution of SFs already in pristine TLAG grown films exceeds any conventional growth approach.
To confirm that the increased amount of SFs in TLAG films has an influence on the current carrying performance of films, we take advantage of the anisotropy of the 2D defect, its peculiarity of providing additional lattice distortions and its interference with twin-boundaries (TBs).[13] This requires probing of the critical surface $J_c(\theta, H, T)$ (3.3) and application of the Blatter scaling approach to allow for separation into isotropic and anisotropic pinning contributions [239, 240]. Ultimately, the TFA-CSD system is used again as reference to evaluate whether the observed changes are relevant or not.
Although most of the measurements are carried out on pristine films from different processing routes (T - and $P_{O2}(BaCu_2O_2)$ -route), first results on a TLAG 6%BZO NC film are also included for the sake of completeness. NC films require, however, a thorough characterization of current transport characteristics to further validate the role of NPs as isotropic core pinning sites, as we have suggested earlier.

7.3.1 $J_c(H)$ in-field dependence of TLAG films

Several pristine TLAG films and a 6%BZO NC where micropatterned through use of a standard photolithography procedure (3.3) to give 4-point collinear bridges of known dimensions (Fig. 3.10). The processed samples can then be mounted on an electrical probe (PUCK) and any selected bridge connected via external wiring to the contact pads of the PUCK. This allows, in combination with the Physical Property Measurement Systems (PPMS), to record IV-curves and explore the temperature-, angular- and magnetic field behaviour of the critical current density.
In-field critical current densities of all samples, considered in the following, are summarized in Fig. 7.10 at 77 K, both for $H//c$ and $H//ab$. The choice is limited to films with varying current densities of 1.2 -5.5 MA cm^{-2}.[14] Also a pristine TFA-CSD film with a critical current density at self-field, J_c^{self}, of 3.8 MA cm^{-2} is included for comparison. Complementary $J_c(H)$ raw data at temperatures from 5-65 K is laid out in Appendix E, Fig. E.1.

[13] TBs are intrinsic to any orthorhombic YBCO crystal structure.

[14] Films below this margin are not considered due to increased granular contributions that complicate a comparison to standard TFA films.

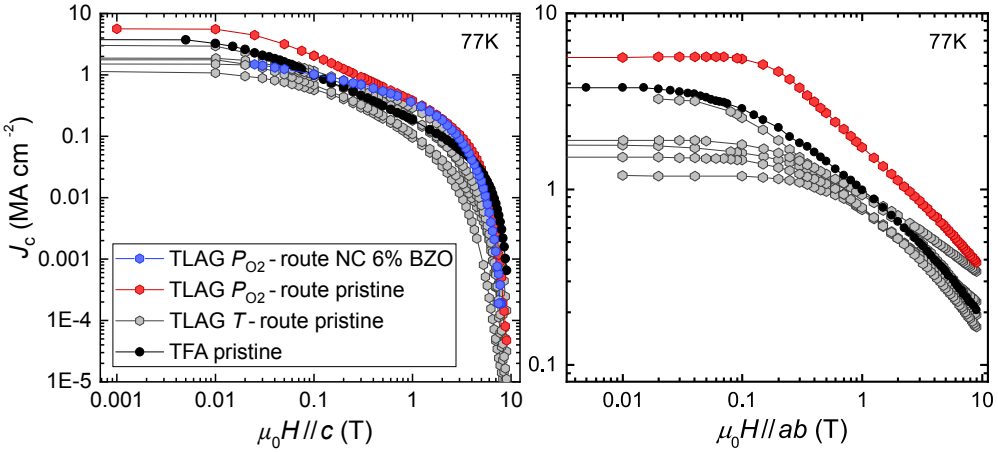

FIGURE 7.10: In-field dependence of the critical current density, $J_c(H)$, at 77 for a) H//c and b) H//ab. Included are pristine TLAG films from the T- and $P_{O2}(BaCu_2O_2)$-route, a TLAG 6%BZO NC and a TFA pristine film.

Most of the characterised TLAG films reach lower J_c^{self} as compared to the TFA pristine film (up to a factor of 2-4). This is, as we have concluded in 6.1.4, attributed to percolating hindrances that reduce the conducting cross-section and should be further addressed through a second run optimization of growth conditions. As the work presented here contributes to our first understanding of the process and optimization of films properties, we have included those samples that already reach competitive current carrying performance.
It is, therefore, remarkable that although the initial J_c^{self} is lowered, a cross-over with the pristine TFA film is reached by several films in the middle magnetic field range (0.2-3 T) for H//c (Fig. 7.10a)), particularly pronounced in the NC case. The trend is reversed for H//ab where TLAG films become competitive in the high magnetic field range above 1 T.
The overall smoother dependence of J_c in applied field conditions becomes further evident considering the elongation of the single-vortex pinning plateau. Fig. 7.11 summarizes $\mu_0 H^*_{0.8}$ values for both applied field directions and a temperature range of 5-77 K. The margin governed by standard TFA-CSD films is marked through the dark-shaded regions and black markers. A comparison exclusively of pristine samples shows that an elevation of up to a factor of 5.1 and 6.7 can be reached in H//c and H//ab from the TFA to TLAG case at 77 K, respectively. The value decreases to 2.1 and 2.8 at 20 K. In the NC case an increase in $\mu_0 H^*_{0.8}$ by a factor of 10 at 77 K and H//c is even higher than for pristine samples.

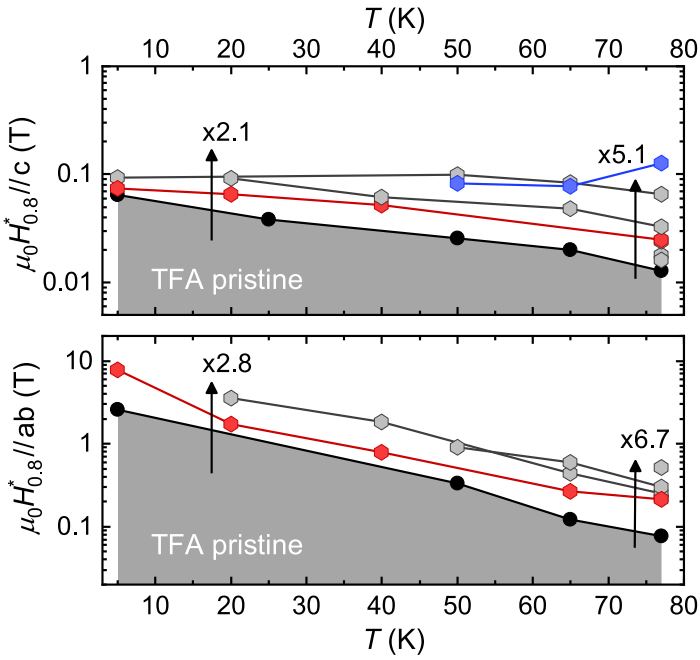

FIGURE 7.11: Temperature dependence of $\mu_0 H^*$ values for both magnetic field orientations, $H//\mathrm{c}$ and $H//\mathrm{ab}$. The values are obtained from raw measurements (Fig. 7.10) at different temperatures. The grey-shaded region confines the single-vortex pinning margin for the pristine TFA case. Arrows and multiplication factors denote the elevation of $\mu_0 H^*$ from the TFA to the maximum TLAG pristine value.

Regardless of the processing route and growth conditions, it appears that TLAG films provide more pinning sites, yielding to the smoother decay of $J_c(H)$. The effect is more pronounced in the high temperature region, around 77 K, where the highest elongation of the single-vortex pinning plateau is registered (Fig. 7.11).

The temperature dependence of different pinning contributions can be described by two theoretical models that distinguish between weak and strong pinning centers. In the, so-called, weak collective pinning model the decay of J_c with temperature is predicted according to

$$J_c^{\mathrm{weak}}(T) = J_c^{\mathrm{weak}}(0) \cdot \exp\left(-\frac{T}{T_0}\right) \tag{7.2}$$

where $J_c^{\mathrm{weak}}(0)$ is the weak pinning contribution at 0 K and T_0 related to characteristic vortex pinning energy of weak defects [240]. Especially 0D point-defects, with a size smaller than the vortex coherence length ξ, apply as weak

pinning centers. In YBCO, these are primarily vacancies and substituted interstitial atoms.
In contrast, for strong pinning centers a weaker dependence of J_c with temperature is predicted theoretically [247, 248]:

$$J_c^{strong}(T) = J_c^{strong}(0) \cdot \exp\left(-3\left(\frac{T}{T^*}\right)^2\right) \tag{7.3}$$

Accordingly, $J_c^{strong}(0)$ and T^* denote the strong pinning contribution to J_c at 0 K and the temperature associated to the characteristic vortex pinning energy, respectively.
The stronger temperature dependence of J_c^{weak} results in weak pinning being more pronounced at low temperatures, while strong pinning governs the mid-to-high temperature range. Various defects, 1D and 2D dimensional, have been identified in YBCO to provide strong pinning. This includes correlated pinning by the YBCO structure itself (intrinsic pinning and TBs, both 2D), SFs in $H//ab$ (2D), nanostrain (3D ramified network) and partial dislocations (1D).
Taking into account that the observed increase in $\mu_0 H^*_{0.8}$ values of pristine TLAG films is more pronounced at high temperatures (Fig. 7.11), it can be suggested that these films have a higher density of strong pinning centers. In addition, the trend is given, both, for $H//c$ and $H//ab$ orientation. The strong pinning contribution must, hence, either act anisotropically in both directions or be completely isotropical. A conclusion should, however, consider all the experimental results shown in the following.

7.3.2 $J_c(T)$ temperature dependence of TLAG films

In the aforegoing part we have seen that TLAG films present an improved current carrying capacity in applied field conditions. This was demonstrated at 77 K where some TLAG samples outperform conventional TFA-CSD pristine films in the intermediate magnetic field range (0.2 - 3 T) for $H//c$ and high magnetic fields (1 - 9 T) for $H//ab$.[15] However, for $H//c$, the proximity to the irreversibility line might yield to an underestimation of this positive trend. For instance, at 9 T the irreversibility temperature, T_{irr}, of a pristine TFA film lies at 78 K [249], while TLAG samples settle around 76 K. For that reason, we probed the temperature dependence of J_c at the maximum reachable field of $H//c = 9$ T.

[15] Although most TLAG films have reduced J_c^{self} values as compared to the TFA case.

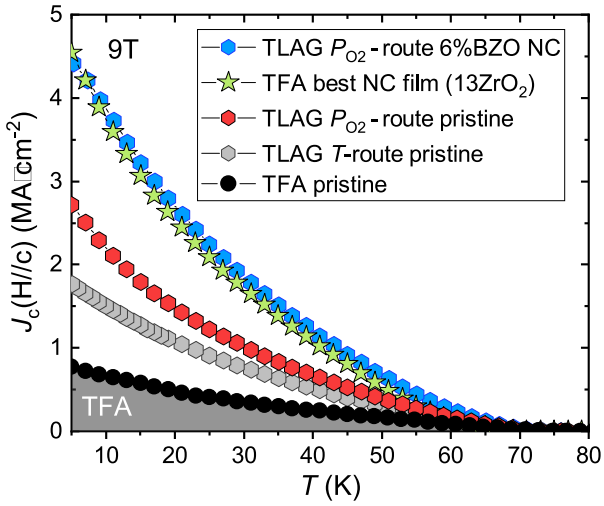

FIGURE 7.12: Temperature dependence of critical current density, $J_c(T)$, for $H//c = 9$T. Included are pristine TLAG films from the T- and $P_{O2}(BaCu_2O_2)$-route, a TLAG 6%BZO NC and a TFA pristine sample (grey-shaded region). The best performing NC that was achieved trough the TFA-CSD methodology is added for comparison [30].

An overview of $J_c(T)$ measurements is given in Fig. 7.12 for pristine and NC films. At 77 K, the pristine TFA film slightly outperforms TLAG samples. This is best seen in the log-log scale of the $J_c(H)$ behaviour for $H//c$ and 9 T (Fig. 7.10) and can be attributed to coherent TBs that provide strong pinning in the TFA case [45]. For TLAG films, however, the coherence along the c-axis of this defect might be perturbed by the high amount of SFs, as suggested by the TEM results (7.1). The absence of TB coherence would then, in turn, be responsible for the minor decrease of the irreversibility line.

Away from the high temperature region, however, pristine TLAG films clearly show an improved lift in J_c as compared to the TFA reference, approximately by a factor of 2 - 3 for T < 50 K. The increase is most significant for the T - route grown pristine sample since $J_c^{self}(77\,K)$ reaches only half of the TFA value,[16] while the $P_{O2}(BaCu_2O_2)$-route pristine film lies 45% above.

The elevation of $J_c(T)$ is even more pronounced in the TLAG 6%BZO NC, reaching 4.4 MA cm^{-2} at 9 T and 5 K. Hence, NP addition is confirmed as feasible approach to further increase the in-field performance of TLAG films. In fact, one of the best performing NC films, ever obtained with the TFA-CSD process, is included for comparison showing a similar efficiency as the

[16] $J_c^{self} = 1.9$ MA cm^{-2} and 3.8 MA cm^{-2} for T - route and TFA standard film, respectively.

TLAG NC. This is, once more, an indication that the improved in-field performance is partially governed by NP core pinning given the low fraction of added phase (only 6%BZO).

7.3.3 $J_c(\theta)$ angular dependence of TLAG films

Considering the improved in-field performance of TLAG samples for $H//c$ over a wide range of temperatures (Fig. 7.12), in addition to a slight reduction of T_{irr} at 9 T, it can be suggested that pinning in these films must be promoted from a different source than coherent TBs. These are reported to sustain strong, anisotropic pinning at $H//c$ in standard films from the TFA approach [45, 249]. To further reinforce this assumption, complementary angular information is included here.

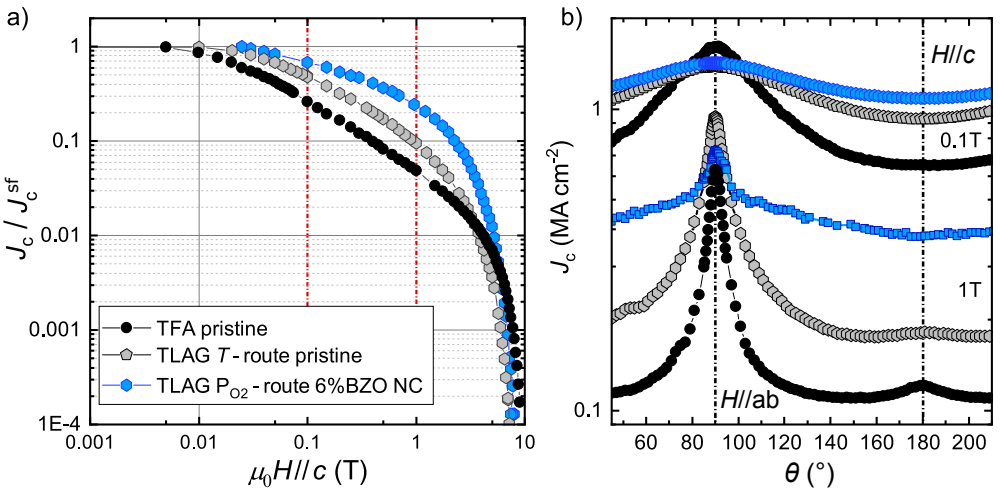

FIGURE 7.13: Three films that show a difference in the a) normalised $J_c(H//c, 77K)$ behaviour are further compared in their b) full angular dependence at 77 K. The comparison is made at 0.1 T and 1 T (red dashed lines in a)). The black-dashed lines in b) mark the angles where $H//ab$ and $H//c$ directions at 90 ° and 180 °, respectively.

In a first attempt to probing the isotropic behaviour of TLAG samples and deriving a potential model for the pinning landscape, three films are compared in their angular dependence, $J_c(\theta)$, at 77 K. Fig. 7.13a) shows the normalized $J_c(H//c, 77K)$ behaviour of the three reference films, a TFA pristine, T -route TLAG pristine and the TLAG 6%BZO NC. As discussed previously, the elevation of the critical surface in the TLAG case at high temperatures must be governed by strong pinning (eq. 7.2 and 7.3). Angular measurements are performed at 0.1 T and 1 T, that is where the smoother $J_c(H)$ decay is obtained

for TLAG samples (red-dashed lines in Fig. 7.13a)).
Absolute $J_c(\theta)$ curves at 0.1 T and 1 T are shown in Fig. 7.13b) with the same color code as the $J_c(H)$ measurements. The previously observed elevation of J_c in-field appears to be angular independent. This is already given for the T-route grown pristine sample and most pronounced in the NC case. The increase in strong pinning should, hence, be of isotropic nature.

At this point, a possible pinning scenario can be illustrated for TLAG films given the aforegoing findings of this chapter. From the TEM analysis we have evidenced an increased density of SFs. Inductive measurements of $J_c(H)$, XRD evaluation of local strain deviations and irreversibility line scaling all suggested that SFs indeed affect macroscopic properties of the grown layer. This could not be implied through TEM analysis alone since the technique has a low spatial coverage as compared to the full film.

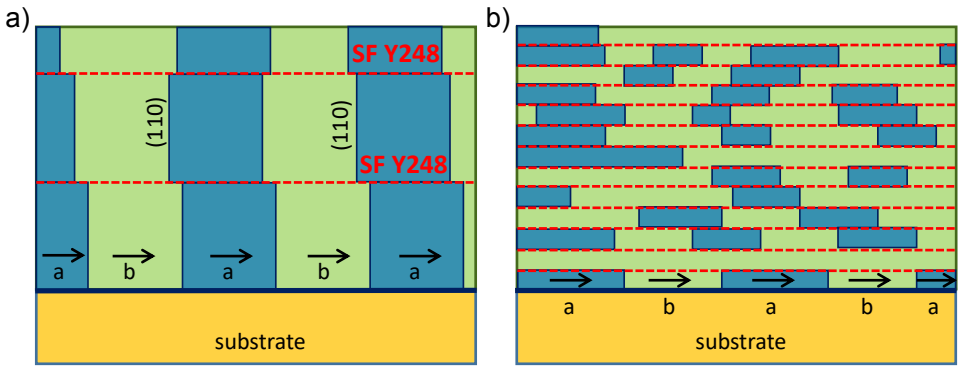

FIGURE 7.14: Illustration of stacking fault (SF) interference with twin boundaries (TBs): a) Low SF density case where TB are mostly coherent along the whole YBCO layer thickness. Red-dashed and black lines mark SFs and TBs, respectively. a and b label domains of alternating in-plane lattice parameters. b) High SF density case where the TB coherence is lost. Courtesy of V.Rouco [249].

The influence of SFs on the YBCO crystal structure, generation of secondary defects and contribution to pinning are widely understood from studies on TFA pristine and NC films [40, 41, 243]. From the structural point of view, SFs yield two main changes: On the one hand, the coherence length of twin boundaries (TBs) shrinks yielding to a displacement of the domains. This is illustrated in Fig. 7.14a) and b) comparing a film of low and high SF density, respectively. The loss of the vertical coherence is attributed to the localized strain regions ensuing from partial dislocations at the periphery of SFs [54]. This is, in turn, the second structural change that SFs induce in YBCO, namely

local variations of lattice parameters in- and out-of-plane. Hence, the defect affects the XRD line broadening as discussed in 3.5.4.
Regarding pinning characteristics, the increase in nanostrain is known to result in the overall elevation of the critical surface in a wide $H-T$ range, given its role as strong, isotropic pinning source [40, 41]. Hence, a defect constellation, as illustrated in Fig. 7.14b), might be responsible for the observed trends in TLAG grown films. Although this can already be affrimed through the smoother decay of $J_c(H)$ (7.3.1), improved $J_c(T)$ dependence (7.3.2) and flattening of $J_c(\theta)$ curves (7.3.3), the next two sections are devoted to more advanced probing methods of the pinning landscape.

7.3.4 Loss of twin boundary coherence in TLAG films

Twin boundaries are formed at the oxygenation stage of the film, accommodating to those defects that evolved in the growth process [54]. It has been shown for TFA-CSD films that while the coherence of TBs extends to the full layer in the pristine, defect-free case, the constellation changes for nanocomposite films [54]. Here, interfaces between NPs and YBCO provide additional sites for TB nucleation due to broken symmetry, strain, and altered chemical structure decreasing the nucleation barrier. Furthermore, the high density of intergrowths, allows for alternative paths of oxygen migration needed for TBs to form. As a result, a more complex domain structure evolves where TB coherence through the full thickness is no longer satisfied and the twin spacing is also reduced (Fig. 7.14b)).
The impact of TB distribution, spacing and coherence has been found to strongly affect $J_c(H,T,\theta)$ characteristics, observable through variation of magnetic field orientation and temperature [250, 251]. For instance, in the defect-free case of TB coherence through the full thickness, the twin planes act as strong, anisotropic pinning centres at high temperatures (>65 K) for magnetic field alignments around $120\,^\circ < \theta < 170\,^\circ$, while they act as easy vortex sliding channels at low temperatures and high magnetic fields [45, 54, 252]. Subsequently, this yields to an increase or reduction of J_c for $H//c$, respectively.
Taking the example $J_c(\theta)$ measurements at 77 K and 1 T (Fig. 7.13b)), the contribution of TBs as strong, anisotropic pinning centers becomes evident at $\theta = 180\,^\circ$. A slight increase in J_c, best visible in the TFA pristine film, can be attributed to TB pinning close to the irreversibility line [45]. However, from these measurements alone it cannot be distinguished whether the twin planes have a high length of coherence or not. Also in the TLAG pristine case, a scarce TB contribution to J_c at $H//c$ is observable.
The response to TB coherence is more pronounced in the vortex sliding

regime, hence lowered temperatures and increased fields. Normalised measurements of $J_c(\theta)$ at 20 K and 9 T are shown in Fig. 7.15a) for a TLAG/TFA pristine film and TFA NC. Under these conditions, only the TFA pristine sample shows a strong decrease of J_c at θ =180 °. This is a signature of TBs that extend coherently throughout the full YBCO layer allowing for vortex sliding [45]. The TLAG pristine film and TFA NC show, however, an elevation of the overall $J_c(\theta)$ and no such dip around $H//c$.

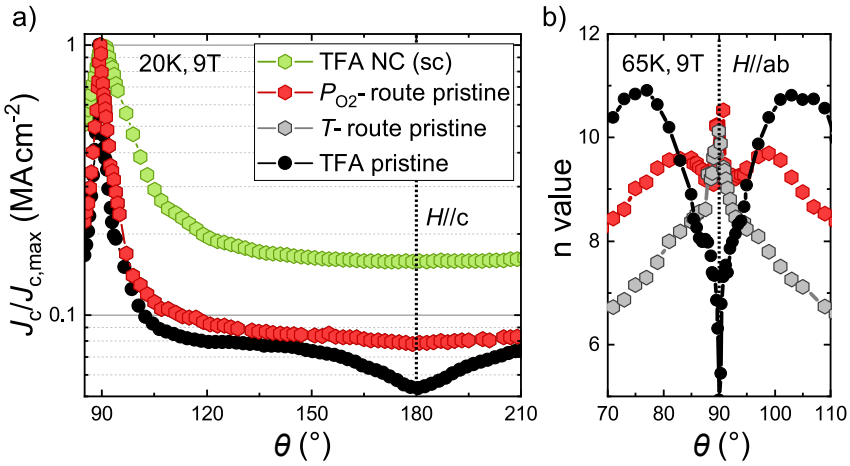

FIGURE 7.15: Influence of stacking faults (SFs) on the a) normalized angular dependence of the critical current density, $J_c(\theta)$, at 20 K and 9 T and b) the n-value around $H//ab$ at 65 K and 9 T.

The absence of a dip in the TFA NC case was successfully attributed to a more complex TB constellation prohibiting vortex channeling under these conditions (Fig. 7.14b)) [45]. In the TLAG case this is, however, given by default without introduction of any secondary phases. To confirm that the effect is indeed related to the increased density of SFs, we make use of a recently developed method to probe vortex creep characteristics [30, 243]. For a complete introduction to the subject of vortex movement and different pinning regimes, the reader is advised to consult the references mentioned below.

As introduced in 3.4.4, the shape of IV-curves upon ramping of the current follows the power-law behaviour $E \propto J^n$ around the critical current value. The exponent n, also referred to as n-value, is related to a current regime where flux creep takes place. The power-law approximation was initially derived through consideration of the standard flux creep model together with a logarithmic current dependence of the pinning potential, U_P, yielding

$$n \propto \frac{U_P}{k_B T} \tag{7.4}$$

with $k_B T$ the thermal energy [243, 253, 254]. In the practical sense, the n-value represents the degree of vortex immobilization in this energy-dissipative regime. Yamasaki and Mawatari further postulated an inverse relation of n to the flux creep rate S [255], opening up a new field to study vortex dynamics through electrical transport measurement [243].[17]

Recent studies of the vortex creep characteristics around $H//\text{ab}$ and high temperatures (50 - 80 K) have revealed that there is an $H-T$ dependent crossover between stacking fault pinning (SF) and intrinsic pinning (IP) by the ab-plane structure [30, 243]. In particular, the crossover from SF pinning to IP is defined through a peak-to-dip transition of $n(\theta)$ for $H//\text{ab}$.

The $n(\theta)$ evolution for two pristine TLAG films from both routes and one TFA reference are shown in Fig. 7.15a) at $T = 65$ K and $\mu_0 H = 9$ T. A clear diminishment of the n-value is observed in the TFA case as the magnetic field gets aligned with the ab-planes. The decrease in n translates into a larger vortex creep, hence, stronger curvature of the IV-curve. Attributed to thermally activated double-kink excitations, the effect is observable for films where intrinsic pinning by the laminar crystal structure is the prime defect in this direction [240, 257, 258]. On the contrary, both TLAG films show a peak-like shape of the $n(\theta)$ at $\theta = 90°$, 65 K and 9 T. This inverse correlation is a fingerprint of SFs disrupting double kink formations, as shown formerly for TFA NC films [243].

In summary, the breaking of long-length twin-boundary coherence (Fig. 7.14b)) together with a characteristic increase in n-values reinforces that transport characteristics of TLAG films are influenced by the high density of SFs. Once again, TLAG pristine films are suggested to resemble a pinning constellation that is typical for TFA NC films (Fig. 7.14b)), rather than pristine YBCO (Fig. 7.14a)).

7.3.5 Blatter scaling separation of isotropic and anisotropic pinning contributions

The combined understanding of the aforegoing part can further be used to evaluate the isotropic/anisotropic contributions to pinning in defined angular ranges where we expect SFs or local strain deviation to impact most prominently the performance. The approach relies on Blatter scaling separation [239, 240] and is frequently used to interpret J_c data [259–261]. A complete introduction to the separation approach and construction of

[17] Flux creep rates are typically studied through magnetic relaxation measurements [256]

$H-T$ dependent color-maps, discussed in this section, are presented in the appendix E.
In 7.2.1 we have introduced an effective magnetic field, $\mu_0 H_{\text{eff}}$, to obtain anisotropy factors, γ_{eff}, from an isotropic collapse of irreversibility lines (ILs). The value of γ_{eff} determines the strength of magnetic field modulation to reach this overlap (eq. 7.1).

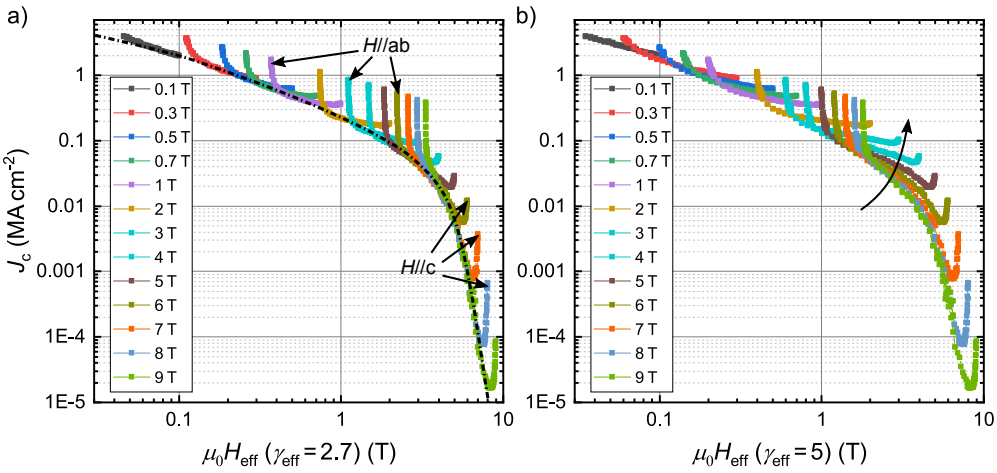

FIGURE 7.16: Blatter scaling of $J_c(\theta)$ curves through introduction of an effective magnetic field $\mu_0 H_{\text{eff}}$ for a $P_{O2}(BaCu_2O_2)$-route grown pristine film. The scaling is carried out with (a) $\gamma_{\text{eff}} = 2.7$ and (b) $\gamma_{\text{eff}} = 5$ to show the decreased anisotropy of TLAG films as compared to the TFA-CSD case [242]. Deviations from the isotropic collapse, due to anisotropic defects along $H//c$ and $H//ab$, are labeled with arrows in a).

The same methodology can be used to scale $J_c(\theta)$ data obtained at different magnetic fields. Fig. 7.16a) shows J_c versus $\mu_0 H_{\text{eff}}$ data at 77 K for a pristine TLAG films grown through the $P_{O2}(BaCu_2O_2)$-route. A γ_{eff} value of 2.7 is used, as determined previously through IL scaling (Fig. 7.6). As a result, the $J_c(\theta)$ curves, measured at 0.1 - 9 T, overlap in those regions where J_c is entirely governed by isotropic pinning [41]. Accordingly, $J_c(\theta)$ regions close to $H//ab$ and $H//c$, that is where most anisotropic pinning centers are settled in YBCO films, deviate gradually away from the collapse (arrows in Fig. 7.16a)). To show that the scaling does not succeed for higher γ_{eff} values, as used for TFA pristine films, the calculation is repeated with $\gamma_{\text{eff}} = 5$. As seen in Fig. 7.16b), the overlap of $J_c(\theta)$ curves is not achieved in any of the angular ranges, in agreement with the IL studies (Fig. 7.5).
Fig 7.16a) allows to obtain a $J_c(H_{\text{eff}})$ curve for the isotropic contribution to pinning through interpolation of the collapsed regions (black-dashed line).

The curve can then be used to recalculate the isotropic curves for the $J_c(H)$ and $J_c(\theta)$ dependencies at the same temperature where the Blatter scaling is performed.

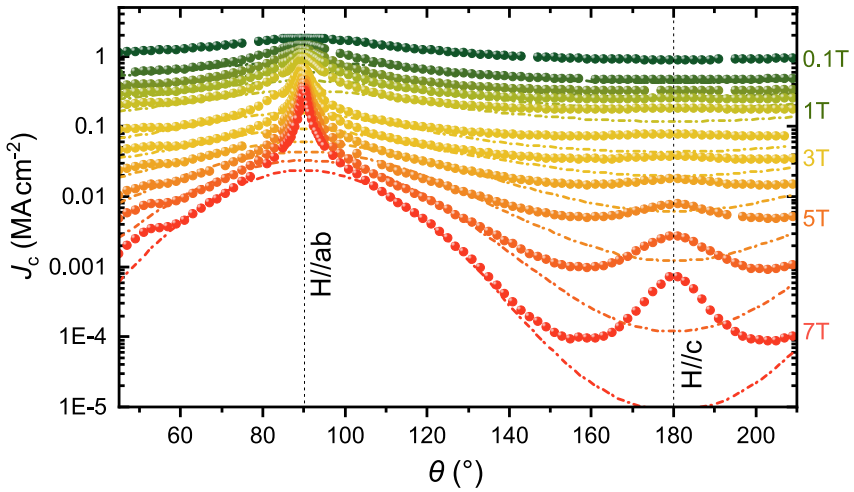

FIGURE 7.17: $J_c(\theta)$ evolution of a T-route grown film at 77 K for varying magnetic fields of 0.1 - 7 T (see labels) at 77 K. Data points and dashed lines correspond to the measured $J_c(\theta)$ and isotropic contribution $J_{c,iso}(\theta)$, respectively.

The isotropic contribution to $J_c(\theta)$ is depicted exemplary in Fig. 7.17 for varying magnetic fields at 77 K. Each measured curve is included through solid symbols and the isotropic fraction as dashed line of the same color. As observed in Fig. 7.16a), some parts of the curve did not collapse. This is now visible in the separation of J_c to $J_{c,iso}$ close to $H//$ab and $H//$c. The discrepancy is attributed to anisotropic pinning centers that act in these directions and also allow for off-angle accommodation of vortices.[18] Hence, absolute values for $J_{c,aniso}$ can be obtained through substraction of J_c and $J_{c,iso}$.[19] The $J_{c,aniso}$ angular-dependence is shown in Fig. 7.18 for the same pristine sample at 77 K. Two peak-like contributions arise from intrinsic pinning + SFs at $H//$ab and TBs along $H//$c. The high density of correlated defects in ab-direction is responsible for the more pronounced anisotropic peak.

[18] As will be discussed in the following, vortices can be pinned in a staircase-like manner away from the main axes.

[19] The linear subtraction is a rough approximation since interactions between defects are not considered. Nevertheless, it is valid whenever one of the defect types is dominant [30].

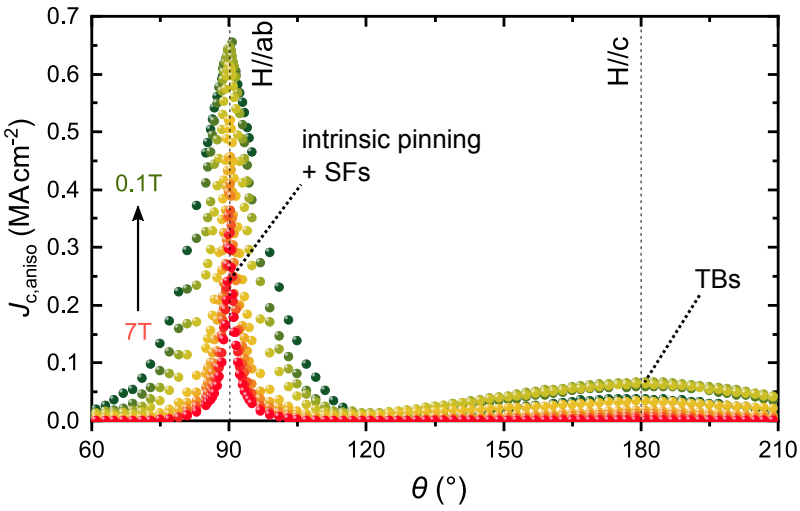

FIGURE 7.18: Anisotropic contribution, $J_{c,aniso}(\theta)$, at 77 K for varying magnetic fields of 0.1 - 7 T. The curves are obtained through subtraction of $J_c(\theta)$ and $J_{c,iso}(\theta)$ (Fig. 7.17). The most relevant anisotropic pinning centers along $H//c$ and $H//ab$ are labeled.

Already from Fig. 7.18 it becomes apparent that the peak width in $H//ab$ decreases with increasing magnetic field. In fact, the width variation seems to be less noticeable in the high magnetic field limit going towards 7 T. To understand this behaviour, vortex accommodation in correlated defects needs to be addressed.

Taking the example of intrinsic ab-plane pinning, a schematic overview of different vortex accommodation regimes is given in Fig. 7.19: When H encloses an angle $\Delta\theta = \theta - 90\,^\circ$ with the ab-plane direction three pinning regimes can be drawn dependent on the extent of the tilt [258, 262]. Up to a threshold, θ_L, vortices are in lock-in with the defect direction (Fig. 7.19a)). This, so-called, lock-in angle is estimated in the order of $\theta_L < 0.1\,^\circ$ [258], far too small to be responsible for the large width seen in the anisotropic ab-peak (Fig. 7.18). Instead, the broadening in angular dependence can be fully ascribed to a regime where vortices remain trapped in a staircase-like manner, consisting of pinned segments and vortex kinks (Fig. 7.19b)). This upper threshold is referred to as trapping angle, θ_T, and its exceedance results in vortices loosing their accomodation and aligning with the outer magnetic field (Fig. 7.19c)).

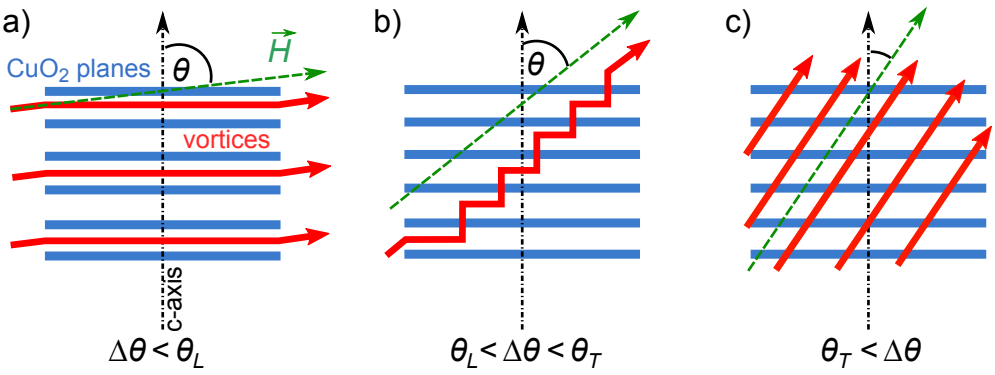

FIGURE 7.19: Illustration of different vortex accommodation regimes for intrinsic pinning along $H//ab$. The applied magnetic field is tilted by $\Delta\theta = \theta - 90\,^\circ$ with respect to the ab-planes. For angles a) $|\Delta\theta| < \theta_L$, b) $\theta_L < |\Delta\theta| < \theta_T$ and c) $\theta_T < |\Delta\theta|$ vortices remain in the lock-in, staircase and straight-vortex regime, respectively. Adapted from [30].

In order to quantify the possible degree of vortex misalignment, the trapping angle θ_T can be estimated through the full width at half maximum (FWHM) of the anisotropic ab-peak [41, 258, 262]. This is done at 77 K for several TLAG pristine films and three TFA pristine samples as reference. Shown in Fig. 7.20, the TLAG films present a clear increase in trapping angle for the full range of probed magnetic fields (0.1 - 9 T). The raw data at 2 T is normalized to the maximum value, $J_{c,aniso}(90\,^\circ)$, and shown in the inset for comparison. Already here the width increase from TFA to TLAG films is observable.

The decline of θ_T with magnetic field is a signature of vortex-vortex interactions [258]. Below the matching field, $\mu_0 H_\phi$, vortices are pinned individually by defects and J_c would be field-independent. For $H > H_\phi$, however, some vortices outside the pinning potential interact with those being pinned. This, in turn, yields to energy dissipation.

Regarding the evolution in Fig. 7.20, the initial decrease of θ_T for 0.1 - 4 T is more abrupt for all films, followed by an asymptotic behaviour at high fields. In the case of mixed pinning landscapes, constituted of intrinsic ab-plane pinning and other anisotropic pinning contributions, this effect is attributed to the existence of several matching fields, strongly differing in their magnitude [30, 243, 258, 262]. The matching field of intrinsic pinning in YBCO is estimated to reach up to 1000 T, while H_ϕ of SF pinning depends on the actual density and distribution and can lie below 1 T [30, 258]. Hence, the $\theta_T(H)$ dependence is governed by a crossover from a region where SF pinning transitions into pure intrinsic pinning. Since the large number of intrinsic pinning centers cannot be saturated, given the high matching field, the peak width starts to saturate.

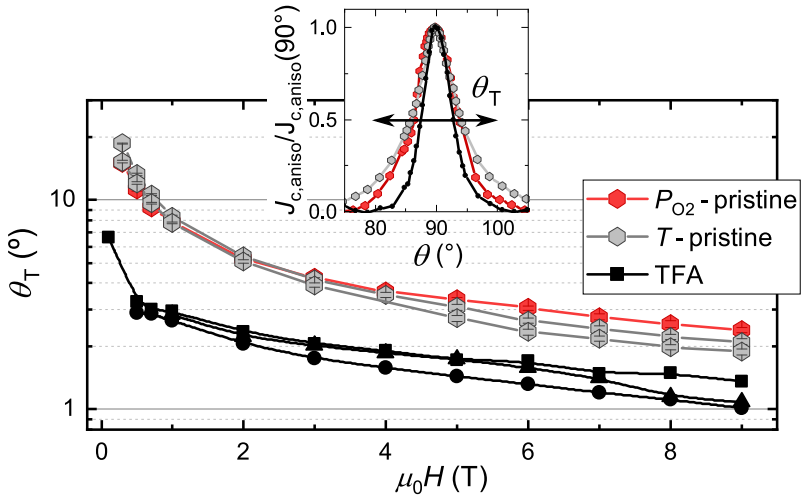

FIGURE 7.20: FWHM values, θ_T, of the anisotropic peaks at $H//$ab and 77 K (e.g. as shown in Fig. 7.18) for TLAG and TFA pristine films. Normalized, anisotropic $H//$ab peaks at 2 T are further shown in the inset. The double-headed arrow highlights the θ_T increase from TFA to TLAG pristine films.

It should be stressed that θ_T values of pristine TLAG films exceed the TFA ones at all magnetic fields. Regarding the low magnetic field region (< 4 T) this might be a direct result of the increased SF density in TLAG films that we have motivated throughout this chapter. Towards 9 T, however, the increase of θ_T is uncertain. A possible explanation might lie in enhanced lattice bending associated to the high SF density. Intrinsic pinning would then allow for a higher margin in vortex accommodation angles as also concluded for the increased anisotropic peak widths of TFA nanocomposite films [30, 243].
Similar to the Blatter scaling separation of $J_c(\theta)$ curves, the approach can be applied to the in-field behaviour at various temperatures (5 - 77 K). For a single TLAG pristine film from the $P_{O2}(BaCu_2O_2)$-route, the complete separation, both for $H//$c and $H//$ab, is presented in Fig. 7.21. The $J_{c,aniso}$ contribution is calculated according to $J_{c,aniso} = J_c - J_{c,iso}$.
Some of the aforegoing discussion reflects in the presented Blatter separation. At $H//$c, J_c is predominantly governed by isotropic pinning since the only anisotropic contribution is provided through twin boundaries, perturbed in coherence in the TLAG case (7.3.4). As expected, their contribution is primarily located at high temperatures and fields [45, 252]. The $J_{c,aniso}$ fraction at $H//$ab, however, is considerably increased given the combined contribution of intrinsic and SF pinning.

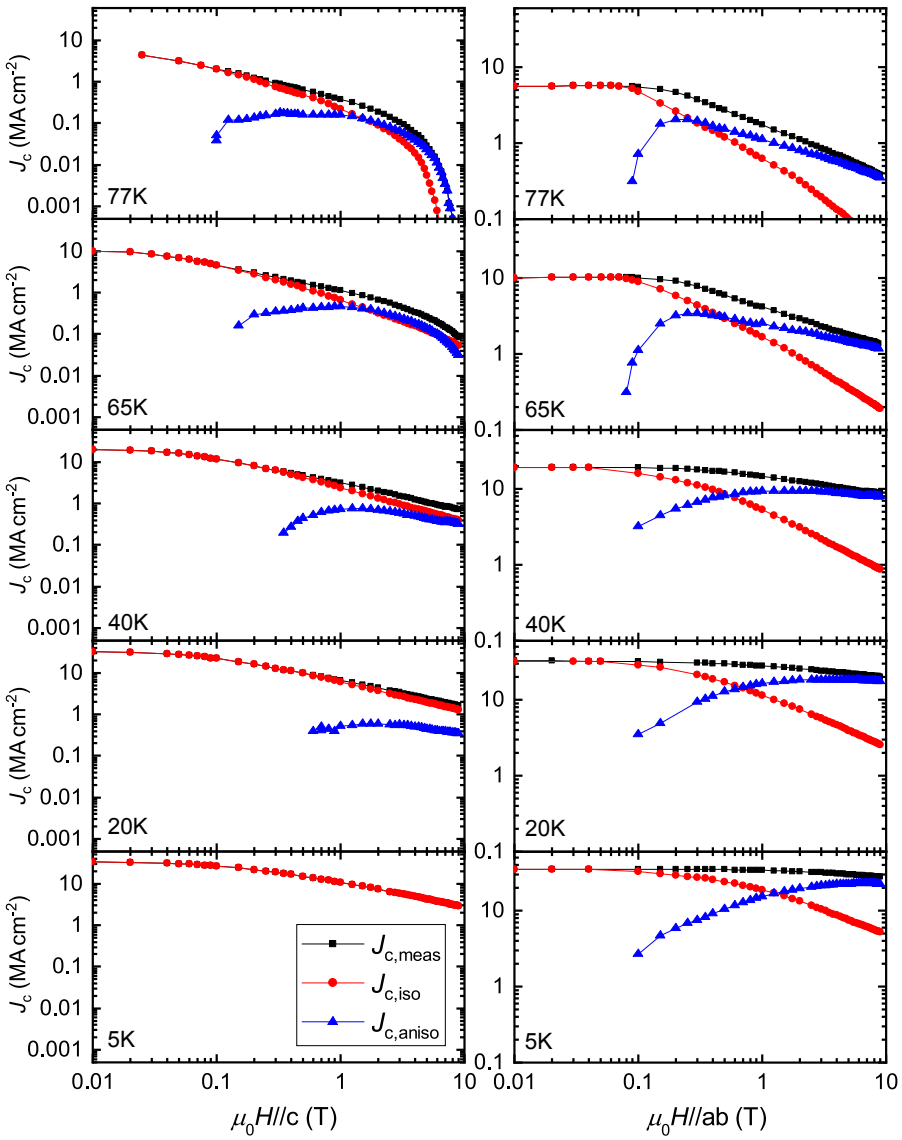

FIGURE 7.21: Separation of the in-field critical current density, $J_c(H)$, into isotropic ($J_{c,iso}$) and anisotropic ($J_{c,aniso}$) parts using the Blatter scaling approach with $\gamma_{eff} = 2.7$. The method is carried out at temperatures from 5 - 77 K and for $H//c$ and $H//ab$ for a pristine film grown through the $P_{O2}(BaCu_2O_2)$ -route, 100 nm in thickness.

The field- and temperature-dependent separation has been repeated for a T - route grown TLAG and a TFA pristine reference sample. This allows to set the isotropic and anisotropic pinning contributions of both processes in comparison. Considering first the results for $H//ab$, we calculate the anisotropic

fraction at $\mu_0 H^*_{0.8}$ according to

$$\eta_{\mathrm{H//ab}} = \frac{J_{\mathrm{c,aniso}}(\mu_0 H^*_{0.8})}{J_{\mathrm{c}}(\mu_0 H^*_{0.8})}. \tag{7.5}$$

Hence, the analysis probes the amount of anisotropic pinning centers acting in that direction. Values of η are calculated in a range of 5 - 77 K and depicted in Fig. 7.22. For TLAG films the anisotropic fraction of defects is increased as compared to the pristine TFA case. The increase is more pronounced at high temperatures (> 50 K) where η drops below 10% in the TFA film and settles around 60% for TLAG pristine films.

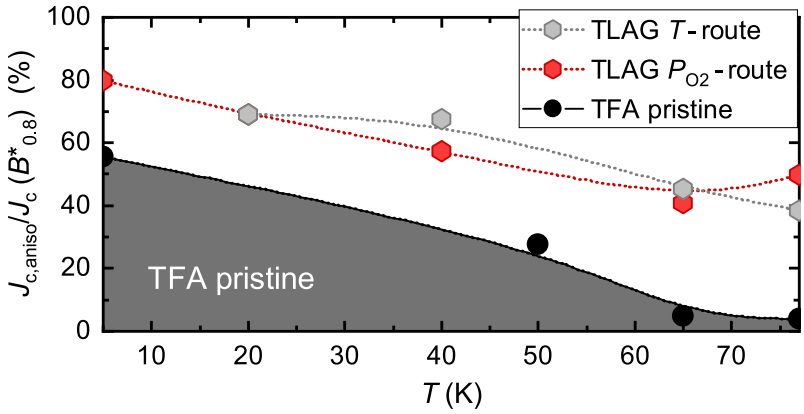

FIGURE 7.22: Anisotropic pinning contribution to J_c at $H^*_{0.8}$ for H//ab, expressed as ratio $J_{c,aniso}/J_c$ in percent. The dark-shaded region covers the margin of pristine TFA films.

The overall elevation of η values can be attributed to the increased SF density in TLAG grown films. The combined effect of intrinsic and SF pinning was previously shown to influence the evolution of trapping angles (Fig. 7.20) and is evidenced here to result in the higher amount of anisotropic pinning centers.

Also the more pronounced η increase for T > 50 K might be attributed to a higher SF density. The vortex core diameter along the ab-planes, 2ξ, is calculated to reach a minimum of 3.2 nm at 0 K and monotonically increase with temperature [30, 240]. Consequently, the pinning efficiency of larger defects will be more significant at high temperatures than of smaller ones. Intrinsic pinning is known to give a modulation of the order parameter, ϕ, on the subnanometer scale reaching a maximum at the Cu_2O planes and a minimum in between. SFs, on the contrary, even though only constituted of a Cu-O double-chain layer, induce structural changes in their vicinity

increasing the effective width of the potential well to pin vortices [54, 55]. Hence, SFs pinning will dominate the high temperature region, in agreement with the recently developed $H-T$ phase diagram for different pinning contributions in YBCO [243].

Finally, using the Blatter separation of $J_c(H)$ data (Fig. 7.21), a comparison can also be drawn for the $H//c$ direction. Here, the focus is set on the isotropic changes, given the low amount of anisotropic pinning centers in this direction.[20] In particular, the isotropic contribution to J_c is summarized through $H-T$ dependent color-maps, the construction of which is discussed in Appendix E.
Fig. 7.23 shows the $H-T$ diagrams in a range of 0 - 9 T and 5 - 75 K for the same three films that were analysed previously in their anisotropic pinning characteristics (Fig. 7.22). The upper $J_{c,iso}/J_c$ ratios (50 - 90%) are labeled at the corresponding contour lines. From a comparison of both processes, TFA and TLAG, the increase in isotropic pinning becomes apparent. Following the 80% contour lines for the TFA and $P_{O2}(BaCu_2O_2)$-route grown pristine film the region extends from 10 K to 15 K at high fields and is overall widened in magnetic field at any temperature. This is even more pronounced in the T-route grown pristine sample where the 80% threshold reaches 38 K at 9 T.
The change in pinning characteristics resembles the differences observed from TFA-pristine to TFA-nanocomposite films where a high density of SFs and local strain deviations perturbs the twin boundary coherence [30, 249]. While displaced and non-coherent TBs result in a direct decrease in anisotropic pinning, the localized strain around the SFs (nanostrain) is a source of strong isotropic pinning that affects the whole $H-T$ diagram [40, 41]. For TLAG films, this can further be corroborated given the increased nanostrain values (Fig. 7.8), broken TB coherence (Fig. 7.15) and widening in vortex accommodation angles along $H//ab$ (Fig. 7.20).
Finally, it can also be suggested from Fig. 7.23 that the increase in isotropic pinning is more pronounced for the T-route grown film. This might be attributed to the overall tendency of this approach towards shorter SFs, increased amounts of lattice distortions and presence of embedded ab-grains (7.1.1).
For the sake of completeness a similar analysis was carried out to produce H - T color maps of the $J_{c,aniso}/J_c$ ratio for H//ab, though the main results for that magnetic field orientation are summarized in the aforegoing part. The H - T diagrams are included in Appendix E, Fig. E.5.

[20] Mainly twin boundary pinning.

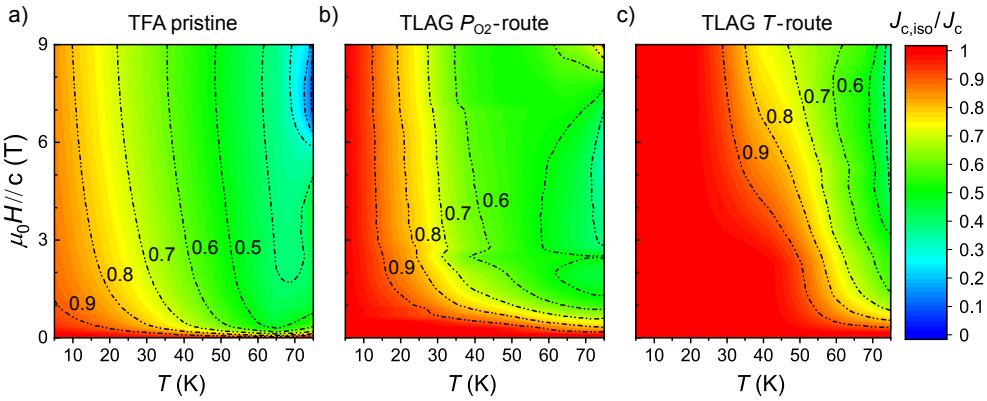

FIGURE 7.23: H - T color mapping of the $J_{c,iso}/J_c$ ratio for a TFA-CSD pristine and a TLAG $P_{O2}(BaCu_2O_2)$-route and T-route pristine film, H//c. Contour lines of different ratios are included as guide to the eye.

In summary, we have conducted a Blatter scaling separation of $J_c(\theta, H, T)$ data to study the isotropic and anisotropic contributions. This allows us to affirm that TLAG films have a more complex pinning landscape as compared to YBCO grown through the TFA-CSD approach. Most notably, the high amount of SFs is shown to induce changes in vortex accommodation angles for $H//ab$ and increase the overall isotropic fraction at $H//c$.
An equivalent study should be carried out on TLAG NC films, whose microstructure and physical properties (nanostrain, γ_{eff}) are shown to exhibit promising trends with regard to pinning performance. In particular, we have motivated that the recent miniaturization of NPs together with the non-equilibrium process kinetics might pave the way for NP pinning, an effect that is highly desired to fabricate NC films with strong, isotropic core pinning contributions.

7.4 Conclusions

With the aim of characterizing the pinning characteristics of TLAG films, we carried out a set of microstructural and electrical transport measurements on patterned bridges using high J_c samples (1.2 - 5.5 MA cm^{-2}) from the two main growth approaches, $P_{O2}(BaCu_2O_2)$ - and T-route (Fig. 4.4.1). In contrast to TFA-CSD films, the TLAG process is shown to trigger a higher density of nanometric defects that are advantageous for vortex pinning.
Microstructurally, all films present increased amounts of 248 stacking faults (SFs) and YBCO lattice distortions. In the case of T-route grown films we also identify embedded ab-grain (5-10 nm is size), antiphase boundaries and

224 intergrowths. Although the latter do not constitute the prime defect landscape, their presence is indicative for the non-equilibrium nature of the process.
Several physical measures are demonstrated to change due to the highly faulted YBCO crystal structure. In particular, we find that TLAG samples have a reduced effective anisotropy, γ_{eff}, and increased nanostrain values as compared to pristine reference films from the TFA-CSD process.[21] Up to now, such tendencies have primarily been achieved in TFA-CSD films only through addition of nanoparticles (NPs) where SFs are generated as a means of stress relaxation.
We further show that the TLAG process is compatible with NP addition from colloidal solutions giving rise to more defects and an elongation of the single-vortex pinning plateau. In fact, since TLAG nanocomposite films span a similar nanostrain range as their pristine counterpart, while profoundly increasing the single-vortex pinning plateau, we suggest that a fraction of the added NPs can act as core pinning centers. This is in agreement with the recent success in synthesizing nanoparticles of only 3-4 nm in diameter and the successful conservation of the nanometric size until embedment in the YBCO crystal structure, hence, avoiding coarsening during growth.

Finally, the identified microstructural changes are found to beneficially impact the superconducting performance of TLAG films yielding to an improved performance in applied field conditions as compared to TFA-CSD YBCO. This is shown through a 2-7 fold increase in $\mu_0 H^*_{0.8}$ values,[22] both for $H//\text{ab}$ and $H//\text{c}$ at 5 - 77 K, a 2-3 fold increase of $J_c(T)$ at 9 T and an overall flattening of the $J_c(\theta)$ dependence.
We attribute the improved angular isotropy and in-field behaviour to the high density of SFs which, in turn, induce localized strain at the nanoscale (nanostrain) and perturb the coherence of twin boundaries (TBs), a naturally formed, anisotropic defect of the YBCO orthorhombic structure. This is further confirmed through angular dependent transport measurements and Blatter scaling separation of isotropic and anisotropic pinning contributions of J_c.
The enhanced in-field performance of pristine TLAG films appears to be intrinsic to the growth process. Similar tendencies are reported for YBCO growth through rapid heating and liquid-mediated techniques of high supersaturation, both of which are given in the TLAG case. The use of non-equilibrium growth kinetics might, hence, become a viable strategy for defect landscape tailoring, complementary to the already established techniques.
Additional transport measurements and a thorough analysis of the pinning

[21] The two physical measures range from 2.5 - 3.5 and 0.12 - 0.25, respectively
[22] Associated to a higher density of defects that elongate the single-vortex pinning plateau.

characteristics should further be carried out for NC films in future work. These are shown to exhibit an even more complex pinning landscape than pristine TLAG films and potentially allow for NP core pinning, a yet unexplored strategy to improve the isotropic pinning performance of YBCO films.

Chapter 8

General Conclusions

With the aim of developing a novel growth approach, that can provide $YBa_2Cu_3O_{7-\delta}$ (YBCO) films at ultrahigh growth rates and of competitive performance, we have combined Chemical Solution Deposition (CSD) with the non-equilibrium growth kinetics of the Transient-Liquid Assisted Growth process (TLAG-CSD). It is based on the capability of the ternary $BaCO_3$, CuO, and Y_2O_3 system to form a transient (Ba-Cu-O) liquid phase prior to the growth of YBCO, i.e. a liquid that does not exist in the equilibrium ternary phase diagram. Ultrahigh YBCO epitaxial growth rates are rendered possible due to $BaCO_3$ decomposition and reaction with CuO to form a transient liquid in the presence of dispersed Y_2O_3 nanoparticles. Due to the kinetic hindrance to crystallize YBCO, the liquid formation precedes and accelerates the reaction path towards the final product phase.
In this thesis, we have thoroughly looked into integral parts of the process, including *in-situ* studies of the involved reactions and growth kinetics, tracking of physical properties (structural, electrical and inductive analysis) of grown films and characterization of the vortex pinning performance using micropatterned four-point probes. In particular, our efforts aimed to address several key issues:

1. **Fundamental understanding of TLAG-CSD:** Scarce information was available on the combination of transient liquids with non-equilibrium processing conditions, such as rapid heating and pressure variations. We had to define viable routes on reaching stable YBCO growth conditions, disclose the underlying reactions and identify the most influential processing parameters. The demonstration of large growth rates and possibility to study such processes in a systematic way was further required as a proof of concept.

2. **Limitations and capabilities in obtaining high current density films:** TLAG-CSD relies on $BaCO_3$ decomposition and formation of a melt that

is highly reactive with crucible and substrate materials. Both characteristics can result in obstacles to obtain high critical current density films. We had to demonstrate that CO_2 retention and liquid induced reactivity can be avoided. In addition, oxygen incorporation and the percolation state of grown films had to be examined to evaluate potential limitations to the process.

3. **Feasibility of reaching competitive SC performance:** Liquid assisted growth techniques, especially those that work at low supersaturation, are known to give rise to poor pinning landscapes and offer restricted possibilities for defect tailoring. It was therefore essential to study the pinning efficiency of TLAG grown YBCO films. We further aimed to test the compatibility of the process with preformed nanoparticle addition from colloidal solutions, a strategy that could allow large-scale, controlled tuning of the defect constellation.

In the course of this thesis we have established a foundation for YBCO growth through TLAG-CSD and developed experimental strategies to study the process. Using a high luminosity X-ray beam (18 keV) in combination with fast acquisition times (100 - 500 ms) per 2D-XRD frame we carried out *in-situ* growth experiments under non-equilibrium processing conditions at the DiffAbs beamline, Soleil Synchrotron. The experiments proved essential to resolve reactions on the scale of seconds and demonstrate that the TLAG process enables YBCO growth at rates above $100\,\mathrm{nm\,s^{-1}}$.
The *in-situ* measurements were successfully employed to show that full $BaCO_3$ decomposition is achievable through different $P_{O2} - T$ paths into the YBCO stable region, either through heating at constant P_{O2} to a target growth temperature, so-called T - route, or through a 2-step procedure where the sample is first heated in a low P_{O2} step, followed by YBCO growth upon pressure increase into the high P_{O2} region, termed $P_{O2}(BaCu_2O_2)$ -route. Both processing routes were elucidated in their main reaction paths and optimized to allow for growth of high current density YBCO films (1 - 5 $\mathrm{MA\,cm^{-2}}$).
The T - route, in particular, was studied in greater detail to obtain *in-situ* information about TLAG growth kinetics under variation of temperature, oxygen partial pressure and heating ramp. In a first approach, two type of nanocrystalline precursor systems were analysed during thermal treatment: Binary mixtures containing $BaCO_3$ and CuO and ternary ones with the full Y_2O_3, $BaCO_3$ and CuO composition. The former system is used to facilitate the observation of melting and possible binary reactions, while the latter mixtures serve to explore YBCO growth. These efforts led to an elaborate construction of so-called kinetic phase diagrams, a visual representation of the process that comprises all appearing phases during thermal treatment

at different heating ramps and P_{O2} partial pressures. The diagrams were constructed for the case of binary mixtures of (3-7) composition and a heating ramp of $4.5\,^{o}C\,s^{-1}$ and ternary mixtures of (2-3) and (3-7) composition for heating ramps of $0.4\,^{o}C\,s^{-1}$ and $4.5\,^{o}C\,s^{-1}$.[1] The kinetic phase diagrams revealed that transient liquid assisted growth of YBCO can be realised in a wide range of $P_{O2} - T$ conditions. The temperature margin is found highly increased as compared to conventional solid-solid and liquid-mediated processes, such as Pulsed Laser Deposition (PLD) or Liquid Phase Epitaxy (LPE). We attribute this fact to the nanometric size and homogenous spread of precursor phases, which can undergo rapid transformations when high heating ramps, as used in this work, are employed.

In a second approach of analysing synchrotron data we have focused our efforts on narrowing down process parameters to foster

1. **Growth at reduced temperatures**
2. **Growth at increased epitaxial growth rates**
3. **Epitaxial YBCO as primary nucleating phase**

The first two issues are of particular interest for the industrial use of TLAG to further improve fabrication cost and throughput, while the last point deals with strategies to avoid formation of undesired phases that can be obstructive to reaching high current percolation in grown films. We could successfully demonstrate that growth temperatures and growth rates can both be tuned through film composition, heating ramps and P_{O2}, being key parameters of the kinetic phase diagrams. High epitaxial layer growth rates are achieved through heating ramp increase and placement of the $P_{O2} - T$ growth conditions in the "full - liquid" region. In this context we also suggest that the Cu valance state in the "full - liquid" region might be essential to liquid characteristics, such as viscosity, diffusivity and the equilibrium concentration of Y. Only the exploration of YBCO growth in wider regions of the phase diagram, which is currently addressed with new experiments, might provide further insights on this matter and allow for the refinement of processing conditions.
A decrease in growth temperatures can be achieved by two different means: Variation of the (Ba - Cu) ratio or reduction of the P_{O2}. We suggest that precursor films with enriched copper content tend to promote epitaxial YBCO growth at lowered temperatures and that the effect is attributed to a higher equilibrium concentration of Y in the copper-rich melt, hence, decreased

[1] The nomenclature (x - y) relates to the (Ba-Cu) ratio of each film.

supersaturation of the system. On the other hand, the influence of P_{O2} on growth temperatures might be a result of changes in liquid characteristics (e.g. viscosity, Y solubility) or a shift of the YBCO stability window. Using both strategies, we could demonstrate that epitaxial growth of YBCO can be achieved at temperatures as low as 650 °C and growth rates of 10 nm s^{-1}.
Finally, we have observed that the TLAG process is capable of reorienting homogeneously nucleated YBCO grains and preformed nanoparticles towards the epitaxial layer alignment. The unexpected, kinectically driven mechanism was further explored in its efficiency to reach full epitaxy in films that had previously nucleated homogeneous YBCO along the thermal profile. As a result, we observed that reorientation is favoured upon heating ramp increase and use of the stoichiometric (2 - 3) composition. While increased heating ramps are suggested to reduce coarsening effects and allow for enhanced liquid assistance in the "full-liquid" region, (2 - 3) compositions were shown to avoid the segregation of solid CuO grains which, in turn, can perturb the reorientation process. These findings enabled us to formulate new experiments with growth conditions that were previously abandoned due to the impeding homogeneous nucleation.

In the proceeding course of the thesis, structural, electrical and electromagnetic properties of grown films were analyzed to pinpoint process limitations that can yield reduced current carrying performance. In particular, we addressed the critical issues of carbon retention, liquid induced reactivity, epitaxial quality of films, proper oxygen doping of the YBCO crystal structure and percolation hindrances. Some of these points can be suspended as potential limitation, others avoided through variations of process parameters. Films from all processing routes are evidenced to have a high degree of texture,[2] show no signs of carbon contamination and enable sufficient oxygen incorporation. Also liquid induced reactivity issues can be prevented through use of reduced heating ramps or growth through the TLAG pressure routes. In addition, we advice to explore growth on $LaMnO_3$ buffer layers as alternative path to avoid liquid reactivity issues. This, in turn, might allow for reconsideration of growth conditions that had to be omitted to avoid liquid induced reactivity (e.g. heating ramps higher than 20 °C s^{-1}).
Remaining performance constraints could be ascribed to route-specific, undesired phases that reduce the epitaxial cross-section. We further motivated that film percolation can be improved through choice of growth conditions that favour decreased YBCO grain sizes in the grown film. Competing, undesired phases are then encapsulated without evolving into large current blockades

[2] Demonstrated also for thick films up to 1 μm and films on hastelloy metallic substrates.

and deterioration of the grain boundary quality can be avoided. Having understood the intrinsic limitations of the process we have been able to obtain ultrahigh critical current density films with up to 5.5 MA cm^{-2} at 77 K and self-field. The follow-up research now extends our present understanding to obtaining the high performance with increased reproducibility, for thick films and for YBCO grown on metallic substrates.
Studies of the physical properties were further extended to YBCO nanocomposite films including $BaZrO_3$/$BaHfO_3$ nanoparticles (NP) from colloidal solutions. In agreement with synchrotron studies of reorientation processes, we confirmed that NPs are epitaxially incorporated into the YBCO crystal structure during growth reaching record small sizes of 4 - 6 nm and inducing strong lattice distortions. Structural, inductive and electrical transport measurements suggest an improved isotropy and in-field performance of NC films as well as indications of NP core pinning contributions. Hence, the TLAG-CSD process is demonstrated to be compatible with NP addition, a scalable methodology to further improve the pinning efficiency. The embedment of NPs at such small sizes and possibility to induce core pinning in CSD-based films has been evidenced just recently for the TFA route under particular processing conditions and low YBCO growth rates.

In the final part of this work we performed an in-depth analysis of the vortex pinning characteristics using a set of standard YBCO films of high critical current density (1.2 - 5.5 MA cm^{-2}). For reference, the results were compared with CSD YBCO films from the trifluoracetate metalorganic decomposition approach (TFA-CSD).
TLAG grown YBCO is shown to exhibit a complex microstructure with a high density of 248 stacking faults (SFs) throughout the full thickness. Also more exotic defects such as small ab-oriented YBCO grains (5 - 10 nm), antiphase boundaries and 224-intergrowths could be identified, indicative for the non-equilibrium nature of the process. In turn, the decay of J_c as function of magnetic field is smoothed and the angular isotropy improved as compared to conventional TFA-CSD grown YBCO. We attribute the improved in-field and angular characteristics to the high density of SFs which are found to induce local strain gradients and perturb the coherence of twin boundaries (TBs) already in pristine TLAG YBCO films.

Overall, we can conclude that the TLAG-CSD process has the potential to overcome present cost and throughput constraints in the fabrication process of Coated Conductors. We demonstrated that growth rates exceed those of

currently employed growth techniques by a factor of 10 - 100 and that superconducting films of competitive performance can be obtained through different processing routes. In addition, we gained fundamental understanding of the involved process mechanisms, developed methods to study these and addressed various intrinsic limitations to obtain high current density films. We further suggest that the non-equilibrium nature of the process enables unique strategies to improve the pinning efficiency of YBCO films, either through formation of natural defects during growth or inclusion of preformed nanoparticles to produce nanocomposites.

Appendix A

Appendix to Chapter 3

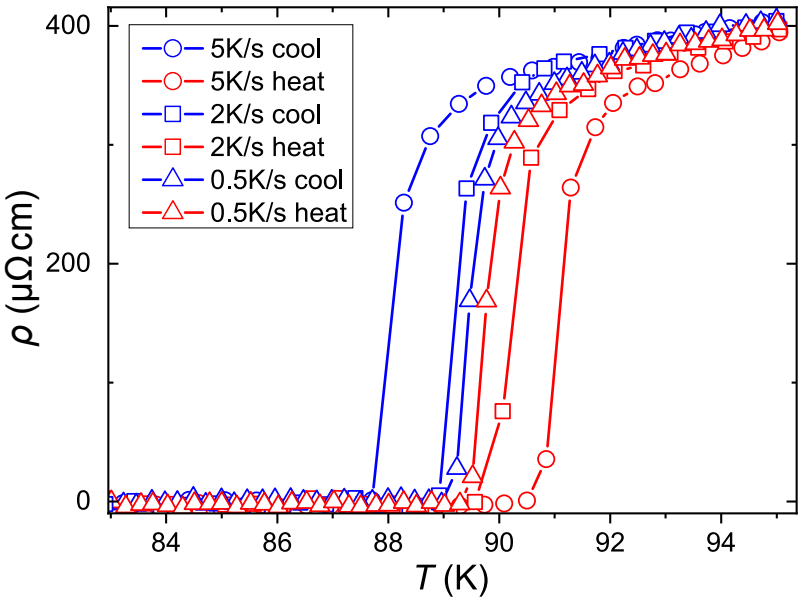

FIGURE A.1: Van der Pauw measurement of the critical temperature at different cooling and heating rates. T_c values show a systematic under- and over-estimation upon cooling or heating, respectively. An accuracy of $\pm 0.2\,°C$ on the determination of the transition temperature can be obtained at rates lower than $0.5\,°C/min$.

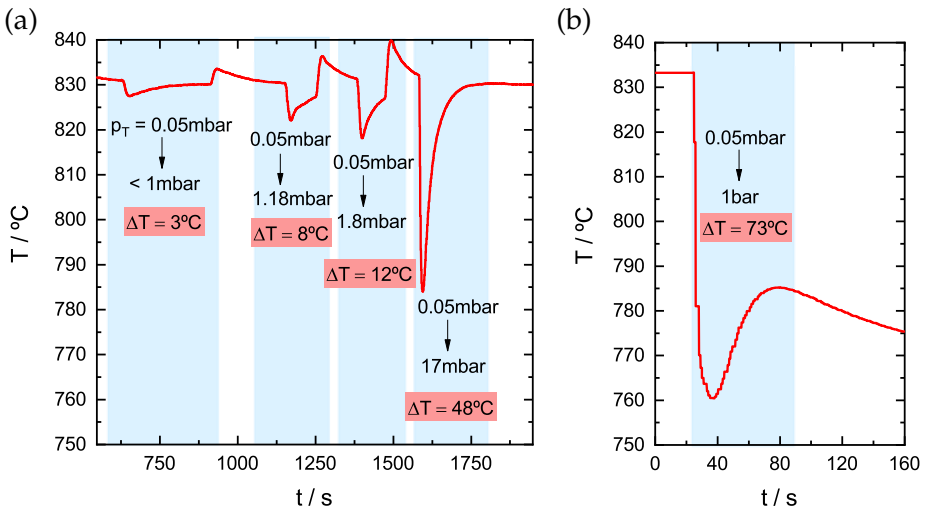

FIGURE A.2: Temperature decrease arising from pressure jumps from P_{total} =0.5 mbar to final pressures ranging from <1 mbar to 1 bar

Appendix B

Appendix to Chapter 4

B.1 Thermal history of binary films on MgO

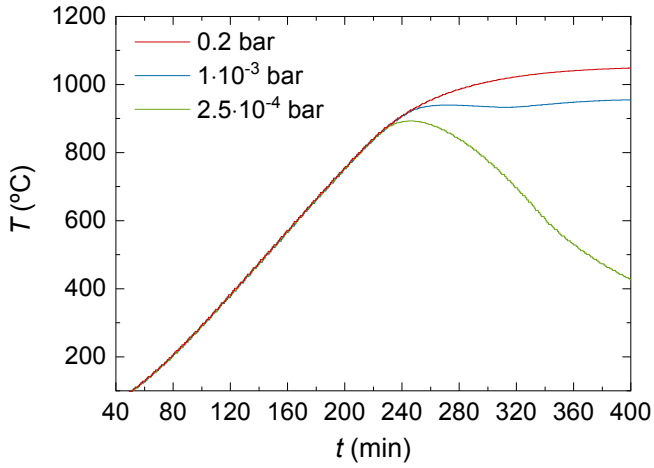

FIGURE B.1: Temperature profiles of binary films heat-treated in X-ray transparent furnace at Soleil synchrotron, Diffabs beamline. All experiments are carried out at 1 bar of total pressure varying the oxygen partial pressures (denoted in the legend). Temperature set points were increased with P_{O2} to ensure that T_E is crossed in all conditions [161]

Appendix C

Appendix to Chapter 5

C.1 $BaCO_3$ decomposition in $P_{O2}(BaCu_2O_2)$ - route

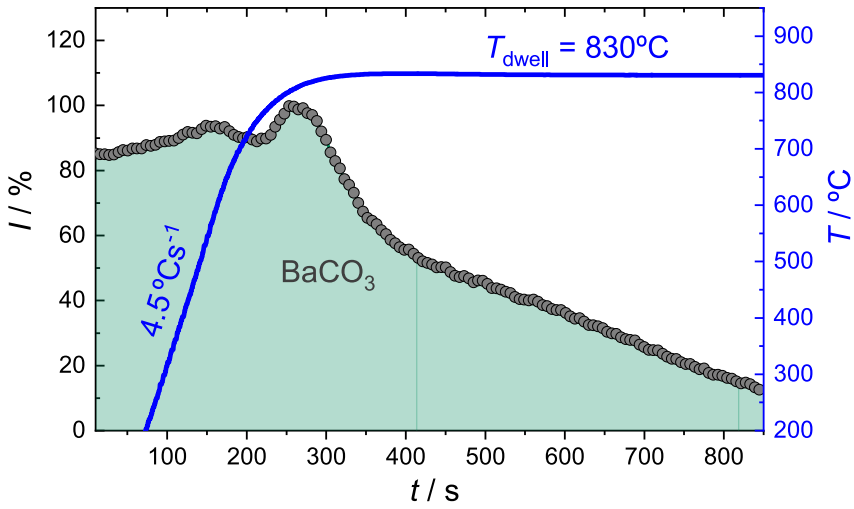

FIGURE C.1: $BaCO_3$ decomposition in $BaCu_2O_2$ - route: A temperature dwell is realized at $T_{final} = 830\,°C$, $P_{O2} = 10^{-5}$ bar and $P_{total} = 5 \cdot 10^{-5}$ bar. The evolution is obtained through tracking of the maximum $BaCO_3$ (111) plane intensity.

C.2 Heating ramp changes during growth

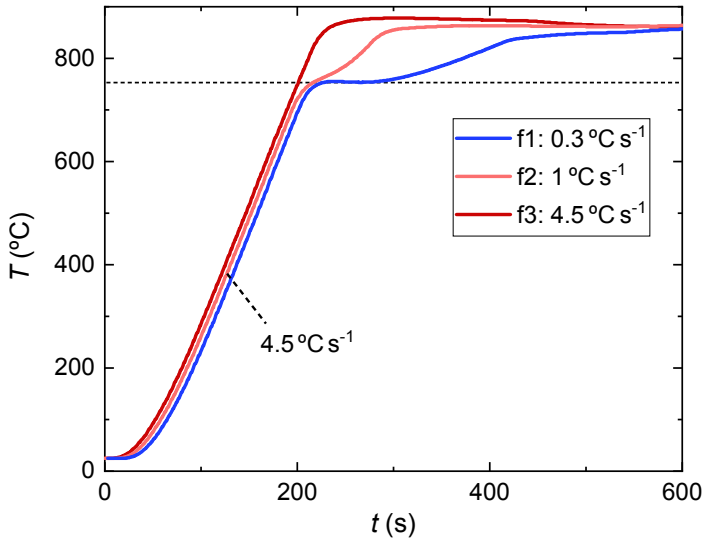

FIGURE C.2: Temperature profiles of three (3-7) films (f1-f3) of 1.75 M molar concentration treated at $P_{O2} = 1$ mbar: All films are first heated with a ramp of 4.5 °C s^{-1} to 750 °C. An average heating ramp of 4.5 °C s^{-1}, 1 °C s^{-1} and 0.3 °C s^{-1} is then applied until 860 °C for the film f1, f2 and f3, respectively.

Appendix D

Appendix to Chapter 6

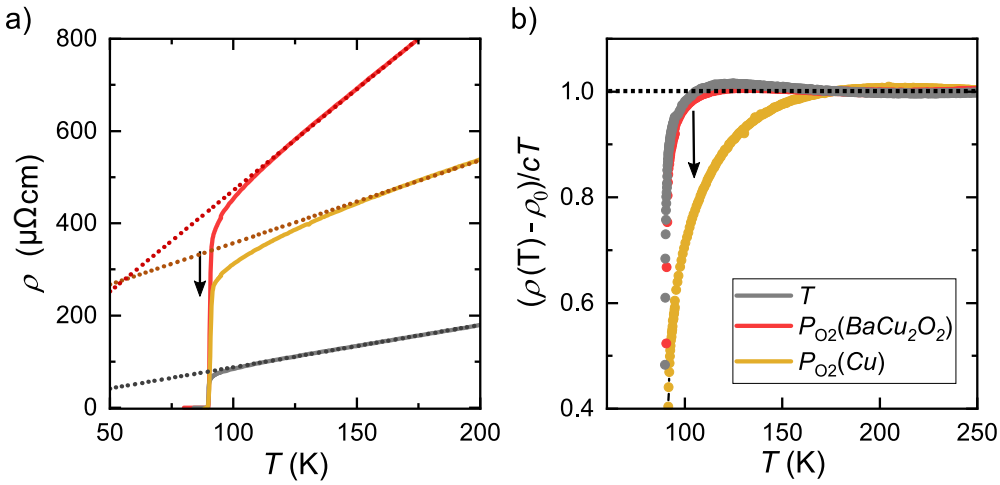

FIGURE D.1: Resistivity measurements of three thick samples (800-1000 nm) from different routes. a) $\rho(T)$ dependence indicating a deviation from linearity towards T_c. Dashed lines are linear fits carried out at 150 - 300 K. b) Normalized resistivity $(\rho(T) - \rho_0)/cT$ as a function of temperature for the same three films.

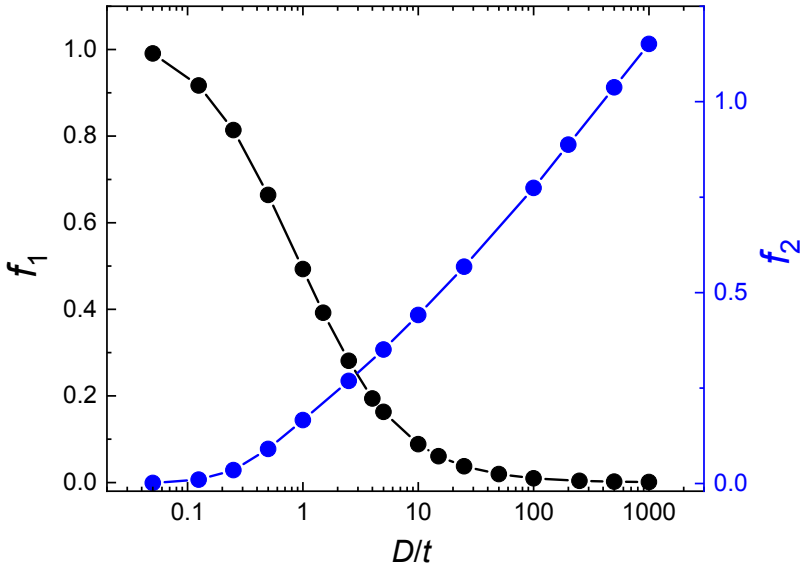

FIGURE D.2: Numerically calculated dimensionless functions, f_1 and f_2, that depend on the ratio between grain diameter and thickness (D/t) [16]. The values are used to calculate J_c^{Grain} and D according to eq. 6.3a and eq. 6.3b.

Appendix E

Appendix to Chapter 7

E.1 In-field $J_c(H)$ data of TFA-CSD and TLAG films at 5K, 50K and 65K

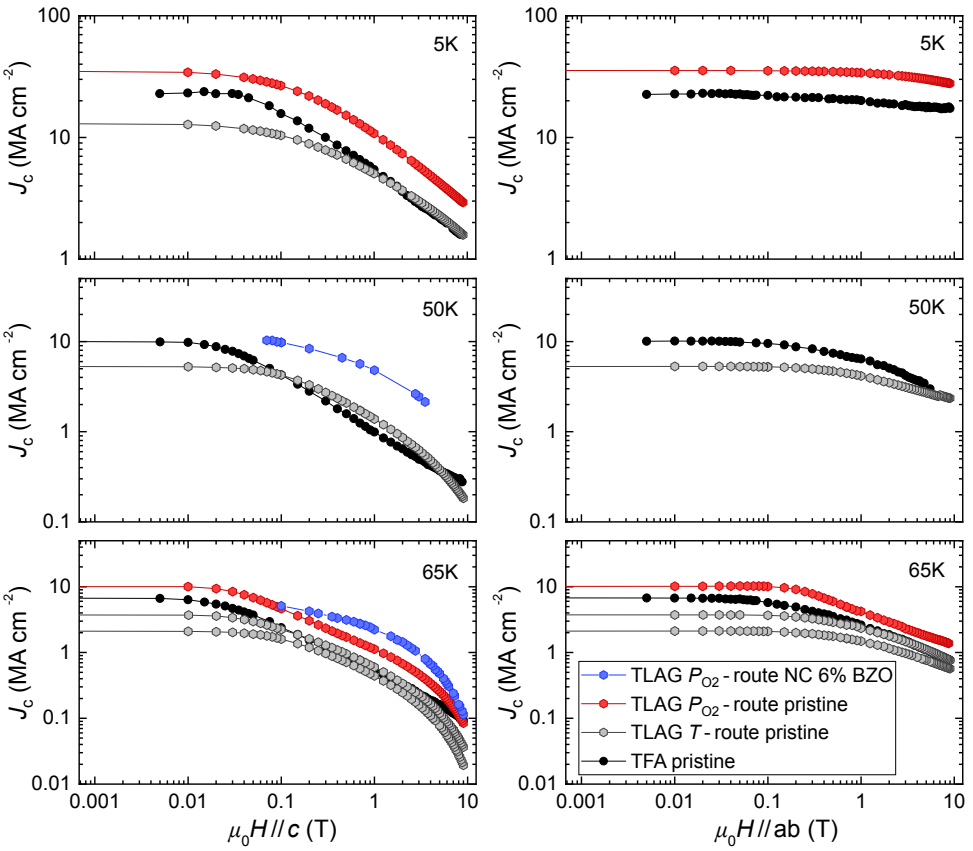

FIGURE E.1: In-field dependence of the critical current density, $J_c(H)$, at 5 K, 50 K and 55 K for a) $H//c$ and b) $H//ab$. Included are pristine TLAG films from the T - and $P_{O2}(BaCu_2O_2)$ -route, a TLAG 6%BZO NC and a TFA pristine film.

E.2 Blatter scaling and generation of H - T color maps

Isotropic pinning centres, such as vacancies, nanoparticles and localized strain regions, reduce superconductivity equally for any magnetic field orientation θ, enclosed by the magnetic field and YBCO crystal lattice (see inset in Fig. 7.5a)). Nevertheless, the characteristic vortex parameters ξ and λ scale with θ due to the electronic mass anisotropy of YBCO [240]. This is illustrated in Fig. E.2 were ξ and λ change dependent on the direction of the magnetic field H. When H is applied parallel to ab-planes, $H//\mathrm{ab}$, the vortex core adopts a pancake-like shape with ξ and λ splitting into ξ_{ab}/ξ_c and λ_{ab}/λ_c, respectively. Accordingly, ξ and λ evolve into ξ_{ab} and λ_{ab} for $H//\mathrm{c}$.

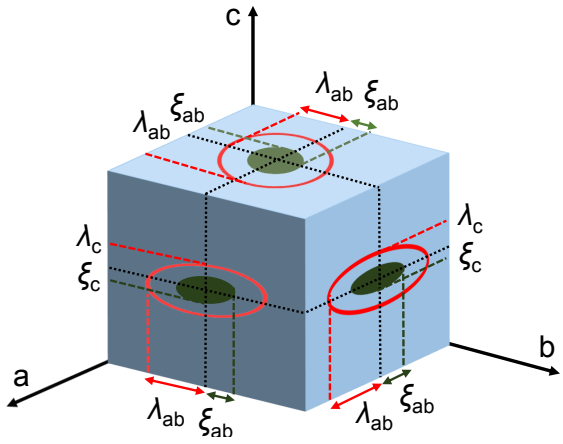

FIGURE E.2: Angular dependence of the vortex coherence length ξ and penetration depth λ with respect to the crystallographic directions in YBCO. Modified from [30].

Blatter et al. proposed a scaling approach which accounts for any isotropic pinning contribution and takes the natural modulation of vortex characteristic lengths into account [239, 240]. The method introduces an angular dependent scaling factor $\epsilon(\theta)$ which modulates according to

$$\epsilon(\theta) = [\cos^2\theta + \gamma^{-2}\sin^2\theta]^{1/2}. \tag{E.1}$$

with the anisotropic constant γ determining the strength of the modulation. The value of γ can be measured through the direction-dependent intrinsic properties:

$$\gamma = \sqrt{\frac{m_c}{m_{ab}}} = \frac{\lambda_c}{\lambda_{ab}} = \frac{\epsilon_{ab}}{\epsilon_c}. \tag{E.2}$$

Here, m_c and m_{ab} are the effective electron masses along the c- and ab-direction, respectively. However, the more common approach to obtain γ relies on isotropic scaling of $J_c(\theta)$, irreversibility field H_{irr} or upper critical field H_{c2}, all of which are influenced by the angular dependencies $\xi(\theta) = \epsilon(\theta)\xi_{ab}$ and $\lambda(\theta) = \epsilon(\theta)\lambda_{ab}$. This is typically done through introduction of a magnetic field that follows the modulation $\epsilon(\theta)$ according to

$$H_{scaled}(\theta) = \epsilon(\theta)H. \tag{E.3}$$

For standard YBCO films,[1] scaling of any of the above mentioned physical parameters yields γ values in the range of 5-6, being in agreement with the intrinsic mass anisotropy of YBCO [241]. Recent studies on nanocomposite films have shown, however, that the scaling of $J_c(H,\theta)$ and $H_{irr}(T,\theta)$ yields reduced γ values even down to 1.5 [242], while the same approach with $H_{c2}(T,\theta)$ gives the intrinsic values in the range of 4-6. This led to the differentiation between an intrinsic γ, which is only dependent on the electron mass anisotropy and an effective anisotropy parameter γ_{eff} that is altered when isotropic pinning is dominant. Hence, whenever the Blatter scaling approach is applied to $J_c(H,\theta)$ and $H_{irr}(T,\theta)$, the scaling field (eq. E.3) is substituted by an effective field H_{eff} with effective anisotropy parameter γ_{eff}:

$$H_{eff}(\theta) = \epsilon_{eff}(\theta)H = [\cos^2\theta + \gamma_{eff}^{-2}\sin^2\theta]^{1/2} \cdot H. \tag{E.4}$$

The modulation of $H_{eff}(\theta)$ for varying γ_{eff} values (2-6) is shown in Fig. E.3. The orientation and characteristic change of the vortex core along the main crystallographic directions of YBCO are further depicted in the inset. While $H_{eff}(\theta)$ is identical at $H//c$, due to the vanishing term in eq.E.4, the deviation becomes progressively stronger towards $H//ab$. The modulation of $H_{eff}(\theta)$ is weakest for the lowest value of γ_{eff}. This is in agreement with the enhanced angular isotropy of nanocomposite films where an increased density of isotropic pinning centers is observed [40, 41, 263, 264].

[1] Without introduction of artificial pinning centers.

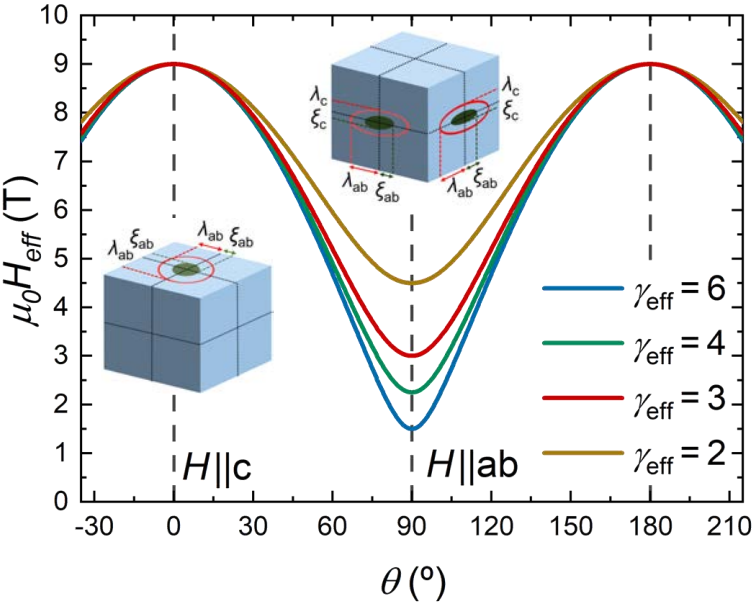

FIGURE E.3: Evolution of H_{eff} with θ for an applied field of $H = 9\,\text{T}$ and varying γ_{eff}. The curves are calculated from eq. E.4. Insets show the corresponding vortex modulation for H //c and H //ab, from Fig. E.2. Adapted from [30].

In this thesis, the Blatter scaling approach is used for two purposes, determination of γ_{eff} values as a measure of the overall isotropy of films and separation of J_c data into isotropic and anisotropic contributions, $J_{\text{iso,c}}$ and $J_{\text{aniso,c}}$, respectively.

The effective anisotropy parameter is determined through scaling of $H_{\text{irr}}(T,\theta)$ curves which are obtained from field- and angular- dependent resistance measurements $R(T)$. Such scans are carried out using patterned 4-terminal bridges in maximum Lorentz force configuration. Some of the raw measurements are shown in Fig. E.4a) for H //c. Here, the superconducting transition is remeasured in applied field conditions from 0 - 9 T. The irreversibility temperature, T_{irr}, is obtained following the criterion $R(T_{\text{irr}})/R_{95\text{K}} = 10^{-3}$, as commonly used to obtain the critical temperature in YBCO. The corresponding irreversibility line for H //c is plotted in Fig. E.4b) showing the decrease in transition temperature upon field increase.

Fig. E.4 comprises the irreversibility line determination only for one orientation of the magnetic field with respect to the YBCO crystal lattice. In order to carry out the Blatter scaling approach, the set of $R(T)$ measurements is repeated for varying angles θ from H //c to H //ab orientation. The applied field in Fig. E.4b) is then substituted through H_{eff} (eq. E.4) and the value of γ_{eff}

modified until the best isotropic collapse is achieved. The approach is shown in Fig. 7.5 for a γ_{eff} value of 5 and 2.7. As mentioned above, the isotropic scaling can yield reduced γ_{eff} values when isotropic defects dominate the pinning landscape.[2] This is observed for all TLAG grown films characterised in the present work.

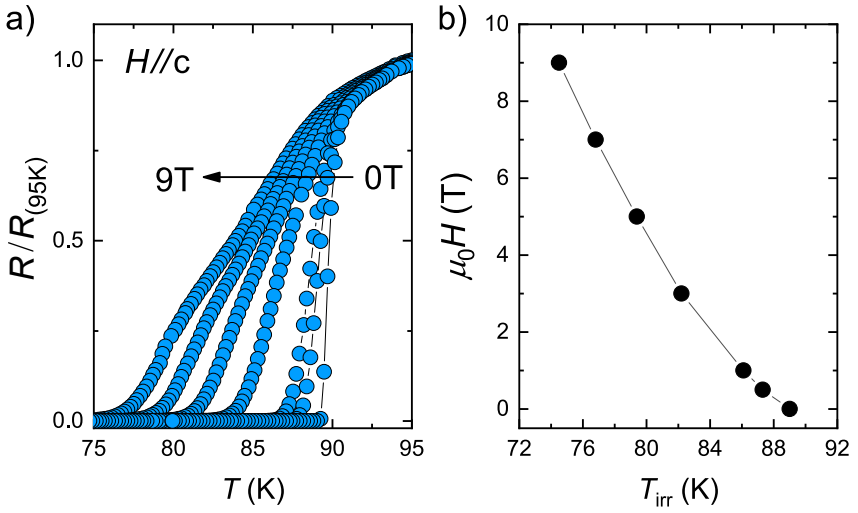

FIGURE E.4: Determination of the irreversibility line for H // c: a) Normalized $\rho(T)$ measurements for applied DC fields of 0 - 9 T. The measurements are carried out in maximum Lorentz force configuration. b) Irreversibility line obtained with the $R(T_{\text{irr}})/R_{95\text{K}}$ =10^{-3} criterion.

A similar approach, as discussed above, is used to obtain the isotropic and anisotropic contributions to pinning from the collapse of $J_c(\theta)$ measurements. $J_c(\theta)$ curves are obtained for a set of fields in the range of 0.1 - 9 T at a fixed temperature and plotted against $\mu_0 H_{\text{eff}}$ (Fig. 7.16a)). The overlapping sections belong to those parts of the $J_c(\theta)$ dependence which are purely governed by isotropic pinning. The isotropic contribution to pinning can then be obtained manually through setting of anchor points and spline interpolation.[3]
This is done with a Matlab routine, developed in this thesis, which also facilitates the reverse calculation into $J_{c,\text{iso}}(\theta)$, $J_{c,\text{aniso}}(\theta)$, $J_{c,\text{iso}}(H)$ and $J_{c,\text{aniso}}(H)$. For that, θ and H values of any measured I-V curve are used to calculate the effective field H_{eff}. The corresponding $J_{c,\text{iso}}$ value is then obtained from the isotropic curve in Fig. 7.16a). The separation of J_c dependencies is used in 7.3.5 to disentangle pinning contributions in TLAG films. Some of the Blatter scaling analysis is summarized in Fig. 7.17, 7.18 and 7.21.

[2]Observed in TFA-CSD films upon increase of the nanostrain [40].
[3]Where the curves show the best overlap.

In particular, $J_c(H)$ measurements at different temperatures are further used to construct H - T dependent color maps of the isotropic contribution to pinning. In this representation, differences can be visually set in comparison (Fig. 7.23). The maps are generated through use of $J_c(H,T)$ measurements as shown in Fig. 7.21. The absolute measurements are first normalised to the maximum J_c value at each temperature, enabling comparability of films with different J_c at self-field. A cubic spline interpolation is then carried out in temperature, keeping the magnetic field of each spline constant. Consequently, an H - T dependent matrix of the $J_{c,iso}/J_c$ ratios can be generated and visualized in form of a contour plot (Fig. 7.23).

E.3 H - T color maps for TFA-CSD and TLAG films for H//ab

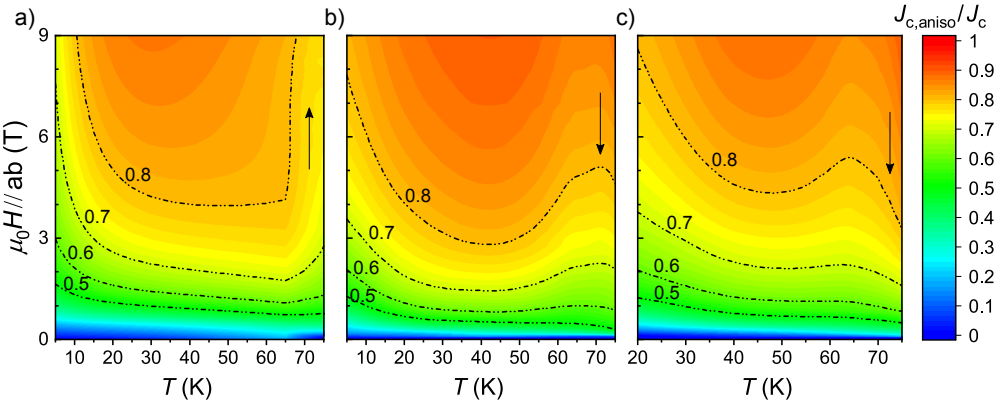

FIGURE E.5: H - T color mapping of the $J_{c,aniso}/J_c$ ratio for a TFA-CSD pristine and a TLAG $P_{O2}(BaCu_2O_2)$-route and T-route pristine film, H//ab. Contour lines of different ratios are included as guide to the eye.

Bibliography

[1] Stephen Blundell. *Superconductivity: A Very Short Introduction*. Oxford University Press, USA, 2009. ISBN: 9780199540907.

[2] J.R. Waldram. *Superconductivity of metals and cuptrates*. Taylor & Francis Ltd, 1996. ISBN: 978-0852743355.

[3] J. G. Bednorz, M. Takashige, and K. A. Müller. "Possible High Tc Superconductivity in the Ba-La-Cu-O System". In: *Z.Phys.B - Condensed Matter* 64.189-193 (1986). DOI: 10.1007/BF01303701.

[4] Hiroaki Nishikawa et al. *Correlated functional oxides: Nanocomposites and heterostructures*. Springer, 2016. ISBN: 978-3319829081. DOI: 10.1007/978-3-319-43779-8.

[5] S. Ogale, T. Venkatesan, and M. Blamire. *Functional Metal Oxides: New Science and Novel Applications*. Wiley-VCH, 2013. ISBN: 9783527654864.

[6] X. Obradors et al. "Growth, nanostructure and vortex pinning in superconducting YBa2Cu3O7 thin films based on trifluoroacetate solutions". In: *Superconductor Science and Technology* 25.12 (2012). ISSN: 09532048. DOI: 10.1088/0953-2048/25/12/123001.

[7] Xavier Obradors and Teresa Puig. "Coated conductors for power applications: Materials challenges". In: *Superconductor Science and Technology* 27.4 (2014), p. 044003. DOI: 10.1088/0953-2048/27/4/044003.

[8] R Kleiner and W Buckel. *Superconductivity: An Introduction*. Wiley-VCH, 2016. ISBN: 9783527411627.

[9] Thomas P. Sheahen. *Introduction to High-Temperature Superconductivity*. Kluwer Academic Publishers, 2002. ISBN: 0306470616.

[10] James William Rohlf. *Modern Physics from α to Z^0*. John Wiley & Sons, Inc., 1994. ISBN: 9780471572701.

[11] G.B.Yntema. "Superconducting Winding for Electromagnet". In: *Physical Review* 98.4 (1955). DOI: 10.1103/PhysRev.98.1144.

[12] J. E. Kunzler Wernick et al. "Superconductivity in Nb3Sn at High Current Density in a Magnetic Field of 88 kgauss". In: *Phys. Rev. Lett.* 7.215 (1961). DOI: 10.1103/PhysRevLett.6.89.

[13] D. Dew-Hughes. "Flux pinning mechanisms in type-II superconductors". In: *Philosophical Magazine* 30.2 (1974). DOI: 10.1080/14786439808206556.

[14] T.Matsushita. *Flux Pinning in Superconductors*. Vol. 178. Springer Series in solid-state sciences, 2014. ISBN: 978-3642453113.

[15] C P Bean. "Magnetization of Hard Superconductors". In: *Phys. Rev. Lett.* 8.6 (1962), pp. 250–253. DOI: 10.1103/PhysRevLett.8.250.

[16] A.Palau. "Critical currents and dissipation of grain boundary networks in coated conductors". In: (2005). URL: https://ddd.uab.cat/record/38161.

[17] Carles Navau and Alvaro Sanchez. "Magnetic properties of finite superconducting cylinders. I. Uniform applied field". In: *Physical Review B* 64.21 (2001). DOI: 10.1103/PhysRevB.64.214506.

[18] Alvaro Sanchez and Carles Navau. "Critical-current density from magnetization loops of finite high-Tc superconductors". In: *Superconductor Science and Technology* 14.7 (2001). DOI: 10.1088/0953-2048/14/7/304.

[19] Paul Seidel. *Applied Superconductivity: Handbook on Devices and Applications*. Wiley-VCH, 2015. ISBN: 9783527412099.

[20] M. K. Wu et al. "Superconductivity at 93K in a new mixed-phase Yb-Ba-Cu-O compound system at ambient pressure". In: *Physical Review Letters* 58.9 (1987). DOI: 10.1103/PhysRevLett.58.908.

[21] "Engineering critical current density versus applied magnetic field". In: (2020). URL: https://nationalmaglab.org/.

[22] Goran Majkic et al. "Engineering current density over 5 kA mm-2 at 4.2 K, 14 T in thick film REBCO tapes". In: *Superconductor Science and Technology* 31.10 (2018). DOI: 10.1088/1361-6668/aad844.

[23] A I Golovashkin et al. "Low temperature measurements of Hc2 in HTSC using megagauss magnetic fields". In: *Physica B: Condensed Matter* 177.1 (1992), pp. 105–108. DOI: 10.1016/0921-4526(92)90076-5.

[24] Seungyong Hahn et al. "45.5-Tesla direct-current magnetic field generated with a high-temperature superconducting magnet". In: *Nature* 570.7762 (2019). DOI: 10.1038/s41586-019-1293-1.

[25] J. L. MacManus-Driscoll et al. "Strong pinning in very fast grown reactive co-evaporated GdBa 2Cu3O7 coated conductors". In: *APL Materials* 2.8 (2014). DOI: 10.1063/1.4893339.

[26] A. Sykes et al. "Compact fusion energy based on the spherical tokamak To". In: *Nucl. Fusion* 58.016039 (2017).

[27] Cesar A. Luongo et al. "Next generation more-electric aircraft: a potential application for hts superconductors". In: *IEEE Transactions on Applied Superconductivity* 19.3 (2009), pp. 1055–1068. DOI: 10.1109/TASC.2009.2019021.

[28] David Larbalestier et al. "Superconducting Materials for Electric Power Applications". In: *Nature* 414 (2001), pp. 368–377. DOI: 10.1038/35104654.

[29] Alex Gurevich. "To use or not to use cool superconductors?" In: *Nature Materials* 10.4 (2011). DOI: 10.1038/nmat2991.

[30] F.Vallès. "Vortex Pinning and Creep in YBCO Nanocomposite Films grown by Chemical Solution Deposition". In: (2019). URL: https://ddd.uab.cat/record/213601.

[31] J. D. Jorgensen et al. "Structural properties of oxygen-deficient YBa2Cu3O7-d". In: *Physical Review B* 41.4 (1990). DOI: 10.1103/PhysRevB.41.1863.

[32] M. Magnuson et al. "Self-doping processes between planes and chains in the metal-to-superconductor transition of YBa2Cu3O6.9". In: *Scientific Reports* 4 (2014), pp. 2–7. ISSN: 20452322. DOI: 10.1038/srep07017.

[33] *International Centre for Diffraction Data (ICDD)*. URL: http://www.icdd.com/.

[34] Jeffery L. Tallon. "Thermodynamics and Critical Current Density in High-Tc Superconductors". In: *IEEE Transactions on Applied Superconductivity* 25.3 (2015). DOI: 10.1109/TASC.2014.2379660.

[35] B. Keimer et al. "From quantum matter to high-temperature superconductivity in copper oxides". In: *Nature* 518.7538 (2015). DOI: 10.1038/nature14165.

[36] Chandra Varma. "High-temperature superconductivity: Mind the pseudogap". In: *Nature* 468.7321 (2010), pp. 184–185. DOI: 10.1038/468184a.

[37] V. Breit et al. "Evidence for chain superconductivity in near-stoichiometric YBa2Cu3Ox single crystals". In: *Physical Review B* 52.22 (1995), pp. 4–7. DOI: 10.1103/PhysRevB.52.R15727.

[38] Michael Tinkham. *Introduction to superconductivity*. McGraw Hill, 1996. ISBN: 9780070648784.

[39] S R Foltyn et al. “Materials science challenges for high-temperature superconducting wire”. In: 6 (2007), pp. 631–642. DOI: 10.1038/nmat1989.

[40] A. Llordés et al. “Nanoscale strain-induced pair suppression as a vortex-pinning mechanism in high-temperature superconductors”. In: *Nature Materials* 11.4 (2012), pp. 329–336. DOI: 10.1038/nmat3247.

[41] J. Gutiérrez et al. “Strong isotropic flux pinning in solution-derived YBa2Cu3O7-x nanocomposite superconductor films”. In: *Nature Materials* 6.5 (2007), pp. 367–373. DOI: 10.1038/nmat1893.

[42] P. Mele et al. “Insertion of nanoparticulate artificial pinning centres in YBa2Cu3O7-x films by laser ablation of a Y2O3-surface modified target”. In: *Superconductor Science and Technology* 20.7 (2007). DOI: 10.1088/0953-2048/20/7/006.

[43] P. Mele et al. “Incorporation of double artificial pinning centers in YBa2Cu3O7-d films”. In: *Superconductor Science and Technology* 21.1 (2008). DOI: 10.1088/0953-2048/21/01/015019.

[44] Lars Opherden et al. “Large pinning forces and matching effects in YBa2Cu3O7-δ thin films with Ba2Y(Nb/Ta)O6 nano-precipitates”. In: *Scientific Reports* 6 (2016). DOI: 10.1038/srep21188.

[45] V. Rouco et al. “Role of twin boundaries on vortex pinning of CSD YBCO nanocomposites”. In: *Superconductor Science and Technology* 27.12 (2014). DOI: 10.1088/0953-2048/27/12/125009.

[46] C.J.Jou and J.Washburn. “Formation of coherent twins in YBa2Cu307-d superconductors”. In: *J. Mater. Res* 4.4 (1989). DOI: 10.1557/JMR.1989.0795.

[47] E. D. Specht et al. “Stacking faults in YBa2Cu3O7-x: Measurement using x-ray diffraction and effects on critical current”. In: *Applied Physics Letters* 89.16 (2006). DOI: 10.1063/1.2364185.

[48] M. Tachiki and S. Takahashi. “Strong vortex pinning intrinsic in high-Tc oxide superconductors”. In: *Solid State Communications* 70.3 (1989). ISSN: 00381098. DOI: 10.1016/0038-1098(89)90330-X.

[49] L. Civale. “Vortex pinning and creep in high-temperature superconductors with columnar defects”. In: *Superconductor Science and Technology* 10.7A (1997). DOI: 10.1088/0953-2048/10/7A/003.

[50] L. Piperno et al. “Polymer-assisted surface decoration for critical current enhancement in YBa2Cu3O7-x films”. In: *Applied Surface Science* 484 (2019). DOI: 10.1016/j.apsusc.2019.04.027.

[51] B. Maiorov et al. "Synergetic combination of different types of defect to optimize pinning landscape using BaZrO3-doped YBa2Cu3O7". In: *Nature Materials* 8.5 (2009), pp. 398–404. DOI: 10.1038/nmat2408.

[52] J. L. Macmanus-Driscoll et al. "Strongly enhanced current densities in superconducting coated conductors of YBa2Cu3O7-x + BaZrO3". In: *Nature Materials* 3.7 (2004), pp. 439–443. ISSN: 14761122. DOI: 10.1038/nmat1156.

[53] T. Puig et al. "Vortex pinning in chemical solution nanostructured YBCO films". In: *Superconductor Science and Technology* 21.3 (2008). ISSN: 09532048. DOI: 10.1088/0953-2048/21/3/034008.

[54] R. Guzman et al. "Strain-driven broken twin boundary coherence in YBa2Cu3O7-δ nanocomposite thin films". In: *Applied Physics Letters* 102.8 (2013). DOI: 10.1063/1.4793749.

[55] Paolo Mele et al. *Superconductivity: From Materials Science to Practical Applications*. Springer, 2020, pp. 169–188. ISBN: 978-3030233020.

[56] S. Samoilenkov et al. "Customised 2G HTS wire for applications". In: *Superconductor Science and Technology* 29.2 (2015). DOI: 10.1088/0953-2048/29/2/024001.

[57] V. Chepikov et al. "Introduction of BaSnO3 and BaZrO3 artificial pinning centres into 2G HTS wires based on PLD-GdBCO films. Phase I of the industrial R&D programme at SuperOx". In: *Superconductor Science and Technology* 30.12 (2017). DOI: 10.1088/1361-6668/aa9412.

[58] V. V. Sychugov et al. "Variation of critical current and n-value of 2G HTS tapes in external magnetic fields of different orientation". In: *Journal of Physics: Conference Series* 747.1 (2016). DOI: 10.1088/1742-6596/747/1/012048.

[59] T.Winkler. "The EcoSwing Project". In: *IOP Conf. Series: Materials Science and Engineering* 502 (2019). DOI: 10.1088/1757-899X/502/1/012004.

[60] Mark Stemmle et al. "AmpaCity - Installation of Advanced Superconducting 10 kV System in City Center Replaces Conventional 110 kV Cables". In: *IEEE International Conference on Applied Superconductivity and Electromagnetic Devices* (2013). DOI: 10.1109/ASEMD.2013.6780785.

[61] T. Puig et al. "Coated conductor technology for the beamscreen chamber of future high energy circular colliders". In: *Superconductor Science and Technology* 32.9 (2019). DOI: 10.1088/1361-6668/ab2e66.

[62] Artur Romanov et al. “High frequency response of thick REBCO coated conductors in the framework of the FCC study”. In: *Scientific Reports* 10.1 (2020). DOI: 10.1038/s41598-020-69004-z.

[63] N. Yanagi et al. “Progress of the Design of HTS Magnet Option and R&D Activities for the Helical Fusion Reactor”. In: *IEEE Transactions on Applied Superconductivity* 24.3 (2014). DOI: 10.1109/TASC.2013.2292775.

[64] Pierluigi Bruzzone et al. “High Temperature Superconductors for fusion magnets”. In: *Nucl. Fusion* 58 (2018). DOI: 10.1088/1741-4326/aad835.

[65] H. Hilgenkamp and J. Mannhart. “Grain boundaries in high- Tc superconductors”. In: *Reviews of Modern Physics* 74.2 (2002), pp. 485–549. DOI: 10.1103/revmodphys.74.485.

[66] A. Goyal et al. “Texture formation and grain boundary networks in rolling assisted biaxially textured substrates and in epitaxial YBCO films on such substrates”. In: *Micron* 30.5 (1999). DOI: 10.1016/S0968-4328(99)00047-5.

[67] Yasuhiro Iijima et al. “Reel to reel continuous formation of Y-123 coated conductors by IBAD and PLD method”. In: *IEEE Transactions on Applied Superconductivity* 11 (2001). DOI: 10.1109/77.919649.

[68] Jae Hun Lee et al. “RCE-DR, a novel process for coated conductor fabrication with high performance”. In: *Superconductor Science and Technology* 27.4 (2014). DOI: 10.1088/0953-2048/27/4/044018.

[69] Brian G. Marchionini et al. “High-Temperature Superconductivity: A Roadmap for Electric Power Sector Applications, 2015-2030”. In: *IEEE Transactions on Applied Superconductivity* 27.4 (2017). DOI: 10.1109/TASC.2017.2671680.

[70] C. F. Sánchez-Valdés, T. Puig, and X. Obradors. “In situ study through electrical resistance of growth rate of trifluoroacetate-based solution-derived YBa2Cu3O7 films”. In: *Superconductor Science and Technology* 28.2 (2015). DOI: 10.1088/0953-2048/28/2/024006.

[71] O. Stadel et al. “Continuous YBCO deposition by MOCVD for coated conductors”. In: *Physica C* 372-376 (2002), pp. 751–754. DOI: 10.1016/S0921-4534(02)00898-5.

[72] A. Kursumovic et al. “Study of the rate-limiting processes in liquid-phase epitaxy of thick YBaCuO films”. In: *Journal of Crystal Growth* 218.1 (2000). DOI: 10.1016/S0022-0248(00)00519-4.

[73] S. J. Rothman, J. L. Routbort, and K. C. Goretta. "Tracer diffusion of Ba and Y in YBa2Cu3Ox". In: *Journal of Materials Research* 7.9 (1992), pp. 2308–2316. DOI: 10.1557/JMR.1992.2308.

[74] Y. Shiohara and A. Endo. "Crystal growth of bulk high-Tc superconducting oxide materials". In: *Materials Science and Engineering R: Reports* 19 (1997), pp. 1–86. DOI: 10.1016/S0927-796X(96)00198-2.

[75] W. R. Studenmund et al. "Progress in photothermal microscopy of YBa2Cu3O7-x". In: *Journal of Physics and Chemistry of Solids* 59.10-12 (1998), pp. 2012–2014. DOI: 10.1016/S0022-3697(98)00157-7.

[76] L.Soler. "Liquid assisted ultrafast growth of superconducting films derived from chemical solutions". PhD thesis. Universitat Autònoma de Barcelona, 2019. URL: https://ddd.uab.cat/record/213642.

[77] X. Qi and J. L. MacManus-Driscoll. "Liquid phase epitaxy processing for high temperature superconductor tapes". In: *Current Opinion in Solid State and Materials Science* 5.4 (2001), pp. 291–300. DOI: 10.1016/S1359-0286(00)00040-1.

[78] A. Kuršumović et al. "Study of the rate-limiting processes in liquid-phase epitaxy of thick YBaCuO films". In: *Journal of Crystal Growth* 218.1 (2000), pp. 45–56. DOI: 10.1016/S0022-0248(00)00519-4.

[79] Y.Yamada. "Liquid-phase epitaxy processing of RBa2Cu3O7-δ". In: *Superconductor Science and Technology* 13 (2000), pp. 82–87. DOI: 10.1088/0953-2048/13/1/311.

[80] T. Ohnishi et al. "High rate in situ YBa2Cu3O7 film growth assisted by liquid phase". In: *Journal of Materials Research* 19.4 (2004), pp. 977–981. ISSN: 08842914. DOI: 10.1557/JMR.2004.0127.

[81] A. Kursumovic et al. "Hybrid liquid phase epitaxy processes for YBa2Cu3O7 film growth". In: *Superconductor Science and Technology* 17.10 (2004), pp. 1215–1223. DOI: 10.1088/0953-2048/17/10/024.

[82] K. S. Yun et al. "Vapor-liquid-solid tri-phase pulsed-laser epitaxy of RBa2Cu 3O7-y single-crystal films". In: *Applied Physics Letters* 80.1 (2002), pp. 61–63. ISSN: 00036951. DOI: 10.1063/1.1432111.

[83] Yusuke Ichino et al. "Possibility of high deposition rate in SmBa2Cu3O y, films prepared using the vapor-liquid-solid growth mode". In: *Japanese Journal of Applied Physics* 45.2A (2006), pp. 758–760. DOI: 10.1143/JJAP.45.758.

[84] A. Kursumovic et al. "High critical current densities in YBa2Cu3O7-x films grown at high rates by hybrid liquid phase epitaxy". In: *Applied Physics Letters* 87.25 (2005), pp. 1–3. ISSN: 00036951. DOI: 10.1063/1.2149975.

[85] X. Obradors et al. "Chemical solution route to self-assembled epitaxial oxide nanostructures". In: *Chemical Society Reviews* 43.7 (2014), pp. 2200–2225. DOI: 10.1039/c3cs60365b.

[86] Theodor Schneller et al. *Chemical solution deposition of functional oxide thin films*. 2013. DOI: 10.1007/978-3-211-99311-8.

[87] Robert W. Schwartz. "Chemical Solution Deposition of Perovskite Thin Films". In: *Chemistry of Materials* 9.11 (1997), pp. 2325–2340. DOI: 10.1021/cm970286f.

[88] A. Gupta et al. "Superconducting oxide films with high transition temperature prepared from metal trifluoroacetate precursors". In: *Applied Physics Letters* 52.24 (1988), pp. 2077–2079. ISSN: 00036951. DOI: 10.1063/1.99752.

[89] Pieter Vermeir et al. "Elucidation of the mechanism in fluorine-free prepared YBa 2Cu3O7-δ coatings". In: *Inorganic Chemistry* 49.10 (2010), pp. 4471–4477. DOI: 10.1021/ic9021799.

[90] J. Tafto et al. "Grain Boundaries, Planar Defects and Superconducting Properties of YBa2Cu3O7". In: *MRS Proceedings* 99 (1987). DOI: 10.1557/proc-99-511.

[91] C. Pop et al. "Growth of all-chemical high critical current YBa2Cu3O7-δ thick films and coated conductors". In: *Superconductor Science and Technology* 32.1 (2019). DOI: 10.1088/1361-6668/aaea4e.

[92] Yuanqing Chen et al. "An advanced low-fluorine solution route for fabrication of high-performance YBCO superconducting films". In: *Superconductor Science and Technology* 25.6 (2012). DOI: 10.1088/0953-2048/25/6/069501.

[93] Teruo Izumi et al. "Progress in development of coated conductors by TFA-MOD processing". In: *Physica C: Superconductivity and its Applications* 412-414.SPEC. ISS. (2004), pp. 885–889. ISSN: 09214534. DOI: 10.1016/j.physc.2003.12.095.

[94] S.Rasi. "Advanced Thermal Analysis of REBCO Superconductor Precursor Films and Functional Oxides". PhD thesis. Universitat de Girona, 2019. URL: https://dugi-doc.udg.edu/handle/10256/17825.

[95] Julia Jareño. "Transient liquid assisted growth of superconducting nanocomposite films". PhD thesis. Universitat Autònoma de Barcelona, 2020.

[96] Sandeep Rekhi, G. L. Bhalla, and G. C. Trigunayat. "Recovery of superconductivity in the water degraded YBCO samples". In: *Physica C: Superconductivity and its Applications* 307.1-2 (1998), pp. 51–60. DOI: 10.1016/S0921-4534(98)00404-3.

[97] R. Ramesh et al. "Epitaxy of Y-Ba-Cu-O thin films grown on single-crystal MgO". In: *Applied Physics Letters* 56.22 (1990), pp. 2243–2245. ISSN: 00036951. DOI: 10.1063/1.102932.

[98] H. Huhtinen, H. Palonen, and P. Paturi. "The Growth Rate and Temperature Induced Microcracks in YBCO Films Pulsed Laser Deposited on MgO Substrates". In: *IEEE Transactions on Applied Superconductivity* 23.3 (2012), pp. 7200104–7200104. DOI: 10.1109/tasc.2012.2228891.

[99] CrysTec GmbH. *No Title*. URL: http://www.crystec.de/crystec-e.html.

[100] A. Llordés et al. "Evolution of metal-trifluoroacetate precursors in the thermal decomposition toward high-performance YBa2Cu3O7 superconducting films". In: *Chemistry of Materials* 22.5 (2010), pp. 1686–1694. ISSN: 08974756. DOI: 10.1021/cm903080k.

[101] J.L. MacManus-Driscoll, J.C. Bravman, and R.B. Beyers. "Phase equilibria in the Y-Ba-Cu-O system and melt processing of Ag clad Y1Ba2Cu3O7-x tapes at reduced oxygen partial pressures". In: *Physica C: Superconductivity* 241.3-4 (1995), pp. 401–413. DOI: 10.1016/0921-4534(94)02369-7.

[102] Albert Queraltó. "Growth of functional oxide heterostructures from chemical solutions using advanced processing methodologies". PhD thesis. Universitat Autònoma de Barcelona, 2015. URL: https://ddd.uab.cat/record/129856.

[103] Ruixing Liang, D. A. Bonn, and W. N. Hardy. "Evaluation of CuO2 plane hole doping in YBa2Cu3O6+x single crystals". In: *Physical Review B - Condensed Matter and Materials Physics* 73.18 (2006), pp. 1–4. DOI: 10.1103/PhysRevB.73.180505.

[104] E. F. Talantsev et al. "Oxygen deficiency, stacking faults and calcium substitution in MOD YBCO coated conductors". In: *IEEE Transactions on Applied Superconductivity* 23.3 (2013). DOI: 10.1109/TASC.2012.2233843.

[105] A.Stangl. "Oxygen kinetics and charge doping for high critical current YBCO films". PhD thesis. Universitat Autònoma de Barcelona, 2019. URL: https://ddd.uab.cat/record/213664.

[106] R. C. Jaklevic et al. "Quantum interference effects in Josephson tunneling". In: *Physical Review Letters* 12.7 (1964), pp. 159–160. ISSN: 00319007. DOI: 10.1103/PhysRevLett.12.159.

[107] A. Palau et al. "Magnetic granularity analysis of YBCO coated conductors". In: *Physica C: Superconductivity and its Applications* 408-410.1-4 (2004), pp. 866–868. DOI: 10.1016/j.physc.2004.03.224.

[108] A. Palau et al. "Simultaneous determination of grain and grain-boundary critical currents in YBa2Cu3O7 -coated conductors by magnetic measurements". In: *Physical Review B - Condensed Matter and Materials Physics* 75.5 (2007), pp. 1–12. DOI: 10.1103/PhysRevB.75.054517.

[109] E. Bartolomé et al. "Artificial magnetic granularity effects on patterned epitaxial YBa2Cu3O7-x thin films". In: *Physical Review B - Condensed Matter and Materials Physics* 76.9 (2007), pp. 1–9. ISSN: 10980121. DOI: 10.1103/PhysRevB.76.094508.

[110] Frédéric Sirois, Jonathan Coulombe, and Antoine Bernier. "Characterization of the superconducting to normal transition of HTS coated conductors by fast pulsed current measurements". In: *IEEE Transactions on Applied Superconductivity* 19.3 (2009), pp. 3585–3590. ISSN: 10518223. DOI: 10.1109/TASC.2009.2018304.

[111] J. W. Ekin et al. "High Tc superconductor/noble-metal contacts with surface resistivities in the 10-10 Ω cm2 range". In: *Applied Physics Letters* 52.21 (1988), pp. 1819–1821. ISSN: 00036951. DOI: 10.1063/1.99725.

[112] L.J. van der Pauw. "A Method for Measuring Specific Resisitivity and Hall Effect of Discs of Arbitrary Shape". In: *Philips Res.Repts* 13 (1958), pp. 1–9.

[113] E.H.Hall. "On a New Action of the Magnet on Electric Currents". In: *American Journal of Mathematics* 2.3 (1879), pp. 287–292. DOI: 10.2307/2369245.

[114] S.L. Drechsler and T. Mishonov. "High-Tc Superconductors and Related Materials". In: (2001), p. 298. DOI: 10.1007/978-94-010-0758-0.

[115] S. Murase et al. "Critical temperature measurement method of composite superconductors". In: *Physica C: Superconductivity and its Applications* 357-360 (2001), pp. 1197–1200. ISSN: 09214534. DOI: 10.1016/S0921-4534(01)00483-X.

[116] F. Vallès et al. "Angular flux creep contributions in YBa2Cu3O7-δ nanocomposites from electrical transport measurements". In: *Scientific reports* 8.1 (2018). DOI: 10.1038/s41598-018-24392-1.

[117] A.Llordes. "Superconducting Nanocomposite Films Grown by Chemical Solution Deposition: Synthesis, Microstructure and Properties". PhD thesis. Universitat Autònoma de Barcelona, 2010. URL: http://www.ecole.ensicaen.fr/~chateign/pdf/Llordes_Anna_PhD.pdf.

[118] C Michaelsen and D Anders. "Improved Graded Mirrors for Xrd Applications". In: *Advances* 42.C (2000), pp. 308–320.

[119] Ziliang Li. "Growth and Characterization of Nanocomposite YBa2Cu3O7-δ – BaMO3 (M = Zr, Hf) Thin Films from Colloidal Solutions". PhD thesis. 2018. URL: https://ddd.uab.cat/record/201515.

[120] M. A. Moram and M. E. Vickers. "X-ray diffraction of III-nitrides". In: *Reports on Progress in Physics* 72.3 (2009). DOI: 10.1088/0034-4885/72/3/036502.

[121] W H Bragg and W L Bragg. "Reflection of X-rays by crystals". In: *Proceedings of the Royal Society A* 88.605 (1913), pp. 428–438. ISSN: 00280836. DOI: 10.1098/rspa.1913.0040.

[122] B. E. Warren. "X-Ray Diffraction". In: *Dover* (1990).

[123] Vitalij K. Pecharsky. *Fundamentals of Powder Diffraction and Structural Characterization of Materials*. Springer, 2009. ISBN: 978-0-387-09578-3. DOI: 10.1007/978-0-387-09579-0.

[124] M. Calamiotou et al. "Phase separation, microstructure and superconductivity in the Y1-xPrxBa2Cu3Oy compounds". In: *Journal of Physics Condensed Matter* 20.39 (2008). DOI: 10.1088/0953-8984/20/39/395224.

[125] J. B. Nelson and D. P. Riley. "An experimental investigation of extrapolation methods in the derivation of accurate unit cell dimensions of crystals". In: *Proceedings of the Physical Society* 57.3 (1945), pp. 160–177. DOI: 10.1088/0959-5309/57/3/302.

[126] A. L. Patterson. "The scherrer formula for X-ray particle size determination". In: *Physical Review* 56.10 (1939), pp. 978–982. DOI: 10.1103/PhysRev.56.978.

[127] A. R. Stokes and A. J.C. Wilson. "The diffraction of x rays by distorted crystal aggregates". In: *Proceedings of the Physical Society* 56.3 (1944), pp. 174–181. ISSN: 09595309. DOI: 10.1088/0959-5309/56/3/303.

[128] J. I. LANGFORD and A. J. C. WILSON. "Scherrer after Sixty Years: A Survey and Some New Results in the Determination of Crystallite Size". In: *J. Appl. Cryst. (1978).* 11 (1978), pp. 102–113. DOI: 10.1107/S0021889878012844.

[129] S. Christiansen, M. Albrecht, and H. P. Strunk. "Defect structure of epitaxial GaN films determined by transmission electron microscopy and triple-axis X-ray diffractometry". In: *Philosophical Magazine A: Physics of Condensed Matter, Structure, Defects and Mechanical Properties* 77.4 (1998), pp. 1013–1025. ISSN: 01418610. DOI: 10.1080/01418619808221225.

[130] Roger Guzmán. "In-depth investigation of the origin, evolution and interaction of structural defects in YBCO nanocomposite thin films". PhD thesis. Universitat Autònoma de Barcelona, 2013. URL: https://ddd.uab.cat/record/116398.

[131] Teresa Puig. *ULTRAfast growth of ultrahigh performance SUPERconducting TAPEs*. 2014. URL: https://cordis.europa.eu/project/id/669504.

[132] L. Soler et al. "Ultrafast transient liquid assisted growth of high current density superconducting films". In: *Nature Communications* 11.1 (2020). DOI: 10.1038/s41467-019-13791-1.

[133] F. Parmigiani et al. "Observation of carboxylic groups in the lattice of sintered Ba2YCu3O7-y high-Tc superconductors". In: *Physical Review B* 36.13 (1987), pp. 7148–7150. DOI: 10.1103/PhysRevB.36.7148.

[134] I. A. Parinov. *Microstructure and Properties of High-Temperature Superconductors*. Springer, 2012, p. 280. ISBN: 978-3-642-34440-4. URL: https://link.springer.com/book/10.1007/978-3-642-34441-1.

[135] I. Arvanitidis, Du Sichen, and S. Seetharaman. "A study of the thermal decomposition of BaCO3". In: *Metallurgical and Materials Transactions B: Process Metallurgy and Materials Processing Science* 27.3 (1996), pp. 409–416. DOI: 10.1007/BF02914905.

[136] T Itoh. "Role of CuO for the decarbonation of BaCO3 and CaCO3 in the solid-state reaction of CuO with BaCO3 and that of CuO with CaCO3". In: *Journal of Material Science Letters* 22 (2003), pp. 185–189. DOI: 10.1023/A:1022293724698.

[137] Shin-ichi -i Hirano, Takashi Hayashi, and Masashi Miura. "Preparation of Ba2YCu3O7-δ Thin Films with Preferred Orientation through an Organometallic Route". In: *Journal of the American Ceramic Society* 73.4 (1990), pp. 885–888. DOI: 10.1111/j.1151-2916.1990.tb05130.x.

[138] Jeffrey L Sobolik, Hong Wang, and William J Thornson. "Effect of Particle Size on Binary Reactions Common to the Y-Ba-Cu-O System". In: *J.Am.Ceram.Soc.* 77.10 (1994), pp. 2738–2746. DOI: 10.1111/j.1151-2916.1994.tb04669.x.

[139] T.B. Lindemer et al. "Synthesis of Y-Ba-Cu-O superconductors in subatmospheric oxygen". In: *Physica C: Superconductivity* 174.1-3 (1991), pp. 135–143. DOI: 10.1016/0921-4534(91)90429-3.

[140] M. Nevřiva et al. "On the determination of the CuO-BaCuO2 and CuO-YCuO2.5 binary phase diagrams". In: *Journal of Crystal Growth* 91.3 (Aug. 1988), pp. 434–438. DOI: 10.1016/0022-0248(88)90265-5.

[141] Peir Yung Chu and Relva C. Buchanan. "Reactive liquid phase sintering of YBa2Cu307-x superconducting thin films: Part II. Sintering mechanism and film properties". In: *Journal of Materials Research* 9.4 (1994), pp. 844–851. DOI: 10.1557/JMR.1994.0844.

[142] A. D. Gamalski et al. "Formation of metastable liquid catalyst during subeutectic growth of germanium nanowires". In: *Nano Letters* 10.8 (2010), pp. 2972–2976. DOI: 10.1021/nl101349e.

[143] K.Benz and W.Neumann. *Introduction to Crystal Growth and Characterization*. Ed. by Wiley-VCH Verlag GmbH & Co. 2014. ISBN: 9783527318407. DOI: 10.1002/9783527689248.

[144] Gabriele C. Sosso et al. "Crystal Nucleation in Liquids: Open Questions and Future Challenges in Molecular Dynamics Simulations". In: *Chemical Reviews* 116.12 (2016), pp. 7078–7116. DOI: 10.1021/acs.chemrev.5b00744.

[145] Q. S. Mei and K. Lu. "Melting and superheating of crystalline solids: From bulk to nanocrystals". In: *Progress in Materials Science* 52.8 (2007), pp. 1175–1262. DOI: 10.1016/j.pmatsci.2007.01.001.

[146] Max Born. "Thermodynamics of crystals and melting". In: *The Journal of Chemical Physics* 7.8 (1939), pp. 591–603. DOI: 10.1063/1.1750497.

[147] J. G. Dash. "History of the search for continuous melting". In: *Reviews of Modern Physics* 71.5 (1999), pp. 1737–1743. DOI: 10.1103/revmodphys.71.1737.

[148] Joost W. M. Frenken and J. F. der Veen Van. "Observation of Surface Melting". In: *Phys. Rev. Lett.* 54.134 (1995). DOI: https://doi.org/10.1103/PhysRevLett.54.134.

[149] M. Polcik, L. Wilde, and J. Haase. "Partial order of the quasiliquid during surface melting of Al(110)". In: *Physical Review Letters* 78.3 (1997), pp. 491–494. ISSN: 10797114. DOI: 10.1103/PhysRevLett.78.491.

[150] T. Kaneyoshi. *Introduction to Surface Magnetism*. CRC Press, Inc, 1991, p. 24. ISBN: 0-8493-6687-9.

[151] R. Kofman et al. "Surface melting enhanced by curvature effects". In: *Surface Science* 303.1-2 (1994), pp. 231–246. ISSN: 00396028. DOI: 10.1016/0039-6028(94)90635-1.

[152] P. Pawlow. "Über den Dampfdruck der Körner einer festen Substanz". In: *Zeitschrift für Physikalische Chemie* 65.545 (1909). DOI: 10.1515/zpch-1909-6824.

[153] H. W. Sheng, K. Lu, and E. Ma. "Melting and freezing behavior of embedded nanoparticles in ball-milled Al-10 WT% M (M = In, Sn, Bi, Cd, Pb) mixtures". In: *Acta Materialia* 46.14 (1998), pp. 5195–5205. ISSN: 13596454. DOI: 10.1016/S1359-6454(98)00108-6.

[154] K. Lu and Z. H. Jin. "Melting and superheating of low-dimensional materials". In: *Current Opinion in Solid State and Materials Science* 5.1 (2001), pp. 39–44. ISSN: 13590286. DOI: 10.1016/S1359-0286(00)00027-9.

[155] J. Zhong et al. "Superheating of Ag nanoparticles embedded in Ni matrix". In: *Acta Materialia* 49.15 (2001), pp. 2897–2904. ISSN: 13596454. DOI: 10.1016/S1359-6454(01)00212-9.

[156] Yusuke Ichino et al. "Orientation Mechanism of REBa2Cu3Oy (RE = Nd, Sm, Gd, Y, Yb) Thin Films Prepared by Pulsed Laser Deposition". In: *TRANSACTIONS ON APPLIED SUPERCONDUCTIVITY* 13.2 (2003). DOI: 10.1109/TASC.2003.811972.

[157] K F Kelton and A L Greer. *Nucleation in Condensed Matter*. Vol. Volume 15. 2010, p. 726. ISBN: 9780080421476.

[158] F. T. Yuan et al. "Low-temperature ordering of FePt thin films induced by glow-discharge ion bombardment". In: *Applied Physics Letters* 101.9 (2012). ISSN: 00036951. DOI: 10.1063/1.4749274.

[159] Yuh Shiohara and Eugene A. Goodilin. *Chapter 189 Single-crystal growth for science and technology*. Vol. 30. Elsevier, 2000, pp. 67–227. DOI: 10.1016/s0168-1273(00)30006-x.

[160] Norbert Kolassa et al. *Elements of X-Ray Diffraction*. Ed. by Pearson. Vol. 108. 2. 2014, pp. 495–500. ISBN: 9781292040547.

[161] T.B. Lindemer, F.A. Washburn, and C.S. MacDougall. "Study of phase behavior in the YBa2Cu3O7-x-BaCuO2+y-CuO-Ag system". In: *Physica C Superconductivity* 196.3-7 (1992), pp. 390–398. DOI: 10.1016/0921-4534(92)90462-L.

[162] Wei Zhang, Kozo Osamura, and Shojiro Ochiai. "Phase Diagram of the BaO-CuO Binary System". In: *Journal of the American Ceramic Society* 73.7 (1990), pp. 1958–1964. ISSN: 15512916. DOI: 10.1111/j.1151-2916.1990.tb05252.x.

[163] A. B. Bykov et al. "Crystallization of high temperature superconductors from nonstoichiometric melts". In: *Journal of Crystal Growth* 91.3 (1988), pp. 302–307. DOI: 10.1016/0022-0248(88)90242-4.

[164] H. Yoshikazu et al. "Single crystal growth of (La1-xAx)2CuO4 (A=Ba or Sr) and Ba2YCu3O7-y". In: *Journal of Crystal Growth* 85.4 (1987), pp. 581–584. DOI: 10.1016/0022-0248(87)90025-X.

[165] Pieter Vermeir et al. "Influence of sintering conditions in the preparation of acetate-based fluorine-free CSD YBCO films using a direct sintering method". In: *Materials Research Bulletin* 47.12 (2012), pp. 4376–4382. DOI: 10.1016/J.MATERRESBULL.2012.09.033.

[166] T.B.Lindemer and E.D.Specht. "The BaO-Cu-CuO system. Solid-liquid equilibria and thermodynamics of BaCuO2 and BaCu2O2". In: *Physica C: Superconductivity* 255.1-2 (1995), pp. 81–94. DOI: 10.1016/0921-4534(95)00460-2.

[167] H.J.T. Ellingham. "Reducibility of Oxides and Sulphides in Metallurgical Processes". In: *Journal of the Society of Chemical Industry* 63.5 (1944), pp. 125–160. DOI: 10.1002/jctb.5000630501.

[168] Y. Yoshida et al. "Surface morphology and growth mechanism of YBa2Cu3O7-y films by metalorganic chemical vapor deposition using liquid sources". In: *Applied Physics Letters* 69.6 (1996), pp. 845–847. DOI: 10.1063/1.117911.

[169] Fadila Tair et al. "Melting temperature of YBa2Cu3O7-x and GdBa2Cu3O7-x at subatmospheric partial pressure". In: *Journal of Alloys and Compounds* 692 (2017), pp. 787–792. DOI: 10.1016/j.jallcom.2016.08.072.

[170] Vyacheslav F. Solovyov et al. "Strong influence of the YBa2Cu3O7 grain size on critical current densities of thick YBa2Cu3O7 layers made by a metal-organic deposition process". In: *Superconductor Science and Technology* 21.12 (2008). DOI: 10.1088/0953-2048/21/12/125013.

[171] Takao Itoh and Hiroshi Uchikawa. "Effects of coexisting nonsuperconducting phase on the superconductivity of YBa2Cu3O7". In: *Journal of Applied Physics* 66.10 (1989), pp. 4900–4902. DOI: 10.1063/1.343758.

[172] T. Ito, K. Takenaka, and S. Uchida. "Systematic deviation from T-linear behavior in the in-plane resistivity of YBa2Cu3O7-y: Evidence for dominant spin scattering". In: *Physical Review Letters* 70.25 (1993), pp. 3995–3998. ISSN: 00319007. DOI: 10.1103/PhysRevLett.70.3995.

[173] T. Puig et al. "The influence of growth conditions on the microstructure and critical currents of TFA-MOD YBa2Cu3O7 films". In: *Superconductor Science and Technology* 18.8 (2005), pp. 1141–1150. DOI: 10.1088/0953-2048/18/8/020.

[174] Y. Yoshida et al. "Surface morphology and growth mechanism of YBa2Cu3O7-y films by metalorganic chemical vapor deposition using liquid sources". In: *Applied Physics Letters* 69.6 (1996), pp. 845–847. ISSN: 00036951. DOI: 10.1063/1.117911.

[175] K. M. Jadhav et al. "Influence of hole filling by Ti on the superconductivity of YBa2Cu3O7-δ". In: *Journal of Superconductivity* 8.3 (1995), pp. 373–375. DOI: 10.1007/BF00728174.

[176] X. Yao and Y. Shiohara. "Process for high growth rate and high superconducting properties of REBCO single crystals". In: *Materials Science and Engineering B* 53.1-2 (1998), pp. 11–17. ISSN: 09215107. DOI: 10.1016/S0921-5107(97)00294-8.

[177] C Klemenz and H J Scheel. "Solubility of YBCO and NdBCO in the BaO/CuO flux". In: *J. Cryst. Growth* 200 (1999), pp. 435–440.

[178] Masaru Nakamura, Christian Krauns, and Yuh Shiohara. "Oxygen partial pressure dependence of the yttrium solubility in Y-Ba-Cu-O solution". In: *Journal of Materials Research* 11.5 (1996), pp. 1076–1081. ISSN: 08842914. DOI: 10.1557/JMR.1996.0136.

[179] Jingyuan Chu et al. "Insight into the Interfacial Nucleation and Competitive Growth of YBa2Cu3O7-δ Films as High-Performance Coated Conductors by a Fluorine-Free Metal-Organic Decomposition Route". In: *Crystal Growth and Design* 19.11 (2019), pp. 6752–6762. DOI: 10.1021/acs.cgd.9b01120.

[180] T. Puig et al. "The influence of growth conditions on the microstructure and critical currents of TFA-MOD YBa2Cu3O7 films". In: *Superconductor Science and Technology* 18.8 (2005), pp. 1141–1150. ISSN: 09532048. DOI: 10.1088/0953-2048/18/8/020.

[181] D Dimos et al. "Orientation dependence of grain-boundary critical currents in YBa2Cu3O7-d bicrystals". In: *Physical review letters* 61.2 (1988), pp. 219–222. DOI: 10.1103/PhysRevLett.61.219.

[182] Jingyuan Chu et al. "Interface reaction-governed heteroepitaxial growth of YBa2Cu3O7-δ film on CeO2-buffered technical substrate". In: *Journal of the American Ceramic Society* 102.10 (2019), pp. 5705–5715. ISSN: 15512916. DOI: 10.1111/jace.16452.

[183] A. Queraltó, J. Banchewski, and A. Pacheco. "Combinatorial Screening of Cuprate Superconductors by Drop-On-Demand Inkjet Printing". In: *submitted to ACS Applied Materials and Interfaces* (2020).

[184] A. M. Campbell and J. E. Evetts. "Flux vortices and transport currents in type II superconductors". In: *Advances in Physics* 21.90 (1972), pp. 199–428. DOI: 10.1080/00018737200101288.

[185] X. Obradors et al. "Nanostructured Superconductors with Efficient Vortex Pinning". In: *Comprehensive Nanoscience and Technology* 1-5 (2011), pp. 303–349. DOI: 10.1016/B978-0-12-374396-1.00112-4.

[186] D.L. Andrews, G.D. Scholes, and G.P. Wiederrecht. *Comprehensive nanoscience and technology*. Elsevier, 2011. ISBN: 978-0-12-374396-1.

[187] P. H. Boullay et al. "Substitution of CO3 Groups for Copper in YBCO: The Oxycarbonates YnBa2nCu3n-1CO3O7n-3". In: *Chemistry of Materials* 5.11 (1993), pp. 1683–1686. DOI: 10.1021/cm00035a016.

[188] Nikolai M Plakida and Alexander N Ermilov. "High-Temperature Superconductivity: Experiment and Theory". In: *Springer* (1995). DOI: 10.1007/978-3-642-78406-4.

[189] T. R. Chien, Z. Z. Wang, and N. P. Ong. "Effect of Zn impurities on the normal-state Hall angle in single-crystal YBa2Cu3-xZnxO7-". In: *Physical Review Letters* 67.15 (1991), pp. 2088–2091. ISSN: 00319007. DOI: 10.1103/PhysRevLett.67.2088.

[190] L Experimental et al. "Imaging the effects of individual zinc impurity atoms on superconductivity in Bi2Sr2CaCu2O8+d". In: *Nature* 403.February (2000). DOI: 10.1038/35001534.

[191] A. S. Parikh, B. Meyer, and K. Salama. "A method to improve grain boundary current-carrying capability in melt-textured YBa2Cu3O7-d". In: *Superconductor Science and Technology* 7.7 (1994), pp. 455–461. ISSN: 09532048. DOI: 10.1088/0953-2048/7/7/002.

[192] Vyacheslav F. Solovyov, Harold J. Wiesmann, and Masaki Suenaga. "Nucleation of YBa2Cu3O7-x on buffered metallic substrates in thick precursor films made by the BaF2 process". In: *Superconductor Science and Technology* 18.3 (2005), pp. 239–248. ISSN: 09532048. DOI: 10.1088/0953-2048/18/3/006.

[193] A. Pomar et al. “Porosity induced magnetic granularity in epitaxial YBa2Cu3O7 thin films”. In: *Physical Review B - Condensed Matter and Materials Physics* 73.21 (2006), pp. 1–5. ISSN: 10980121. DOI: 10.1103/PhysRevB.73.214522.

[194] Sung Hun Wee et al. “Engineering nanocolumnar defect configurations for optimized vortex pinning in high temperature superconducting nanocomposite wires”. In: *Scientific Reports* 3 (2013), pp. 1–9. DOI: 10.1038/srep02310.

[195] Jae Hun Lee et al. “RCE-DR, a novel process for coated conductor fabrication with high performance”. In: *Superconductor Science and Technology* 27.4 (2014). DOI: 10.1088/0953-2048/27/4/044018.

[196] J. L. MacManus-Driscoll et al. “Strong pinning in very fast grown reactive co-evaporated GdBa2Cu3O7 coated conductors”. In: *APL Materials* 2.8 (2014). ISSN: 2166532X. DOI: 10.1063/1.4893339.

[197] J. Gutierrez. “Vortex pinning and critical currents in YBa2Cu3O7-x MOD-TFA thin films and Coated Conductors”. PhD thesis. 2008.

[198] J. Plain et al. “Microstructural influence on critical currents and irreversibility line in melt-textured YBa2Cu3O7-x reannealed at high oxygen pressure”. In: *Physical Review B - Condensed Matter and Materials Physics* 65.10 (2002), pp. 1–10. DOI: 10.1103/PhysRevB.65.104526.

[199] K. A. Mueller, M. Takashige, and J. G. Bednorz. “Flux trapping and superconductive glass state in La2CuO4-y:Ba”. In: *Physical Review Letters* 58.11 (1987), pp. 1143–1146. DOI: 10.1103/PhysRevLett.58.1143.

[200] David Larbalestier et al. “High Tc Superconducting Materials for Electric Power Applications”. In: *Nature* 414 (2001), pp. 368–377. DOI: 10.1038/35104654.

[201] Yue Zhang et al. “Unprecedented high irreversibility line in the nontoxic cuprate superconductor (Cu,C)Ba2Ca3Cu4O11+δ”. In: *Science Advances* 4.9 (2018), pp. 1–6. DOI: 10.1126/sciadv.aau0192.

[202] S. Badoux et al. “Change of carrier density at the pseudogap critical point of a cuprate superconductor”. In: *Nature* 531.7593 (2016), pp. 210–214. DOI: 10.1038/nature16983.

[203] H Castro and G Deutscher. “Anomalous Fermi liquid behavior of overdoped high-Tc superconductors”. In: (2004), pp. 1–8. DOI: 10.1103/PhysRevB.70.174511.

[204] Guy Deutscher. “Impact of pseudo-gap states on the pinning energy and irreversibility field of high temperature superconductors”. In: *APL Materials* 2.9 (2014). DOI: 10.1063/1.4894781.

[205] A. C. Westerheim et al. "Relation between electrical properties and microstructure of YBa2Cu3O7-x thin films deposited by single-target off-axis sputtering". In: *Journal of Applied Physics* 75.1 (1994), pp. 393–403. DOI: 10.1063/1.357012.

[206] N. Tsuda et al. *Electronic Conduction in Oxides*. Springer, 2000. ISBN: 9783642086274.

[207] F. Miletto Granozio et al. "Competition between a-axis and c-axis growth in superconducting thin films". In: *Physical Review B - Condensed Matter and Materials Physics* 61.1 (2000), pp. 756–765. DOI: 10.1103/PhysRevB.61.756.

[208] Vyacheslav F. Solovyov et al. "Nature of Y1Ba2Cu3O7 nucleation centers on ceria buffers". In: *Superconductor Science and Technology* 23.1 (2010). DOI: 10.1088/0953-2048/23/1/014008.

[209] X. Obradors et al. "Epitaxial YBa2Cu3O7-x nanocomposite films and coated conductors from BaMO3 (M = Zr, Hf) colloidal solutions". In: *Superconductor Science and Technology* 31.4 (2018). DOI: 10.1088/1361-6668/aaaad7.

[210] Ziliang Li et al. "Control of nanostructure and pinning properties in solution nanocomposites with preformed perovskite nanoparticles". In: *Scientific Reports* 9 (2019), pp. 1–14. DOI: 10.1038/s41598-019-42291-x.

[211] Mukarram Zaman Khan et al. "Enhanced flux pinning isotropy by tuned nanosized defect network in superconducting YBa2Cu3O6+x films". In: *Scientific Reports* 9.1 (2019), pp. 1–12. DOI: 10.1038/s41598-019-51978-0.

[212] Max Sieger et al. "BaHfO3-doped thick YBa2Cu3O7-δ films on highly alloyed textured Ni-W tapes". In: 25.3 (2015), pp. 3–7. DOI: 10.1109/TASC.2014.2372903.

[213] Kaname Matsumoto and Paolo Mele. "Artificial pinning center technology to enhance vortex pinning in YBCO coated conductors". In: *Superconductor Science and Technology* 23.1 (2010). ISSN: 09532048. DOI: 10.1088/0953-2048/23/1/014001.

[214] Yutaka Yoshida et al. "Approaches in controllable generation of artificial pinning center in REBa2Cu3Oy coated conductor for high flux pinning". In: *Superconductor Science and Technology* 30.104002 (2017). DOI: 10.1088/1361-6668/aa8236.

[215] L. R. Motowidlo et al. "An intermetallic powder-in-tube approach to increased flux-pinning in Nb3Sn by internal oxidation of Zr". In: *Superconductor Science and Technology* 31.1 (2018). DOI: 10.1088/1361-6668/aa980f.

[216] T. Izumi and K. Nakaoka. "Control of artificial pinning centers in REBCO coated conductors derived from the trifluoroacetate metal-organic deposition process". In: *Superconductor Science and Technology* 31.3 (2018). DOI: 10.1088/1361-6668/aa9dd2.

[217] P. Pahlke et al. "Influence of artificial pinning centers on structural and superconducting properties of thick YBCO films on ABAD-YSZ templates". In: *Superconductor Science and Technology* 31.044007 (2018). DOI: 10.1088/1361-6668/aaafbe.

[218] J. Feighan, A. Kursumovic, and J. L. MacManus-Driscoll. "Materials design for artificial pinning centres in superconductor PLD coated conductors". In: *Superconductor Science and Technology* 30.12 (2017). DOI: 10.1088/1361-6668/aa90d1.

[219] J. Wu and J. Shi. "Interactive modeling-synthesis-characterization approach towards controllable in situ self-assembly of artificial pinning centers in RE-123 films". In: *Superconductor Science and Technology* 30.10 (2017). DOI: 10.1088/1361-6668/aa8288.

[220] J. Wu et al. "The effect of lattice strain on the diameter of BaZrO3 nanorods in epitaxial YBa2Cu3O7-δ films". In: *Superconductor Science and Technology* 27.4 (2014). DOI: 10.1088/0953-2048/27/4/044010.

[221] Jack J. Shi and Judy Z. Wu. "Influence of the lattice strain decay on the diameter of self assembled secondary phase nanorod array in epitaxial films". In: *Journal of Applied Physics* 118.16 (2015). ISSN: 10897550. DOI: 10.1063/1.4934640.

[222] S. Engel et al. "Enhanced flux pinning in YBa2Cu3O7 layers by the formation of nanosized BaHfO3 precipitates using the chemical deposition method". In: *Applied Physics Letters* 90.10 (2007). DOI: 10.1063/1.2711761.

[223] M. Erbe et al. "BaHfO3 artificial pinning centres in TFA-MOD-derived YBCO and GdBCO thin films". In: *Superconductor Science and Technology* 28.11 (2015). DOI: 10.1088/0953-2048/28/11/114002.

[224] Ziliang Li et al. "Accelerated growth by flash heating of high critical current trifluoroacetate solution derived epitaxial superconducting YBa2Cu3O7 films". In: *Journal of Materials Chemistry C* 7.16 (2019), pp. 4748–4759. DOI: 10.1039/c9tc00488b.

[225] Alok K. Jha and Kaname Matsumoto. "Superconductive REBCO thin films and their nanocomposites: The role of rare-earth oxides in promoting sustainable energy". In: *Frontiers in Physics* 7 (2019), pp. 1–21. DOI: 10.3389/fphy.2019.00082.

[226] J.L. MacManus-Driscoll et al. "Studies of structural disorder in ReBa2Cu307-x thin films (Re=rare earth) as a function of rare-earth ionic radius and film deposition conditions". In: *Physica C 232* 232 (1994), pp. 288–308. DOI: 10.1016/0921-4534(94)90789-7.

[227] Y. Yamada et al. "Epitaxial nanostructure and defects effective for pinning in Y(RE)Ba2Cu3O7-x coated conductors". In: *Applied Physics Letters* 87.13 (2005). DOI: 10.1063/1.2061874.

[228] L. Civale et al. "Vortex confinement by columnar defects in YBa2Cu3O7 crystals: Enhanced pinning at high fields and temperatures". In: 67.5 (1991). DOI: 10.1103/PhysRevLett.67.648.

[229] J. Giapintzakis et al. "Production and identification of flux-pinning defects by electron irradiation in YBa2Cu3O7-x single crystals". In: *Physical Review B* 45.18 (1992). DOI: 10.1103/PhysRevB.45.10677.

[230] D. X. Fischer et al. "The effect of fast neutron irradiation on the superconducting properties of REBCO coated conductors with and without artificial pinning centers". In: *Superconductor Science and Technology* 31.4 (2018). ISSN: 13616668. DOI: 10.1088/1361-6668/aaadf2.

[231] J. Gutierrez et al. "Anisotropic c-axis pinning in interfacial self-assembled nanostructured trifluoracetat-YBa2Cu3O7-x films". In: *Applied Physics Letters* 94.17 (2009), pp. 75–78. DOI: 10.1063/1.3130085.

[232] C. Pop et al. "Growth of all-chemical high critical current YBa2Cu3O7-δ thick films and coated conductors". In: *Superconductor Science and Technology* 32.1 (2019). DOI: 10.1088/1361-6668/aaea4e.

[233] J. Gazquez et al. "Structural defects in trifluoroacetate derived YBa2Cu3O7 thin films". In: *Superconductor Science and Technology* 25.6 (2012). ISSN: 09532048. DOI: 10.1088/0953-2048/25/6/065009.

[234] Subhash L. Shinde and David A. Rudman. *Interfaces in High-Tc Superconducting Systems*. Springer-Verlag, 1994. ISBN: 978-0387940007. DOI: 10.1007/978-1-4612-2584-3.

[235] R. Ramesh et al. "Direct observation of structural defects in laser-deposited superconducting Y-Ba-Cu-O thin films". In: *Science* 247 (1990). DOI: 10.1126/science.247.4938.57.

[236] J. Tafto, M. Suenaga, and R. L. Sabatini. "Characterization of planar crystal lattice defects in the high-temperature superconductor YBa2Cu3O7". In: *Applied Physics Letters* 52.8 (1988). DOI: 10.1063/1.99369.

[237] Claudia Cantoni et al. "Strain-Driven Oxygen Deficiency in Self-Assembled, Nanostructured, Composite Oxide Films". In: *ACS Nano* 5.6 (2011), pp. 4783–4789. ISSN: 19360851. DOI: 10.1021/nn2007628.

[238] L Civale et al. "Influence of crystalline texture on vortex pinning near the ab-plane in YBa2Cu3O7 thin films and coated conductors". In: 414 (2004). DOI: 10.1016/j.physc.2003.12.076.

[239] G. Blatter, V. B. Geshkenbein, and A. I. Larkin. "From isotropic to anisotropic superconductors: A scaling approach". In: *Physical Review Letters* 68.6 (1992). DOI: 10.1103/PhysRevLett.68.875.

[240] G. Blatter et al. "Vortices in high temperature superconductors". In: *Physical Review Letters* 66.1125 (1994). DOI: 10.1103/RevModPhys.66.1125.

[241] Aixia Xu et al. "Broad temperature range study of Jc and Hirr anisotropy in YBa2Cu3Ox thin films containing either Y2O3 nanoparticles or stacking faults". In: 052603 (2015), pp. 2–7. DOI: 10.1063/1.4907891.

[242] E Bartolomé et al. "Intrinsic anisotropy versus effective pinning anisotropy in YBa2Cu3O7 thin films and nanocomposites". In: 100 (2019). DOI: 10.1103/PhysRevB.100.054502.

[243] F. Vallès et al. "Angular flux creep contributions in YBa2Cu3O7-δ nanocomposites from electrical transport measurements". In: *Scientific Reports* 8.1 (2018), pp. 1–7. DOI: 10.1038/s41598-018-24392-1.

[244] Ziliang Li et al. "Suppression of superconductivity at the nanoscale in chemical solution derived YBa2Cu-O7-d thin films with defective Y2Ba4Cu8O16 intergrowths". In: *Nanoscale Advances* (2020). DOI: 10.1039/D0NA00456A.

[245] A Palau et al. "Disentangling vortex pinning landscape in chemical solution deposited superconducting YBa2Cu3O7-x films and nanocomposites". In: *Superconductor Science and Technology* 31 (2018). DOI: 10.1088/1361-6668/aaa65e.

[246] X. Obradors et al. "Nucleation and mesostrain influence on percolating critical currents of solution derived YBa2Cu3O7 superconducting thin films". In: *Physica C: Superconductivity and its Applications* 482 (2012), pp. 58–67. DOI: 10.1016/j.physc.2012.04.020.

[247] David R. Nelson and V. M. Vinokur. "Boson localization and pinning by correlated disorder in high-temperature superconductors". In: *Physical Review Letters* 68.15 (1992). DOI: 10.1103/PhysRevLett.68.2398.

[248] David R. Nelson and V. M. Vinokur. "Boson localization and correlated pinning of superconducting vortex arrays". In: *Physical Review B* 48.17 (1993). DOI: 10.1103/PhysRevB.48.13060.

[249] Víctor Rouco. "Controlling Vortex Pinning and Dynamics of Nanostructured YBCO Thin Films Grown by Chemical Solution Deposition Víctor Rouco Gómez". PhD thesis. 2014. URL: https://ddd.uab.cat/record/127057.

[250] M. Miura et al. "Mixed pinning landscape in nanoparticle-introduced YGdBa2Cu3Oy films grown by metal organic deposition". In: *Physical Review B* 83.18 (2011). DOI: 10.1103/PhysRevB.83.184519.

[251] H. Safar et al. "Ab-plane anisotropy of the critical currents in twinned YBa2Cu3O7-δ superconductors". In: *Applied Physics Letters* 68.13 (1996). DOI: 10.1063/1.116035.

[252] A. Palau et al. "Crossover between channeling and pinning at twin boundaries in YBa2Cu3O7 thin films". In: *Physical Review Letters* 97.25 (2006). DOI: 10.1103/PhysRevLett.97.257002.

[253] E. Zeldov et al. "Flux creep characteristics in high-temperature superconductors". In: *Applied Physics Letters* 56.7 (1990). ISSN: 00036951. DOI: 10.1063/1.103310.

[254] P. W. Anderson. "Theory of flux creep in hard superconductors". In: *Physical Review Letters* 9.7 (1962). DOI: 10.1103/PhysRevLett.9.309.

[255] H. Mawatari and Y. Yamasaki. "Current-voltage characteristics and flux creep in melt-textured YBa2Cu3O7-x". In: *Superconductor Science and Technology* 13.202 (2000). DOI: 10.1088/0953-2048/13/2/315.

[256] Y. Yeshurun Shaulov, A. P. Malozemoff, and A. "Magnetic relaxation in high-temperature superconductors". In: *Rev. Mod. Phys.* 68.911 (1996). DOI: 10.1016/S0375-9601(99)00140-1.

[257] Satoshi Awaji et al. "Anisotropy of the critical current density and intrinsic pinning behaviors of YBa2Cu3Oy coated conductors". In: *Applied Physics Express* 4.1 (2011). DOI: 10.1143/APEX.4.013101.

[258] L. Civale et al. "Identification of intrinsic ab-plane pinning in YBa2Cu3O7 thin films and coated conductors". In: *IEEE Transactions on Applied Superconductivity* 15 (2005). DOI: 10.1109/TASC.2005.848218.

[259] P. Paturi, M. Irjala, and H. Huhtinen. "Greatly decreased critical current density anisotropy in YBa2Cu3O6+x thin films ablated from nanocrystalline and BaZrO3-doped nanocrystalline targets". In: *Journal of Applied Physics* 103.12 (2008). DOI: 10.1063/1.2943266.

[260] M. Kidszun et al. "Critical current scaling and anisotropy in oxypnictide superconductors". In: *Physical Review Letters* 106.13 (2011). DOI: 10.1103/PhysRevLett.106.137001.

[261] Jun Wang et al. "Improvement of the pinning property in YBa2Cu3O7-x films below 35K by doping with graphene oxide". In: *AIP Advances* 9.1 (2019). DOI: 10.1063/1.5063485.

[262] L. Civale et al. "Angular-dependent vortex pinning mechanisms in YBa2Cu3O7 coated conductors and thin films". In: *Applied Physics Letters* 84.12 (2004). DOI: 10.1063/1.1655707.

[263] Z. Chen et al. "Three-dimensional vortex pinning by nano-precipitates in a Sm-doped YBa2Cu3O7-x coated conductor". In: *Superconductor Science and Technology* 20.9 (2007). DOI: 10.1088/0953-2048/20/9/S14.

[264] C. Tarantini et al. "Anisotropy of the irreversibility field for Zr-doped (Y,Gd)Ba2Cu 3O7-x thin films up to 45T". In: *Physical Review B - Condensed Matter and Materials Physics* 84.22 (2011), pp. 1–8. DOI: 10.1103/PhysRevB.84.224514.